

AD-A118 157

LOUISIANA STATE UNIV. BATON ROUGE DEPT OF CIVIL ENGIN--ETC F/6 8/10
CLASSIFICATION OF COASTAL SEDIMENTS.(U)
MAR 82 J N SUHAYDA, M TUMAY

N00014-80-C-0846

NL

UNCLASSIFIED

1 of 5

AD-A118 157

1 of 5

AD-A118 157

AD-A118 157

AD-A118 157

AD-A118 157

AD-A118 157

AD-A118 157

AD-A118 157

AD-A118 157

AD-A118 157

AD-A118 157

AD-A118 157

AD-A118 157

AD-A118 157

AD-A118 157

AD-A118 157

AD-A118 157

AD-A118 157

AD-A118 157

AD-A118 157

AD-A118 157

AD-A118 157

AD-A118 157

AD-A118 157

AD-A118 157

AD-A118 157

AD-A118 157

AD-A118 157

AD-A118 157

AD-A118 157

AD-A118 157

AD-A118 157

AD-A118 157

AD-A118 157

AD-A118 157

AD-A118 157

AD-A118 157

AD-A118 157

AD-A118 157

AD-A118 157

AD-A118 157

AD-A118 157

AD-A118 157

AD-A118 157

AD-A118 157

AD-A118 157

AD-A118 157

AD-A118 157

AD-A118 157

AD-A118 157

AD-A118 157

AD-A118 157

AD-A118 157

AD-A118 157

AD-A118 157

AD A118157

DTIC FILE COPY

SECURITY CLASSIFICATION OF THIS PAGE (When Data Entered)

REPORT DOCUMENTATION PAGE		READ INSTRUCTIONS BEFORE COMPLETING FORM
1. REPORT NUMBER	2. GOVT ACCESSION NO.	3. RECIPIENT'S CATALOG NUMBER
4. TITLE (and Subtitle)		5. TYPE OF REPORT & PERIOD COVERED
CLASSIFICATION OF COASTAL SEDIMENTS		FINAL REPORT/1980-1981
7. AUTHOR(s)		6. PERFORMING ORG. REPORT NUMBER
Joseph N. Suhayda and Mehmet Tumay		8. CONTRACT OR GRANT NUMBER(s)
9. PERFORMING ORGANIZATION NAME AND ADDRESS		10. PROGRAM ELEMENT, PROJECT, TASK AREA & WORK UNIT NUMBERS
Dept. of Civil Engineering Louisiana State University Baton Rouge, LA 70803		ONR Code 422 (CS)
11. CONTROLLING OFFICE NAME AND ADDRESS		12. REPORT DATE
Office of Naval Research, Coastal Sci. Prog. Code 422 (CS) Arlington, VA 22217		March 1982
14. MONITORING AGENCY NAME & ADDRESS (if different from Controlling Office)		13. NUMBER OF PAGES
		420
		15. SECURITY CLASS. (of this report)
		Unclassified
		15a. DECLASSIFICATION/DOWNGRADING SCHEDULE
16. DISTRIBUTION STATEMENT (of this Report)		
Approved for public release, distribution unlimited.		
17. DISTRIBUTION STATEMENT (of the abstract entered in Block 20, if different from Report)		
18. SUPPLEMENTARY NOTES		
19. KEY WORDS (Continue on reverse side if necessary and identify by block number)		
Penetrometers Geotechnical Data Sediments, Coastal, Acoustic Properties		
20. ABSTRACT (Continue on reverse side if necessary and identify by block number)		
This report presents the results of measurements of geotechnical properties of coastal sediments and penetration depths of cylinders into sediments in support of Buried Mine Minehunting System (BURMMS). Penetration into sediments was found to be described with a formula using the penetrometer mass, diameter and impact velocity, and the depth of penetration and shear strength of the sediment. The formula allows depth of penetration to be used to classify coastal sediments. Shear modulus of muds were found and related to shear strength.		

DD FORM 1473
1 JAN 73EDITION OF 1 NOV 65 IS OBSOLETE
S/N 0102-014-6601

SECURITY CLASSIFICATION OF THIS PAGE (When Data Entered)

CLASSIFICATION OF COASTAL SEDIMENTS

BY

JOSEPH N. SUHAYDA

and

MEHMET TUMAY

Department of Civil Engineering
Louisiana State University

FINAL REPORT
OFFICE OF NAVAL RESEARCH
CONTRACT N00014-80-C-0846
PROJECT NR 388-166

Approved for Public Release
Distribution Unlimited

March 1982

PREFACE

This report presents the results of studies conducted by the Civil Engineering Department, Louisiana State University, to support the development of the Buried Mine Minehunting System (BURMMS). The research was conducted in cooperation with the Naval Coastal Systems Center, the U. S. Naval Oceanographic Office and the Naval Ocean Research and Development Activity. Funding for this study was provided by the Office of Naval Research under Contract No. N00014-80-C-0846 and their support is gratefully acknowledged.



Accession For	<input checked="checked" type="checkbox"/>
NTIS GRA&I	<input type="checkbox"/>
DTIC TAB	<input type="checkbox"/>
Unannounced	<input type="checkbox"/>
Justification	
By	
Distribution	
Availability	
Dist	

A

CONTENTS

	Page
INTRODUCTION	1
BURIAL MECHANISMS	3
TECHNOLOGY REVIEW	5
HARBOR AND SHELF ENVIRONMENTS	9
IMPACT BURIAL SENSITIVITY	11
CLASSIFICATION OF SEDIMENTS USING A PENETROMETER	14
DYNAMIC PROPERTIES OF MARINE SEDIMENTS	17
RECOMMENDATIONS	19
BIBLIOGRAPHY	21
TABLES	24
FIGURES	26
APPENDIX A - Classification of Ocean Bottom Sediments by Dynamic Penetrometers	A-1
APPENDIX B - Dynamic Analysis of Sediments of Gulf of Mexico and Numerical Simulation of Mud Flows	B-1

INTRODUCTION

This report presents the results of research to support the development of the Buried Mine Minehunting System (BURMMS). This work was conducted in cooperation with the Naval Coastal Systems Center (NCSC), the U. S. Naval Oceanographic Office (NAVOCEANO) and the Naval Ocean Research and Development Activity (NORDA). The objective of the group effort was to conduct a variety of RDT&E activities associated with the environmental factors affecting the performance of BURMMS and the development of a tactical environmental subsystem for BURMMS. An overview of the group effort is presented in (1).

The kind of bottom sediment existing at a coastal site greatly influences the types and magnitudes of the coastal processes occurring at the site. The behavior of several Naval Inshore Warfare systems are also greatly affected by the nature of bottom sediments. At the present time bottom sediment surveys are conducted in coastal waters worldwide to define the type and distribution of bottom sediments in strategic areas. But bottom sediments are difficult and costly to sample. Natural processes can cause a change in the amount and type of sediment at a specific site in a few days time making and thereby make previous survey data

inaccurate. The overall objective of this research was to develop techniques for rapidly and accurately determining the in-situ properties of coastal bottom sediments.

The specific objectives of the LSU study were to conduct basic and applied research in support of the development of the environmental subsystem. The specific objectives were: 1) Review burial mechanisms and identify the relevant environmental variables; 2) Review existing technology for acquiring the environmental data needed to support BURMMS; 3) Characterize the harbor and shelf environments of operation of BURMMS; 4) Determine the sensitivity of impact burial to bottom sediment shear strength profiles; 5) Conduct tests of a dynamic penetrometer to evaluate the capability of this technology to support BURMMS; 6) Determine the dynamic properties of shelf sediments at a BURMMS test site.

BURIAL MECHANISMS

The environmental requirements for BURMMS are primarily determined by the types of burial mechanisms possible in inshore waters. These mechanisms determine the location, rate and depth of burial; which are important considerations to the effective use of BURMMS. The burial mechanisms also determine the extent and type of environmental "scar" associated with the burial event; which may be important in the detection and classification of buried objects. For these reasons, the types of burial mechanisms expected in inshore waters and their associated environmental variables were considered initially.

Four types of burial mechanisms were identified: impact, scour, bed form migration and liquifaction. These four types are illustrated in Figure 1. The definition of burial being used here is that the object eventually has at least 25 to 50 % of its volume below the water/sediment interface. This definition is different from an operational definition of burial which may be based upon the ability of minehunting systems to locate and classify proud objects. The environmental variables associated with each type of burial are listed in Table 1. The Table indicates whether each variable is of primary or secondary importance to predicting the rate or extent of a

particular burial mechanism.

The sediment variables which are of primary importance are shear strength, grain size, bulk density and the presence of bedforms. The water column variables which are of primary importance are water depth and current.

TECHNOLOGY REVIEW

Once the environmental variables needed to predict burial were identified, a review was conducted of the existing technology which may be capable of measuring these variables. The technology review was conducted with the other participants in the BURMMS effort. The technology review summary was prepared by Dynatrend Inc., 21 Cabot Road, Woburn, Massachusetts and is available from the BURMMS library.

The sediment variables which need to be determined at a site for BURMMS are shear strength, grain size, bulk density and the presence of bedforms. A variety of existing instruments were found which could provide this information. However, the instruments which offered the best capability for acquiring the environmental data needed for BURMMS and which were compatible with field use were acoustic devices (side scan sonar and sub-bottom sonars) and instrumented penetrometers. The acoustic devices provide remote sensing data over large geographic areas and through the sediment column, while the penetrometers provide seabed truth from direct contact measurements.

There is a long history of studies of bottom sediment

properties and their distribution in coastal waters using bottom sediment samples, such as cores, grab samplers and dredges (2), however studies of the remote determination of sediment properties is relatively new. A review of the relationship between acoustic and geotechnical properties of marine sediments indicates several definite correlations exist (3). This review suggests that a quantitative analysis of acoustic signals can provide quantitative measurements of bottom sediment properties. At the present time the link between acoustic properties and geotechnical properties is qualitative. There is also a relationship between sediment properties and resistance to penetration which has been extensively studied on land (4, 5 and 6). However, the use of instrumented penetrometers in the marine environment is relatively new and is still developing (7 and 8).

Measurements of the backscatter of acoustic energy from the bottom as a function of grazing angle have been made at two deep ocean locations (9). One site was on the Blake Plateau where the bottom was covered with ripples having a height of 5 cm and a length of about 30 cm. Backscattering strength varied from -10 db at 80 deg to -20 db at 70 deg and finally reaching -30 db at about 45 deg. The acoustic frequency was 1.78 kHz and the pulse lengths used were 30 and 60 msec. The 60 msec pulse length showed

greater backscatter strength at the same grazing angle. The second site was on the Challenger Bank where the sea bed was generally featureless being covered with silt and clay with an occasional outcrop of rock. The frequency used was 2.5 kHz and the pulse length was varied from 10 to 300 msec. The backscatter strength decreased to -10 db at 70 deg, -20 db at 45 deg, increased to -17 db at 30 deg and decreased to -25 db at 5 deg. These studies indicate that a 10 db change in bottom backscatter energy can occur at the same grazing angle for different bottom sediments.

Backscatter of acoustic signals at 90 deg from different types of bottom sediments have shown a qualitative relationship with bottom sediment type (10 and 11). The effect of beam width on bottom and sub-bottom response has been studied (12). It was shown that bottom sediments which appeared to be well layered in conventional wide beam (30 deg) surveys were actually quite variable horizontally when surveyed with a narrow beam (3 deg) sonar.

The use of penetrometers to determine the properties of marine sediments is fairly new, however they are routinely used on land. Field tests of instrumented dynamic penetrometers have been made using an on-board accelerometer to measure the total force (7 and 8). These

tests indicate that the resistance to penetration varies linearly with depth in many sediments. The rate of increase in resistance seems to increase with sediment shear strength.

HARBOR AND SHELF ENVIRONMENT

A major consideration in the design of BURMMS is the environment that the system will operate within (14). The environment of operation will not only provide a threat to the effectiveness of the system, but will also provide opportunities to be exploited to increase its effectiveness. Thus the range, resolution and depth penetration of BURMMS at a site may be quite different from nominal because of local conditions.

Because of the potential importance to BURMMS of the harbor and shelf environments that the system will be operated within, a brief review was conducted to define the characteristics of a typical operational site. The major aspect of the site considered was type and spatial distribution of bottom sediments. Additional aspects considered included magnetic anomalies, coastal current regime, water column properties and acoustic properties of the water column and sediments.

Survey data were obtained from a commercial company for the area in and offshore of the harbor of Freeport, Texas. The area contained several tens of magnetic anomalies ranging in strength from a few to over 100 gammas. Sediment types varied over spatial scales of 100 ft

both offshore and in the harbor approaches. The data indicate that surveys should be conducted to provide complete coverage of the area of interest at a resolution of a few feet.

IMPACT BURIAL SENSITIVITY

One of the important burial mechanisms considered in this study was impact burial. This mechanism occurs primarily in soft bottom sediments consisting of muds or silts and results in immediate burial of the mine. A computer model for predicting impact burial of cylinders was developed by the Environmental Sciences Division of the Naval Coastal Systems Center (15) and this model was used to determine the sensitivity of the depth of burial to the shear strength profile in the bottom sediments.

The sensitivity tests consisted of using the model to predict the depth of penetration of a mine-like cylinder into sediments whose shear strength profiles varied linearly with depth below the water/sediment interface. The burial predictions were made for a given shear strength profile for several (usually 5) fall attitudes of the cylinder. The depth of the penetration of the cylinder at its deepest point was recorded. A total of 22 test predictions were run.

The tests were run with the following conditions being held constant:

Water depth = 50 ft

Fall velocity = 20 ft/s

Sediment density = 3 slugs/cu ft

The cylinder for all tests had the following properties:

Air weight = 2000 lb

Wet weight = 900 lb

Length = 6.5 ft

Diameter = 2.0 ft

Surface area = 40.84 ft*ft

Volume = 17.14 ft*ft*ft

The cylinder had the shape of a right cylinder.

A schematic diagram of the test result, showing the depth of penetration, Z_9 , the attitude angle, A , and the vertical length, VL , is given in Figure 2. The vertical length of the cylinder is computed from

$$VL = L \cdot \cos(A) + D \cdot \sin(A)$$

where L is the cylinder length and D is the cylinder diameter.

The sediment shear strength profiles used in the test are shown in Figure 3. The shear strength was a constant over depth intervals of .5 ft and increased with depth in a linear manner, i. e.,

$$\text{Shear Strength} = \text{Constant} \cdot \text{Depth}$$

where the constants had the values of 4, 6, 10, 20 and 30 psf/ft.

The results of the tests are given in Table 2. The

Table gives the test number, the shear strength constant (C), the fall attitude angle (A), the predicted depth of penetration (Z9), and the ratio of the depth of penetration to the vertical length for that fall attitude (Z9/VL).

The tests showed that for all fall attitudes for the weakest shear strength profile (constant = 4 psf/ft) the cylinder was buried, that is, $Z9/VL > .5$. For the strongest profile (constant = 30 psf/ft) the cylinder was buried only slightly, $Z9/VL < .25$, for all fall angles except for $A=90$ deg. For this fall angle the burial ratio $Z9/VL = .56$. For the other shear strength profiles the cylinder burial varied with fall angle so that the ratio $Z9/VL$ varied as given in Table 2.

The tests indicated that the deepest penetration (greatest $Z9/VL$ ratio) occurs at a fall angle of 90 deg and that the depth of burial is roughly 2.5 times the burial at lower fall angles. The shear strength profile which seems to separate burial from non-burial for the test cylinder is one that increases with depth at a rate of about 20 to 30 psf/ft.

CLASSIFICATION OF SEDIMENTS USING A PENETROMETER

The primary objective of the phase of the study was to investigate the possibility of using a dynamic penetrometer to classify ocean bottom sediments. A secondary objective was to estimate the shear strength of the sediment from the penetrometer results.

Dimensional analysis was used to develop dimensionless parameters relating the mass M , diameter D and impact velocity V of the penetrometer to the depth of penetration h and shear strength S of the sediment. The equation of motion for the penetrometer, considering the force of gravity and a sediment resistance which varied linearly with depth, was solved. The solution of the equation gives the position, velocity and acceleration of the penetrometer during the penetration event. The total depth of penetration is given by

$$h = \frac{V^2}{2} \cdot \frac{M}{NP \cdot D \cdot S}$$

The total depth of penetration was measured in a variety of sediments using a non-instrumented penetrometer. Penetrometers were used having diameters of 1.60, 2.54 and 5.10 cm. Attachable weights up to 23 kg were used to

achieve different mass to diameter ratios. Impact velocities were varied between 2 and 8 m/s. The penetrometer tip shapes used were a blunt end and a cone having a 60 deg apex angle. The sediment types tested included a clay, a clayey sand and sand. Additional penetration data were taken from published sources for strong clays.

Classification of sediments was achieved by utilizing the dimensionless ratios h/D , V^2/gh and S^2D^3/Mg and the dimensional ratio hD/Mg . Graphs of V^2/gh versus $\log hD/Mg$ provided a clear distinction between saturated sand and clay up to a shear strength of about 25 kPa. The classification of sediment is based upon the value of the ratio

$$\frac{V^2}{gh} \frac{M}{hD}$$

Estimates of the shear strength of the sediments were based upon using a graph of h/D versus V^2/gh for various sediments. By normalising the mass of the penetrometer and plotting V^2/gh versus $\log hD/Mg$, the shear strength of clay was estimated. The results compared within about 20% with direct measurements of sediment shear strength.

A complete description of the study is presented in

Appendix A.

DYNAMIC PROPERTIES OF MARINE SEDIMENTS

Sediment samples from a single boring near Pass A Loutre of the Mississippi River at a water depth of 33 ft were tested in a resonant column apparatus for their dynamic properties. The total length of the boring was 338 ft. The sediments were selected as typical of those for which impact burial would be very likely. Index properties of the samples were determined and indicated they had high water contents of 60 to 80 % and shear strengths that ranged from less than 100 psf at the top of the core to over 2000 psf at the bottom of the core.

The shear modulus of each sediment sample was also determined. The shear modulus is the geotechnical parameter which is most directly involved with the penetration process. The value of the shear modulus was measured at several shear strain amplitudes (ranging from .0001 to 1 %). The maximum shear modulus was computed by fitting a hyperbolic curve to the experimental values of the shear modulus. Using the shear modulus data, cyclic shear stress versus shear strain were also correlated. The non-linear stress-strain curves were represented as bilinear curves following Von-Mises yield criterion. Experimental curves of damping with shear strain amplitude were used to estimate the minimum damping ratio and damping

characteristics.

The maximum shear modulus was related to the shear strength of each sample. The ratio of the shear modulus to the shear strength varied between 140 at the top of the core to 470 at the bottom. The average of the ratio through the top 200 ft of core was about 250.

A detailed description of this phase of the study can be found in Appendix B.

RECOMMENDATIONS

As a result of this study several additional research tasks were identified as needed to develop an environmental subsystem for BURMMS. These recommended additional studies are as follows.

- 1). Continue development of the acoustic remote sensing systems of side scan sonar and sub-bottom sonar incorporating parametric acoustics and digital processing of output data. The objectives of acoustic surveys should emphasize quantitative rather than qualitative results.
- 2). A dynamic penetrometer to serve as a ground truth instrument should be built and tested in a variety of bottom sediment types.
- 3). Additional research should be performed concerning the relationship between acoustic and geotechnical properties of coastal sediments, particularly the in-situ relations.
- 4). The penetration of objects into coastal

sediments should be investigated using
instrumented penetrometers and improved
numerical models.

BIBLIOGRAPHY

1. Tooma, S., BURMMS environmental subsystem, Unpublished manuscript, Naval Ocean Research and Development Activity, June, 1980.
2. Shepard, F. P., SUBMARINE GEOLOGY, Harper and Row, New York, 1963.
3. Caruthers, J. W., A survey of acoustical techniques for measuring marine sediment mechanical properties relevant to mine burial prediction, Report of the Radian Corporation to W. Howard, Naval Coastal Systems Center, Nov., 1980.
4. Janbu, N. and K. Senneset, Effective stress interpretation of in-situ static penetration tests, Proc. European Sym. Penetration Testing, 1974.
5. Wu, T. J., SOIL DYNAMICS, Allyn and Bacon, Inc., Boston, Mass., 1971.
6. Lareal, P., G. Sangerlat and J. Gielly, Comparison of penetration test data obtained by different static or dynamic penetrometers, Proc. European Sym. Penetration Testing, Stockholm, 1974.

7. Wilkes, P. T., Marine sediment penetrometer development at Sandia Laboratories, Proc. Conf. Rapid Penetration Terrestrial Materials, Texas A&M University, 1972.

8. McNeill, R. L., Enhancement of geophysical soil profiles using instrumented marine sediment penetrometers, Preprint 11th Offshore Technology Conf., 1979.

9. Patterson, R. B., Relationship between acoustic backscatter and geological characteristics of the deep ocean floor, J. Acoustic Soc. Amer., 46, 1969.

10. Strickler, D. C., Negative bottom loss, critical angle shift and interpretation of the bottom reflection coefficient, J. Acoustic Soc. Amer., 61, 1977.

11. Addy, S. K., E. Pehrens and R. Haines, Correlation of some lithologic and physical characteristics of sediment with high frequency sub-bottom reflection types, Preprint 3569, 11th Offshore Technology Conf., 1979.

12. Bolus, R. K., K. Sivaprasad and A. Frost, A theoretical vertical and lateral model for the analysis of acoustic sub-bottom data through simulation, J. Acoustic Soc. Amer.,

67, 1980.

13. Hamilton, E. L., Sound velocity-density relations in sea-floor sediments and rocks, J. Acoustic Soc. Amer., 63, 1978.

14. Fleischer, P., Evaluation and selection of test sites for BURMMS, NORDA Tech. Note 90, Naval Ocean Research and Development Activity, January 1981.

15. Annone, R. A., Prediction model of the time history of penetration of a cylinder through the air water sediment phases, Report NCSC-LR-734-36, Naval Coastal Systems Center, May 1980.

Table 1.

ENVIRONMENTAL PARAMETER NEEDED TO PREDICT BURIAL

BURIAL MECHANISMS	SEDIMENT													WATER				
	Bulk density	Shear strength	Void ratio	Grain size	Shear modulus	Compressibility	Permeability	Viscosity	Friction angle	Sensitivity	Pore water prop.	Bed forms		Water depth	Current	Bottom pressure	Density	Suspended sediment
Impact	●	●	○	○	●	○	●	○	○	●	○						○	
Scour	○	○		●					●			●		●	●		○	●
Bed Form Migration	○	○		●								●		●	●	○	○	●
Liquifaction	●		●	○	●	●	●	○						○		●	○	

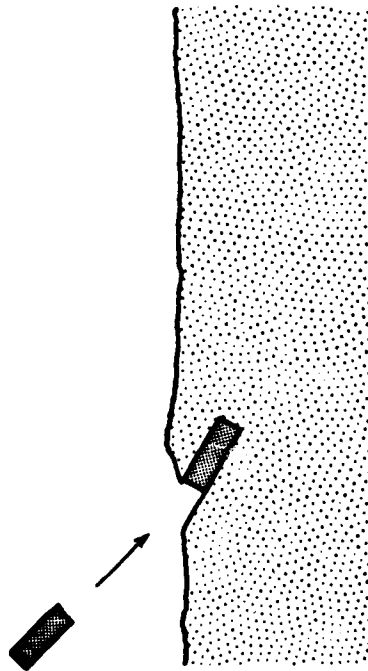
● PRIMARY
○ SECONDARY

Table 2. Penetration Sensitivity Test Runs.

Test	Strength Profile	Angle A	Z9	Z9/VL
1	30	0	1.43 ft	.22
2	30	22.5	1.03	.15
3	30	45	.97	.16
4	30	67.5	1.09	.25
5	30	90	1.12	.56
6	4	0	6.04	.93
7	4	22.5	5.57	.83
8	4	45	4.51	.75
9	4	67.5	3.31	.76
10	4	90	3.31	1.66
11	10	0	1.93	.30
12	10	45	1.64	.27
13	10	67.5	1.35	.31
14	10	90	1.36	.68
15	6	0	2.20	.34
16	6	45	2.06	.34
17	6	90	1.88	.94
18	20	0	2.56	.39
19	20	22.5	1.54	.23
20	20	45	1.43	.24
21	20	67.5	1.29	.30
22	20	90	1.33	.66

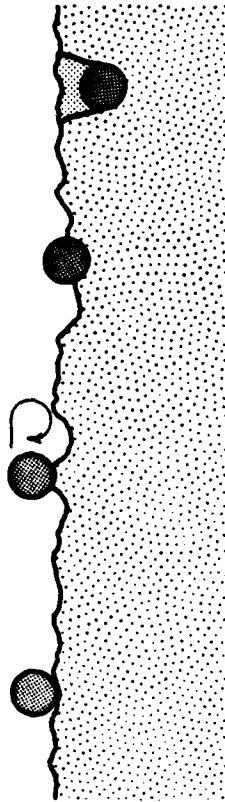
BURIAL MECHANISMS

IMPACT BURIAL



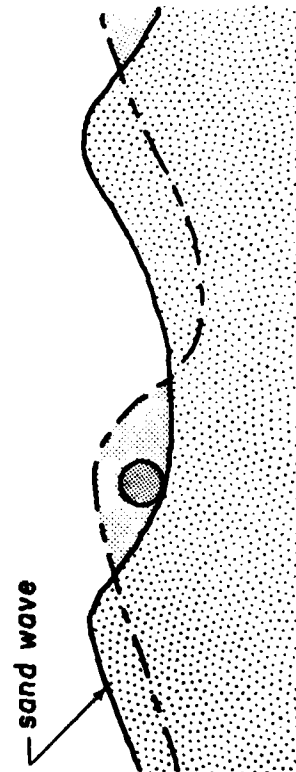
SCOUR

current →
waves ↔



BED FORM MIGRATION

current →



LIQUIFACTION

storm waves

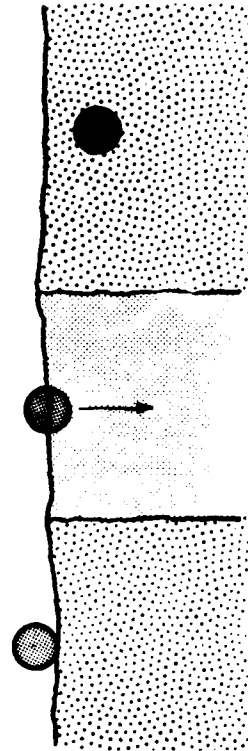


Figure 1. Schematic illustration of burial mechanism types.

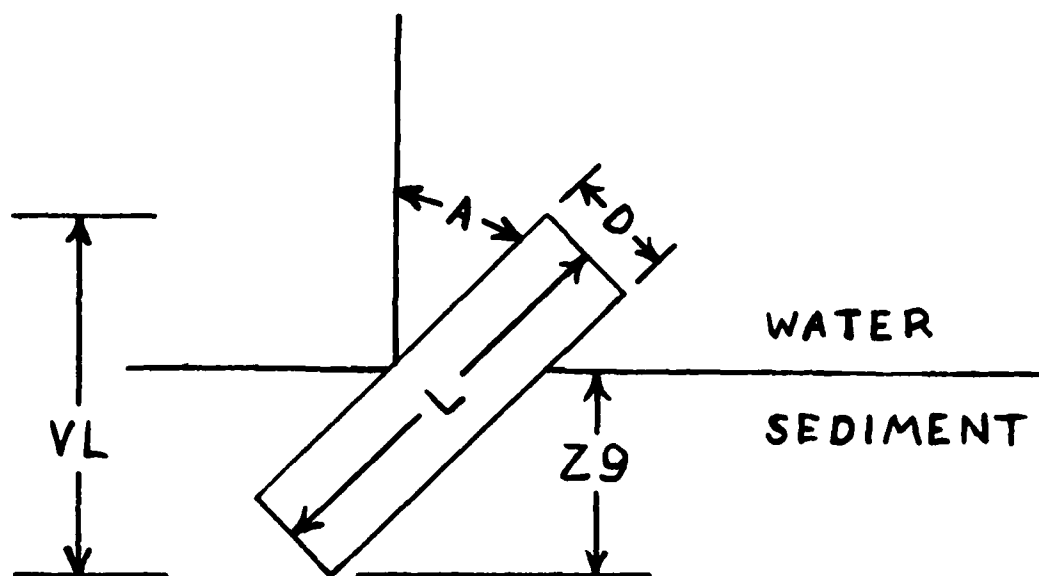


Figure 2. Diagram of variables used in penetration test runs.

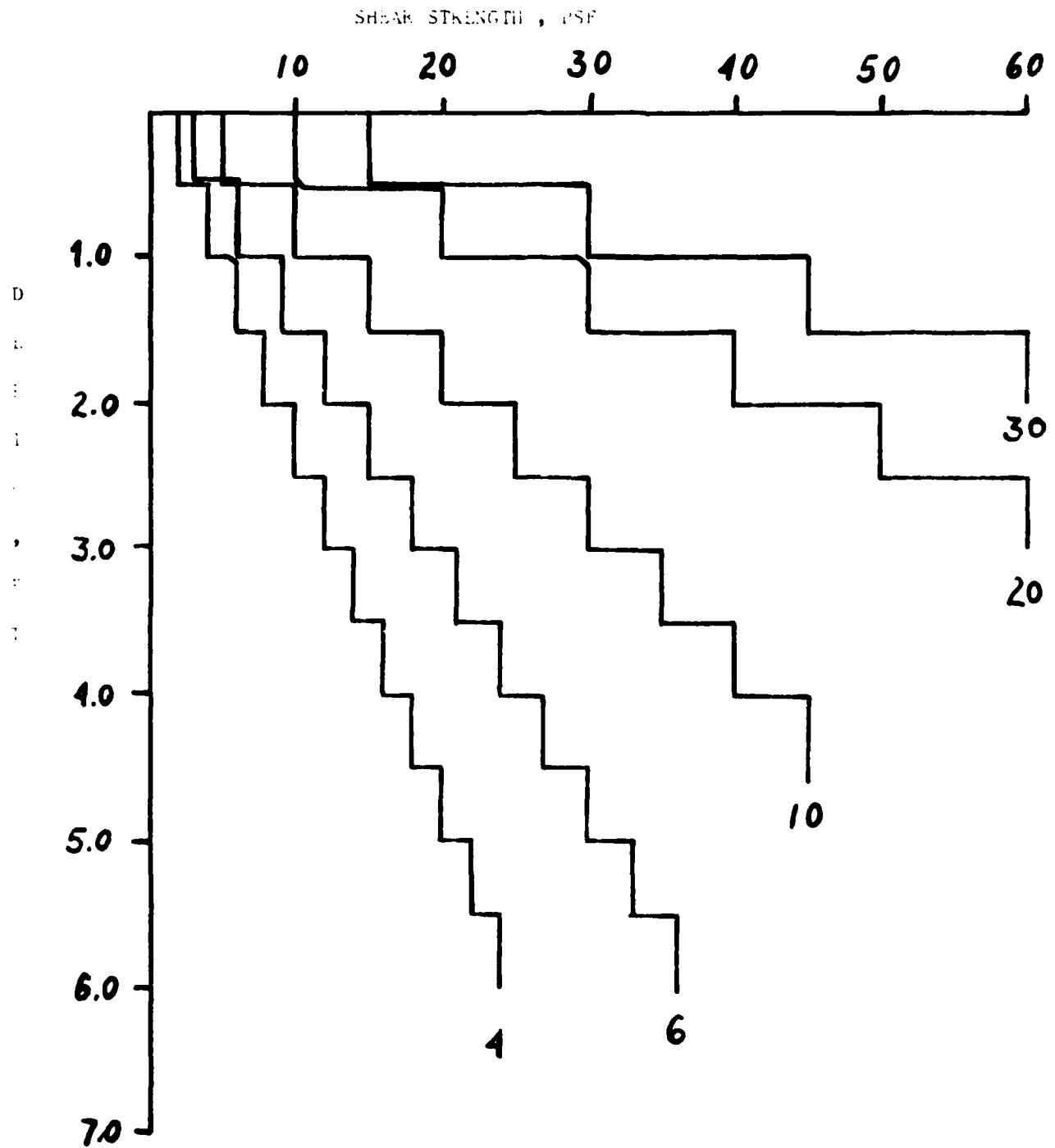


Figure 3. Shear strength profiles used in penetration test runs.

APPENDIX A

Classification of Ocean Bottom Sediments by Dynamic Penetrometers

**CLASSIFICATION OF OCEAN BOTTOM SEDIMENTS
BY DYNAMIC PENETROMETERS**

A Thesis

**Submitted to the Graduate Faculty of the
Louisiana State University and
Agricultural and Mechanical College
in partial fulfillment of the
requirements for the degree of
Master of Science**

in

The Department of Civil Engineering

by

**Behnam Nikakhtar
B.S., Louisiana State University, 1979
December 19, 1981**

ACKNOWLEDGEMENTS

The author is grateful to his major professor, Dr. Joseph N. Suhayda for his cooperation, understanding and guidance during this study. Without his assistance and generous support, this research could not have been done. Acknowledgement goes to Professor Mehmet T. Tumay, Dr. Roger K. Seals and Dr. Y. Acar for their advice and suggestions during this investigation.

The author's thanks and appreciation go to his family for the support and encouragement they gave him during his studies.

The author expresses gratitude to the Environmental Protection Agency and the Office of Naval Research for financing this research project. The author expresses gratitude to the Department of Civil Engineering for making his stay at Louisiana State University a pleasant one.

A special thank you is extended to Mr. Bob Taylor for building the penetrometers, to Mrs. Susan Sartwell for doing a superb job in typing the thesis, to Ms. Norma Duffy and her assistant, Ms. Evete Ledoux, for doing an excellent job on the drawings.

TABLE OF CONTENTS

	Page
ACKNOWLEDGEMENTS	ii
LIST OF TABLES	v
LIST OF FIGURES	vi
LIST OF SYMBOLS	viii
ABSTRACT	ix
 Chapter	
1. INTRODUCTION	1
2. LITERATURE REVIEW	5
2.1 EFFECT OF VELOCITY	6
2.2 PENETRATION RESISTANCE	12
2.2.1 Modes of Failure	12
2.2.2 Strain Rate Effect	13
2.3 PENETRATION MODELS	14
3. THEORETICAL CONSIDERATIONS	20
3.1 DIMENSIONAL ANALYSIS	20
3.2 PREDICTION OF PENETRATION	22
4. DATA ACQUISITION AND ANALYSIS	27
4.1 PENETROMETER CHARACTERISTICS	27
4.2 LABORATORY EQUIPMENT AND PROCEDURE	27
4.3 FIELD EQUIPMENT AND PROCEDURE	30
5. DISCUSSION OF RESULTS	33
5.1 GENERAL OBSERVATIONS AND CHARACTERISTICS OF RESULTS	33
5.2 DIMENSIONAL ANALYSIS RESULTS	41

5.3	N_p RESULTS	43
5.4	CLASSIFICATION RESULTS	50
5.5	SHEAR STRENGTH	56
5.5.1	Determination of Shear Strength at Zero Impact Velocity	56
5.5.2	Pore Pressure Effects	58
6.	CONCLUSION OF RESULTS	60
REFERENCES	62
APPENDICES		
A	GRAIN SIZE DISTRIBUTION CURVES	65
B	CALCULATION OF SAND SATURATED UNIT WEIGHTS	68
VITA	70

LIST OF TABLES

Table		Page
2.1	Variation of Friction Ratio with Penetration Velocity (8)	10
3.1	Units of Primary Variables	22
5.1	Range of Penetration Variables	33
5.2	h/D Ratios for Dry Sand and Dense Sand	42
5.3	Summary of Test Details for Clay Target	44
5.4	Summary of Test Details for Saturated Sand (St. Andrews Bay, Florida)	45
5.5	Summary of Test Details for Saturated Sand (Pass Christian, Mississippi)	46
5.6	Summary of Test Details for Clay Target (6)	47
5.7	Summary of Test Details for Loose Dry Sand (27)	48
5.8	Summary of Test Details for Dense Dry Sand (27)	49

LIST OF FIGURES

Figure	Page
1.1 Sea Bottom Interaction	2
1.2 Ocean Bottom Engineering Characteristics (Bea and Andibert, 20)	3
2.1 Details of Laboratory Impact Penetrometers (De Ruiter, 33)	7
2.2 Constant Velocity Penetration Test Results for Loose Sand (Dayal and Allen, 8)	8
2.3 Constant Velocity Penetration Test Results for Very Soft Clay (Dayal and Allen, 8)	8
2.4 Penetration Depth Versus Velocity for Different Nose Shapes (Murff, Harry and Coyle, 18)	11
2.5 Effect of Velocity on Force Depth Record in Soft Kaolin Clay (Murff, Harry and Coyle, 18)	11
2.6 Impact Test Results for Soft Clay (Dayal and Allen, 8)	17
2.7 Variation of Deceleration, Velocity and Depth Curves with Drop Heights (Knight, 14)	19
3.1 Penetrometer and Soil Properties Used in the Dimensional Analysis	21
4.1 Photograph of Field and Laboratory Penetrometers	28
4.2 Field Penetration Equipment	31
5.1 Impact Velocity Versus Depth of Penetration in Clay	34
5.2 Impact Velocity Versus Depth of Penetration in Sand (Pass Christian)	36
5.3 Impact Velocity Versus Depth of Penetration in Sand (St. Andrews)	38

5.4	Impact Velcocity Versus Depth of Penetration in clay ($s = 28$ kpa)	39
5.5	Impact Velocity Versus Depth of Penetration in Dry Loose and Dense Sand	40
5.6	Classification of Soil Type by the Penetrability Constant	51
5.7	Plot of Two Dimensionless Ratios for Determination of Clay Shear Strength (5-52 kPa)	52
5.8	Determination of Clay Shear Strength by Normalization of all Penetrometer Characteristics	54
5.9	Distinction Between Sand Types by Normalization of Penetrometer Characteristics	55
5.10	Classification of Soil Type by Normalization of Penetrometer Characteristics	57

LIST OF SYMBOLS

a	Projectile cross-section
D	Projectile diameter
D'	Coefficient in terms of sand particles diameter before and after fracture
dT_1	Energy dissipation due to inertial resistance
dT_2	Energy dissipation due to overcoming the strength of soil
g	Acceleration of gravity
h	Total depth of penetration
M	Projectile mass
N_p	Penetrability constant
S	Shear strength
V_o	Velocity at impact
x	Depth of Penetration
\dot{x}	Velocity at any time
\ddot{x}	Deceleration
σ_N	Stress on projectile nose
σ_s	Stress on projectile sides
γ	Soil unit weight
ϕ	Angle of internal friction
ρ	Mass density of soil

ABSTRACT

The primary objective of this study was to investigate the possibility of using a dynamic cone penetrometer to classify ocean bottom sediments. As a secondary objective the penetration results were used to estimate the shear strength of the soil.

Dimensional analysis was used as a tool to combine the affect of mass, diameter, and the impact velocity of the penetrometer together with the total depth of penetration and the shear strength of the soil into dimensionless ratios. The equation of motion was also solved by considering the forces involved in dynamic penetration. The solution of the equation of motion was expressed in three dimensionless ratios.

The total depth of penetration was obtained in a variety of soils by non-instrumented penetrometers. The 1.60, 2.54 and 5.10 cm diameter penetrometers used in this study were fabricated of stainless steel. Attachable weights up to 23 kg were used for different mass to diameter ratios. The range of velocities tested were 2 m/s to 8 m/s. The tips used were the 60° apex angle and the 180°. The targets were laboratory prepared clay of 5 kPa shear strength and saturated sand in two field sites at Florida and Mississippi. Penetration data into higher strength clay of up to 52 kPa by other investigators were also utilized in this analysis.

Classification of soils was achieved by utilizing the dimensionless ratios h/D , v_o^2/gh and SD^2/Mg and the dimensional ratio hD/Mg . Plot of v_o^2/gh versus $\log hD/Mg$ provided a clear distinction between saturated sand and clay of shear strength up to about 25 kPa.

By plotting h/D versus V_o^2/gh in terms of the third dimensionless ratio SD^2/Mg , the shear strength of clay as high as 52 kPa was estimated. By normalizing the mass of the penetrometer and plotting V_o^2/gh versus $\log hD/Mg$ the shear strength of clay was directly estimated from the plot.

Chapter 1

INTRODUCTION

Experience shows that as offshore work moves into deeper water, conventional methods of determining in-situ soil type and strength are becoming more difficult, time consuming, less reliable and less efficient.

Soil strengths are presently measured by boring, sampling and testing of undisturbed samples. This process of boring, sampling and testing has several inherent deficiencies such as high cost and undesirable effects of mechanical sample disturbance especially if gases are present in the soil.

The most sensitive, delicate and very easily disturbed layer in the ocean bottom sediments in which boring, sampling and testing is very difficult is the few top meters. Due to the fact that these soils are commonly under-consolidated as shown in Figure 1.1, the shear strength of the soil is very low and consequently very difficult to measure. For this reason the shear strength of the top meter is grossly estimated. Figure 1.2 shows the profile of shear strength in the ocean bottom sediments. Generally these soils have strengths less than 0.05 kg/cm^2 (100 psf) down to a depth of 50 meters (20). It is in these soils that pipelines are embedded and the estimated shear strength are relied upon.

It is therefore generally agreed among practitioners and researchers that there is a clear need to develop new and improved in-situ methods for determining soil types, strength and other necessary soil properties.

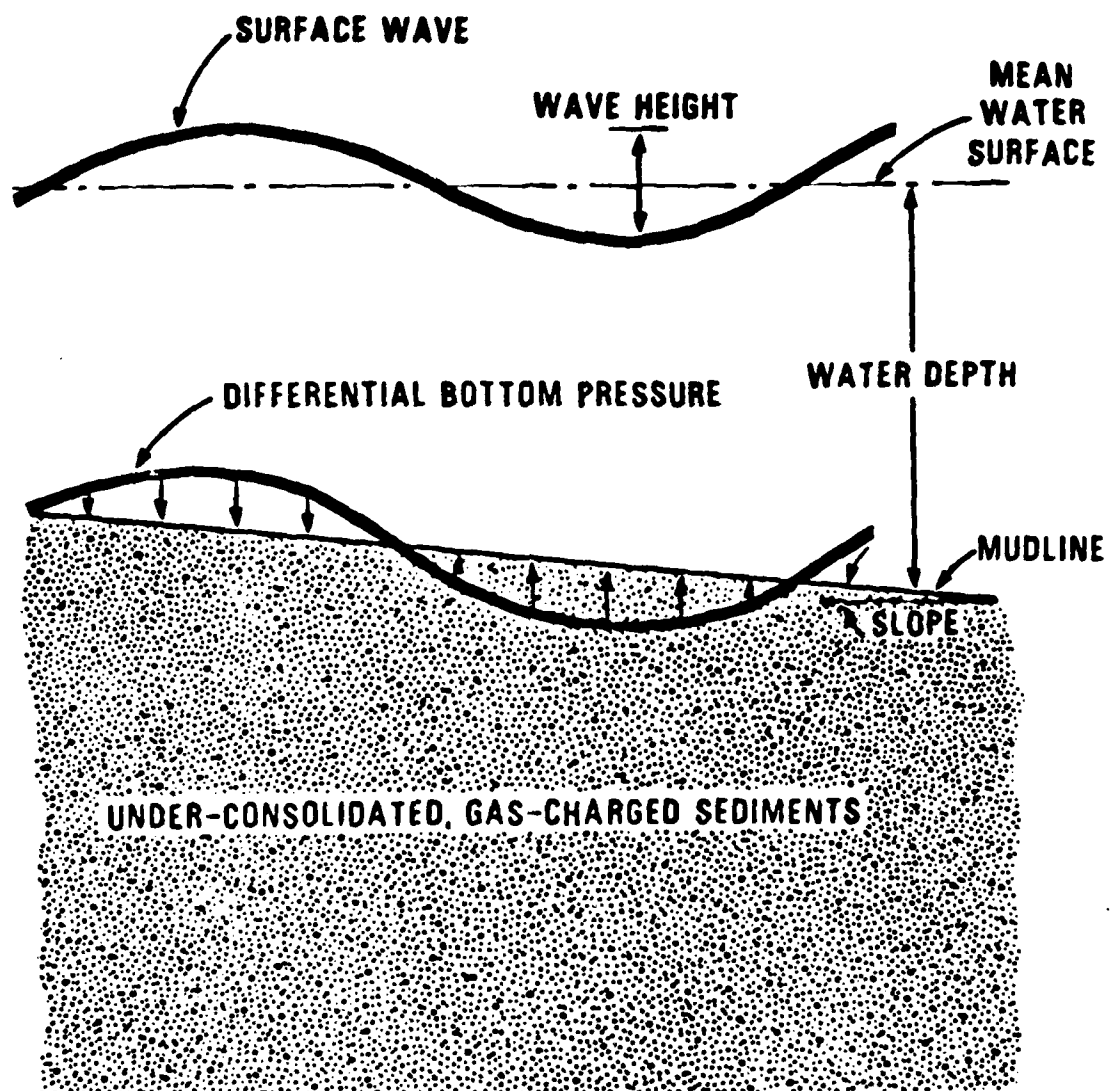


Figure 1.1 Sea Bottom Interaction

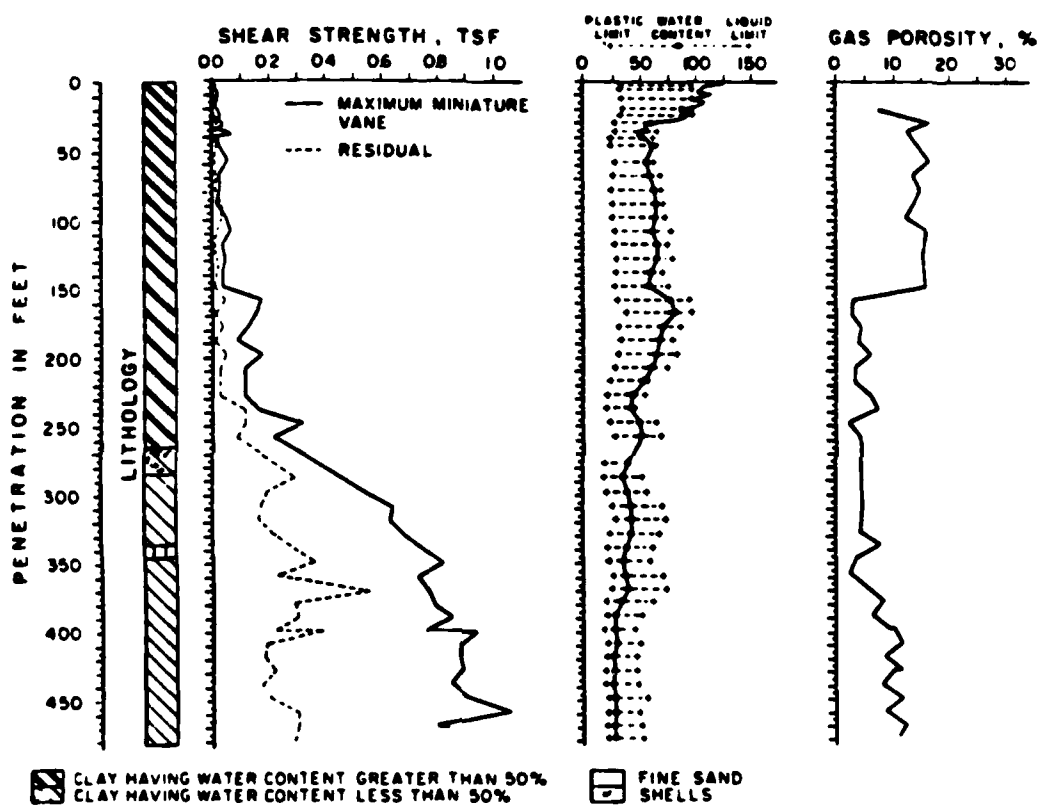


Figure 1.2 Ocean Bottom Engineering Characteristics
(After Bea and Audibert, 20)

In this research focus was directed toward dynamic penetrometers. Dynamic penetrometers are penetrators that have velocities which vary and are usually greater than a hundred centimeters per second with inertial effects that must be considered. Field and laboratory penetration data on sand and clay were obtained by using a variety of impact velocities ranging from 2 m/s to 8 m/s with different weight to area ratios. These data were then analyzed with the aid of dimensional analysis and theoretical consideration in order to classify the type of ocean bottom sediments.

Historically, the impact phenomena of projectiles have been man's concern mostly in the field of armor penetration and passive protection against bombing (21). The major objective has been to find the penetration depths of given projectiles under given conditions. Recovering the space vehicles by soft landing on either lunar or earth surface has brought considerable attention to the projectile penetration (27). Also the disposal of nuclear power supplies re-entering the earth's atmosphere from orbit have concerned with the projectile penetration (26).

Although some penetration equations have been published, the state of the art of projectile penetration into soils is still in its infancy (32).

Chapter 2

LITERATURE REVIEW

There have been many dynamic penetrator experiments, but only few with soil data are available (17,32). Several models and theoretical relationships have been derived for the analysis and solution to the projectile penetration (6,7,10,18,22,27,32), but none have been able to present a solution to satisfactorily fulfill the objective of dynamic penetration.

The objective of the dynamic penetration is to find the soil's properties (strength, type, etc.) provided certain variables of the projectile are known. These variables are projectile weight, diameter, impact velocity and depth of penetration. To this day many researchers and investigators have failed to satisfy this objective. Because of the complexity of the nature of penetration, much emphasis has been placed on the use of empirical equations in predicting penetration which has been the earlier objective of researchers. Those formulas express the maximum penetration in terms of projectile weight, diameter and impact velocity. The starting point of these investigations has been Newton's second law of motion in which the total force on the projectile was assumed in some functional form.

The instrumentation for measuring the forces (decelerations) on the penetrating unit are well developed (28,32). Accelerometer instrumentation enables the use of the projectile as a tool for estimation of the velocity profile with depth and maximum depth of penetration. Other instruments such as load cells for measuring the

total force, dynamic cone pressure, and dynamic local side friction (sleeve friction) have also been used. Figure 2.1 shows such an instrumented marine penetrometer.

2.1 EFFECT OF VELOCITY

Wang (27) performed penetration experiments on loose and dense dry sand with impact velocities up to 763 cm/sec. On clay Dayal and Allen (6,8) experimented with impact velocities to a maximum of 610 cm/sec. In 1973 Murff, Harry and Coyle (18) investigated the dynamic penetration phenomena on Kaolin clay at impact velocities which ranged from 1,500 cm/sec to 61,000 cm/sec. McNeil (16) also tested with high impact velocities of about 2500 cm/sec into seafloor sediments.

A study done by Dayal and Allen (8) showed that the effects of velocity on friction ratios are very significant. Friction ratio is defined as the dimensionless ratio of the unit friction/adhesion along the smooth steel friction jacket to the unit bearing capacity of the standard cone point. Although the study was done with constant velocity penetration, the 600-fold increase in penetration velocity is a good basis for observing the effect of increase in velocity. The range of velocities tested were 0.13 cm/sec to 81 cm/sec. Targets were clay of various strengths (0.03 to 0.81 kg/cm^2) and sand in loose and dense state. It was concluded that an increase in penetration velocity results in an increase in friction ratio in clay. Figure 2.2 shows that for granular soils, the effect of velocity on cone and sleeve friction resistances are insignificant. The percentage increase is about 4 percent. Figure 2.3 shows that for cohesive soils the effect of penetration velocity causes an increase in cone and friction resistances. An increase of 80 percent was observed. Therefore, the

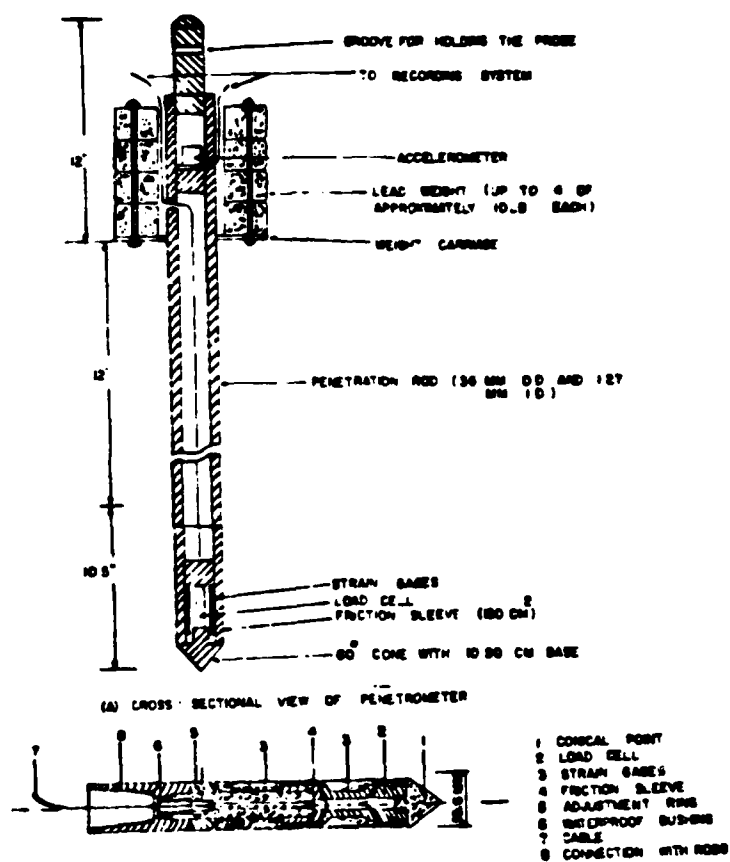


Figure 2.1 Details of Laboratory Impact Penetrometer
(After De Ruiter, 33)

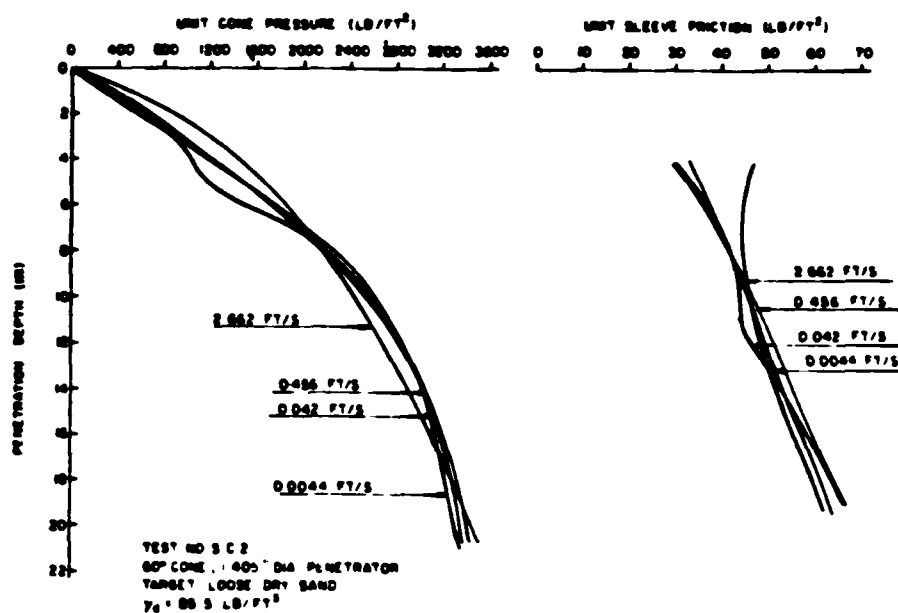


Figure 2.2 Constant Velocity Penetration Test Result for Loose Sand (After Dayal and Allen 8)

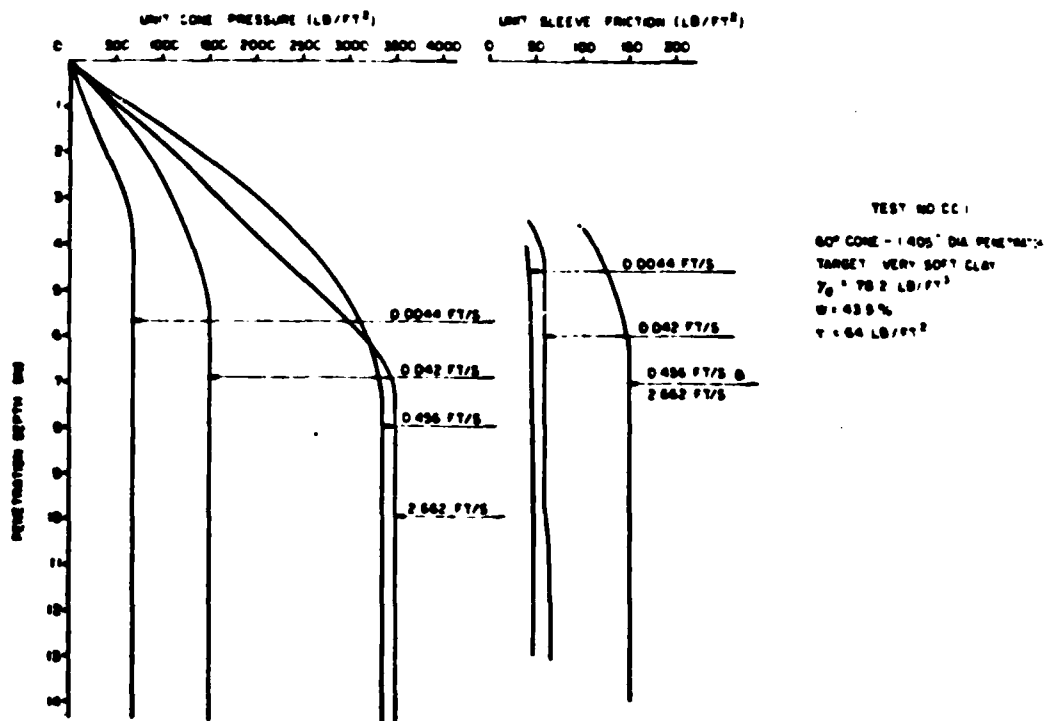


Figure 2.3 Constant Velocity Penetration Test Results for Very Soft Clay (After Dayal and Allen 8)

effect of velocity on clay are very significant. Table 2.1 shows the variation of friction ratio with penetration velocity and soil type. On the topic of effects of velocity, other researchers such as Murff, Harry and Coyle (18) have postulated the existence of some critical velocity. They hypothesize that if the projectile enters the soil mass at a velocity which encapsulates the projectile by a cavity, no side resistance occurs and the penetrometer continues to penetrate until the reduction in velocity causes the cavity to collapse and the contribution of side resistance which is now significant, causes the penetrometer to stop more quickly. This velocity is called the critical velocity which is a function of projectile geometry and soil properties. Soil properties are very important in the critical velocity concept. For soft or very soft clay the velocity at which separation occurs (critical velocity) is much lower than for stiff or medium clays. It has also been found that the velocity at which separation occurs is influenced by the projectile nose shape. The blunter nose has a greater tendency to cause separation and consequently the resistance along the projectile sides is less (18). This surprising result is best illustrated by plot of depth versus velocity for two different nose shapes. Figure 2.4 shows plot of this type which represent tests in two different soil targets. It is readily seen that for both targets a critical velocity is reached for the blunter projectile. Past this velocity the blunter projectiles penetrate further than the sharp nose projectiles. The blunter nose projectile experiences a high deceleration at impact but has a lower resistance during penetration apparently due to a less sidewall resistance.

Table 2.1
Variation of Friction Ratio with Penetration Velocity
(After Dayal and Allen (8))

Soil Type	Moisture Content (%)	Dry Density (lb/ft ³)	Vane Shear Strength (psf)	Friction Ratio (%) for:		
				Penetration velocities (fps) of		
				0.0044	0.042	0.456 2.662
Pottery clay	43.5	78.2	64	6.4	4.0	4.4 4.2
Pottery clay	25.5	90.8	962	5.4	6.0	6.3 9.7
Pottery clay	23.9	91.0	1066	5.5	5.7	5.8 8.1
Pottery clay	22.4	90.6	1671	5.7	6.7	7.0 10.0
Medium to fine sand (dense)		90.7		(mean)	1.8	
Medium to fine sand (loose)		85.5		(mean)	2.0	
Sandy gravel		109.0		(mean)	0.8	

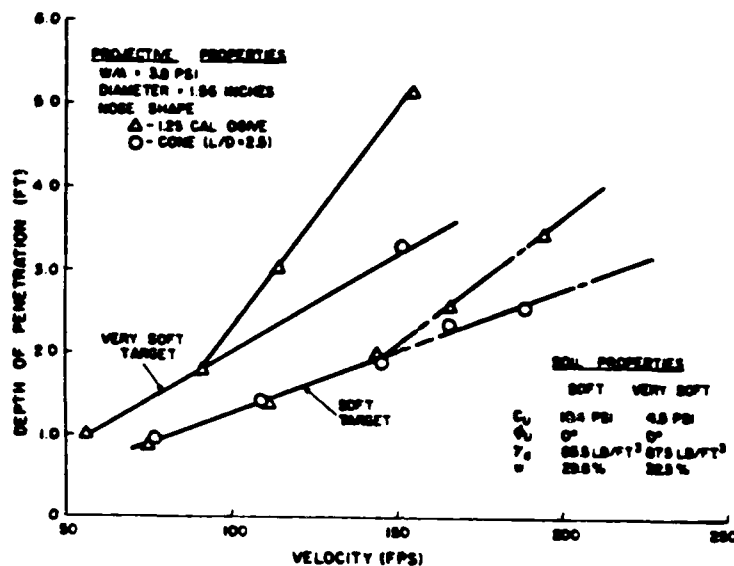


Figure 2.4 Penetration Depth Versus Velocity for Different Nose Shapes (After Murff, Harry, and Coyle 18)

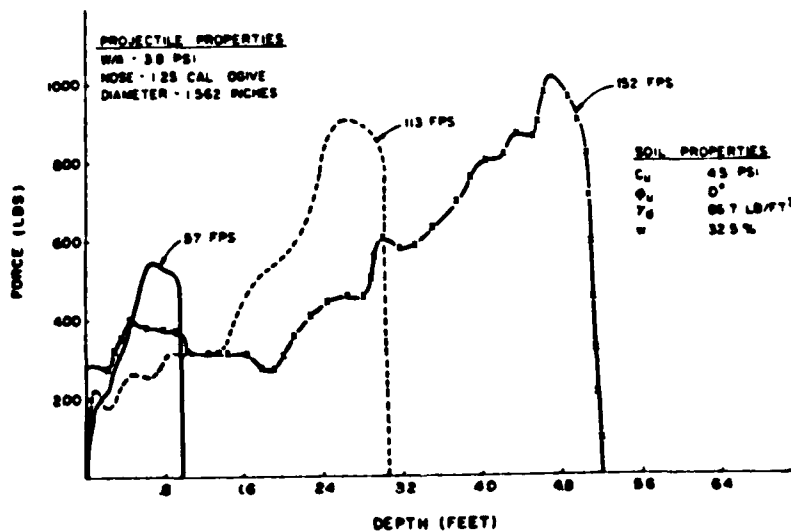


Figure 2.5 Effect of Velocity on Force Depth Record in Soft Koalin Clay (After Murff, Harry and Coyle 18)

As another illustration of the effect of velocity, Figure 2.5 shows a comparison of several force-depth records at varying impact velocities. Note that as the velocity increases the slope becomes flatter until it finally becomes approximately horizontal. This horizontal portion is felt to be due to a cavity totally encapsulating the projectile. At a certain depth (and velocity) the resistance begins to increase indicating that the cavity is beginning to collapse on the projectile. Murff (18) concluded that for clay after collapse the sidewall resistance is a significant portion of the total resistance.

2.2 PENETRATION RESISTANCE

During the impact penetration, the penetrometer is subject to resistance due to "dynamic" soil bearing capacity all the way from entry until the conclusion of penetration. Well established formulae are available for estimating the bearing capacity for "static" loading, however, no formula is known to be adequate for "dynamic" loading. Furthermore, the behavior of soil under dynamic loading is still not well understood. It is believed that the "dynamic" case at low velocity is similar to the "static" case (7). The two major factors that could cause differences between the "static" and "dynamic" are modes of failure and strain rate effect on characteristic strength parameter.

2.2.1 Modes of Failure

Thompson (25) has performed both two and three-dimensional model impact penetration tests and full scale impact penetration tests on sand and gelatine target materials to study the failure pattern. The motion of soil particles and penetrometer has been studied from high speed photographs with penetrometer velocities ranging from 6096 to 24384 cm/s.

The motion of the target in the two-dimensional tests as well as the length of the surface crack and surface deformation in full scale tests indicate the phenomena of impact penetration are primarily one of shear deformation. There appears to be a shear front, defined as the line bounding the zone in which no shearing of medium has occurred, traveling with the penetrometer. The shape of the leading edge of the front seems to be a log spiral in the case of a blunt nose projectile penetrating a half space. Similar observations have been reported by Colp (5) and Chou (4) from steady penetration tests performed on simulated cohesionless and cohesive soils, respectively.

2.2.2 Strain Rate Effect

During the past two decades, increased attention has been given to the study of strain rate effects on soil strength parameters. Taylor (24) and Casagrande and Shannon (2) were among the first to perform comprehensive investigations of the dynamic strength properties of clays and sands. By their experimental results, these investigators demonstrated that the strength of clay increases significantly under dynamic loading while only a slight increase in the strength of sand is observed. Whitman (29,30) has reported dynamic-static strength ratios of 1.5 to 2 to various types of clay, whereas for sand Whitman and Healy (31) have shown that the value of ϕ changes by only 2 to 3 percent with increase in loading speed to 254 cm/s (100 in/s). Schimming, Hass, and Sexa (23) reached the same conclusion stating that dynamic effects are minimal for cohesionless soils.

2.3 PENETRATION MODELS

Upon impact on a soil mass, a projectile pushes against soil particles, ruptures the soil structure, crushes the soil particles, and comes to rest when the projectile inertia is totally dissipated (29).

The major factors that contribute to energy dissipation of the projectile and causing it to stop are: (1) inertial resistance, (2) the bearing capacity or overcoming the strength of soil, and in the case of sand (3) pulverization of sand particles.

Based upon these aforementioned energy dissipation factors, researchers such as Wang (29) proposed penetration models by taking the change of kinetic energy of the projectile to be equal to the sum of the energy dissipation factors as a function of depth of penetration.

1. Inertial resistance:

$$dT_1 = a \rho dx V^2$$

where

dT_1 = energy dissipation due to inertial resistance

ρ = mass density of soil

a = cross-sectional area of projectile

dx = traveling distance during dt

V = impact velocity of projectile

2. Overcoming the strength of soil:

$$dT_2 = (A + Cx)$$

where

dT_2 = energy dissipation due to overcoming the strength of soil

x = depth of penetration

A, C = constants, depending on the soil property and
projectile shape and size

and for the case of sand,

3. Crushing sand particles:

$$dT_3 = D' a dx V^2$$

where

dT_3 = energy dissipation due to pulverization of sand

D' = coefficient in terms of sand particles diameter

before and after fracture, porosity, and the

ratio of new surface area to the energy producing
fracture

The sum of dT_1 , dT_2 and dT_3 is equal to change in kinetic energy,

$$-d \frac{1}{2} (MV^2) = D' a dx V^2 + \rho a dx V^2 + (A + Cx) dx$$

The differentiation of the above equation results in a relationship between the impacting velocity and maximum penetration which is not obtainable in a closed form.

Murff, Harry and Coyle (18) proposed an elementary penetration model for clay in which for simplicity they assumed that the entire resistance is concentrated over the nose of the projectile and is constant,

$$\frac{1}{2} MV_o^2 = \int_0^{x_f} c_N \frac{D^2}{4} dx$$

where

M = projectile mass

V_0 = impact velocity

σ_N = stress on nose

D = diameter

x_f = depth of penetration

x = coordinate direction

Next they considered the entire constant resistance distributed along the sides of projectile

$$\frac{1}{2} M V_0^2 = \int_0^{x_f} \sigma_s \pi D x dx$$

where

σ_s = stress on projectile sides

The equation of motion proposed by Dayal and Allen (6) which was based on momentum considerations was derived from the assumption of the path of soil movement to the surface. The momentum of all of the regions of the soil movement were calculated with the assumption that the soil is incompressible and a volume of soil equal to the volume of the penetrated projectile moves above the original surface. By equating the contributions of the weight of the projectile and different soil masses to the soil resistance, a non-linear differential equation for which neither an exact nor an approximate analytical solution could be found was presented. This equation is not presented here because of the length and the complexity of the equation.

Figure 2.6 shows the record of the forces on the penetrometer from the same study done by Dayal and Allen (6). The penetrometer starts to decelerate after a small penetration. The deceleration remains nearly

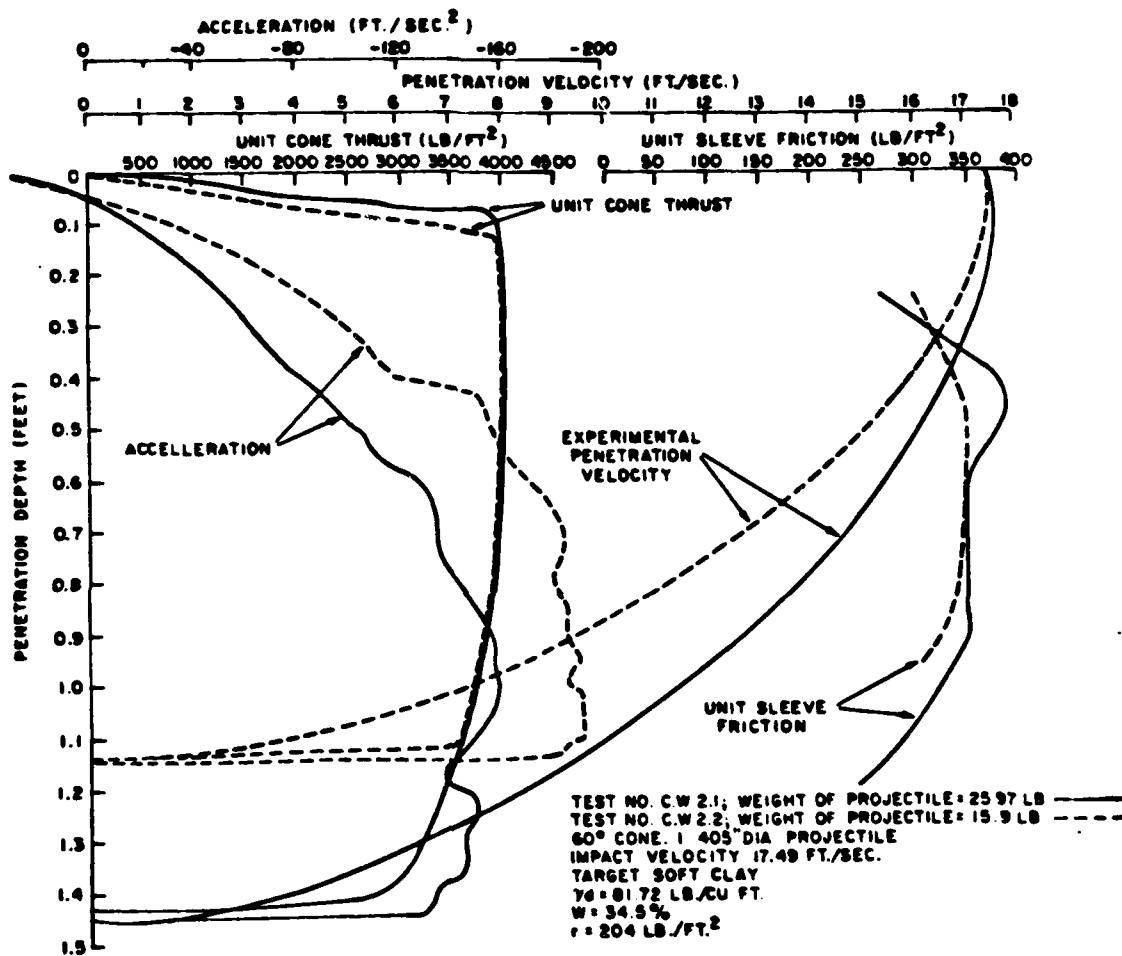


Figure 2.6 Impact Test Results For Soft Clay
(After Dayal and Allen 8)

linear with depth. At some further penetration the penetrometer comes to an abrupt zero acceleration. The figure shows that the resistances of the soil on the penetrometer which are the cone and sleeve are nearly constant with depth.

Recently, accelerometer output has been recorded by Knight (14). The velocity and depth of penetration at any instant were calculated for the deceleration record. Results are shown in Figure 2.7 from a series of tests on a dry sand target for a range of impact velocities up to 12 m/s. Figure 2.7 shows that at higher impact velocities there is a noticeable secondary peak in the deceleration record. A satisfactory explanation given by Knight is that the early part of the impact on dry sand is so violent that resistance decreases until some further penetration has taken place.

In this study a new approach for classification of ocean bottom sediments by considering the equation of motion is presented.

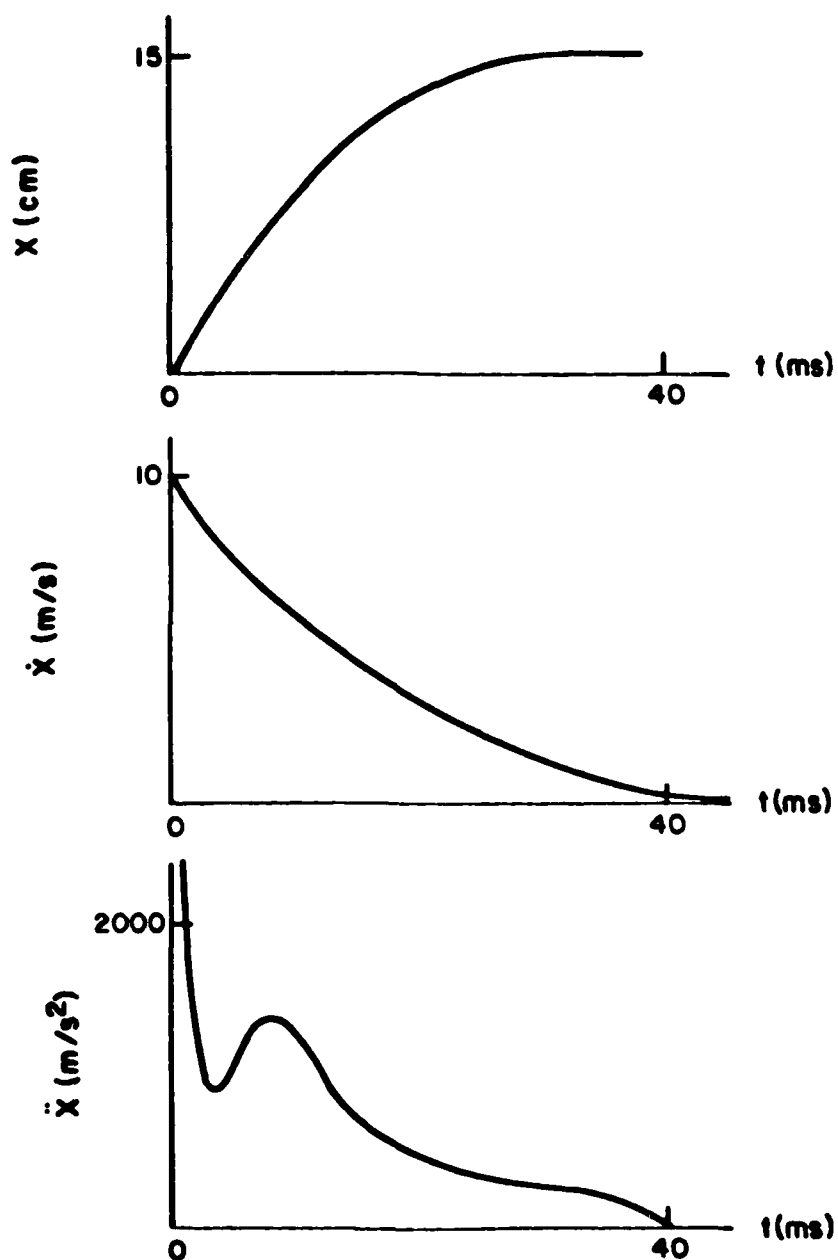


Figure 2.7 Variation of Deceleration (\ddot{X}), Velocity (\dot{X}), and Depth (X) Curves with Drop Heights (After Knight)

Chapter 3

THEORETICAL CONSIDERATIONS

This section considers the relationship between the physical characteristics of the penetrometer and the geotechnical properties of the sediments. In the first section a dimensional analysis of the problem is conducted as an aid in interpreting experimental data. In the second section the equation of motion of the penetrometer is solved to yield a prediction of penetration as a function of soil and penetrometer characteristics.

3.1 DIMENSIONAL ANALYSIS

A general technique which can be used to analyze mechanical problems is dimensional analysis. In this technique the major variables affecting the problem are identified and combined into dimensionless ratios.

The primary variables considered in this analysis are the air mass of the penetrometer (M), the diameter of the penetrometer (D), the impact velocity (V_0), the soil shear resistance (S), the maximum depth of penetration (h), and the acceleration of gravity (g) (see Figure 3.1). The unit weight of the soil is neglected in this analysis. The units and the dimensions of these variables are listed in Table 3.1. Using M , D , and g as repeating variables, the dimensionless ratios are h/D , V_0^2/hg and SD^2/Mg .

The first term h/D represents the number of penetrometer diameter the penetrometer penetrates. This ratio can be viewed as the depth

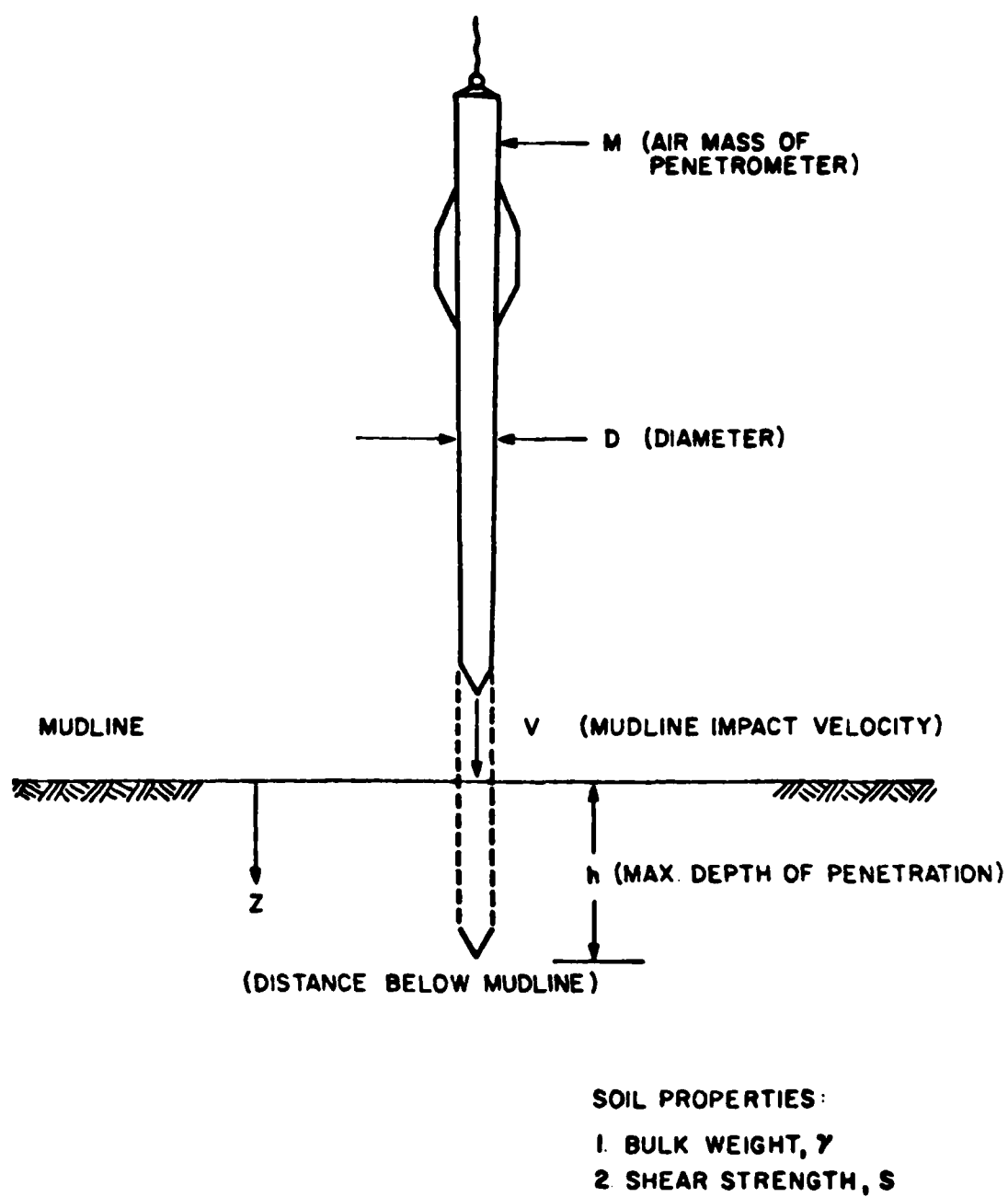


Figure 3.1 Penetrometer and Soil Properties Used in the Dimensional Analysis

factor for bearing capacity. The second term, V_o^2/hg represents the kinetic energy over the potential energy of the penetrometer. The third term, SD^2/mg represents static weight versus shear strength. This ratio is related to the bearing capacity of the soil. The primary relationship will be sought between h/D and V_o^2/Dg .

Table 3.1
Units of Primary Variables

Variable	Dimensions	Units
M	Mass	kg
D	Length	m
V_o	Length/Time	m/sec
S	Force/Area Length	kN/m ²
h	Length	m
g	Length/Time ²	m/sec ²

3.2 PREDICTION OF PENETRATION

Most of the proposed solutions of projectile penetration are based upon the following general relationship summarized by Fuchs (2)

$$M \frac{dV}{dt} = R \quad (1)$$

where M = mass of projectile, V = velocity of projectile, t = time, and R = sum of the forces on the projectile.

For this first order analysis R will be assumed to have two components; the downward force of gravity, and the upward resistance of soil. The downward force of gravity is taken to be the immersed mass of

the penetrometer (M') multiplied by acceleration of gravity (g). The upward soil resistance will be taken to be related to the soil shear stress (τ). Therefore, the total force on the penetrometer will be related to by the shear stress multiplied by the cylindrical area of the penetrometer, πDz .

The final form of soil resistance will be given by

$$\tau \pi Dz = N_p Dz S$$

where N_p is the penetrability factor, which may include the effect of friction angle, cohesion, velocity, etc.; S is the shear strength of the soil; and z is the depth of penetration at any time.

The equation of motion for the penetrometer is as follows:

$$M \frac{dV}{dt} = M'g - N_p Dz S \quad (2)$$

The initial conditions are that at $t = 0$ and at $Z = 0$, $V = V_0$. The final conditions are that at $t = T$ and at $z = h$, $V = 0$.

The solution of equation (2) is as follows. Rewrite equation (2) as

$$\frac{d^2 h}{dt^2} = a - bz \quad (3)$$

where

$$a = (M'/M) g$$

$$b = N_p (D/M) S$$

$$\text{let } Q = a - bz$$

$$\frac{dQ}{dt} = -b \frac{dz}{dt}$$

$$\frac{d^2 Q}{dt^2} = -b \frac{d^2 z}{dt^2}$$

Therefore

$$\frac{d^2 z}{dt^2} = -\frac{1}{b} \frac{d^2 Q}{dt^2} \quad (4)$$

Then substituting equation (4) into (3)

$$-\frac{1}{b} \frac{d^2 Q}{dt^2} = Q$$

$$\frac{d^2 Q}{dt^2} = bQ$$

The general solution of the above equation is

$$Q = Q_0 \sin b^{\frac{1}{2}} t + P_0 \cos b^{\frac{1}{2}} t$$

The solution for z is

$$a - bz = Q_0 \sin b^{\frac{1}{2}} t + P_0 \cos b^{\frac{1}{2}} t$$

or

$$z = \frac{a}{b} - \frac{1}{b} (Q_0 \sin b^{\frac{1}{2}} t + P_0 \cos b^{\frac{1}{2}} t)$$

The equation for velocity as a function of time is

$$\frac{dz}{dt} = V = -\frac{1}{b} (b^{\frac{1}{2}} Q_0 \cos b^{\frac{1}{2}} t + P_0 b^{\frac{1}{2}} \sin b^{\frac{1}{2}} t)$$

Applying the initial conditions at $t = 0$, $z = 0$ and $V = V_0$ gives

$$z = \frac{a}{b} - \frac{1}{b} (P_0) = 0$$

solving for $P_0 = a$

$$V = -\frac{1}{b} (b^{\frac{1}{2}} Q_0) = V_0$$

solving for $Q = -V_0 b^{\frac{1}{2}}$

The particular solution for the depth and velocity are

$$z = \frac{a}{b} + \frac{V_0}{b^{\frac{1}{2}}} \sin b^{\frac{1}{2}} t - \frac{a}{b} \cos b^{\frac{1}{2}} t \quad (5)$$

$$V = V_0 \cos b^{\frac{1}{2}} t + \frac{a}{b^{\frac{1}{2}}} \sin b^{\frac{1}{2}} t \quad (6)$$

where $a = (M'/M) g$ and $b = N_p (D/M) S$

These solutions define a relationship between the penetrometer characteristics, the sediment properties and the maximum depth of penetration, i.e., at $t = T$, $z = h$ and $V = 0$, equation (5) and (6) will be equal to the following

$$h = \frac{a}{b} (1 - \cos b^{\frac{1}{2}} T) + \frac{V_0}{b^{\frac{1}{2}}} \sin b^{\frac{1}{2}} T \quad (7)$$

$$0 = V_0 \cos b^{\frac{1}{2}} T + \frac{a}{b^{\frac{1}{2}}} \sin b^{\frac{1}{2}} T \quad (8)$$

Solving equation (8) for T

$$T = \tan^{-1} (b^{\frac{1}{2}} V_0 / a) / b^{\frac{1}{2}}$$

Assuming a is small ($a \rightarrow 0$) then

$$T = \frac{\tan^{-1}(\infty)}{b^{\frac{1}{2}}} = \frac{\pi/2}{b^{\frac{1}{2}}}$$

Substituting for b

$$T = \frac{\pi}{2(N_p (D/M) S)^{1/2}}$$

Using this in equation (7)

$$h = \frac{a}{b} (1 - \cos \frac{\pi}{2}) + \frac{v_o}{b^{1/2}} \sin \frac{\pi}{2}$$

and since a = 0 then

$$h = \frac{v_o}{b^{1/2}} = v_o \left(\frac{M}{N_p D S} \right)^{1/2} \quad (9)$$

Equation (9) relates the maximum depth of penetration to the impact velocity.

Equation (9) can be rewritten as the dimensionless ratios obtained in the first section:

$$h/D = (v_o^2/gh)/(SD^2/Mg)N_p$$

Therefore the penetrability factor, N_p can be calculated by the following formula of dimensionless ratios:

$$N_p = (v_o^2/gh)/(SD^2/Mg)(h/D) \quad (10)$$

Chapter 4

DATA ACQUISITION AND ANALYSIS

4.1 PENETROMETER CHARACTERISTICS

This study deals with the classification of ocean bottom sediments by free fall of a penetrometer. The non-instrumented penetrometers used in this study were fabricated from stainless steel. These penetrometers had the capability of additional weight attachment for penetration testing of different mass to diameter ratios. In the case of the penetrometer with the diameter of 5.1 cm this capability was conveniently achieved by adding weights inside the hollow penetrometer tube. In the case of the other penetrometers which had diameters of 2.54 cm and 1.60 cm this was achieved by designing cylindrical lead weights with penetrometer diameter openings. These weights were fitted with set screws so that they could easily be slipped up the penetrometer and screwed onto the penetrometer. The weight of the 5.10 cm, 2.54 cm and 1.60 cm diameter penetrometers were 4.85 kg, 7.5 kg and 0.875 kg, respectively. The overall length of the penetrometers were 2 meters for the 5.10 cm and 2.54 cm diameter penetrometer, and 1 meter for the 1.60 cm diameter penetrometer. Two cones of blunt and 60° tip were used in the tests. Figure 4.1 shows the photograph of the three penetrometers.

4.2 LABORATORY EQUIPMENT AND PROCEDURE

In the laboratory testing dry powdered bentonite clay was placed in a large concrete mixer and mixed with a measured amount of water to

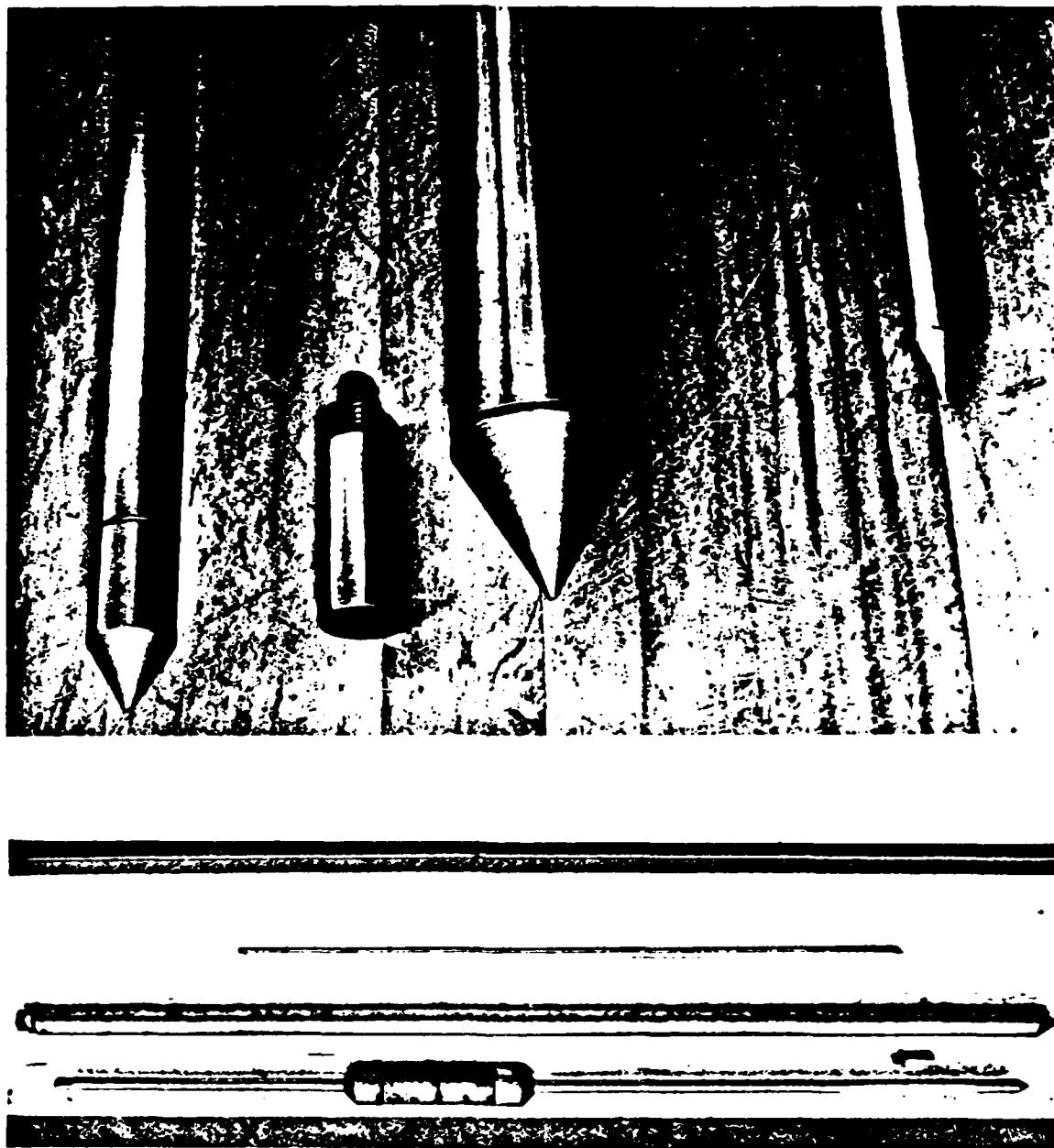


Figure 4.1 Photograph of Field and Laboratory Penetrometers

obtain a very low shear strength, simulating the ocean bottom conditions. The material was recycled until the mixture was homogeneous and was then removed from the mixer.

Target was constructed in cylindrical steel mold of 46 cm (18 in) diameter and 81 cm (32 in) height. The mold was placed on a set of wheels for mobility. The soil mixture was placed in the mold in layers and compacted. At the end of compaction of every layer samples were collected for determination of shear strength. The fall cone test was performed three times on each sample to obtain a reasonable and statistically reliable shear strength of the soil in the mold. These shear strength values were all very close to 5.0 kPa which was chosen to represent the shear strength of the target.

In this soil the dynamic penetration tests were performed with the 1.6 cm diameter penetrometer. Different weights were attached to the penetrometer to diversify the penetration for variety of velocities. The penetrations were performed as many times as possible without adversely influencing the results.

The release mechanism of the penetration was composed of a pulley attached to the ceiling of the laboratory 4 meters high and a stiff cable covered by plastic lining to restrain the elastic strain and to reduce friction in the pulley. The penetrometer was released by an electrical device that was connected to the end of the cable by a very short non-elastic string of high tensile stress.

The impact velocities were determined by the height of fall. The total depth of penetration was measured by initially measuring the total height of the penetrometer and subtracting the buried height of the penetrometer.

4.3 FIELD EQUIPMENT AND PROCEDURE

The field experimentations were performed on two sites. The sites were located at St. Andrews, Panama City, Florida and at Pass Christian, Gulf Port, Mississippi.

The classification of the top 40 cm of soil in the field for both sites according to AASHTO Soil Classification system were A-3. According to the Unified Soil Classification system, both sites were poorly graded soils with 80-90 percent fine sand. Shells were also present but the percentage was not appreciable. The grain size distribution graphs are available in the Appendix.

The tests were performed at low tide and low wave period. The maximum height of water above the sand during penetration testing was about 20 cm.

The 2.54 cm and 1.60 cm diameter penetrometers were used in the field. The bigger diameter penetrometer (5.10 cm) did not penetrate into the soil appreciably because of the low mass to diameter ratios and the low range of velocities tested. For this reason the 5.10 cm diameter penetrometer was not used. The effect of different cones on the depth of penetration were also tested.

A steel pipe frame was constructed to support the penetrometer for penetration testing. A pulley was suspended from the top horizontal member of the frame. On the vertical member of the frame five release mechanisms were attached for adjusting the height of fall of the penetrometer. Figure 4.2 shows the schematic diagram and the details of the system. The frame was erected on top of the soil and the height of penetrometer fall was adjusted. After the release of the penetrometer the depth of penetration was measured by knowing the total height of the

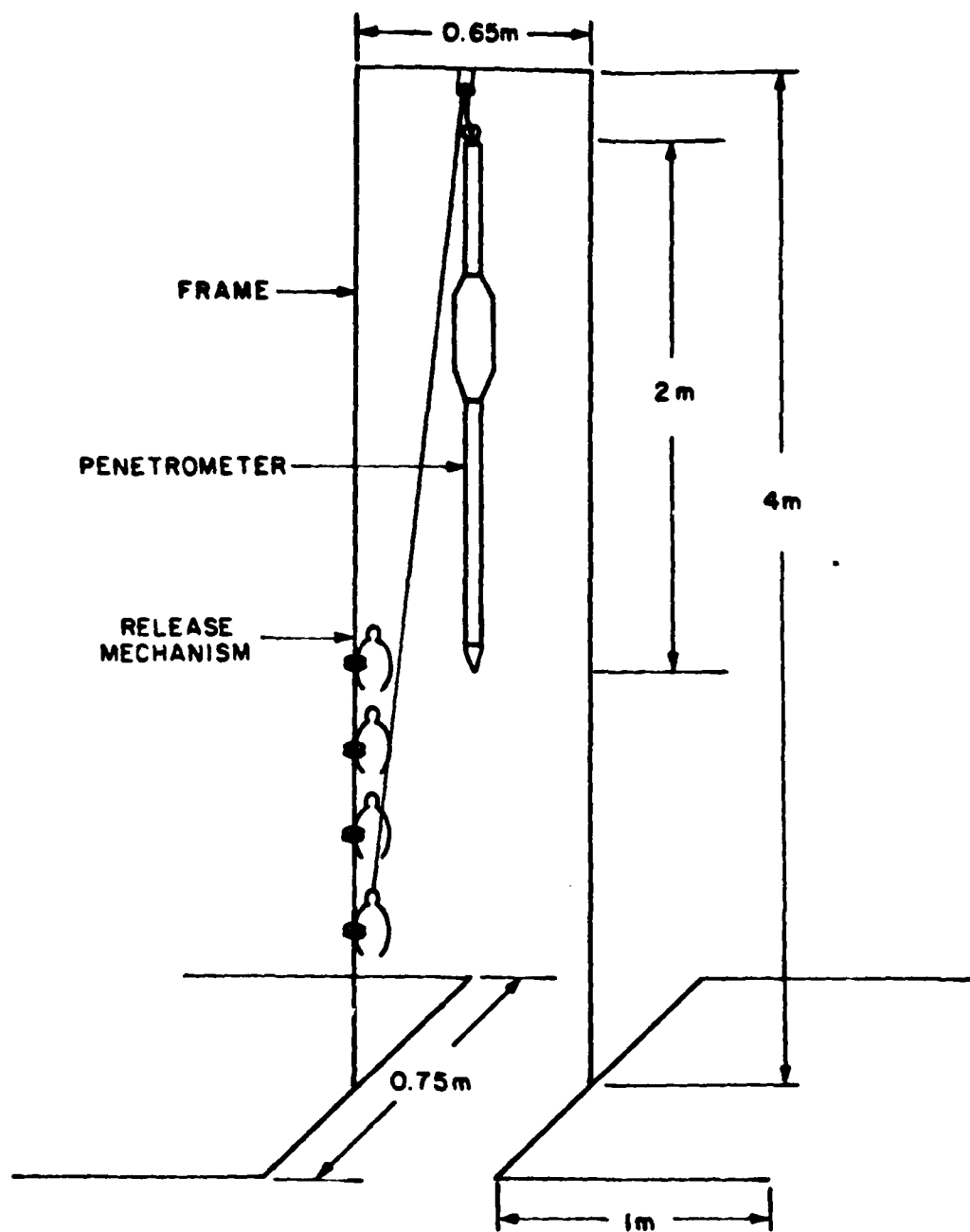


Figure 4.2 Field Penetration Equipment

penetrometer and subtracting the measured unburied height of the penetrometer. The frame was then lifted and relocated on a different spot in the same vicinity without disturbing the path of penetration which was chosen along the shoreline. This time another height of fall was adjusted and the penetrometer was released and the depth of penetration was measured.

Due to the fact that shells existed in the site, the true depth of penetration in sand was not always obtained by the first drop. The true depth of penetration in sand was obtained by dropping the penetrometer three times and using the largest value. For example, if the first depth of penetration was 10 cm and the second and third depth of penetration was 20 cm and 22 cm, respectively, the largest value which is 22 cm was used in the analysis to represent the penetration in sand.

Chapter 5

DISCUSSION OF RESULTS

5.1 GENERAL OBSERVATIONS AND CHARACTERISTICS
OF RESULTS

The total depth of penetration is an essential information for classification of soils. In this study the penetrometers discussed in the previous chapter were utilized to obtain the total depth of penetration. A variety of velocities and mass to diameter ratios were tested to yield different depth of penetrations without changing the soil properties. The range of these variables are summarized in the table below.

Table 5.1
Range of Penetration Variables

Variable	Clay		Sand	
	Min.	Max.	Min.	Max.
Impact Velocity (m/sec)	2.23	7.83	2.78	5.68
Mass/Diameter (kg/m)	54.70	243.80	385.80	1011.80
Total Depth of Penetration (m)	0.09	0.55	0.06	0.42

Figure 5.1 shows the plot of impact velocity versus the total depth of penetration in clay. The penetrometer was loaded to four different

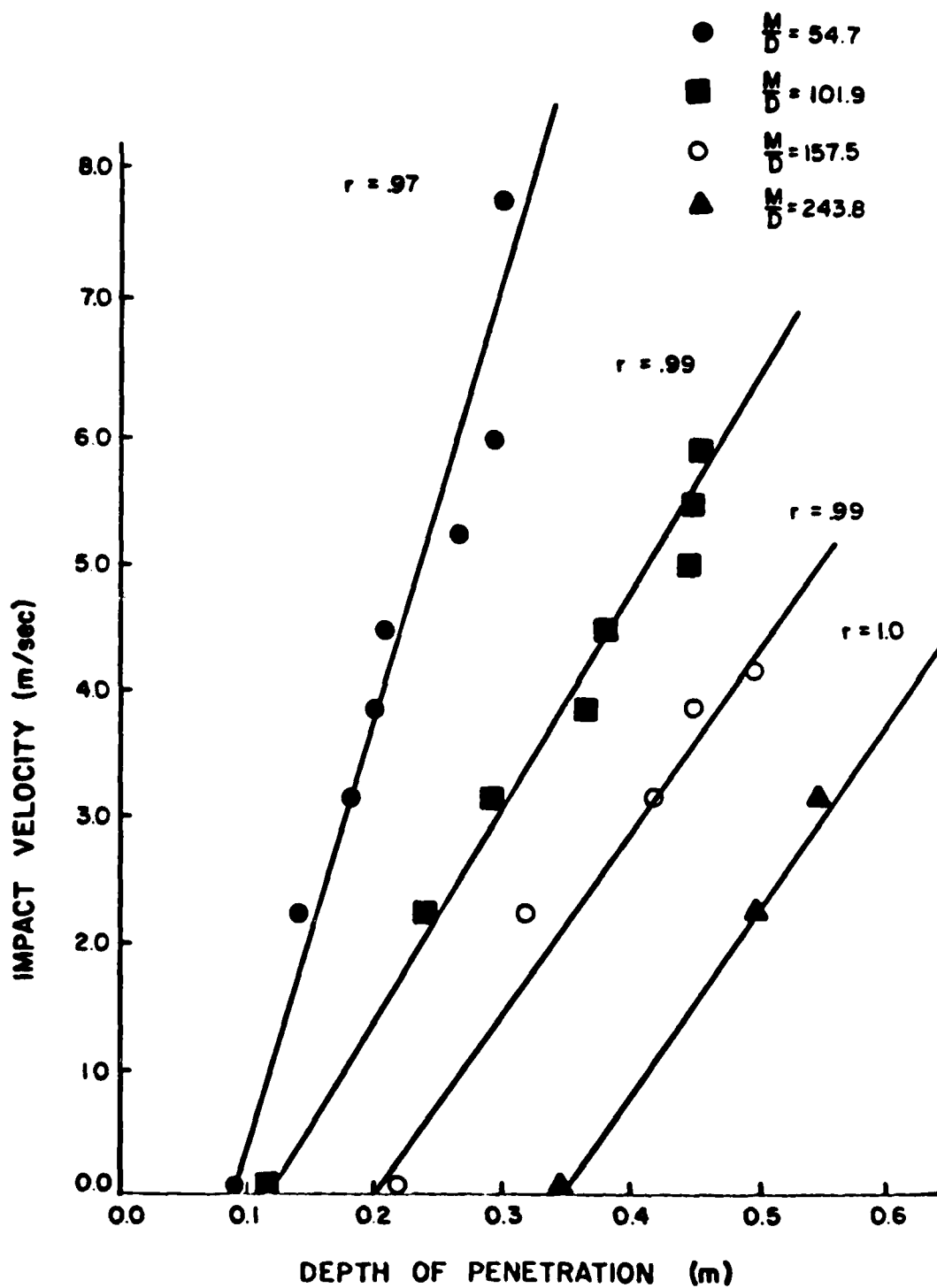


Figure 5.1 Impact Velocity Versus Depth of Penetration in Clay

weights and dropped into laboratory prepared clay target of 5 kPa shear strength. For each weight a nearly linear relationship for a variety of velocities was observed. The linear coefficient of correlation ranging between 0.97 and 1.0 confirmed this relationship. The plots show that as the velocity increases the total depth of penetration also increases.

It was observed that at velocities higher than 5 m/s the effect of velocity on the depth of penetration becomes less significant. That is to say the increase in the depth of penetration was almost non-existent as the velocity increased over 5 m/s. Recall that the height of mold was 81 cm and therefore the boundary conditions cannot be attributed as an explanation for this behavior. However, this phenomenon can possibly be attributed to the fact that the strength of clay increases significantly under dynamic loading (8). At high velocities of 5-8 m/s, as tested in this study, the clay can gain additional strength due to the inertial forces. This explanation does not however suggest that at velocities significantly higher than the velocities mentioned in this study, the depth of penetration will not increase. At some velocity the inertial forces may overcome the dynamic strength of clay and higher depth of penetration will result.

Figure 5.2 shows the plot of impact velocity and the total depth of penetration in sand at Pass Christian. These points represent the data obtained at Pass Christian site. This figure shows the linearity between the depth of penetration and impact velocity as was observed in clay.

The saturated unit weight of the sand was calculated and the internal friction angle of the sand was obtained from a table by

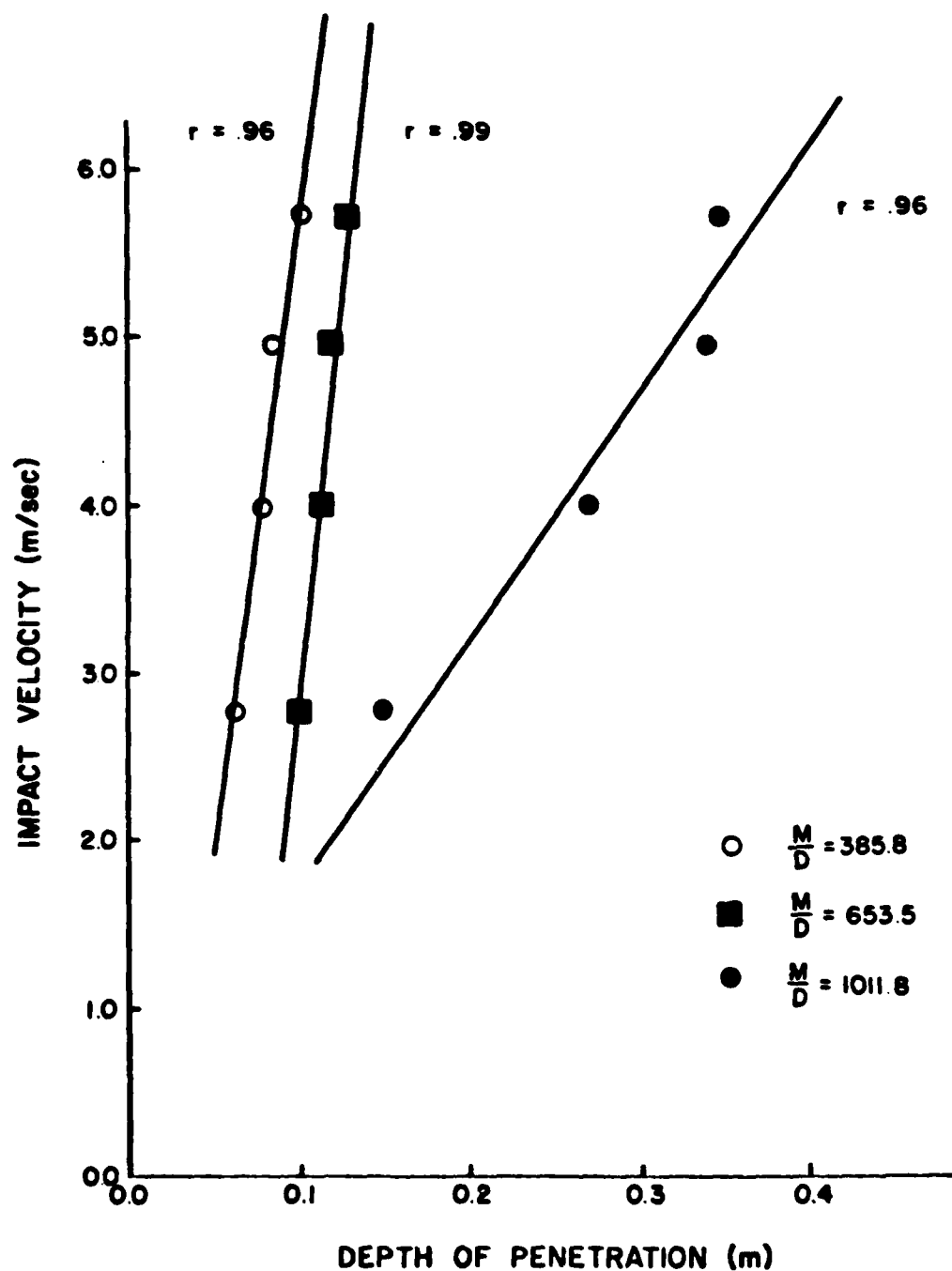


Figure 5.2 Impact Velocity Versus Total Depth of Penetration in Sand
(Pass Christian)

Meyerhof for calculating the shear strength of sands. For Pass Christian the internal friction angle was 40° and for St. Andrews it was 35° .

One important fact that must always be considered in dynamic penetration is the variability of depth of penetration in field and natural conditions as it was demonstrated to us in this study. Many times the depth of penetration was drastically reduced because of collision of the penetrometer with shells which existed in the beach. The true depth of penetration was obtained by dropping the penetrometer at the same velocity and the same weight until a consistent result was attained. In ocean bottom sediments this problem can also exist. There are hard objects that will stop the penetrometer and the actual depth of penetration for that particular sediment strength and type will not be obtained. It is advised that as many penetrations as possible be made in the same vicinity of interest to obtain a representative penetration result.

In the field, the effect of the blunt tip and the 60° cone tip on the depth of penetration was examined. A 25.71 kg penetrometer with the 60° cone dropped at a velocity of 5.68 m/s resulted in 34.3 cm penetration, while the same penetrometer with a blunt tip penetrated into the same soil resulted in 35.5 cm penetration. These penetration depths were the largest depth of penetration after dropping the penetrometer three times. At velocities lower than 5.68 m/s with different weights, no significant change in depth of penetration took place.

Figures 5.3, 5.4 and 5.5 show the penetration results at St. Andrews, in clay and in dry loose and sand sand, respectively.

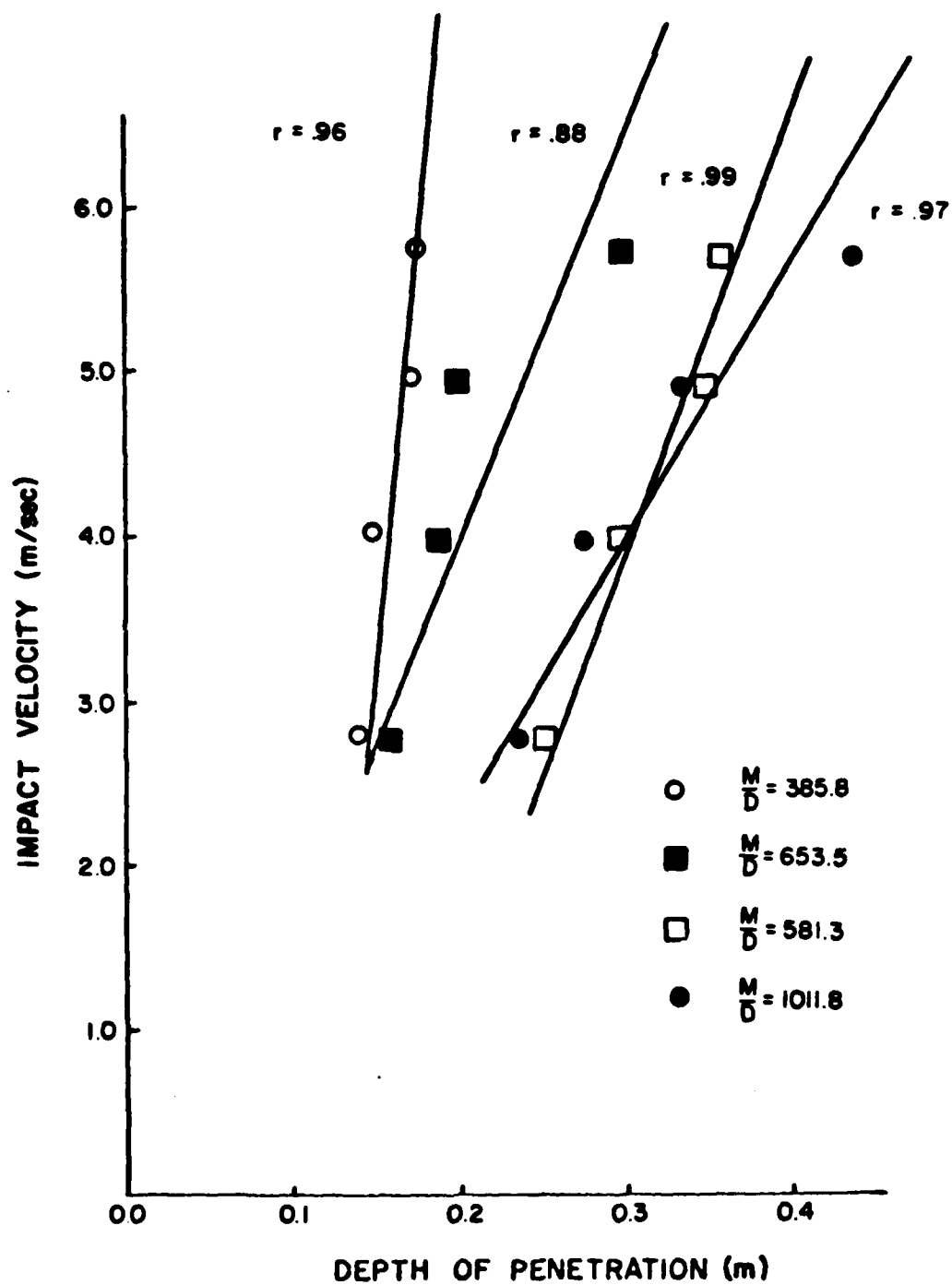


Figure 5.3 Impact Velocity Versus Depth of Penetration in Saturated Sand (St. Andrews)

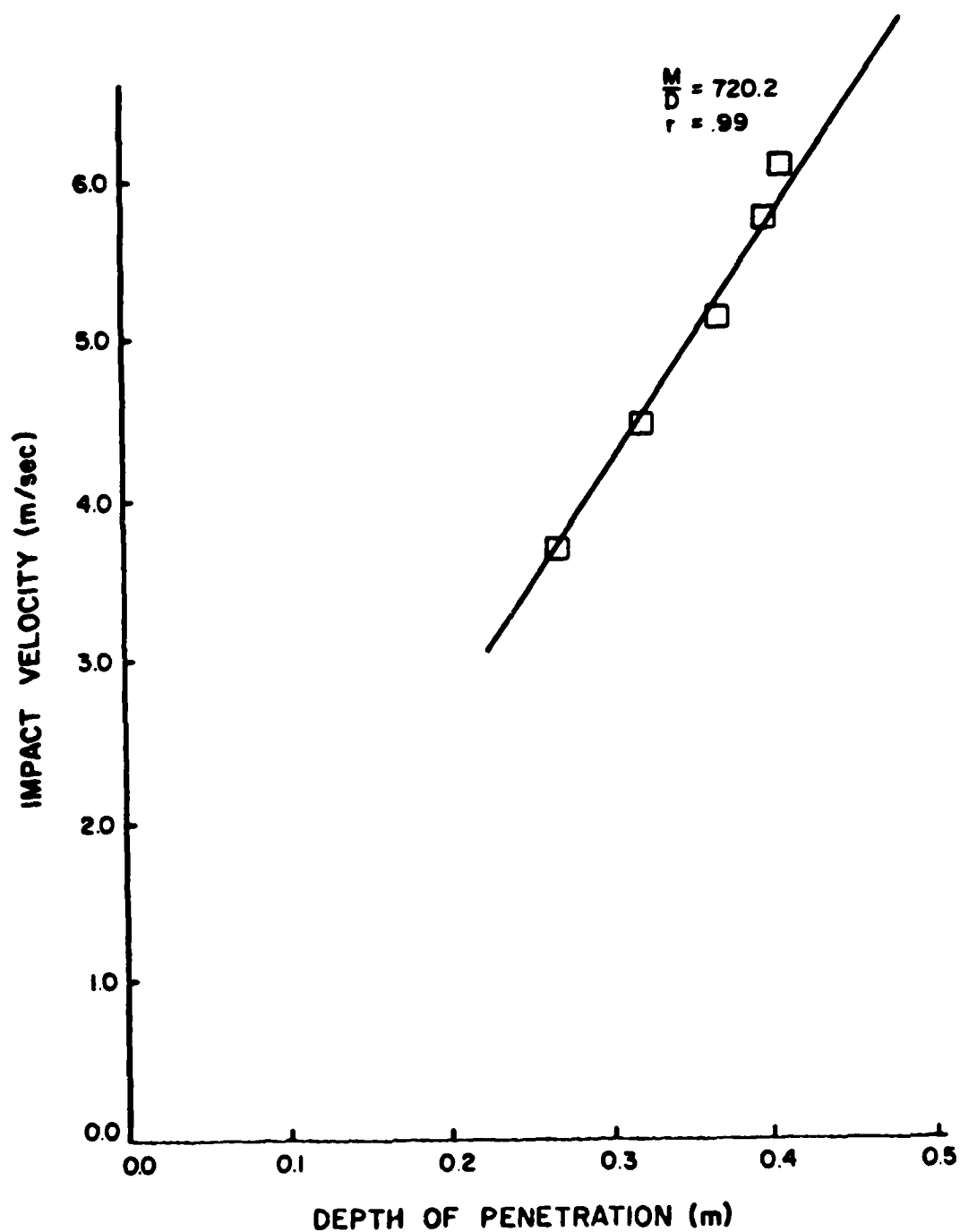


Figure 5.4 Impact Velocity Versus Depth of Penetration in Clay
($S = 28$ kpa)

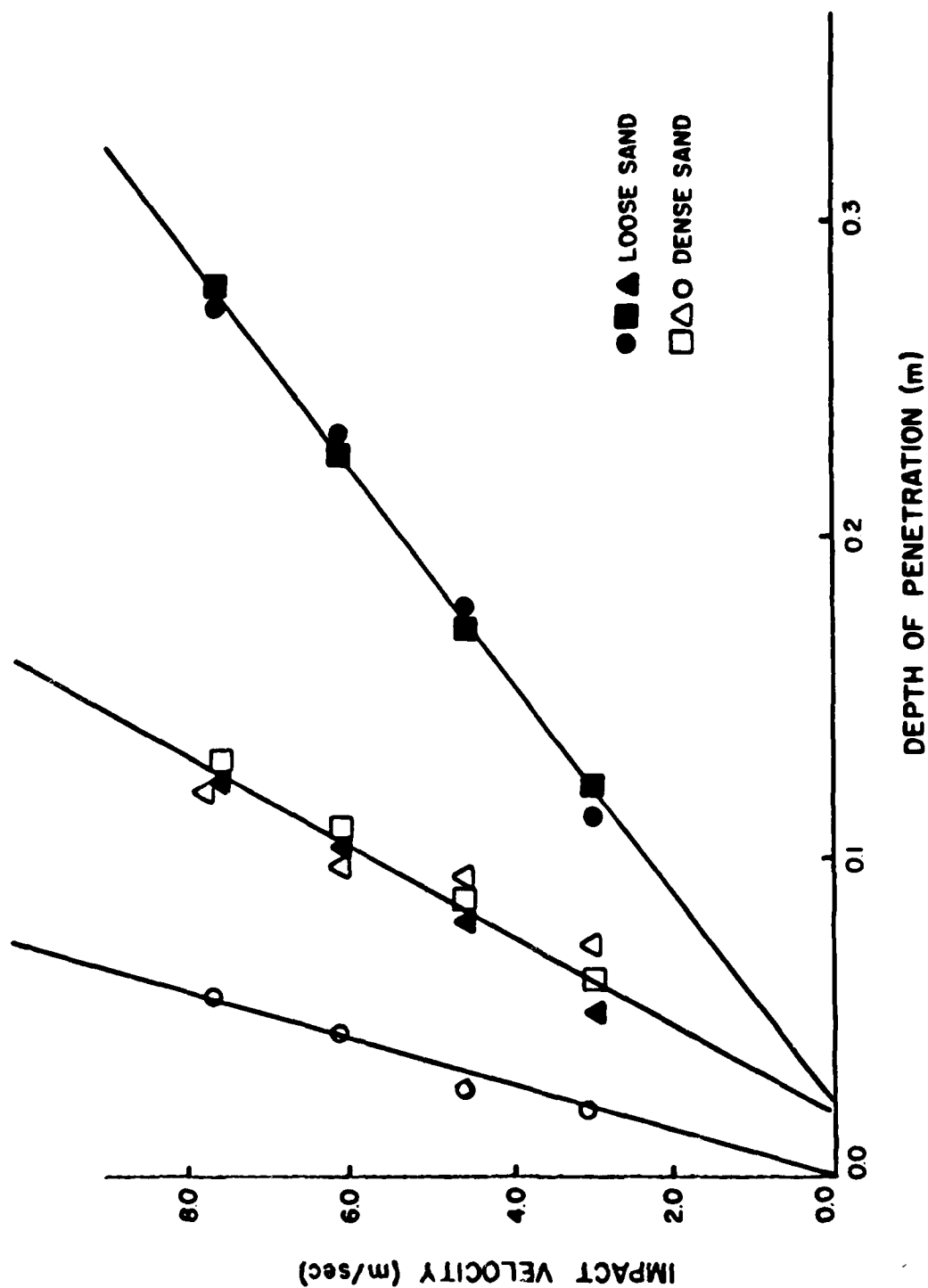


Figure 5.5 Impact Velocity Versus Depth of Penetration in Dry Loose and Dense Sand (27)

5.2 DIMENSIONAL ANALYSIS RESULTS

Three dimensionless ratios were considered. The first of these ratios was h/D where h is the total depth of penetration and D is the diameter of penetrometer. This ratio represents the number of penetrometer diameters the penetrometer penetrates. The majority of the values for this ratio were between 5 and 30 indicating that dynamic penetration passes the limit of shallow foundation problem. The values of h/D for saturated sand and clay were approximately the same, however, the mass of the penetrometer in the case of sand ranged from 9.8 kg to 25.7 kg while in the case of clay it ranged from 0.875 kg to 3.9 kg.

Wang (27) performed penetration testings on dry dense sand with unit weight of 17.27 kN/m^3 and internal friction angle of 40° , and on dry loose sand with unit weight of 15.54 kN/m^3 and internal friction angle of 30° . The values of h/D ratios are tabulated in Table 5.2. As shown in column 5 the ratios of h/D for loose sand divided by the ratios of h/D for dense sand is approximately 2. This result indicates a direct relation between internal friction angle ϕ and h/D .

The second dimensionless ratio was V_o^2/gh where V_o is the impact velocity, g is the gravitational acceleration, and h is the total depth of penetration. This ratio represented the kinetic energy of the penetrometer over the potential energy of the penetrometer. The values for this ratio for both clay and sand ranged from 2 to 100. This indicated the prevailing control of kinetic energy over potential energy. For saturated sand this ratio was much larger than for clay for the same mass, diameter and velocity.

The third dimensionless ratio was SD^2/Mg where S is the shear strength of the soil, and m is the mass of the penetrometer. This ratio

Table 5.2

h/D Ratios for Dry Loose and Dense Sand

M/D (kg/m)	V ₀ (m/Sec)	h/D (Loose Sand)	h/D (Dense Sand)	$\frac{h/D \text{ (Loose)}}{h/D \text{ (Dense)}}$
26.18	3.05	2.24	1.26	1.8
26.18	4.58	3.47	1.66	2.1
26.18	6.10	4.47	2.09	2.1
26.18	7.63	5.37	2.51	2.1
18.90	3.05	3.24	1.86	1.7
18.90	4.58	4.57	2.34	2.0
18.90	6.10	6.03	2.62	2.3
18.90	7.63	7.41	3.31	2.2
6.30	3.05	1.38	0.52	2.7
6.30	4.58	2.14	0.74	2.9
6.30	6.10	2.69	1.20	2.2
6.30	7.63	3.24	1.48	2.2

represented the shear strength over the weight/area ratio of the penetrometer. The values of this ratio for clay ranged from 0.16 to 0.50 and for saturated sand it ranged from 0.006 to 0.014. The inverse of this ratio Mg/SD^2 represented the load over the strength of soil or the bearing capacity of the soil. These values were ranging from 2 to 6 for clay and 71 to 166 for saturated sand. This means that the dynamic penetration considerably exceeded the bearing capacity of the soil.

Tables 5.3 through 5.8 show the summarized values of all the dimensionless ratios for all penetration data.

5.3 N_p RESULTS

N_p is also a dimensionless number. It is a function of impact velocity, depth of penetration, diameter of penetrometer, mass of penetrometer, and the soil shear strength. Equation 10 in Chapter 3 described N_p as the function of the three dimensionless ratios discussed in the previous section.

The results show that for clay of shear strength ranging from 5 kPa to 52 kPa, N_p varies from 1 to 7. For saturated sand N_p varies from 22 to 1153. For dry loose and dense sand N_p varies from 4 to 45. The variation of N_p for every soil is dependent on the impact velocity and the mass to diameter ratio. The values of N_p clearly distinguishes between clay and sand. For sand the values are much larger than for clay.

Solving equation 9 of Chapter 3 for N_p gives

$$N_p = \frac{MV_o^2}{DSh^2}$$

Table 5.3
Summary of Test Results for Clay Target
(60° Cone - Projectile of 0.016 m Diameter)

Test Number	Mass of Projectile (kg)	Impact Velocity (m/sec)	Full Cone Indentation Shear Strength (kPa)	Depth of Penetration (m)	$\frac{h}{D}$	$\frac{V^2}{g}$	$\frac{W^2}{g}$	$\frac{W}{g} = 10^3$	$\frac{W^2}{g} = 10^3$	h_p
1	0.075	0.00	5.0	0.09	5.43	0.00	0.15	16.00	0.00	0.00
2	0.075	2.23	5.0	0.16	0.75	3.62	0.15	26.12	13.87	2.16
3	0.075	3.16	5.0	0.18	11.25	5.66	0.15	33.60	16.06	3.35
4	0.075	3.87	5.0	0.20	12.63	7.64	0.15	37.90	19.87	4.03
5	0.075	4.47	5.0	0.21	13.44	9.48	0.15	40.10	23.64	4.10
6	0.075	5.24	5.0	0.27	16.69	10.40	0.15	49.00	21.06	4.19
7	0.075	6.02	5.0	0.29	18.25	12.66	0.15	54.53	23.26	4.62
8	0.075	6.70	5.0	0.29	18.25	15.69	0.15	54.53	26.79	5.73
9	0.075	7.00	5.0	0.29	18.25	21.26	0.15	54.53	36.02	7.77
10	1.630	0.00	5.0	0.13	7.94	0.00	0.00	12.71	0.00	0.00
11	1.630	2.23	5.0	0.24	15.00	2.11	0.00	26.06	0.79	1.76
12	1.630	3.16	5.0	0.29	18.13	3.61	0.00	29.61	12.00	2.49
13	1.630	3.87	5.0	0.34	21.44	4.46	0.00	34.42	12.97	2.60
14	1.630	4.47	5.0	0.30	23.75	5.37	0.00	38.10	16.09	2.83
15	1.630	5.00	5.0	0.45	27.81	5.73	0.00	44.66	12.06	2.41
16	1.630	5.47	5.0	0.45	27.81	6.06	0.00	44.66	15.39	3.00
17	1.630	5.90	5.0	0.46	28.94	7.70	0.00	46.42	16.00	3.35
18	2.520	0.00	5.0	0.22	13.50	0.00	0.05	14.06	0.00	0.00
19	2.520	2.23	5.0	0.34	21.44	1.40	0.05	22.25	6.64	1.30
20	2.520	3.16	5.0	0.42	26.91	2.43	0.05	27.10	9.96	1.80
21	2.520	3.87	5.0	0.45	27.81	3.43	0.05	28.00	11.91	2.47
22	2.520	4.10	5.0	0.50	30.94	3.62	0.05	32.11	11.20	2.34
23	3.900	0.00	5.0	0.34	21.44	0.00	0.03	16.42	0.00	0.00
24	3.900	2.23	5.0	0.50	31.25	1.01	0.03	20.90	4.04	0.90
25	3.90	2.94	5.0	0.55	34.38	1.60	0.03	23.02	6.94	1.41

Table 5.4
Summary of Test Details for Saturated Sand
(St. Andrews, Florida)

Test Number	Diameter of Projectile (m)	Mass of Projectile (kg)	Impact Velocity (m/sec)	Sat. Unit Weight (kN/m ³)	Depth of Penetration (m)	$\frac{h}{D}$	$\frac{V_o^2}{gh}$	$\frac{SD^2}{mg}$	$\frac{hD}{mg} \times 10^5$	$\frac{MV_o^2}{2Dh} \times 10^3$	W_p
1	0.0254	25.70	2.78	18.60	0.24	9.55	3.28	0.008	2.42	135.78	43.2
2	0.0254	25.70	3.99	18.60	0.28	10.96	5.80	0.009	2.82	205.46	58.8
3	0.0254	25.70	4.90	18.60	0.34	13.49	7.21	0.011	3.43	210.15	48.6
4	0.0254	25.70	5.68	18.60	0.42	16.60	7.84	0.014	4.24	185.05	33.7
5	0.0254	16.60	2.78	18.60	0.16	6.30	4.93	0.008	2.50	197.31	97.8
6	0.0254	16.60	3.99	18.60	0.19	7.41	8.55	0.009	2.97	288.21	121.4
7	0.0254	16.60	4.90	18.60	0.20	7.94	12.25	0.010	3.12	392.28	154.0
8	0.0254	16.60	5.68	18.60	0.30	11.75	10.97	0.015	4.68	234.27	62.2
9	0.0254	9.80	2.78	18.60	0.14	5.50	5.63	0.012	3.70	152.21	85.3
10	0.0254	9.80	3.99	18.60	0.15	5.09	10.83	0.013	3.97	272.99	163.7
11	0.0254	9.80	4.90	18.60	0.17	6.76	14.41	0.014	4.51	320.54	152.3
12	0.0254	9.80	5.68	18.60	0.17	6.76	19.37	0.014	4.51	430.72	204.7
13	0.0160	9.30	2.78	18.60	0.25	15.49	3.15	0.009	4.39	71.87	22.6
14	0.0160	9.30	3.99	18.60	0.30	18.62	5.42	0.011	5.27	102.81	26.4
15	0.0160	9.30	4.90	18.60	0.34	21.38	7.21	0.012	5.97	120.72	28.1
16	0.0160	9.30	5.68	18.60	0.36	22.39	9.27	0.013	6.23	148.80	32.0

Table 5.5
Summary of Test Details for Saturated Sand
(Pass Christian, Mississippi)

Test Number	Diameter of Projectile (m) D	Mass of Projectile (kg) M	Impact Velocity (m/sec) V_o	Sat. Unit Weight (kN/m ³) γ	Depth of Penetration (m) h	$\frac{h}{D}$	$\frac{V^2}{gh}$	$\frac{SD^2}{mg}$	$hD \times 10^5 \frac{m^2}{mg}$	$\frac{MV^2}{Dh^2} \times 10^3$	N_p
1	0.0254	25.70	2.78	20.20	0.152	6.03	5.19	0.006	1.53	338.46	143.4
2	0.0254	25.70	3.99	20.20	0.267	10.47	6.08	0.010	2.69	225.95	58.2
3	0.0254	25.70	4.90	20.20	0.343	13.49	7.14	0.013	3.56	206.49	48.3
4	0.0254	25.70	5.68	20.20	0.343	13.49	9.60	0.013	3.46	277.46	54.7
5	0.0254	16.60	2.78	20.20	0.100	3.98	7.89	0.006	1.56	505.08	330.1
6	0.0254	16.60	3.99	20.20	0.115	4.57	14.13	0.007	1.80	786.72	441.7
7	0.0254	16.60	4.90	20.20	0.120	4.68	20.42	0.007	1.87	1089.69	623.3
8	0.0254	16.60	5.68	20.20	0.130	5.13	25.32	0.008	2.03	1247.62	617.1
9	0.0254	9.80	2.78	20.20	0.063	2.48	12.52	0.006	1.67	751.27	855.1
10	0.0254	9.80	3.99	20.20	0.076	3.02	21.38	0.007	2.01	1063.43	855.3
11	0.0254	9.80	4.90	20.20	0.082	3.24	29.88	0.008	2.17	1377.70	1153.2
12	0.0254	9.80	5.68	20.20	0.102	3.98	32.28	0.010	2.70	1196.43	811.4

Table 5.6
Summary of Test Details for Clay Target
(60° Cone - Projectile of 0.0357 m Diameter)
(after Dayal and Allen, 1980)

Test Number	Mass of Projectile (kg) M	Impact Velocity (m/sec) V_o	Vane Shear Strength (kpa) S	Depth of Penetration (m) h	$\frac{h}{D}$	$\frac{V_o^2}{gh}$	$\frac{SD^2}{mg}$	$\frac{hD}{mg} \times 10^5$	$\frac{MV_o^2}{Dh^2} \times 10^3$	R_p
1	25.71	5.79	52.0	0.27	7.56	12.69	0.26	3.83	331	6.2
2	21.07	5.79	52.0	0.24	6.72	14.25	0.32	4.15	343	6.6
3	16.26	5.79	52.0	0.21	5.88	16.29	0.42	4.70	346	6.6
4	25.71	6.10	28.0	0.41	11.54	9.22	0.14	5.84	157	5.7
5	25.71	5.75	28.0	0.40	11.12	8.50	0.14	5.63	155	5.5
6	25.71	5.12	28.0	0.37	10.42	7.19	0.14	5.27	136	4.8
7	25.71	4.66	28.0	0.32	9.05	6.86	0.14	4.58	149	5.4
8	25.71	3.77	28.0	0.27	7.62	5.33	0.14	3.85	138	5.0
9	11.79	5.34	10.0	0.44	12.32	6.61	0.11	13.60	48	4.8
10	7.22	5.34	10.0	0.35	9.8	8.31	0.18	17.66	47	4.7

Table 5.7
Summary of Test Details for Loose Dry Sand
(after W. L. Wang, 1971)

Test Number	Diameter of Projectile (m) D	Mass of Projectile (kg) M	Impact Velocity (m/sec) V_o	Dry Unit Weight (kN/m ³) γ	Depth of Penetration (m) h	$\frac{h}{D}$	$\frac{V_o^2}{gh}$	$\frac{SD^2}{mg}$	$\frac{MD}{mg} \times 10^5$	$\frac{MV^2}{2Dh} \times 10^3$	R_p
1	0.0508	1.33	3.05	14.3	0.114	2.24	8.33	0.20	44.4	18.74	18.6
2	0.0508	1.33	4.58	14.3	0.178	3.47	12.02	0.32	69.4	17.33	10.8
3	0.0508	1.33	6.10	14.3	0.229	4.47	16.58	0.41	89.3	18.57	9.1
4	0.0508	1.33	7.63	14.3	0.274	5.37	21.68	0.49	106.8	20.30	8.2
5	0.0381	0.72	3.05	14.3	0.122	3.24	7.78	0.22	65.9	11.81	10.9
6	0.0381	0.72	4.58	14.3	0.175	4.57	12.23	0.32	94.5	12.94	8.5
7	0.0381	0.72	6.10	14.3	0.229	6.03	16.58	0.42	123.7	13.41	6.6
8	0.0381	0.72	7.63	14.3	0.280	7.41	21.22	0.52	151.2	14.05	5.5
9	0.0381	0.24	3.05	14.3	0.053	1.38	17.91	0.29	85.9	20.86	44.7
10	0.0381	0.24	4.58	14.3	0.081	2.14	26.43	0.45	131.2	20.13	27.4
11	0.0381	0.24	6.10	14.3	0.102	2.69	37.22	0.56	165.2	22.53	24.7
12	0.0381	0.24	7.63	14.3	0.124	3.24	47.91	0.63	200.9	23.85	23.5

Table 5.8
Summary of Test Details for Dense Dry Sand
(after W. L. Wang, 1971)

Test Number	Diameter of Projectile (m)	Mass of Projectile (kg)	Impact Velocity (m/sec)	Dry Unit Weight (kN/m ³)	Depth of Penetration (m)	$\frac{h}{D}$	$\frac{V^2}{gh}$	$\frac{SD^2}{mg}$	$\frac{hD}{mg} \times 10^5$	$\frac{MV^2}{Dh} \times 10^3$	M_p
1	0.0508	1.33	3.05	17.3	0.063	1.26	14.95	0.18	24.8	61.36	65.9
2	0.0508	1.33	4.58	17.3	0.084	1.66	25.48	0.24	32.7	77.83	63.9
3	0.0508	1.33	6.10	17.3	0.107	2.09	35.49	0.31	41.7	85.09	54.8
4	0.0508	1.33	7.63	17.3	0.127	2.51	46.78	0.36	49.5	94.50	51.7
5	0.0381	0.72	3.05	17.3	0.071	1.86	13.37	0.21	38.5	34.87	34.2
6	0.0381	0.72	4.58	17.3	0.090	2.34	23.78	0.27	48.6	48.94	37.6
7	0.0381	0.72	6.10	17.3	0.101	2.62	37.59	0.30	54.5	68.93	47.3
8	0.0381	0.72	7.63	17.3	0.127	3.31	46.78	0.38	68.6	68.21	37.3
9	0.0381	0.24	3.05	17.3	0.020	0.52	47.46	0.18	32.4	146.51	507.1
10	0.0381	0.24	4.58	17.3	0.028	0.74	76.44	0.25	45.4	168.53	413.7
11	0.0381	0.24	6.10	17.3	0.046	1.20	82.54	0.41	74.5	110.77	167.8
12	0.0381	0.24	7.63	17.3	0.056	1.48	106.08	0.50	90.7	116.94	143.3

Solving further for the product of two unknowns,

$$N_p S = \frac{MV_o^2}{Dh^2}$$

For sand S is the shear strength at h .

Figure 5.6 shows the plot of $\log MV_o^2/Dh^2$ which is N_p multiplied by shear strength of the soil versus the $\log N_p$. For clay $\log N_p$ is less than one, and for sand it is greater than one. Shear strength of both soils increase to the right.

5.4 CLASSIFICATION RESULTS

Figure 5.7 shows the plot of two dimensionless ratios h/D and V_o^2/gh for clay. The third dimensionless ratio SD^2/Mg combines the effect of shear strength, diameter and mass of penetrometers into one constant that decreases from 0.42 to 0.05. These data points are from two sources. First the results of this study with 5 kPa clay shear strength and secondly the result of a study done by Dayal and Allen (6) with 10, 28 and 52 kPa clay shear strength. This figure is a valuable result for obtaining the shear strength of clay with dynamic penetrometer. A penetrometer with any mass, diameter and velocity limited to the range of the values in this study can penetrate into clay and by referring to this figure and determining the value of SD^2/Mg , the shear strength of the clay can be estimated. All of the points that appear in the figure are from different velocities that range from 2.23 m/s to 7.80 m/s and from different mass that vary from 0.875 kg to 25.71 kg and by two diameters that are 1.60 cm and 3.57 cm.

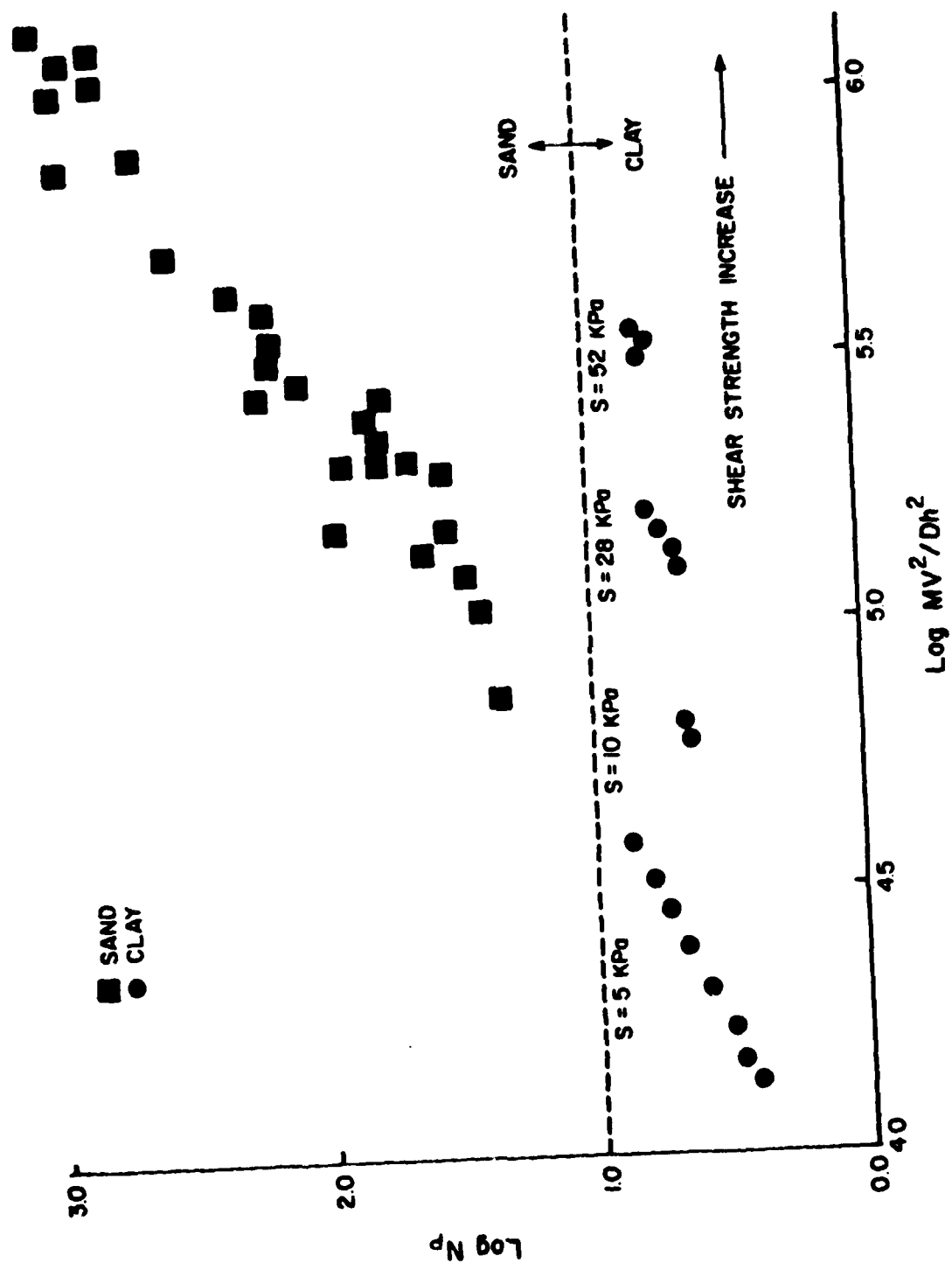


Figure 5.6 Classification of Soil Type by the Penetrability Constant

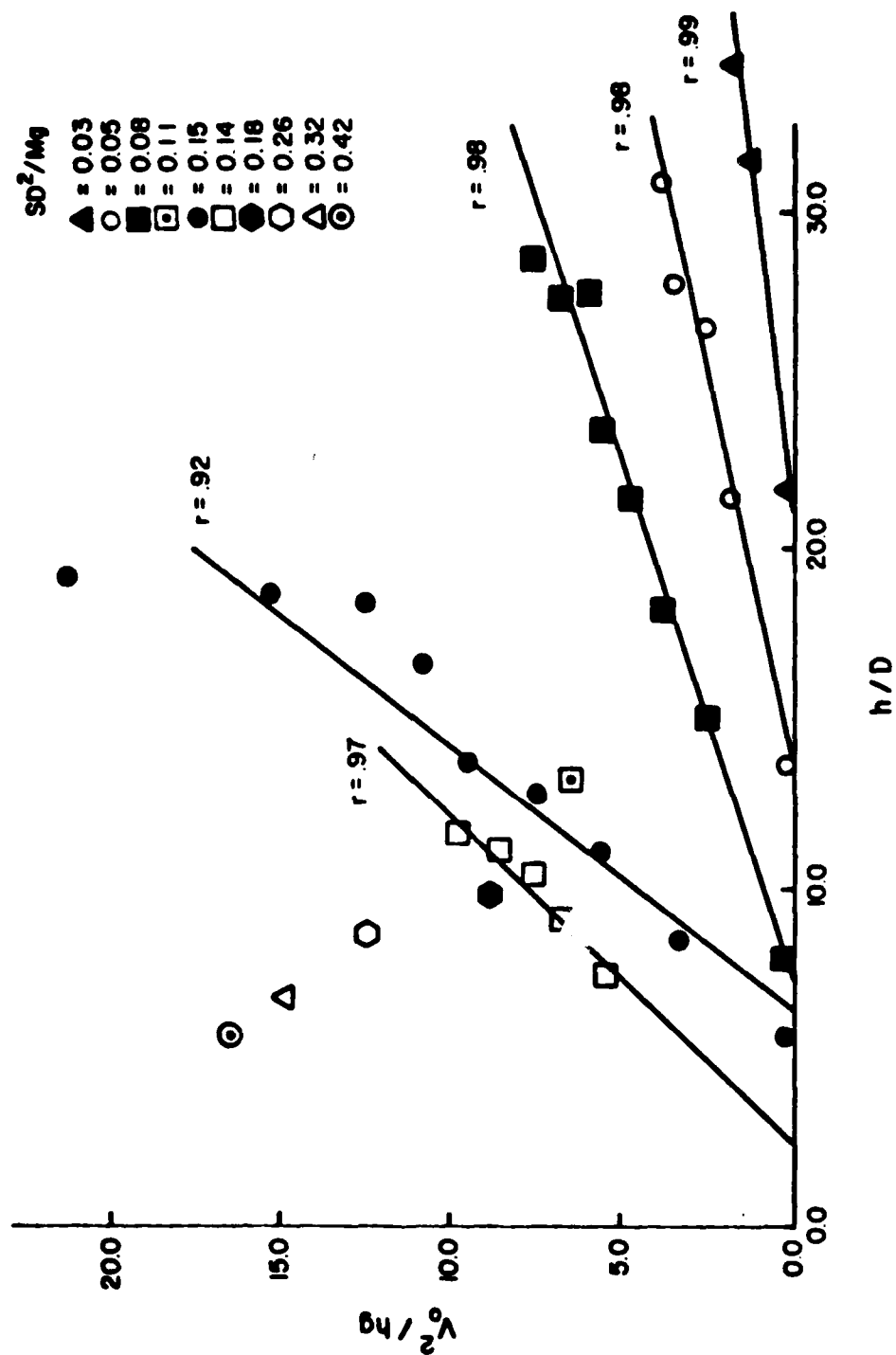


Figure 5.7 Plot of Two Dimensionless Ratios for Determination of Clay Shear Strength
(Shear Strength Varies from 5-52 kpa)

For example, a penetrometer with a mass of 20 kg and diameter of 3.0 cm penetrates into clay with impact velocity of 5.0 m/s. It penetrates 25 cm. What is the shear strength of the clay?

$$\frac{V_o^2}{gh} = \frac{(5.0)^2}{(9.8)(0.25)} = 10.20$$

$$\frac{h}{D} = \frac{0.25}{0.03} = 8.33$$

By referring to Figure 5.4, $\frac{SD^2}{Mg} \approx 0.24$

$$S = (0.24)(20)(9.8)/(0.03)^2$$

$$S = 52,266 \text{ N/m}^2 = 52 \text{ kPa}$$

In Figure 5.7 a distinction was lacking between sand and clay. The depth of penetration in clay with the same penetrometer is much more than the depth of penetration in sand. However, different penetrometers with different masses and diameters can create confusion in distinction between sand and clay. Therefore, the effect of mass and diameter were normalized for classification purposes. Ultimately the ratio hD/Mg was obtained which is not a dimensionless ratio.

Figure 5.8 shows the result of this normalization in clay. The shear strength of clay is directly obtainable by knowing V_o , h , D and M , and calculating the two ratios of V_o^2/gh and hD/Mg . The best line is fitted through each soil shear strength.

Figure 5.9 shows the result of the same normalization in sand. The sand with the higher strength behaves in a linear fashion. However, because of the variability of testing, the lower strength sand does not

AD-A116 157

LOUISIANA STATE UNIV BATON ROUGE DEPT OF CIVIL ENGIN--ETC F/6 8/10
CLASSIFICATION OF COASTAL SEDIMENTS.(U)
MAR 82 J N SUHAYDA, M TUNAY

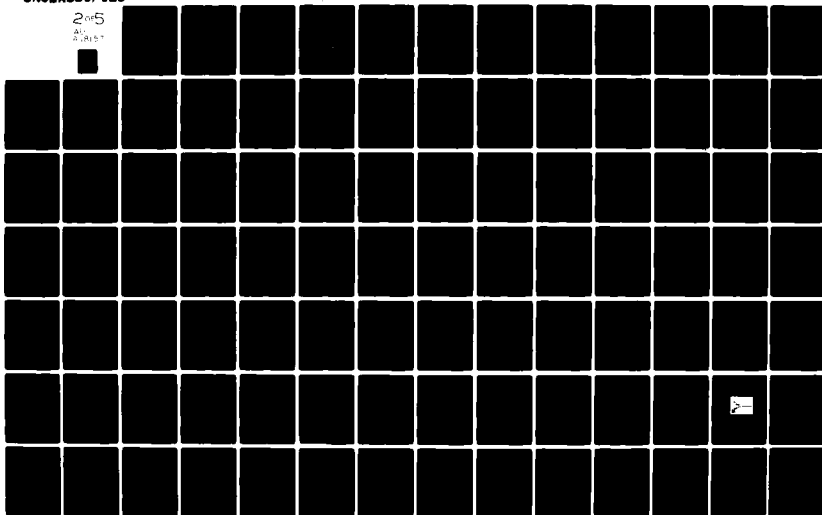
N00014-80-C-0846

UNCLASSIFIED

NL

2 of 5

ALL
RIGHTS



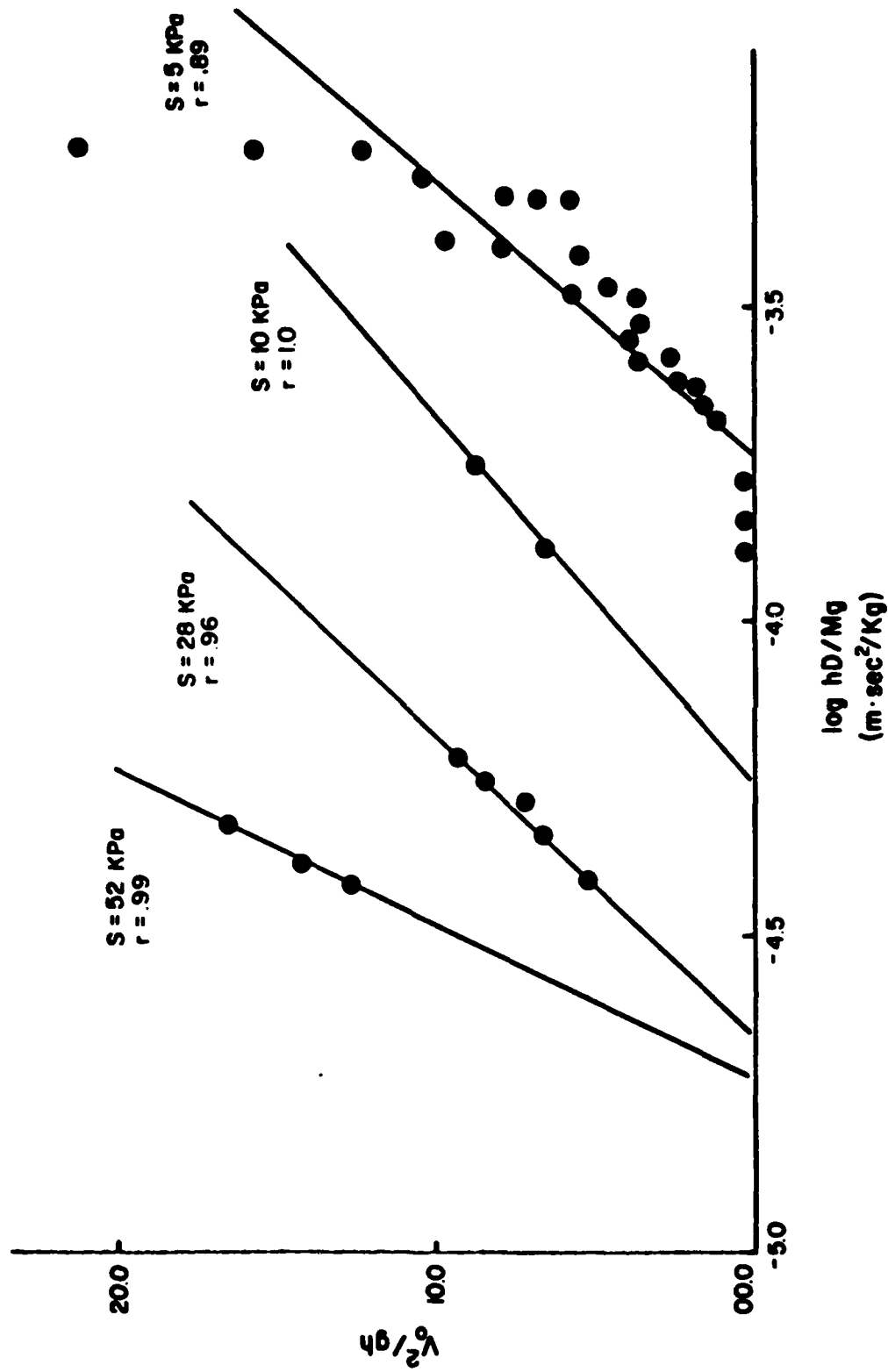


Figure 5.8 Determination of Clay Shear Strength by Normalization of all Penetrometer Characteristics

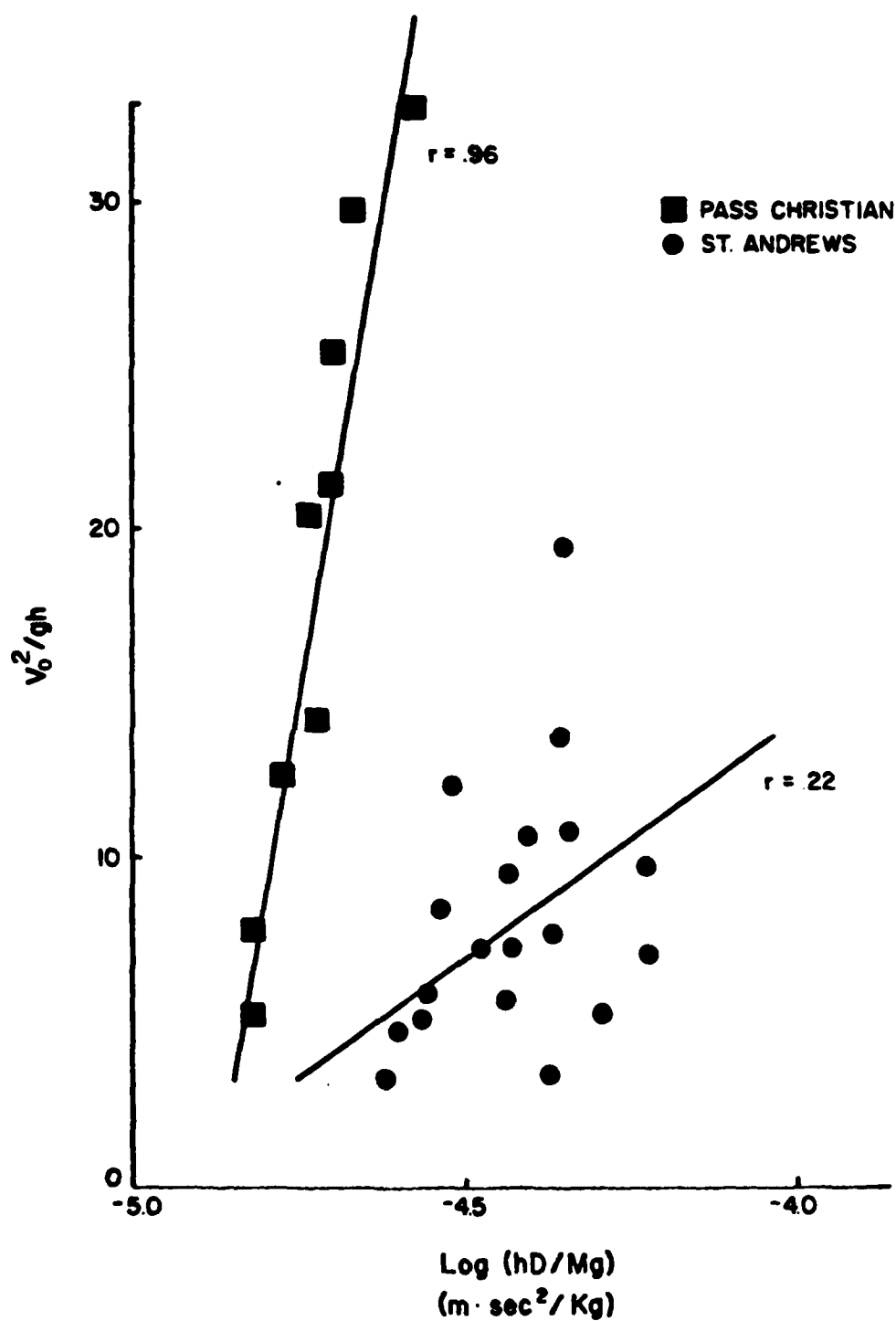


Figure 5.9 Distinction Between Sand Types by Normalization of Penetrometer Characteristics

behave linearly. This result can indicate that not all of the points have the same shear strength.

Because of the discrepancy between the values of hD/mg for sand and clay, the log values were observed.

Figure 5.8 and 5.9 are combined to present Figure 5.10. This figure classifies the soil type by dynamic penetration. For clay shear strength of 5, 10, 28 and 52 kPa are presented. As it can be observed the lower strength sand mixes with highest strength of clay. This suggests that in dynamic penetration low strength saturated sand behaves as high strength clay.

In the ocean bottom sediment, however, overconsolidated clay with shear strength of 52 kPa (1000 psf) is very rarely encountered. Therefore, by omitting the points of 52 kPa clay, any soil that falls to the right of the dotted line is considered clay and any soil that falls on the left side of dotted line is sand. The lower strength of clay are to the extreme right and the higher strength of sand are to the extreme left in Figure 5.10.

5.5 SHEAR STRENGTH

5.5.1 Determination of Shear Strength at Zero Impact Velocity

The depth of penetration under zero impact velocity describes a quasi-static penetration. In clay the depth of penetration with no impact velocity is higher than for sand. The ratio Mg/hD with h at zero impact velocity gives the shear strength of clay. For best results, h at $V_o = 0$ must be tested a few times to get a reliable values.

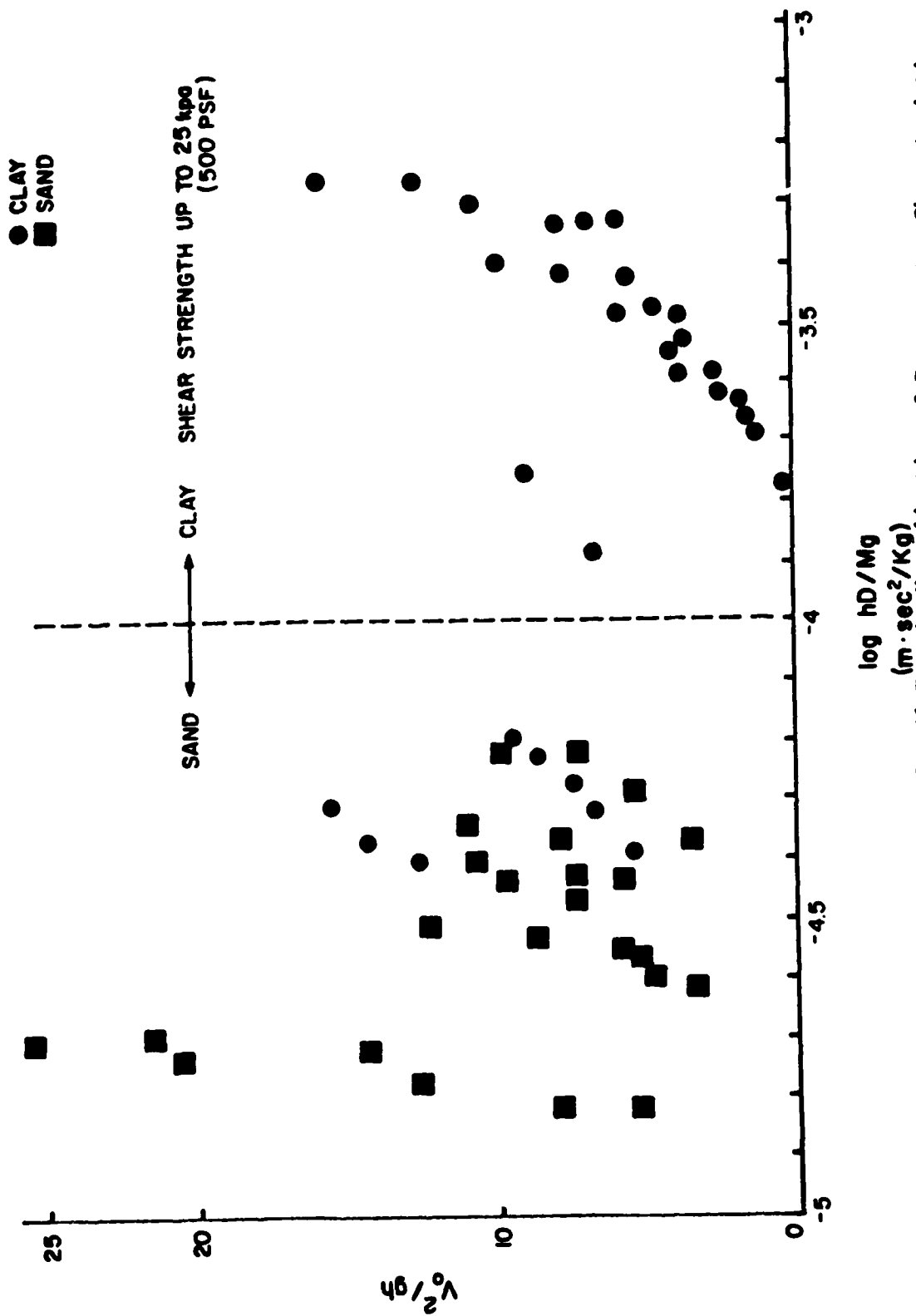


Figure 5.10 Classification of Soil Type by Normalization of Penetrometer Characteristics

For example, the laboratory testing of penetration with zero impact velocity results in 9 cm of penetration. The mass of the penetrometer was 0.875 kg with the diameter of 1.6 cm. Therefore,

$$s = \frac{Mg}{hD} = \frac{(0.875)(9.8)}{(0.09)(0.016)} = 5,950 \text{ N/m} = 5.95 \text{ kPa}$$

The measured fall cone shear strength of this clay was 5 kPa.

5.5.2 Pore Pressure Effects

The effect of dynamic pore pressures in sands are highly significant. The depth of penetration decreases greatly when pore pressures are present.

In the laboratory experimental testing in dry dense and loose sand were compared with saturated dense and loose sand.

In dry loose and dense sand the depth of penetrations were similar under the same penetrator conditions. This is attributed to the small confining pressures that were present and therefore no significant change in depth of penetration between dry loose and dense sand was observed. After addition of water to the loose dry sand and immediately dropping the penetrometer into the saturated sand, the depth of penetration was observed to be very high. This was due to the lower effective stresses that existed. The container was then vibrated and the sand was compacted. The sand consolidated in the tank for one month. The penetration tests were again performed. This time the depth of penetration was significantly reduced. Because of dilatancy effects, the negative pore pressures were created to increase the effective stress and consequently reduce the penetration.

The effect of pore pressures were observed in the field when the penetrometer was stopped momentarily at impact at the surface of sand and then continued to penetrate with less momentum. This suggests that the pore pressures were high enough to exceed the normal stresses and stop the penetrometer momentarily at surface.

Chapter 6

CONCLUSION OF RESULTS

1. Ocean bottom sediment types can be classified by dynamic penetrometers, given the total depth of penetration, the mass of penetrometer, the diameter of the penetrometer, and the velocity at impact provided it does not exceed the range of velocities tested in this study which was at maximum of 8 m/s.
2. In this study the most repeatable and adequate depth of penetrations were obtained by the heaviest penetrometer with the smallest diameter and the highest impact velocity. The following penetrometer characteristics are recommended.

Mass = 25 kg

Diameter = 2.5 - 3.0 cm

Impact Velocity = 5 - 10 m/s

Penetration into ocean bottom sediment with the above penetrometer characteristic will assure an adequate depth of penetration in both sand and clay.

3. Because of pore pressures, the total depth of penetration in saturated sand is significantly less than in clay with the same shear strength at that depth.
4. Shear strength of clay can be obtained by dynamic penetration, provided the penetrometer has adequate velocity and mass to sufficiently penetrate into clay.
5. The total depth of penetration under zero impact velocity condition can provide the shear strength of clay.

6. The dimensionless ratios h/D , V^2/gh and SD^2/Mg describe the distinction between sand and clay.
7. The effect of penetrometer nose shape is insignificant on the depth of penetration in sand for velocities up to 8 m/s.
8. The total depth of penetration increases with increasing velocity, increases with increasing mass and decreases with increasing diameter.
9. Logarithm of N_p , the penetrability factor, is less than one for clay and greater than one for dry and saturated sand. It increases with increasing velocity and decreases with increasing mass to diameter ratio.
10. Dynamic penetration resistance significantly exceeds the static bearing capacity of the soil due to pore pressure effects.
11. Dynamic pore pressures in sand are significantly high to cause large reductions in penetration. Further research of penetration into saturated sand is recommended.
12. The need for further research with instrumented dynamic penetrometer to measure tip resistance, sleeve friction and pore pressure is recommended.

REFERENCES

1. Backman, M. E., and Morrison, H. L., "The Fracture of Aggregates of Brittle Particles," Research Department, Properties of Matter Branch, U.S. Navy Ordnance Test Station, Inyokern, China Lake, CA, Nov., 1953.
2. Casagrande, A., and Shannon, W. L., "Strength of Soil Under Dynamic Loads," Transactions, ASCE, Vol. 114, 1949, p. 755.
3. Caudle, W. N., et al., "The Feasibility of Rapid Soil Investigation Using High-Speed Earth Penetrating Projectiles," SC-R-68-1736, Sandia Laboratories, Albuquerque, NM, Aug., 1967.
4. Chou, Y. T., "Penetration in Clay by the Visioplasticity Method," Proc. Conf. Rapid Penetration Terr. Mater., Texas A & M Univ., TX, 1972, p. 431.
5. Colp, J. L., "An Experimental Investigation of the Continuous Penetration of a Blunt Body into a Stimulated Cohesionless Soil," SC-RR-65-260, Sandia Corporation, Albuquerque, NM, 1965.
6. Dayal, V., Allen, J. H., Reddy, D. V., "Low Velocity Projectile Penetration of Clay," Journal of the Soil Mechanics and Foundation Division, ASCE, Vol. 106, No. GT8, Aug., 1980, pp. 919-937.
7. Dayal, V., "Instrumented Impact Cone Penetrometer," Thesis presented to the Memorial University of Newfoundland at St. John's, Newfoundland, Canada, in 1974, in partial fulfillment of the requirements for the degree of Doctor of Philosophy.
8. Dayal, V., and Allen, J. H., "Penetration Rate Effect on Soil Strength," Proceedings of the 27th Canadian Geotechnical Conference, 1974.
9. French, A. P., "Penetration of Ballistic Projectiles," Technical Note No. 10-57-P3, Department of Physics, University of South Carolina, Columbia, SC, 1957.
10. Fuchs, Otto P., "Impact Phenomena," AIAA Journal, Vol. 1, No. 9, 1963, pp. 2124-2176.
11. Goldsman, W., "Analytical Version of Penetration Process," AD273718, Armed Services, Technical Information Agency, Arlington Hall Station, Arlington, VA, Feb., 1962.
12. Harris, C. M., and Crede, C. E., Shock and Vibration Handbook, Vol. 2, McGraw-Hill Publishing Co., Inc., New York, 1961.

13. Healy, K. A., "The Dependence of Dilation in Sand on Rate of Shear Strain," Thesis presented to the Massachusetts Institute of Technology at Cambridge, Mass., in 1963, in partial fulfillment of the requirements for the degree of Doctor of Philosophy.
14. Knight, D. G., "Impact Penetration of Sand," Canadian Geotechnical Journal, Vol. 17, 1980, pp. 127-131.
15. Meyerhof, G. G., "The Ultimate Bearing Capacity of Wedge Shaped Foundation," Proceedings of the Fifth International Conference on Soil Mechanics and Foundations Engineering, Vol. 2, 1961, pp. 105-109.
16. McNeil, R. L., "Enhancement of Geophysical Soil Profiles Using Instrumented Marine Sediment Penetrations," OTC35261 Proc., Offshore Technology Conference, 1979.
17. McNeil, R. L., "Rapid Penetration of Terrestrial Materials, The State of the Art," Proc., Conf. on Rapid Penetration of Terrestrial Materials, Texas A & M University (1972).
18. Murff, J. D., and Coyle, H. M., "Low Velocity Penetration of Kaolin Clay," Journal of the Soil Mechanics and Foundations Division, ASCE, Vol. 99, No. SM5, Proc. paper 9737, 1973, pp. 375-389.
19. Murff, J. D., and Coyle, H. M., "A Laboratory Investigation of Low Velocity Penetration," Proceedings Conference on Rapid Penetration of Terrestrial Materials, Texas A & M Univ., College Station, TX, 1972, pp. 319-359.
20. Bea, R. G., and Audibert, J. M., "Offshore Platforms and Pipelines in Mississippi River Delta," Journal of the Soil Mechanics and Foundations Division, ASCE, Vol. 106, No. GT8, Aug., 1980, pp. 853-869.
21. Robertson, H. P., "Terminal Ballistics," Commission on Passive Protection Against Bombing, National Research Council, Washington, DC, 1941.
22. Schmid, W. E., "Penetration of Objects into Ocean Bottom," Civil Engineering in the Ocean II, ASCE, 1969, pp. 167-208.
23. Schimming, B. B., Hass, H. J., and Sexa, H. C., "Study of Dynamics and Static Failure Envelopes," Journal of the Soil Mechanics and Foundations Division, ASCE, Vol. 92, No. SM2, Proc. paper 4735, March, 1966, pp. 105-124.
24. Taylor, D. W., Fundamentals of Soil Mechanics, John Wiley & Sons, New York, 1948.
25. Thompson, L. J., "Dynamic Penetration of Selected Projectile into Particulate Media," Sandian Lab. Rep. Sc-R-R-66-376, Albuquerque, NM, 1976.

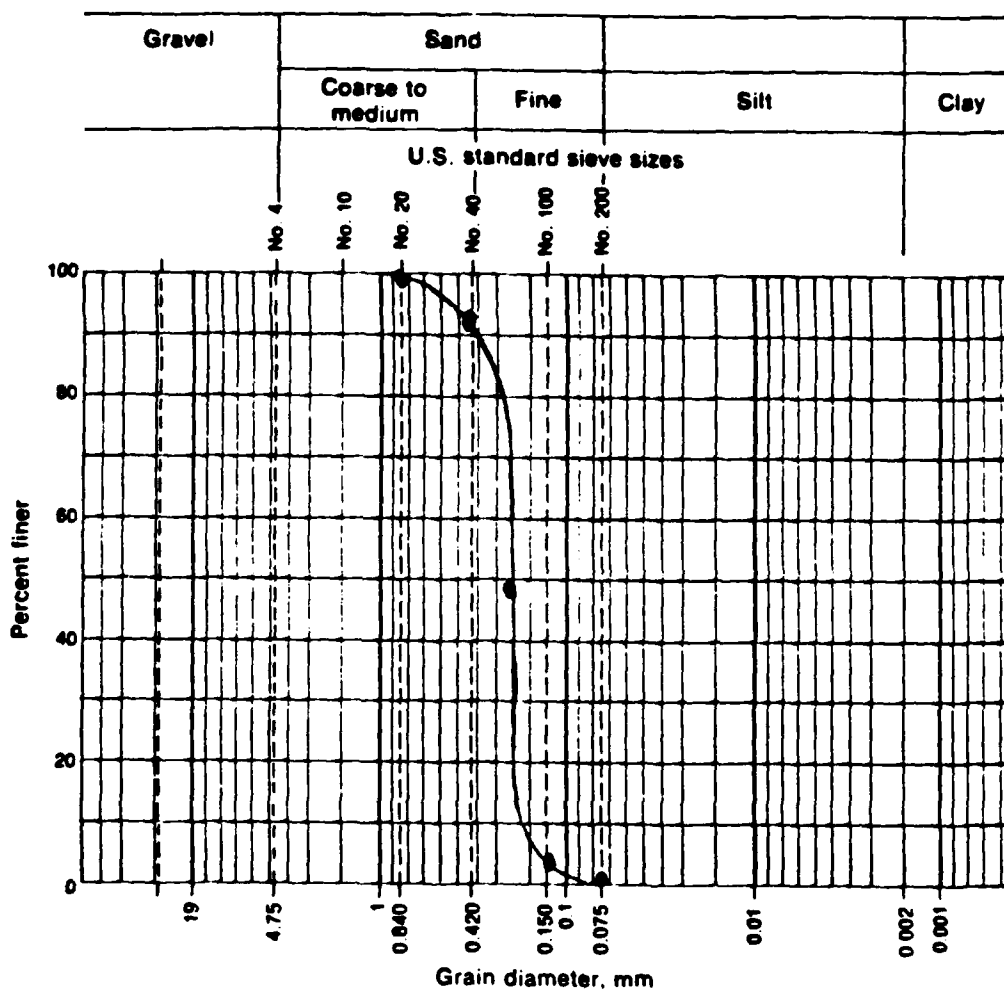
26. Thompson, L. J., and Colp, J. L., "Preliminary Evaluation of Earth Targets for Impact Effects Studies," SC-DR-316-63, Sandia Laboratories, Albuquerque, NM, March, 1964.
27. Wang, W. L., "Low Velocity Projectile Penetration," Journal of the Soil Mechanics and Foundation Division, Vol. 97, No. SM12, Dec., 1971.
28. Wilkes, P. R., "Marine Sediments Penetrometer Development of Sandia Laboratories," Proc. Conf. on Rapid Penetration of Terrestrial Materials, Texas A & M Univ., 1972.
29. Whitman, R. V., "The Response of Soils to Dynamic Loading Final Report," U.S. Army Engr. WES, Vicksburg, Miss., Contract No. DA-22-079-ENG-224, 1970.
30. Whitman, R. V., "The Behavior of Soils Under Transient Loading," Proc. 4th Int. Conf. Soil Mech. Found. Eng., London, England, Vol. 1, pp. 207-212.
31. Whitman, R. V., and Healy, K. A., "Shearing Resistance of Sand During Rapid Loadings," Mass. Institute of Technology, R62-113MIT, Cambridge, Mass.
32. Young, C. W., "Empirical Equations for Predicting Penetration Performance in Layered Earth Material for Complex Penetrator Configuration," SC-DR-77-0523, Sandia Laboratories, Albuquerque, NM, 1972.
33. De Ruiter, J., "Electric Penetrometer for Site Investigations," Journal of Soil Mechanics and Foundations Division, ASCE, Vol. 97, No. SM2, Proc. Paper 7907, Feb. 1971, pp. 457-472.

APPENDIX A
GRAIN SIZE DISTRIBUTION CURVES

GRAIN SIZE DISTRIBUTION

Data Sheet 6

Project _____ Job No. _____

Location of Project St Andrews Boring No. _____ Sample No. _____Description of Soil fine SAND Depth of Sample 40 cmTested By. _____ Date of Testing July 18 51

Visual soil description _____

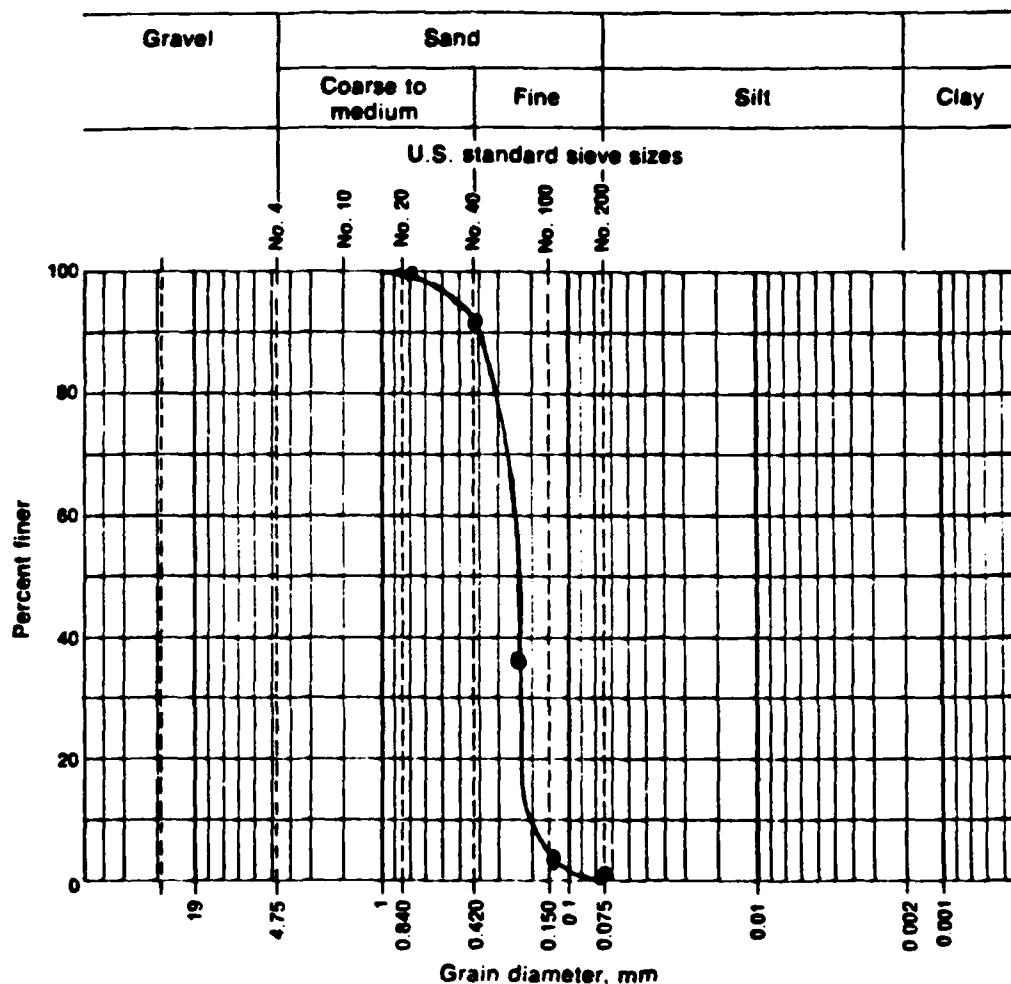
Soil classification:

_____ System _____

GRAIN SIZE DISTRIBUTION

Data Sheet 6

Project _____ Job No. _____

Location of Project Pass Christian Boring No. _____ Sample No. _____Description of Soil fine sand Depth of Sample 70 cmTested By. _____ Date of Testing July 20 41

Visual soil description _____

Soil classification: _____

System _____

APPENDIX B
CALCULATIONS OF SATURATED UNIT WEIGHT OF SAND

DETERMINATION OF SATURATED UNIT WEIGHT

St. Andrews

$$w = 32\%$$

$$G_s = 2.67$$

$$e = w G_s (2.67)(0.32) = 0.85$$

$$\gamma_{sat} = \frac{(G_s + e) \gamma_w}{1 + e} = \frac{(2.67 + 0.85) 62.4}{1 + 0.85}$$

$$\gamma_{sat} = 118.9 \text{ lb/ft}^3 = 18.60 \text{ kN/m}^3$$

Pass Christian

$$w = 21\%$$

$$G_s = 2.65$$

$$e = (2.65)(0.32) = 0.56$$

$$\gamma_{sat} = \frac{(2.65 + 0.56) 62.4}{1 + 0.56} = 128.5 \text{ lb/ft}^3 = 20.2 \text{ kN/m}^3$$

VITA

Behnam Nikakhtar was born on February 28, 1958 in Zahedan, Iran. He graduated from Robert E. Lee, Baton Rouge, Louisiana in May 1975. He enrolled in the Civil Engineering curriculum at Louisiana State University, Baton Rouge and received his Bachelor of Science degree in Civil Engineering in August 1979.

He became a Graduate Research Assistant in the Department of Civil Engineering of Louisiana State University in September 1979; he is now a candidate for the Master of Science degree.

DYNAMIC ANALYSIS OF SEDIMENTS OF GULF OF MEXICO
AND NUMERICAL SIMULATION OF MUD FLOWS

A Thesis

Submitted to the Graduate Faculty of the
Louisiana State University and
Agricultural and Mechanical College
in partial fulfillment of the
requirements for the degree of
Master of Science

in

The Department of Civil Engineering

by

Sibel Pamukcu
Bachelor of Science
Bogazici University
Istanbul, Turkey, 1978
December 19, 1981

APPENDIX B

Dynamic Analysis of Sediments of the Gulf of Mexico
and Numerical Simulation of Mud Flows

ACKNOWLEDGEMENTS

The author wishes to express her sincerest gratitude to her advisor and major professor Dr. Joseph N. Suhayda, for his valuable guidance, advice and expertise through the project. Without his generous academic and moral support this research could not have been done. Very special thanks are due to Dr. Jack K. Poplin, who spared his valuable time to teach, assist and improve the laboratory work and whose comments and suggestions have materially improved this research.

The author would also like to extend her sincerest gratitude to Prof. M. T. Tumay for his valuable support in every way which all along has played a very important role in her academic achievements.

Thanks are due to Prof. Roger K. Seals and Prof. R. L. Thoms whose comments and suggestions have been very beneficial through this research. A special thank you is extended to Prof. Ara Arman for his support and concern during the author's studies.

The author wishes to express her very special thanks and appreciation to her husband Mr. Derya Pamukcu for his continuous and valuable assistance in the computer work phase of this research and naturally his love, patience and encouragement throughout the entire period.

Special thanks are due to Mrs. Susan Sartwell for her beautiful and incredibly fast job in typing this thesis and her guiding editorial comments. Thanks are extended to Ms. Norma Duffy and her assistants for their excellent job in preparing the drawings.

This research was financed by the Office of Naval Research and the soil samples were provided by McClelland Engineers, Inc. The author expresses gratitude to both parties for making this study possible.

TABLE OF CONTENTS

	Page
ACKNOWLEDGEMENTS	ii
LIST OF FIGURES	vii
LIST OF TABLES	xi
LIST OF SYMBOLS	xii
ABSTRACT	xviii
 Chapter	
1. INTRODUCTION	1
2. THEORETICAL CONSIDERATIONS	10
2.1 BEHAVIOR OF SOFT CLAYS DURING CYCLIC LOADING	10
2.2 THEORETICAL CONSIDERATIONS IN WAVE PROPAGATION ANALYSIS AND MEASUREMENT OF DYNAMIC PROPERTIES	26
2.2.1 Wave Propagation Analysis in Elastic Media	26
2.2.2 Dynamic Testing Methods to Evaluate the Dynamic Moduli and Damping Characteristics of Soils	31
2.2.2.1 Resonant column test of soils	33
2.3 CRITICAL STATE MODEL FOR CYCLIC LOAD RESPONSE OF SOILS	54
2.3.1 Concepts of Critical State Soil Mechanics	56
2.3.2 Critical State Model for Cyclic Loading	64
3. METHODOLOGY	71
3.1 GEOGRAPHIC AND GEOLOGICAL INFORMATION OF SAMPLE SITE	71

3.2	EXPERIMENTAL PHASE	75
3.2.1	Sample Information and Utilization	75
3.2.2	Dynamic Experiments	76
3.2.2.1	Description of the apparatus and experiment setup	76
3.2.2.2	Specimen preparation and apparatus assembly	83
3.2.2.3	Testing procedures	86
3.2.2.4	Data reduction procedure	92
3.2.3	Experiments and Analytical Procedures to Evaluate Soil Index Properties and Shear Strength	95
3.2.3.1	Undrained triaxial tests	95
3.2.3.2	Plasticity analysis, classification and other index properties	96
3.2.3.3	Sensitivity experiments	97
3.2.3.4	Assumptions and formulations to estimate K_0 and μ	99
3.2.4	One Dimensional Consolidation Experiments Used in Critical State Soil Mechanics Analysis	100
3.3	NUMERICAL ANALYSIS PHASE	103
3.3.1	Wave-Propagation Viscoelastic Sea- Bottom Interaction Analysis	104
3.3.2	NONSAP - Nonlinear Structural Analysis Program	113
3.3.3	Utilization of NONSAP Using the Stress-Strain and Index Property Data Obtained for Boring B-6 Samples	119
3.3.3.1	Discretization	120
3.3.3.2	Mass and damping effects	122

3.3.3.3	Material model and layering	122
3.3.3.4	Loading curves and use of "restart" option	124
4.	RESULTS AND CONCLUSION	128
4.1	INDEX PROPERTIES OF THE CORE SAMPLES	128
4.2	RESONANT COLUMN TEST RESULTS	130
4.3	CRITICAL STATE ANALYSIS RESULTS	140
4.4	NUMERICAL ANALYSIS RESULTS	140
4.4.1	Wave-Propagation Viscoelastic Sea-Bottom Interaction Results	140
4.4.2	Results of NONSAP	142
5.	CONCLUSIONS AND RECOMMENDATIONS	154
	REFERENCES	158
	APPENDICES	
A	EXPERIMENTAL RESULTS	165
B	NUMERICAL ANALYSIS RESULTS	261
C	COMPUTER PROGRAMS, TYPICAL STRESS-STRAIN CURVES FROM UNDRAINED TRIAXIAL TESTS	286
VITA	315

LIST OF FIGURES

Figure		Page
1.	Rate of Pore Pressure Buildup (from Seed, et al. (50))	3
2.	Isopleth Map of Block 70 Based on Pre and Post Camille Surveys (from Bea, et al. (7))	5
3.	Schematic Diagram of Delta Front Instability Features (from Roberts, et al. (42a))	3
4.	A Typical Stress-Strain Hysteresis Loop (from Idriss, et al. (22))	11
5.	(a) Stress-Strain Curve of a Soil, (b) Bilinear Model (from Thiers, et al. (60))	12
6.	Hyperbolic Stress-Strain Relation (from Hardin, et al. (19))	12
7.	Determination of Material Damping from Torsion Shear Tests (from Stokoe (55))	14
8.	Idealized Shear Modulus Reduction Curve	14
9.	Summary of Normalized Shear Modulus Variation with Shear Strain (from Stokoe (55))	16
10.	Hysteresis Loops Measured During First Cycle (from Idriss, et al. (22))	16
11.	Stress-Strain Loop End Points at 10 and 100 Cycles of Loading (from Hardin, et al. (19))	17
12.	Stress-Strain Curves for Bilinear Models in San Francisco Bay Mud (a) Cycle No. 1, (b) Cycle No. 50, (c) Cycle No. 200 (from Thiers, et al. (60))	17
13.	Hysteresis Loops Measured During First and Tenth Cycles (from Idriss, et al. (22))	19
14.	Variation in Shear Modulus with Number of Cycles of Loading and Shear Strain (from Stokoe (55))	19

15. Variation in Degradation Factor with Shearing Strain (from Stokoe (55))	21
16. Schematic Illustration of Construction of Degraded Backbone Curves (from Idriss, et al. (22))	21
17. Effect of Cyclic Loading on Dynamic Moduli (a) Dynamic Modulus G_1 , (b) Dynamic Modulus G_2 (from Thiers, et al. (60))	23
18. Summary of Normalized Damping Ratio Variation with Shearing Strain (from Stokoe (55))	23
19. Longitudinal Vibration of a Rod (from Richart, et al. (42))	28
20. Torsion in Circular Rod (from Richart, et al. (42))	28
21. Normal Modes for Fixed-Free Rod (from Richart, et al. (42))	36
22. Schematic of Resonant Column End Conditions (from Hardin (17))	36
23. Forced Vibrations of a Single-Degree-of-Freedom System with Viscous Damping (from Richart, et al. (42))	39
24. Response Curves for a Viscously Damped Single-Degree-of-Freedom System (from Richart, et al. (42))	39
25. Dynamic Magnification Factor and Phase Angle Between Force and Displacement of an Undamped Single-Degree-of-Freedom System (from Richart, et al. (42))	42
26. Free Vibrations of a Viscously Damped System (a) Overdamped, (b) Critically Damped, (c) Underdamped (from Richart, et al. (42))	42
27. Typical Vibration-Decay Curve from Resonant Column Test (from Mississippi Delta Specimen Test)	45
28. Variation in Normalized Shear Modulus with Shearing Strain and Effective Confining Pressure (from Stokoe (55))	47

29.	Variation in Damping Ratio with Shearing Strain and Effective Confining Pressure (from Stokoe (55))	47
30.	Normalized Shear Modulus and Shear Strain Relation (from Hardin, et al. (19))	50
31.	Typical Modulus and Height Changes with Time for Clay at Constant Confining Pressure (from Anderson, et al. (1))	50
32.	Critical States (from Schofield and Wroth (47))	57
33.	Sections of the Yield Surfaces	57
34.	Critical State Yield Surface (from Schofield and Wroth (47))	61
35.	Yield Curves for Granta-Gravel and Cam-Clay (from Schofield and Wroth (47))	61
36.	Upper Half of State Boundary Surface for Cam-Clay (from Schofield and Wroth (47))	63
37.	Yield Curve for Cam-Clay (from Schofield and Wroth (47))	63
38.	State Space Response of an Isotropically Normally Consolidated Soil Cycled at the Critical Level of Repeated Loading (from Egan, et al. (15))	66
39.	Vicinity Map for Block 75 Main Pass of Mississippi Delta (from McClelland Engineers Geotechnical Report (30))	72
40.	Depth Profile of Boring B-6 and Location of Samples	74
41.	Drnevich Resonant Column Apparatus	77
41A.	Details of the Sample Setup and Coil System	78
42.	Electronic Device Setup of the Resonant Column	79
43.	Electrical Wiring Diagram for a Typical Drnevich Resonant Column Apparatus	82
44.	Typical Lissajous-figure (obtained from one of the tests with a Mississippi Delta Sediment Specimen)	90

45.	Cross-Section of Water Clay System (from Schapery (45a))	106
46.	Stress-Strain Diagram for a Linear Viscoelastic Material under Harmonic Straining (from Schapery (45a))	109
47.	Schematic Representation of the Stress- Strain Diagram for Sediment Under Cyclic Straining (from Schapery (45a))	109
48.	Stress-Strain Behavior of Von Mises Material Model	117
49.	Stress-Strain Behavior of Drucker- Prager Material Model	117
50.	Finite Element Discretization of Soil Matrix for NONSAP Model	121
51.	The Imaginary Configuration of the Finite Element Model to Estimate Nodal Masses	127
52.	Sinusoidal and Modified Loading Functions for Finite Element Analysis	127

LIST OF TABLES

Table		Page
1.	Summary of Index and Critical State Parameters for Clays and Silty Clays (from Egan (14))	70
2.	Confining Pressures of Samples in Resonant Column Test	88
3.	Sensitivity Analysis Results	98
4.	Some Index Properties of Samples of Boring B-6	147
5.	Regression Constants for Curve Fitting of G versus γ	148
6.	Damping Information and Rayleigh Damping Coefficients	149
7.	Regression Constants for Curve Fitting of τ versus γ	150
8.	Shear Strength Data of Core Samples	151
9.	Consolidation Test Parameters	152
10.	Critical State Parameters	153

LIST OF SYMBOLS

A	Hyperbolic equation constant
A	Amplitude of displacement
A_L	Area contained within hysteresis loop
A_T	Area contained under equivalent secant modulus
A	Area
a	Acceleration displacement
B	Hyperbolic equation constant
C	Hyperbolic equation constant
[C]	Damping matrix
C_c	compression index
C_r	Rebound index
c	Cohesion
c	Damping
c_c	Critical damping
c_u	Undrained shear strength
D	Damping ratio
D_{min}	Minimum damping ratio
d	Diameter
d	Water depth
E^*	Complex elastic modulus
E	Elastic modulus
e	Void ratio
e_o	Void ratio at in-situ mean effective stress
$(E_s)_N$	Secant modulus at cycle N

$(E_s)_1$	Secant modulus at the first cycle
$F(t)$	Load function
F	Nodal point force vector
F_A	Age factor
f_n	Natural fundamental frequency
G	Shear modulus
G^*	Complex shear modulus
$ G $	Magnitude of complex shear modulus
$G(t)$	Relaxation modulus
G'	Real part of complex modulus
G''	Imaginary part of complex modulus
G_1	Elastic component of complex modulus
G_2	Viscous component of complex modulus
G_1	Equivalent linear viscoelastic modulus
G_o	Strain dependent modulus
G_c	Shear modulus at critical state
G_s	Secant shear modulus
G_{max}	Maximum shear modulus
H	Wave height from crest to trough
I_p	Polar moment of inertia
I_G	Coefficient of shear modulus increase with time
J	Mass polar moment of sample
J_o	Mass polar moment of attached weight on the sample
$[K]$	Stiffness matrix
K_o	Lateral earth pressure coefficient
k	Stiffness
L	Length

L	Wave length
l	Length
l	Wave number
l_1	Real part of wave number
l_2	Imaginary part of wave number
[M]	Mass matrix
M	Magnification factor
M	Frictional soil constant
m	Mass
N	Number of cycles
N	Number of cycles required for liquefaction
n	Constant related to liquidity index of material
p'_o	Mean effective stress
Q_o	Amplitude of harmonic force
q	Deviator stress
R	External load vector
r_u	Pore pressure ratio
r	Radius
r_a	Acceleration radius
S	Sensitivity
s_u	Undrained shear strength
s_c	Stress term
T_p	Wave period
t	Degradation parameter
t	Time
t'	Reference time
T	Torque

u	Axial displacement
u_c	Horizontal displacement component
U_{od}	Distortion energy
V	Velocity
v_c	Vertical displacement component
v	Volume
V_p	Velocity of compression waves in infinite elastic medium
V_s	Velocity of shear waves in infinite elastic medium and elastic rod
V_c	Velocity of compression waves in elastic rod
V_r	Ratio of compression wave velocity to shear wave velocity in infinite elastic media
W	Weight
x_1, y_1	Reference data point
α	Rayleigh damping coefficient
β	Rayleigh damping coefficient
β	Experimental constant for resonant column test
γ	Shear strain
γ_r	Reference shear strain
γ_y	Yield shear strain
γ_c	Critical state shear strain
γ_{max}	Maximum shear strain
γ	Unit weight
Γ	Basic soil property constant
Γ	Gamma function
δ	Degradation index
δ_L	Phase angle
δv	Volumetric strain

ϵ_1	Axial strain
ϵ_2, ϵ_3	Radial strains
ϵ_v	Volumetric strain potential
n	Frictional constant, ratio of deviator stress to mean stress
θ	Angular rotation
κ	Rebound index
λ	Compression index
λ	Constant related to wave number
μ	Poisson's ratio
μ	Viscosity
π	Volume change potential
ρ	Mass density
σ	Stress
$\bar{\sigma}_o$	Effective octahedral normal stress
$(\sigma_d)_N$	Deviator stress at cycle N
$(\sigma_d)_1$	Deviator stress at cycle 1
σ_{yp}	Yield stress
σ'_{yp}	Tensile yield stress
σ''_{yp}	Compressive yield stress
$\sigma_1, \sigma_2, \sigma_3$	Principal stresses
τ	Shear stress
$\bar{\tau}_o$	Octahedral shear stress
τ_{oct}	Octahedral shear stress
τ_{yp}	Yield shear stress
τ_y	Yield shear stress
τ_{max}	Maximum shear stress
τ_c	Critical state shear stress

τ_f	Failure shear stress
ϕ	Phase angle
ϕ	Friction angle
ω	Circular frequency
ω_n	Natural fundamental circular frequency
ω_{\min}	Minimum circular frequency

ABSTRACT

Samples from a single borehole located near Main Pass of the Mississippi River at water depth of 10 m were tested in Drnevich resonant column apparatus for their dynamic properties. Index properties of the samples indicated high water contents of 60-80 percent, and shear strength data indicated very soft weak material for the top 60 m of borehole. The maximum shear modulus values at each depth were predicted by hyperbolically fitting the experimental values of shear modulus measured at different shear strain amplitudes (ranging from 10^{-4} to 1.0 percent). Using the shear modulus-shear strain variation data, cyclic shear stress versus shear strain were also correlated. The nonlinear stress-strain curves were represented as bilinear curves following Von-Mises yield criterion. Experimental curves of damping with shear strain amplitude were used to estimate the minimum damping ratio and damping characteristics for several specimens. The material properties obtained through the testing procedures were then incorporated in two distinct numerical solution techniques, a viscoelastic subbottom wave interaction solution technique, and a nonlinear finite element program, NONSAP. The apparent advantages and disadvantages of each technique in the process of providing foundation design data for offshore structures with regard to mudflow problems of the area are discussed. A preliminary study to incorporate critical state soil mechanics concepts into mudflow analysis was also conducted and results were discussed.

Chapter 1

INTRODUCTION

Marine sediment instabilities are known to be one of the major design concerns for offshore structures. The severity of the problem is limited to the local material properties and loading conditions. Several theories providing methods to analyze marine subbottom movements are as follows:

1. Infinite slope stability analysis (35,39)
2. Simple rheological model analysis (59)
3. Wave-propagation and viscoelastic subbottom interaction analysis (45,54,26)
4. Spontaneous liquefaction due to progressive pore pressure build up under cyclic wave loading

A recent approach suggests employing Critical State Soil Mechanics method (14). Since, no literature concerning the application of the method to the specific problem of marine instabilities is encountered, it is not included in the above list of theories. Nevertheless, a pioneering study on some ways of employing the critical state method will be included here in this study.

Infinite slope stability analysis is one of the early attempts to study the mechanism of submarine sediment slides. Mitchell, et al. (35), did not observe infinite slope stability failure along circular arcs conducting model tests. In a more recent study by Prior, et al. (39), a failure condition from the geometry of the slope was formulated, and an equation of pore pressure in soil matrix at failure was derived.

Analytical pore pressure results at failure in Mississippi Delta sediments, were well above geostatic stresses. Consequently, one could conclude that the progressive pore pressure buildup raising the condition of liquefaction, would provide an analogical approach to the high pore pressure criteria of failure in this study. Considering the fact that the sediment slides in the Mississippi Delta area, generally initiate at very low slopes ranging from 0.5 to 2.0 percent, attributing the initial failure to high pore pressures would be favorable.

Liquefaction theory is one of the well developed analysis in soil dynamics area. Numerous studies on liquefaction behavior of saturated cohesionless soils, under various types of dynamic loadings, are frequently encountered throughout geotechnical literature. Cyclic wave loading analysis of marine sediments of cohesionless type, consequently, related design procedures for offshore structures employ liquefaction theory (40,27,32,51). Various numerical solution techniques evaluate the pore pressure response of soil matrix before and/or after the liquefaction under the induced cyclic loading (27,10,33,51). When saturated sands are subjected to cyclic loading, as earthquake vibrations or wave pressures on offshore sediments, they tend to compact and decrease in volume. If drainage is unable to occur, the volume change is replaced by an increase in pore water pressure. When pore pressure builds up so that it is equal to the overburden stress, the effective stress which is transmitted through grain contact points, diminishes to zero and the sand loses its strength, passes to a "liquefied state". The relation between the number of cycles of loading versus the pore pressure ratio r_u , is illustrated in Figure (1), where N_L is the number of cycles of loading required for the material to reach a

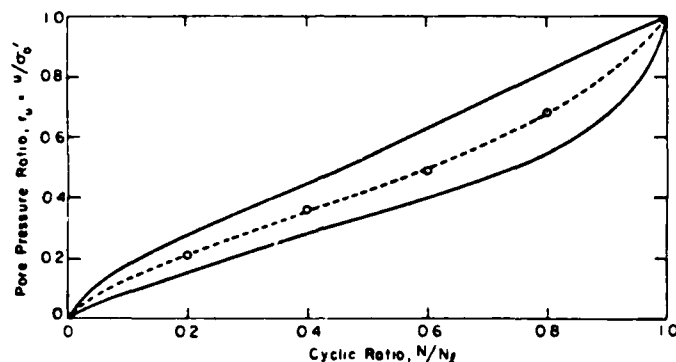


Figure 1. Rate of Pore Pressure Buildup (from Seed, et al. (50))

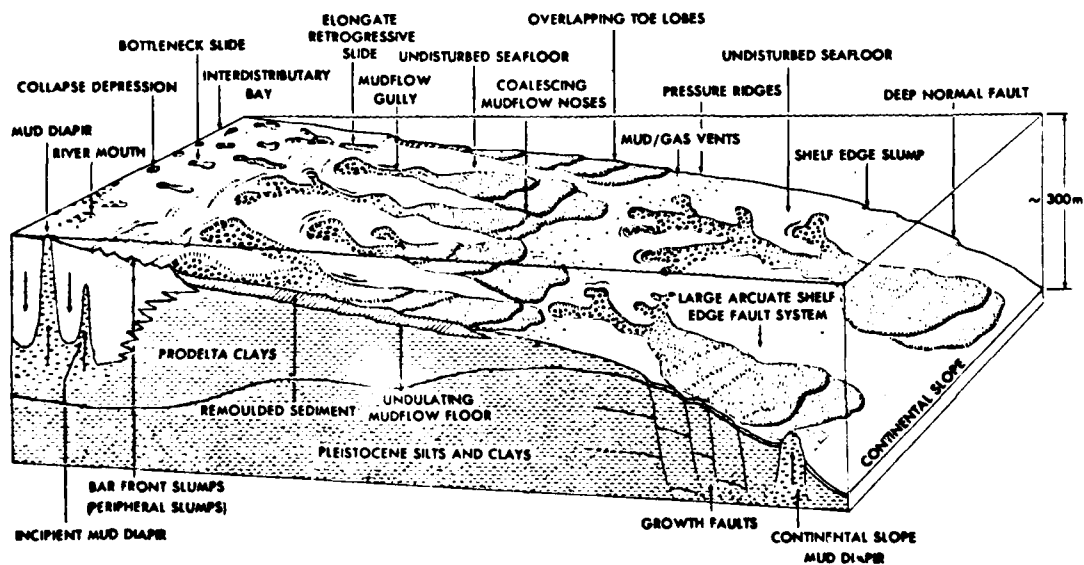


Figure 3. Schematic Diagram of Delta Front Instability Features (from Roberts, et al. (42.a))

"liquefied" state. Response of saturated cohesive soils under cyclic loading is not termed as "liquefaction". Nevertheless, reduction in effective stress with increasing pore pressure under undrained conditions, reduction of shear modulus with increasing shear strain and number of cycles of loading, and damping affects are common responses for both cohesive and cohesionless saturated soils under dynamic loading. These common aspects, plus in-situ and experimental observations of high pore water pressures in several areas of cohesive nature (39,20,8,41) allows one to study the mechanism of failure in cohesive marine sediments through dynamic response analysis coupled with an analogy to "liquefaction" behavior.

Massive sediment movements initiated by the cyclic wave loading in Mississippi Delta region, are known to cause failure of anchoring and supporting piles of oil platforms located in that area. Two of the very well known incidents are the failure of Shell Oil Co. South Pass Block 70B and Gulf Oil Co. South Pass Block 61 oil platforms after hurricane Camille in 1969 (53). A survey by Shell Oil Co. on the bottom of Block 70 of South Pass area of Delta, before and after the hurricane, indicated a sediment wave front movement toward southeast, building up over a width of 8,000 ft., to a depth of 10 to 35 ft. Behind the moving mud front the bottom was depressed up to 5 ft. over an area of more than 750 acres (7). Movement of the sediment mass is illustrated in Figure (2). The slides are known to occur in slopes which, according to conventional slope stability analysis, should be stable. The average value for these slopes is 1.0 percent. A technical report investigating the engineering properties of shallow sediments in some

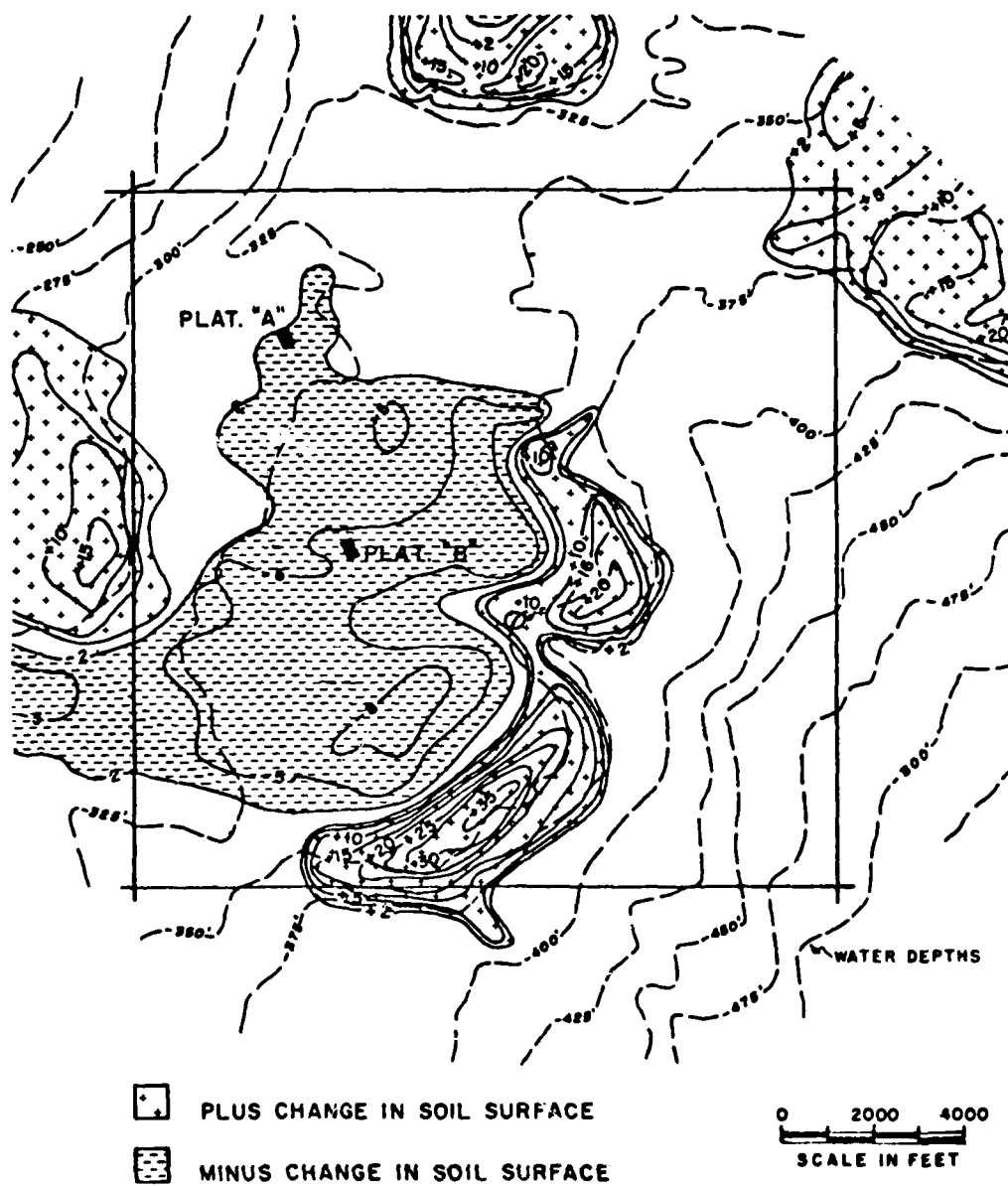


Figure 2. Isopleth Map of Block 70 Based on Pre and Post Camille Surveys (from Bea, et al. (7))

parts of Mississippi Delta area, describes the nature of the subbottom soil as generally weak, highly plastic and underconsolidated clays (52).

The main concern of the investigation reported herein is about the dynamic response of these highly plastic, weak clay sediments of Mississippi Delta region. As stated earlier, the cohesive nature of the material limits the application of already existing analytical and numerical solution techniques used in liquefaction to evaluate the mechanism of instability. Consequently, other theories, particularly applicable to the soft sediments are reviewed. One of the major studies in this area was done at Texas A & M University, under the supervision of R. A. Schapery (45,54,26). A numerical solution technique that finds the displacements, strains, velocities and accelerations in soil matrix of a specified thickness in response to the cyclic loading of a continuous wave train was formulated. The numerical solution employs continuum mechanics with nonlinear viscoelastic material properties. Based on soil displacements, the technique further evaluates the lateral forces induced on oil platform piles. Since the stability of the platforms depend on the anchoring piles that would resist the very large lateral and overturning loads, the evaluation of soil displacements, velocities and in turn, their impact on the piles become very important parameters in offshore design techniques.

A more recent investigation uses a rheological model to derive equations defining the initial failure of slope, mass movement thickness, accelerations, velocities and the shape of sediment deposition after the completion of flow in channels termed as "gullies" (59). A schematic diagram describing the various features of marine instabilities as reviewed by the investigators of this study is given in

Figure (3). Some of the features are identified as collapse depressions, bottleneck slides, elongate slides, shallow rotational slumps and mudflow gullies.

Earlier numerical solutions developed include the finite element model by Bea, et al., in which the soil properties are translated to terms of lateral movements through application of static, nonlinear and two dimensional mathematical formulation. The model estimates the amount of lateral force developed by moving soils (6). The solution technique stands to be one of the pioneering works to the viscoelastic subbottom wave interaction solution of Schapery, et al. It also represents a significant improvement over infinite slope stability analysis.

In this study, an attempt to employ another numerical solution technique, namely the finite element program, NONSAP (Nonlinear Structural Analysis Program) developed by Bathe, et al. at the University of California, Berkeley, will be presented. NONSAP evaluates the displacements, velocities and accelerations induced by design loads within a nonlinear continuum. This in turn enables one to predict the unbalanced forces that cause the soil mass to move and its impact on offshore structures. The effort to predict the lateral and overturning forces is not within the scope of this work. Only the displacement and velocity profiles obtained using NONSAP and WAVE AND VISCOELASTIC SEA BOTTOM INTERACTION solution methods, to provide a basis for further work on evaluation of forces, will be presented.

Dynamic forces induced on the sediments by cyclic wave loading brings about the need to evaluate the dynamic properties of these sediments in concern. The phase one effort of this study will provide

the theoretical information section on the general behavior of cohesive soils under cyclic loading. Phase two will cover the dynamic experiment procedures conducted in laboratory and their evaluated results.

Application of the numerical solution techniques using these dynamic properties will constitute the phase three effort of this study. Deep core samples taken from Main Pass Block 75 of Gulf of Mexico by McClelland Eng. Co. for Texaco Oil Co. were donated to LSU Geotechnical Laboratory for research purposes. These samples were from a single boring, ranging from 0.2 to 110 meters in depth, from mudline. Dynamic properties for the samples were obtained through a series of torsional vibration resonant column tests. Reduction of shear modulus, G with increasing shear strain amplitude, γ ; backbone curve of a series of hysteresis loops, and variation of damping ratios, D , with shear strain amplitude for each sample were obtained as a result of these tests. Results provided the data used in numerical solution schemes, discussed earlier. Consequently, a nonhomogeneous layered media was represented in the numerical models.

Finally, intermitted within the consecutive phases of this study, another mechanical evaluation of the mud slides employing critical soil mechanics theory is presented. The theoretical background information about critical soil mechanics concept is included in phase one section. Related experimental procedures and using the data obtained in program NONSAP are presented in the following two phases, respectively. A series of consolidation tests on several arbitrarily chosen samples were conducted. Analysis of the undisturbed and remolded sample compression curves provided the data used in the numerical solution. As stated previously, findings through critical state method will be presented

only as a basis for further work on the subject matter, since it would require detailed and comprehensive work to formulate the final solution for the particular problem of mud flows using this technique.

The study presented herein will provide a transitional step in applying different experimental procedures to already existing numerical solution technique, in order to evaluate the instability of Mississippi Delta sediments in the Gulf of Mexico. These various approaches will be comparative in nature, but no conclusion as to which would provide the most applicable design criterias will be drawn, since it would require further work on the loading mechanism of offshore piles. It is the author's conclusion that, more effort should be directed on the integrity of the engineering property data obtained from the soft, gaseous, and easily disturbed sediments obtained from the Mississippi Delta subbottom. Consequently, in-situ evaluation of shear strength and pore water and gas pressures coupled with the dynamic property data obtained either through undisturbed laboratory samples or indirect in-situ procedures, would provide higher reliability and integrity to the numerical solution results.

In summary, the main objective of this study is to provide information on the measurement of dynamic soil properties through resonant column apparatus, and emphasize the various uses of data obtained through this experimental procedure in numerical solution techniques for mudflow analysis. These techniques in turn yield the necessary foundation design parameters for offshore structures with regard to mud flow problems. Note that evaluation of these design parameters is not within the scope of this work.

Chapter 2

THEORETICAL CONSIDERATIONS

Behavior of soft clays during cyclic loading, evaluation of dynamic properties through dynamic testing and the discussion of a representative critical state soil mechanics model are presented in this section in an effort to provide theoretical information for the experimental phase of this study.

2.1 BEHAVIOR OF SOFT CLAYS DURING CYCLIC LOADING

During cyclic loading, the stress strain behavior of clays is nonlinear and hysteretic. A hysteresis loop consists of 3 stages during one cycle of loading. They are the initial loading, unloading and reloading stages. The initial loading constitutes the "backbone" curve of the loop. An idealized stress-strain hysteresis loop obtained for a soil specimen subjected to a symmetric cyclic shearing load along a plane free of initial shear stress is given in Figure (4). The backbone curve characterizes the nonlinear stress-strain behavior of clays. G_{\max} is the maximum shear modulus defined as the slope of the initial tangent to the backbone curve. G_s is the secant modulus equal to the τ_c / γ_c ratio, where τ_c and γ_c are the maximum cyclic shear stress and maximum cyclic shear strain, respectively.

Masing criterion is the most widely accepted rule for generating hysteresis loops from backbone curve (34). It simply states that the unloading and reloading branches of the loop are the same backbone curve with both stress and strain scales expanded by a factor of two and the

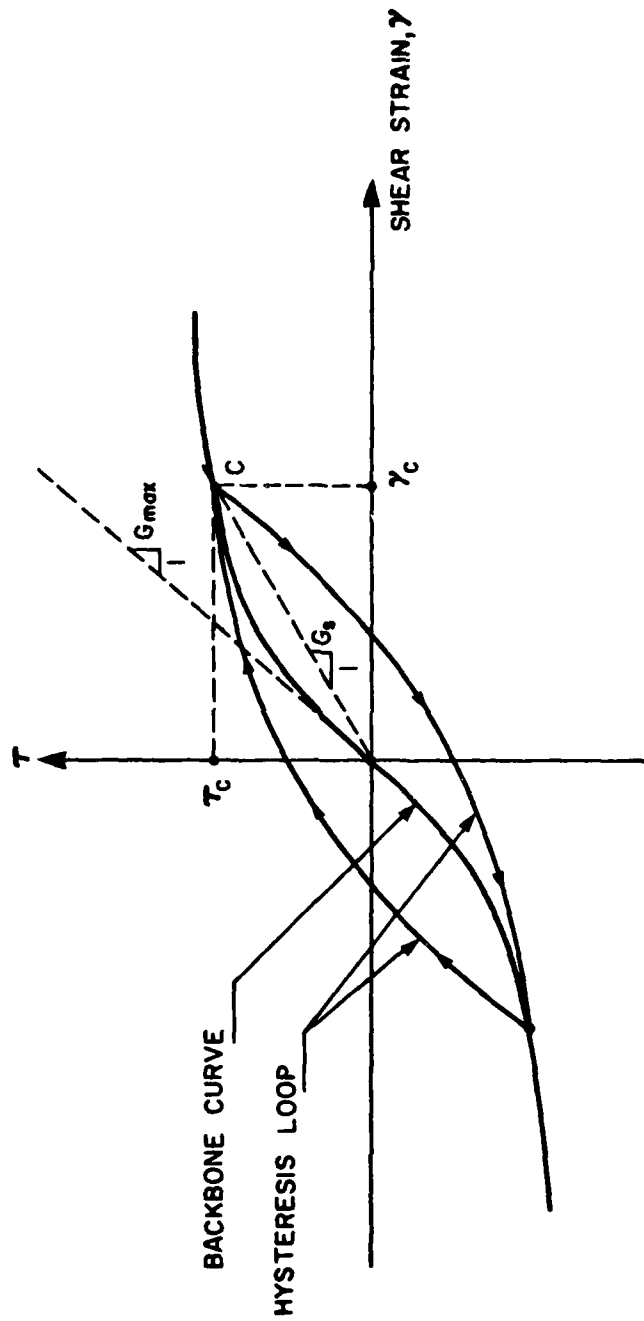


Figure 4. Typical Stress - Strain Hysteresis Loop (from Idriss, et al. (22))

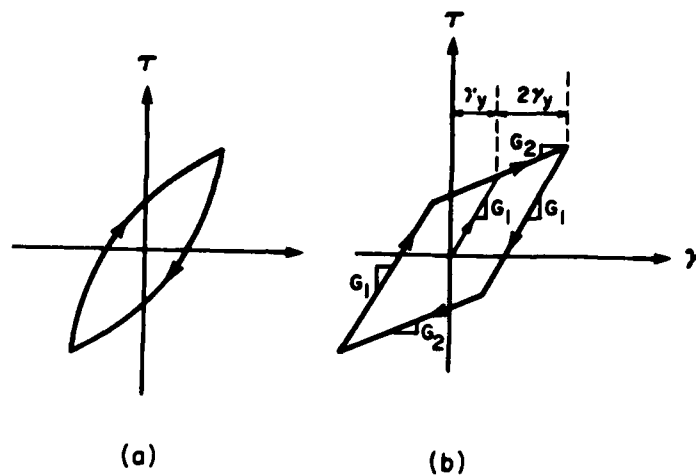


Figure 5. (a) Stress - Strain Curve of a Soil
 (b) Bilinear Model
 (from Thiers, et al. (60))

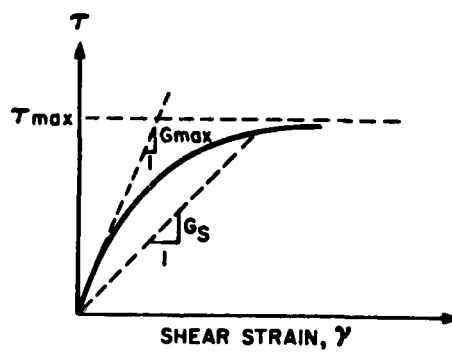


Figure 6. Hyperbolic Stress - Strain Relation (from Hardin, et al. (19))

origin translated. After the stress reversal, the tangent modulus at the tips of the loop is equal to G_{\max} . The backbone curve is expressed in several mathematical formulations which include bilinear (Figure (5)) (60), multilinear, hyperbolic (Figure (6)) (19) and Ramberg-Osgood (Figure (4)) (22) formulations.

In this study, the hyperbolic formulation will be adapted. The equation of the backbone curve according to hyperbolic formulation is as follows:

$$\tau = \frac{\gamma}{\frac{1}{G_{\max}} + \frac{1}{\tau_{\max}} \gamma} \quad (1)$$

where, τ_{\max} is the shear stress at failure.

Damping ratio D , is defined as the ratio of the energy dissipated to energy input during one cycle of loading. D is computed on the basis of the area contained within the hysteresis loop, A_L , and the equivalent secant modulus, A_T , as shown in Figure (7). The equation for the damping ratio given by Hardin and Drnevich (19) is:

$$D = \frac{1}{4\pi} \frac{A_L}{A_T} \quad (2)$$

Systems that satisfy the Masing criterion behave as though they had an equivalent viscous damping ratio independent of the frequency vibration at a given shear strain value (19,22).

Reduction of moduli with increasing strain amplitude is a major characteristic displayed by the nonlinear nature of the stress-strain relationship of soils. In clays, reduction of moduli is generally accompanied by degradation of backbone curve. Concentrating first on the reduction of moduli aspect, the following figures are presented to illustrate this affect. Figure (8) gives an idealized shear modulus reduction curve, where by extrapolating the curve to zero strain, the

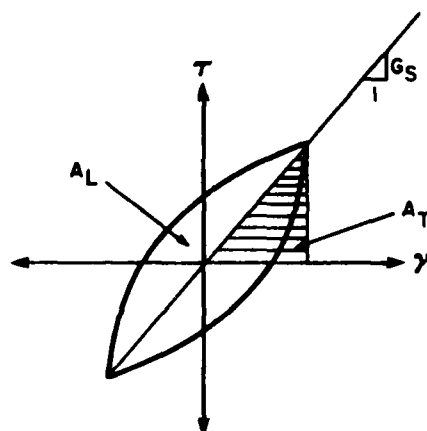


Figure 7. Determination of Material Damping from Torsional Shear Tests
(from Stokoe (55))

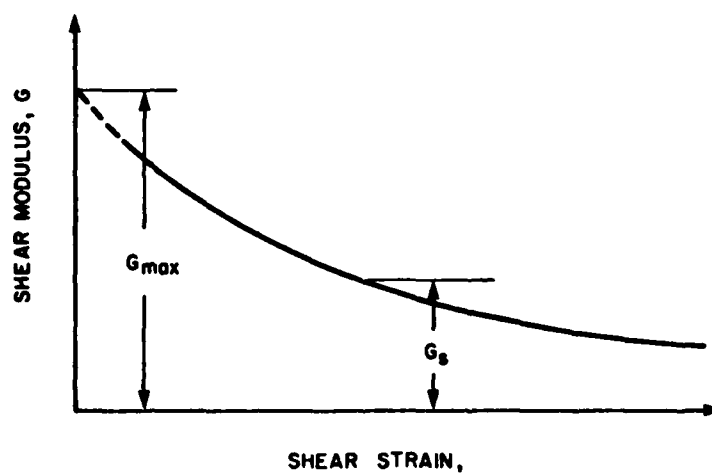


Figure 8. Idealized Shear Modulus Reduction Curve

maximum shear modulus, G_{\max} can be estimated at the intercept. Represented on a semi-logarithmic scale, normalized curves from Seed-Idriss (48), Stokoe-Lodde (57), and Isenhowe (24), show the variation of shear modulus with shearing strain in Figure (9). Block samples from San Francisco Bay marine silty clay were tested for their dynamic properties. Consecutive hysteresis loops obtained for the first cycle of dynamic loading at different controlled strain levels illustrates the stiffness reduction as the loops deform and tilt with increasing strain amplitude (Figure (10)) (22).

Same correlations between shear modulus and shear strain are also obtained through in-situ dynamic tests conducted and reported by Prakash and Puri (38) for several sites located in India. The test procedures included wave propagation tests, cyclic plate load tests, free and forced vibration tests.

Degradation of backbone curve is typical for dynamic behavior of soft clays. Progressive degradation of soil stiffness with increasing number of cycles of loading can be defined as progressive "softening" of soil. Degradation is known to be mainly a function of the number of cycles of loading. An early study done by Hardin and Drnevich (19), on dry, clean graded sand shows hardening of the material with increasing number of cycles. In Figure (11), taken from Hardin, et al. (19), the backbone curve for 10 cycles is below the backbone curve for 100 cycles of loading at the same shear strain amplitudes. On the other hand, saturated soft clays display softening through numerous experimental plots of hysteresis loops. Typical stress-strain curves for bilinear models in San Francisco Bay mud illustrates the degradation of stiffness with increasing number of cycles (Figure (12)) (60). Another example of

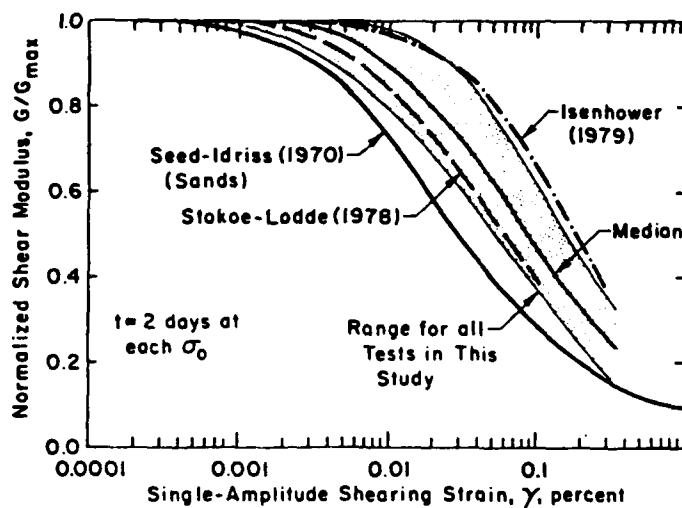


Figure 9. Summary of Normalized Shear Modulus Variation With Shearing Strain (from Stokoe (55))

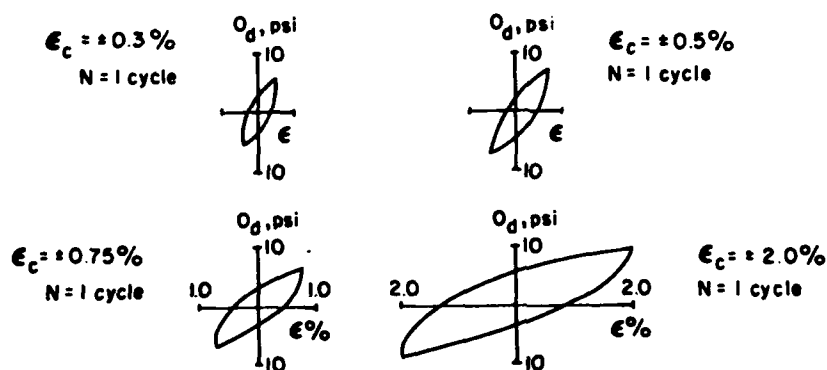


Figure 10. Hysteresis Loops Measured During First Cycle (from Idriss, et al. (22))

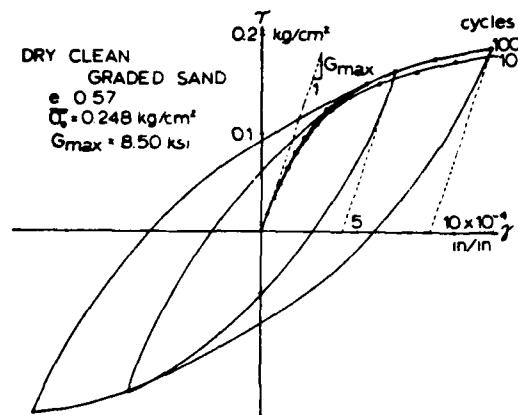


Figure 11. Stress - Strain Loop End Points at 10 and 100 Cycles of Loading (from Hardin, et al. (19))

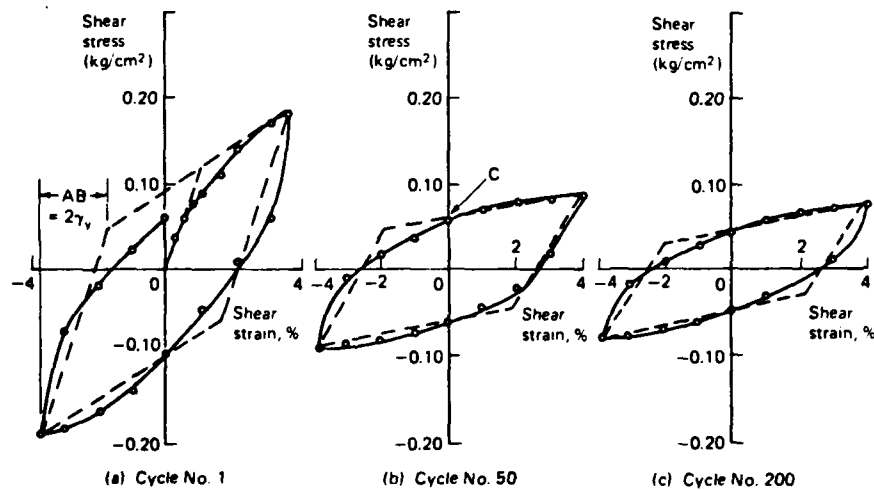


Figure 12. Stress - Strain Curves for Bilinear Models in San Francisco Bay Mud (a) Cycle No 1 (b) Cycle No 50 (c) Cycle No 200 (from Thiers, et al. (60))

the affect is shown in Figure (13), where the first and the tenth cycle hysteresis loops, tips of which correspond to the same strain amplitude, are plotted (22). The experimental data is again obtained from San Francisco Bay mud, but modeled using Ramberg-Osgood formulation. It is observed that the tenth cycle backbone curve is below the first.

Degradation affects are formulated using degradation index δ , which is the ratio of the secant modulus in the N'th cycle $(E_S)_N$ or $(G_S)_N$, to the initial secant modulus $(E_S)_1$ or $(G_S)_1$. δ is a function of number of cycles N, and is defined as:

$$\delta = N^{-t} \quad (3)$$

where, t is the degradation parameter. "t" is defined as the slope of the logarithmic plot of $(E_S)_N$ versus N. By the following relation it is also the slope of the logarithmic plot of maximum cyclic stress $(\sigma_d)_N$ versus N:

$$\delta = \frac{(E_S)_N}{(E_S)_1} = \frac{(\sigma_d)_N / \epsilon_c}{(\sigma_d)_1 / \epsilon_c} = \frac{(\sigma_d)_N}{(\sigma_d)_1} = N^{-t}$$

The modified expression used with torsional shear test data on San Francisco Bay mud is illustrated by the plot of $(G_S)_N$ versus N for different peak shear strains in Figure (14). It is observed that degradation parameter t, is strongly dependent on peak strain amplitude. Idriss, et al. (22) predicted that it is also essentially independent of the confining pressure or water content of the specimen. Plotting t versus peak shear strain, Stokoe observed the variation of t for two different samples of San Francisco Bay mud (Figure (15)), where specimen 3 was clayey and specimen 1 was silty material. The variations in Figure (15) are explained in part by one soil tending to generate

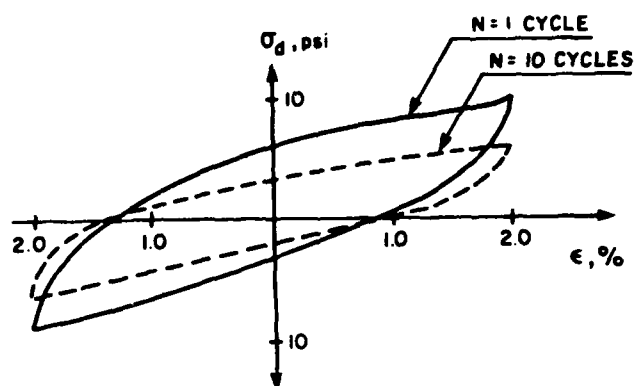


Figure 13. Hysteresis Loops Measured During First and Tenth Cycles (from Idriss, et al. (22))

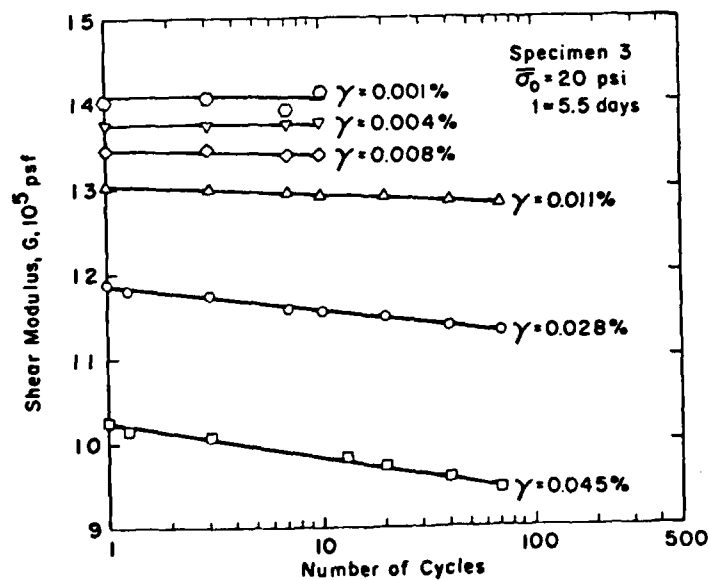


Figure 14. Variation in Shear Modulus With Number of Cycles of Loading and Shear Strain (from Stokoe (55))

negative pore pressure, thus showing a hardening effect (specimen 1) while the other tending to generate positive pore pressures, thus showing a softening effect (specimen 3). These effects come about by the changes in the effective stress state on the soil specimens during cyclic loading. Idriss, et al. (22), readjusted the Ramberg-Osgood formulation to produce series of degraded backbone curves for different values of degradation index δ , for San Francisco Bay mud soil. As observed from Figure (16), the backbone curve shifts down and flattens progressively with increasing values of δ .

Degradation affect diminishes with increasing number of cycles. The major decrement in the stiffness of the material comes about during the first 10 cycles of loading. Figure (17) illustrates this observation affectively, where the modulus reduction curves of a bilinear model for different number of cycles are given.

Therefore, one can predict a reasonable value of number of cycles at which the material can be assumed to have reached a steady state condition with insignificant degradation of stiffness. Verification of this assumption can be shown quantitatively through a simple calculation of percentage decrement of shear modulus as the number of cycles are increased. Referring back to Figure 14, it is observed that the total reduction in shear modulus ranges from 11.0 to 0.7 percent based on its initial value, up to 500 cycles of loading for maximum and minimum peak strain amplitudes, respectively. About 85 - 90 percent of the reduction is completed by the time the material undergoes its 100th cycle of loading. In determining the dynamic properties of soils from laboratory tests, one can obtain a hypothetical stress-strain curve, so that the tips of all strain-controlled hysteresis loops at the steady state

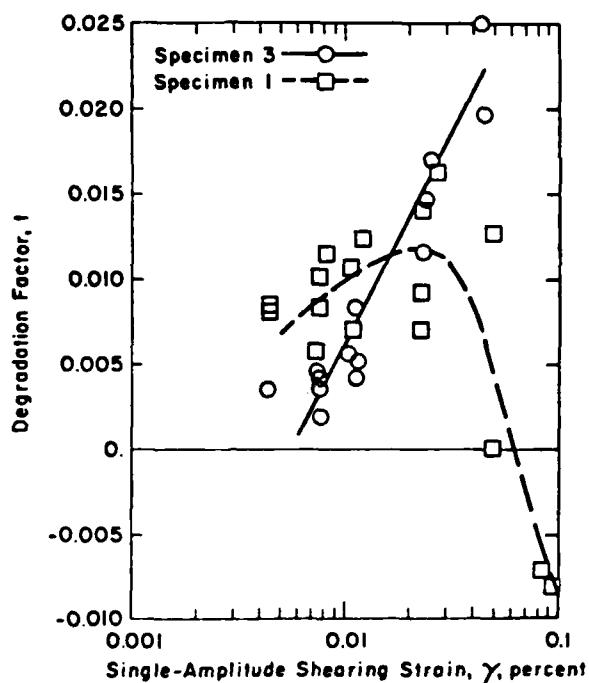


Figure 15. Variation in Degradation Factor With Shearing Strain (from Stokoe (55))

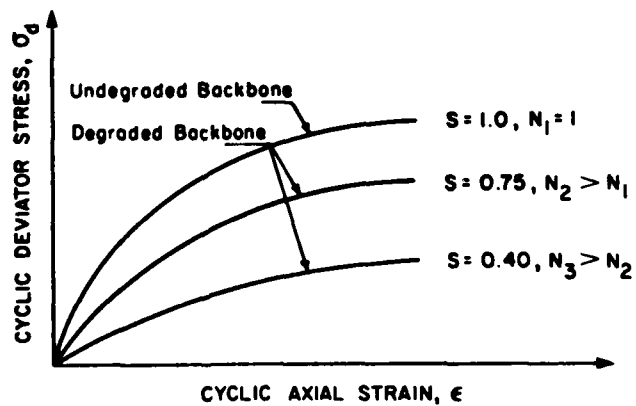


Figure 16. Schematic Illustration of Construction of Degraded Backbone Curves (from Idriss, et al. (22))

condition would end on the same curve. The steady state condition, in this case, is defined as the condition at which the material no longer experiences significant stiffness reduction with increasing number of cycles of loading. Degradation of stiffness is observed to gain more importance at high amplitude strain levels (strains greater than 0.001 percent). Unless one can measure the dynamic properties accurately at the first cycle of each strain-controlled hysteresis loop, as the strain levels are progressively increased during cyclic loading, one has to take into consideration the degradation of stiffness effects. For practical purposes, the steady-state condition assumption may serve to obtain an approximate hypothetical stress-strain curve. In order to define limiting criteria or correction factors for the assumption, a degradation study that would help to obtain the order of magnitude of stiffness reduction based on number of cycles of loading, becomes necessary to conduct. Several numerical solution techniques consider the degradation of stiffness effect in soft clays under cyclic loading. A recent finite difference technique namely DETRAN, developed by Tsai, et al. (61), includes an algorithm for describing the progressive softening of cohesive soils under high amplitude cyclic loading. The technique is originally developed to predict the seismic response of cohesive marine soils, under earthquake induced loading.

Damping of soils under cyclic loading is the second important dynamic property besides moduli of soils. The relation defining damping is given by equation (2). Damping, like stiffness, is strongly dependent on strain amplitude. In Figure (10), the tilting of the hysteresis loops are accompanied by the enlargement of the area they enclose, as the strain amplitude increases. Since damping, by

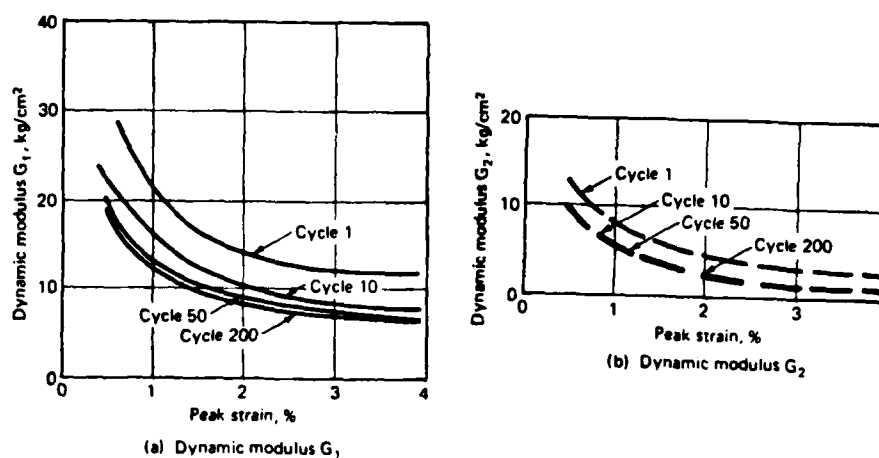


Figure 17. Effect of Cyclic Loading on Dynamic Moduli
 (a) Dynamic Moduli G_1 (b) Dynamic Moduli G_2
 (from Thiers, et al. (60))

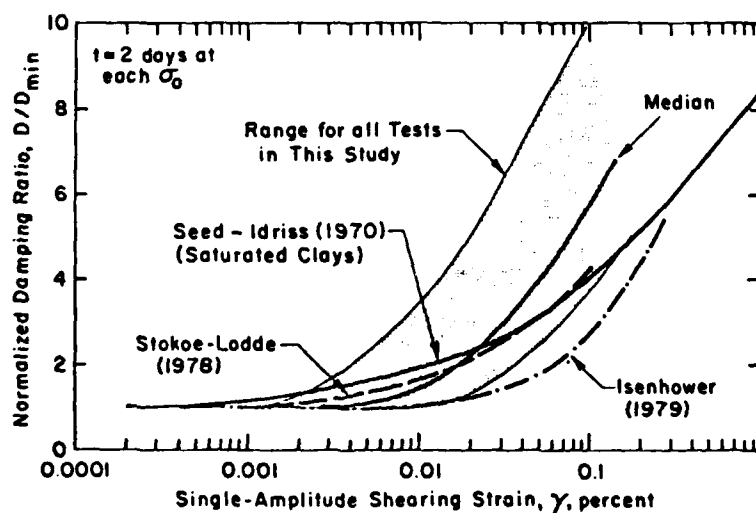


Figure 18. Summary of Normalized Damping Ratio With Shearing Strain
 (from Stokoe (55))

definition, is related to the ratio of the area enclosed by the loop to the area under the secant modulus line, the strain dependence of damping is readily observed from Figure (18). The figure summarizes the normalized damping ratio variation with shear strain from the works of several different investigators. Opposed to the trend of stiffness moduli, damping ratio of soils increases with increasing strain amplitude under cyclic loading. In most of the dynamic tests, it is observed that damping ratio stays independent of strain up to a threshold range. That value of damping ratio which is independent of strain and corresponding to the low strain amplitudes (below 0.001 percent) is the minimum damping ratio, D_{min} of the soil being tested.

Damping response is one of the important factors that must be included in all dynamic analysis of soils. The damping of soils vary to some extent with depth and lateral distance from the source of excitation. Therefore, Seed, et al. (49) utilized the variable Rayleigh Damping Method to include the effects of depth and lateral distance in soil medium in a numerical analysis for earthquake type of dynamic loading. Rayleigh Damping method utilizes the stiffness and mass of a system to express damping as a linear combination of those two properties of the system. The following equation, in matrix notation, defines this relation,

$$[C] = \alpha [M] + \beta [K] \quad (4)$$

where

$[C]$ = damping matrix

$[M]$ = mass matrix

$[K]$ = stiffness matrix

α and β are constants expressed in terms of minimum material damping ratio D_{\min} , and corresponding fundamental frequency ω_{\min} of the system. Using a modal analysis Seed, et al. and Lysmer (49,29) expressed damping ratio, D , as a continuous function of frequency, ω , where:

$$D(\omega) = \frac{1}{2} \left[\frac{\alpha}{\omega} + \omega\beta \right] \quad (5)$$

This function has a minimum at,

$$\omega_{\min} = \sqrt{\alpha/\beta} \quad (6)$$

and the minimum value is,

$$D_{\min} = \sqrt{\alpha\beta} \quad (7)$$

Equations (6) and (7) can be solved for α and β as follows:

$$\begin{aligned} \alpha &= D_{\min} \omega_{\min} \\ \beta &= D_{\min} / \omega_{\min} \end{aligned} \quad (8)$$

Substitution of equation (8) into (5) yields:

$$D(\omega) = \frac{1}{2} \left[\frac{\omega_{\min}}{\omega} + \frac{\omega}{\omega_{\min}} \right] D_{\min} \quad (9)$$

where, ω_{\min} is defined as the fundamental frequency of the system.

If the fundamental frequency of the system is much lower than the frequencies which are of interest for system response, equation (9) would lead to significantly high damping values at these high frequencies. This outcome constitutes a contrast with the general observation that the soil damping ratios vary only slightly over a range of high frequency response (corresponding to low strain-amplitude response). To avoid this deficiency, α and β can be computed using equation (5) such that the damping equals the desired damping at two different frequencies, and solving the two equations simultaneously.

Another method of introducing damping response of a system under cyclic loading in a numerical analysis is Complex Response Method. In

this method damping is included through the use of complex stiffness matrices, $[E^*]$ or $[G^*]$. These matrices are formed exactly like real-valued matrices except that complex moduli are used, where,

$$G^* = G e^{2i\theta} = G(\cos 2\theta + i \sin 2\theta) \quad (10)$$

$$E^* = E e^{2i\theta} = E(\cos 2\theta + i \sin 2\theta) \quad (11)$$

and

$$D = \sin \theta \approx \theta \quad (12)$$

The use of complex moduli leads to effective damping ratios which are frequency independent and this method serves to simulate the observed damping behavior of soils better than the previous method (45,29).

2.2 THEORETICAL CONSIDERATIONS IN WAVE PROPAGATION ANALYSIS AND MEASUREMENT OF DYNAMIC PROPERTIES

In order to evaluate the dynamic response of soils during cyclic loading as earthquake, ocean-wave or vibratory machine loading with stability requirements such that very small displacements could be permitted, dynamic measurements of soil properties must be conducted. Dynamic tests which are done both in-situ and in laboratory employ the same principles of theory of wave propagation. Next discussion will provide information about wave propagation analysis in elastic media (42).

2.2.1 Wave Propagation Analysis in Elastic Media

Infinite elastic media can sustain two kinds of waves which represent different types of body motions and that travel at different velocities. They are dilatational (primary, P, compression, irrotational) waves, and distortional (secondary, S, shear, equivoluminal) waves. The propagation velocity of a dilatational wave in an infinite elastic medium is given by the following formula

$$v_p = \frac{\sqrt{\lambda + 2G}}{\sqrt{\rho}} \quad (11)$$

where ρ is the mass density of the medium and,

$$\lambda = \frac{\mu E}{(1 + \mu)(1 - 2\mu)} \quad (12)$$

where μ is Poisson's ratio, and E is Young's Modulus.

The propagation velocity of a distortional wave in infinite elastic medium is

$$v_s = \sqrt{G/\rho} \quad (13)$$

In order to understand these velocity terms more thoroughly, one has to analyze the equation of motion in elastic media. In problems of wave propagation, it is instructive to start with the specific problem of waves in bounded medium in order to develop a general solution (42). The equation of motion in various forms of physical systems subject to vibration is called the "wave equation", and it is expressed by

$$\frac{\partial^2 u}{\partial t^2} = v^2 \frac{\partial^2 u}{\partial x^2} \quad (14)$$

where u is the displacement along the longitudinal axis of the rod, and V is the wave-propagation velocity. To simulate a bounded medium, an elastic rod with cross-sectional area A , will be considered. Three independent kinds of wave motion are possible in rods. They are longitudinal, torsional and flexural motions. The longitudinal and torsional motions result in typical wave equation, therefore only those two will be considered here.

Longitudinal waves. An infinitesimal transverse section, Δx of an elastic rod experiences stress σ_x on a transverse plane at x , and stress $[\sigma_x + (\partial \sigma_x / \partial x) \Delta x]$ on a transverse plane at $(x + \Delta x)$, as shown in Figure (19). Using Newton's Second Law:

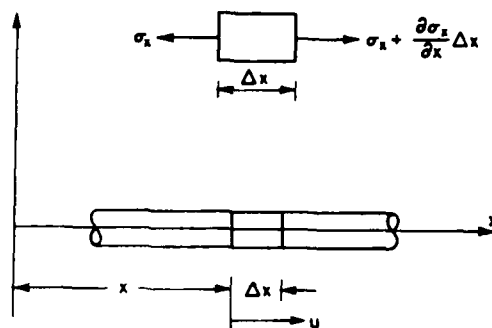


Figure 19. Longitudinal Vibration of a Rod (from Richart, et al. (42))

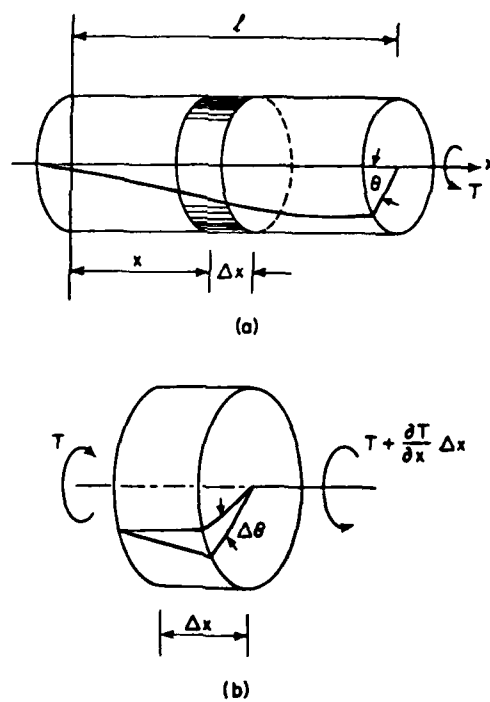


Figure 20. Torsion in Circular Rod (from Richart, et al. (42))

$$-\sigma_x A + \left[\sigma_x + \frac{\partial \sigma_x}{\partial x} \Delta x \right] A = F \quad (15)$$

where

$$F = (\rho A \Delta x) \frac{\partial^2 u}{\partial t^2} \quad (16)$$

Substituting (16) into (15), and rearranging:

$$\frac{\partial \sigma_x}{\partial x} = \rho \frac{\partial^2 u}{\partial t^2} \quad (17)$$

where

$$\frac{\partial \sigma_x}{\partial x} = \frac{\partial}{\partial x} \left[E \frac{\partial u}{\partial x} \right] = E \frac{\partial^2 u}{\partial x^2} \quad (18)$$

Substituting (18) into (17), and rearranging:

$$\frac{\partial^2 u}{\partial t^2} = \frac{E}{\rho} \frac{\partial^2 u}{\partial x^2} \quad (19)$$

Substituting equation (19) into equation (14),

$$v_c = \sqrt{E/\rho} \quad (20)$$

where v_c is the longitudinal wave propagation velocity in an elastic rod.

Comparing equation (20) to equation (11), it is readily observed that the dilatational waves--in the case of elastic rod longitudinal waves--travel faster in infinite media than they do in a rod. This is because, in infinite media there are no lateral displacements, but in a rod they are possible.

Torsional waves. The torque on a transverse section of a rod produces an angular rotation θ , as shown in Figure (20). Torque is expressed by the following formula,

$$T = G I_p \frac{\partial \theta}{\partial x} \quad (21)$$

where I_p is the polar moment of inertia of the cross-section, and G is the shear modulus. Torque due to the rotational inertia of an element

of rod of length Δx is

$$T = \rho I_p \Delta x \frac{\partial^2 \theta}{\partial t^2} \quad (22)$$

Using Newtons Second Law:

$$-T + [T + \frac{\partial T}{\partial x} \Delta x] = \rho I_p \Delta x \frac{\partial^2 \theta}{\partial t^2} \quad (23)$$

Substituting equation (21) into (23) and rearranging:

$$\frac{\partial^2 \theta}{\partial t^2} = \frac{G}{\rho} \frac{\partial^2 \theta}{\partial x^2} \quad (24)$$

Comparing equations (24) and (14), the relation for torsional wave velocity is derived,

$$V_s = \sqrt{G/\rho} \quad (25)$$

where V_s is the torsional wave propagation velocity. At this point, one observes that the distortional waves---in the case of elastic rod torsional waves---travel at the same speed in an elastic infinite medium as they do in an elastic rod.

In elastic half-space there is a third kind of wave possible which was first studied by Lord Rayleigh in 1885, and later analyzed by Lamb in 1904 thoroughly. It is called the Rayleigh or R-wave and is confined to a zone near the boundary or the surface of the half-space. Some of the characteristics of Rayleigh waves are as follows:

1. Their influence decrease rapidly with depth.
2. Velocity of R-waves is independent of frequency and it is nearly equal to the velocity of distortional waves.
3. R-waves are nondispersive and propagate radially outward along a cylindrical wave-front.
4. R-waves are the most powerful of all three types of waves. They constitute 67 percent of the total energy that generates the waves.

Both dilatational and distortional waves encounter an increasingly larger volume of material as they travel into the half-space, thus the energy density in each wave decreases with distance to the source. This decrease in displacement amplitude is called geometrical damping. The amplitude of P (dilatational) and S (distortional) waves decrease in proportion to the ratio $1/r$ outward into the half-space, and $1/r^2$ on the surface, r being the distance from source. On the other hand, the Rayleigh wave displacement amplitude decreases in proportion to the ratio $1/\sqrt{r}$. Therefore, Rayleigh waves can travel longer distances without experiencing the geometrical damping effect as strong as the other two wave types experience.

2.2.2 Dynamic Testing Methods to Evaluate the Dynamic Moduli and Damping Characteristics of Soils

The major soil properties used in soil dynamics are (64):

1. Dynamic Moduli - Young's Modulus, shear modulus, bulk modulus and constrained modulus
2. Poisson's ratio
3. Damping and attenuation
4. Liquefaction parameters - cyclic shearing stress ratio, cyclic deformation, and pore pressure response
5. Shearing strength in term of strain-rate effects.

Some of these are best measured or studied in the field, others in the laboratory and some can be measured in both laboratory and in-situ.

Among the parameters listed above, shear modulus, damping and cyclic deformation are the three important characteristics that are of interest to this study. All three parameters have been discussed in general in the previous section of this chapter. In this subsection, evaluation of

shear modulus and damping will be discussed in detail, since they are the two parameters measured in the dynamic testing phase of this study.

An important consideration of water propagation analysis in soils is the effect of fluid phase of soil matrix on wave velocity. The temperature and salinity of the pore water are the side factors that influence the analysis also. A theoretical study which treated the wave-propagation in a fluid-saturated porous medium, showed that the presence of the fluid exerted an important influence on the dilatational wave velocity but produced only a minor effect on the distortional or shear wave velocity (9). The fluid effects the shear wave velocity only by adding to the mass of the particles in motion. Therefore, it would be satisfactory not to consider the saturation effects in measurements of V_s or G in soils. With one of the moduli evaluated through dynamic analysis, the other moduli can be estimated by equation (26), with a calculated or even assumed value of Poisson's ratio, μ .

$$E = 2 (1 + \mu) G \quad (26)$$

In an extensive study done by Cunny and Fry (12) on dynamic in-situ and laboratory moduli measurements and their comparison, it is suggested that Poisson's ratio can be calculated using the following equation,

$$\mu = \frac{V_r^2 - 2}{2 (V_r^2 - 1)} \quad (27)$$

where

$$V_r = \frac{V_c}{V_s} \quad (28)$$

where, V_c is the dilatational wave velocity determined through conventional in-situ refraction seismic techniques, and V_s is the shear wave velocity determined by in-situ dynamic tests.

The common in-situ dynamic testing methods to evaluate shear velocity of soils include shear wave refraction method, steady state subsurface vibrations (Rayleigh wave method), up-hole and down-hole method, and cross-hole method. Since it is not of interest to this study reported herein, no discussion on in-situ dynamic measurement techniques will be presented. However, the comparison of the in-situ measurements with laboratory measurements stand out to be an important factor in dynamic soil testing methods. As reported by Cunny and Fry (12), the difference between in-situ and laboratory moduli range from +50% to -50%, and this generalization seems to hold for either undisturbed or remolded, cohesive or cohesionless materials. This conclusion was made after a large number of samples from 19 different sites and various depths were tested in laboratory utilizing resonant column apparatus, while a series of in-situ Rayleigh Wave Vibration tests were conducted at the same sites.

2.2.2.1 Resonant column test of soils

The resonant column method was conceived by Ishimoto and Iida in 1936, and was first employed by Iida (23) to study the wave propagation in vertical columns of sand set into longitudinal or torsional oscillations. The frequency at "resonance" and the height of the specimen provided the information for calculation of the wave velocity. During the decade following Iida's tests, little published information was available on the evaluation of soil properties by resonant column method. By the mid 1950's, the device picked up interest and has been used since for both research and routine soil evaluation, (e.g., Shannon, Yamane, Dietrich, 1959; Wilson and Dietrick, 1960; Hardin and Richart, 1963; Hardin and Black, 1968; Hardin and Drenevich, 1972;

Drenevich, 1977; Anderson and Stokoe, 1977; Stokoe and Lodde, 1978; Stokoe, 1980).

The resonant column test for determining moduli and damping of soils is based on the theory of wave propagation in elastic rods. In a resonant column apparatus, the sample response is monitored for a range of frequencies of both longitudinal and torsional modes of excitation to determine the resonant frequency of the soil specimen. The modulus is computed from the resonant frequency and the geometric properties of the specimen and driving apparatus. Several versions of the resonant column test are possible using different end conditions to constrain the specimen. These end conditions are free-free, fixed-free and fixed-fixed type of boundaries. The resonant column apparatus--later to be described in detail in methodology phase--employed in the dynamic experiments in this study was a fixed-free end type of apparatus. Therefore, only fixed-free end condition type of test and its modifications will be discussed.

The solution of the wave equation for finite rods of various boundary conditions is given as follows (42),

$$u = U (C_1 \cos \omega_n t + C_2 \sin \omega_n t) \quad (29)$$

where

U = the displacement amplitude along the length of the rod

C_1, C_2 = amplitude constants

ω_n = the circular frequency of a natural mode of vibration

Substituting this solution into the wave equation (equation (14)),

$$U = C_3 \cos \frac{\omega_n x}{V} + C_4 \sin \frac{\omega_n x}{V} \quad (30)$$

where V is the wave propagation velocity, and x is the longitudinal axis of the rod.

The normal modes of vibration in a fixed-free end condition rod is given in Figure (21). At the fixed end of the rod the displacement U , and at the free end the strain $\partial U / \partial x$, is zero. Using these two boundary conditions, the expression for displacement amplitude is derived (42),

$$U_n = C_4 \sin \frac{\omega_n x}{V} \quad (31)$$

where

$$\omega_n = \frac{n \pi V}{2 \ell} \quad (32)$$

Substituting (30) into (29)

$$U_n = C_4 \sin \frac{n \pi x}{2 \ell} \quad (33)$$

where, C_4 is the maximum amplitude of the sin function, n is the number of the harmonic, ℓ is the length of the rod. The first three harmonics derived from equation (31) are shown in Figure (21).

Major problems came about with resonant column technique when driving and motion monitoring instruments were attached to the specimen in order to excite and measure the corresponding response. These attachments naturally altered the specimen boundary conditions. The problem was solved when these attachments were lumped into a mass at the free end of the specimen. This configuration, while compensating for the attachments, also turned out to be advantageous for Drnevich in 1967, as he was able to obtain uniform strain distribution throughout the length of the specimen. Figure (22) illustrates the difference in the angular rotation, θ distribution in a fixed-free end rod, and a fixed-free end rod with a mass attached to the free end. The $1/4$ sine wave distribution of θ reduces considerably to almost a linear distribution when a mass with mass polar moment of inertia, J_0 , is attached to the free end of the rod with mass polar moment of inertia, J (64).

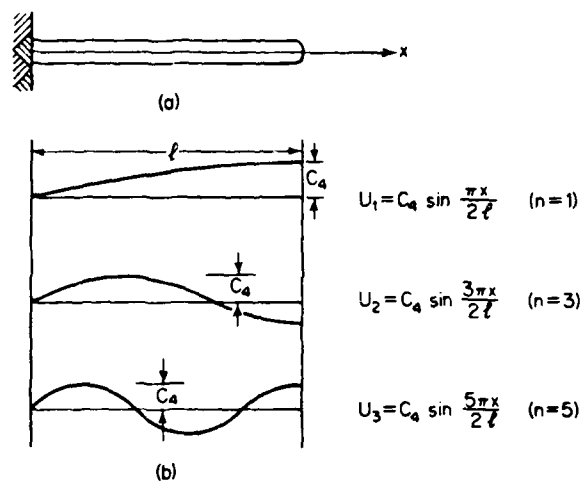


Figure 21. Normal Modes of a Fixed - Free Rod
(from Richart, et al. (42))

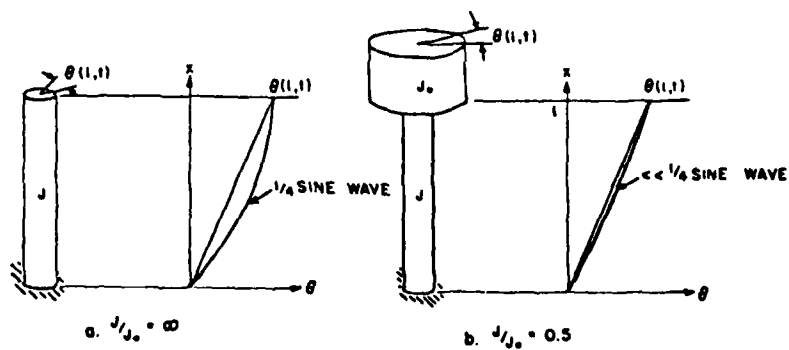


Figure 22. Schematic of Resonant Column End Conditions
(from Hardin (17))

Previous equations for fixed-free end condition need to be modified to apply to the mass-attached case. The derivations are presented for longitudinal excitation and eventually modified for torsional excitation. In longitudinal excitation displacement is zero at the fixed end, but at the free end a force is exerted on the rod which is equal to the inertia force of the concentrated mass.

$$F = \frac{\partial u}{\partial x} AE = -m \frac{\partial^2 u}{\partial t^2} \quad (34)$$

where A is cross sectional area, E is the Young's Modulus of the rod, and m is the mass of the attachment. Differentiating equation (29), and substituting into equation (34), gives:

$$AE \frac{\partial U}{\partial x} = m \omega_n^2 U \quad (35)$$

Finally, substituting U from equation (31) at $x = l$ and $V = V_c$, the following relation is obtained

$$AE \frac{\omega_n}{V_c} \cos \frac{\omega_n l}{V_c} = \omega_n^2 m \sin \frac{\omega_n l}{V_c} \quad (36)$$

This equation, by proper manipulation, can be reduced to

$$\frac{A l \gamma}{W} = \frac{\omega_n l}{V_c} \tan \frac{\omega_n l}{V_c} \quad (37)$$

where

$A l \gamma$ = weight of the rod

W = weight of the attached mass

For torsional excitations, $A l \gamma / W$ ratio is substituted by J / J_o , and V_c is substituted by V_s . Then the corresponding equation comparable to equation (37) is

$$\frac{J}{J_o} = \frac{\omega_n l}{V_s} \tan \frac{\omega_n l}{V_s} \quad (38)$$

For convenience, the right hand side of equation (38) can be written as $(\beta \tan \beta)$ where $\beta = \omega_n l / V_s$. Equation (38) is solved by plotting a curve

of β versus J/J_0 . With the proper value of β , wave velocity V_s , can now be written as

$$V_s = \frac{2\pi f_n \ell}{\beta} \quad (39)$$

where f_n is the natural mode frequency of the rod. Substituting equation (39) into equation (25), and rearranging, an expression for shear modulus G is obtained

$$G = \rho \left[\frac{2\pi f_n \ell}{\beta} \right]^2 \quad (40)$$

It is important to note that f_n is the natural frequency measured at resonance in a resonant column test.

At this point, it is beneficial to include a brief section on vibration formulation and resonance of systems, before moving further into the discussion of measurement of dynamic moduli employing resonant column apparatus. The equation of motion for a viscously damped single-degree-of-freedom system under forced vibration is given as (42),

$$m\ddot{z} + c\dot{z} + kz = Q_0 \sin \omega t \quad (41)$$

where

m = mass, c = damping, k = stiffness of the system

z = displacement

Q_0 = amplitude of harmonic force

ω = circular frequency

This system approximates closely the properties of many real systems. A schematic diagram of the idealized system is shown in Figure (23a). The solution to equation (41) is

$$z = A \sin (\omega t - \phi) \quad (42)$$

where, A is the displacement amplitude and ϕ is the phase angle between the exciting force and displacement vector. Differentiating equation

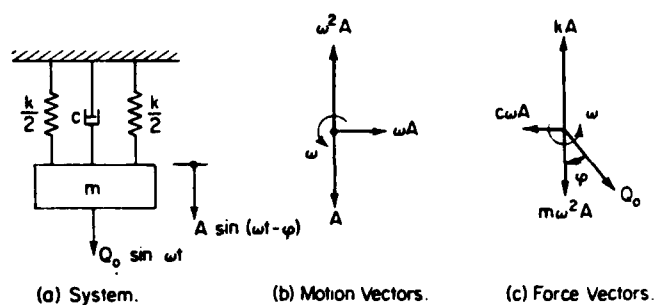


Figure 23. Forced Vibrations of a Single-Degree-of-Freedom System With Viscous Damping (from Richart, et al. (42))

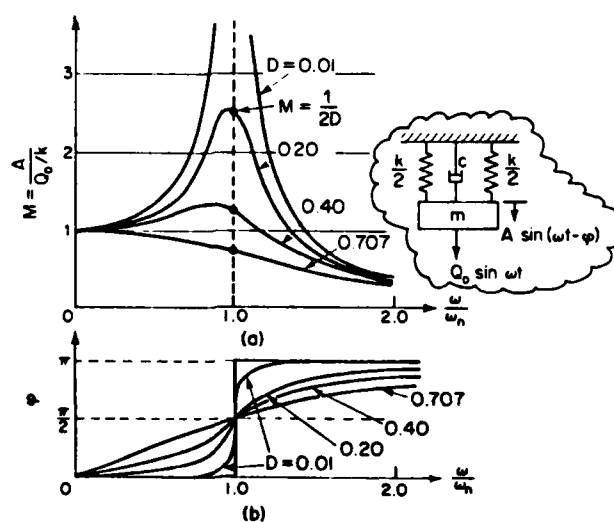


Figure 24. Response Curves for a Viscously Damped Single-Degree-of-Freedom System (from Richart, et al. (42))

(42) with respect to time twice, velocity and acceleration vectors are obtained. The motion and force vectors are shown in Figures (23b) and (23c). Summation of the force vectors in the horizontal and vertical directions give two equations that can be solved simultaneously to obtain the unknowns, A and ϕ in equation (42). Solving for A and ϕ , then substituting damping ratio D, and natural circular frequency, ω_n , given as

$$\omega_n = \sqrt{k/m} \quad \text{or} \quad f_n = 1/2\pi\sqrt{k/m} \quad (43)$$

and

$$D = c/c_c \quad (44)$$

in which c is the damping coefficient and c_c is the critical damping coefficient

$$c_c = 2\sqrt{km} \quad (45)$$

the following relations are obtained

$$M = \frac{A}{\frac{Q_0}{k}} = \frac{1}{[1 - (\frac{\omega}{\omega_n})^2]^2 + [2D \frac{\omega}{\omega_n}]^2} \quad (46a)$$

$$\tan \phi = \frac{2D \frac{\omega}{\omega_n}}{1 - (\frac{\omega}{\omega_n})^2} \quad (46b)$$

in which, M is called the dynamic magnification factor. Plots of these equations for various values of D are given in Figure (24). These curves are referred to as constant-force-amplitude excitation response curves for steady state vibration, where Q_0 is a constant, independent of ω .

It is observed from Figure (24a) that as the exciting force frequency, ω , approaches to the natural circular frequency ω_n , the magnification factor M peaks to a maximum value denoted by M_{\max} . The

frequency at this maximum amplitude of displacement will be referred to as the resonant frequency and is given by the expression

$$f_m = f_n \sqrt{1 - 2D^2} \quad (47)$$

Resonance of a damped system occurs at a frequency slightly less than the natural frequency of the system, as observed by equation (47). On the other hand, resonance of an undamped system occurs exactly at the natural frequency of the system, with the amplitude of the motion increasing without bound. The value of M_{\max} at the resonant frequency f_m , in a damped system is given by

$$M_{\max} = \frac{1}{2D \sqrt{1 - D^2}} \quad (48)$$

while the value of M_{\max} at resonance in an undamped system is undefined, that it is infinitely large. Figure (25a) illustrates the response curve for an undamped system ideally represented on the corner of the same figure.

The phase angle between the exciting force and displacement vector is also different for the two cases of forced vibration of a single-degree-freedom system. In the damped system all the response curves merge at one point where $\omega = \omega_n$ and the corresponding ϕ value is $\pi/2$ (Figure (24b)). In the undamped system, at $\omega = \omega_n$, there is an instantaneous increase of ϕ from 0 to π . Therefore, for $\omega < \omega_n$ the exciting force is in phase with displacement, and for $\omega > \omega_n$ the exciting force is 180° out of phase with displacement. The phase difference is 90° for the damped system.

Internal damping of systems is associated with the magnitude of their ability to dissipate energy. Earlier, damping ratio of materials was defined as the ratio of the energy dissipated by the system to the

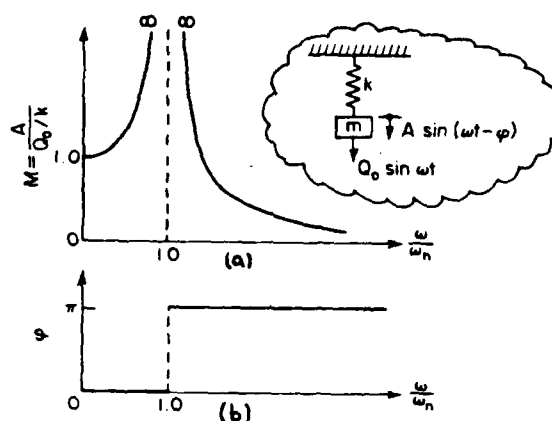


Figure 25. Dynamic Magnification Factor and Phase Angle Between Force and Displacement of an Undamped Single-Degree-of-Freedom System (from Richart, et al. (42))

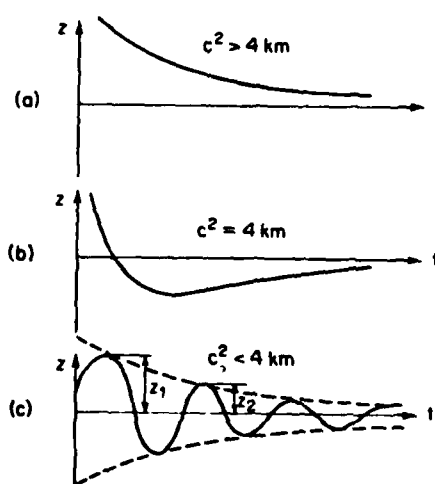


Figure 26. Free Vibrations of a Viscously Damped System
(a) Overdamped (b) Critically Damped (c) Underdamped
(from Richart, et al. (42))

excitation energy exerted on the system. The higher the dissipative character of the material, the higher the damping ratio associated with it. Another analytical formulation for damping ratio is expressed through equations (44) and (45). Natural systems are either overdamped or critically damped or underdamped in response to vibratory excitations. In overdamped response the displacement of the system decrease exponentially without change in sign, as shown in Figure (26a). In underdamped response, the motion is oscillatory and decay in amplitude with time, as shown in Figure (26c). The critically damped response occurs when the damping coefficient of the system, c , satisfies the condition of motion so that there is only one possible sign change, as shown in Figure (26b). That value of c is called the critical damping coefficient c_c and is expressed by equation (45). Referring back to Figures (24) and (25), it is observed that at low damping ratio values, the damped system responds like the undamped system, that is it experiences resonance at the natural frequency of the system. Another important observation is made through equations (47) and (48) where for $D = 1/\sqrt{2}$ and $f_m = 0$, M_{\max} is 1.0 corresponding to a static response.

Two methods are available for measuring damping ratio in a resonant column apparatus. They are amplitude decay method and magnification factor method. Both give essentially the same results but the latter is simpler and quicker. Magnification factor method relies on the similar behavior of undamped and damped systems at low damping ratios ($D < 0.1$) which in turn corresponds to low shear strain amplitudes ($\gamma < 0.001$). This method was utilized to measure the damping ratio values in the experimental phase of this study. Therefore, it will be discussed in detail in the methodology phase. The amplitude decay method being less

practical than the magnification factor method, is generally used for occasional spot-checking in resonant column analysis. With the apparatus vibrating at the resonant frequency, the power to the excitation device is cut off and the decay curve for the free vibration of the specimen is recorded. Figure (27) shows a typical vibration-decay curve obtained from resonant-column tests of Mississippi Delta marine sediments.

The decay of free vibration of a single-degree-freedom system with viscous damping is described by the logarithmic decrement, δ , which is defined as the natural logarithm of two successive amplitudes of motion, z_1 and z_2 , and given by,

$$\delta = \ln \frac{z_1}{z_2} = \frac{2 D}{\sqrt{1 - D^2}} \quad (49)$$

Typical relations of G and D with shear strain amplitude, obtained by resonant column tests were given in Figures (9) and (18), respectively. In these tests cylindrical specimens were excited torsionally, G and D values at each strain amplitude were calculated employing the measured resonant frequency, the geometric properties of the sample and apparatus, and the theoretical principles discussed above. Hardin and Black (18) have indicated several parameters which exert an influence on the shear modulus of soils in the form of a functional relation for G ,

$$G = f(\bar{\sigma}_o, e, H, S, \tau_o, C, A, f, t, \nu, T) \quad (50)$$

where

$\bar{\sigma}_o$ = effective octahedral normal stress (average effective confining pressure

e = void ratio

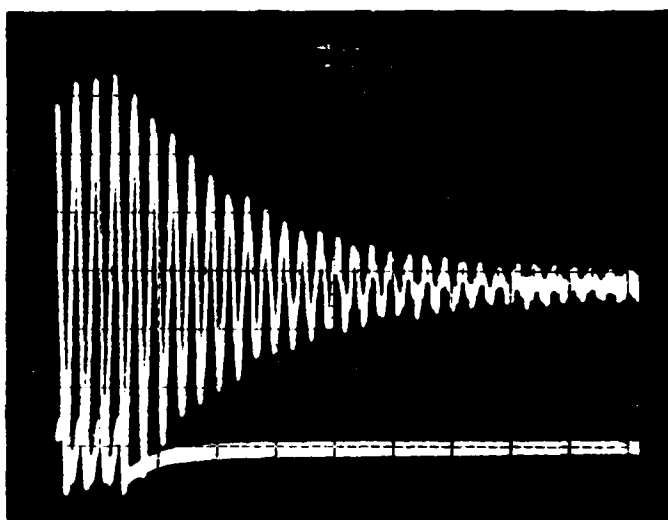


Figure 27. Typical Vibration - Decay Curve from Resonant Column Test
(from Mississippi Delta Sediment Specimen Test)

H = ambient stress history and vibration history

S = degree of saturation

C = grain characteristics, grain shape, grain size, grading
minerology

τ_o = octahedral shear stress

A = amplitude of strain

f = frequency of vibration

t = secondary effects that are functions of time and magnitude of
load increment

V = soil structure

T = temperature

Among the parameters listed above, the effective confining pressure $\bar{\sigma}_o$, strain amplitude A, ambient stress history and vibration history, H, and void ratio, e, are known to be the major parameters that exert significant influence on shear modulus of cohesive soils. The insignificant effect of saturation on shear wave velocity thus shear modulus measurements was discussed earlier. Several investigators found that (42), frequency of vibration had no measurable effects on G for frequencies less than about 2500 Hz. The other parameters listed in equation (50) still need to be studied extensively to pinpoint their influence on shear modulus of cohesive soils. Some of the parameters listed in equation (50), if not all, can also be considered as parameters influencing the damping nature of the soils. The variation trends of shear modulus, and damping ratio with strain amplitude are the most consistent results of resonant column tests. A recent study done by Stokoe (55), involves the resonant column testing of San Francisco Bay Mud samples. Figures (28) and (29) illustrate the influence of

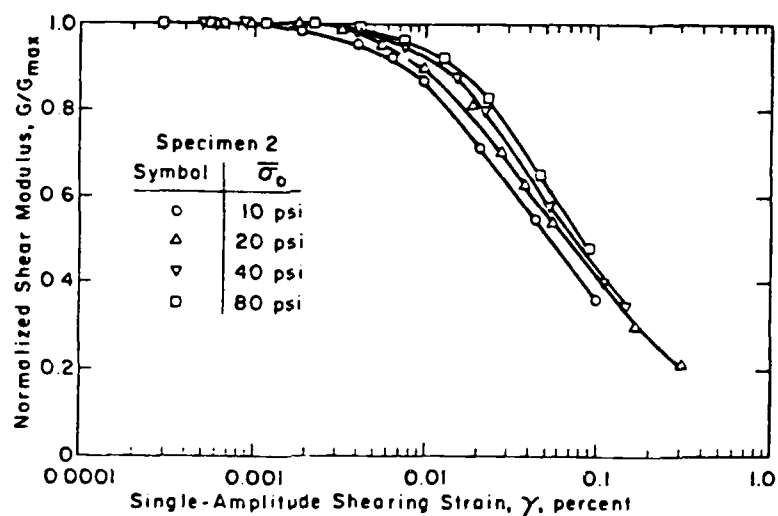


Figure 28. Variation in Normalized Shear Modulus With Shearing Strain and Effective Confining Pressure (from Stokoe (55))

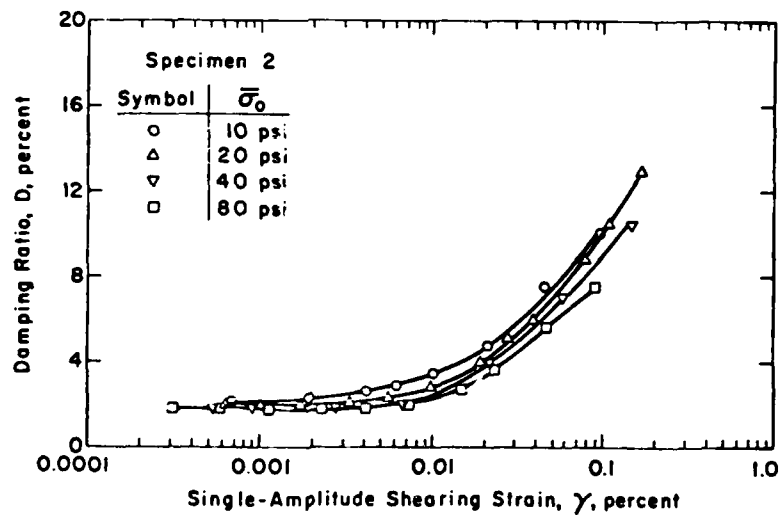


Figure 29. Variation in Damping Ratio With Shearing Strain and Effective Confining Pressure (from Stokoe (55))

confinement of the specimens, on the dynamic shear modulus, and damping ratio, respectively. It is observed from the figures that the shear modulus increase while the damping ratio decrease with increasing effective confining stress, $\bar{\sigma}_o$.

The number of curves for different confining pressures in Figures (28) and (29) can be reduced to a single curve by normalizing the shear strain with reference strain, γ_r , as suggested by Hardin and Drnevich (19). Reference strain is defined as the ratio of τ_{max} to G_{max} , in a hyperbolic stress-strain relationship.

$$\gamma_r = \frac{\tau_{max}}{G_{max}} \quad (51)$$

where τ_{max} was defined by equation (1) in Section 2.1. Figure (30) illustrates a normalized plot of G versus γ , using γ_r for normalizing parameter of γ , by Hardin and Drnevich (19). The samples tested were from 14 different sites of both cohesive and cohesionless nature and they were obtained from different depths.

Tests of cohesive soils have shown that stress-history effects can be an important factor in response to vibratory loading. However, additional tests have indicated that some of these effects may be "shaken out" by a few cycles of high amplitude loading. Drnevich, in 1967, determined that a prestrain amplitude of 10^{-4} or lower did not induce significant stress-history effects on G at low amplitude vibrations.

Empirical formulas to estimate the maximum shear modulus of soils serve as a means of checking the value of G_{max} obtained using the experimental curves of G versus γ . The well known formula developed by Hardin and Black (18), is equally applicable to cohesive and

cohesionless soils and takes into consideration the affects of void ratio, stress history and effective confining pressure.

$$G_{\max} = 1230 \frac{(2.973 - e)^2}{(1 + e)} (\text{OCR})^K \bar{\sigma}_o^{-0.5} \quad (52)$$

where

G_{\max} and $\bar{\sigma}_o$ are in psi

e = void ratio

OCR = overconsolidation ratio

K = constant value of which depends on plasticity index, PI , of the soil

Various empirical formulas defining damping in terms of logarithmic decrement, δ , employ viscoelastic models. Hardin (17) using a Kelvin-Voight model formulated the following relation in which μ is the viscosity of the soil

$$\delta = \pi \left[\frac{\mu \omega}{G} \right] \quad (53)$$

Use of complex shear modulus, assuming the soil to be a linear viscoelastic solid is another analytical procedure to obtain damping relation which was discussed in part in Section 2.1. The complex shear modulus, G^* , is considered to be composed of a real and an imaginary component, each of which is a function of frequency,

$$G^*(\omega) = G_1(\omega) + i G_2(\omega) \quad (54)$$

where $G_1(\omega)$ is the elastic component and $G_2(\omega)$ is the viscous component.

The angle by which the strain lags the stress in a soil sample undergoing sinusoidal excitation is δ_L , which is given by

$$\tan \delta_L = \frac{G_2}{G_1} \quad (55)$$

and it is related to the logarithmic decrement, δ , as

$$\delta = \pi \tan \delta_L \quad (56)$$

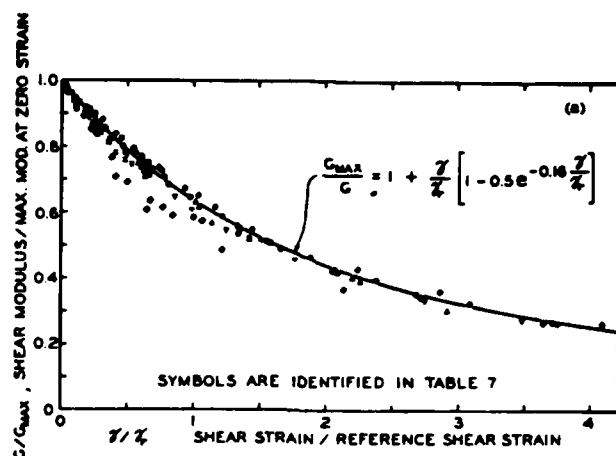


Figure 30. Normalized Shear Modulus and Shear Strain Relation (from Hardin, et al. (19))

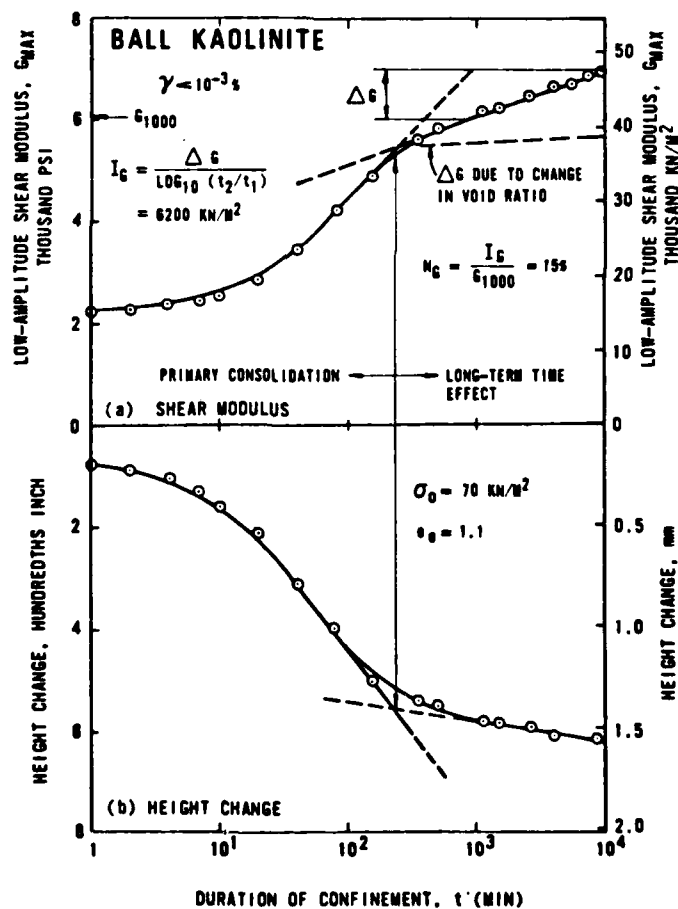


Figure 31. Typical Modulus and Height Changes With Time for Clay at Constant Confining Pressure (from Anderson, et al. (1))

However, the use of complex modulus approach for dynamic situations involving large amplitude vibrations is not recommended by Richard, et al. (42).

Having discussed the general aspects of dynamic testing and in particular resonant column testing, this section will be completed with a brief discussion of the general problems encountered in resonant column testing. As in most tests, calibration and operation of the instrument as well as the integrity of the sample and appropriate confining stress are the major factors that influence the results. In resonant column testing particularly, other problems are encountered which are in terms of "time effects", stiffness of the specimen and, coupling between the specimen and end platens for torsion (for end platens refer to the description of the apparatus in the methodology section). If the stiffness of the specimen and the apparatus parts are nearly the same, then the possibility of those parts deforming during the test would introduce errors in the measurements made on the specimen. Likewise, if complete coupling between the end platens and the specimen is not achieved, then the possibility of slipping between platens and specimen would introduce further errors in the results. Both sources of errors would produce lower moduli values and higher damping values than actually exist. To overcome the slipping affect, end platens with embedded razor blade vanes are utilized (13). The stiffness of the specimen in torsion is given by

$$K_{\text{torsion}} = \pi d^4 G / (32 L) \quad (57)$$

where d, L are in inches and G is in psi.

To reduce the specimen stiffness, readjusting d/L ratio is sufficient. On the other hand, the problem of deformation of apparatus

parts during testing is naturally non-existing when soft specimens are tested, which will be the case in this study reported herein.

In recent years, attention has been drawn to the fact that "time effects" can help to account for the difference between moduli obtained in the laboratory and in the field. In order to determine the magnitude of time effects, longer-term laboratory tests (on the order of days or more) must be performed. This procedure, in turn, gives rise to air-migration through the confining medium and membrane into the specimen pore space, thus reducing the degree of saturation. This problem is most critical when the confining medium is compressed air. Several techniques are useful in reducing the air migration. They are, coating the membrane with grease on the exterior, and using another confining medium, such as deaired water, mineral oil or silicone oil.

Influence of duration of confining pressure, termed as "time effects" earlier, is of fundamental importance in laboratory evaluation of shear modulus and damping ratio. Various tests on undisturbed specimens of sands and clays showed that when they were confined at constant pressures, the shear moduli measured at shearing strain amplitudes below 0.001 percent (low-amplitude moduli) increased, and the corresponding damping decreased with time of specimen confinement (1). This behavior is attributed to the primary and secondary consolidation of the specimen during the confinement time. Figure (31) illustrates typical changes in shear modulus and vertical height of the specimen with time under constant pressure. The time effects are expressed in two parts. First is the primary consolidation time effect and the second is the long-term time effect corresponding to secondary compression of the specimen.

Anderson and Stokoe (1), through numerous tests with both artificial and natural soil samples, formulated the following procedure to estimate maximum shear modulus in the field using the maximum shear modulus obtained from resonant column testing after the primary consolidation of a specimen. This procedure is based on studies predicting that the in-situ modulus is higher than that measured in laboratory (Stokoe and Richart, (58); Stokoe and Abdel-razzak, (56)). The ± 50 percent difference between the in-situ and laboratory measurements, as estimated by Cunny and Fry (12), is not taken to be the criteria in this estimation procedure. Moduli variation due to sample disturbance is not taken into account, also. The procedure utilizes the following formula,

$$G_{\max(\text{field})} = G_{\max(\text{primary})} + F_A \times I_G \quad (58)$$

where

$G_{\max(\text{primary})}$ = maximum shear modulus measured at the end of the primary consolidation, as shown in Figure (31)

F_A = age factor for site

I_G = coefficient of shear modulus increase with time

F_A and I_G are given by the following formulas, respectively

$$F_A = \log_{10} (t_c / t_p) \quad (59)$$

where t_c is the time since start of most recent significant change in stress history at the site, and t_p is the time to complete primary consolidation at site as a result of stress change.

$$I_G = \frac{\Delta G}{\log_{10} (t_2 / t_1)} \quad (60)$$

where t_1 and t_2 are times after primary consolidation and ΔG is the change in low-amplitude shear modulus from t_1 and t_2 , as shown in Figure (31).

Observation of equations (59) and (60) shows that the second term in equation (58) is added to take care of the long term-time effects estimated to occur in the field. In a dynamic situation such that the "stress changes are faster than the consolidation of the soil" as in the case of Mississippi Delta sediments--which is the main interest of this study reported herein--equation (58), accounting for primary and secondary consolidation effects in field, proves to be invalid. In the case of these highly soft and mainly underconsolidated sediments, the effects of sample disturbance stands to be the major factor to be accounted for in adjusting laboratory measurements to estimate field values. However, since it is not possible to prevent completely the structural reorientation and stress relief to occur during sampling and specimen preparation, integrity of the results obtained through laboratory tests of so called "undisturbed" samples would have to depend on the technique and judgement of the investigator. In the case of testing the very soft and weak samples of Mississippi Delta, specially, the judgement and techniques used, could only serve to define a consistent trend of behavior within the limits of data obtained which is reproducible under the same conditions.

2.3 CRITICAL STATE MODEL FOR CYCLIC LOAD RESPONSE OF SOILS

Methods for evaluating pore pressure and strength change responses for fine grained soils under cyclic loading are significantly scarce compared to methods for coarse grained soils. Increasing concerns about the behavior of soft clay submarine floors under wave loading brings about the need to study the pore pressure and effective stress changes they undergo, as well as the mechanics of their dynamic response.

Effective stress methods developed by Martin, Finn and Seed (31), Finn, Lee and Martin (16), Rahman, Seed and Booker (40), Liou, Streeter, Richart (28), Seed, Martin, Lysmer (50), and a number of other investigators all evaluate, specifically, volume changes and pore pressure responses in coarse-grained soils. The major concern of all effective stress methods used to predict cyclic load response is the development and/or dissipation of excess pore water pressure expressed in terms of volume change characteristics of the soil media. High pore water pressures that lead to low effective stresses are observed to occur in Mississippi Delta sediments, initially due to the fact that the deposition is faster than the consolidation of the sediment. Cyclic wave loading adds to the severity of the condition by inducing volume change forces and increasing the pore pressures even more. The progressive pore pressure increase leads to progressive effective stress decrease and continuous distortion under the static and dynamic load. This in turn results in a condition that the soil starts behaving like a "frictional fluid", and flows. In order to predict the volume changes which bring about pore pressure build up and softening, a hypothetical model that applies to cohesive or fine-grained soils must be formulated.

Egan and Sangrey (15), developed a model within the framework of critical state soil mechanics to predict volume change and pore pressure response of soils under cyclic loading. The model is applicable to all soil types. At this point, it is beneficial to review major theoretical concepts of critical state soil mechanics briefly, before discussing the model that employs these concepts.

2.3.1 Concepts of Critical State Soil Mechanics

The basic consideration in critical state soil mechanics is that if soil or other granular materials are continuously distorted, at some state of stress and volume, the material will start flowing as a frictional fluid. During the process of continuous deformation, due to particle rubbing against each other, some power dissipation occurs, which is simply defined as "friction". The fully remolded condition of the soil can be claimed to be the state at which it starts flowing like a frictional fluid. This ultimate state of stress and volume is defined the critical state of soil and serves as the base upon which critical state soil mechanics concepts are built. The problem now reduces to define the stress and volume change in soil from any initial state to the ultimate critical state, and/or how much of that total change can be expected when the distortion process is not carried to the fully remolded state of the soil.

Critical state is basically defined by two equations (47),

$$q = Mp \quad (61)$$

$$\Gamma = v + \lambda \ln p'_0 \quad (62)$$

where M , Γ and λ are basic soil property constants, v is the specific volume, p'_0 is the mean effective stress and q is the deviator stress. These relations are illustrated in Figures (32a) and (32b), respectively. The first equation determines the magnitude of deviator stress, q , to keep the soil from flowing under the mean effective stress, p'_0 . The second equation states that the specific volume, v , occupied by unit volume of flowing particles will decrease as the logarithm of mean effective stress increases. The term "wet" defines the state of soil which is looser than critical state and the term "dry"

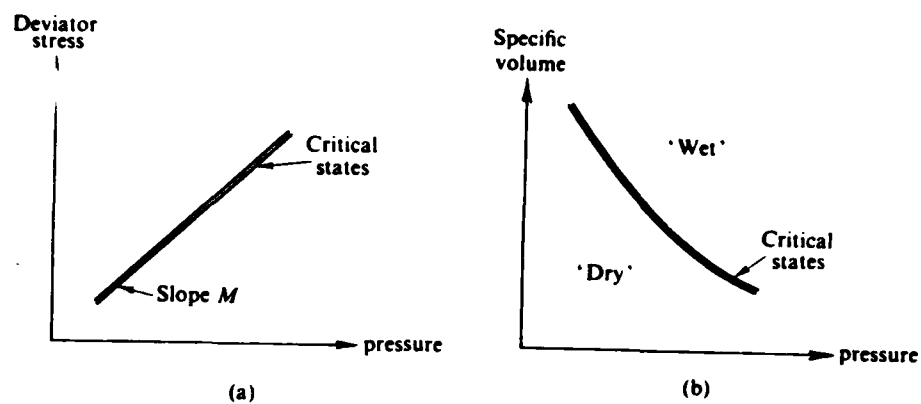


Figure 32. Critical States (from Schofield and Wroth (47))

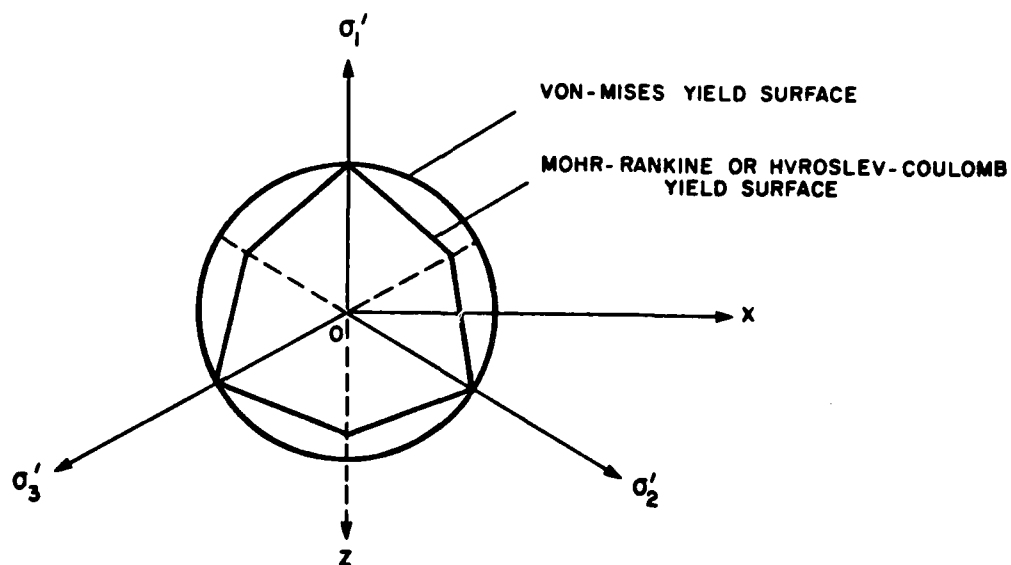


Figure 33. Sections of the Yield Surfaces

defines the state of soil which is denser than critical state. The range of stress states for both cases are indicated in Figure (32b).

When the initial state of soil is wetter than critical during deformation specific volume will tend to decrease thus creating positive pore pressures. For the dry case, the specific volume will tend to increase and create negative pore pressures.

Critical State Soil Mechanics is based on yield criteria and plasticity concepts, which can be inferred from the discussion above. Failure of soils by yielding are generally expressed by two well known yielding theories, Mohr-Rankine and Von Mises criteria. Yield surfaces corresponding to these criteria are given in Figure (33). The Mohr-Rankin Criterion is a maximum principal stress theory which states that the material fails by yielding when the maximum principal stress exceeds the tensile yield strength or when the minimum principal stress exceeds the compressive yield strength (62). That is at yielding

$$|\sigma'_1| = \sigma'_{yp} \quad \text{or} \quad |\sigma'_3| = \sigma''_{yp} \quad (63)$$

where σ'_{yp} and σ''_{yp} are the tensile and compressive yield strengths, respectively. The Mohr-Rankine theory is based on Hvorslev-Coulomb theory which defines a range of states of failure in the near vicinity of critical states. Extending the basic theory, Mohr-Rankine criterion predicts the state of stress when the soil continuum is yielding to failure. Von Mises Criterion predicts that, failure by yielding occurs when at any point in a body in a state of combined stress, the distortion energy per unit volume becomes equal to that associated with yielding in simple torsion (62). The fundamental equation of the theory is

$$(\sigma_1 - \sigma_2)^2 + (\sigma_2 - \sigma_3)^2 + (\sigma_3 - \sigma_1)^2 = 2 \sigma_{yp}^2 \quad (64)$$

where σ_{yp} is the tensile strength. It is observed from equation (64) that since only the differences of the principal stresses are involved, an equal increase or a decrease in each stress does not effect the yielding condition. In other words, yielding does not depend upon hydrostatic tensile or compressive stresses. Von Mises criterion is also expressed in terms of distortion energy.

$$U_{od} = \frac{3}{2} \frac{1 + \mu}{E} \tau_{oct}^2 \quad (65)$$

where τ_{oct} is the octahedral stress, and in simple tension it can be expressed as

$$\tau_{oct} = 0.47 (\sigma_{yp}) \quad (66)$$

The shear stress at yield, τ_{yp} , is related to the tensile strength, σ_{yp} , by the following equations according to Mohr-Rankine and Von Mises yield theories, respectively (62).

$$\tau_{yp} = \sigma_{yp} \quad (67)$$

$$\tau_{yp} = 0.577 (\sigma_{yp}) \quad (68)$$

Materials capable of undergoing an appreciable amount of yielding or permanent deformation are regarded as ductile, if they suffer only small yielding before failure they are regarded as brittle materials. Most brittle materials exhibit greater resistance to compression than to tension. Therefore, σ''_{yp} is larger than σ'_{yp} . The ductile materials exhibit a characteristic strengthening called strain hardening as the loading is increased beyond yield. Experiments show that for ductile materials, shear stress at yield, obtained in torsion tests, are on the order of 0.5 to 0.6 times the tensile stress at yield obtained in simple tension tests. Equation (68) derived by assuming equal tensile and compressive yield strengths, seem to agree with the experimental results for ductile materials the best. Therefore, one can correctly conclude

that Von Mises yield criterion in the most suitable formulation to express the nonlinear stress-strain behavior of soils with one major assumption that the soil is of ductile nature and/or σ'_{yp} is equal to σ'_{yp} . Then yield strength can be denoted by a single term, σ'_{yp} .

Two of the basic critical state soil mechanics models are Granta-Gravel and Cam-Clay. The first represents an ideal rigid-plastic continuum, while the latter represents an ideal elastic-plastic continuum. For the purpose of the study reported herein, the elastic-plastic continuum model will be adopted since it represents the stress-strain and volume change behavior of clays. A typical critical state yield surface in three dimensional sketch is given in Figure (34). An elastic-plastic material, in a state of stress within the boundaries of the yield surface is considered to behave elastically, and outside the boundaries it is considered to deform plastically. In addition to illustrating the main difference between Granta-Gravel and Cam-Clay models, Figure (35) aids to understand the stress-strain and volume change characteristic of the two models. In this figure the yield surfaces are represented with respect to (p,q) plane, where

$$p'_0 = \frac{\sigma'_1 + \sigma'_2 + \sigma'_3}{3} \quad (69)$$

and

$$q = \sigma'_1 - \sigma'_3 \quad (70)$$

These stress parameters were defined as mean effective stress and axial deviator stress, respectively, earlier. The tips of yield surfaces correspond to the isotropic virgin consolidation of the materials under uniform pressure, $p = \sigma'_1 = \sigma'_2 = \sigma'_3$. Cam-Clay displays recoverable, non-linear volumetric strains, while Granta-Gravel remains at its final volume state, v_0 , when the mean effective stress is reversed.

AD-A118 157

LOUISIANA STATE UNIV BATON ROUGE DEPT OF CIVIL ENGIN--ETC F/G 8/10
CLASSIFICATION OF COASTAL SEDIMENTS.(U)
MAR 82 J N SUMAYDA, M TUMAY

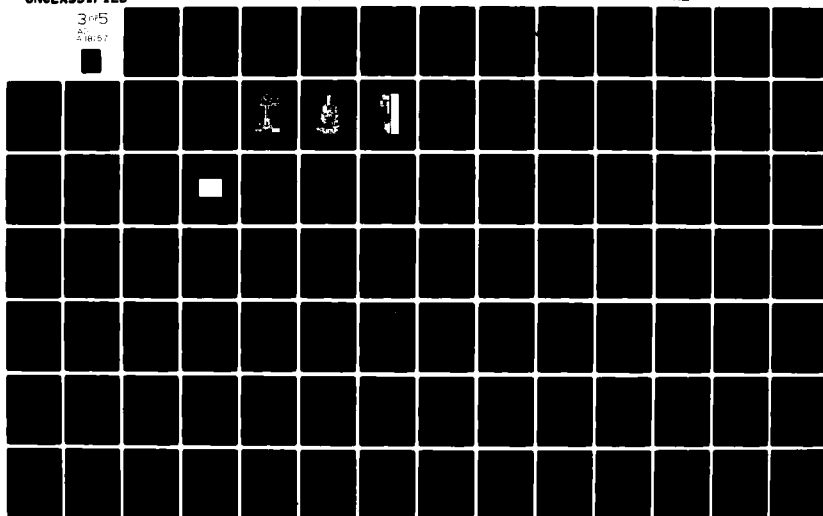
N00014-80-C-0846

ML

UNCLASSIFIED

3 of 5

218107



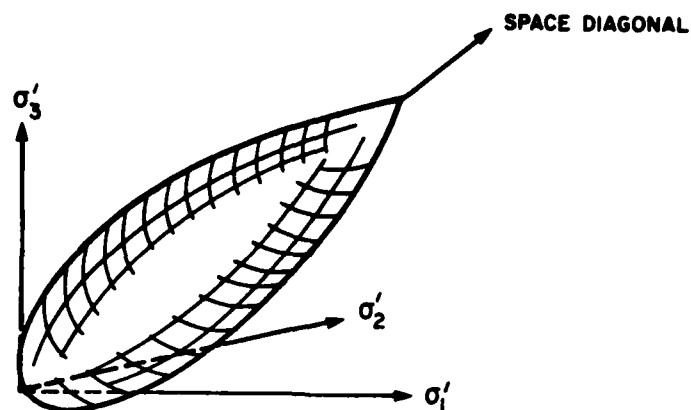


Figure 34. Critical State Yield Surface (from Schofield and Wroth (47))

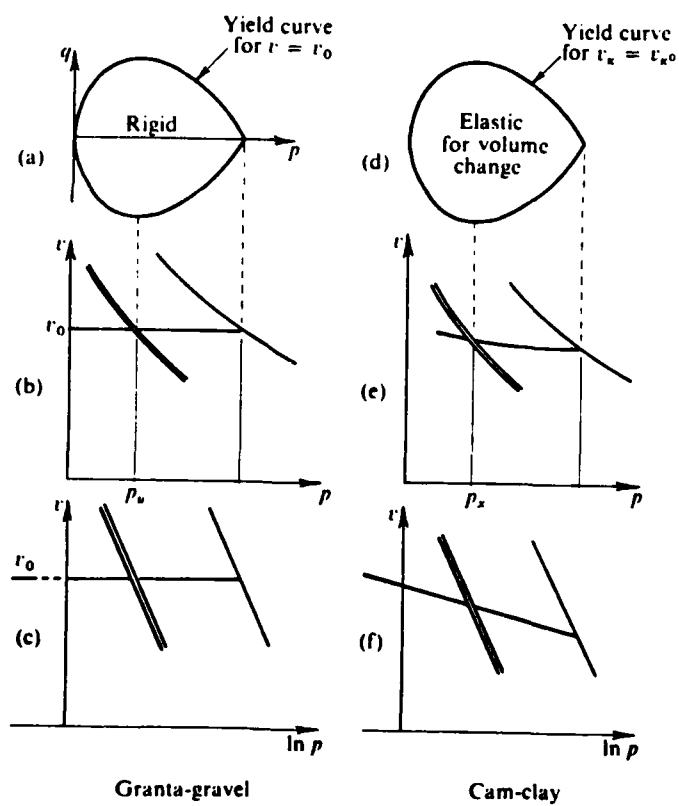


Figure 35. Yield Curves for Granta-Gravel and Cam-Clay (from Schofield and Wroth (47))

A representation of yield curves in (p, q, v) space for Cam-Clay is given in Figure (36). Each yield surface is a curved one to account for the recoverable volumetric strains. The material displays a rigid response to any change in shear stress, q , and an elastic (non-linear) response to any change in mean effective stress, p'_0 , within the yield surface. If the state of stress falls outside the yield surface boundaries, then a change of magnitude Δv occurs in specific volume of the specimen, so that it is permanently distorted into a "new" specimen with a new yield curve of its own. The successive yield surfaces in Figure (36) represent this effect as the volume of the material change under increasing value of p . The points, C_1, C_2 , etc. on the same figure are the points at which the line given by equation (61) crosses the yield surface. The line that connects these points is called the critical state line.

Since the use of three dimensional state space is rather cumbersome, a two dimensional representation will be adopted. Figure (37) illustrates a typical yield surface and the corresponding volumetric compression curves for Cam-Clay model. The critical state line (denoted by double lines), is the projection of the actual state line given in three dimensional illustration. From Figure (37) it is observed that point C is the intersection of the yield surface and the $q = Mp$ line, where M is the slope of the effective stress failure envelope. Point V, at the tip of the yield curve, corresponds to the virgin compression of the specimen at p'_0 mean effective stress, and zero shear stress. At the critical state, denoted by point C on yield surface, the soil specimen reaches to its ultimate state of stress under shear, where it resists deformation with its minimum strength,

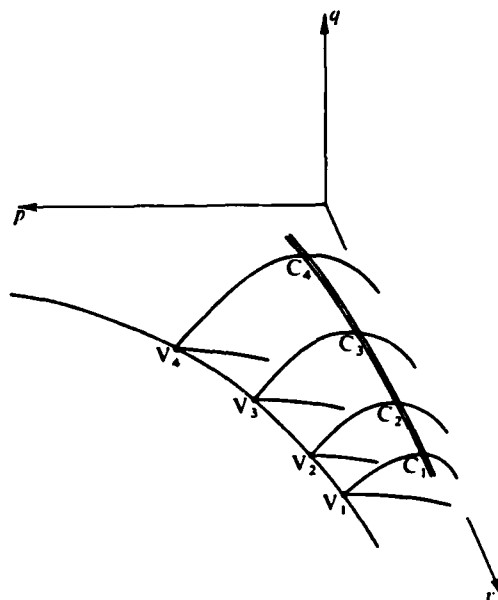


Figure 36. Upper Half of State Boundary Surface for Cam-Clay (from Schofield and Wroth (47))

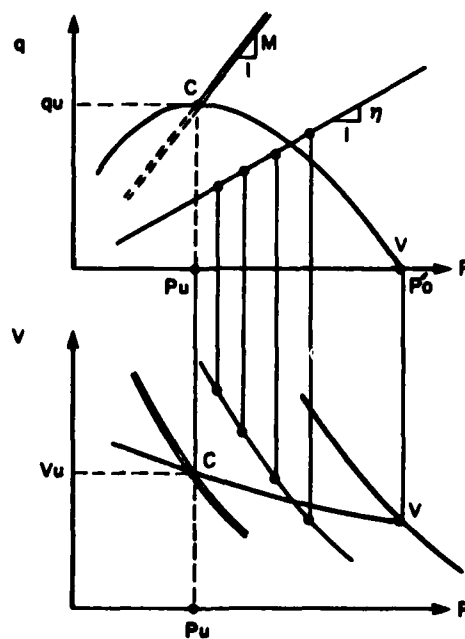


Figure 37. Yield Curve for Cam-Clay (from Schofield and Wroth (47))

corresponding to remolded strength. The ultimate shear stress and mean effective principal stress at critical state are denoted by q_u and p_u , respectively. Critical state is also defined as the condition at which the soil deforms continuously with no change in volume, deviator and mean effective principal stresses. It is the lowest effective stress condition that can cause failure of the soil for a particular consolidation stress history, as stated by Egan (14). The term η is the ratio of q to p at yield under a succession of load increments that produce continuous yielding and in turn a series of yield surfaces (refer to Figure (36)). The corresponding volume compression curve under this constant stress increment is called the peak failure line. This line usually corresponds to the critical state line for insensitive remolded soils, as observed by Egan (14). For sensitive soils it falls between the virgin compression (VCL) and critical state line (CSL). Note that these assumptions and observations are made for the elastic-plastic (Cam-Clay) model of critical state soil mechanics theory.

2.3.2 Critical State Model for Cyclic Loading

Volumetric compression is generally characterized by two curves, the virgin compression curve and the rebound compression curve (non-linear elastic response). The virgin compression consists of both plastic and elastic volumetric strains. Expressing the volume change in terms of void ratio, e , the fundamental relation for virgin-compression is given by

$$e_\lambda = e_0 - \lambda \ln (p/p'_0) \quad (71)$$

where λ is the slope of the straight line portion of the plot of $\ln p$ versus e , and e_0 and p'_0 are the initial void ratio and mean effective

principal stress, respectively. The rebound compression is similarly expressed by

$$e_k = e_o - \kappa \ln (p/p_o') \quad (72)$$

where κ is the slope of the rebound curve on semi-logarithmic scale.

In reviewing the critical state model for cyclic loading developed by Egan and Sangrey (15), the virgin compression curve for an isotropically normally consolidated soil will be considered and it will be referred to as IVCL. Similarly, the critical state line and the rebound compression line, will be referred to as CSL and RSL, respectively.

An element of soil that is isotropically normally consolidated lies on the isotropic virgin compression curve, and its initial state is defined by e_o , q_o and p_o' , where $q_o = 0$. The soil element is then subjected to repeated cycles of loading under undrained conditions. This forces the behavior of rebound curve to be a stress path of constant void ratio, as indicated by the line segment A-C in Figure (38a). Assuming that the amplitude of the repeated loading, q_{cyc} , is equal to the critical shear stress level, q_u , the soil element experiences both plastic and elastic work during each cycle of loading. Figure (38b) illustrates the cyclic loading with respect to critical state conditions in p, q space.

Since drainage is not possible during the rapid loading, the volume change tendencies result in storage of strain energy within the soil element, which in turn correspond to excess pore pressure buildup. When the deviator stress, q_{cyc} , is removed, due to fractional increase in pore pressure, the effective stress migrates to a lower value, as represented by p_1 in Figure (38b). The cumulative result of each

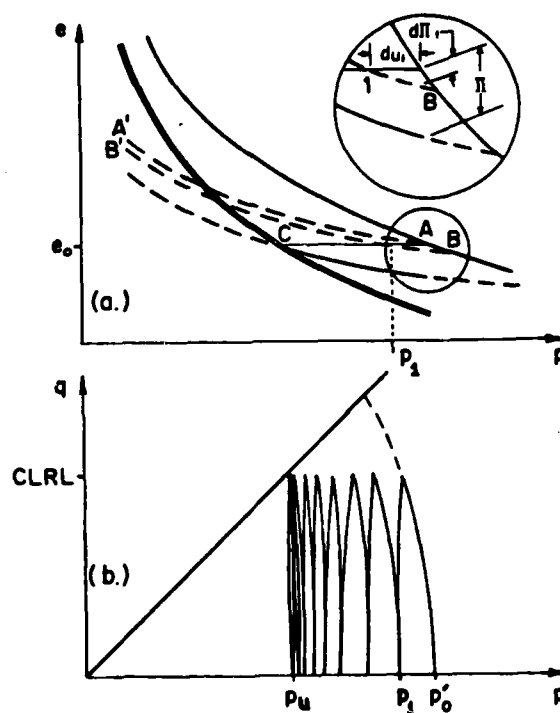


Figure 38. State Response of an Isotropically Normally Consolidated Soil Cycled at the Critical Level of Repeated Loading (from Egan, et al. (15))

migration is the effective stress value at critical state, p_u , as indicated in Figure (38b), or by point C on CSL, in Figure (38a). The migration of effective stress level comes about by the work of unrecoverable plastic strain energy. The volume change potential associated with the total plastic work is defined by π and it is the sum of all the increments for each cycle. Observing Figure (38a), π can be expressed by the following relation

$$\pi = \kappa \ln [p'_0/p_u] \quad (73)$$

The total residual excess pore pressure due to the plastic strain is

$$du_r = p'_0 - p_u \quad (74)$$

or, substituting p_u from equation (73)

$$du_r = [1 - \exp(-\pi/\kappa)] p'_0 \quad (75)$$

The maximum excess-pore pressure response is obtained by adding the elastic strain affects (which are maximum at the top of each loading cycle and recovered at the end) to the total residual excess pore pressure. The elastic pore pressure response at the top of each loading cycle is assumed to be 1/3 of the cycling stress amplitude, q_{cyc} , or the critical state stress, q_u . The resulting equation for maximum excess pore pressure response after replacing q_u by $(M_{exp}(-\pi/\kappa))$ is

$$du_{max} = [1 - \exp(-\pi/\kappa) (1 - M/3)] p'_0 \quad (76)$$

When the soil element is allowed to drain, the accumulated excess pore pressure will dissipate, the volume of the soil element will decrease by amount of π , so that the new void ratio value will be e_f . If the initial volume of the soil element is given by $1 + e_0$, the volumetric strain potential, which will be denoted by ϵ_v , can be written as follows.

$$\epsilon_v = \frac{\pi}{1 + e_0} \quad (77)$$

Furthermore, if a cylindrical soil specimen of initial volume V , undergoes a volume change of Δv , the volumetric strain, δv , is given by

$$\delta v = \frac{\Delta v}{V} = \frac{\delta e}{1 + e_0} \quad (78)$$

In terms of axial and radial strains, denoted as $\delta \epsilon_1$, $\delta \epsilon_2$, and $\delta \epsilon_3$, respectively, the same equation can be written as

$$\delta v = \delta \epsilon_1 + 2\delta \epsilon_3 \quad (80)$$

Shear strain, $\delta \gamma$, can also be derived using axial and radial strains (43),

$$\delta \gamma = \frac{2}{3} (\delta \epsilon_1 - \delta \epsilon_3) \quad (81)$$

Rearranging and substituting equation (80) into (81), the relationship between volumetric strain and shear strain is obtained.

$$\delta \gamma = \delta \epsilon_1 - \frac{\delta v}{3} \quad (82)$$

Under constrained boundary conditions where no radial strains are allowed, as in a conventional one dimensional consolidation test δv is equal to $\delta \epsilon_1$, therefore equation (82) reduces to

$$\delta \gamma = \frac{2}{3} \delta v \quad (83)$$

From Figure (38a) and the earlier argument about the volume change potential being activated when dissipation of pore water pressure is allowed, one can conclude that

$$\pi = e_0 - e = \delta e \quad (84)$$

Through manipulation of equations (77), (78) and (83) one can readily derive the relation between volume change potential and the corresponding shear strain of a soil element for one dimensional consolidation.

$$\gamma = \frac{2}{3} \left[\frac{\pi}{1 + e_0} \right] \quad (85)$$

This information will aid in predicting critical state yield stress-strain parameters and material properties when coupled with the dynamic analysis data, which is to be presented later in the results phase of this study.

Volume change potential values and related material properties of several different clays including San Francisco Bay Mud, are given in Table 1. The data represent both cyclic as well as static loading testing programs both of which are equally sufficient to obtain critical state parameters.

Table 1
Summary of Index and Critical State Parameters for Clays and Silty Clays
(from Egan (14))

Soil Name and Reference	w_L^* (%)	w_p^* (%)	G_g^*	ϕ'^*	λ	κ	π
San Francisco Bay Mud Egan (1977)	98	42	2.69	37.5	0.3847	0.0217	0.0164
Concord Blue Clay Egan (1977)	33	22	2.76	24.8	0.0707	0.0173	0.0150
Agnew Hospital Clay Egan (1977)	54	30	2.73	25.0	0.0688	0.0213	0.0195
Illite Clay France (1976)	57	26	2.78	24.5	0.1826	0.0322	0.0193
Newfield Clay Sangrey (1968)	28	18	2.75	29.0	0.0521	0.0083	0.0061
Seattle Clay Sherif, et al. (1972)	52	26	2.71	25.7	0.1263	0.0271	0.0138
Norwegian Drammen Clay Brown, et al. (1977)	55	28	2.76	30.7	0.1770	0.0210	0.0137
Bangkok Clay Balasubramaniam, et al. (1976)	118	43	2.78	25.4	0.2215	0.0395	0.0215
London Clay Parry (1956)	78	26	2.75	22.5	0.1610	0.0620	0.0381
Kaolin London (1967)	74	42	2.61	26.0	0.2600	0.0500	0.0404

* w_L = liquid limit, w_p = plastic limit, G_g = specific gravity, ϕ' = effective ϕ angle
 λ , κ = basic soil property constants, π = volume change potential

Chapter 3

METHODOLOGY

3.1 GEOGRAPHIC AND GEOLOGICAL INFORMATION OF SAMPLE SITE

The specimens tested in laboratory for index and dynamic properties were obtained from a bore hole located near Main Pass of Mississippi River at a water depth of 10 m. Sampling was done by McClelland Engineers, Inc., for the geologic and foundation study phase of investigation conducted for Texaco, Inc. Among the six borings, three of them were undisturbed sample borings and the rest were wash logs. A number of samples from hole B-6, location of which is given in the general vicinity map in Figure 39, were donated to LSU Geotechnical Engineering Laboratory for research purposes. The depth of the samples ranged from 0.2 m to 110 m. A schematic depth profile for the samples are given in Figure 40.

Sediments deposited by Mississippi River are advanced seaward from the river mouth, at a rate of 4 miles in 150 years, as observed by the movement of 30 ft. contour eastward into the Gulf of Mexico over that extent of time (30). Great thicknesses of very soft clays below sea floor are encountered immediately to the east of the boring location in concern. They are known to accumulate by large-scale delta front movements in forms of mud flows and turbidity flows. Generally, the mud flow strata overlies on earlier sedimentary sequence of continental shelf marine clays that were deposited prior to the arrival of the modern delta. Mud flow strata are gassy from biogenic methane production and

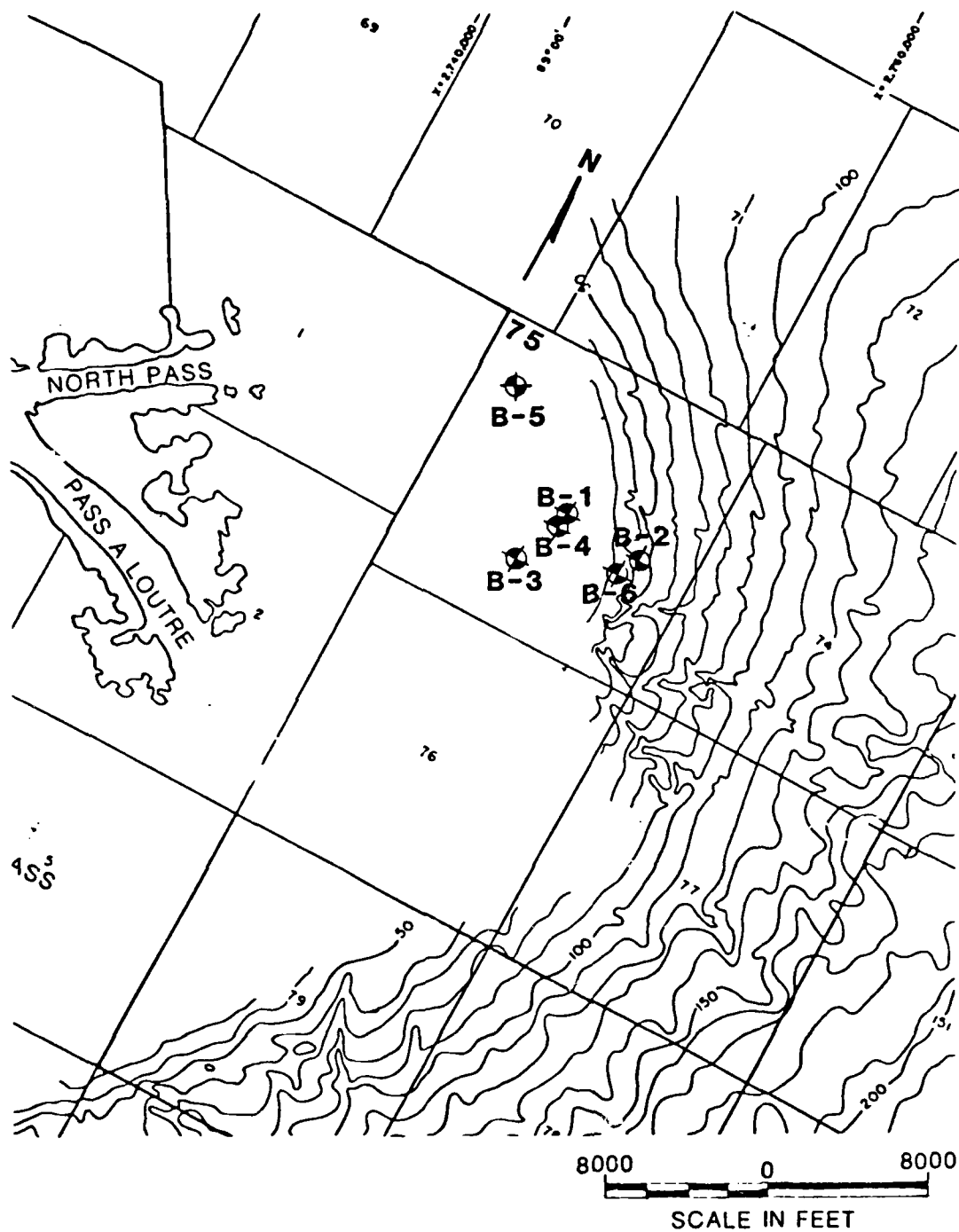


Figure 39. Vicinity Map for Block 75 Main Pass of Mississippi Delta
(from McClend Engineers' Geotechnical Report (30))

are highly underconsolidated due to the fact that deposition is faster than consolidation.

Most borings in the region encounter a dense material, characteristically sand near the depth of 75 to 90 m from mudline. This formation is attributed to an earlier delta on the continental shelf that occurred near the end of the Late Wisconsin glacial period. This early deltaic stratum was encountered at 75 m of depth from mudline in Boring B-6, as reported by McClelland Engineers, Inc. (30). Presence of wood and shell fragments both in the sand strata and below 90 m of depth suggested probable exposure of the shelf during low water stages in the Late Wisconsin. A highly plastic, non-gassy clay layer is reported to overlie the sand in Boring B-6 below 60 m of penetration, in the same investigation. This stratum is composed of continental shelf marine clays that were deposited during and after the rise of ocean level at the close of the Pleistocene. The recent deposits of Mississippi Delta, probably less than 100 to 150 years old, constitute the upper 60 m of material which is gassy in nature and mostly composed of mud flows.

When the water depths decrease in front of the distributary bar due to mudflows and turbidity flows that carry sediments to deeper water, then silt and fine sand are deposited directly onto the seafloor from river and ocean currents. This deposition process in turn produce a layer of stronger material overlying much weaker sediments. The silty, sandy zone close to the surface is a typical occurrence in Mississippi Delta front, and is called the "crustal" zone. The shear strength profiles for Boring B-6, from the investigation of McClelland Engineers Inc., indicated this crustal zone to be near 9-12 m of penetration with a peak shear strength of 14 kPa. The strengths decreased to as little

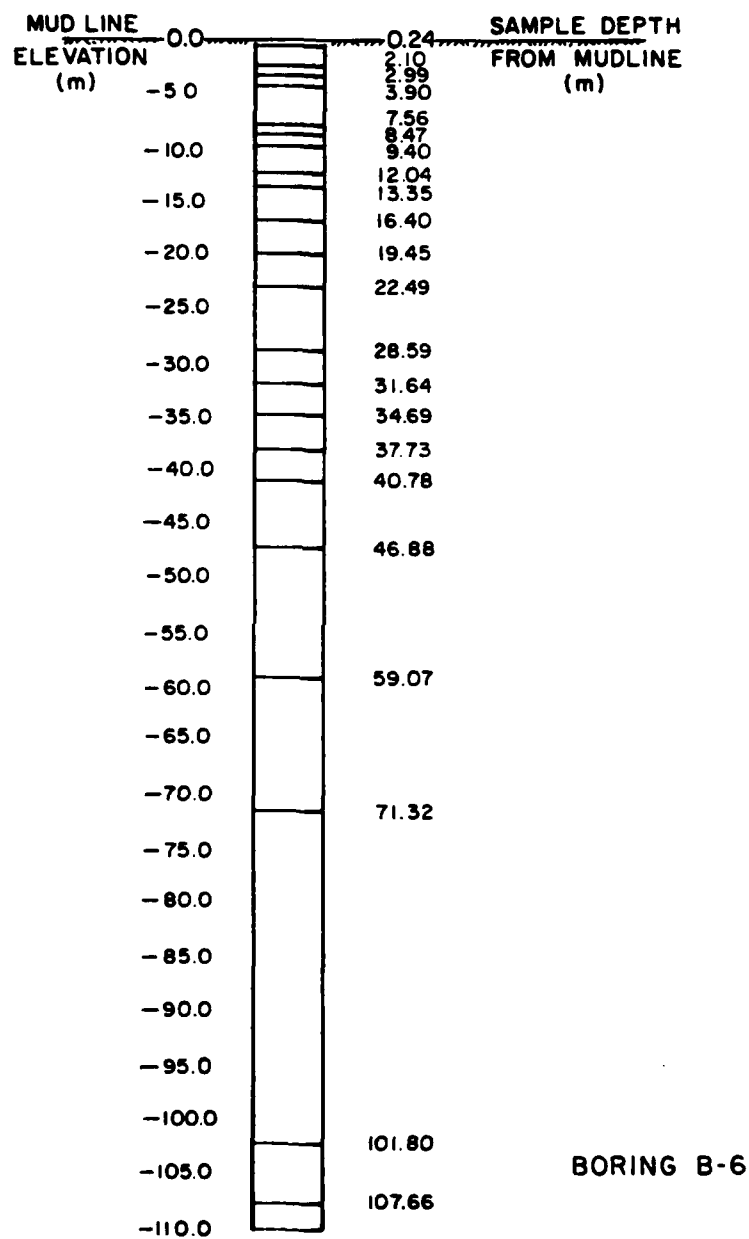


Figure 40. Depth Profile of Boring B-6 and Location of Samples

as 5 kPa below the crust zone. Investigation also indicated that the strength distribution was nearly linear down to the sandy layer around 75 m of depth. Below the sandy layer, stiff to very stiff clay was encountered starting around 85 m of depth. Extending down to the bottom of the bore hole (down to an approximate depth of 120 m) this clay layer exhibited very high shear strength values.

The gassy nature of the samples recovered from the top layer was suggested by their saturation values of 80-90 percent, which was in contrast to near 100 percent saturations of the prodelta clays encountered below 60 m of depth.

3.2 EXPERIMENTAL PHASE

3.2.1 Sample Information and Utilization

Samples were recovered in "hard plastic" tubes of outside diameter 5.74 cm, inside diameter 5.37 cm and an approximate length of 12.50 cm. They were sealed tightly on both sides to eliminate drying. Samples were extracted out of the tubes by manual means, taking great care to avoid disturbance. In spite of the careful manipulation, due to their extremely weak nature, disturbance in form of peeling and shear cracks did occur on the surface of most samples during the process of extraction. The disturbance was eliminated to a degree, when the samples were trimmed to a smaller diameter (~3.80 cm), and the top and bottom portions were cut off to prepare for dynamic testing procedures.

A total of 29 samples were provided from Boring B-6. The depths of these samples from mudline are given in Figure 40. Out of 29 samples, 22 of them were tested for dynamic and index properties. After being recovered from the resonant column apparatus, 17 of these samples were

subjected to undrained shear strength tests using a triaxial apparatus. Four of the samples from different depths were used in the consolidation study to obtain critical state parameters. Two consolidation tests were conducted for each sample, one with undisturbed, the other with remolded sample.

Initially, upon extraction from the recovery tubes, the water contents of the samples were measured. After trimming and preparing for dynamic testing the weight and dimensions of the samples were measured to determine the bulk unit weights. Air dried samples were subjected to plasticity analysis, in which their liquid limits (w_L), plastic limits (w_p) and plasticity and liquidity indices were determined. Specific gravity tests were conducted on mixtures of air dried samples, each mixture representing a layer of material more or less homogeneous in properties. This information was used in consolidation data reduction, where each consolidation test data was also assumed to represent several layers of material as one homogeneous layer in the numerical analysis phase. Finally, a sensitivity analysis was conducted for the upper soft clay layer, using a laboratory drop-cone apparatus.

3.2.2 Dynamic Experiments

3.2.2.1 Description of the apparatus and experiment setup

The dynamic properties of the samples were determined through a Drnevich Resonant Column apparatus. This apparatus was a torsional vibration type resonant column, where the samples were subjected to torsional cyclic loading. Figures 41, 41.A and 42 show the resonant column apparatus, details and the electronic device setup in connection to it, respectively.

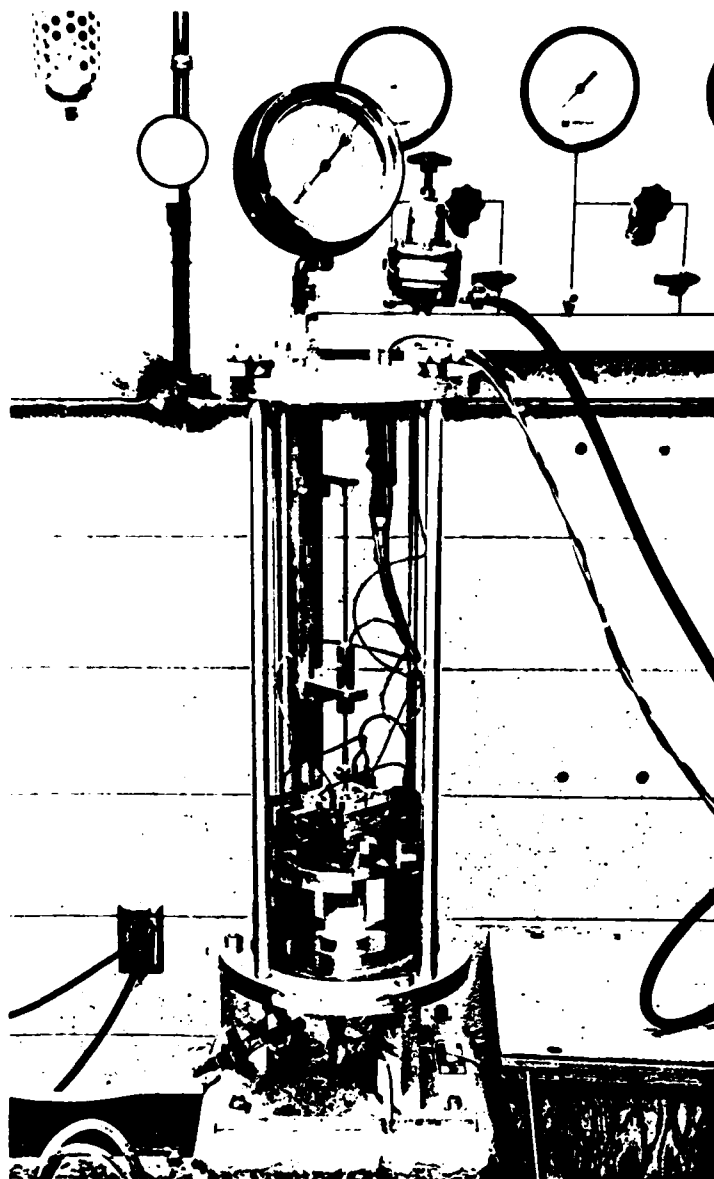


Figure 41. Drnevich Resonant Column Apparatus

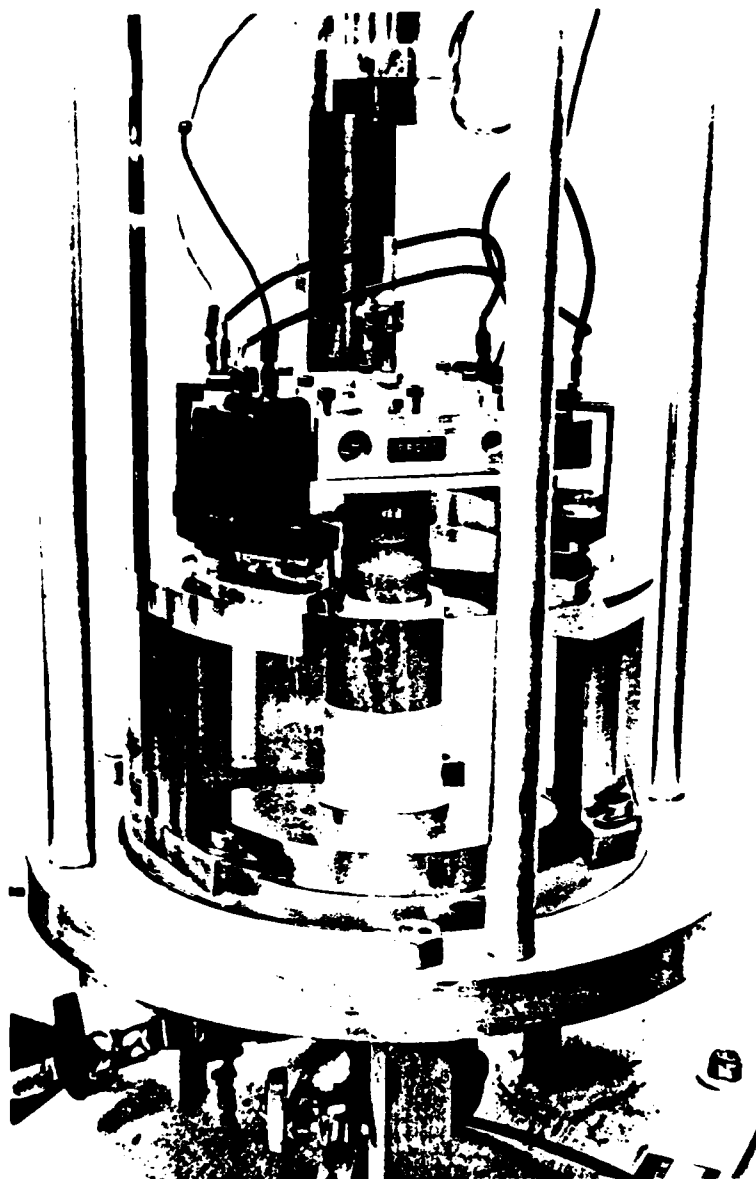


Figure 41.A. Details of the Sample Setup and Coil System

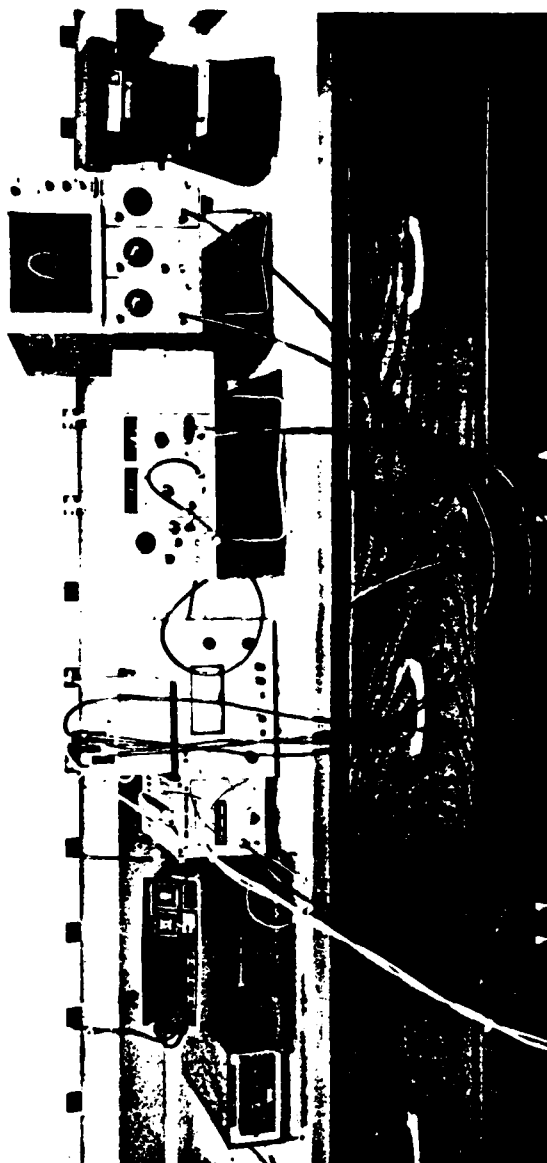


Figure 42. Electronic Device Setup of the Resonant Column

The resonant column apparatus was mounted on a concrete base that stood 0.45 m from the floor. This massive base helped to keep the apparatus free of the floor vibrations. A regulated compressed air supply capable of pressurizing from near zero to 690 kPa (7 bars), was provided to confine the samples within the column. However, due to equipment limitations, only a maximum of 414 kPa pressure was available. This deficiency did not produce serious errors since only 2 of the samples required higher confining pressures than 414 kPa. Due to fairly recent installment of the instrument, the system of burettes normally used to measure volume changes under static consolidation were not available. Nevertheless, since both confinement and tests were conducted under undrained conditions, lack of this setup did not interfere with the testing procedures. A pore pressure transducer attached to the base of the specimen, and a pressure readout unit connected to the transducer were provided. This set up was used occasionally to check the pore pressure response of the specimen under undrained conditions. A pore pressure reading close to the confining pressure would suggest the saturation of the sample to be nearly 100 percent. An attempt to measure pore pressure changes during cyclic loading was unsuccessful, due to the fact that the change in readings were insignificant in magnitude and did not follow a consistent path for the long durations of vibration at high amplitude strains (i.e., 1-2 hours at 0.1 percent strain amplitude). The confining medium for the specimens was distilled water. This choice of medium eliminated in part the possibility of air migration into the pore space of the specimens during long term confinement.

Figure 43 shows the electrical wiring diagram for a typical Drnevich Resonant Column apparatus. The wave generator is the source of the power that drives the coils. The device used in this research was a Tektronix FG 503 model multiple function generator which had sine, square and triangle waveforms with a frequency range of 1 Hz to 3 MHz. The sine waveform was used to drive the coils. A frequency dial on the generator made it possible to fine adjust the frequency at resonance. A power amplifier of Hewlett-Packard Model 6824A was used to amplify the low output power of the wave generator. The power input is then connected to the resonant column apparatus control box, where a switch on the box controls the power to the driving coils. A Tektronix DM501 Model digital multimeter that measures DC and AC voltage and current is also connected to the control box. Another switch on the box selects either the readout of the current (mv rms) applied to the driving coils, or of the voltage output from the accelerometer (mv rms) in connection to the specimen response in vibration. The voltmeter was used in the AC mode. A Tektronix DC504 Model counter/timer was used to either measure the resonant frequency or the resonant period. It is a digital readout unit with frequency and period ranges of 0.1 Hz to 80 MHz, 1 μ s to 999.99 s, respectively.

The driving coils are mounted on a permanent magnet that is in turn fit and fastened tightly over a cylindrical cap on top of the specimen. The magnet also houses a rotational acceleration transducer (accelerometer). The rotation of the top of the specimen is measured by measuring the rotational acceleration and then converting to displacement dividing by $(2\pi f_n)^2$, where f_n is the natural frequency in Hz. Accelerometer signals are read out from the voltmeter, as discussed

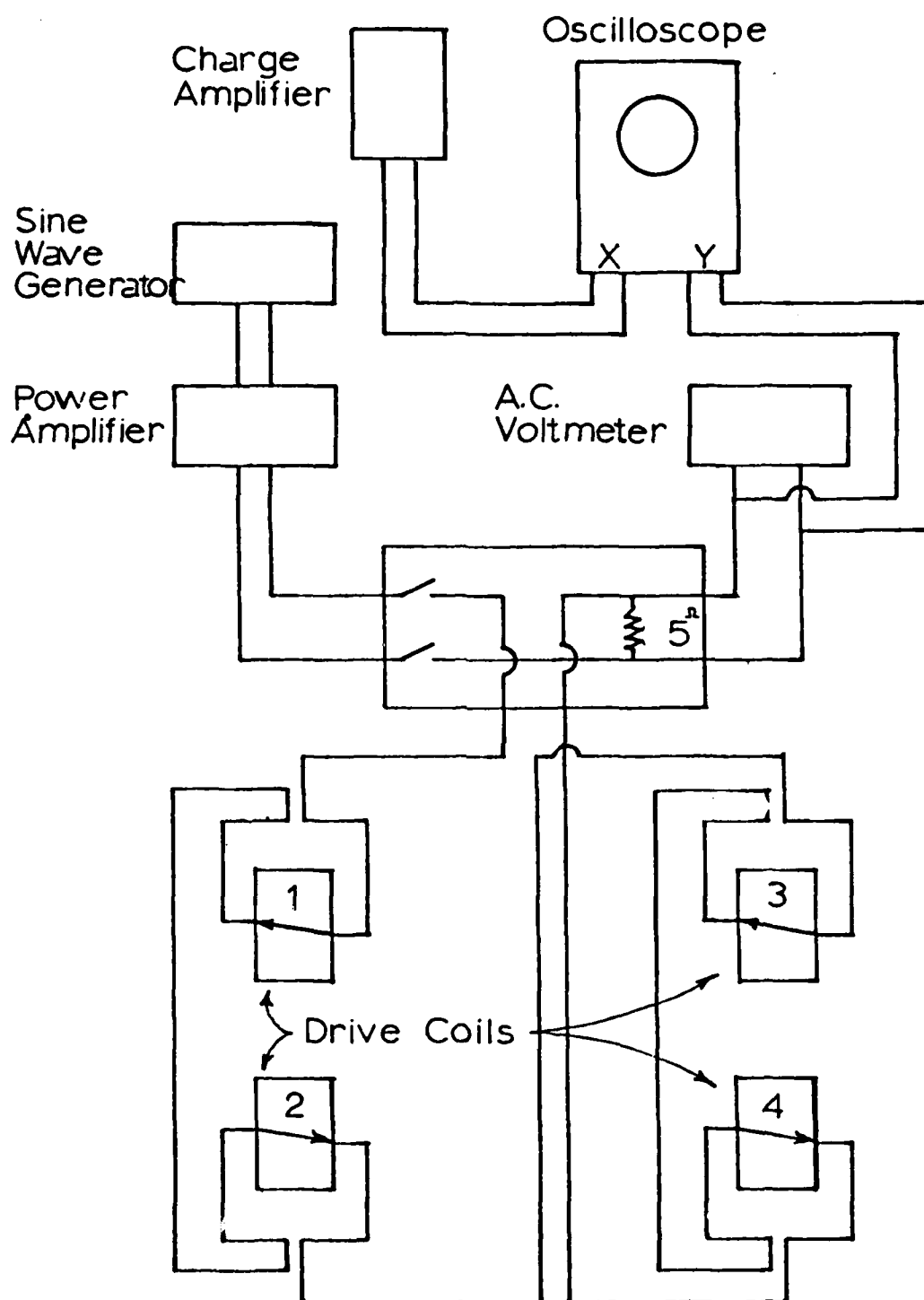


Figure 43. Electrical Wiring Diagram for Typical Drnevich Resonant Column

above. The weight of the permanent magnet is carried by a vertical spring which in turn is connected to a length change transducer (LVDT) and fastened safely onto a reference bar at the top of the column. The length change transducer is a Schaevitz, Type 300 HR Model that has a linear range of ± 0.762 cm. The LVDT is also connected to a separate readout unit. Since the tests were conducted under undrained conditions, static length change measurements were not made. Observing that they were insignificant in magnitude and did not have noticeable influence on the data, the LVDT measurements were discontinued after a number of tests.

The final and the most important electronic device used in connection to the resonant column is the storage oscilloscope. The type used in the research was Tektronix Model 5111, with large screen 8 x 10 division display and each division being equal to 1.27 cm. This device is used to detect the "Lissajous" figure which is an ellipse on the x-y display at resonance of the specimen. It is also used to estimate damping of the material by conducting "run-down" or logarithmic amplitude decay tests on x-time display and storing the image on the screen which can then be captured on a photographic film. This is done using a special camera that can be mounted on the oscilloscope screen. The oscilloscope used in this research had two 5A15N type amplifiers which regulated the x-y display, and one 5B10N time base amplifier which regulated the time display.

3.2.2.2 Specimen preparation and apparatus assembly

As soon as a sample was extracted out of its recovery tube, a small portion was cut off for water content determination. Then it was trimmed down to a diameter of 3.80 cm and a length of 7.50 cm, on the

average (diameter and length of each specimen actually differed slightly from these average values). After the trimming was completed the dimensions and weight of the specimen were measured for bulk unit weight calculation, where

$$\gamma_b = \left[\frac{W_{\text{total}}}{V_{\text{total}}} \right]_{\text{wet specimen}} \quad (86)$$

Then the sample was mounted on the heavy stainless steel base of the resonant column with outlets to the pore pressure transducer and vacuum. This was done outside the resonant column device, since the base piece was removable and provided higher flexibility for fine work. The base piece was equipped with razor blade embedded porous stones upon which the specimen was set. The necessity of coupling between the apparatus parts and the sample was discussed earlier in the theoretical considerations section. The beneficial results of using razor blade embedded porous stones for that matter was emphasized. The solid metal cylindrical cap that was placed on top of the specimen was also equipped with a razor blade embedded porous stone. Using a membrane expander, the membrane and rubber O-rings were installed on the specimen. Before moving and fastening the setup to the resonant column, a stainless steel split mold was tightened about the specimen with hose clamps in order to secure the specimen from further disturbances until the apparatus assembly was completed. After the set up was tightened onto the resonant column base, the permanent magnet was aligned and fastened onto the top cap of the specimen. The magnet was then connected to the spring and the LVDT. Driving coils were installed on the magnet and checked for any rubbing points between the coils and the magnets. This check is most important to ensure the free vibration of the magnet without any friction forces developed that would alter the current,

acceleration and frequency readings, as well as the shape of the Lissajous figure essential to determine the resonance condition. At this point, normally a routine calibration for LVDT readout is conducted. However, this step was eliminated for a number of experiment setups due to the reasons stated earlier in this section. After the completion of the inner installations, the split mold around the sample was removed and the plexi-glass pressure chamber was placed over the assembly. The wiring connections were made on the top lid of the column. The lid was then tightened over the chamber by use of four vertical rods that extended along the height of the column. Two O-rings, one at the top and the other at the bottom provided the insulation of the chamber. Note that the wiring connection for the pore pressure readout is underneath the base plate where the pore pressure transducer is attached to the base upon which the specimen is set. The base in turn sits on another rubber O-ring with the transducer connection extending out through a hole on the base plate of the resonant column (refer to Figure 41). The acceleration, current and LVDT readout wiring connections are made on the top lid. Distilled water was let in to fill the chamber until it covered the top O-ring of the specimen through a valve beneath the base plate. The filling procedure was carefully manipulated so that the water never came in contact with the driving coils. The water valve was then closed and the air pressure supply with pressure regulator was connected to the top lid. Finally, the chamber was pressurized at the desired confining pressure.

3.2.2.3 Testing procedures

All the samples were confined at their calculated effective overburden stresses for a period of 24 hours under undrained conditions.

The following list of reasons account for this practice.

1. Failure or yielding of the material in the site is theoretically assumed to occur under undrained conditions since rapid cyclic loading of clay--or other granular material for that matter-- doesn't allow for pore pressure dissipation.
2. The recovered samples are assumed to represent the original site conditions even though they had undergone significant disturbance during sampling and preparation procedures. This conclusion was derived due to the insensitive nature (sensitivity = 1-4) of the material (refer to Table 3).
3. In order to determine the maximum shear modulus presumed to exist in-situ, the sample should not be consolidated. Otherwise consolidation will naturally strengthen the sample and result in higher shear modulus values than actually exist.

However, confining for a period of time under undrained conditions did also induce strengthening effect on the samples. The confinement period for several of the samples was extended longer than 24 hours in order to observe the effect. The strengthening effect can be explained by a number of assumptions. One of them is that an experimental error occurred such that complete undrained conditions could not be simulated and some drainage was inevitable. Another one is that the soil particle frame transformed gradually from a relaxed structure to a firmer structure without a net change in the void ratio, under the sustained

pressure. This change can be attributed to the gaseous nature of the samples; possible partial saturation effects (indicated by the saturation values of some samples in Table 9), and electro-chemical characteristics and complex behavior of the clay-water system. The gas content and pressure within the pore space is a factor that influences the mechanical behavior of the clay matrix significantly. Under sustained confinement the gas could go into solution by dissolving in the pore water thus increasing the saturation. On the other hand the same process could also bring about some electro-chemical changes within the clay matrix. Changes in the thickness of the diffuse double layers and adsorbed water layer due to ion attraction to the clay surface (34a) thus altering the electrical attraction and repulsion characteristics of individual particles could result in a possible "thixotropic" behavior. This in turn would cause the formation of a firmer structural frame with stronger particle bonds. The influence of temperature changes on marine clays as observed by Bischoff, et al. (9a) and Fanning and Pilson (15a) is also an important factor that could account partially for the shear modulus results of this study. Since it is not within the scope of this research, no detailed reasoning can be presented at this stage. However if the "strengthening" or "thixotropic" change is considered to have taken place, then one can safely assume that confining the samples a reasonable amount of time would help to "shake off" the sampling and preparation disturbances significantly. Note that a consistent duration of confinement (24 hours) was chosen for this study. The confining pressures for each sample tested are given in Table 2.

At the completion of the confining period, the samples were subjected to a series of torsional vibration forces consecutively

Table 2
Confining Pressures of Samples
in Resonant Column Test

Depth From Mudline (m)	Confining Pressure, σ_c (kPa)
0.244	13.79
2.100	17.24
2.980	20.69
3.900	27.58
7.560	51.71
8.470	55.16
9.390	69.00
12.040	75.85
13.350	94.05
16.400	96.53
19.440	124.11
22.500	131.01
28.600	124.11
31.640	137.90
34.680	172.40
37.730	179.30
40.780	200.20
46.880	213.75
59.070	324.08
71.320	413.72
101.800	413.72
107.650	413.72

increasing in amplitude. This was achieved by turning the switch on the control box to "standby" position and then setting the voltmeter to a desired power output and finally turning the control switch to "on" position to transfer the power to the driving coils in the resonant column. The driving coils then set the magnet and the sample into torsional vibratory motion. Note that the sample was set up so that its base was fixed and the top end being attached to the magnet was free to move. Referring back to the discussion on resonant column apparatus sample boundary conditions in Chapter 2, this situation is observed to be a fixed-free type of boundary condition and the vibratory motion is pure cyclic torsion with an angle of twist, θ . The undamped resonance condition is achieved when the ratio of the acceleration at the top of the sample to that at the bottom of the sample is maximum, and the phase angle, ϕ , between the sine wave at the top and bottom of the sample approaches 180° (refer to Figure 25b). At resonance the oscilloscope screen displays a figure called the "Lissajous" figure and it is an ellipse with horizontal and vertical axes coinciding with the x-y axes of the screen. Figure 44 illustrates a typical Lissajous figure obtained at the resonance of one of the samples tested. Note that the ellipse can be distorted due to imperfect apparatus assembly or may include some vibration effects from outside or electrical network. To achieve the resonance condition, the fine frequency adjustment dial was turned until an ellipse with the description above, appeared on the oscilloscope screen. The input current and the corresponding undamped natural frequency or period values were read from the digital multimeter (voltmeter) and the digital counter (timer), respectively. Switching to the accelerometer output on the control box, the acceleration value of

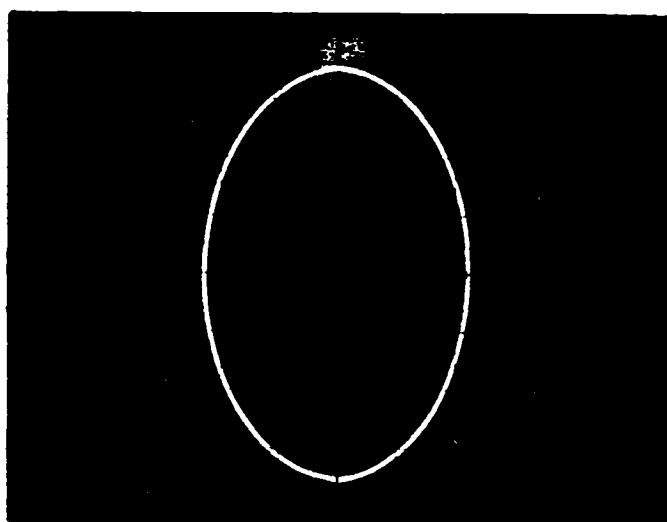


Figure 44. Typical Lissajous-figure (obtained from one of the tests with a Mississippi Delta sediment specimen)

the sample was read from the digital multimeter, also. The same procedure was repeated for a range of input power values in ascending order. In addition to these, another set of readings were taken at $\sqrt{2} \times f_n$ for the smallest input power value. This was done by setting the frequency to $\sqrt{2}$ times the undamped natural frequency and reading the current and acceleration values at that value of frequency. The set of data obtained in this manner were then used in the calculations of damping ratio, which will be discussed in the next subsection.

Several of the samples were tested for their degradation behavior with increasing number of cycles of loading. This was done by keeping the input power constant and recording the frequency and acceleration values at resonance randomly. In doing so, the Lissajous figure had to be restored to its original position by adjusting the frequency before each set of readings. The reason for this practice was that due to long periods of vibration, the material properties would change slightly so that the sample adopting a new fundamental frequency would drop out of resonance condition. This in turn would cause a slight distortion in the shape of the Lissajous figure. As stated earlier, by adjusting the frequency, the figure was restored back to its original shape, which in turn yielded the set of readings for the new resonance condition. The results and discussion of the number of cycle dependency of the shear modulus will be given in Chapter 4. However, at this point, it is beneficial to note that, the sequence of readings made to measure the input power (or strain amplitude) dependence of shear modulus were assumed not to be influenced by the extra number of cycles of loading while they were taken. This assumption is supported first by the fact that the low amplitude shear modulus values are essentially independent

of the number of cycles of loading. The high amplitude measurements, on the other hand, were done fast enough so that degradation effects that could have altered the readings were eliminated.

3.2.2.4 Data reduction procedure

The constitutive equations and constants for evaluation of dynamic properties using the data obtained from resonant column testing are given below.

(i) Shear modulus and shear wave velocity

$$G = \rho \left[\frac{2 \pi f_n l}{\beta} \right]^2 \quad (87)$$

where

ρ = mass density of sample

l = length of sample

$\beta = f(J/J_0)$

J = mass polar moment of sample

J_0 = mass polar moment of attached weight on top of the sample

$$J_0 = 28.44 \text{ gm cm sec}^2$$

$$J = \frac{M D^2}{8g}$$

where

m = mass of sample

D = diameter of sample

g = acceleration of gravity

$$\frac{J}{J_0} = \beta \tan \beta \quad (88)$$

Equation (88) is solved for β either by iteration or by Drnevich curves (42).

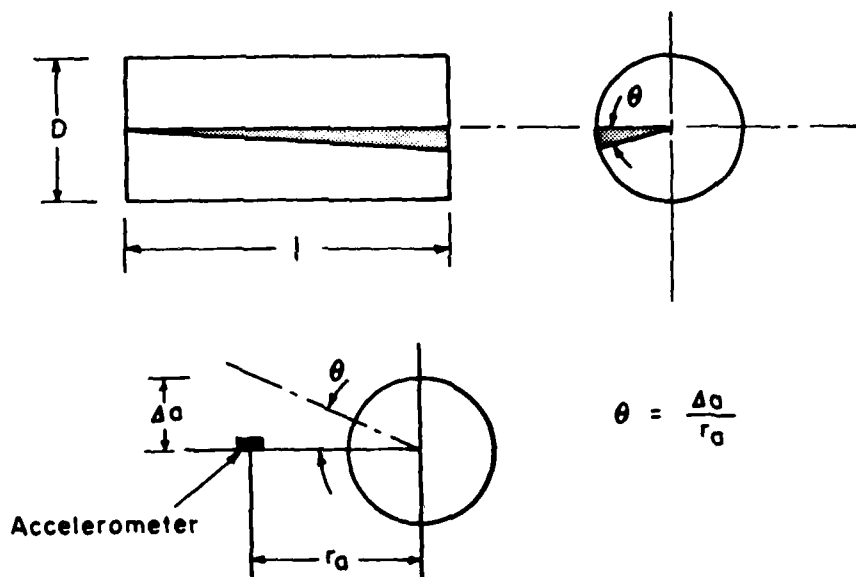
$$V_s = \frac{2 \pi f_n \ell}{\beta} \quad (89)$$

where

V_s = shear wave density

In the calculations above, only measurements for D , ℓ and f_n are needed.

(ii) Strain Amplitude



$$\gamma = \frac{D}{3} \frac{a}{r_a \ell} \quad (90)$$

where

γ = shear strain

a = acceleration displacement

r_a = acceleration radius

$$\Delta a = \frac{35.12 \times \text{Acceleration Reading (mv-rms)}}{\text{ACF} \times f_n^2}$$

ACF = acceleration calibration factor (pk-mv/pk-g)

ACF = 2,500 pk-mv/pk-g

$r_a = 3.75$ cm

Then

$$= 14.74 \left[\frac{D}{l} \right] \frac{1}{f_n^2} (\text{Acceleration rdg. mv-rms}) \quad (91)$$

Measurements for all the parameters in equation (91) are needed.

(iii) Damping Ratio

Using the Magnification Factor Method the damping ratio is calculated as follows

$$D(\%) = DCF(\%) \left[\frac{\text{Current Reading}}{\text{Acceleration Reading}} \right]_{f=f_n} \quad (92)$$

where

$$DCF(\%) = \frac{1}{4R} \left[\frac{\text{Acceleration Reading}}{\text{Current Reading}} \right]_{f=\sqrt{2} f_n}$$

and

$$R = \frac{1}{J \left[1 - 0.27 \left(\frac{0}{J} \right)^{-0.92} \right]}$$

DCF is calculated only once at $\sqrt{2}$ times the low amplitude resonant frequency, i.e., the amplitude where the measured modulus is nearly equal to the maximum modulus.

Data of the resonant column tests were recorded manually on data sheets. The data reduction was done using a mini-computer program in BASIC language. The listing of the program and part of a sample output is given in Appendix C.

3.2.3 Experiments and Analytical Procedures to Evaluate Soil Index Properties and Shear Strength

3.2.3.1 Undrained triaxial tests

The samples were subjected to undrained triaxial test after they were recovered from the resonant column. Since resonant column testing is essentially nondestructive, the samples were sufficiently intact for strength testing. Only the top and bottom portions where the razor blades of the porous stones were embedded needed to be cut off.

The undrained shear strength tests were conducted under approximately the same calculated effective overburden stresses as in resonant column tests. The triaxial apparatus was ELE Tritest 50 Model with a separate constant pressure device. The data was recorded automatically on a data logger of Hewlett-Packard 3467A Model. A mini-computer program of BASIC language was utilized for data reduction in these sets of experiments also. The listing of the program and part of a sample output is given in Appendix C.

Most of the shallow samples failed by bulging outward rather than shearing along a plane. This behavior is typical of soft saturated clays with high values of Poisson ratio, μ (0.4-0.5). Typical stress-strain diagrams obtained for three different depths of samples are given in Appendix C (Plate C-5). For the samples that showed a strain hardening behavior, (e.g., the stress-strain behavior of 0.24 m deep sample) the failure was assumed to have occurred at 20 percent strain level. The undrained shear strengths in terms of cohesion were obtained using Mohr-Coulomb equation for undrained strength tests.

$$s_u = c = \frac{\sigma_d}{2} \quad (93)$$

3.2.3.2 Plasticity analysis, classification and other index properties

Liquid limit and plastic limit tests were performed on air dried samples. They displayed an average plasticity index of 33.0 and liquid limit of 60.0. Average liquidity index for the top 60 m of material was on the order of 1.40.

Using Unified Soil Classification System, the samples tended to cluster within the vicinity of "A" line, with larger portion classifying as CH (high plasticity clay) type of soil. Visual observations of the samples indicated some organic characteristic for certain depths due to the presence of small amounts of shell and wood fragments. In addition to this, the dark olive color and the "spongy" texture of the cross-sections (tiny holes that are presumed to bear gas), strongly suggested organic nature, especially for the top 60 m layer of material. However, fine sand and silty material was encountered around 4 m, 7.5 m and 14 m below mudline in pocket layers. Therefore, combining these visual observations with the plasticity analysis, the soil samples were classified as CH-MH-OH material in general, according to the Unified Soil Classification system.

The natural water contents of the top layer samples generally were higher than their liquid limits. This readily suggested under consolidation for these samples. However, the firmer samples below 60 m of depth were normally or overconsolidated. Note that these conclusions were made only through plasticity analysis and visual observations. Therefore, no quantitative verification can be provided at this point. Details of the plasticity analysis results are given in Chapter 4, and in a depth profile diagram in Appendix A (Plate A-2).

Dry and bulk unit weight profiles were prepared. The typical "crust" formation of Mississippi Delta sediments due to silty and sandy layer of material is indicated between 7 to 14 m of depth from mudline for this location of boring. The diagram of the profile is given in Appendix A (Plate A-1).

Specific gravity analysis were conducted for three separate mixtures of air dried samples. The first mixture consisted of random amounts of soil from 2.98 m, 3.90 m and 7.56 m samples. Likewise, the second and the third mixtures were prepared from 16.39 m, 19.44 m, 22.50 m, and 34.68 m, 37.73 m, 40.78 m, 46.88 m samples, respectively. The choice of the samples to make the mixtures was based on the closeness of the shear modulus values of these samples. Each mixture was assumed to represent a layer of slightly different material properties. However, the specific gravity value for each mixture did not differ significantly from the other two. They are given in Table 9.

3.2.3.3 Sensitivity experiments

Sensitivity analysis was performed using a Geonor A/S Model laboratory cone penetration apparatus (drop cone apparatus). In this procedure, the penetration of a cone of known weight and tip angle dropped from an initial position such that the cone tip touches the surface of the soil, is correlated to the undrained shear strength of the soil. This correlation is expressed by the following formula

$$s_u = k \frac{Q}{h^2} \quad (94)$$

where k is a constant which depends on the angle of the cone and is also influenced by the sensitivity of the soil. Q is the weight and h is the penetration of the cone. This relation is tabulated for various

Table 3
Sensitivity Analysis Results*

Depth From Mudline (m)	Undisturbed Shear Strength (kPa)	Remolded Shear Strength (kPa)	Sensitivity S	Classification
0.244	3.09	2.30	1.34	Insensitive
5.730	3.43	1.54	2.23	Insensitive
7.560	8.92	2.21	4.00	Insensitive
8.47	11.87	4.22	2.80	Insensitive

*Cone apex-angle = 60°
Cone weight = 60 gr.

penetration depths in mm. Several shallow samples were subjected to the laboratory cone penetration test before they were extracted from the recovery tubes. This in turn provided the penetration values that corresponded to undrained shear strength of the undisturbed sample. Same procedure was repeated after the samples were extracted and a portion of them were thoroughly remolded for testing. Penetration values for these portions yielded the undrained shear strength of the remolded sample. Applying the following equation, sensitivities of some of the shallow samples were estimated.

$$S = \frac{\text{undisturbed strength}}{\text{remolded strength}} = \frac{[S_u]_{\text{undisturbed}}}{[S_u]_{\text{remolded}}} \quad (95)$$

The results for this analysis are given in Table 3.

3.2.3.4 Assumptions and formulations to estimate K_o and μ

The most abundantly used formulation to estimate lateral earth pressure K_o , is the one that relates K_o to the friction angle ϕ . Since no experimental information was available about the value of ϕ angle, another formulation was adapted. It was Brooker and Ireland formulation that related K_o to plasticity index, I_p (11). Over the region from $I_p = 0$ to 40 percent the relationship is expressed as

$$K_o = 0.40 + 0.007 I_p \quad (96)$$

In the region $I_p = 40$ to 80 percent, it is approximately

$$K_o = 0.68 + 0.001 (I_p - 40) \quad (97)$$

Poisson's ratio μ is uniquely related to K_o state since it is a condition of no lateral strain. From the general Hooke's law by setting the lateral strains to zero, relation for μ is easily derived

$$\mu = \frac{K_o}{1 + K_o} \quad (98)$$

The estimated value of Poisson's ratio is used to predict mean effective stress which is a parameter for critical state analysis.

3.2.4 One Dimensional Consolidation Experiments used in Critical State Soil Mechanics Analysis

A set of consolidation tests for four samples from randomly chosen depths were conducted. Two consolidations were done for each sample, once in the undisturbed state and once in the remolded state of soil. Consequently, two separate compression curves were obtained for each sample.

Geonor Model Consolidometers were used and data were recorded automatically on a data logger. Data reduction was done using a computer program in FORTRAN language (61a).

Standard consolidation testing procedure was followed as closely as possible. Samples were soaked 24 hours in the consolidometer to induce swelling thus eliminating the potential for it, if any existed. None of the samples showed swelling behavior, instead they consolidated slightly under the weight of the top porous stone and metal cap. Due to the very soft nature of the material, the initial loading stress was chosen to be a small value. With a stress-increment ratio of 1.0, the loading was started from 0.05 kg/cm^2 and continued on to 6.4 kg/cm^2 except for the very top sample (2.99 m) which was loaded up to 3.2 kg/cm^2 . The undisturbed samples were unloaded with the same increment ratio to obtain the rebound curves. The compression curves for each sample are given in Appendix A (Plates A-81/A-84).

Evaluation of the critical state parameters were done using the procedures described by the critical state model for cyclic loading,

presented in Chapter 2. The mean effective stress, p'_o , was evaluated by the following formula.

$$p'_o = 1/3 [\sigma'_1 + 2 K_o \sigma'_1] \quad (99)$$

where σ'_1 is the calculated effective overburden pressure of the sample.

It is

$$\sigma'_1 = [\text{geostatic pressure} - \text{hydrostatic pressure}]_{h=\text{sample depth}}$$

Note that excess pore pressure values are not involved in the calculation of σ'_1 , simply because of the fact that they were not possible to be evaluated either by experimental or analytical methods for this study. However, it is important to note that studies to measure in-situ excess pore pressures in sediments of Mississippi Delta and Gulf of Mexico through use of piezo-cone penetrometer (61b) are underway, which will aid further in predicting design parameters for foundations of offshore structures. At this point, it is instructive to refer back to Figure (38a) of Chapter 2 in order to follow the procedure in predicting volume change potential of the material described here. The in-situ stress and volume state of the material is denoted by point A, with coordinates (p'_o , e_o). It is necessary to point out that the e_o value given on the semi-logarithmic plots of compression curves in Appendix A is not the same e_o referred to here. The value of e_o on those curves is the calculated initial void ratio of the sample before it was subjected to consolidation experiment. Under undrained, rapid loading conditions, the material yields to critical state along path A-C, with no change in its specific volume. In order to reach the same state of stress and volume at point C, the material would have to be at a higher state of stress initially on virgin compression curve so that when volume change is allowed by slow unloading process, it follows the

characteristic rebound curve to point C. The vertical difference between the line segment A-C and the rebound curve at (p'_0, e_0) point on virgin compression curve (or undisturbed compression curve in terms of the experimental analysis), is defined as the volume change potential, π . The graphical analysis includes locating (p'_0, e_0) point on virgin compression curve and extending a horizontal straight line to the critical state curve (or remolded compression curve in terms of the experimental analysis) to find the coordinates of point C denoted as (p_u, e_u) . The following assumptions are made in using this procedure, and they are important to note at this point of discussion.

1. The experimental one-dimensional compression curve is assumed to coincide with the theoretical isotropic virgin compression curve.
2. Due to the insensitive nature of material dealt with, the remolded compression curve is assumed to coincide with the critical state line.
3. The material is assumed to be cyclicly loaded at the ultimate state of stress on the yield surface, that is q_u . This level of loading is known to produce the largest pore pressure, and effective stress changes before failure by yielding (14).

Upon determination of values of the three essential parameters, p'_0 , e_0 , p_u , the following set of equations are used to predict the rest of the parameters defining critical state condition.

$$\text{Excess pore pressure} \quad du_r = p'_0 - p_u$$

$$\text{Volume change potential} \quad \pi = \kappa \ln [p'_0/p_u]$$

$$\text{Volumetric strain potential} \quad \epsilon_v = \frac{\pi}{1 + e_0}$$

$$\text{Shear strain at critical state } \gamma = \frac{2}{3} \left[\frac{\pi}{1 + e_o} \right]$$

Note that κ is the slope of the rebound curve on semi-logarithmic plot, and it is also determined graphically along with e_o and p_u . The equations given above are derived in Chapter 2. A table summarizing the calculated values of these parameters for the samples tested will be given in the results section of this study.

3.3 NUMERICAL ANALYSIS PHASE

Two distinct numerical solution techniques were employed in order to simulate the "movement" of submarine sediments in terms of displacements, strains, velocities and accelerations under cyclic loading. The major difference between the two techniques was that one was specifically developed for evaluating the dynamic response of soft marine sediments under the action of sinusoidal water wave train and the other one was a finite element solution method developed in general for response analysis of nonlinear materials under either dynamic or static loading conditions. The first method was wave-propagation viscoelastic sea bottom interaction analysis developed at Texas A & M University in 1974. The latter one was the finite element program, NONSAP (nonlinear structural analysis program) developed at the University of California, Berkeley in 1974. The choice of these numerical solution techniques to simulate dynamic response of Mississippi Delta sediments depended mostly on their availability. However, distinct capabilities of both techniques to represent material properties and loading conditions provided an insight to predict certain critical aspects that need to be considered in the analysis of dynamic response of these sediments in concern. The flexibility of each technique varied over certain input

phases. The following discussion will aid to understand these techniques and the way they were employed in this study.

3.3.1 Wave-Propagation Viscoelastic Sea-Bottom Interaction Analysis

This analysis was developed and contributed to by a number of investigators. The original investigator being Schapery (45,45a), other names such as King, Dunlap (26), and Stevenson (54) appear throughout the period the analysis was developed and modified. The solution technique is currently used commercially in offshore foundation design procedures.

In this method, the continuum mechanics approach is extended to represent a nonlinear viscoelastic material. The analytical solution for linearly viscoelastic material is derived first and by means of an approximate method, realistic soil nonlinearities are then taken into account. Effects of a sloping subbottom are also considered. Analysis is based on a clay-water system, rather than clay alone. The geometry and coordinate notation used in the analysis are shown in Figure 45.

The theoretical assumptions are as follows (45).

1. Each clay layer and the bottom half-space is homogeneous, linearly viscoelastic and isotropic.
2. The water is homogeneous and inviscid.
3. For both water and clay, volume strains ("dilatations") are negligible compared to shear strains; this assumption permits the use of the equations for "incompressible" clay and water.
4. With the exception of thin layers having relatively low strengths, the shear strains and rotations are small enough

that the standard linear strain-displacement relations can be used.

5. The subbottom is of infinite extent in the horizontal direction and is in a state of plane strain.
6. At a fixed station, defined by the value of x , the vertical water displacement at the surface, $y = 0$, is a sinusoidal function of time with zero mean value for all time.

The continuum mechanics equations for an elastic material were extended to viscoelasticity by means of so-called "correspondence principle" and the shear modulus G was replaced by a complex modulus G^* ,

$$G^* = G' + i G'' \quad (100)$$

where

G' = real part of complex modulus

G'' = imaginary part of complex modulus

and

$$|G| = \sqrt{G'^2 + G''^2} \quad (101)$$

Then the general continuum equations extended to viscoelasticity are given as (45),

$$G^* \nabla^2 u_c + \frac{\partial s'_c}{\partial x} = \rho_c \frac{\partial^2 u_c}{\partial t^2} \quad (102)$$

$$G^* \nabla^2 v_c + \frac{\partial s'_c}{\partial y} = \rho_c \frac{\partial^2 v_c}{\partial t^2}$$

where u_c and v_c are the horizontal and vertical displacement components of clay, ρ_c is the mass density and s'_c is a stress term given by

$$s'_c = s_c + \gamma_c v_c \quad (103)$$

where s_c is the decrement in effective stress on a clay particle due to wave action and γ_c is the unit weight of clay.

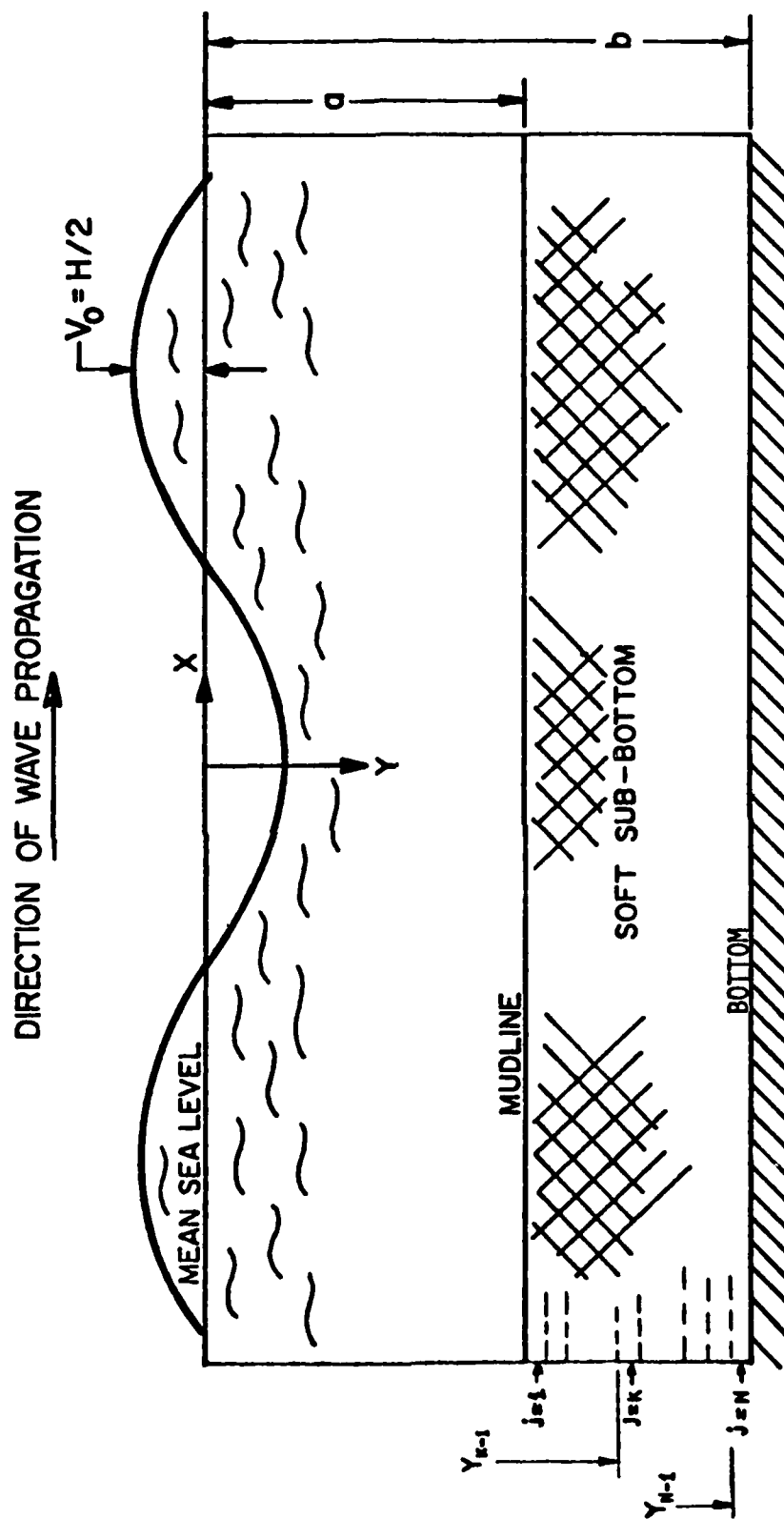


Figure 45. Cross-section of Water Clay System (from Schapery (45.a))

The complex shear modulus of the clay, G^* , is a function of circular frequency, $\omega = 2\pi/T_p$, where T_p is the wave period. G^* is defined as τ/γ when γ is

$$\gamma = |\gamma| e^{i\omega t} \quad (104)$$

G^* is also dependent on the stress level of loading. However, for very small stresses the clay can be assumed to be a linearly viscoelastic material defined by a constant rate of strain $\dot{\gamma}$, (linear relation of strain versus time). In this linear range viscoelastic properties (e.g., G^*) is independent of stress. The stress-strain equation for a linearly viscoelastic material is written in the form (36)

$$\tau = \int_0^t G(t - t') \frac{d\gamma}{dt'} dt' \quad (105)$$

where t' is a reference time, $G(t)$ is the relaxation modulus defined as the ratio of shear stress to strain when the strain is applied at $t = 0$ and held constant thereafter. $G(t)$ obeys a power law, for many materials including clays.

$$G(t) = G_1 t^{-n} \quad (106)$$

where G_1 and n are constants.

Values for G_1 and n obtained through vane shear tests (54) on sea-floor sediments, showed good correlation with vane shear strength and liquidity index, respectively. (Note that vane shear data taken at constant rotation rates is indeed applicable since linear viscoelasticity theory is based on constant strain rates.)

The amplitude of complex shear modulus, $|G|$, can also be expressed in terms of G_1 (36).

$$|G| = G_1 \Gamma(1 - n) \omega^n \quad (107)$$

where $\Gamma(1 - n)$ is Gamma function with argument $(1 - n)$.

The approximate method of nonlinear analysis start by assuming a secant shear modulus which is equal to the amplitude of the complex modulus, $|G|$, such that

$$G = \tau_m / \gamma_m \quad (108)$$

with τ_m and γ_m being maximum shear stress and strain, respectively. Substituting equation (108) into (107) and rearranging, the following relation for G_1 is obtained

$$G_1 = \frac{\tau_m / \gamma_m}{\Gamma(1-n)} \omega^{-n} \quad (109)$$

At this stage it is important to note that G_1 is the amplitude of the time dependent modulus $G(t)$ at constant strain rate. The relation for "n" is obtained by considering the phase angle, ϕ , between stress and strain, which is formulated as

$$\phi = \tan^{-1} (G''/G') \quad (110)$$

Referring back to Chapter 2 about the discussion of damping materials (2.1 and 2.2.2), equation (110) is readily recognized. Substituting the relations given for G'' and G' (36), ϕ is then expressed in terms of n.

$$\phi = \frac{n\pi}{2} \quad (111)$$

The stress-strain diagram for a linear viscoelastic material under harmonic straining is an ellipse, while the stress-strain diagram for cyclic loading (hysteresis behavior) can be estimated to be a parallelogram. These diagrams are given in Figures 46 and 47, respectively. In order to obtain "equivalent" linear parameters for nonlinear stress-strain behavior of soil, the areas enclosed by the parallelogram and ellipse are equated and solved for the ϕ , upon which the following relation is obtained.

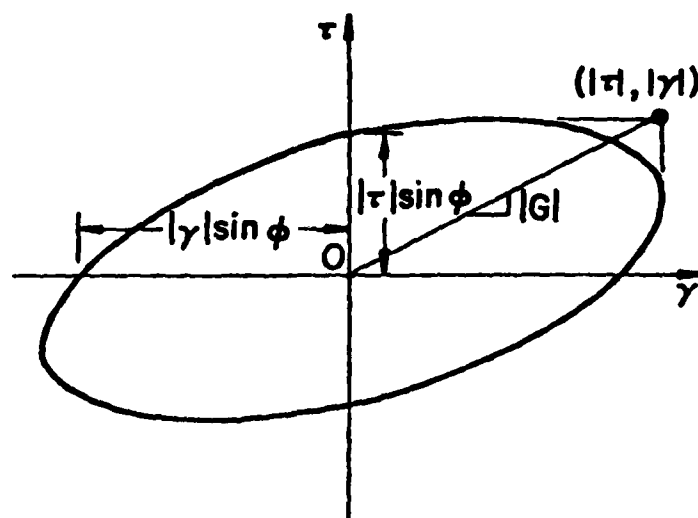


Figure 46. Stress-Strain Diagram for a Linear Viscoelastic Material Under Harmonic Straining (from Schapery (45.a))

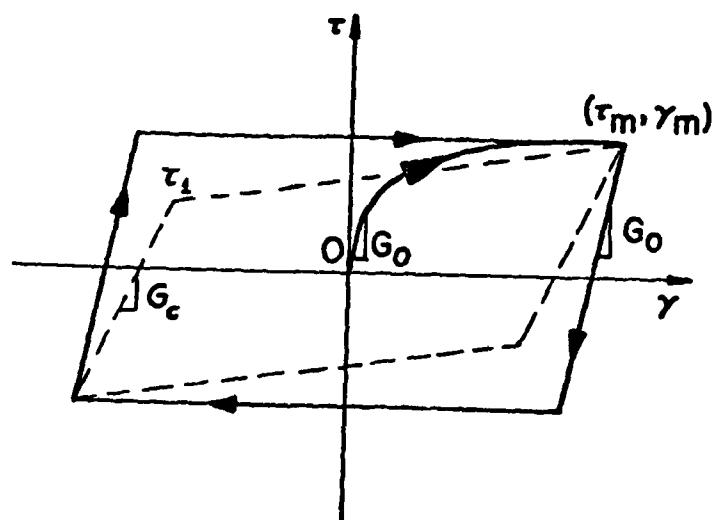


Figure 47. Schematic Representation of the Stress-Strain Diagram for Sediment Under Cyclic Straining (from Schapery (45.a))

$$\phi = \sin^{-1} \left[\frac{4 \tau_m^2}{\pi |\tau|^2} \left(1 - \frac{|G|}{G_0} \right) \right] \quad (112)$$

where G_0 is the initial tangent modulus for the backbone curve. Note that the assumption of $|G|$ being equal to τ_m/γ_m is used in this derivation once again. In order to solve for τ_m/τ ratio, ϕ is set to be 90° which makes the linear viscoelastic diagram a circle. Corresponding to this, a condition of very large strain is adopted, which forces $|G|/G_0$ to be approximately equal to 0. Substituting these boundary conditions into equation (112), the relation between peak linear viscoelastic stress τ and actual peak stress τ_m is obtained

$$\frac{\tau_m}{|\tau|} = \frac{\sqrt{\pi}}{2} \quad (113)$$

Combining equations (111), (112) and (113) an expression for n is obtained

$$n = \frac{2}{\pi} \sin^{-1} \left[1 - \frac{\tau_m/\gamma_m}{G_0} \right] \quad (114)$$

Note that, being a function of ϕ , the parameter n accounts for the damping characteristic of the material. G_1 and n expressed by equations (109) and (114), respectively, serve to define the "equivalent" linear viscoelastic material. Both terms are observed to be a function of the nonlinear secant modulus, defined as τ_m/γ_m . The next discussion will be on the determination of this nonlinear secant modulus as incorporated in the analysis.

The nonlinear behavior is defined by the hyperbolic stress-strain relation.

$$\tau = \frac{G_0 \gamma}{1 + \frac{G_0}{c_u} \gamma} \quad (115)$$

where c_u is the ultimate undrained shear strength. Analytical solutions for vane shear test predict that a plot of experimental values of vane rotation angle, θ , versus $-\log(1 - T/T_u)$, T_u being the ultimate torque at failure, is a straight line, slope of which yields the value for G_o/c_u (54). Indeed experimental data from different sites for some range of constant vane rotation rate, $\dot{\theta}$, produced straight lines with G_o/c_u ratio varying between 26 and 37 (54). Same relation was obtained in cyclic torque experiments where G_o/c_u ratio was estimated to be between 32-40 (26,46). The lowest strain amplitude for the cyclic experiments were approximately 0.4 percent. Note that the lowest strain level for the resonant column experiments presented herein, was about 0.001 percent.

The maximum shear stress and shear strain values, τ_m and γ_m , are assumed to fall on the hyperbolic stress strain curve when G_o and c_u are the values corresponding to remolded clay. This assumption is made to extend equation (115) to cyclic loading. Then using the assumption and equation (115), an expression for nonlinear secant modulus is obtained

$$G = \tau_m / \gamma_m = G_o \left[1 - \frac{\tau_m}{c_u} \right] \quad (116)$$

Substituting equation (113) for τ_m , the final form of the relation is written as

$$G = G_o \left[1 - \frac{\sqrt{\pi}}{2} \frac{|\tau|}{c_u} \right] \quad (117)$$

In order to work back from this equation to the "equivalent" linear viscoelastic properties, the values for G_o and c_u are essential. The numerical analysis requires the values for G_o/c_u , c_u , linear viscoelastic value of n , and an initial estimation for $|\tau|/c_u$. G_o/c_u ratio can either be obtained experimentally, as discussed above, or a

reasonable value can be assumed depending on site conditions or previously obtained information. c_u can be determined by an undrained shear strength analysis. The value of n for the linear viscoelastic range can either be determined experimentally, or estimated through a linear relationship with liquidity index. After a series of substitutions and iterations the "equivalent" linear viscoelastic modulus is obtained and used in the continuum mechanics formulation to determine the displacements, strains, velocities and accelerations induced by the wave loading.

The sinusoidal wave loading is given by a complex equation, where v_w is the vertical displacement and v_o is equal to $H/2$, H being the wave height measured from trough to crest.

$$v_w = v_o e^{i\lambda} \quad (118)$$

in which,

$$\lambda = \omega t - \ell x$$

and

$$\ell = \ell_1 - i \ell_2 \quad (\text{wave number})$$

Combining the equations above and converting to real notation, the relation for a "physical" water wave is obtained

$$\text{Re}(v) = v_o e^{-\ell_2 x} \cos(\omega t - \ell_1 x) \quad (119)$$

The physical wavelength, L , is

$$L = 2\pi / \ell_1 \quad (120)$$

The computer program phase of the analysis automatically generate the sinusoidal wave loading when wave period T_p and wave height H are specified.

Two sets of data were prepared and used in this numerical solution technique. The continuum was represented by ten layers with slightly

different material properties. The top 60 m of the material from boring B-6 was simulated in this procedure. Samples with similar material properties were assumed to constitute a single layer and corresponding undrained shear strengths, maximum shear moduli and liquidity indices were averaged over the thickness of each layer. Material below 60 m was considered to be the base material overlaid by the soft clay. The water depth to the mudline was assumed to be 6 m. The wave period and the wave height were given as 10 sec and 2.5 m, respectively. Both sets of data contained essentially the same information except the G_o/c_u values. Originally G_o/c_u values were estimated using the maximum shear modulus and undrained shear strength values obtained through laboratory experiments. Similar to the other material properties, these ratios varied for each of the ten layers. The values were found to range from about 120 for the top layer to 400 for the bottom layer. For comparison purposes, the G_o/c_u value of 32 obtained through cyclic vane shear tests by several investigators (26,46) was incorporated to constitute a different set of data. In this case, the same value of G_o/c_u was used for all the layers. Results of the analysis will be discussed in Chapter 4.

3.3.2 NONSAP - Nonlinear Structural Analysis Program

NONSAP has been developed to solve static and dynamic, linear and nonlinear problems (2). It incorporates large displacements and large strain nonlinearity solution modes. Nonlinearities are either considered to be material nonlinearities or they arise from large displacements and strains. Material properties and stress-strain behavior are represented through several material models implemented in the program. In general, three types of material behavior can be

simulated by the technique. They are elastic, hyperelastic and hypoelastic material behaviors. The element representation can be done in one, two or three-dimensional form.

System response is obtained using an incremental solution of equations of equilibrium with Wilson or Newmark time integration schemes in a dynamic analysis (3). At specified time intervals the linear stiffness matrix of the system is modified for nonlinearities. The fundamental equation for equilibrium is the equation of motion.

$$m {}^{t+\Delta t}\ddot{u} + c {}^{t+\Delta t}\dot{u} + k {}^t u = {}^{t+\Delta t}R - {}^t F \quad (121)$$

where R is the external load vector and F is the nodal point force vector equivalent to the element stresses at time t . The other parameters were defined in Chapter 2, earlier. During the motion of an element of the system, its volume, surface area, mass density, stresses and strains change continuously. In order to solve for the static and kinematic variables at each time increment, the configuration of the element at time $t+\Delta t$ must be estimated. To obtain a first approximate solution any one of the already calculated equilibrium configurations could be used. Two separate formulations can be utilized for this purpose. They are the total Lagrangian (TL) and updated Lagrangian (UL) formulations (4,5). TL formulation uses the initial configuration of the element and refers all static and kinematic variables to that configuration at time zero. The UL formulation refers all static and kinematic variables to the last calculated configuration. Once an approximate solution is obtained it is improved by equilibrium iteration using either one of the integration schemes, stated above. In dynamic analysis, equilibrium iteration is a critical process due to the fact that the calculated solutions may "drift away" or diverge from the exact

solution if the step-by-step solution becomes unstable during a stage of time integration. This is usually observed to happen if large load time steps are used. Since in dynamic analysis the solution for any prescribed load at a specific time is dependent on the history of solution, a relatively sudden increase in load within a short increment of time, brings about the divergence effect. In order to avoid this problem, a very low rate of loading must be input or the size of the time steps must be reduced considerably.

The UL and TL formulations are used for large displacement and strain solutions where the configuration of the element changes continuously during the time of loading. This effect is known as the geometric nonlinearities of the system. However, in the case of an analysis involving only material nonlinearities, the strains are assumed to be infinitesimal and the configurations of the elements do not change. Consequently, the nonlinear strain components and the displacements at time t are neglected in the formulations.

In NONSAP isoparametric finite element discretization is used (65). Two dimensional elements can be represented by 3 to 8 number nodes in plane strain, plane stress or axisymmetric stress space. Material properties in terms of material models are assigned to the elements of the system. Eight material models are implemented in the program. They are:

1. Linear isotropic
2. Linear orthotropic
3. Variable tangent moduli
4. Curve description model

5. Curve description model with tension cut-off capability (plane strain only)
6. Elastic-plastic (Von-Mises)
7. Elastic-plastic (Drucker-Prager)
8. Incompressible nonlinear elastic (Mooney-Rivlin, plane stress only)

In addition to these, a 9th model, which would be a user supplied model can be implemented in the program. Since, the material, response of which simulated through this numerical analysis, displayed elastic-plastic behavior, Von Mises, and Drucker-Prager material models were adapted for this study. Schematic diagrams of stress-strain behavior of these material models are given in Figures 48 and 49, respectively. Von-Mises material model apply, in general, to ductile materials with strain-hardening characteristic, as discussed in Chapter 2. E , E_t , σ_{yp} and μ are the input parameters for this model. Using the following set of equations, stress-strain information gathered under shear stress conditions can readily be transferred to parameters of axial stress-strain behavior, for Von-Mises material model.

$$\sigma_{yp} = \frac{\tau_{yp}}{0.577}, \quad E = 2G(1 + \mu)$$

(Note that the argument for τ_{yp} and σ_{yp} relation is presented in Chapter 2.)

The Drucker-Prager material model in NONSAP is particularly applicable to geological materials. In Mohr-Coulomb theory, the failure shear strength for soils is defined as

$$\tau_f = c + \sigma \tan \phi \quad (122)$$

Consequently, the input parameters for this material model include cohesion, c , friction angle, ϕ , along with E and μ .

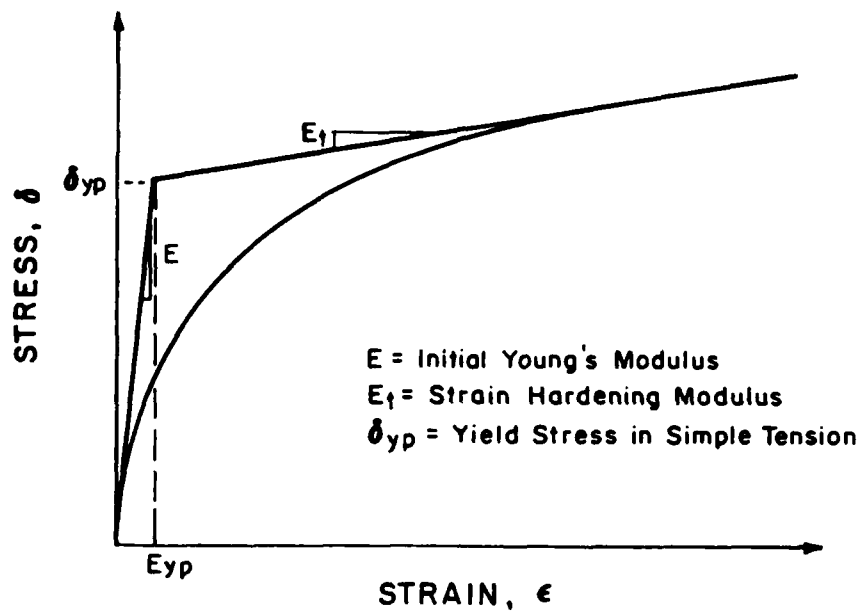


Figure 48. Stress - Strain Diagram of Von Mises Material Model

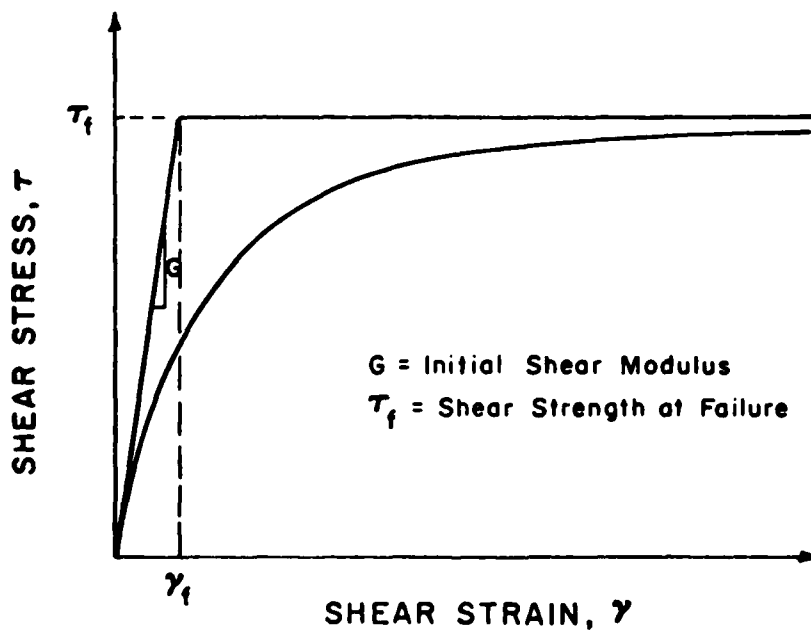


Figure 49. Stress - Strain Diagram of Drucker-Prager Material Model

The advantage of Von-Mises material model over Drucker-Prager model is that, it is capable of utilizing either of the Lagrangian formulations which in turn yield large strain and large displacement solutions. Drucker-Prager model is capable of utilizing only material nonlinearities, therefore is restricted to small strain and displacement solutions.

In addition to the concepts described above, program NONSAP is also equipped with the capability of introducing damping affects of a system in dynamic analysis. The Rayleigh coefficients of α and β are the input parameters for this purpose. Using these parameters, the damping matrix of the system is created as a linear combination of the mass and stiffness matrices (given by equation (4) in Chapter 2).

The mass matrix can be formed either by consistent mass method or lumped mass method. In consistent mass method, the mass density of the element is specified, the program then generates a consistent mass matrix from element data. In lumped mass method, the mass matrix is evaluated by simply lumping $1/N_{th}$ (N = number of nodes in the element) of the element mass at each node. Lumped mass matrix method is an approximate one, but it is well justified for many problems since the other method consumes considerably more computer time. In addition to the elemental masses and dampers, concentrated nodal masses and dampers can be specified also, if need occurs. A lumped mass matrix analysis is also possible by setting the mass density to zero and specifying only nodal masses. This latter procedure was utilized in calculating the response of soft sediments in this study.

Finally, loading is given in successive point values of time versus force. Several different loading curves can be specified for one system.

Note that, not all the solution modes are possible for all element models. For example equilibrium iteration is not allowed for curve description models and Lagrangian formulation is not allowed for Drucker-Prager elastic-plastic model. Limitations such as these constitute certain inefficiencies for the program. However, the option of implementing a user supplied material model stand to be an alternative solution to represent the system of concern most realistically. On the other hand, due to the complexity and size of the program, such a solution is bound to require an extensive amount of work and time. Therefore, choosing the best fit model already implemented in program is presumed to be a more practical and faster solution. Then the problem reduces to making the right assumptions for the real system.

The "restart" option of solution in the program proves to be a useful tool when lengthy runs of data are required for long terms of loading (3). With that option, the program can be terminated at any time of loading sequence, and restarted again with the conditions at termination serving as initial conditions. This option was used extensively in the response analysis of soft sediments, which will be described next.

3.3.3 Utilization of NONSAP Using the Stress-Strain and Index Property Data Obtained for Boring B-6 Samples

3.3.3.1 Discretization

Figure 50 shows the finite element discretization used in the analysis. The simulated system incorporated 16 two dimensional elements of 4 nodes in plane-strain condition. A total of 34 nodes were used. Attempt to represent the system with a finer network of elements was unsuccessful due to the extensive amount of computer time required to obtain the final solution. However, the configuration presented in Figure 50 did produce sufficiently smooth profiles of displacements and velocities. The length of the elements in y-direction was specifically chosen to coincide with the wavelength L , of a wave train of height 2.5 m. This choice of dimensions naturally yielded very elongated elements in y-direction. The total length of the system in z direction was 60 m, coinciding to the mudline at the top. The fine discretization at the very top of the soil column was for the purpose of obtaining smooth kinematic profiles, since the mass effects diminished considerably towards the mudline.

The boundary conditions were chosen so that the system was retained from lateral and vertical displacements at one of the base nodes, and it was retained only from vertical displacements at the other. This, in turn, yielded different static and kinematic profiles (displacement, velocity, acceleration) for the pinned-boundary node sequence on one side of the system, and roller-boundary node sequence on the other side. Since the loading on top of both sequences of nodes were exactly the same, simulation of two distinct kinematic behaviors were attempted for the same column of material for different boundary conditions.

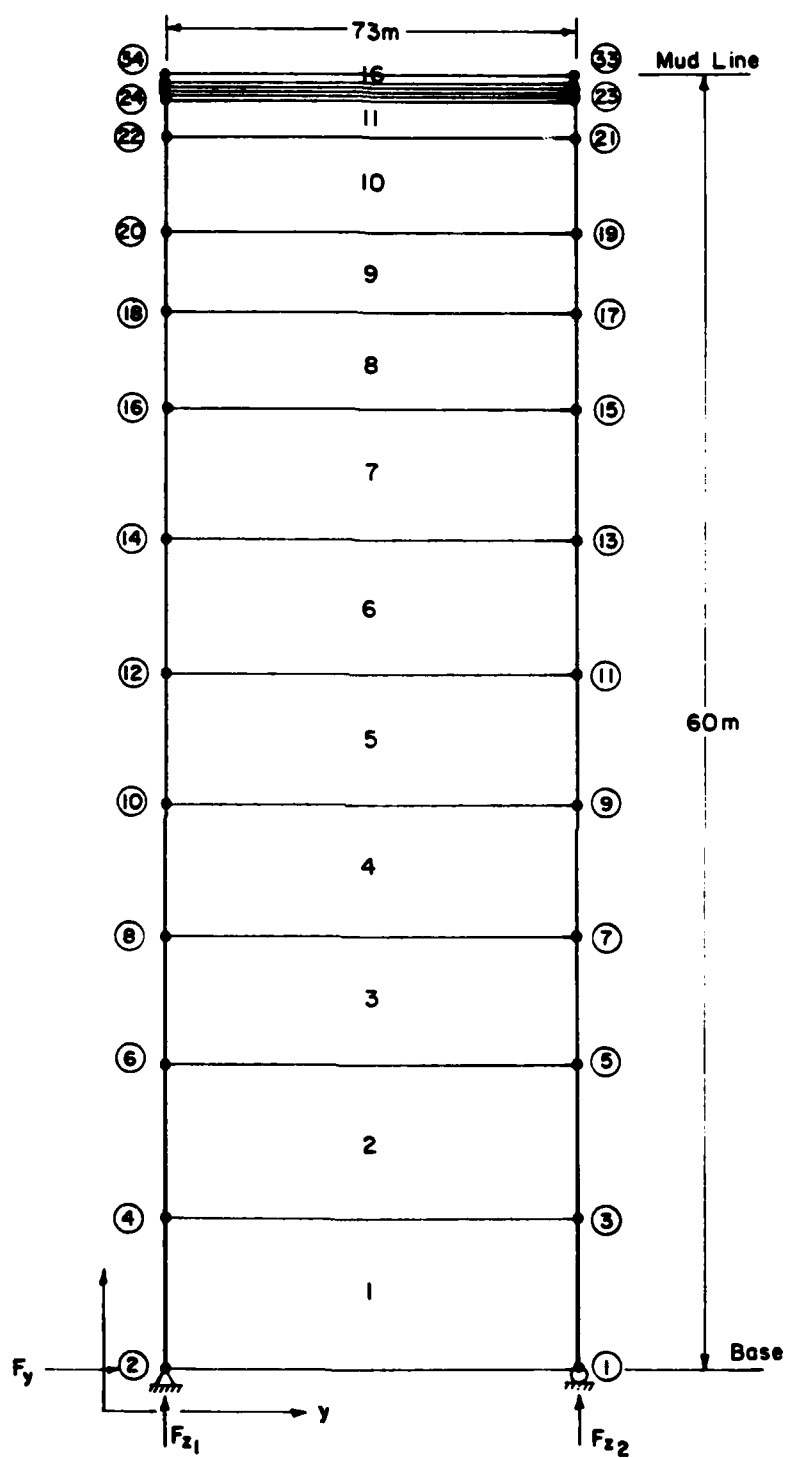


Figure 50. Finite Element Discretization of Soil Matrix

3.3.3.2 Mass and damping affects

The lumped mass option was utilized by setting mass density equal to 0, and specifying only nodal masses. These nodal masses were calculated manually the same way the lumped mass matrix evaluation of the program. However, the system was assumed to extend half wavelength distance on each side along y-axis, and an imaginary element boundary line passed vertically from top to base of system dividing the elements into two equal sections. The imaginary configuration is sketched in Figure 51. The nodal masses are calculated according to this imaginary configuration.

Damping of the material was incorporated through Rayleigh damping coefficients α and β . They were calculated using equation (8) of Chapter 2, for each individual sample and averaged to obtain a single set of α and β values. They were the only parameters to be specified for damping analysis.

The sloping configuration of the system was not specified in discretization phase but rather built into the data by modifying the nodal masses in the y-direction. In order to obtain the displacements and velocity and acceleration values due to sloping bottom, the nodal masses in the y-direction were decreased by an amount of $M_y \sin \delta$, where M_y was the original nodal mass, and δ the angle sloping surface made with the horizontal. The magnitude of the slope was assumed to be one percent.

3.3.3.3 Material model and layering

In order to be able to compare the solutions from viscoelastic material analysis, with NONSAP solutions, the same type of layering was adapted. Corresponding to each layer of material the parameter input

for the material model varied in accordance with the laboratory data obtained. Ten different sets of parameters were prepared for 10 layers of the soil column.

In order to obtain large displacement and large strain solution for the mud-flow analysis, Von-Mises elastic-plastic material model was adapted. The nonlinear shear stress-strain curves derived from resonant column data (discussion and results of this procedure will be given in Chapter 4), were represented bilinearly according to the Von-Mises material model. Schematic illustration of this "equivalency" procedure is given in Figure 48. Consequently, average values of G , G_t and τ_{yp} were obtained for each layer of material. Using the calculated values of μ and the equations (26) and (68), E , E_t , σ_{yp} were estimated. These values and μ , for each layer, constituted the material model input data for the program.

Drucker-Prager model was used to simulate the response of the system at critical state. Since the model represented an elastic-perfectly plastic material (Figure 49), correlation of the critical stress-state and the failure condition of the Drucker-Prager model was presumed. Using the shear strain value obtained from critical state analysis, and the hyperbolic relation of shear stress-strain curves of the corresponding samples (Chapter 4), a "critical state secant shear modulus", denoted as G_c , was obtained. At this stage a major assumption had to be made in order to continue the investigation. It was assumed that, at critical state the material would acquire new stress-strain and volume change characteristics so that the secant shear modulus G_s would be equal to the tangent modulus of this new material. After making this assumption, G_s , now denoted by G_c , was transformed

into E using equation (26). In order to account for c and ϕ , the Mohr-Columb equation for τ_f was equated to the value of τ_c obtained at critical state shear strain, γ_c . The following set of calculations were performed.

$$\tau_c = G_c \gamma_c$$

$$\tau_f = c + \sigma \tan \phi = \tau_c$$

let $\phi = 0$, then solve for c

$$c = \tau_c$$

Consequently, all the parameters (E , c , ϕ) required by Drucker-Prager model could be estimated.

The same discretization was used with four layers of material in this case.

3.3.3.4 Loading curves and use of "restart" option

The cyclic wave loading was simulated by a sinusoidal function of time. The pressure Δp , exerted by the waves on the ocean floor is given by the following formula (51)

$$\Delta p = \gamma_w \frac{H}{2} \frac{1}{\cosh(2\pi \frac{d}{L})} \quad (123)$$

where, γ_w is the unit weight of water, H is the wave length from crest to trough, L is the wavelength and d is the water depth.

Δp multiplied by the sinusoidal function gives the variation of stress at a point with time. This stress function must further be multiplied by the area it is exerted upon, in order to get a force function with respect to time. Considering that the wave train propagates from one node to the other one continuously along the mudline, by setting the distance between the two nodes to be equal to the wavelength, it is readily observed that each node experiences the

same amount of force at the same time. Assuming a standing wave of sinusoidal shape between the two top nodes of the system, the pressurized area is determined to be

$$A = \frac{L}{2} \times \text{thickness} \quad (124)$$

where thickness is assumed to be unit for plane-strain elements.

Therefore, each node is determined to experience a time dependent force of the form

$$F(t) = f(t) \Delta p \frac{L}{2} \quad (125)$$

In the discussion above, $f(t)$ was assumed to be a sine function [$f(t) = \sin \omega t$]. However, due to steep slope of this function within the vicinity of time 0, when it was introduced in program NONSAP divergence in solution occurred. Therefore, a modified function of the form

$$\begin{aligned} f(t) &= 1 - \cos \omega t && \text{for } 0 < \omega t < \pi/2 \\ & && 3\pi/2 \leq \omega t < 2\pi \\ f(t) &= \sin \omega t && \text{for } \pi/2 \leq \omega t < 3\pi/2 \end{aligned} \quad (126)$$

was used. This function along with the sine function is given in Figure 52.

In the calculation phase for load parameters, the same values of water depth, wave height and length of viscoelastic analysis were used. Solving for Δp yielded 10.5 kPa. Substituting this value into equation (125), the amplitude of the forcing function was found to be 383.25 kN.

The wave period T_p , was taken to be 10 sec, which was exactly the same value used in viscoelastic analysis. Then the forcing function between time 0 and 10 sec, was set to be 1 cycle of dynamic loading. With time increment value of 0.01 sec, the CPU time for one cycle of loading to be completed was estimated to be 4 CPU minutes in computer

run phase. For practical purposes, each cycle of loading was divided into 4 sections and utilizing the "restart" option of the program, one cycle was completed in 4 runs. The cyclic loading in this manner was continued up to the end of 11th cycle. Analysis was terminated at that stage of loading, due to cumbersome and extensively time consuming process.

In "restart" option of the program, the final nonlinear stiffness matrix, the kinematic values, strains and stresses at each node are stored on separate disk files when the solution is terminated. The next solution phase takes these matrices and values and automatically uses them as initial conditions.

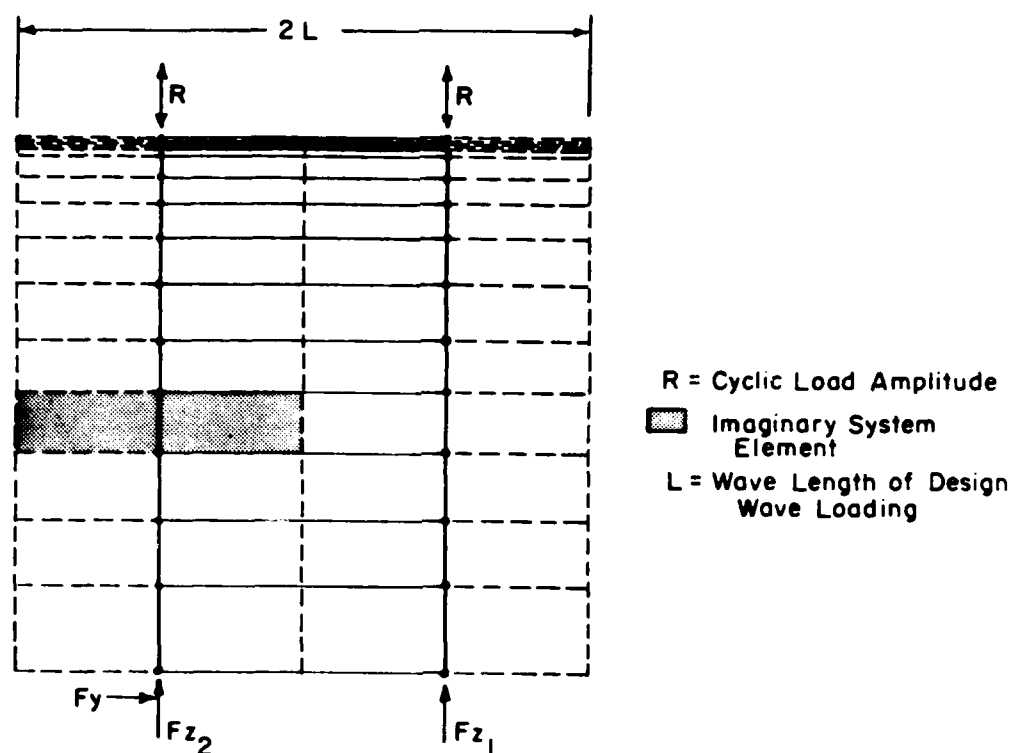


Figure 51. The Imaginary Configuration of the Finite Element Model to Estimate the Nodal Masses

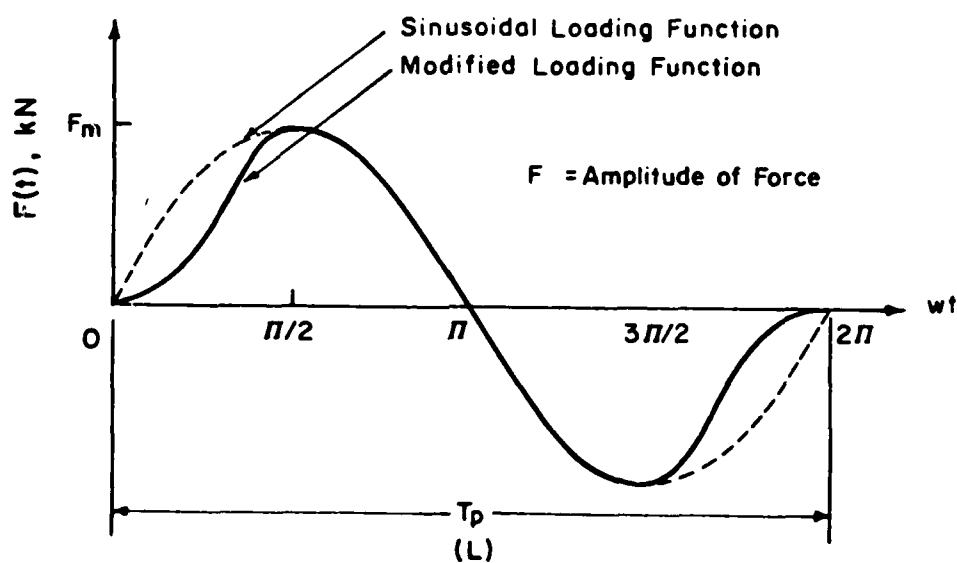


Figure 52. Sinusoidal and Modified Loading Functions for Finite Element Analysis

Chapter 4

RESULTS AND CONCLUSIONS

This study consisted of two major phases, experimental and data acquisition phase, and the numerical analysis phase using the experimental data. In this chapter, the experimental and numerical analysis results will be presented, and integrated into the presentation will be the discussion of these results.

4.1 INDEX PROPERTIES OF THE CORE SAMPLES

Visual and textural observations of the samples prior to any type of experimental analysis, revealed some differences between groups of samples of different depths. The samples from the top soil layer, approximately from 0 to 7 m of depth, was very soft, olive colored clay with "spongy" cross-sectional appearance indicating gaseous nature. Traces of organic matter--fiborous plant parts-- were encountered. From approximately 7 to 14 m of depth, the material showed silty, sandy formation, in "pocket" layers. Below this depth samples were again very soft and dark colored gaseous clay down to approximately 60 m. There was a relatively sudden change in the consistency and color of the soil below 60 m of depth. These samples were much firmer and lighter colored. Traces of organic matter--shell fragments--were encountered in this layer also. Further down, close to 100 m of depth, fragments of stone and other hard substances were scattered within the soil matrix. The type of soil for this layer was again observed to be clay. The sandy layer between 45 and 60 m of depth, reported in the McClelland

Engineers' analysis (30) of the same boring (B-6), was not encountered in this study.

The results of the density and plasticity analysis are given graphically in Appendices A-1 and A-2, respectively. The silty and sandy formation around 7 to 14 m of depth is observed by the increase in dry and bulk unit weights in A-1 plate. This corresponds to the typical "crust" formation in sediments of the Gulf of Mexico. Plate A-2 shows the natural water content and plasticity range variation with depth. The natural water contents of the samples above 60 m are higher or very close to their liquid limits which is an indication of underconsolidation. The firmer samples had natural water contents close to their plastic limits which may be interpreted as overconsolidation depending on the visual observations also. Using the plasticity index information, other properties that are related to the stress-strain nature of the soil samples were derived. These parameters were lateral earth pressure coefficient K_0 , and Poisson's ratio μ . Equations (96), (97) and (98) of Chapter 3 were utilized to estimate their values. Table 4 summarizes these parameters along with PI, effective overburden pressure p' and mean effective pressure p'_0 values for various depths of boring B-6. Note that the effective overburden pressure values do not include the excess pore pressure effects. They were estimated by subtracting the hydrostatic stress from the total stress at each corresponding depth. The total stresses were found by an average distribution of the bulk unit weights along the boring depth to each point of concern. The mean effective pressures, p'_0 , were found by assuming equal lateral effective stresses on a soil element (that is $\sigma'_2 = \sigma'_3$) and using equation (99) of Chapter 3.

4.2 RESONANT COLUMN TEST RESULTS

Hyperbolic curves were fitted to the shear modulus versus shear strain data obtained by resonant column tests. Plates A-3 through A-24 of Appendix A present the data and the fitted curves on semi-logarithmic scale.

Curve fitting was done by using an hyperbolic formula of the form (25)

$$y = \frac{x - x_1}{A' + B'x} + y_1 \quad (127)$$

where (x_1, y_1) is a reference point in the actual data, A' and B' are the constants obtained through linear regression (44). A hyperbolic equation can be transformed into a linear form, such that when plotted, A' and B' correspond to the y-intercept and the slope of a straight line, respectively. Considering a hyperbolic equation of the form

$$y = \frac{x}{A + Bx} + C \quad (128)$$

and substituting (x_1, y_1) in this equation

$$y = \frac{x_1}{A + Bx_1} + C \quad (129)$$

is obtained. Subtracting y_1 from y and rearranging, a linear equation of the following form is obtained

$$\frac{x - x_1}{y - y_1} = A' + B'x \quad (130)$$

where

$$\begin{aligned} A' &= A + Bx_1 \\ B' &= B + (B^2/A) x_1 \end{aligned} \quad (131)$$

Using the procedure described above, the G versus γ data were first plotted as $(\gamma - \gamma_1)/(G - G_1)$ versus γ and subjected to linear regression analysis (44) which yielded the A' and B' constants. Finally,

substituting these constants into equation (127), the equation of the fitted curve was obtained. Table 5 presents the A' and B' values calculated and used in curve fitting procedure of G versus γ along with x_1 and y_1 values, and standard deviation values. An alternate procedure is to evaluate A and B in terms of A' and B' and C in terms of A and B , then use equation (128) for curve fitting. In this case

$$\begin{aligned} A &= \frac{A'^2}{A' + B' x_1} \\ B &= \frac{A' B'}{A' + B' x_1} \\ C &= y_1 - \left[\frac{x_1}{A + B x_1} \right] \end{aligned} \quad (132)$$

A very useful outcome of curve fitting was being able to estimate G_{\max} corresponding to zero shear strain. Conventional methods suggested extrapolation of the curve or using an analytical equation to predict G_{\max} . These methods were discussed in Chapter 2. However, as observed from equation (129) at zero shear strain

$$G = G_{\max} = G_1 - \left[\frac{\gamma_1}{A + G \gamma_1} \right] \quad (133)$$

which can be calculated readily with the proper values of A and B . Hyperbolic curve fitting did agree well for most of the data. However, as observed from plates A-5, 11, 21, 22, 23 and 24 there was some disagreement. This can be attributed either to experimental data scatter, unrepresentative data due to sample disturbance or overconsolidation effects of the deeper firmer samples. (Since it is not within the scope of this work, no discussion on overconsolidation effects will be presented.)

The modulus reduction curves are normalized by G_{\max} on the ordinate. In general, the shear modulus value at 10^{-4} percent strain

amplitude is approximately equal to G_{\max} , and at 1.0 percent strain amplitude the shear modulus is reduced to about 10-20 percent of its maximum value. Due to the nature of the hyperbolic fit, most of the curves display a change of slope within the vicinity of 0.5 percent strain amplitude. This in turn could suggest an "approximate" linear relationship of G versus γ for shear strain values much higher than 1.0 percent. When plotted on normal scale and extended to high strain amplitude levels, the slow asymptotic decrease could indeed be approximated as a linear relationship between G versus γ . This will be illustrated by normalized, normal-scale graphs of reduction curves later in this section.

The modulus reduction curves are further used to develop a family of curves representing different strain amplitudes, in a depth profile analysis of shear moduli. Plates A-25 and A-26 illustrate the products of such a study. In A-25 only the top 60 m of soil column is considered and shear moduli values corresponding to shear strain levels ranging from 0 to 1.0 percent are plotted against depth. The increase in shear modulus between depths of 10 to 20 m is consistent with the silty sandy formation around those depths of soil column. A sudden decrease in shear modulus below 20 m and a gradual increase between 40-60 m are also observed from the graph. Between 0.1 percent and 0.5 percent of shear strain shear modulus values decrease more than they do for other intervals for most of the depths. Plate A-26 reproduces the same data for top 60 m and adds the data obtained for the deeper samples on a different scale of shear modulus. The sudden increase in shear modulus below 60 m indicates the order of magnitude of the difference between the strength of the two distinct layers of materials. Note that due to

the lack of data between depths 60 to 70 m, the two data points were connected merely by a straight line while the actual variation may or may not be approximated by a relation of that type. For practical purposes, it is assumed that the "imaginary" boundary between soft and the firm soil lies somewhere between 60 and 70 m. Compared to the high shear moduli values displayed by the firm layer, the variation of shear moduli for the top layer seem to be almost constant. Due to the sudden increase in shear moduli below 60 m, the interaction between the firm and the soft layer cannot be predicted readily. That is, the soft layer may be acting independent of the firm layer or it may be connected in terms of mechanical response, by a gradual transformation. This in turn brings about the question of whether to assume a frictional or a "frictionless" boundary between the layers. A brief discussion on this matter of choice will be presented in the numerical analysis results section.

These curves are predicted to be of practical use for foundation analysis in regard to design procedures for offshore structures. With the proper knowledge of shear strains induced at different depths of the soil column due to cyclic loading, the existing shear modulus at each corresponding depth can be estimated readily. However, the history of loading at the site should be accounted for in such an analysis--details in relation to this concept is not within the scope of this work. Prediction of final shear modulus values, after a storm loading, for instance, could be of significant importance in further estimations made for the occurrence of mud flow and its "effective" depth.

The degradation effects of number of cycles of loading, discussed in Chapter 2, is looked into through G versus number of cycles of

loading, N , curves produced for several randomly chosen samples. Plates A-27 through A-32 represent these relations. Some of the samples were loaded at a single strain amplitude, while others at several different amplitudes. As observed from plates A-29 and A-31, the degradation affect is more pronounced at higher shear strain loading. The other two multiple strain cases seem to have identical slopes, meaning that the degradation affect is approximately same for both of those strain amplitudes of loading. Apart from this trend, some of the curves display a "leveling" effect at high number of cycles, which may correspond to the "steady state concept" of degradation discussed in Chapter 2. Since the values between cycle number one and cycle number 100 were not measured--mainly due to experimental limitations--that range is represented by dotted lines in all of the curves. Note that this is an ideal approximate representation and does not correspond to the actual variation. For practical purposes, the overall percent decrement in shear modulus up to 10,000 cycles of loading was evaluated. This decrement value for the samples subjected to degradation analysis ranged from 5 to 25 percent. Considering the fact that 10,000 cycles corresponded to approximately 1.0 hour duration of loading and the total time involved during the resonant column measurements was only a small fraction of an hour, the actual degradation affects were safely assumed to be insignificant. Therefore, no corrections with regard to degradation were introduced to the results.

The initial resonant column data also yielded information about the variation of damping ratio, D , with shear strain amplitude. Plates A-33 through A-52 represent the curves of D versus γ for various depths. Due to the soft nature of the material tested, it was not possible to obtain

enough data for the low strain amplitude range (less than 0.001), to extrapolate and estimate the minimum damping ratio. However, the lowest D value was assumed not to be far from the actual minimum value and used in the calculations for Rayleigh damping coefficients, α and β , through equation (8) of Chapter 2. Table 6 lists D_{\min} , ω_{\min} and the corresponding α , β values for different depths.

The D versus γ curves displayed some interesting features that are not observed in curves of same type in soil dynamics literature. These differences may either be attributed to experimental scatter or testing errors involved, method used to estimate the damping ratio (magnification factor method) or merely the soft and weak nature of the samples. One of the relatively consistent traits was that the curves tended to have several inflection points. They did not have a noticeable "leveling" trend below strain values of 10^{-3} percent. However, they all increased with increasing shear strain amplitude. The maximum damping ratios around 0.5 percent of shear strain ranged from 0.6-20 percent, with an average of 3.5 percent. The firmer samples displayed relations which were more consistent with the curves encountered in literature. The average damping ratio of 3.5 percent around 0.5 percent shear strain is regarded to be a rather low value with respect to the soft nature of the material tested. Ordinarily, they were expected to display higher damping values. The reason for this occurrence cannot be predicted readily, but attributed to either insufficient method of estimation or merely some unique characteristics of the samples tested. Since no comparative literature is available for resonant column testing of these soft sediments, the information given in plates A-33 through A-52 will only aid to understand the nature of

the curves and estimate the Rayleigh damping coefficients, α and β used in program NONSAP for mud flow simulation.

Resonant column results yielded a third set of data which constituted the main material input parameters for numerical analysis with NONSAP. Using the general relation between shear modulus and shear strain, and the assumptions made with regard to degradation of backbone curve discussed in Chapter 2, cyclic shear stress versus shear strain relations were obtained for each sample. Then a hyperbolic curve was fit to each of these relations. First, data was plotted as γ/τ versus γ which yielded a straight line with the following equation (21)

$$\frac{\gamma}{\tau} = A + B \gamma \quad (134)$$

Through linear regression (44) of γ/τ versus γ , the constants A and B were obtained. Substituting the values of A and B in the original hyperbolic equation, the fitted curves could be produced. Table 7 lists the A and B constants used in this curve fitting procedure, and the standard deviation values.

Plates A-53 through A-74 of Appendix A, show the analytical cyclic stress-strain curves and the actual data points for different depths. Most of the data were represented quite well by the curves, while some were poor representations as observed in plates A-61, A-64, A-70 and A-73. These are attributed to experimental scatter or insufficient data. The nonlinear stress-strain curves were transformed into a bilinear representation using Von-Mises material model with strain-hardening characteristic. This representation was chosen with the idea of using the yield stress and strain values obtained graphically from these curves in the numerical simulation with program NONSAP. Since only the Von-Mises material model allowed for

large-strain and large-displacement analysis in the program, the choice of representation was inevitable. However, the fairly high Poisson's ratio, μ , values (refer to Table 4), and the observed "bulging" failure mode of the samples in undrained triaxial tests, provided a supportive ground for the justification of the choice of material model with strain-hardening and failure by yielding characteristics. The bilinear representations are also illustrated in the plates. The yield point at which the initial tangent line and the strain-hardening line met, was denoted by (τ_y, γ_y) , namely cyclic shear stress at yield and cyclic shear strain at yield.

In addition to Von-Mises material model representation, the maximum cyclic shear stress τ_{max} was also evaluated using the hyperbolic relationship, where the reciprocal of the constant B was equal to τ_{max} . It was found that τ_{max} did not deviate significantly from the τ_y values estimated graphically. A third shear-strength analysis with undrained triaxial test procedure, yielded the s_u , or undrained shear strength values for several samples. The total shear-strength data, along with the G_{max} values are listed in Table 8. The undrained shear strength values are considerably higher than both of the cyclic shear stress values, as observed from the table. This contradicts with the findings of Whitman (63) who showed that for clays cyclic shear strength values are higher than static shear strength values. A possible reasoning for the results of this study may again lie in errors involved in the various experimental procedures discussed herein. However the closeness of the undrained shear strength values obtained in this study to the ones reported in McClelland Engineers' investigation of the same borehole samples provided verification of the data. On the other hand,

resonant column test data is limited to small strain levels and therefore is a unique procedure compared to other types of cyclic experiments that can be extended to much higher strain amplitude loading. Nevertheless, this contradiction and related conclusions must be investigated further and the limiting and effective parameters must be pin-pointed.

Using the shear strength data, the family of curves for shear modulus depth profile, were normalized and replotted. The results are given in plates A-75 through A-76 of Appendix A. In plate A-75, the shear moduli are normalized by the undrained shear strength, s_u . Plate A-76 provides a closer view of the top 60 m of material for the same relation. It is observed that the G/s_u ratios, for 0 percent shear strain amplitude ranges from 140 to 470 for the entire depth of material. The utilization of this experimental G/s_u ratios came about with the viscoelastic sub-bottom wave interaction numerical model. Results of the numerical analysis in comparison with G/s_u ratio of 32 will be presented later in this chapter. The sudden change of material strength is not observed below 60 m of depth when G values are normalized by s_u in plate A-75. G/s_u ratios almost as high as the deeper values are also encountered around 10 m of depth. The low values of G/s_u correspond generally to the surface of the soil column, while the rest of the data for low shear strain amplitudes tend to range between 200 and 300, with a mean value of 250 for the top 70 m.

The same normalization was done with τ_y , values also. Naturally, the G/τ_y values were much higher than G/s_u values. The new set of data ranged between 600 and 2700 for the low shear strain amplitudes, with a mean value of 1000. These ratios were not utilized in the viscoelastic

sea-bottom analysis due to the fact that the initially estimated τ/s_u [$= \tau/c_u$] values did not converge for solution due to the extremely high values of G/s_u [$= G/c_u$] values provided for the computer program. Plates A-77 and A-78 showing τ_y normalization are included only for comparison purposes.

The yield state parameters, shear strain at yield, γ_y , obtained from the bilinear representation of the nonlinear shear stress-strain curves were used for normalizing the shear strain in order to represent all of shear modulus data on a single graph. The procedure was similar to that used by Hardin and Drnevich (19). However, in their work the shear strain was normalized by reference strain, γ_r ($= \tau_{\max}/G_{\max}$). Plates A-79 and A-80 illustrate the results of the normalization. By normalizing G by G_{\max} and γ by γ_y , shear modulus data for all of the samples could be collected on a single graph. Note that this representation is very similar to that given by Hardin and Drnevich (19) in Figure 30. The curve through the data points was fit by the hyperbolic relation discussed earlier in this section. Extending the hyperbolic curve to higher strain amplitude levels, a "predicted" behavior was observed. Plate A-80 illustrates this relation. Note that at high strain levels the curve can be estimated to be a straight line with linear relationship of G versus γ . However, extrapolating this line to zero shear strain would not aid to find the maximum shear modulus value. Keeping this in mind one can safely assume that shear modulus versus shear strain relation is linear for high strain levels. The hyperbolic curve, eventually, attains an asymptotic value at very high strain levels where shear modulus is independent of strain.

4.3 CRITICAL STATE ANALYSIS RESULTS

Critical state analysis depended mainly on a set of consolidation data. Remolded and undisturbed samples from four different depths were subjected to consolidation tests, simultaneously. Compression curves obtained from these tests are given in A-81, A-82, A-83 and A-84 plates of Appendix A. The parameters in relation to these consolidation experiments are given in Table 9. The first three samples displayed relatively consistent data in relation to the undisturbed and remolded compression curve trends. The last sample, however, displayed a significant separation between the two curves. This was attributed to experimental error.

Using the procedure of estimating critical state parameters discussed in Chapter 2, the corresponding parameters for each sample tested were calculated and tabulated. Table 10 summarizes these parameters and the shear strain, shear stress and shear modulus values at critical state. The shear strength, τ_c , was obtained by substituting the γ_c value into the hyperbolic stress-strain equation with the proper A and B constants. G_c was then estimated by the general relation, $G_c = \tau_c / \gamma_c$. The shear modulus was transformed into Young's modulus and used in numerical analysis, NONSAP, along with the shear strength value, τ_c . Results of this analysis will be presented in the next section.

4.4 NUMERICAL ANALYSIS RESULTS

4.4.1 Wave-Propagation Viscoelastic Sea-bottom Interaction Analysis Results

Two sets of data was utilized in this analysis. First G/s_u [$= G/c_u$] ratios obtained from dynamic analysis were given as the "strength factor" input. These ratios varied for different layers of

materials. In the second set of data the strength factor was kept at the constant value of 32 for all layers. Peak values of horizontal and vertical displacements, resultant velocity and shear strain amplitude for both cases revealed significant differences. Plates B-1, B-2, B-3 and B-4 of Appendix B represent these relations, respectively. In all of the graphs, use of variable strength factor, which was obtained experimentally, yielded considerably lower displacement, velocity and shear strain profiles for the soil column. The maximum horizontal and vertical displacements with variable G/s_u ratio are about 15 percent of those with G/s_u ratio of 32. Likewise the maximum resultant soil velocity and the maximum shear strain amplitude are about 10 percent of those with G/s_u ratio of 32. This occurrence is most significant with regard to foundation analysis of offshore structures. With the proper knowledge of G_{max} value through more refined techniques of evaluation, as illustrated in the study herein, more economical designs can be accomplished. The so called P-y curves for offshore piles are obtained through the knowledge of the lateral soil displacements and velocities and to what depth they are significant and influential to design criterias. By introducing this new technique of evaluating strength factor, favorable changes in estimating foundation design criterias towards a more economical design can be brought about.

The viscoelastic sub-bottom wave interaction analysis considers the loading of a continuous sinusoidal wave train. This type of loading does not involve number of cycles of loading affects, which is critical in soil dynamics analysis due to pore pressure response, degradation of backbone curve, and reduction of shear modulus. Recognizing this limitation and in an effort to represent the soil column with more

detailed mechanical properties, the second numerical analysis approach, namely NONSAP, was adapted.

4.4.2 Results of NONSAP

The use of the finite element program, indeed, offered capability of specifying more mechanical material properties, and flexibility of representing the soil column with different boundary conditions. In addition to this, cyclic loading of the system yielded distinct results from that of viscoelastic sub-bottom model.

As discussed in Chapter 3, two types of boundary conditions were considered in this analysis, a fixed boundary and a laterally free boundary. The latter case can also be described as a "frictionless" boundary, where the material moves with no lateral resistance. The results for this second case of boundary condition are given in plates B-5 through B-10. The number of cycles effects are observed readily through these graphs. The horizontal and vertical clay displacements increase in magnitude with increasing number of cycles. However, the increase is not at a steady state but rather in a decreasing manner. The intervals between cycles 8, 10 and 11 are considerably smaller than the intervals between cycles 1, 2 and 5. The last three cycles also tend to cluster together at about the same values. The same trends are observed for the horizontal and vertical velocity profiles. The acceleration data are very scattered and do not show consistency in relation to the number of cycles of loading, therefore they are not represented by smooth curves but given as data points to illustrate their order of magnitude.

Use of frictionless boundary and allowing the mass to "slide" over the firm base material did not produce critical values of displacement

and velocity. The displacement and velocity terms associated with the fixed boundary case were larger. The frictionless boundary node sequence was expected to behave more critically, but the results did not indicate such occurrence. Further work needed in this area in order to simulate an independent frictionless boundary material. An attempt, to do so with both bottom nodes allowed for lateral movement resulted in instability of the system, and therefore was abandoned.

The fix boundary node sequence, on the other hand did produce satisfactory results of displacement and velocity profiles. Plates B-11 through B-16 of Appendix B present the displacement, velocity and acceleration profiles, respectively. There is a steady increase in horizontal and vertical displacement magnitudes with increasing number of cycles of loading, as observed from plates B-11 and B-12. The "decreasing interval" effect, observed in the previous case, is not encountered in these profiles. On the contrary, a steady state increase is observed. An interesting feature is, for the second cycle of loading the horizontal displacement profile reverses and falls below the first cycle profile. With increasing number of cycles of loading, it picks up and increases steadily. The horizontal velocity profile also shows dynamic effects by moving from positive to negative values steadily. The acceleration profiles again resulted in a very scattered layout of points. An attempt to pass smooth curves through these points resulted in very many different modes and harmonics of the acceleration with increasing number of cycles, and was not very informative. Therefore, they are presented in the original form to give the reader an insight of the order of magnitudes of these acceleration values.

The maximum horizontal clay displacement for $N = 11$, for the fixed end case, was approximately 0.6 m at the surface. This in turn corresponded to a shear strain of 1.0 percent. Information of this type for various depths of material is helpful in finding the existing shear moduli values at each depth using the family of curves of shear modulus presented earlier. This study, suggested herein, was not conducted. However, it is recommended for further work on this subject matter.

The maximum displacement and velocity profiles for the first cycle of loading were plotted for comparison purposes with the viscoelastic model results. They are given in plates B-17 through B-20. The horizontal displacement profile is considerably different than that of viscoelastic model. The maximum displacement for the viscoelastic model corresponds to a depth around 8-10 m, while it corresponds to the surface in NONSAP model. Their values are quite different also. The maximum horizontal displacement for viscoelastic model is about 0.016 m, while it is about 0.210 m for the latter model. Likewise, the vertical displacement values are 0.040 m and 0.182 m, respectively. The horizontal velocity values are 0.026 m/sec for the first model and 0.097 m/sec for the second model.

These differences can generally be attributed to the logic and system of the two different program packages, or to the differences between the loading condition generated by the viscoelastic model and the loading which is specified by the user in program NONSAP. The viscoelastic model is specifically designed for mud flow problems and therefore can be readily chosen to simulate such a case. On the other hand, NONSAP is a general purpose dynamic analysis program with flexibility of defining the material and loading conditions more

realistically. Therefore, the results obtained through both of the models can only be verified with actual data measured in-situ. At this stage of work, this type of verification is not available, at least within the scope of this research. However, for further work one could analyze and compare both results and chose the most critical solution depending on in-situ data and previous records. It is important to note that, NONSAP solutions while incorporating the number of cycles of loading effects, does not reflect any degradation or pore pressure response. Only the reduction of shear moduli are accounted for.

Finally, the critical state parameters were utilized in an attempt to obtain a different type of mud-flow simulation. As discussed in Chapter 3, the shear modulus and shear strength at critical state of the soil constituted the main ingredients for this numerical simulation. The material was initially assumed to have reached its critical state throughout the entire depth and ready to deform continuously with minimum resistance. Using the Drucker-Prager material model (elastic-perfectly plastic), before half of the first cycle of loading was completed, due the large shear stress increments within the top layer (about 7 m) of material, instability occurred and no solution was available in terms of strains and displacements. The material with critical state strength parameters was not able to take stresses by straining or yielding when the loading was continued. The maximum displacement at the end of the first half cycle of loading was approximately 0.20 m at the surface of the soil column. Likewise, the vertical displacement was about 0.23 m, and the horizontal velocity was 0.12 m/sec. The material model was changed to Von Mises type with a very small strain-hardening modulus ($=0.001$ kPa), in order to simulate a

material close to elastic-perfectly plastic model. The rest of the strength parameters were kept at critical state. Under these conditions the maximum horizontal and vertical displacements for the first cycle of loading were 0.41 m and 0.19 m, respectively. The maximum horizontal velocity was 0.12 m/sec. Note that the horizontal displacement is doubled compared to the initial maximum value, while the vertical displacement and the horizontal velocity values are approximately the same.

Attempting to use program NONSAP with critical state soil parameters and continued cyclic loading failed in principle. However, this is only logical since the program is not originally designed for such high loading conditions of materials which are softened down to the state of strength at which continuous deformation or "flow" is expected.

Table 4
Some Index Properties of Samples of Boring B-6

Depth From Mudline (m)	Overburden Effective Stress, p' (kPa)	Lateral Earth Pressure Coefficient K_0	Mean Effective Stress, p' (kPa)	Poisson's Ratio, μ	Plasticity Index PI
0.244	0.97	0.636	0.74	0.389	33.70
2.100	0.40	0.556	5.90	0.357	22.30
2.990	12.40	0.532	8.50	0.347	18.80
3.900	16.90	0.608	12.50	0.378	29.75
7.560	37.10	0.561	26.20	0.359	23.05
8.470	42.10	0.604	31.00	0.377	29.25
9.390	48.50	---	---	---	---
12.040	69.70	0.618	52.00	0.382	31.20
13.350	78.90	0.511	53.20	0.338	15.90
16.400	97.20	0.593	70.80	0.372	27.60
19.450	112.40	0.568	80.00	0.362	24.00
22.500	127.70	0.680	100.40	0.405	40.10
28.600	155.10	---	---	---	---
31.640	165.80	0.663	128.50	0.399	37.60
34.670	176.40	0.623	132.10	0.384	31.90
37.730	188.60	0.672	141.70	0.402	38.80
40.780	200.80	0.681	158.10	0.405	40.90
46.880	225.20	0.644	171.80	0.392	34.90
59.070	280.00	0.683	220.80	0.406	43.00
71.320	353.60	0.686	279.60	0.407	45.80
101.800	582.20	0.672	454.90	0.402	38.80
107.660	629.00	---	---	---	---

Table 5
Regression Constants for Curve Fitting of G versus γ

Depth From Mudline (m)	x_1	y_1	A' (10^{-5})	B' (10^{-4})	Standard Deviation (10^{-5})
0.244	0.01433	912.00	-13.915	-11.490	1.442
2.100	0.00905	920.00	-21.830	-10.934	1.941
2.980	0.00618	1,279.00	- 1.788	- 9.654	1.224
3.900	0.00977	1,007.00	- 8.440	-13.370	3.458
7.560	0.00315	2,256.00	- 2.636	- 5.974	0.959
8.470	0.00359	2,229.00	- 3.908	- 4.520	0.582
9.390	0.00279	3,481.00	- 1.140	- 4.190	0.173
12.040	0.00499	1,726.00	- 5.796	- 6.168	1.040
13.350	0.00242	2,940.00	- 1.076	- 3.486	0.391
16.400	0.00272	3,249.00	- 3.607	- 3.010	0.212
19.440	0.00193	4,303.00	- 1.409	- 2.440	0.581
22.500	0.00317	2,413.00	-52.741	- 4.280	0.743
28.600	0.00419	1,777.00	- 7.408	- 6.215	1.755
31.640	0.00377	1,942.00	- 8.543	- 4.899	0.870
34.680	0.02292	1,361.00	- 8.807	- 7.364	0.633
37.730	0.00286	2,577.00	- 4.806	- 4.182	0.757
40.780	0.00511	2,075.00	- 5.195	- 5.397	0.941
46.880	0.01452	3,069.00	- 2.035	- 3.793	0.149
59.070	0.00312	4,853.00	- 2.164	- 2.331	0.267
71.320	0.000377	26,881.00	- 0.744	- 0.284	0.032
101.800	0.000515	36,531.00	- 0.037	- 0.536	0.019
107.650	0.000234	69,437.00	- 0.225	- 0.112	0.007

Table 6
Damping Information and Rayleigh Damping Coefficients

Depth From Mudline (m)	D_{min} (%)	ω_{min} (Hz)	α	β
0.244	0.1661	5.74	0.0095	0.00029
2.100	0.1801	4.35	0.0078	0.00041
2.980	0.1549	5.47	0.0085	0.00028
3.900	0.0817	4.70	0.0038	0.00017
7.560	0.1588	7.01	0.0011	0.00023
8.470	0.1468	6.99	0.0103	0.00021
9.390	----	--	----	-----
12.040	0.1159	6.57	0.0076	0.00018
13.350	0.1438	9.32	0.0134	0.00015
16.400	0.0994	9.37	0.0093	0.00011
19.440	0.1778	9.99	0.0178	0.00018
22.500	0.2391	7.30	0.0174	0.00033
28.600	0.1660	6.67	0.0111	0.00025
31.640	0.1839	6.97	0.0128	0.00026
34.680	----	--	----	-----
37.730	0.1315	7.73	0.0102	0.00017
40.780	0.1246	7.12	0.0089	0.00018
46.880	0.0854	7.68	0.0065	0.00011
59.070	0.1201	10.99	0.0132	0.00011
71.320	0.2006	25.00	0.0502	0.00008
101.800	----	--	----	-----
107.650	0.1097	40.47	0.0444	0.00003

Table 7
Regression Constants for Curve
Fitting of τ versus γ

Depth From Mudline (m)	A (10^{-4})	B (10^{-1})	Standard Deviation (10^{-5})
0.244	9.761	7.538	2.595
2.100	10.418	5.124	3.302
2.990	10.900	5.615	22.666
3.900	12.047	3.400	14.114
7.560	4.864	4.730	2.588
8.470	4.689	4.496	4.919
9.390	3.417	2.154	4.827
12.040	5.626	4.559	5.011
13.350	3.108	7.866	25.027
16.400	2.915	2.819	1.638
19.440	2.630	2.877	4.806
22.500	3.841	3.119	12.120
28.600	5.692	3.058	1.685
31.640	4.972	3.397	1.761
34.680	6.175	5.112	5.165
37.730	3.872	2.606	1.431
40.780	5.047	3.030	4.426
46.880	2.750	3.674	0.458
59.070	2.007	1.511	0.937
71.320	0.369	0.220	0.108
101.800	0.284	0.770	0.102
107.650	0.135	0.121	0.074

Table 8
Shear Strength Data of Core Samples

Depth From Mudline (m)	Max. Shear* Modulus G_{max} (kPa)	Max. Cyclic* Shear Strength τ_{max} (kPa)	Cyclic Yield* Shear Strength τ_y (kPa)	Undrained+ Shear Strength s_u (kPa)
0.244	1,015.00	1.73	1.04	5.40
2.100	961.50	1.95	1.37	8.06
2.980	1,624.80	1.78	1.27	6.45
3.900	1,122.80	2.94	1.70	8.12
7.560	2,232.50	2.11	1.75	7.50
8.470	2,320.70	2.22	1.81	---
9.390	3,725.40	4.64	3.53	10.16
12.040	1,812.00	2.19	1.71	9.26
13.350	3,165.00	1.27	1.17	13.41
16.400	3,324.50	3.55	2.89	11.80
19.440	4,439.70	3.48	2.94	14.60
22.500	2,473.00	3.21	2.54	---
28.600	1,833.50	3.27	2.32	---
31.640	1,986.00	2.94	2.23	9.70
34.680	1,621.00	1.95	1.54	7.14
37.730	2,636.50	3.84	2.93	8.91
40.780	2,173.30	3.30	2.43	---
46.880	3,782.70	2.72	2.35	11.77
59.070	4,997.00	6.62	2.12	17.22
71.320	26,475.50	45.62	33.25	102.31
101.800	37,918.00	---	---	---
107.650	69,163.30	82.55	66.88	143.20

*Values from Resonant Column Test

+Values from Undrained Shear Strength Test

Table 9
Consolidation Test Parameters

State	Depth From Mudline (m)	P'_2 (kg/cm ²)	P'_{p2} (kg/cm ²)	e'_o	C_c^*	C_r^*	γ_{wet3} (gr/cm ³)	γ_{dry3} (gr/cm ³)	G_s^*	S^* (%)
U N D I S T	2.98	0.13	0.17	1.500	0.393	0.0176	1.630	1.076	2.690	92.30
U R B E D	6.40	1.00	0.50	1.711	0.641	0.0864	1.585	1.005	2.723	92.00
	40.78	2.05	0.21	2.221	0.687	0.1412	1.445	0.853	2.747	85.80
	46.88	2.30	0.15	2.319	0.573	0.1256	1.499	0.828	2.747	96.07
R E M O L D E D	2.98	0.13	--	1.676	0.370	----	1.623	1.005	2.690	---
	16.40	1.00	--	1.848	0.420	----	1.610	0.956	2.723	---
	40.78	2.05	--	2.207	0.580	----	1.511	0.857	2.747	---
	46.88	2.30	--	2.225	0.550	----	1.543	0.852	2.747	---

* p' = Effective Past Pressure
 e'_o = Calculated Initial Void Ratio of the Sample
 C_c = Compression Index (equivalent to λ)
 C_c = Rebound Index (equivalent to κ)
 G_s = Specific Gravity
 S = Saturation

Table 10
Critical State Parameters

Depth From Mudline (m)	P'_o (kPa)	P'^*_u (kPa)	Δu^* (kPa)	e^*_o	κ	π	ϵ_v	γ^*_c	τ^*_c (kPa)	G^*_c (kPa)
2.99	7.94	6.38	1.56	1.44	0.0176	0.00223	0.000914	0.00061	0.426	697.70
16.40	70.60	50.00	20.60	1.39	0.0864	0.01294	0.005414	0.00361	2.757	763.96
40.78	157.90	139.80	18.10	1.38	0.1420	0.00753	0.003164	0.00211	1.844	874.26
46.88	171.60	107.90	63.70	1.40	0.1256	0.02530	0.01054	0.00703	2.460	350.07

* p'_u = Mean Effective Stress at Critical State

Δu = Residual Pore Pressure at Critical State

e_o = Initial Pore Pressure at P'_o

γ_c, τ_c, G_c = Strength Parameters at Critical State

Chapter 5

CONCLUSIONS AND RECOMMENDATIONS

A number of conclusions were drawn from the study presented herein. Mud-flows in the Gulf of Mexico are potentially hazardous to the offshore structures located in the area. Foundation analysis for these structures are conducted with regard to this problem, and continued research provides different solutions to obtain the design parameters. The existing methods are limited either by inability to define the actual conditions closely or by lack of reliable data. In this study the effort mainly concentrated on showing the use of an experimental technique to obtain more realistic data and use of analytical solution techniques with different flexibilities that aid in defining the problem conditions. Finally, the following conclusions were drawn.

1. Resonant column apparatus can be used effectively to obtain dynamic properties of marine sediments in laboratory. The data obtained through this method reflects more realistic properties than other laboratory methods used for the same purpose earlier.
2. More economic designs for offshore piles can be achieved when the resonant column test results for maximum shear modulus are used in an existing numerical solution technique. The displacement, velocity and shear strain profiles obtained through this solution tend to be much lower in magnitude when the experimental G_{\max} values are used instead of an analytical value.

3. The G/s_u ratios obtained through this method tended to range between 140 to 470 for Boring B-6 of Main Pass Block 70 in Gulf of Mexico, from the mud-surface down to a depth of 110 m of soil column. The average value of the ratio was estimated to be 250 for the top 70 m of the material (refer to Plates A-75/A-76 of Appendix A).
4. The maximum cyclic shear strength was estimated to be approximately 3.00 kPa, while the yield cyclic shear strength (Von-Mises Criterion) was estimated around 2.00 kPa for the upper 60 m of soil column. On the other hand, the undrained shear strength, measured through triaxial tests, ranged between 5.00 to 15.00 kPa for the same column of material (refer to Table 8).
5. Dynamic shear modulus values displayed a relative uniformity ranging between 900.00 and 5,000.00 kPa for the top 60 m, and increased suddenly to much higher values ($\approx 70,000.00$ kPa) at around 120 m o depth from mudline (refer to Plates A-25/A-26 of Appendix A). The damping ratio of the upper soft sediments had a mean value of 3.5 percent around the vicinity of 0.5 percent shear strain amplitude. The average minimum damping ratio for the entire material of Boring B-6 was approximately 0.15 percent (refer to A-33/A-52 of Appendix A and Table 6).
6. Family of shear modulus profile curves for various shear strength amplitudes, produced from resonant column data, can be used as a design "tool" with the proper knowledge of shear strains induced within a soil column of a certain depth due to

cyclic wave loading. Existing shear moduli can readily be estimated for different depths after a design storm loading, using these graphs.

7. A finite element program can be adapted to incorporate the number of cycles effects of cyclic loading which is not considered in the existing numerical solution technique for mud flow analysis. The program used in this case is NONSAP.
8. Critical state soil mechanics has a relevant application to mud flow problems. The Cam-Clay model of critical state soil mechanics is readily viewed as one of the modeling procedures to obtain information about the state of soil mass before it starts flowing under cyclic loading effects.
9. The critical state model and the effort to analyze it with the numerical solution method presented herein is by no means final and needs to be studied both experimentally and analytically in detail. The validity of the assumptions made in applying the model to the sediment samples and the problem of mud flows should also be studied further. However, in spite of the shortcomings of the numerical analysis at critical state, the model is viewed to be a powerful tool in explaining some of the mechanisms that prepare mud-flows.

The finite element program, NONSAP, apart from having favorable flexibilities is rather a cumbersome method for cyclic load analysis. The program package being very sensitive to various data input modes (i.e., loading rate), is not a practical solution method for mud-flow analysis. However, other finite element programs, specially devised for cyclic loading concept of soils (i.e., pore pressure and degradation

AD-A118 157

LOUISIANA STATE UNIV BATON ROUGE DEPT OF CIVIL ENGIN--ETC F/8 8/10
CLASSIFICATION OF COASTAL SEDIMENTS.(U)
MAR 82 J N SUHAYDA, M TUMAY

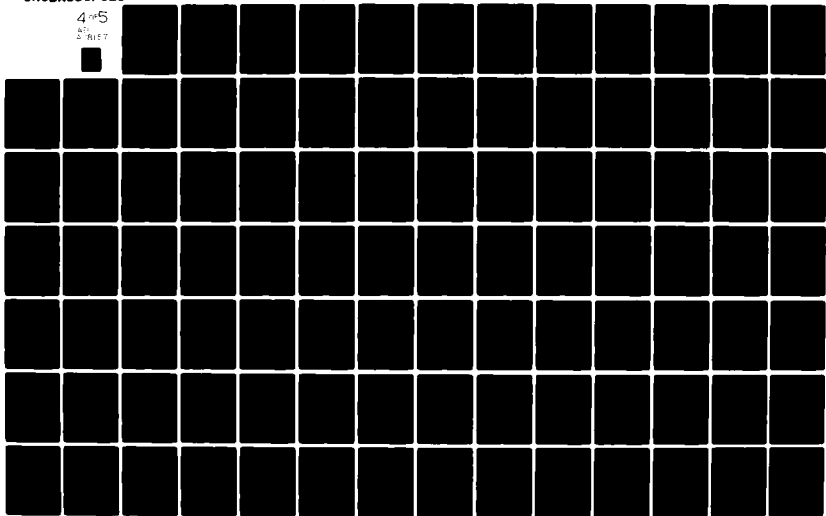
N00014-80-C-0846

NL

UNCLASSIFIED

4 of 5

218157



response) are available, and further search on this subject matter is recommended.

Critical state model having the potential of use for better understanding of sediment behavior under cyclic loading, is recommended to be included in research on the subject matter of mud flows.

Finally, due to the inevitable sample disturbance that complicates most laboratory analysis of soil properties, in-situ techniques of measurements are generally suggested for important foundation design procedures. Experiencing the same "handicap" with the resonant column analysis, and being unable to measure excess pore water and gas pressures that actually exist in the sediments at high magnitudes, more refined techniques of measurements are recommended. These techniques possibly can range from modifications of the resonant column analysis (i.e., using back pressuring, correcting data with regard to disturbance) or turning to in situ techniques (acoustic and seismic moduli measurements, in situ pore pressure measurements, i.e., French self-boring piezo-pressuremeter).

The overall effort of this study was to highlight a better technique of laboratory data acquisition to be used in already existing numerical methods to simulate sediment flows in the Gulf of Mexico.

REFERENCES

1. Anderson, D. G., and Stokoe, K. H., II, "Shear Modulus: A Time-Dependent Soil Property," Dynamic Geotechnical Testing, ASTM Special Technical Publication 654, pp. 66-90.
2. Bathe, K. J., Ozdemir, H., and Wilson, E. L., "Static and Dynamic Geometric and Material Nonlinear Analysis," Report No. UCSESM 74-4, Structures and Materials Research, Department of Civil Engineering Laboratory, Structural Engineering Laboratory, University of California, Berkeley, February 1974.
3. Bathe, K. J., Wilson, E. L., and Iding, R. H., "NONSAP, A Structural Analysis Program for Static and Dynamic Response of Nonlinear Systems," Report No. UCSESM 74-3, Structures and Materials Research Department of Civil Engineering Division of Structural Engineering and Structural Mechanics, University of California, Berkeley, February 1974.
4. Bathe, K. J., and Wilson, E. L., "NONSAP--A General Finite Element Program for Nonlinear Dynamic Analysis of Complex Structures," Paper M3/1, Proceedings 2nd International Conference on Structural Mechanics in Reactor Technology, Berlin, September 1973.
5. Bathe, K. J., Ramm, E., and Wilson, E. L., "Finite Element Formulations for Large Displacement and Large Strain Analysis," SESM Report No. 73-14, Department of Civil Engineering, University of California, Berkeley, September 1973.
6. Bea, R. G., and Arnold, P., "Movements and Forces Developed by Wave Induced Slides in Soft Clays," Fifth Annual Offshore Technology Conference, OTC 1899, April 29 - May 2, 1973.
7. Bea, R. G., Bernard, H. A., Arnold, P., and Doyle, E. H., "Soil Movements and Forces Developed by Wave-Induced Slides in the Mississippi Delta," Journal of Petroleum Technology, April 1975, pp. 500-514.
8. Bennett, R. H., and Faris, J. R., "Ambient and Dynamic Pore Pressures in Fine-Grained Submarine Sediments: Mississippi Delta," Applied Ocean Research, 1979, Vol. 1, No. 3, pp. 115-123.
9. Biot, M. A., "Theory of Propagation of Elastic Waves in a Fluid Saturated Porous Solid," Journal of Acoustical Society of America, Vol. 28, March 1956, pp. 168-191.
- 9a. Bischoff, J. L., Greer, R. E., and Luistro, A. O., "Composition of Interstitial Waters of Marine Sediments: Temperature of Squeezing Effect," Science, 1970, Vol. 167, pp. 1245-1246.

10. Booker, J. R., Rahman, M. S., and Seed, H. B., "GADFLEA - A Computer Program for the Analysis of Pore Pressure Generation and Dissipation During Cyclic or Earthquake Loading," Report No. EERC 76-24, Earthquake Engineering Research Center, University of California, Berkeley, October 1976.
11. Bowles, J. E., Foundation Analysis and Design, McGraw-Hill Book Company, New York, NY, 1977.
12. Cunney, R. W., and Fry Z. B., "Vibratory In-Situ and Laboratory Soil Moduli Compared," Journal of the Soil Mechanics and Foundations Division, ASCE, SM12, Proc. paper 10215, December 1973, pp. 1055-1076.
13. Drnevich, V. P., "Resonant-Column Testing--Problems and Solutions," Dynamic Geotechnical Testing, ASTM Special Technical Publication 654, pp. 384-398.
14. Egan, J. A., "Critical State Model for the Cyclic Loading Pore Pressure Response of Soils," Thesis presented to Cornell University at Ithaca, NY, in 1977, in partial fulfillment of the requirements for the degree of Master of Science.
15. Egan, J. A., and Sangrey, D. A., "A Critical State Model for Cyclic Load Pore Pressure," Proceedings of the ASCE Geotechnical Engineering Division Specialty Conference, Earthquake Engineering and Soil Dynamics, Pasadena, California, June 19-21, 1978, Vol. 1, pp. 411-424.
- 15a. Fanning, F. A., and Pilson, M. E. Q., "Interstitial Silica and pH in Marine Sediments: Some Effects of Sampling Procedures," Science, 1971, Vol. 173, pp. 1228-1231.
16. Finn, W. D. L., Lee, K. K., and Martin, G. R., "An Effective Stress Model for Liquefaction," Journal of the Geotechnical Engineering Division, ASCE, GT6, Proc. paper 13008, June 1977, pp. 517-533.
17. Hardin, B. O., "The Nature of Damping in Sands," Journal of Soil Mechanics and Foundation Division, ASCE, SM1, January 1965, pp. 63-97.
18. Hardin, B. O., and Black, W. L., "Vibration Modulus of Normally Consolidated Clay," Journal of the Soil Mechanics and Foundations Division, ASCE, SM2, March 1968, pp. 353-369.
19. Hardin, B. O., and Drnevich, V. P., "Shear Modulus and Damping in Soils: Design Equations and Curves," Journal of the Soil Mechanics and Foundations Division, ASCE, SM7, Proc. paper 9006, July 1972, pp. 667-692.
20. Herrman, H. G., and Houston, W. N., "Response of Seafloor Soils to Combined Static and Cyclic Loading," Eight Annual Offshore Technology Conference, OTC 2428, May 3-6, 1976.

21. Holman, J. P., Experimental Methods for Engineers, 2nd Edition, McGraw-Hill, Kogakusha, Ltd., Tokyo, 1971.
22. Idriss, I. M., Dobry, R., and Singh, R. D., "Nonlinear Behavior of Soft Clays During Cyclic Loading," *Journal of the Geotechnical Engineering Division, ASCE*, GT12, Proc. paper 14265, December 1978, pp. 1427-1447.
23. Iida, K., "The Velocity of Elastic Waves in Sand," *Bulletin of the Earthquake Research Institute, Tokyo Imperial University, Japan*, Vol. 16, pp. 131-144.
24. Isenhower, W. M., "Torsional Simple Shear/Resonant Column Properties of San Francisco Bay Mud," Thesis presented to University of Texas in 1979, in partial fulfillment of the requirements for the degree of Master of Science.
25. Johnson, L. H., Nomography and Empirical Equations, John Wiley & Sons, New York, NY, 1952.
26. King, J. B., Dunlap, W. A., and Schapery, R. A., "Characterization of Viscoelastic Properties of Submarine Sediments," A Report from Mechanics and Materials Research Center, Texas Engineering Experiment Station, Texas A & M University, TX, April 1976.
27. Lee, K. L., and Focht, J. A., "Liquefaction Potential at Ekofisk Tank in North Sea," *Journal of the Geotechnical Engineering Division, ASCE*, No. GT1, Proc. paper 11054, January 1975, pp. 1-18.
28. Liou, C. P., Streeter, V. L., and Richart, F. E., Jr., "Numerical Model for Liquefaction," *Journal of the Geotechnical Engineering Division, ASCE*, GT6, Proc. paper 12998, June 1977, pp. 589-606.
29. Lysmer, John, "Analytical Procedures in Soil Dynamics," Report No. UCB/EERC-78/29, Earthquake Engineering Research Center, University of California, Berkeley, December 1978.
30. McCllend Engineers, Inc., Geotechnical Consultants, New Orleans, LA, "Geotechnical Investigation Block 75, Main Pass Area," July 1981.
31. Martin, G. R., Finn, W. D. L., and Seed, H. B., "Fundamentals of Liquefaction Under Cyclic Loading," *Journal of the Geotechnical Engineering Division, ASCE*, GT5, Proc. paper 11284, May 1975, pp. 423-437.
32. Martin, G. R., Lam, Ignatius, and Tsai, Chan-Feng, "Pore Pressure Dissipation During Offshore Cyclic Loading," *Journal of the Geotechnical Engineering Division, ASCE*, GT9, Proc. paper 15706, September 1980, pp. 981-995.

33. Martin, P. O., and Seed, H. B., "APOLLO - A Computer Program for the Analysis of Pore Pressure Generation and Dissipation in Horizontal Sand Layers During Cyclic Earthquake Loading," Report No. UCB/EERC-78/21, Earthquake Engineering Research Center, University of California, Berkeley, October 1978.
34. Masing, G., "Eigenspannungen and Verfestigung beim Messing," Proceedings of the Second International Congress of Applied Mechanics, 1926.
- 34a. Mitchell, J. K., Fundamentals of Soil Behavior, John Wiley and Sons, Inc., New York, 1976.
35. Mitchell, R. J., Tsui, K. K., and Sangrey, D. A., "Failure of Submarine Slopes Under Wave Action," Proc. 13th Coastal Engineering Conference, Vancouver, Vol. II, pp. 1515-1542, 1972.
36. Pipkin, A. C., Lectures on Viscoelasticity Theory, Springer-Verlag, 1972.
37. Prakash, Shamsher, Soil Dynamics, McGraw-Hill Book Company, New York, NY, 1981.
38. Prakash, S., and Puri, V. K., "Natural Frequency of Block Foundations Under Free and Forced Vibrations," J. Indian Geotech., Vol. 2, No. 4, October 1972.
39. Prior, D. B., and Suhayda, J. N., "Application of Infinite Slope Analysis to Subaqueous Sediment Instability, Mississippi Delta," Engineering Geology, 14 (1979), pp. 1-10.
40. Rahman, M. S., Seed, H. B., and Booker, J. R., "Pore Pressure Development Under Offshore Gravity Structures," Journal of the Geotechnical Engineering Division, ASCE, No. GT 12, Proc. paper 13411, December 1977, pp. 1419-1435.
41. Richards, A. F., Øioen, K., Keller, G. H., and Lai, J. Y., "Differential Piezometer Probe for an In-Situ Measurement of Sea-floor Pore Pressure," Geotechnique, Vol. 25, No. 2, 1975, pp. 229-238.
42. Richart, F. E., Jr., Hall, J. R., Jr., and Wood, R. D., Vibrations of Soils and Foundation, Prentice-Hall, Inc., Englewood Cliffs, NJ, 1970.
- 42a. Roberts, H. H., Suhayda, J. N., and Coleman, J. M., "Sediment Deformation and Transport on Low Angle Slopes: Mississippi River Delta," Thresholds in Geomorphology, George Alleng Unwin Ltd., 40 Museum Street, London WC1A 1LU.
43. Roscoe, K. H. Schofield, M. A., and Thurairajah, A., "Yielding of Clays in States Wetter Than Critical," Geotechnique, Vol. 13, No. 4, pp. 211-240, 1963.

44. SAS User's Guide, SAS Institute, Inc., 1979.
45. Schapery, R. A., "Wave-Sea Bottom Interaction Study (Phase One), Part I: Theory and Results," A Report from Mechanics and Materials Research Center, Texas Engineering Experiment Station, Texas A & M University, TX, March 1974.
- 45a. Schapery R. A., "Wave-Sea Bottom Interaction Study (Final Report), Part I: Theory and Results," A Report from Mechanics and Materials Research Center, Texas Engineering Experiment Station, Texas A & M University, Texas, September 1976.
46. Schapery, R. A. Riggins, M., and Dunlap, W. A., "Movement of Marine Clay Sediments During Cyclic Loading," A Report from Mechanics and Materials Research Center, Texas Engineering Experiment Station, Texas A & M University, TX, September 1976.
47. Schofield, A., and Wroth, P., Critical State Soil Mechanics, McGraw-Hill Book Company, McGraw-Hill House, Maidenhead, Berkshire, England, 1968.
48. Seed, H. B., and Idriss, I. M., "Soil Moduli and Damping Factors for Dynamic Response Analysis," Report No. EERC 70-10, University of California, Berkeley, September 1970.
49. Seed, H. B., Lysmer, J., and Hwang, R., "Soil-Structure Interaction Analyses for Seismic Response," Journal of the Geotechnical Engineering Division, ASCE, GT5, Proc. paper 11318, May 1975, pp. 439-457.
50. Seed, H. B., Martin, P. P., and Lysmer, J., "Pore-Water Pressure Changes During Soil Liquefaction," Journal of the Geotechnical Engineering Division, ASCE, GT4, Proc. paper 12074, April 1976, pp. 323-346.
51. Seed, H. B., and Rahman, M. S., "Analysis for Wave-Induced Liquefaction in Relation to Ocean Floor Stability," Report No. UCB/TE-77/02, Department of Civil Engineering, Institute of Transportation and Traffic Engineering, University of California, Berkeley, May 1977.
52. Sterling, J. H., Jr., and Bryant, W. R., "Engineering Properties of Shallow Sediments in West Delta and South Pass Outer Continental Shelf Lease Areas, Offshore Louisiana," Technical Report 77-4-T, Department of Oceanography, Texas A & M University, TX, May 1977.
53. Sterling, G. H., and Stohbeck, E. E., "The Failure of the South Pass 70 "B" Platform in Hurricane Camille," Fifth Annual Offshore Technology Conference, OTC 1898, April 29 - May 2, 1973.

54. Stevenson, H. S., "Vane Shear Determination of the Viscoelastic Shear Modulus of Submarine Sediments," Thesis submitted to Graduate College of Texas A & M University in partial fulfillment of the requirement for the degree of Master of Science, December 1973, College Station, TX.
55. Stokoe, K. H., II, "Dynamic Properties of Offshore Silty Samples," 12th Annual Offshore Technology Conference, OTC 3771, May 5-8, 1980.
56. Stokoe, K. H., II, and Abdel-razzak, K. G., in Proceedings, In-Situ Measurements of Soil Properties, American Society of Civil Engineers, Raleigh, NC, Vol. 1, 1975, pp. 422-447.
57. Stokoe, K. H., II, and Lodde, P. F., "Cyclic Stress-Strain Characteristics of Clay," Journal of the Soil Mechanics and Foundation Division, ASCE, SM2, March 1908, pp. 555-569.
58. Stokoe, K. H., II, and Richart, F. E., Jr., in Proceedings, Eighth International Conference on Soil Mechanics and Foundation Engineering, Moscow, Vol. 1, Part 2, 1973b, pp. 403-409.
59. Suhayda, J. N., and Prior, D. B., "Explanation of Submarine Landslide Morphology by Stability Analysis and Rheological Models," Tenth Annual Offshore Technology Conference, OTC 3171, May 8-11, 1978.
60. Thiers, G. R., and Seed, H. B., "Strength and Stress-Strain Characteristics of Clays Subjected to Seismic Loading Conditions," Vibration Effects of Earthquakes on Soils and Foundations, ASTM STP 450, American Society for Testing and Materials, 1968.
61. Tsai, Chan-Feng, Lam, Ignatius, and Martin, R. M., "Seismic Response of Cohesive Marine Soils," Journal of the Geotechnical Engineering Division, ASCE, GT9, Proc. paper 15708, September 1980, pp. 997-1012.
- 61a. Tumay, M. T., "Horizontal and Vertical Permeability Relations During Consolidation," (in Turkish), Technical University of Istanbul, Turkey, 1971.
- 61b. Tumay, M. T., Boggess, R. L., and Acar, Y., "Subsurface Investigations with Piezo-Cone Penetrometer," Cone Penetration Testing and Experience, Proceedings of Geotechnical Engineering Division at the ASCE National Convention, St. Louis, Missouri, October 26-30, 1981, pp. 325-342.
62. Ugural, A. C., and Fenster, S. K., Advanced Strength and Applied Elasticity, Elsevier North Holland Publishing Company, Inc., 52 Vanderbilt Avenue, New York, NY 10017, 1979.
63. Whitman, R. V., "The Response of Soils to Dynamic Loadings," Defense Atomic Support Agency, U.S. Army Waterways Experiment Station, Report No. 26, 1970.

64. Woods, R. D., "Measurement of Dynamic Soil Properties," Proceedings of the ASCE Geotechnical Engineering Division Specialty Conference, Earthquake Engineering and Soil Dynamics, Pasadena, CA, June 19-21, 1978, Vol. 1, pp. 91-178.
65. Zienkiewicz, O. C., The Finite Element Method, 3rd Edition, McGraw-Hill Book Company (UK) Limited, 1977.

APPENDIX A

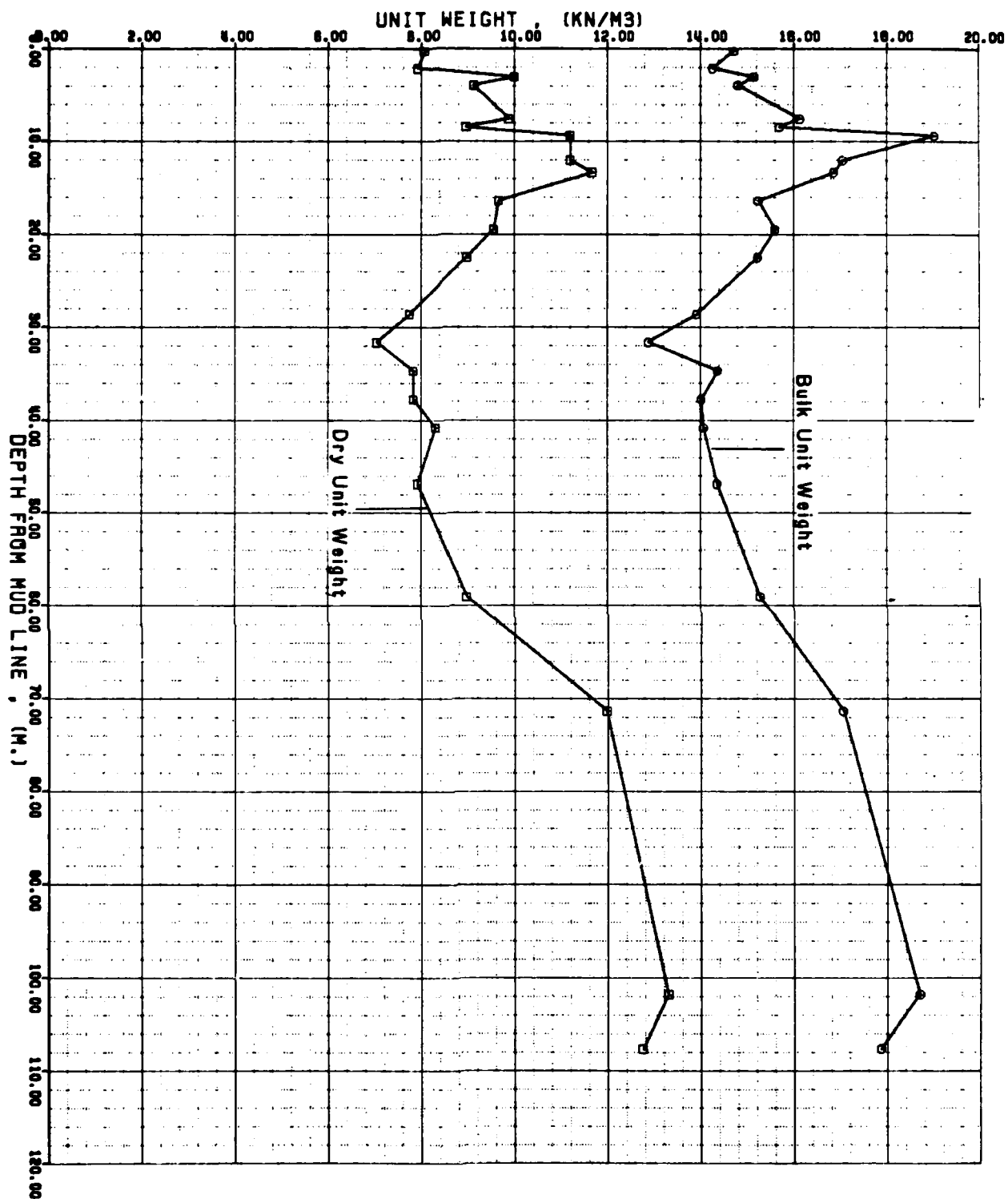
EXPERIMENTAL RESULTS

APPENDIX A-1

BULK AND DRY UNIT WEIGHTS PROFILE

THE VARIATION OF UNIT WEIGHT WITH DEPTH

DEEP CORE SAMPLES OF GULF OF MEXICO

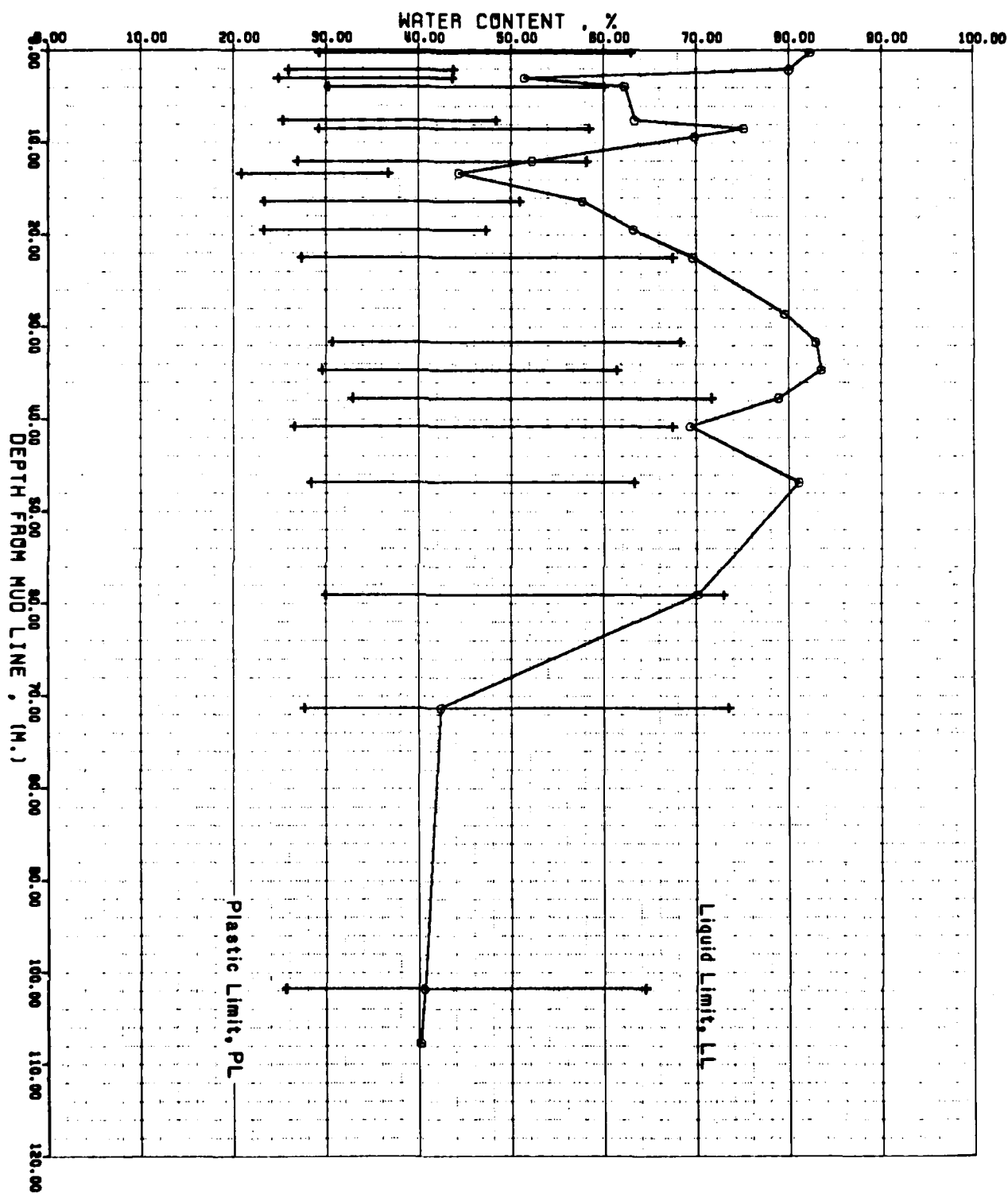


A-1

APPENDIX A-2

WATER CONTENT AND PLASTICITY PROFILE

THE VARIATION OF WATER CONTENT WITH DEPTH DEEP CORE SAMPLES OF GULF OF MEXICO



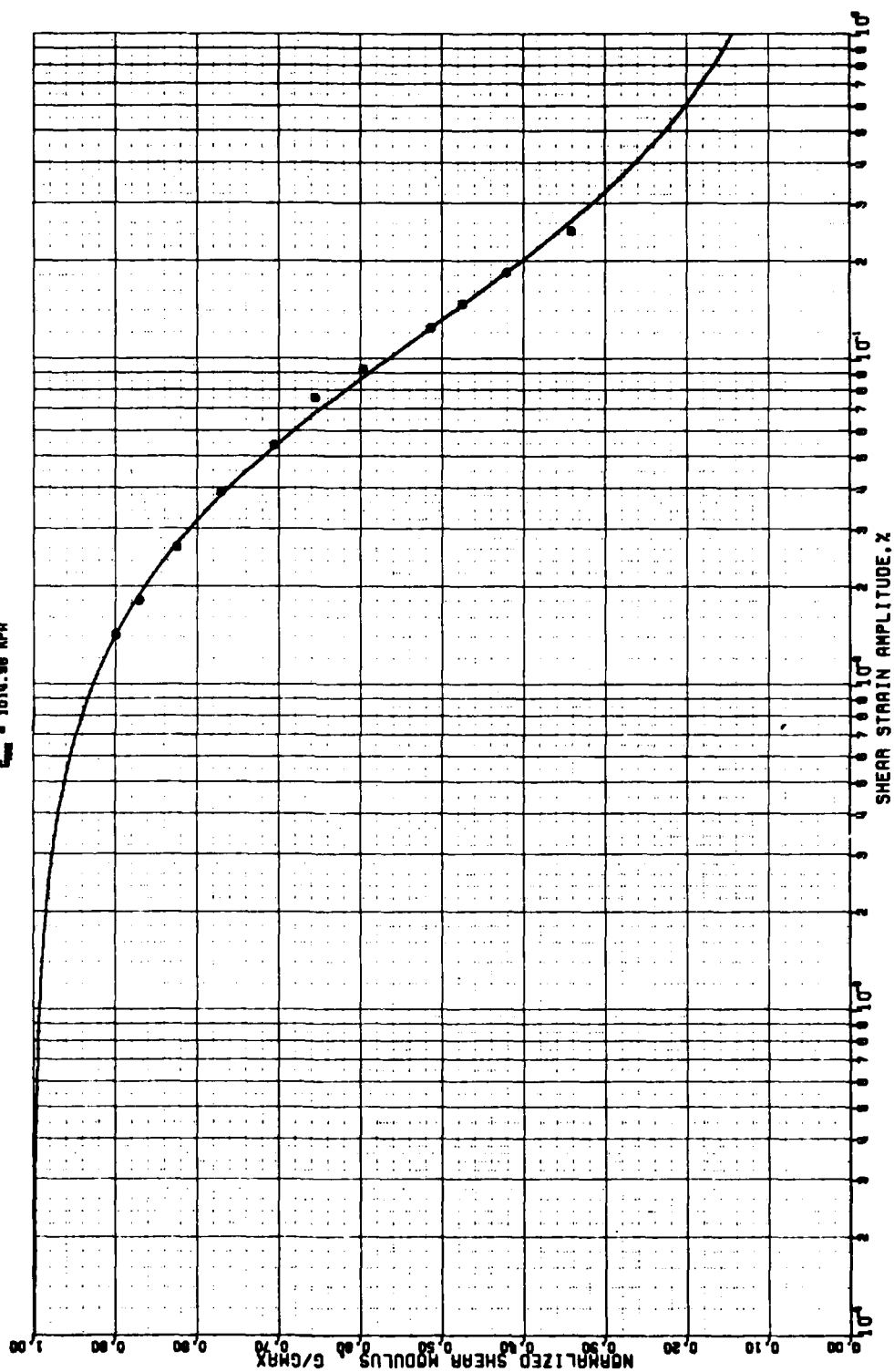
APPENDIX A-3/A-24

VARIATION OF NORMALIZED SHEAR MODULUS WITH SHEAR STRAIN

THE VARIATION OF SHEAR MODULUS WITH STRAIN AMPLITUDE DEEP CONE SAMPLES OF GULF OF MEXICO

SAMPLE DEPTH = 0.24 M.

$E_{\text{max}} = 1014.96 \text{ MPa}$

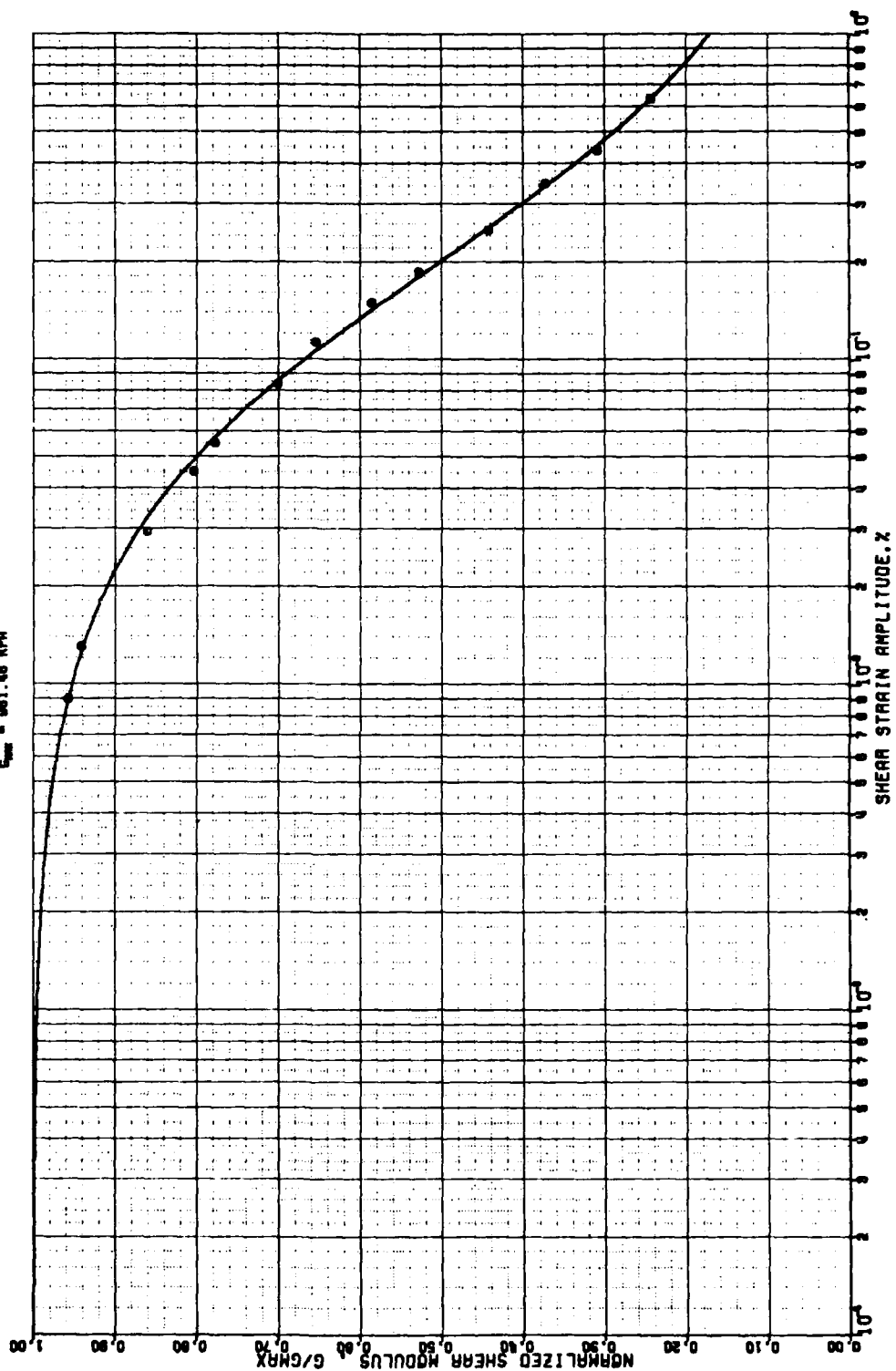


THE VARIATION OF SHEAR MODULUS WITH STRAIN AMPLITUDE

DEEP CORE SAMPLES OF GULF OF MEXICO

SAMPLE DEPTH = 2.10 M.

$G_{max} = 981.46 \text{ KPA}$

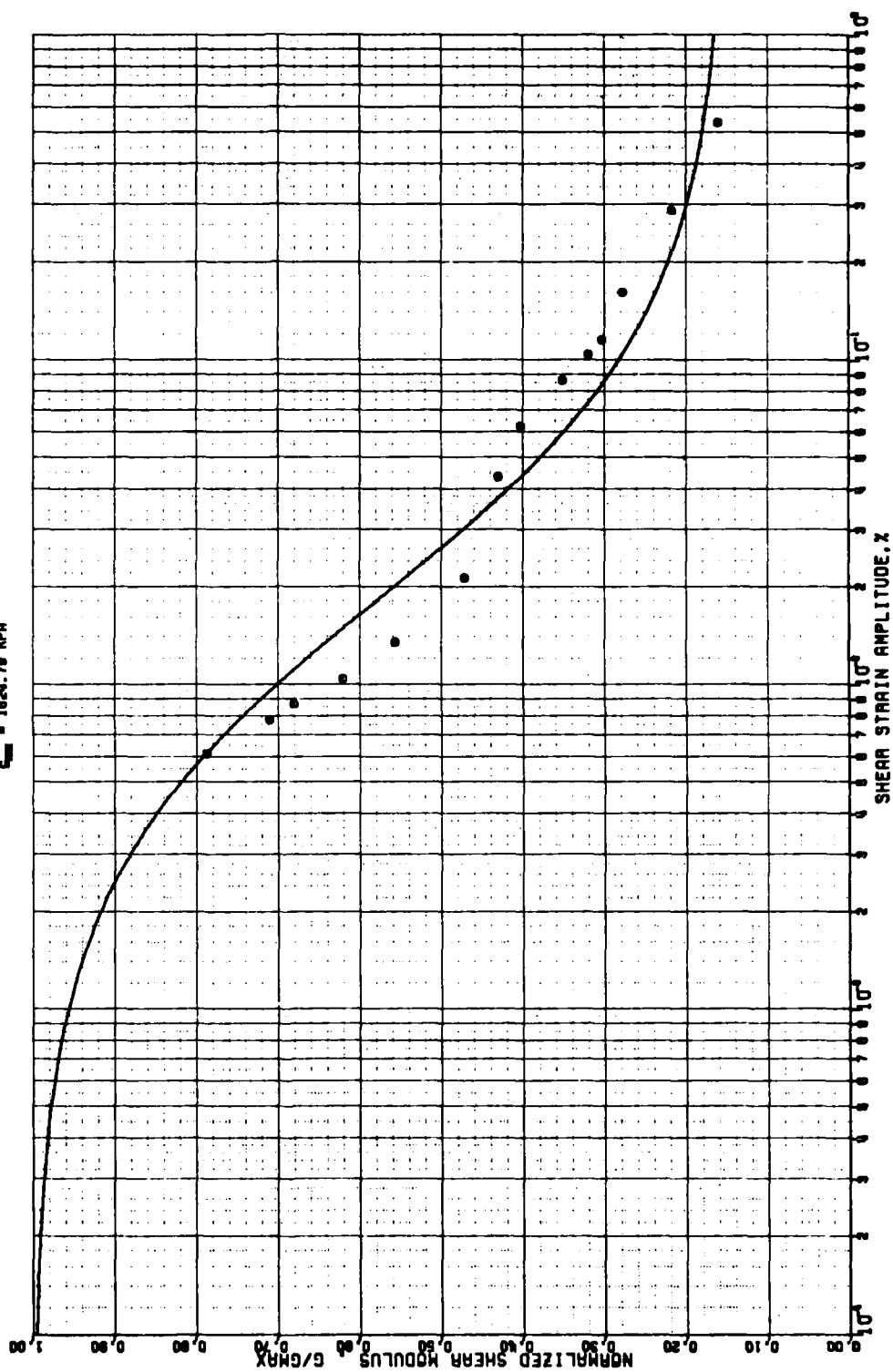


THE VARIATION OF SHEAR MODULUS WITH STRAIN AMPLITUDE

DEEP CORE SAMPLES OF GULF OF MEXICO

SAMPLE DEPTH = 2.88 M.

$\sigma_{vm} = 1624.76 \text{ KPA}$

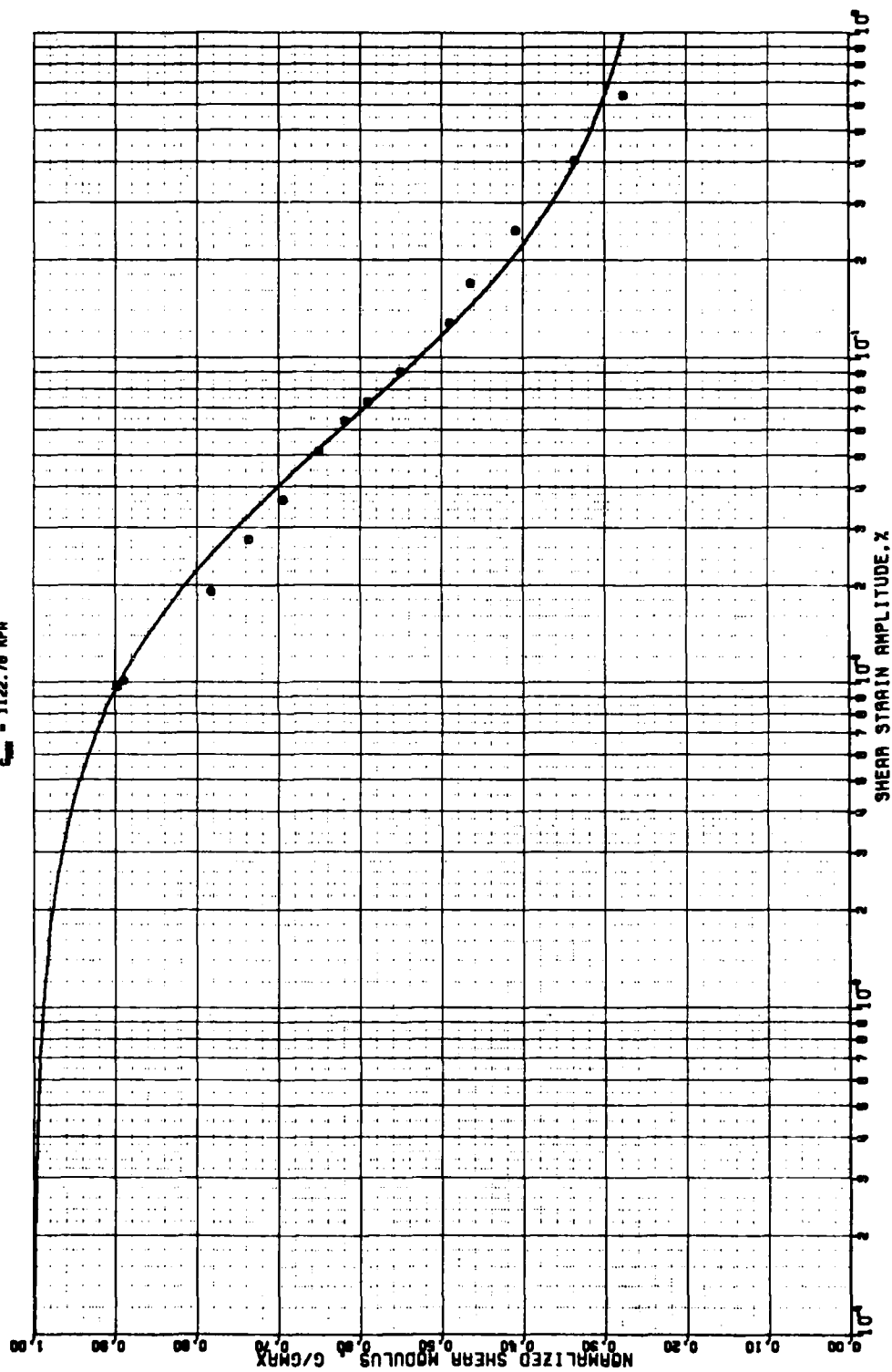


THE VARIATION OF SHEAR MODULUS WITH STRAIN AMPLITUDE

DEEP CORE SAMPLES OF GULF OF MEXICO

SAMPLE DEPTH = 3.80 M.

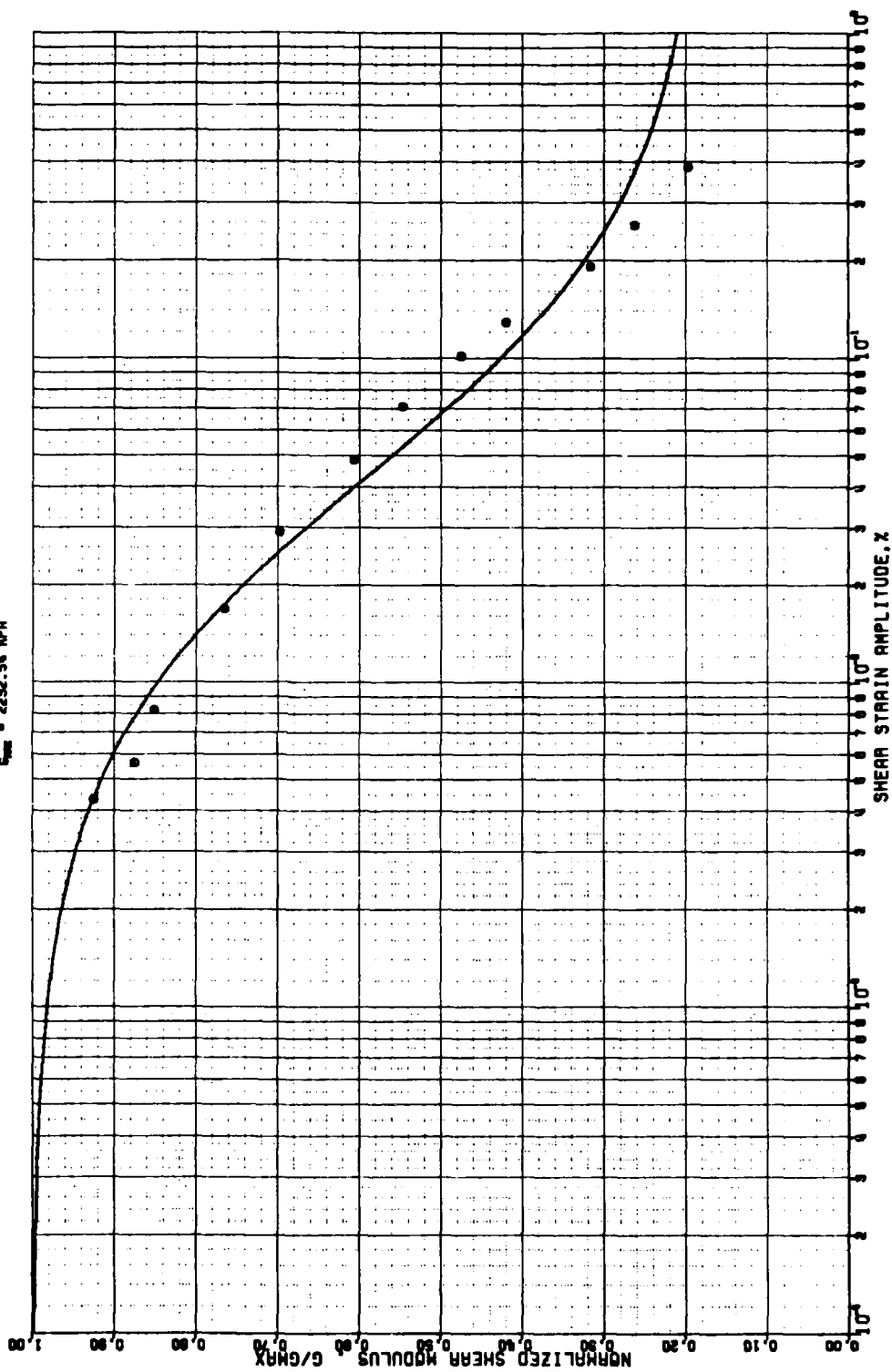
$G_{max} = 1122.78 \text{ MPa}$



THE VARIATION OF SHEAR MODULUS WITH STRAIN AMPLITUDE DEEP CORE SAMPLES OF GULF OF MEXICO

SAMPLE DEPTH = 7.56 M.

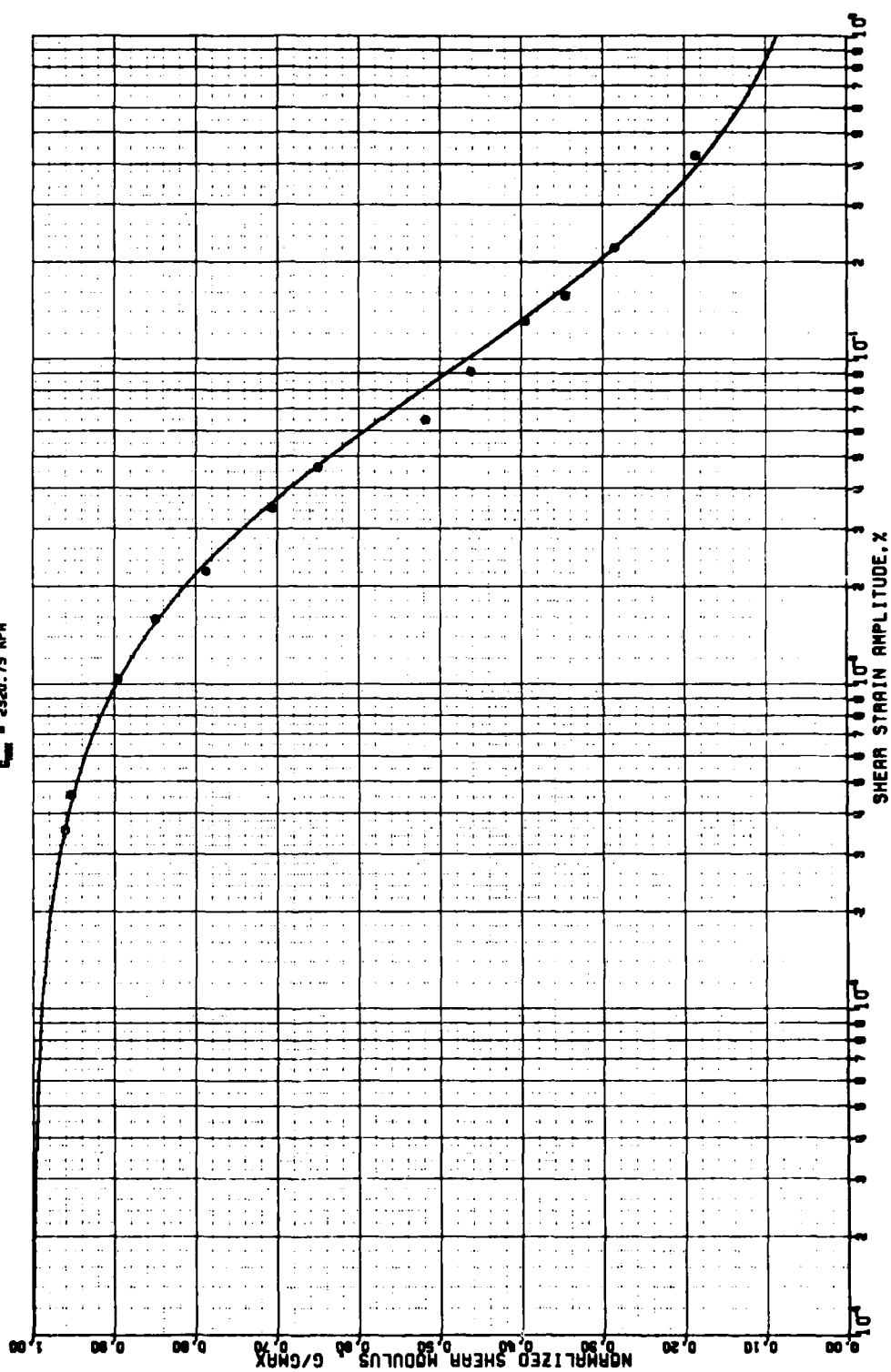
$E_{max} = 2252.56 \text{ MPa}$



THE VARIATION OF SHEAR MODULUS WITH STRAIN AMPLITUDE DEEP CORE SAMPLES OF GULF OF MEXICO

SAMPLE DEPTH = 6.67 M.

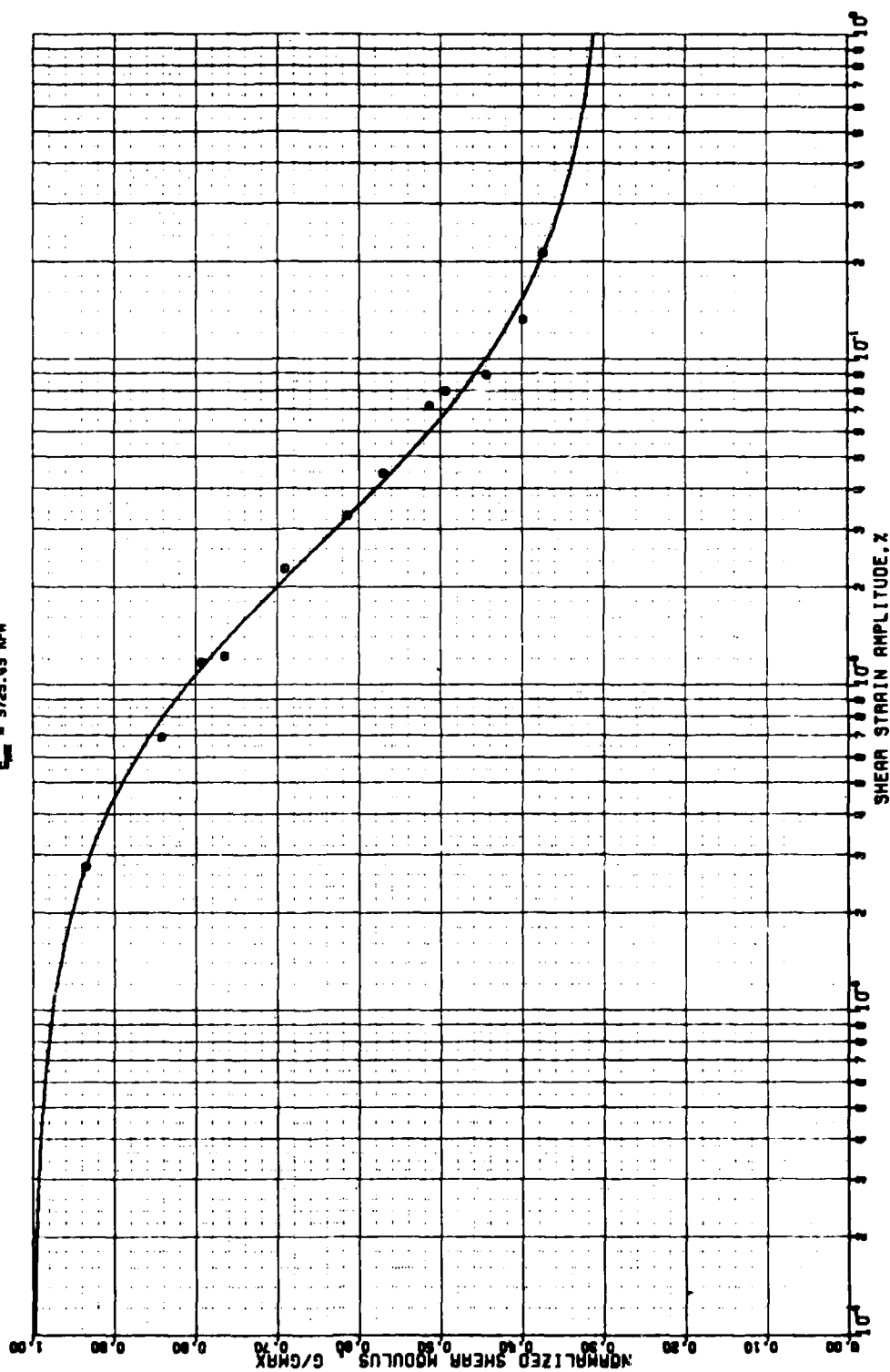
$G_{max} = 2320.75 \text{ KPA}$



THE VARIATION OF SHEAR MODULUS WITH STRAIN AMPLITUDE DEEP CORE SAMPLES OF GULF OF MEXICO

SAMPLE DEPTH = 9.38 M.

$G_{max} = 5725.43 \text{ MPa}$

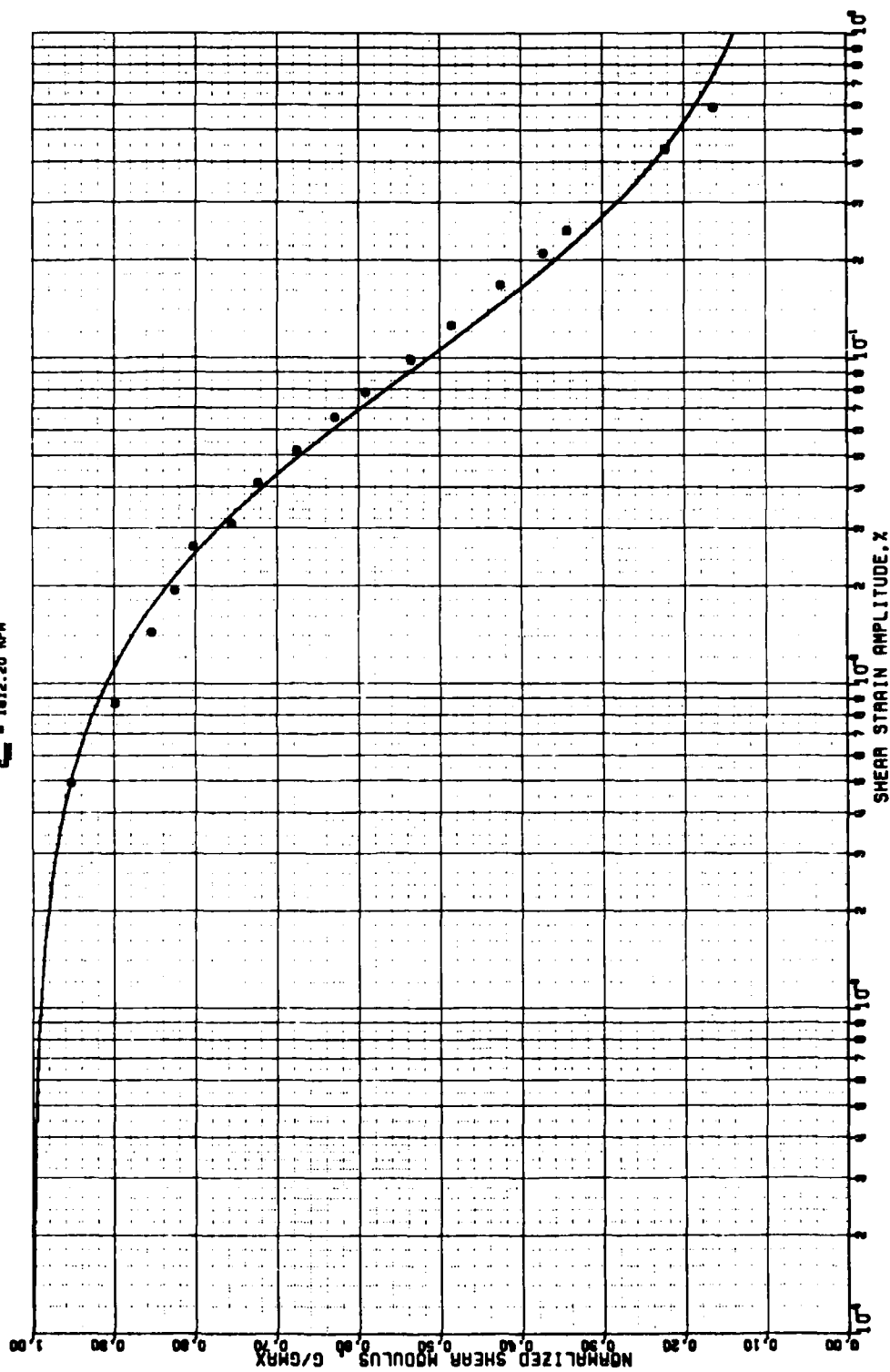


THE VARIATION OF SHEAR MODULUS WITH STRAIN AMPLITUDE

DEEP CORE SAMPLES OF GULF OF MEXICO

SAMPLE DEPTH = 12.04 M.

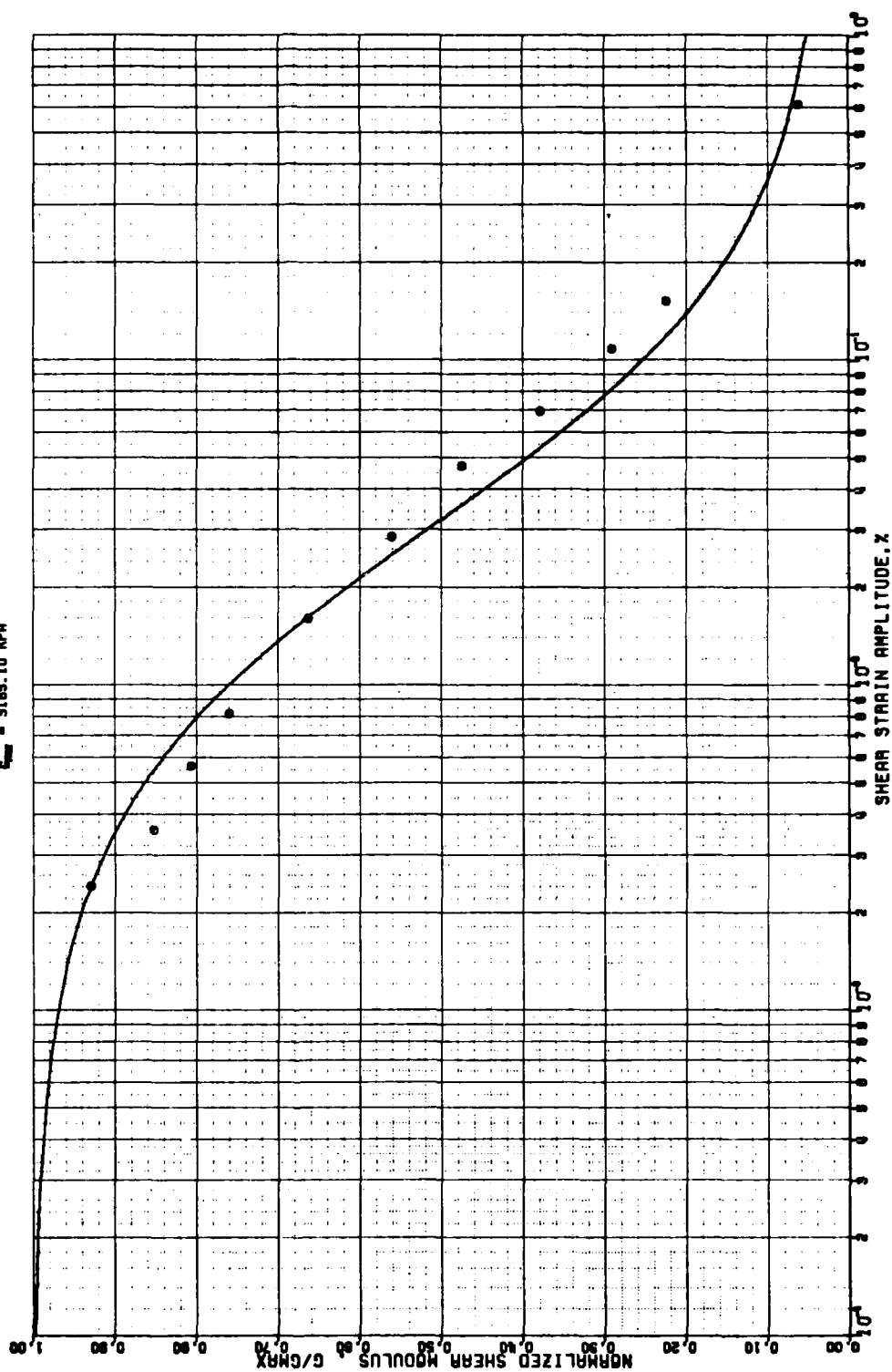
$G_{max} = 1612.20 \text{ KPA}$



THE VARIATION OF SHEAR MODULUS WITH STRAIN AMPLITUDE DEEP CORE SAMPLES OF GULF OF MEXICO

SAMPLE DEPTH = 13.35 M.

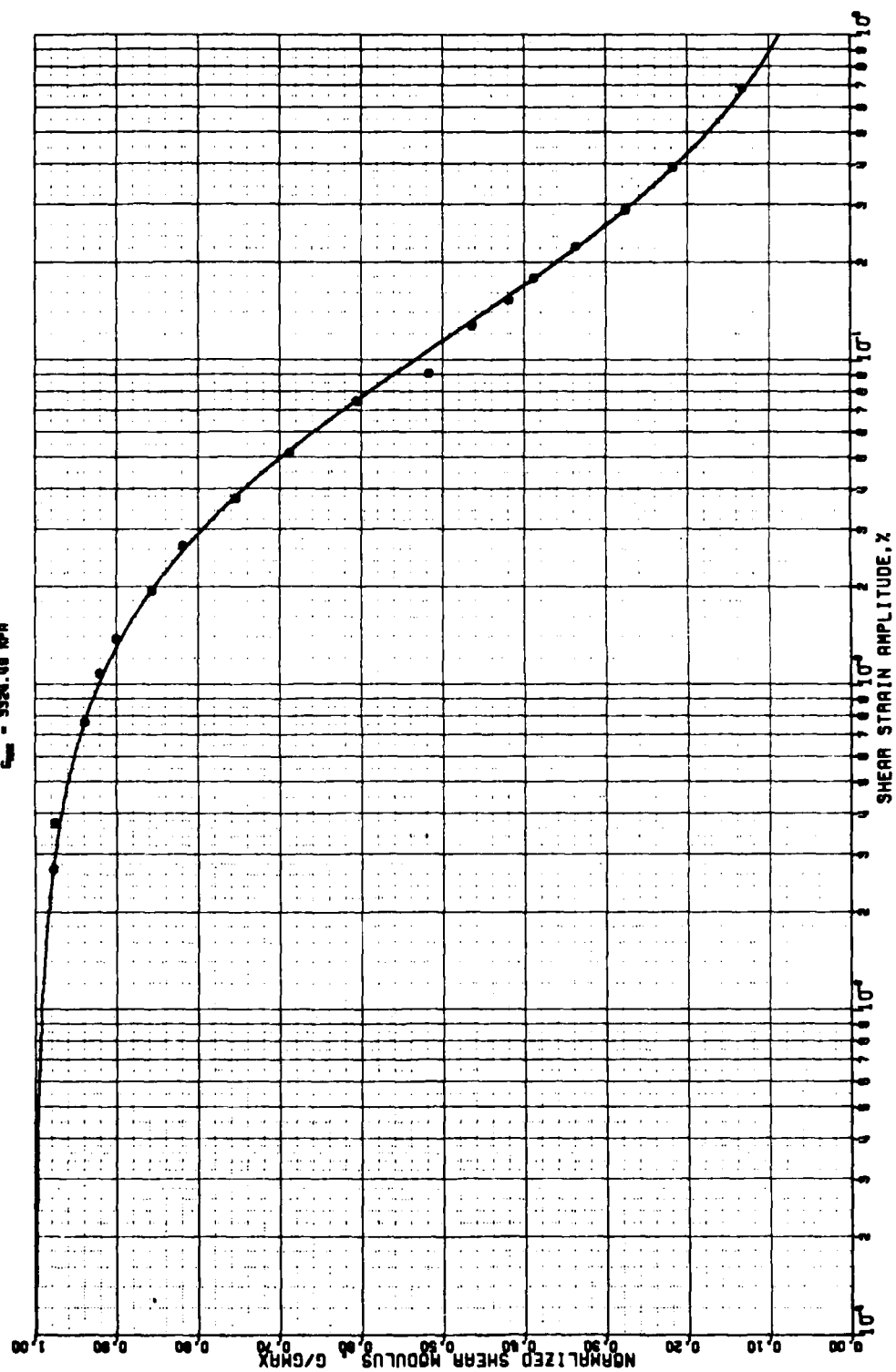
$G_{max} = 5185.10 \text{ KPA}$



THE VARIATION OF SHEAR MODULUS WITH STRAIN AMPLITUDE DEEP CORE SAMPLES OF GULF OF MEXICO

SAMPLE DEPTH = 16.40 M.

$C_{\text{max}} = 3324.48 \text{ KPA}$

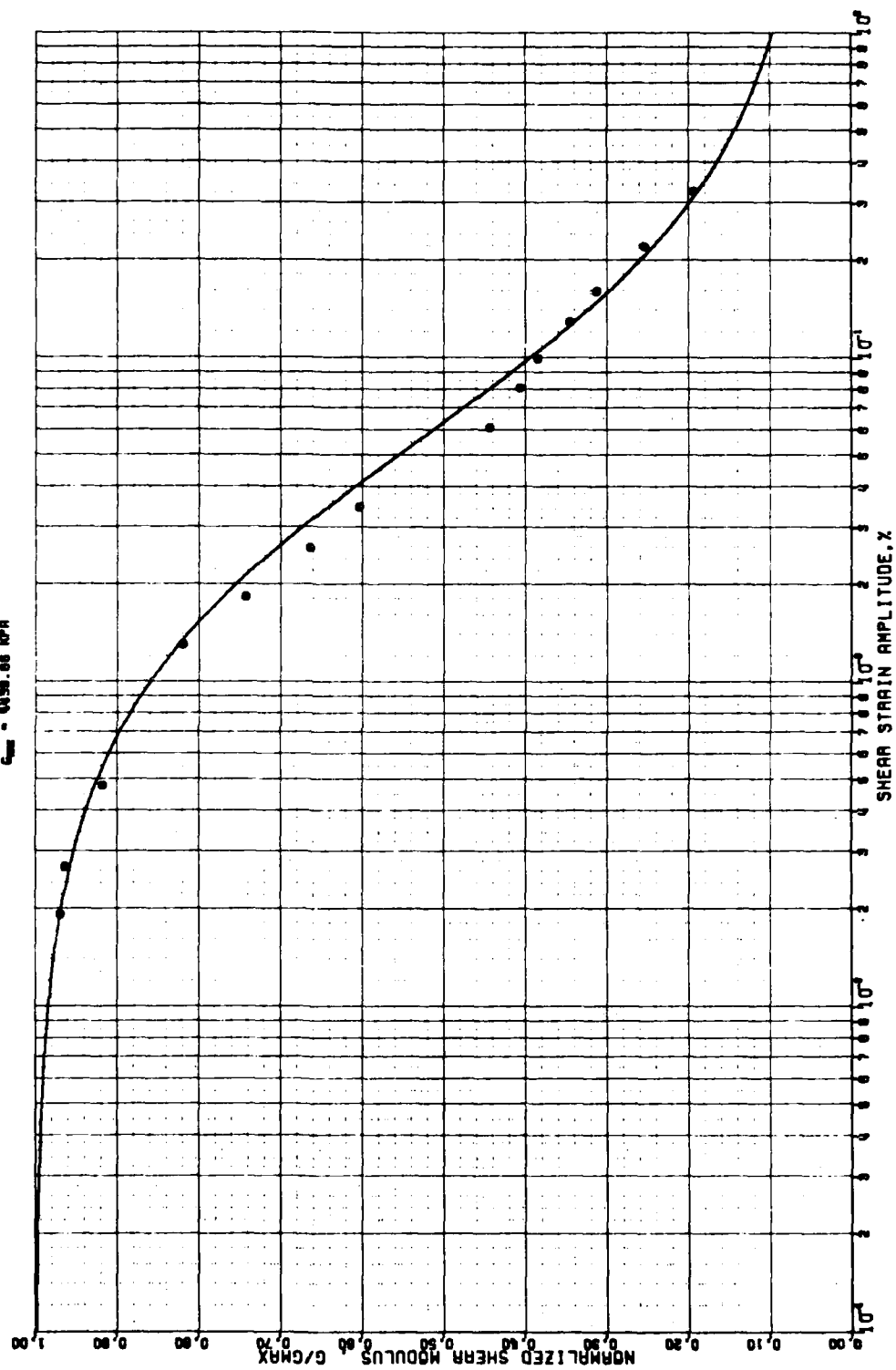


THE VARIATION OF SHEAR MODULUS WITH STRAIN AMPLITUDE

DEEP CORE SAMPLES OF GULF OF MEXICO

SAMPLE DEPTH = 18.45 M.

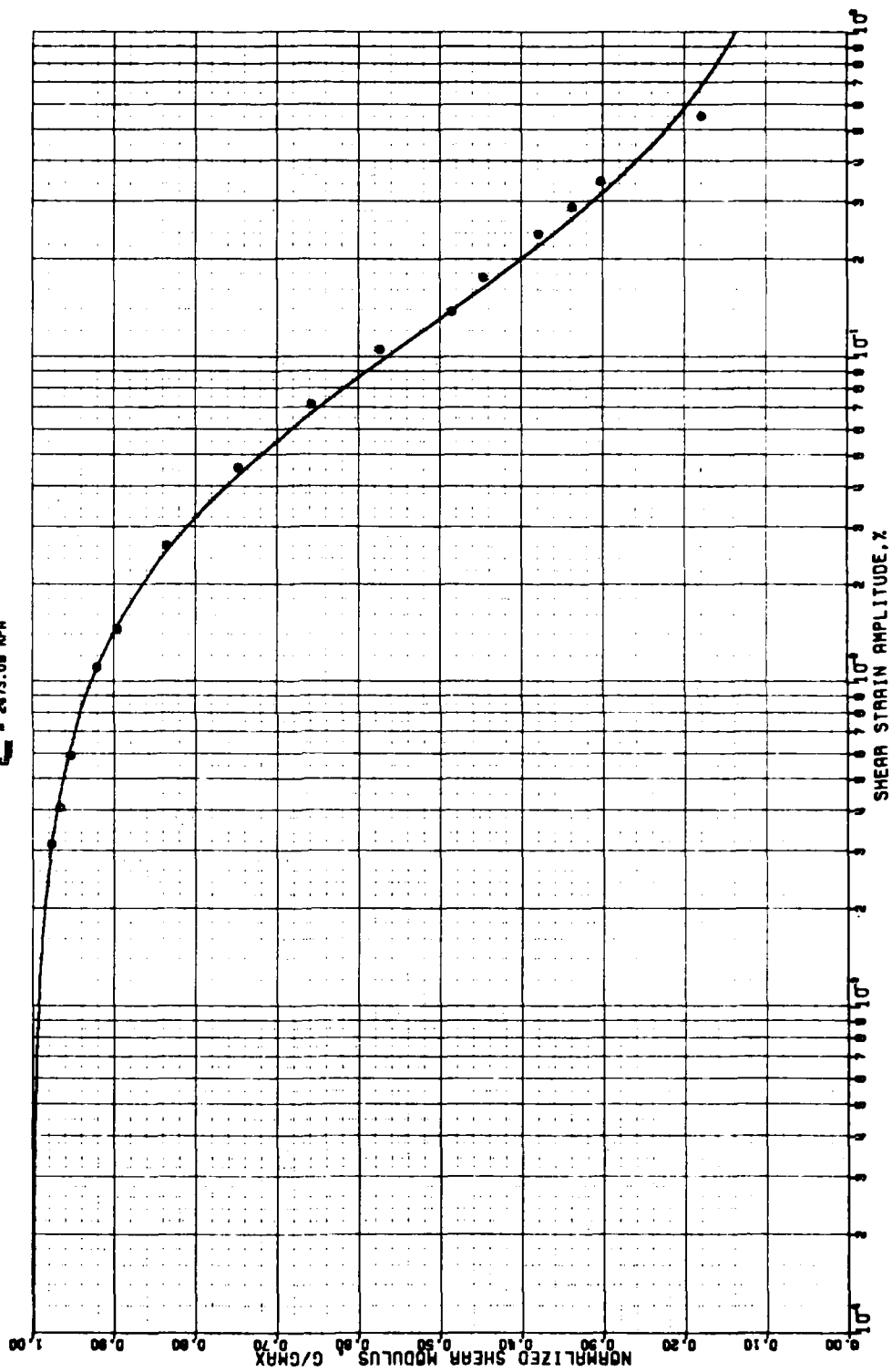
$G_{max} = 6430.00 \text{ KPA}$



THE VARIATION OF SHEAR MODULUS WITH STRAIN AMPLITUDE DEEP CORE SAMPLES OF GULF OF MEXICO

SAMPLE DEPTH = 22.49 M.

$G_{max} = 2475.08 \text{ MPa}$

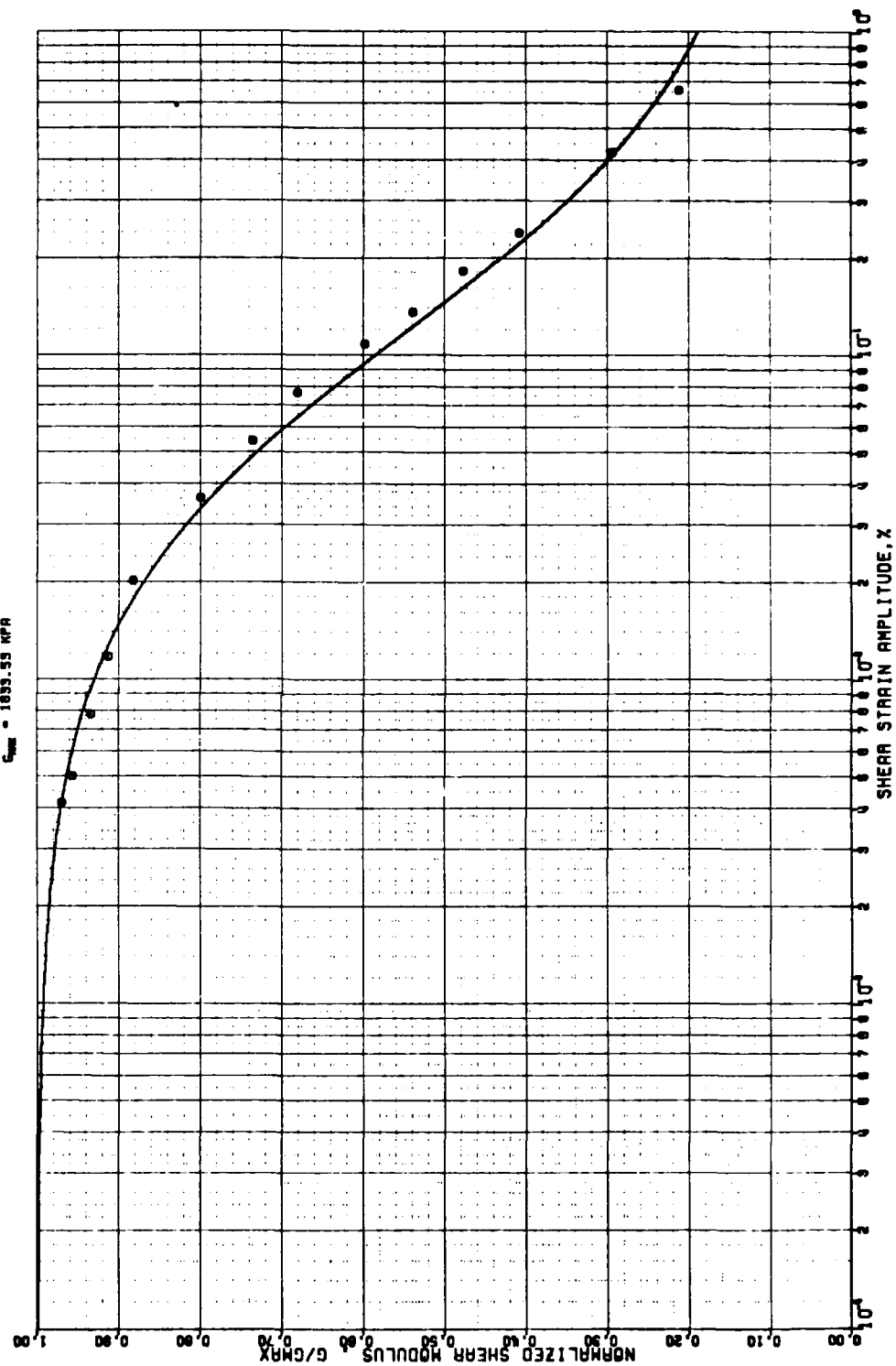


THE VARIATION OF SHEAR MODULUS WITH STRAIN AMPLITUDE

DEEP CORE SAMPLES OF GULF OF MEXICO

SAMPLE DEPTH = 26.50 M.

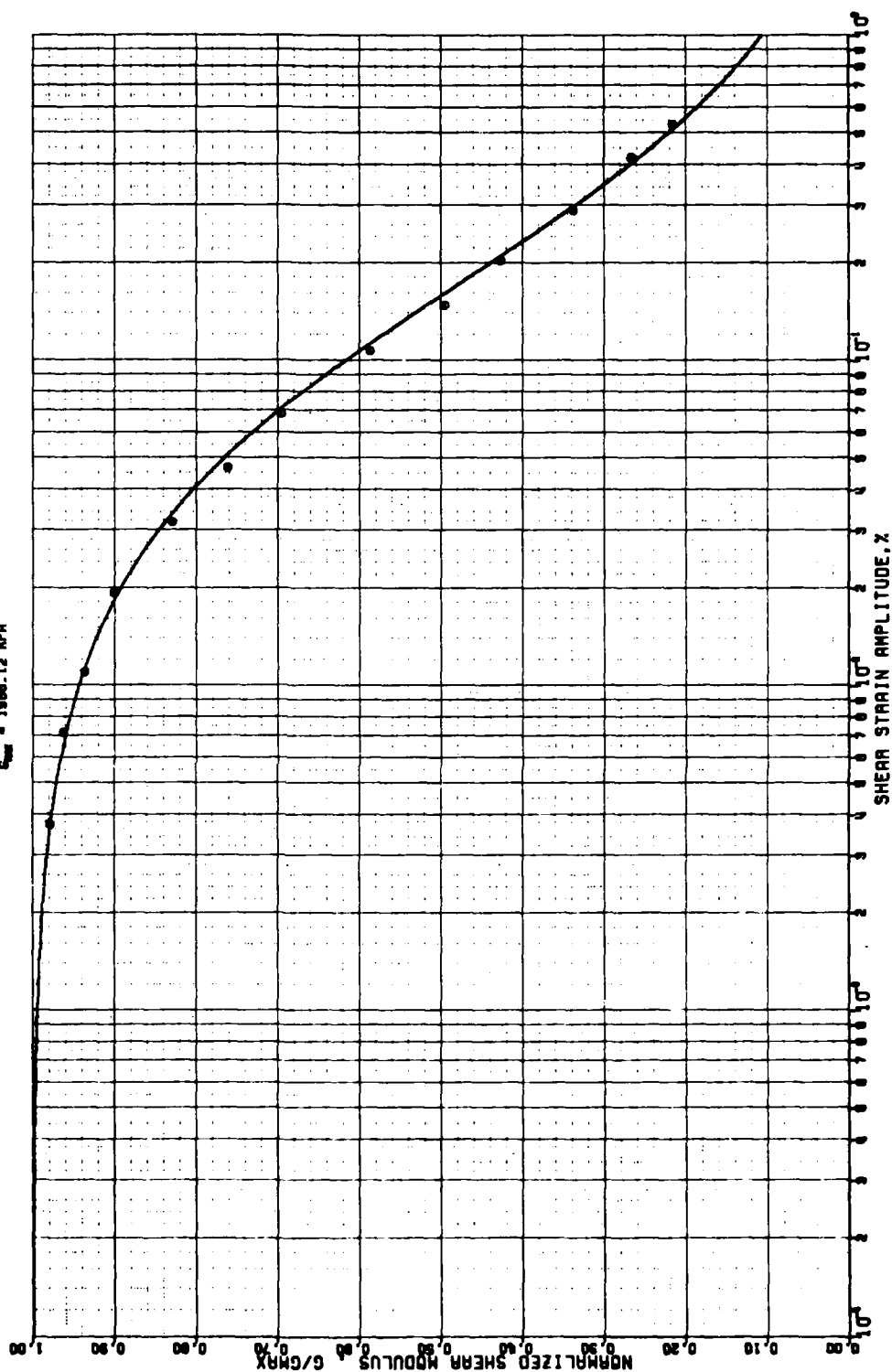
$G_{max} = 1835.55 \text{ KPA}$



THE VARIATION OF SHEAR MODULUS WITH STRAIN AMPLITUDE DEEP CORE SAMPLES OF GULF OF MEXICO

SAMPLE DEPTH = 31.54 M.

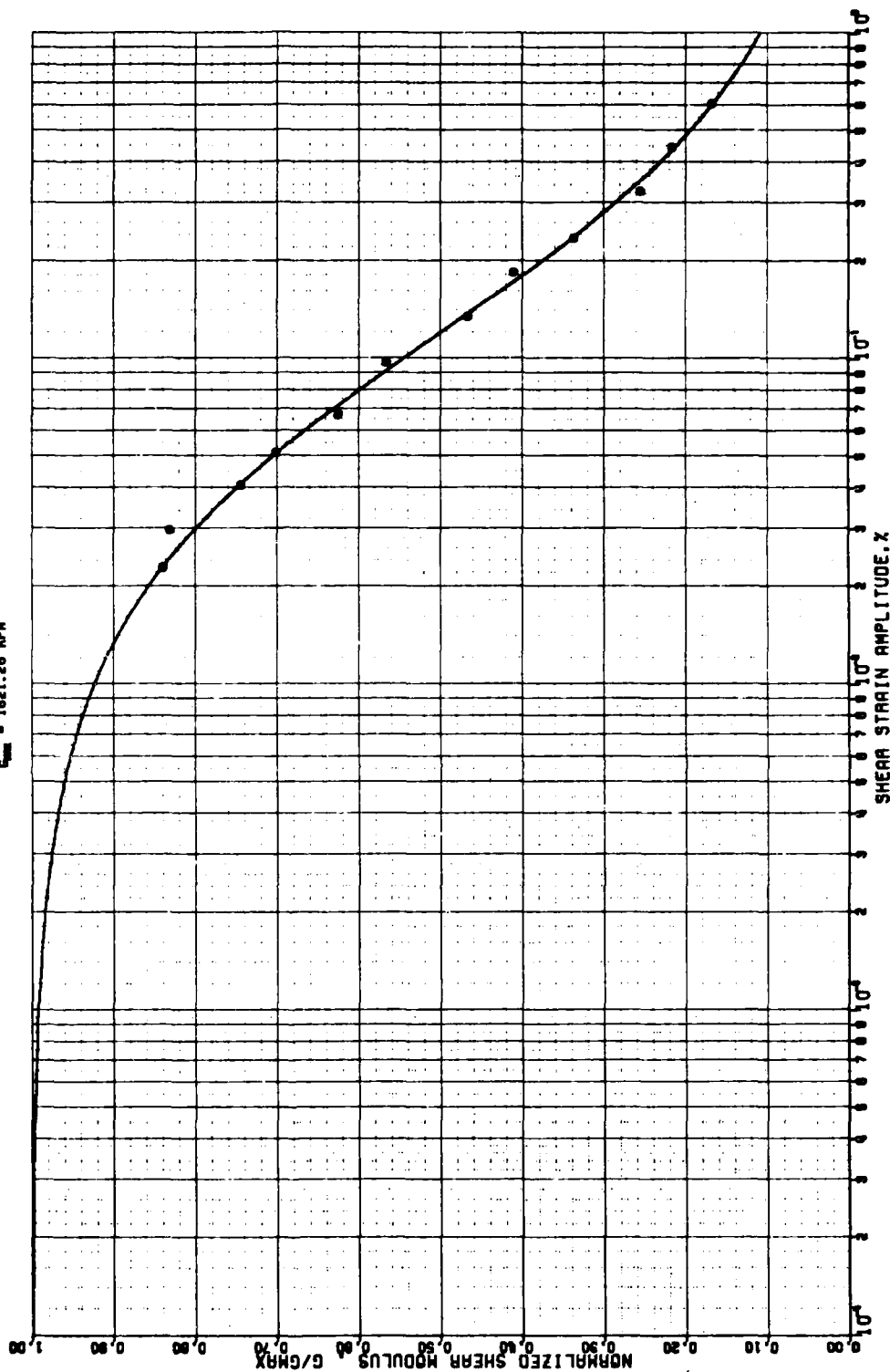
$G_{max} = 1000.12 \text{ MPa}$



THE VARIATION OF SHEAR MODULUS WITH STRAIN AMPLITUDE DEEP CORE SAMPLES OF GULF OF MEXICO

SAMPLE DEPTH = 54.88 M.

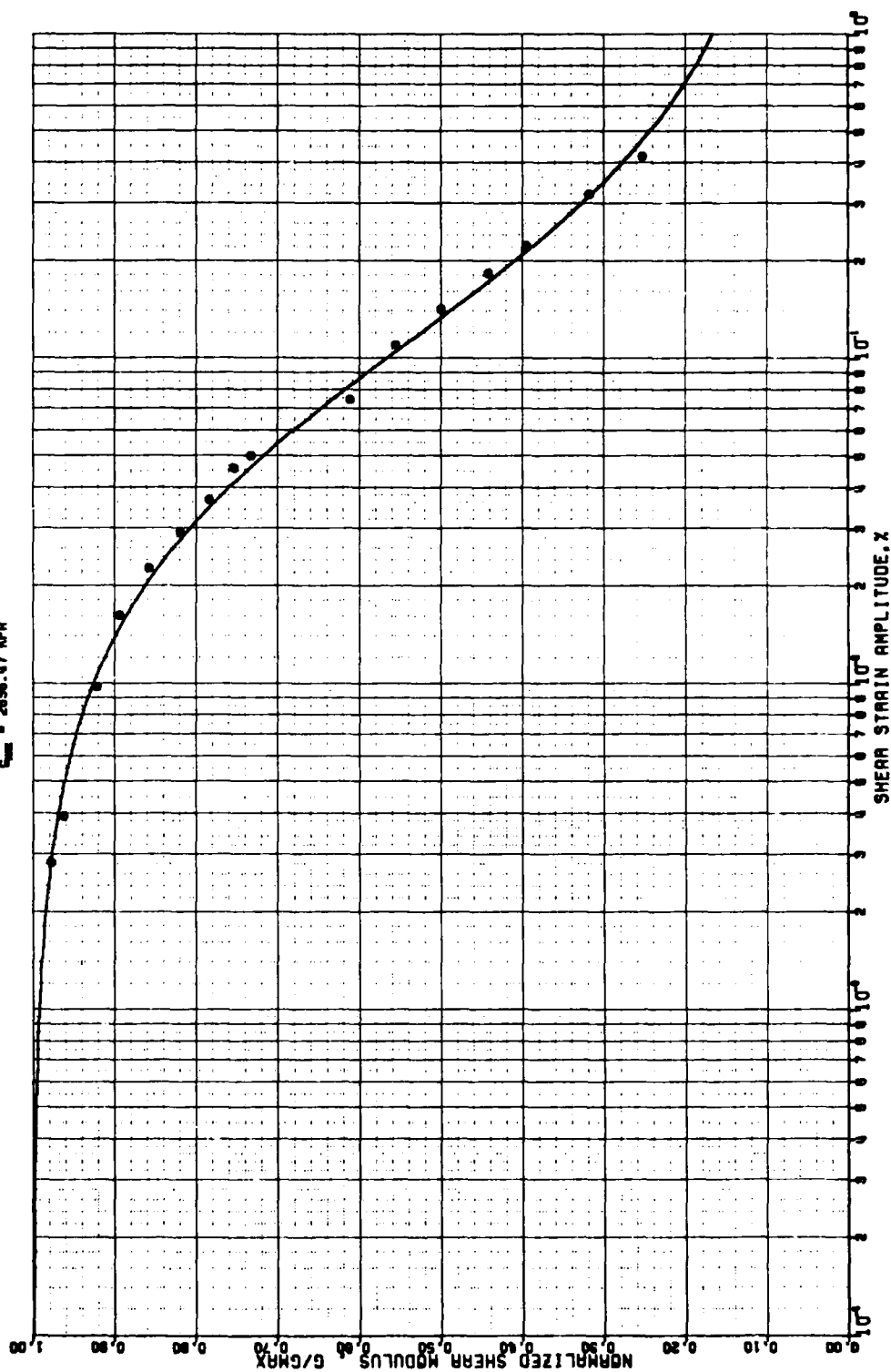
$\sigma_{vm} = 1821.26 \text{ MPa}$



THE VARIATION OF SHEAR MODULUS WITH STRAIN AMPLITUDE DEEP CORE SAMPLES OF GULF OF MEXICO

SAMPLE DEPTH = 37.75 M.

$G_{max} = 2836.47 \text{ KPA}$

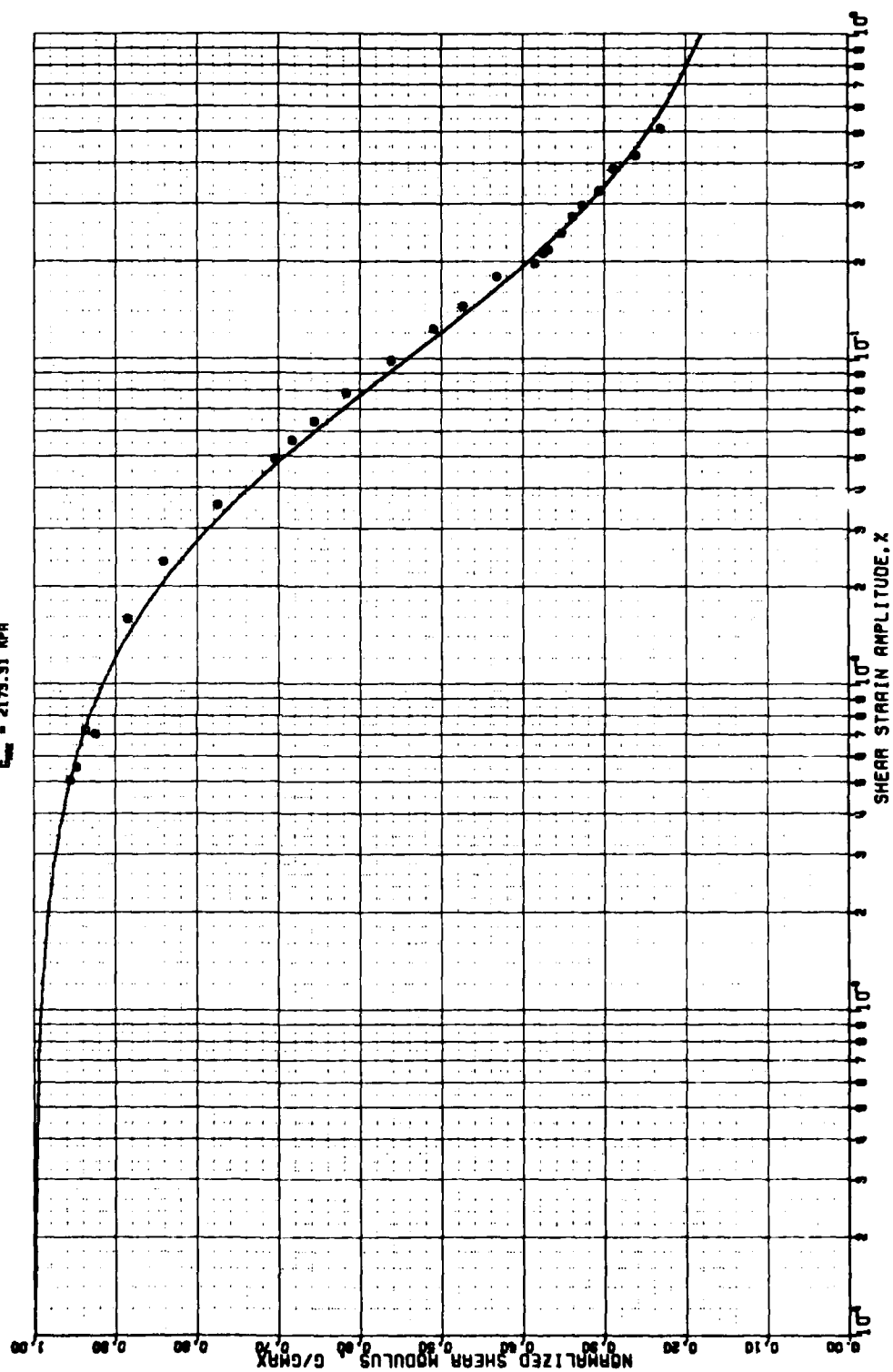


THE VARIATION OF SHEAR MODULUS WITH STRAIN AMPLITUDE

DEEP CORE SAMPLES OF GULF OF MEXICO

SAMPLE DEPTH = 60.76 M.

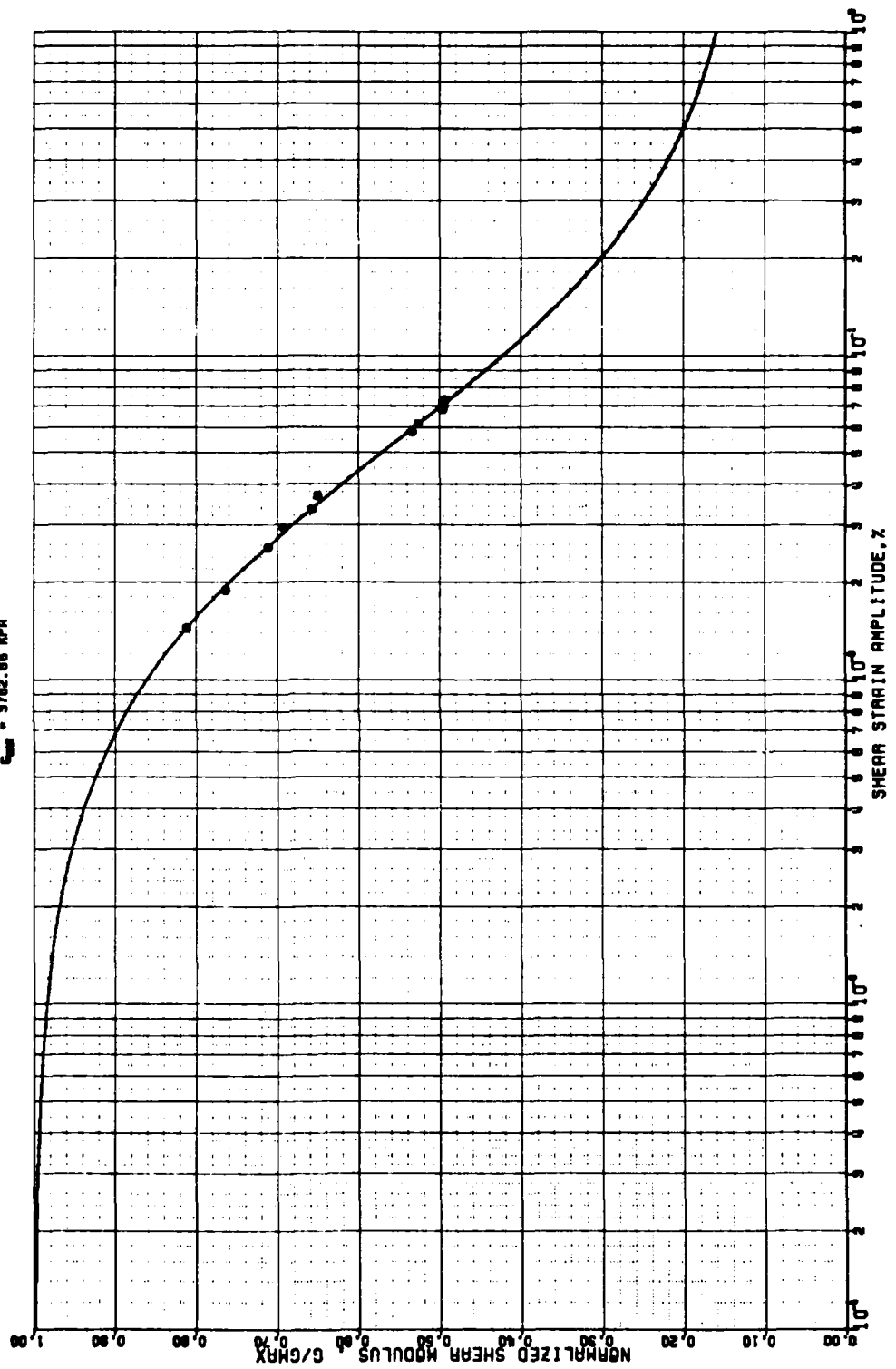
$E_{\text{avg}} = 2173.31 \text{ MPa}$



THE VARIATION OF SHEAR MODULUS WITH STRAIN AMPLITUDE DEEP CORE SAMPLES OF GULF OF MEXICO

SAMPLE DEPTH - 10.00 M.

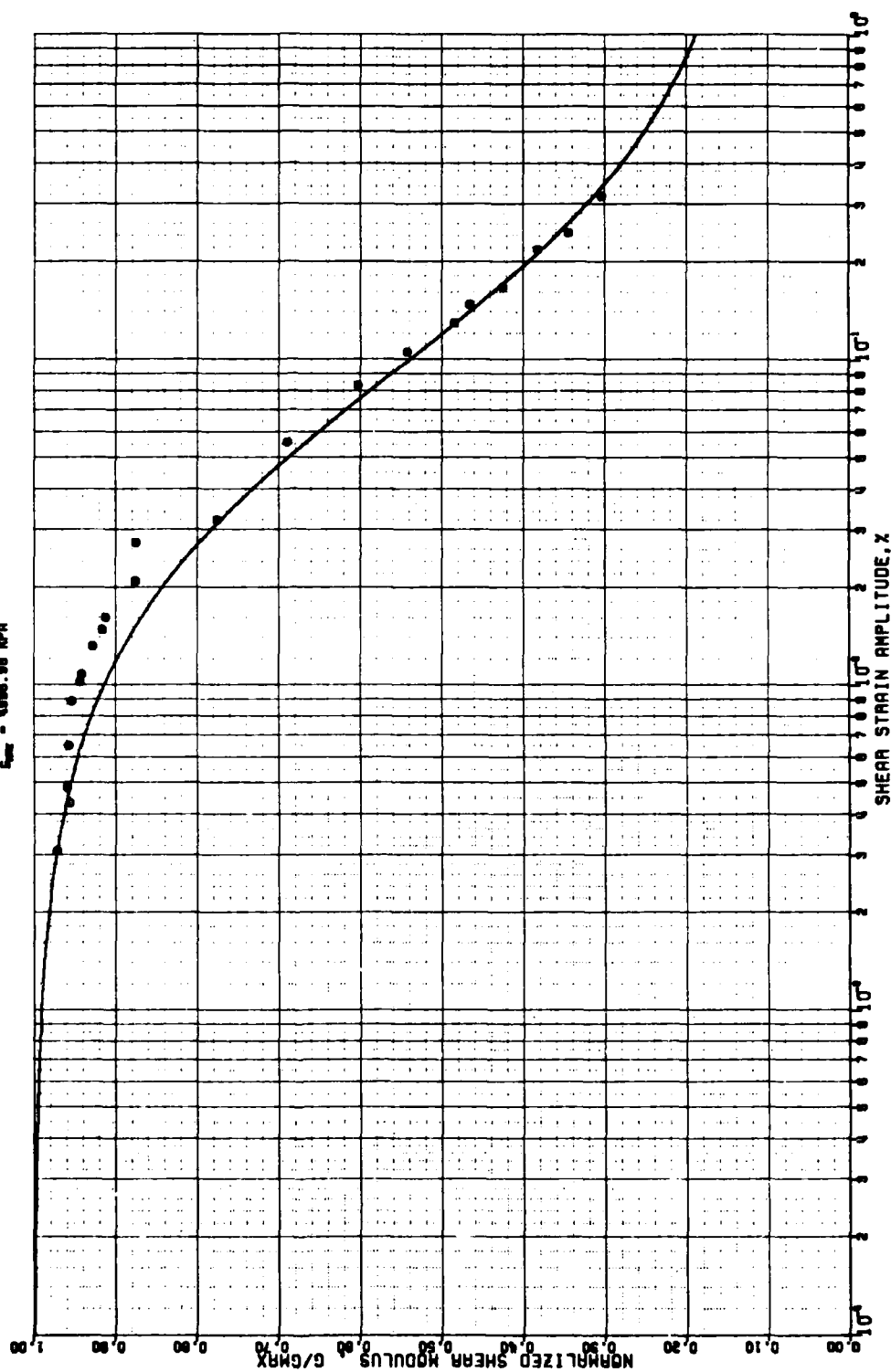
$\sigma_{vm} = 3762.66 \text{ MPa}$



THE VARIATION OF SHEAR MODULUS WITH STRAIN AMPLITUDE DEEP CORE SAMPLES OF GULF OF MEXICO

SAMPLE DEPTH = 59.07 M.

$E_{max} = 1000.00 \text{ MPa}$

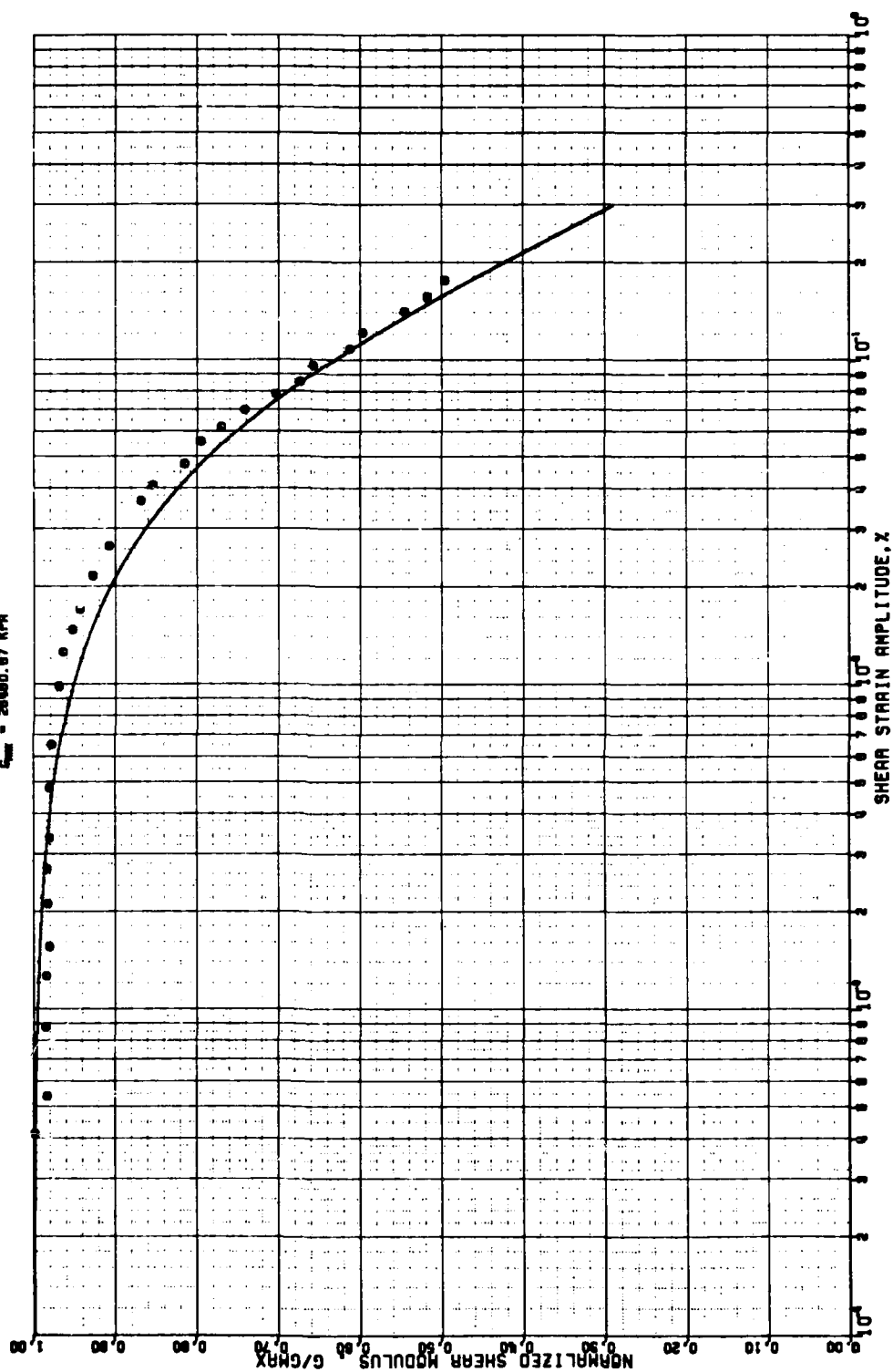


THE VARIATION OF SHEAR MODULUS WITH STRAIN AMPLITUDE

DEEP CORE SAMPLES OF GULF OF MEXICO

SAMPLE DEPTH = 71.32 M.

$\sigma_{vm} = 20900.87 \text{ KPA}$

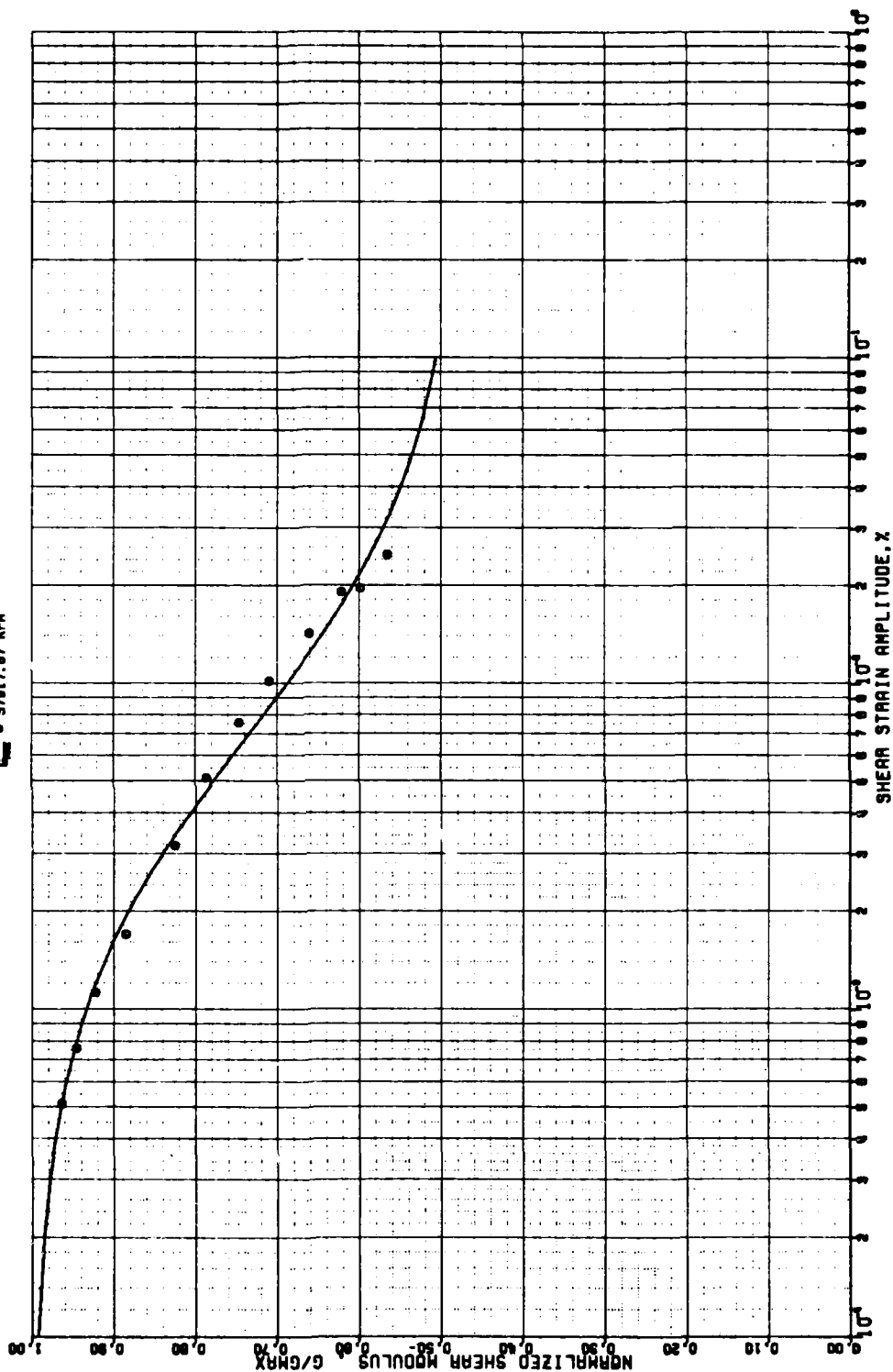


THE VARIATION OF SHEAR MODULUS WITH STRAIN AMPLITUDE

DEEP CONE SAMPLES OF GULF OF MEXICO

SAMPLE DEPTH = 101.60 M.

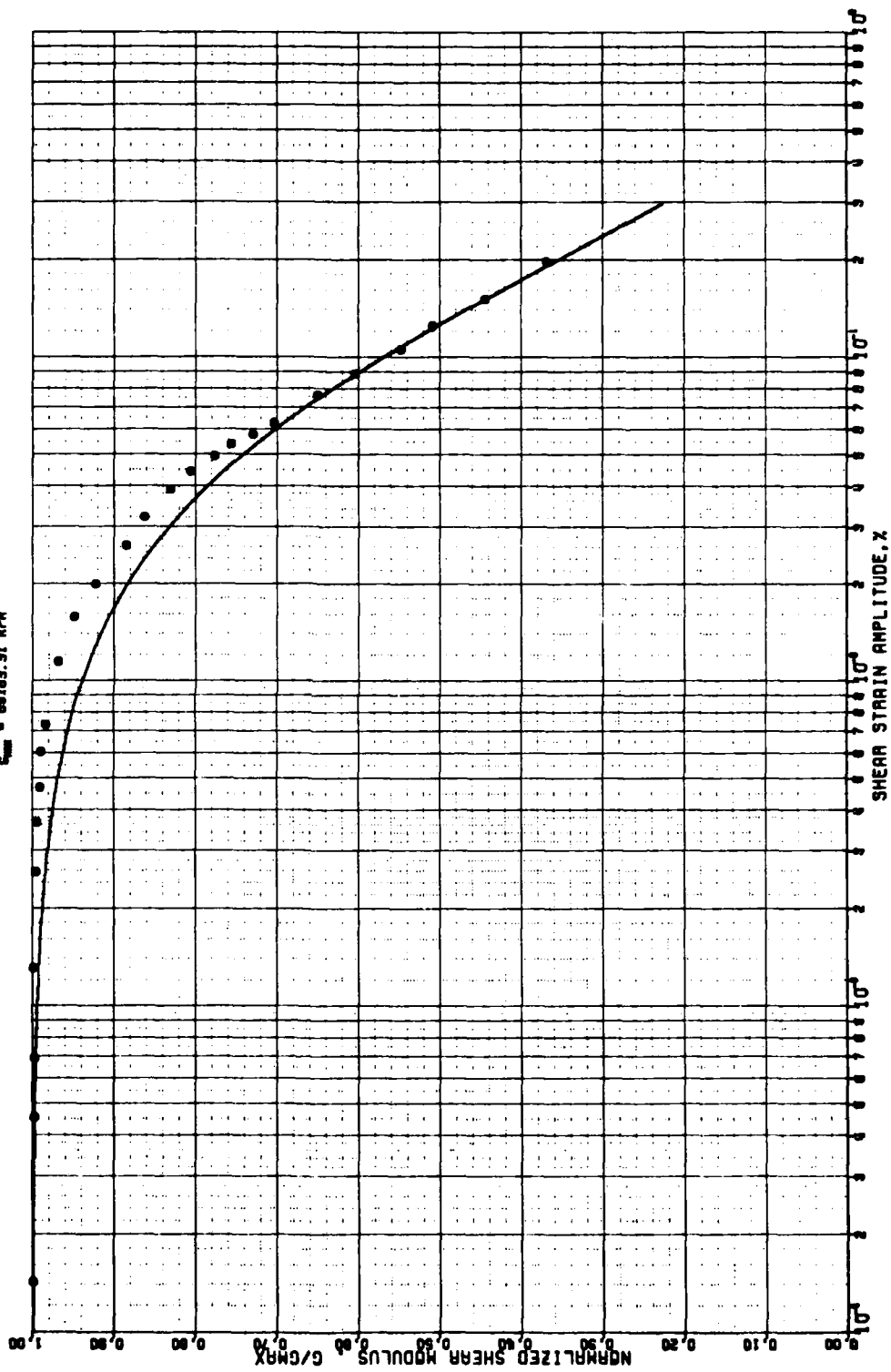
$E_{max} = 57817.87 \text{ MPa}$



THE VARIATION OF SHEAR MODULUS WITH STRAIN AMPLITUDE DEEP CORE SAMPLES OF GULF OF MEXICO

SAMPLE DEPTH = 107.08 M.

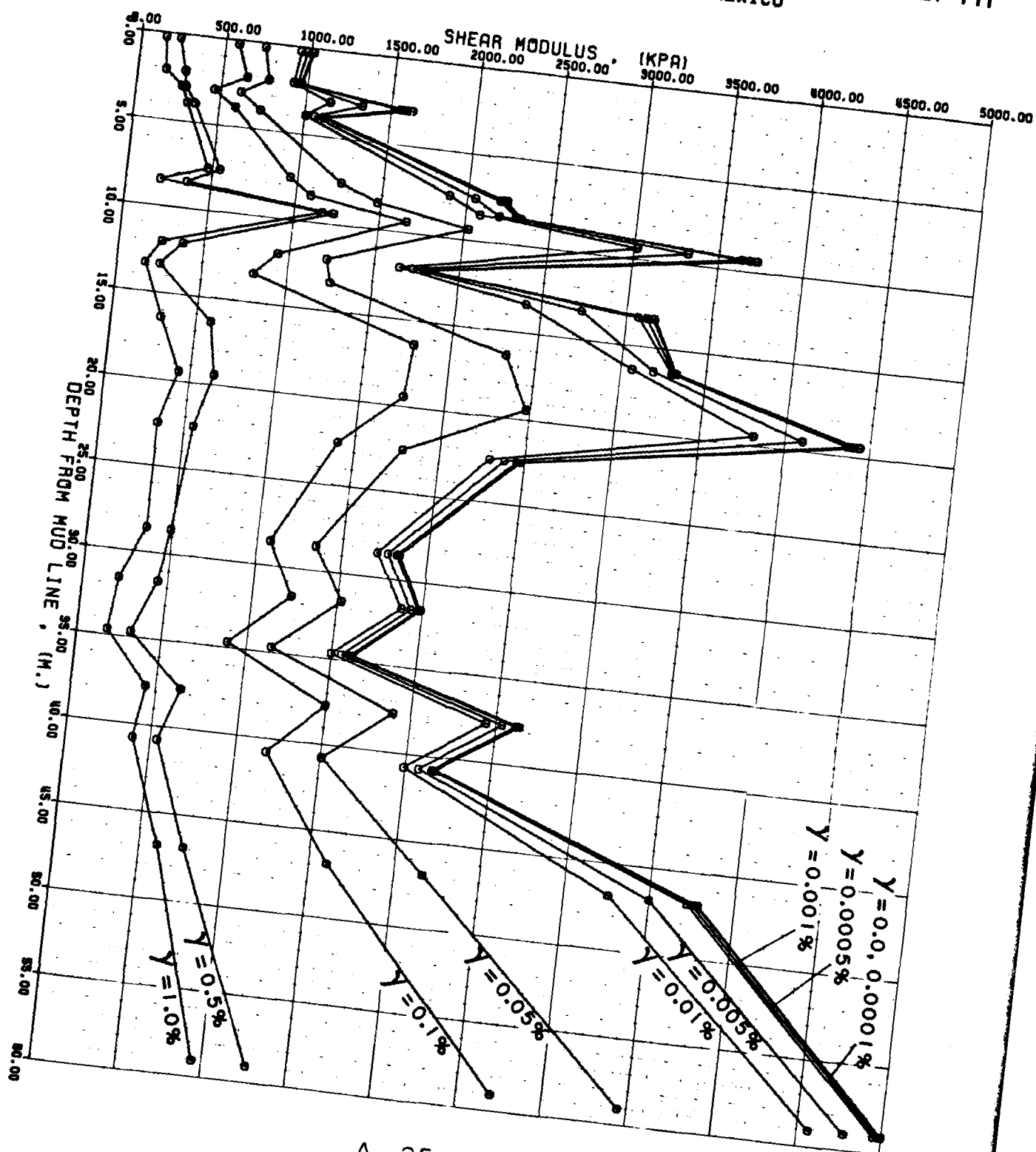
$G_{max} = 88163.91 \text{ KPS}$



APPENDIX A-25/A-26

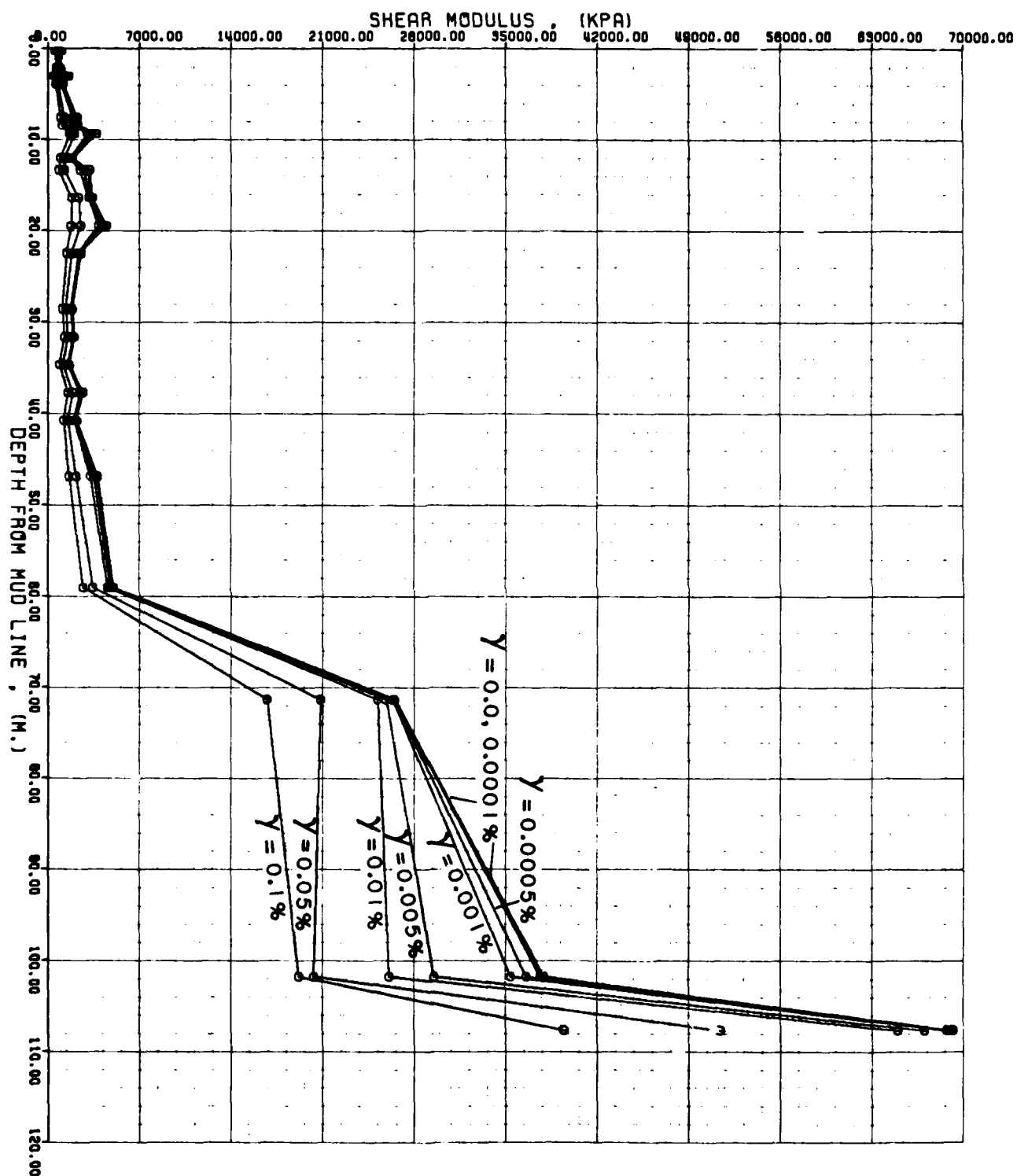
VARIATION OF SHEAR MODULUS WITH DEPTH FOR
DIFFERENT SHEAR STRAIN VALUES

THE VARIATION OF SHEAR MODULUS WITH DEPTH DEEP CORE SAMPLES OF GULF OF MEXICO



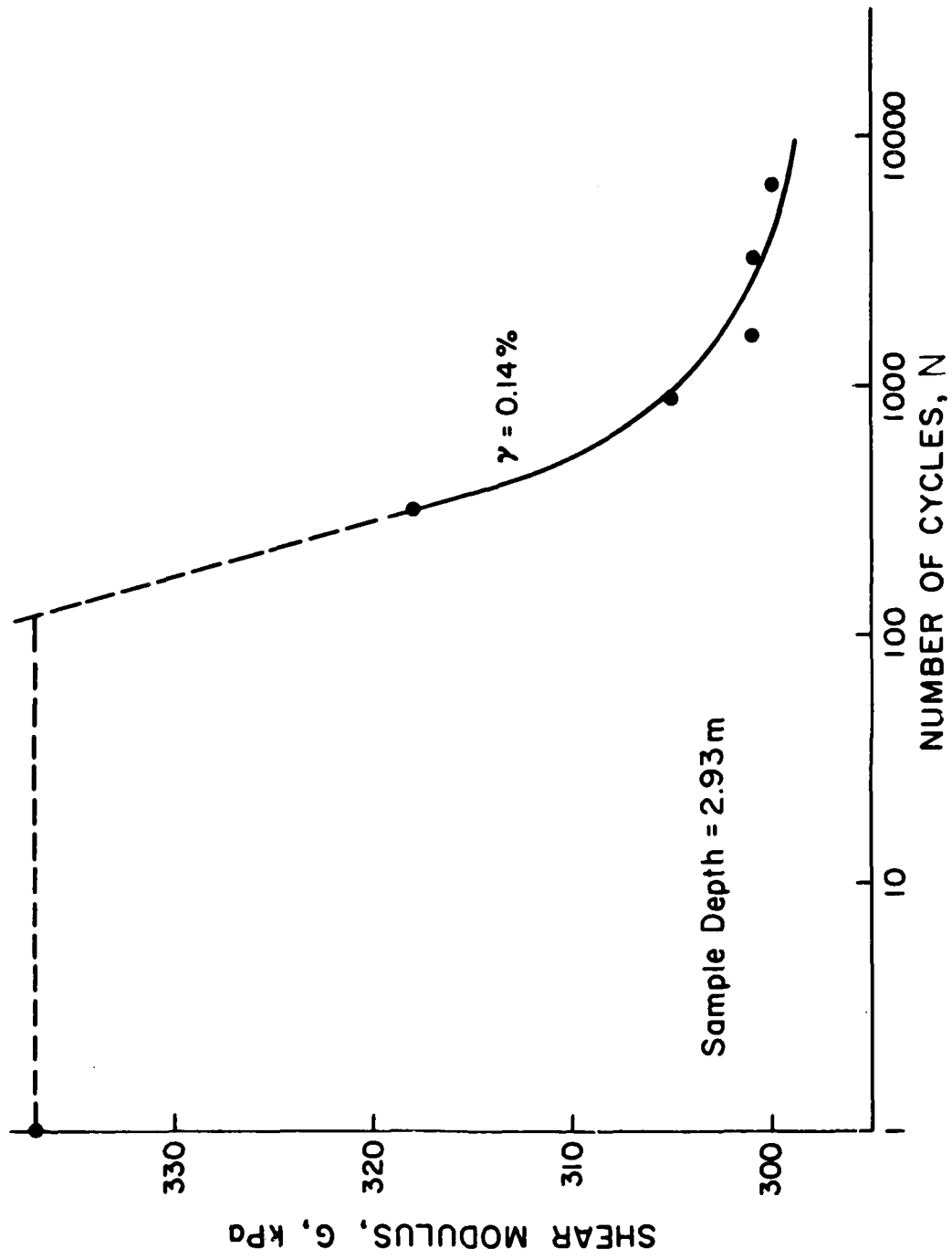
THE VARIATION OF SHEAR MODULUS WITH DEPTH

DEEP CORE SAMPLES OF GULF OF MEXICO

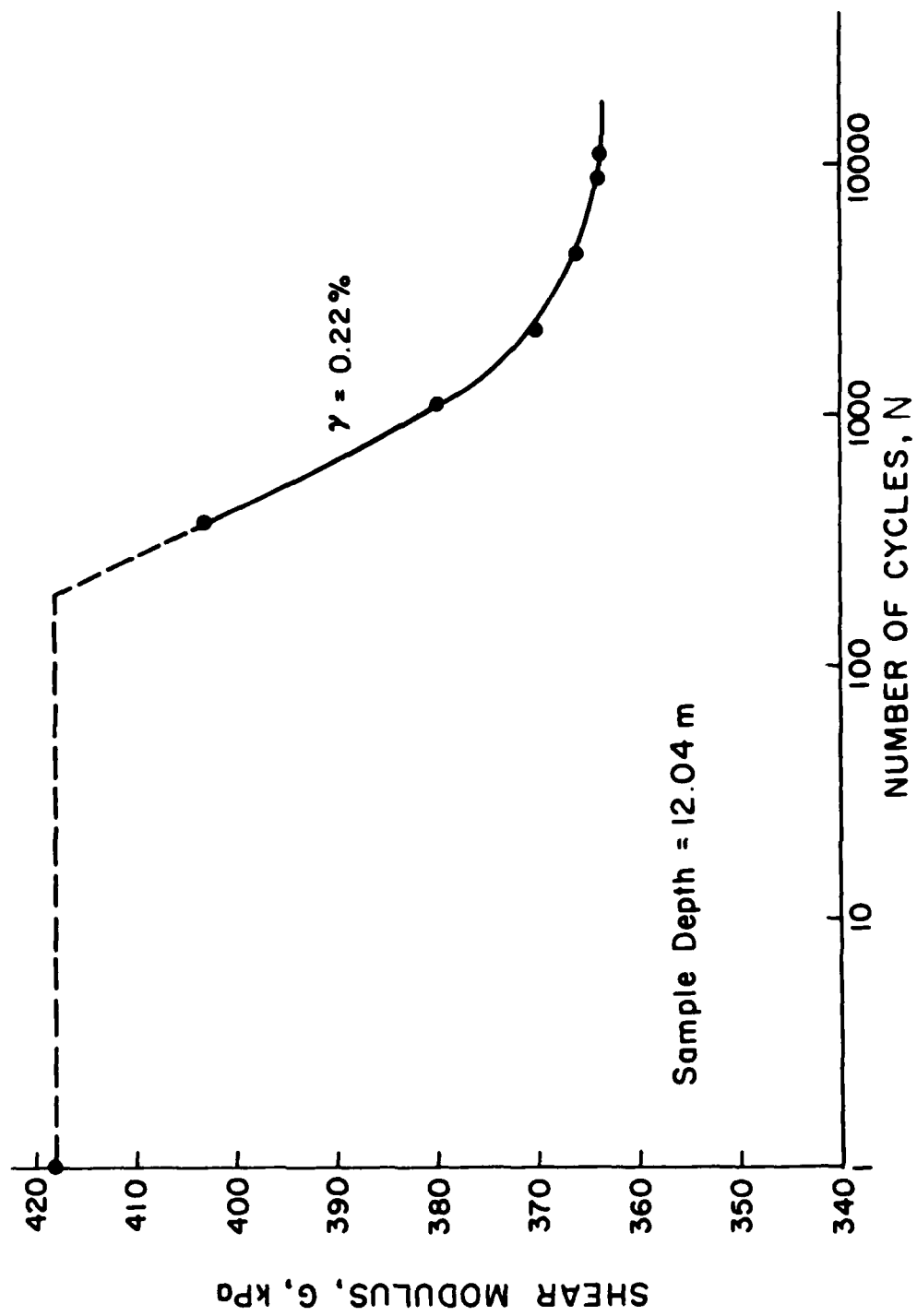


APPENDIX A-27/A-32

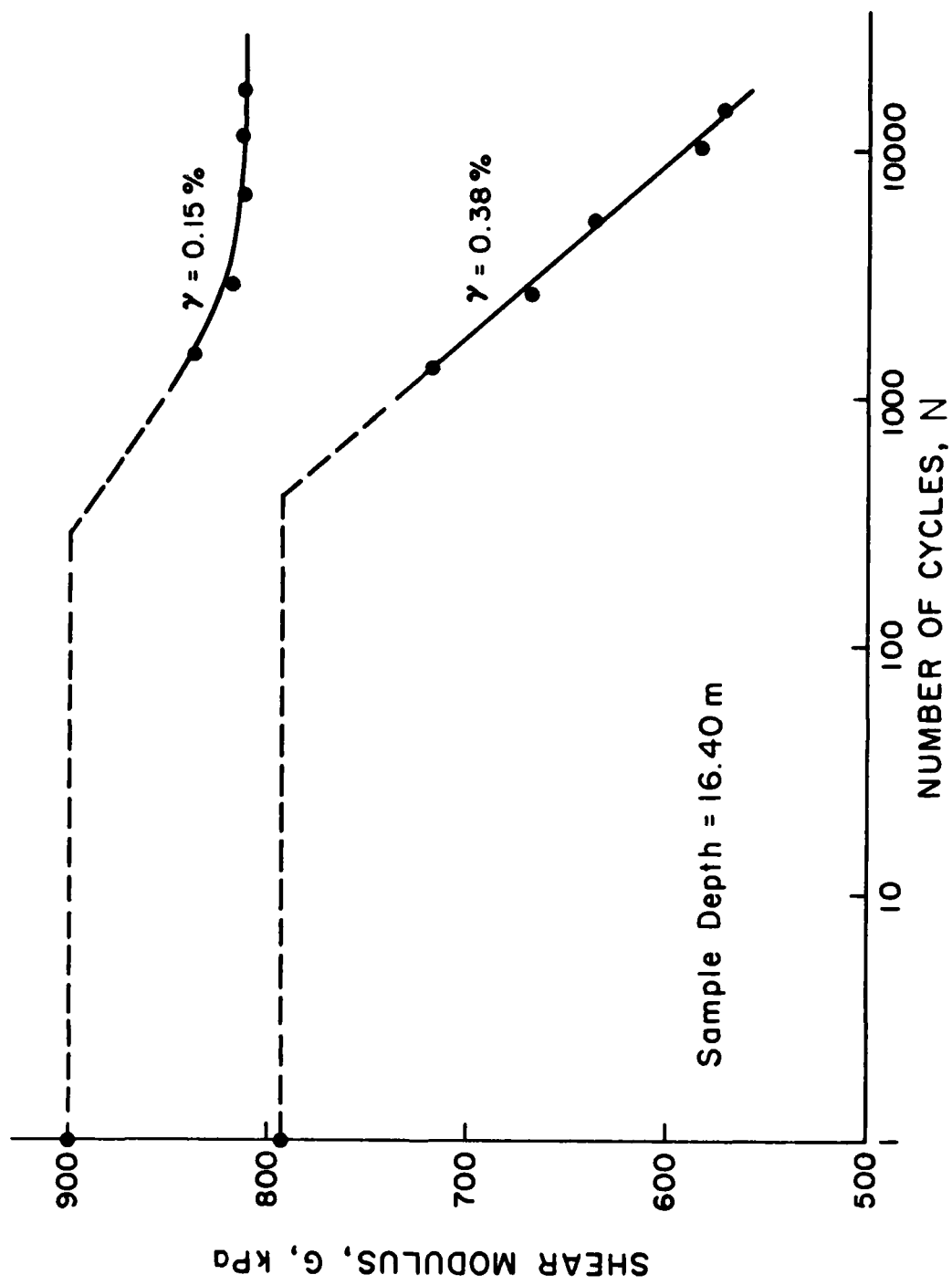
VARIATION OF SHEAR MODULUS WITH NUMBER OF CYCLES



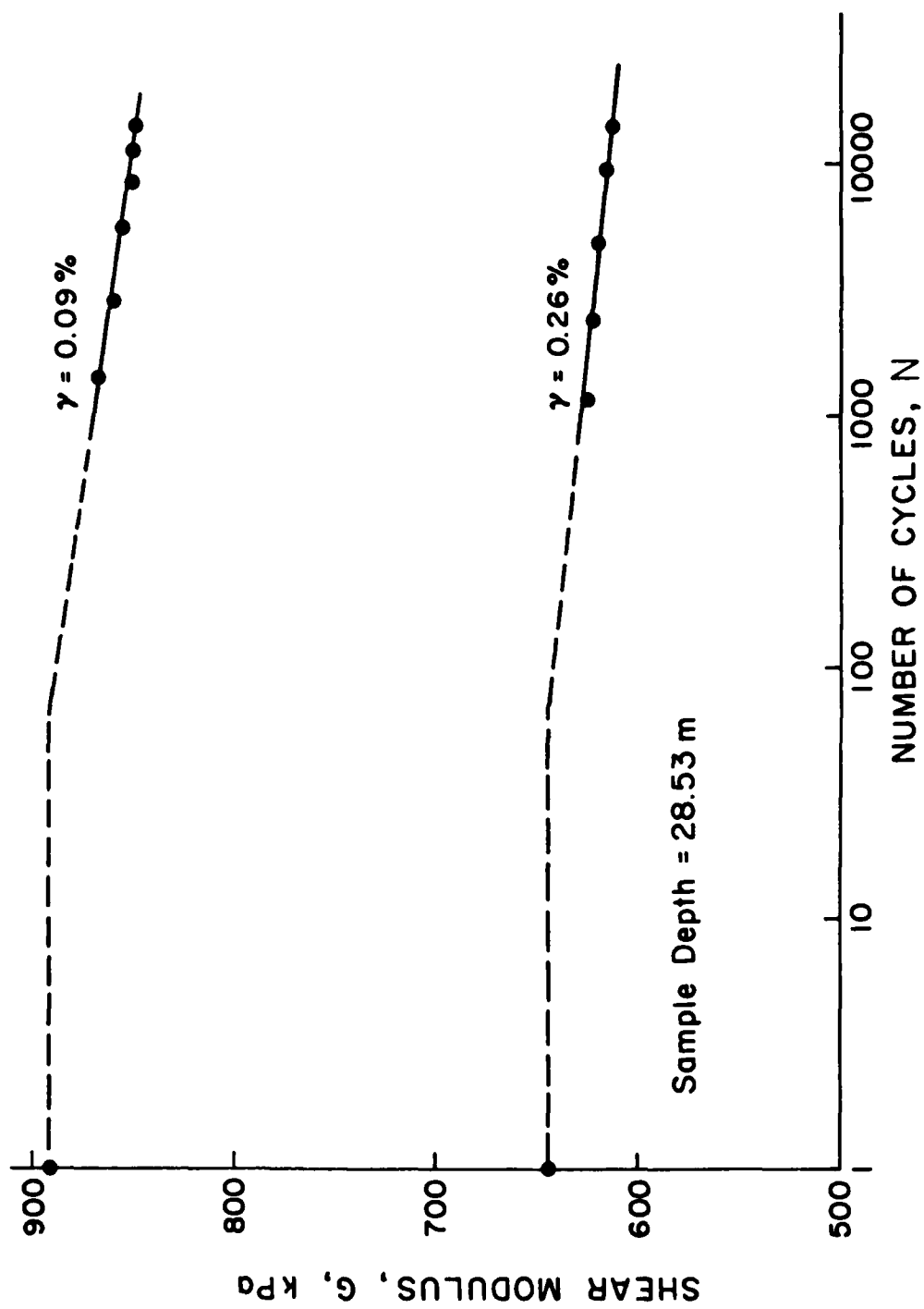
A_27



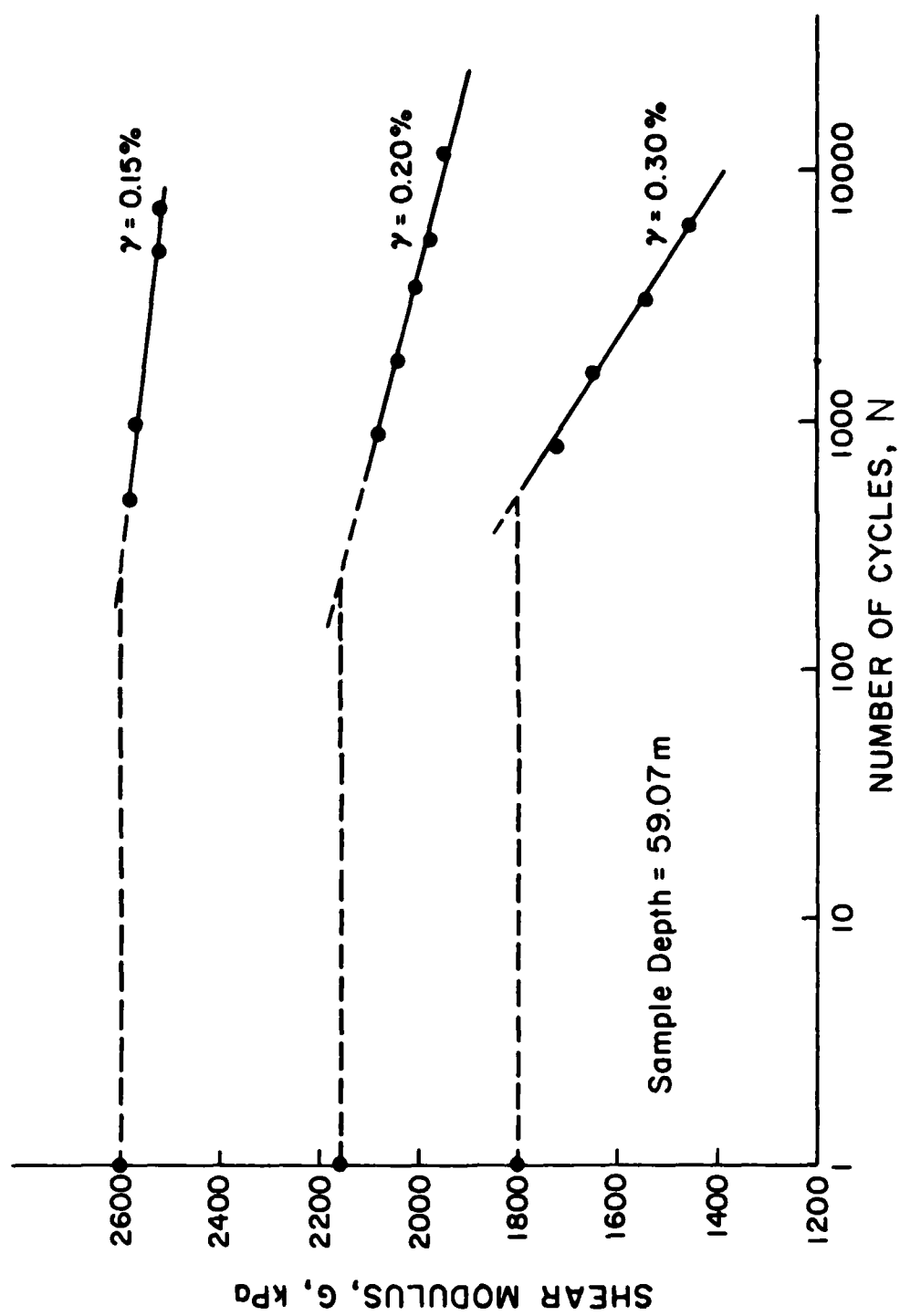
A_28



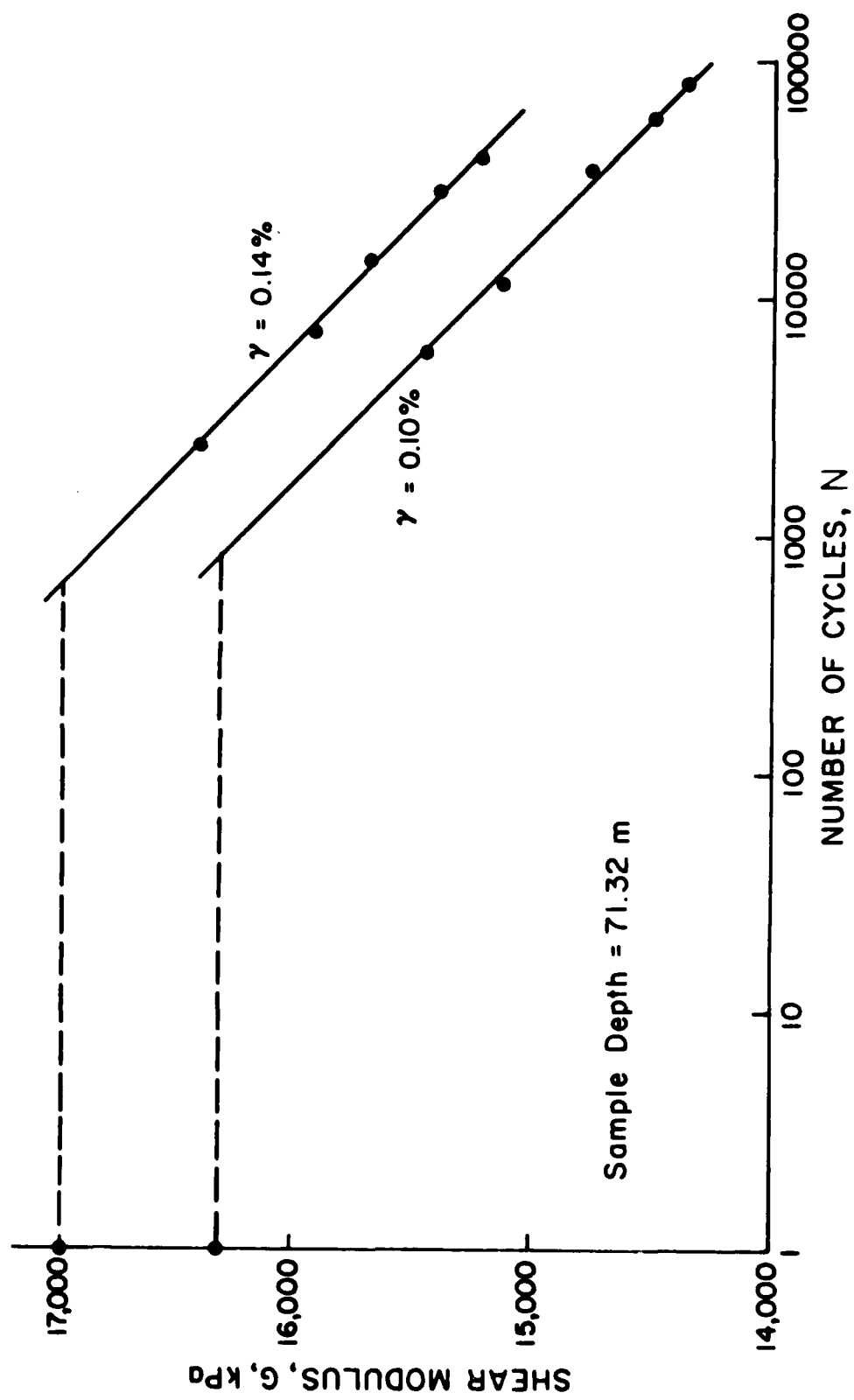
A_29



A_30



A_31



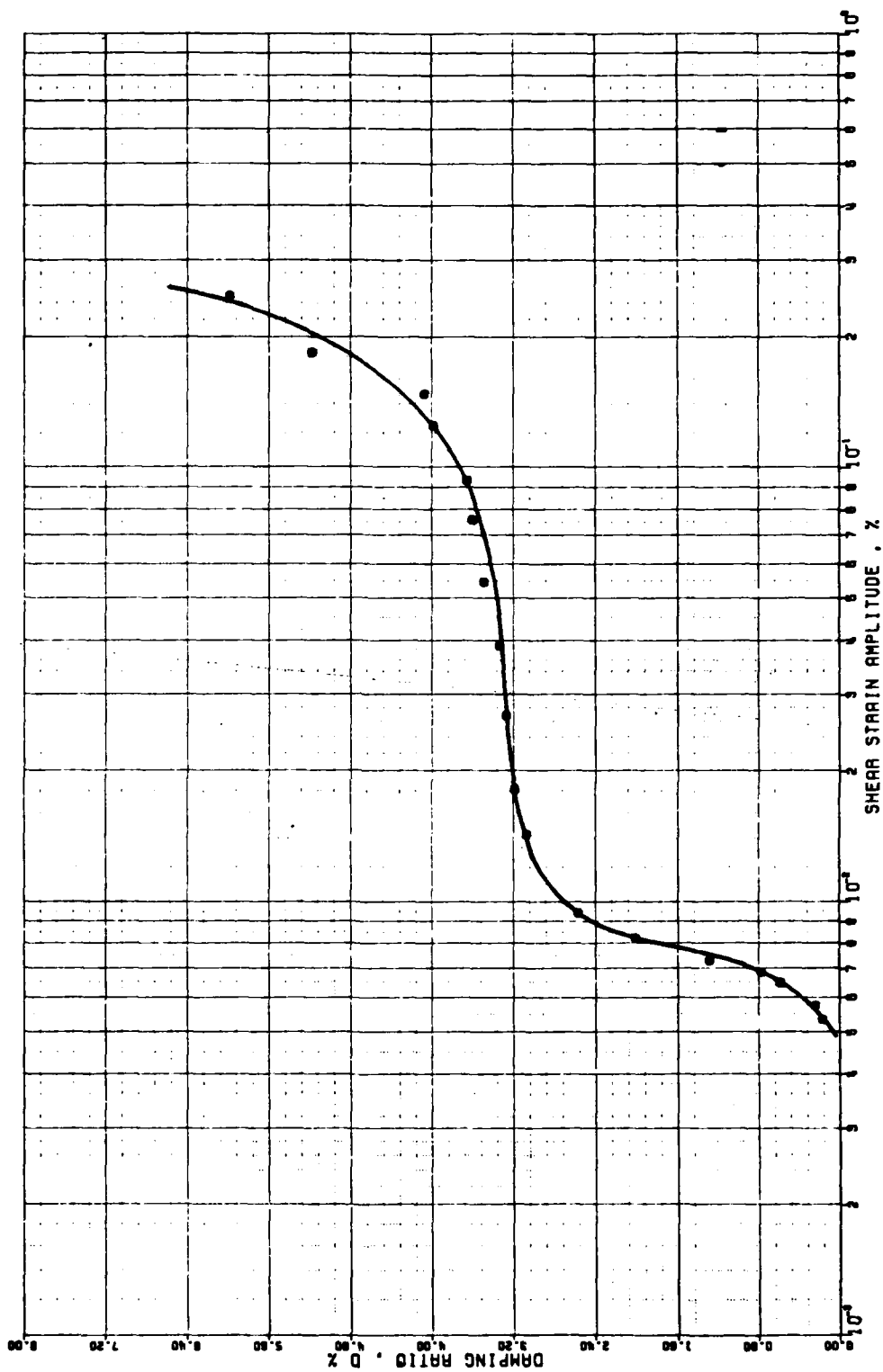
APPENDIX A-33/A-52

VARIATION OF DAMPING RATIO WITH SHEAR STRAIN

THE VARIATION OF DAMPING RATIO WITH STRAIN AMPLITUDE

DEEP CORE SAMPLES OF GULF OF MEXICO

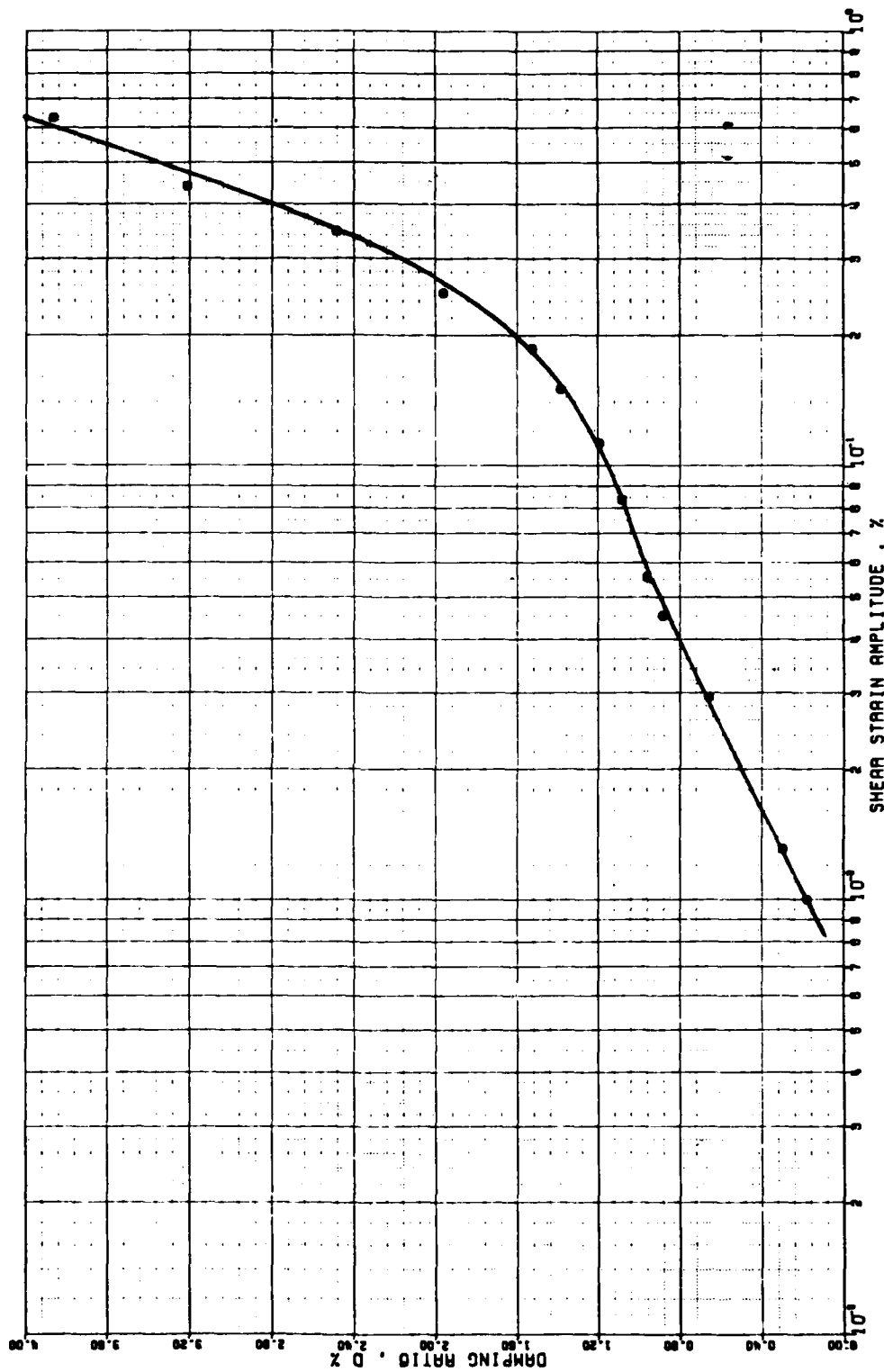
SAMPLE DEPTH = 0.24 M.



THE VARIATION OF DAMPING RATIO WITH STRAIN AMPLITUDE

DEEP CORE SAMPLES OF GULF OF MEXICO

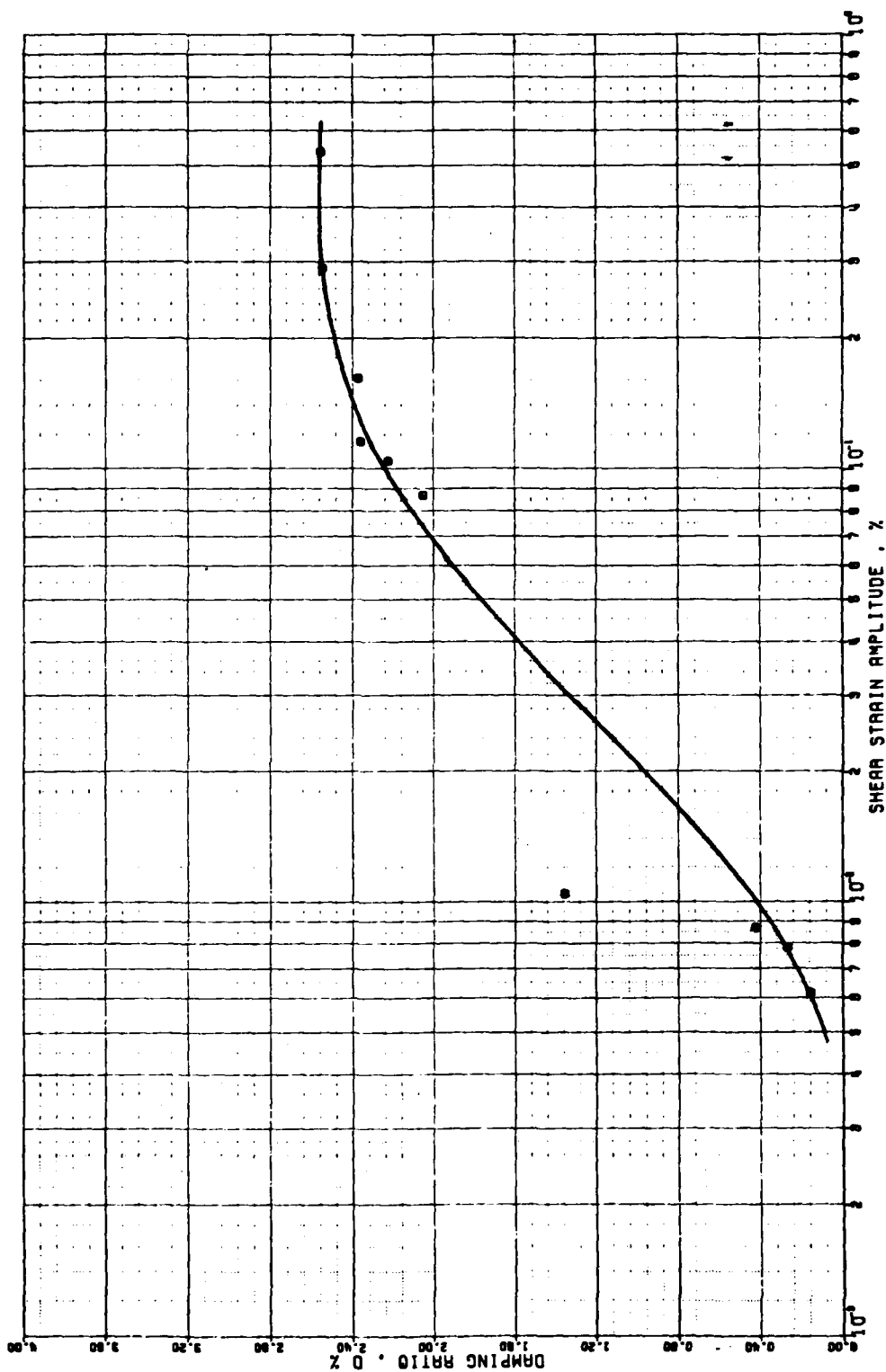
SAMPLE DEPTH = 2.10 M.



THE VARIATION OF DAMPING RATIO WITH STRAIN AMPLITUDE

DEEP CORE SAMPLES OF GULF OF MEXICO

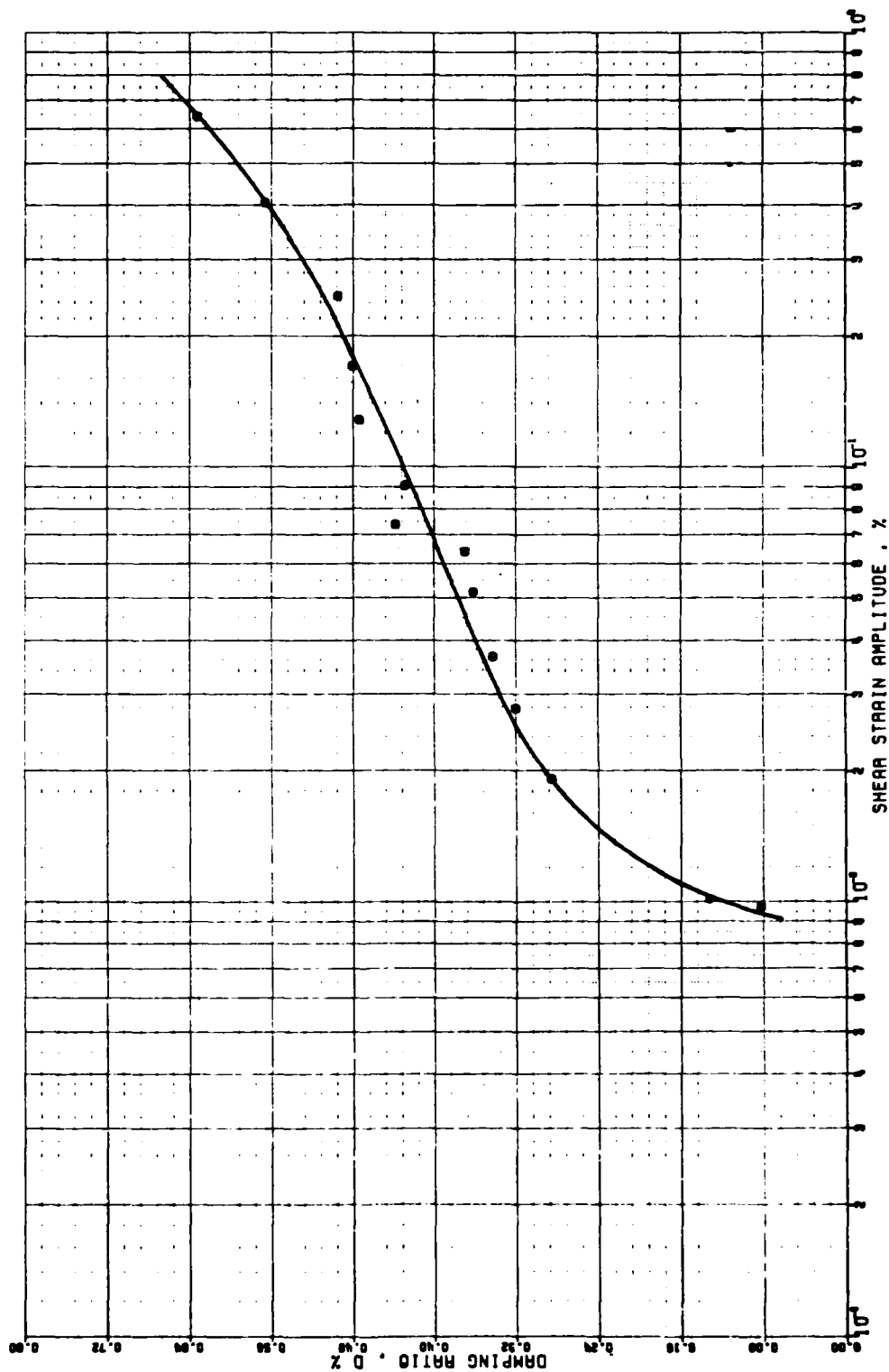
SAMPLE DEPTH = 2.99 M.



THE VARIATION OF DAMPING RATIO WITH STRAIN AMPLITUDE

DEEP CORE SAMPLES OF GULF OF MEXICO

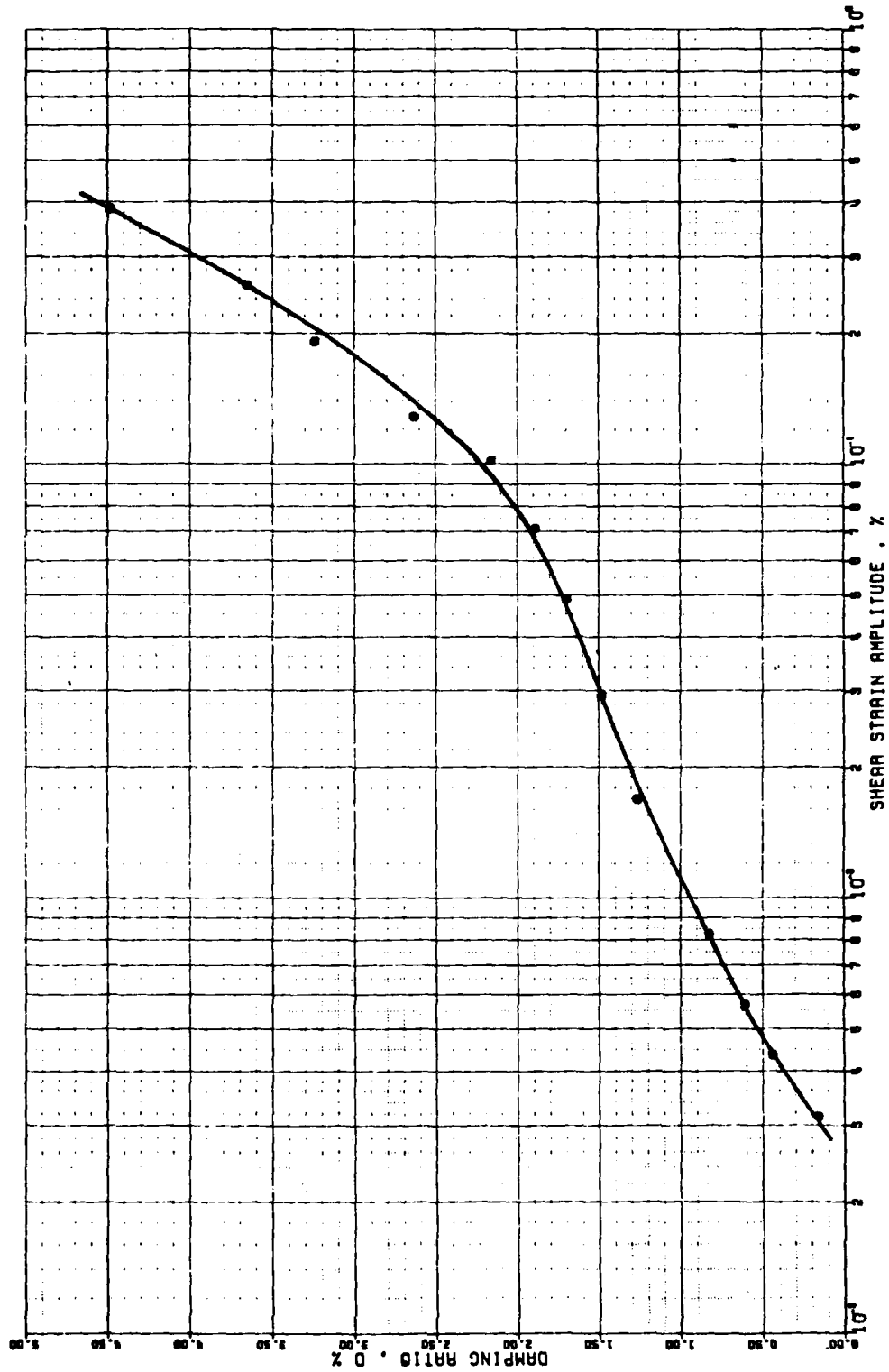
SAMPLE DEPTH = 3.90 M.



THE VARIATION OF DAMPING RATIO WITH STRAIN AMPLITUDE

DEEP CORE SAMPLES OF GULF OF MEXICO

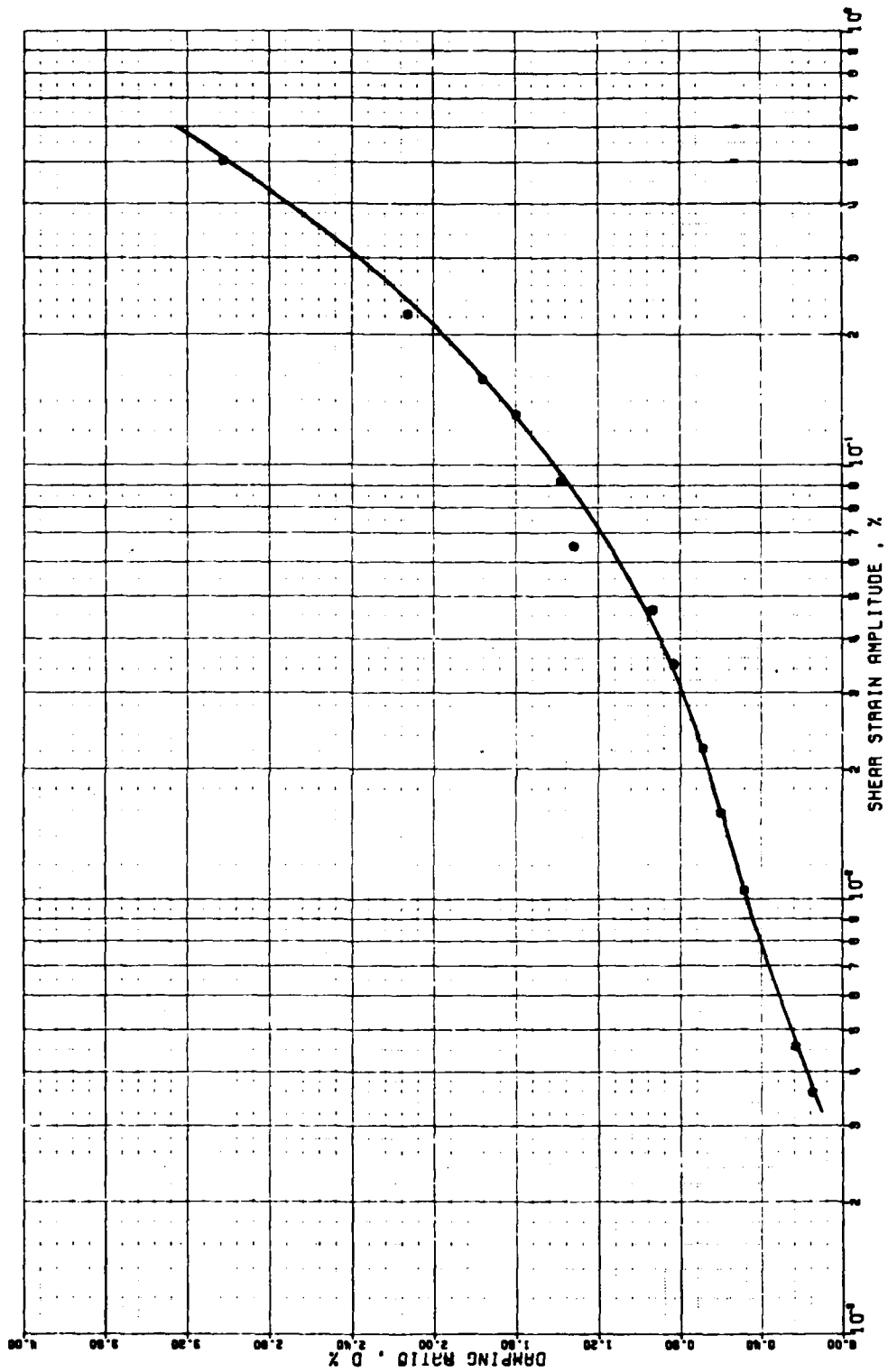
SAMPLE DEPTH = 7.56 M.



THE VARIATION OF DAMPING RATIO WITH STRAIN AMPLITUDE

DEEP CORE SAMPLES OF GULF OF MEXICO

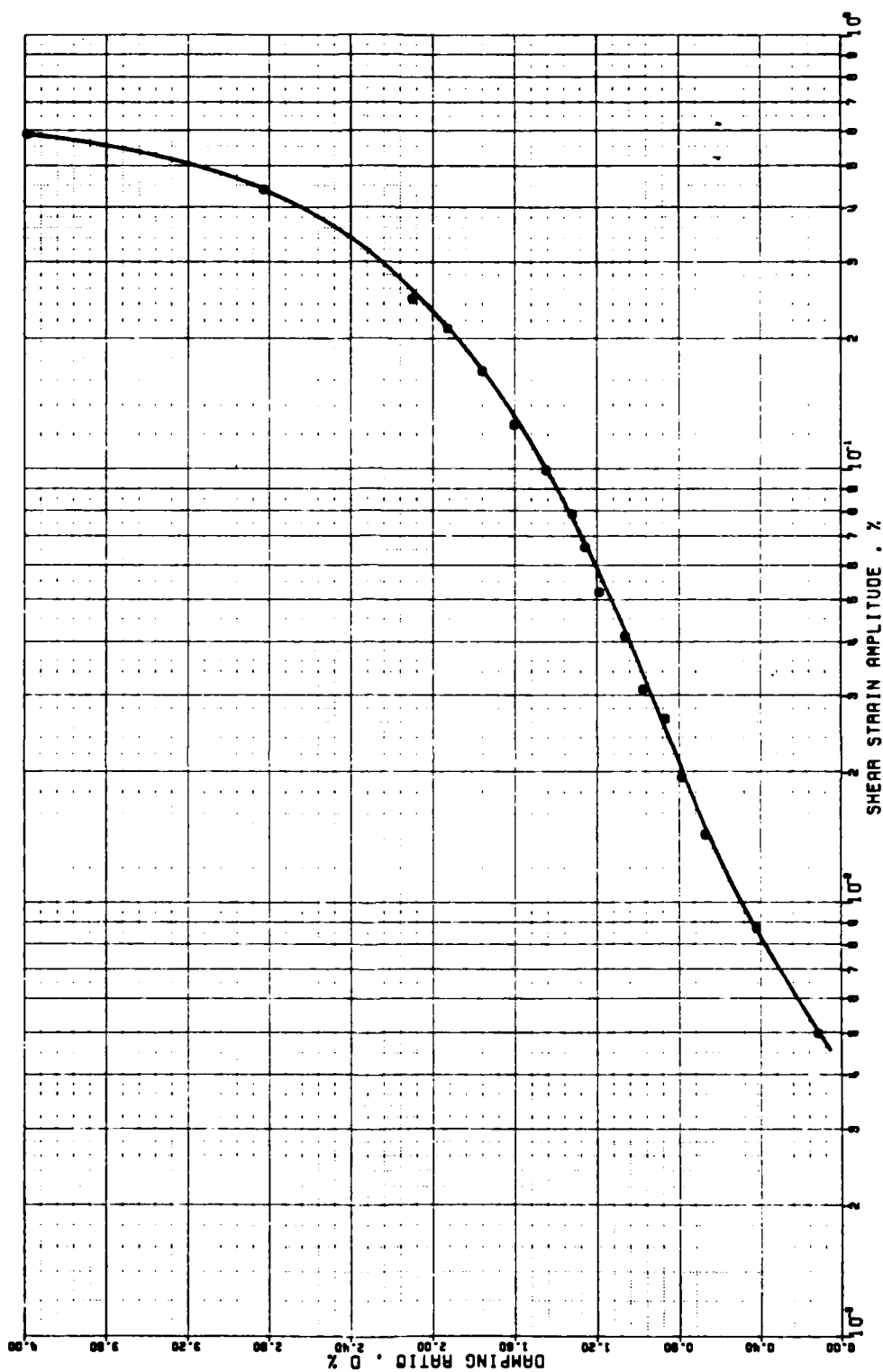
SAMPLE DEPTH = 6.47 M.



THE VARIATION OF DAMPING RATIO WITH STRAIN AMPLITUDE

DEEP CORE SAMPLES OF GULF OF MEXICO

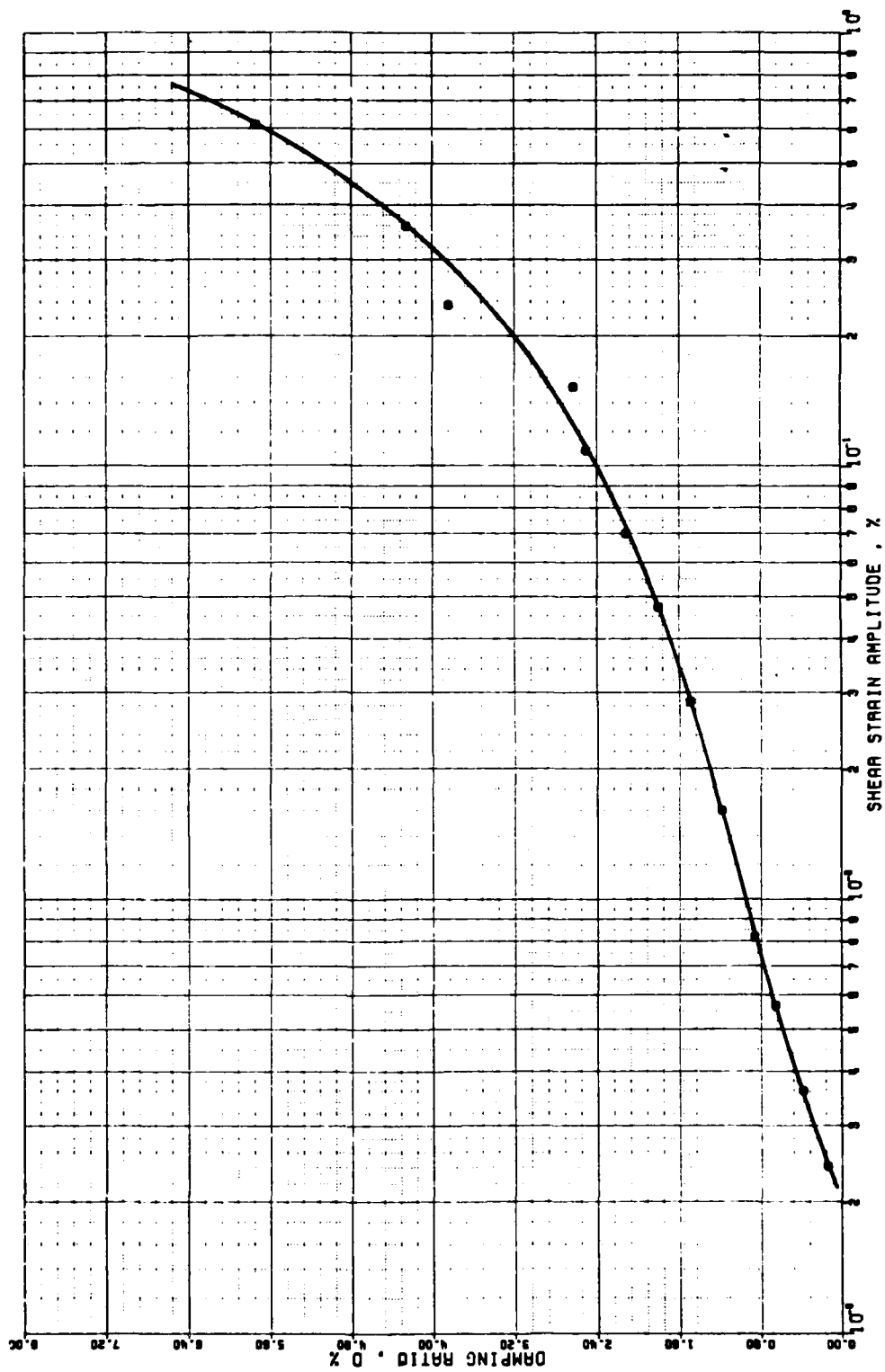
SAMPLE DEPTH = 12.06 M.



THE VARIATION OF DAMPING RATIO WITH STRAIN AMPLITUDE

DEEP CORE SAMPLES OF GULF OF MEXICO

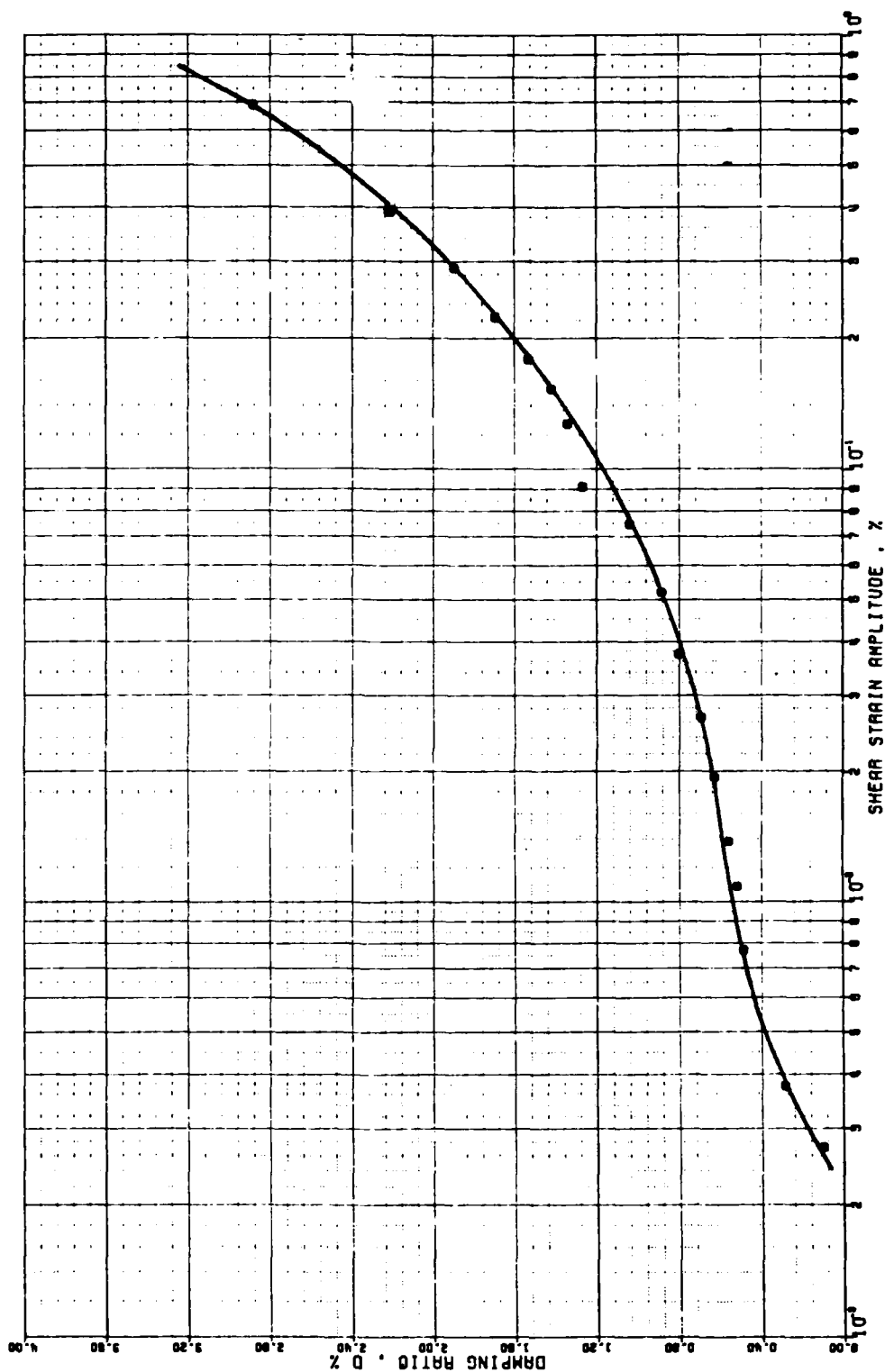
SAMPLE DEPTH = 13.35 M.



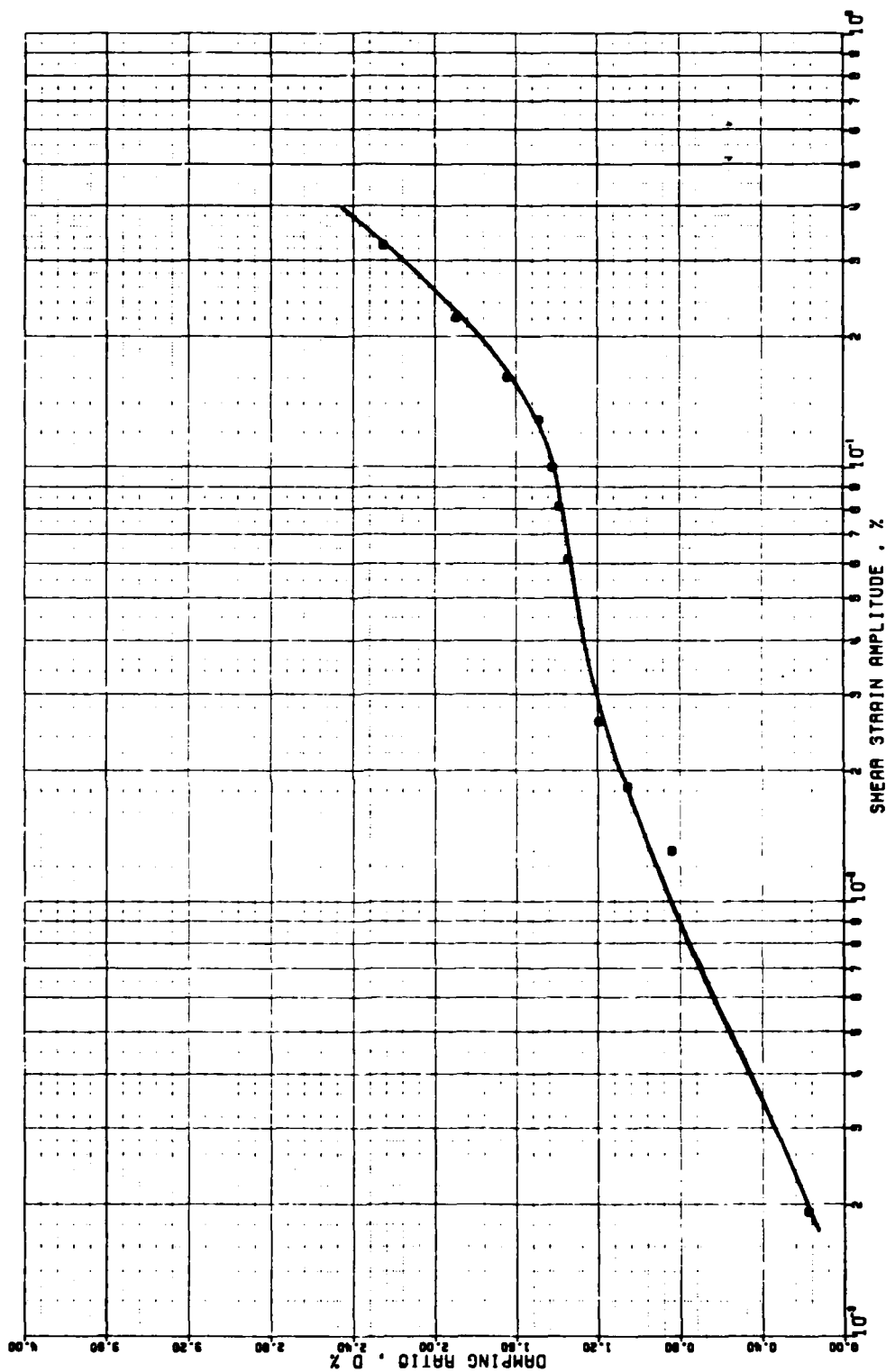
THE VARIATION OF DAMPING RATIO WITH STRAIN AMPLITUDE

DEEP CORE SAMPLES OF GULF OF MEXICO

SAMPLE DEPTH - 16.40 M.

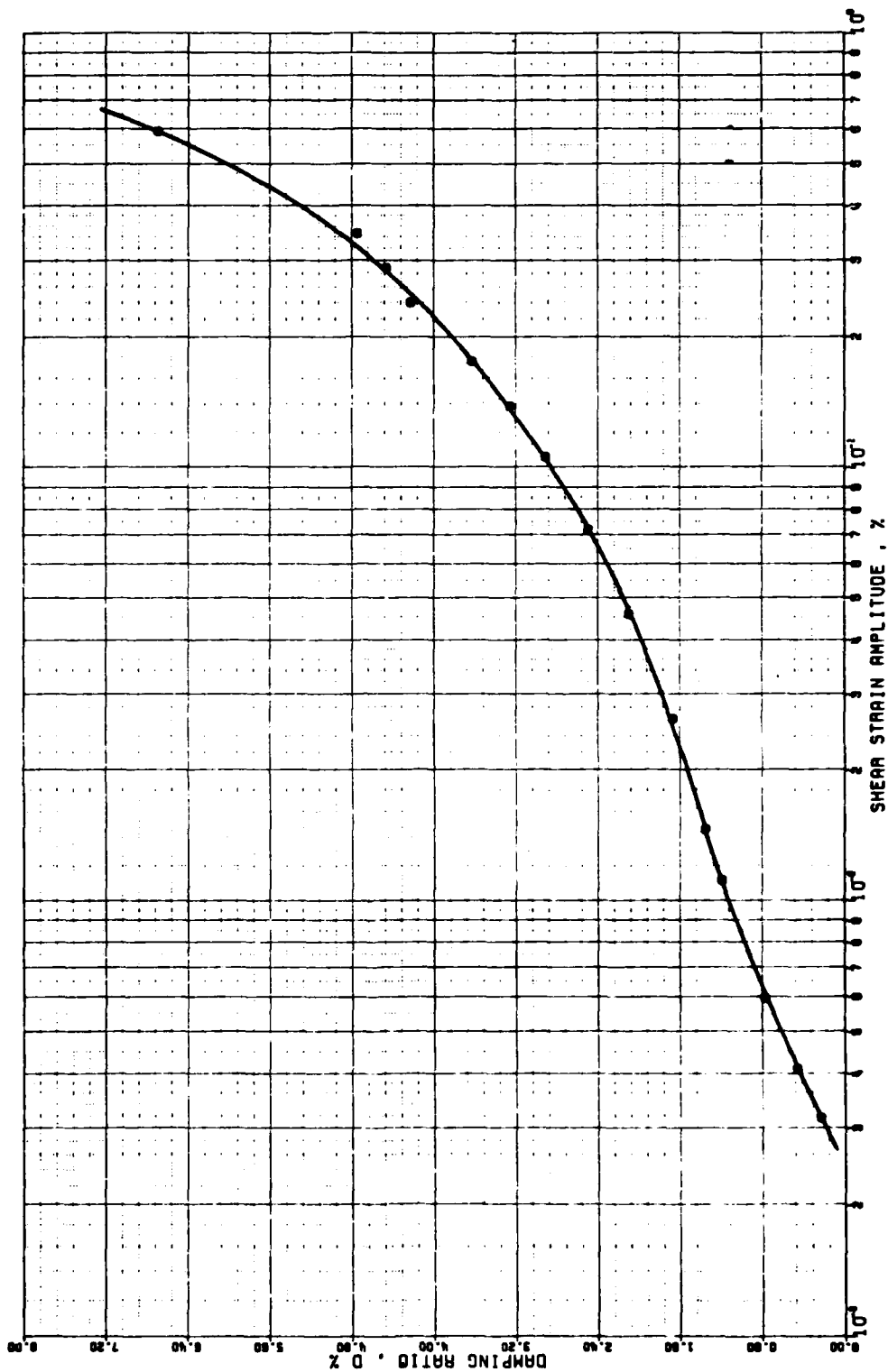


THE VARIATION OF DAMPING RATIO WITH STRAIN AMPLITUDE
 DEEP CORE SAMPLES OF GULF OF MEXICO
 SAMPLE DEPTH = 18.45 M.



THE VARIATION OF DAMPING RATIO WITH STRAIN AMPLITUDE DEEP CORE SAMPLES OF GULF OF MEXICO

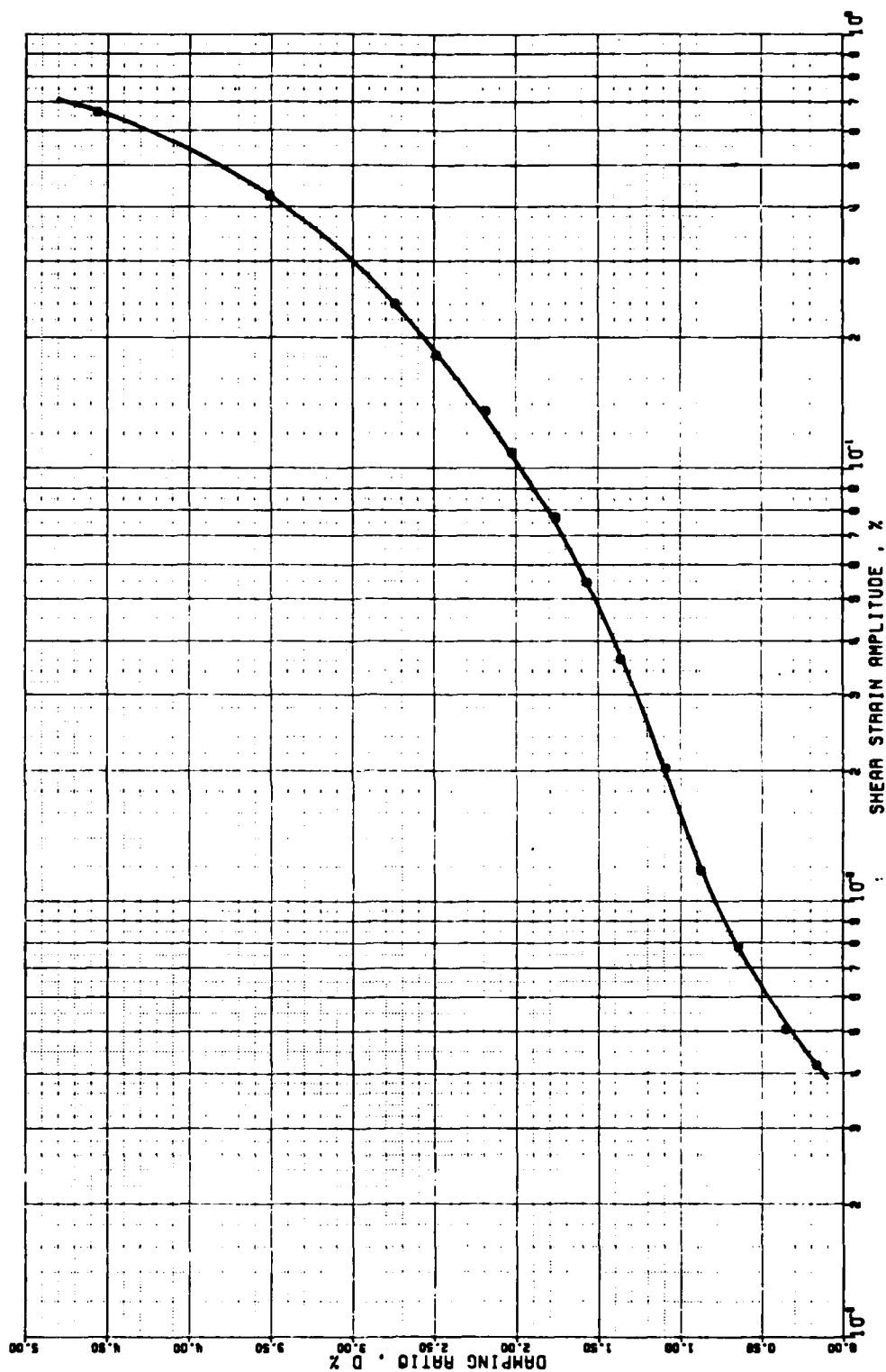
SAMPLE DEPTH = 22.48 M.



THE VARIATION OF DAMPING RATIO WITH STRAIN AMPLITUDE

DEEP CORE SAMPLES OF GULF OF MEXICO

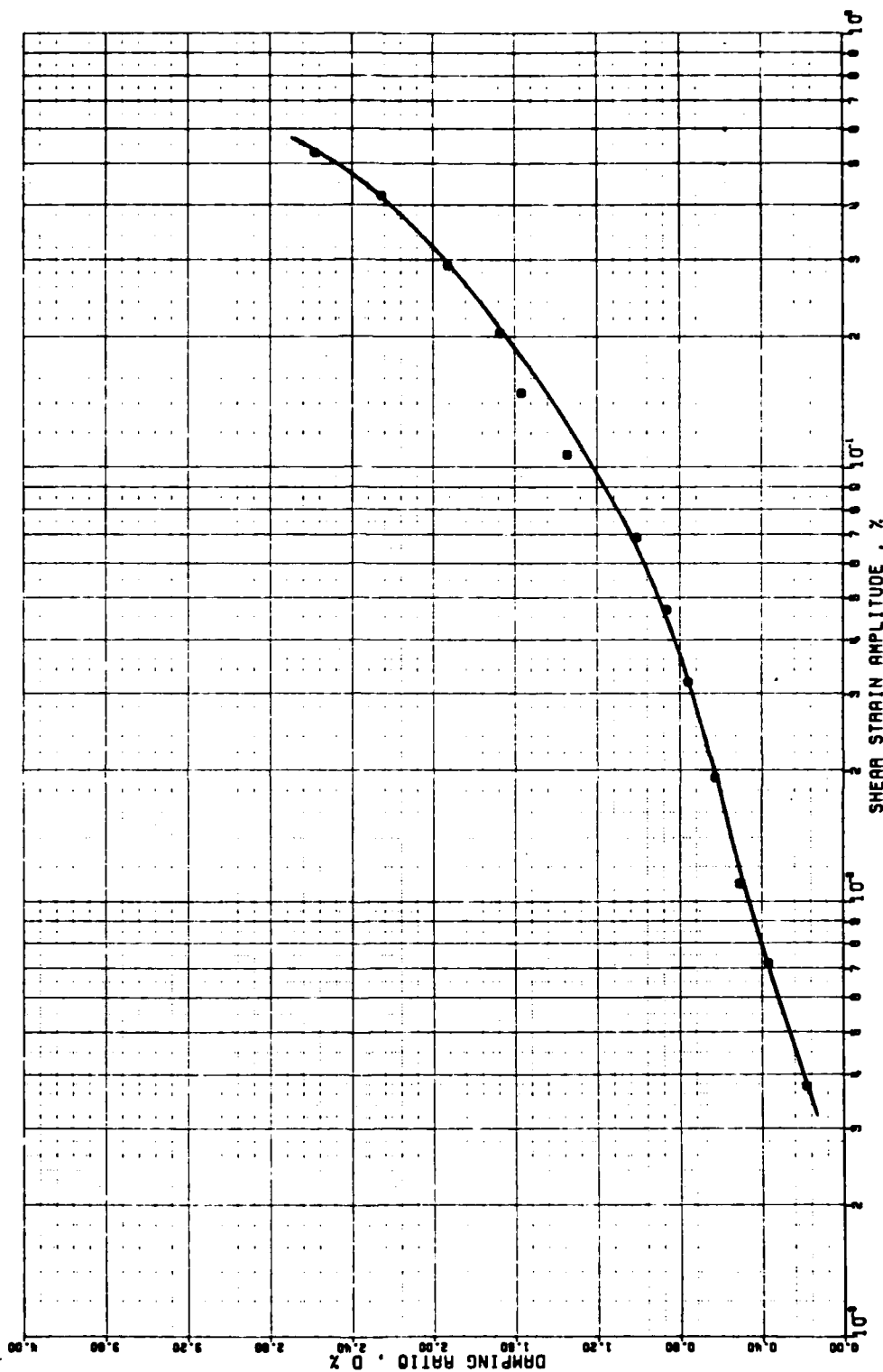
SAMPLE DEPTH = 26.59 M.



THE VARIATION OF DAMPING RATIO WITH STRAIN AMPLITUDE

DEEP CORE SAMPLES OF GULF OF MEXICO

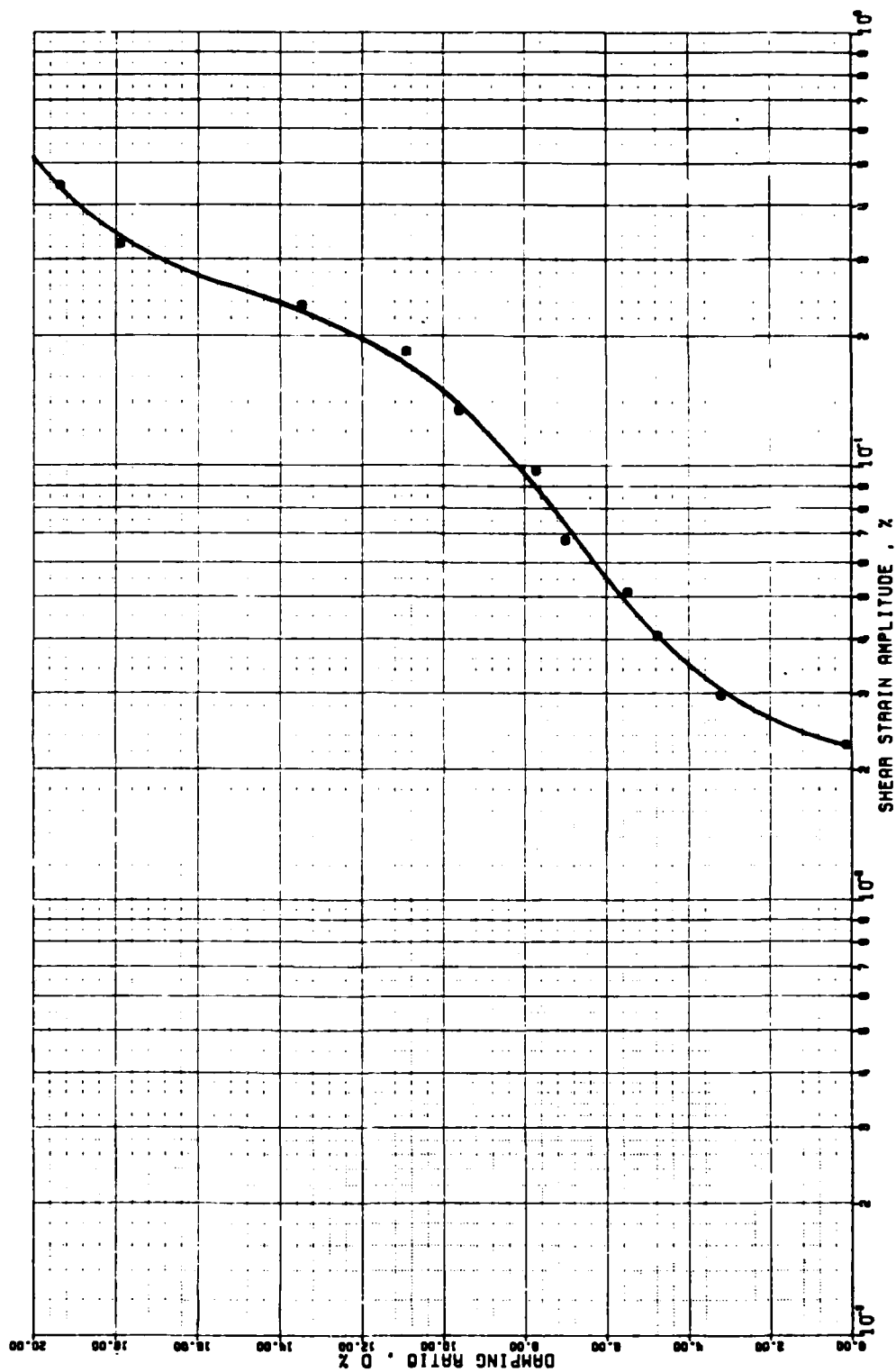
SAMPLE DEPTH = 31.64 M.



THE VARIATION OF DAMPING RATIO WITH STRAIN AMPLITUDE

DEEP CORE SAMPLES OF GULF OF MEXICO

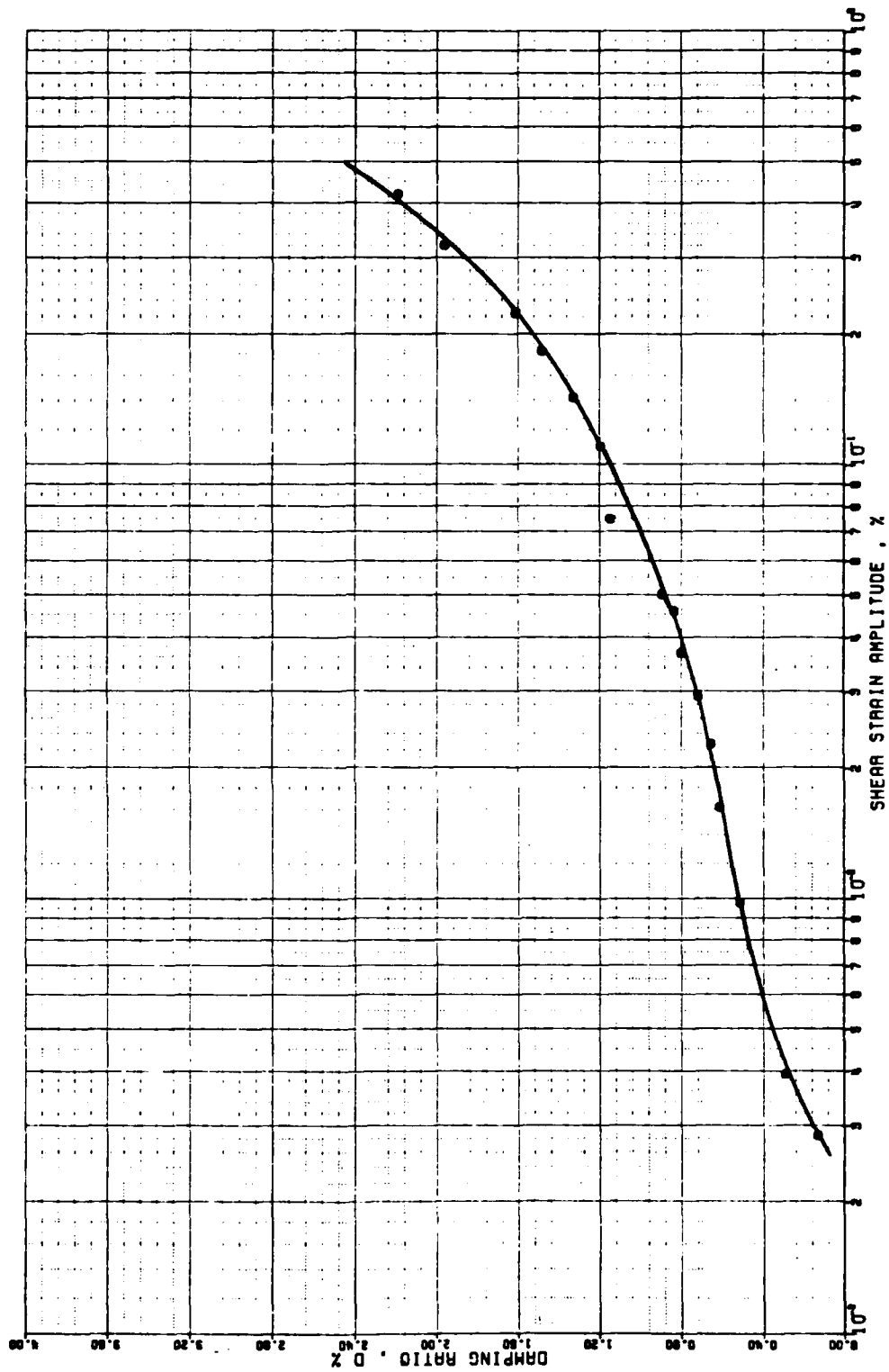
SAMPLE DEPTH - 54.00 M.



THE VARIATION OF DAMPING RATIO WITH STRAIN AMPLITUDE

DEEP CORE SAMPLES OF GULF OF MEXICO

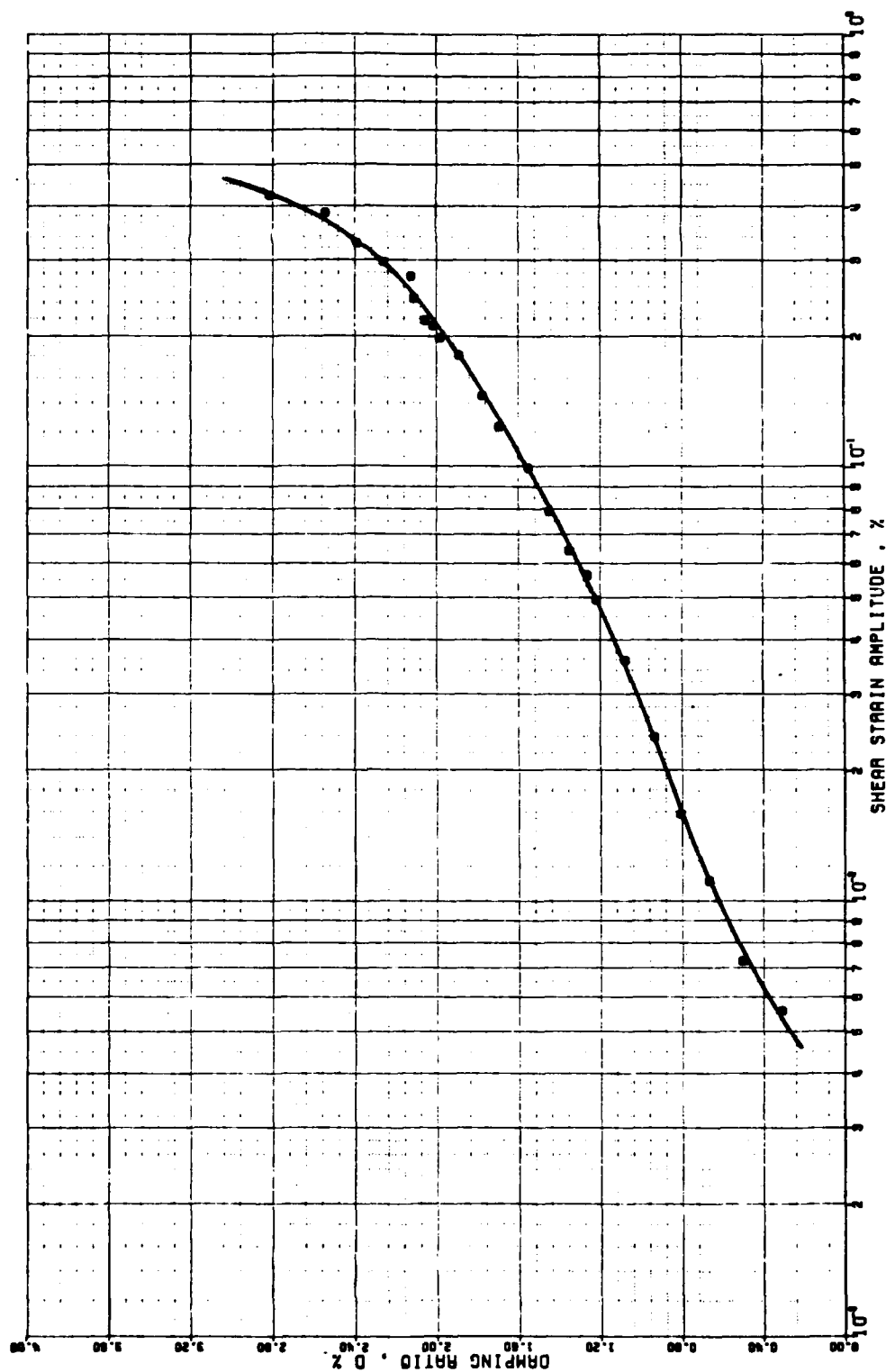
SAMPLE DEPTH = 37.73 M.



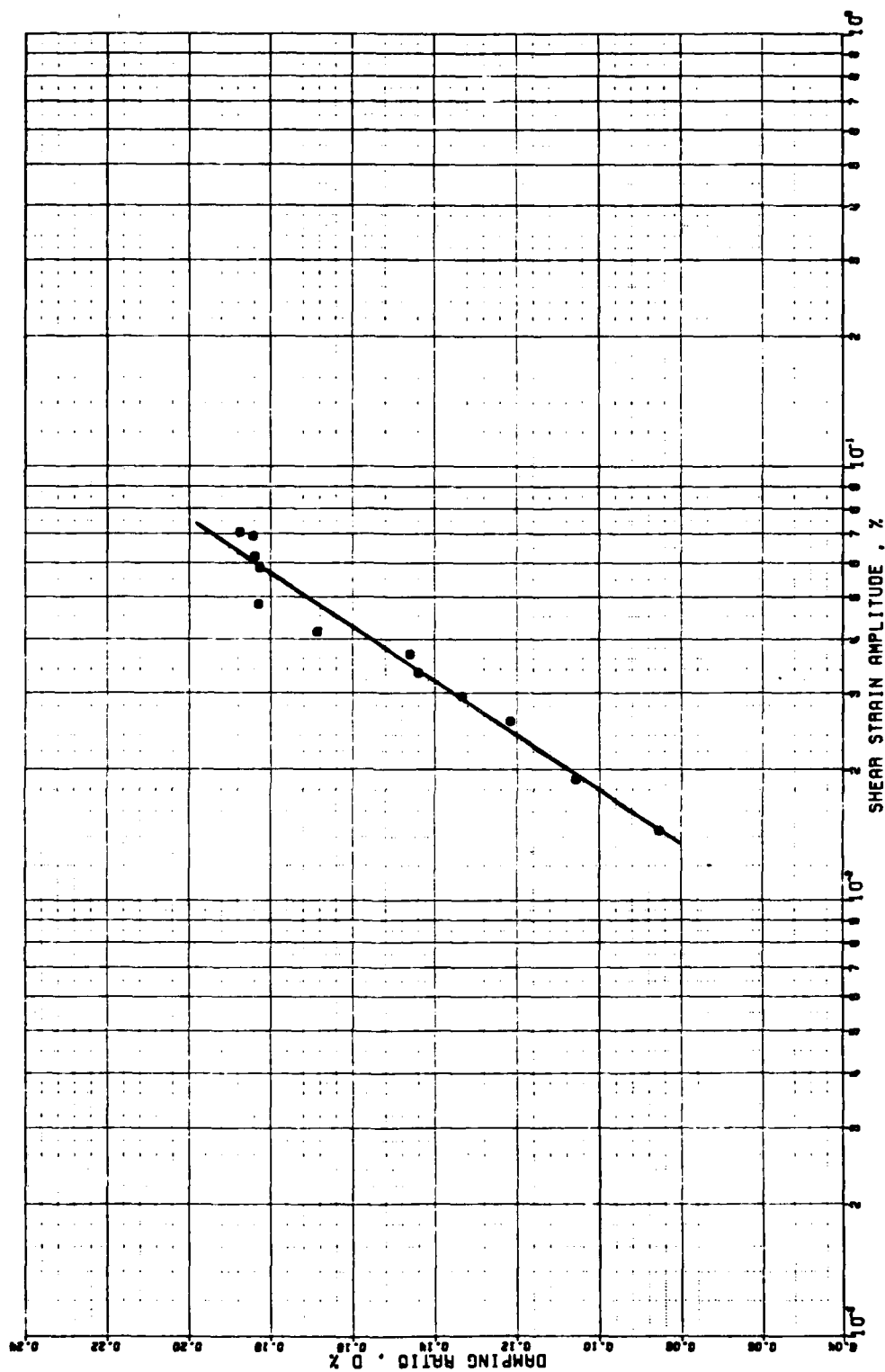
THE VARIATION OF DAMPING RATIO WITH STRAIN AMPLITUDE

DEEP CORE SAMPLES OF GULF OF MEXICO

SAMPLE DEPTH = 40.76 M.



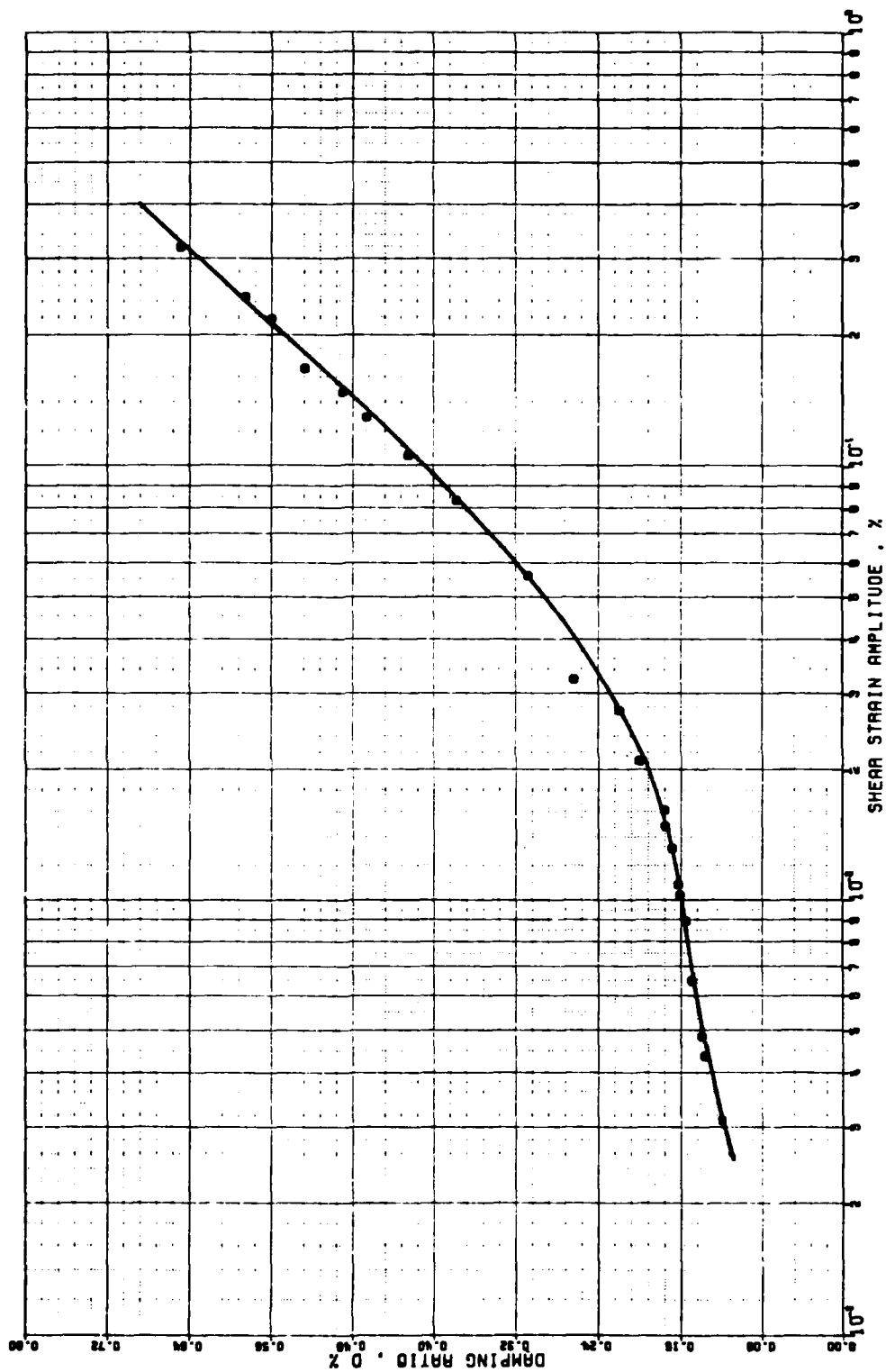
THE VARIATION OF DAMPING RATIO WITH STRAIN AMPLITUDE
 DEEP CORE SAMPLES OF GULF OF MEXICO
 SAMPLE DEPTH = 46.66 M.



THE VARIATION OF DAMPING RATIO WITH STRAIN AMPLITUDE

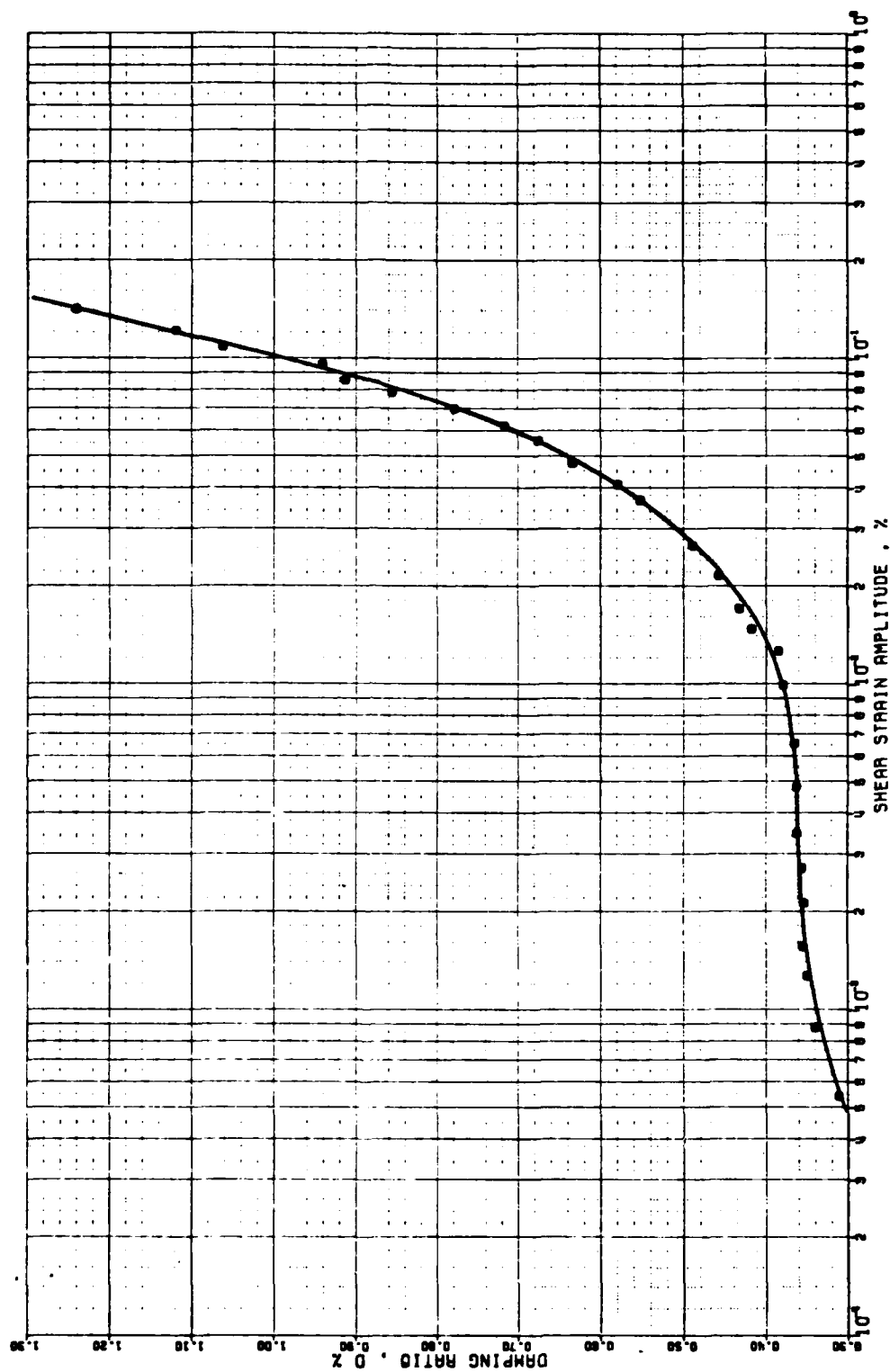
DEEP CORE SAMPLES OF GULF OF MEXICO

SAMPLE DEPTH = 58.07 M.



THE VARIATION OF DAMPING RATIO WITH STRAIN AMPLITUDE DEEP CORE SAMPLES OF GULF OF MEXICO

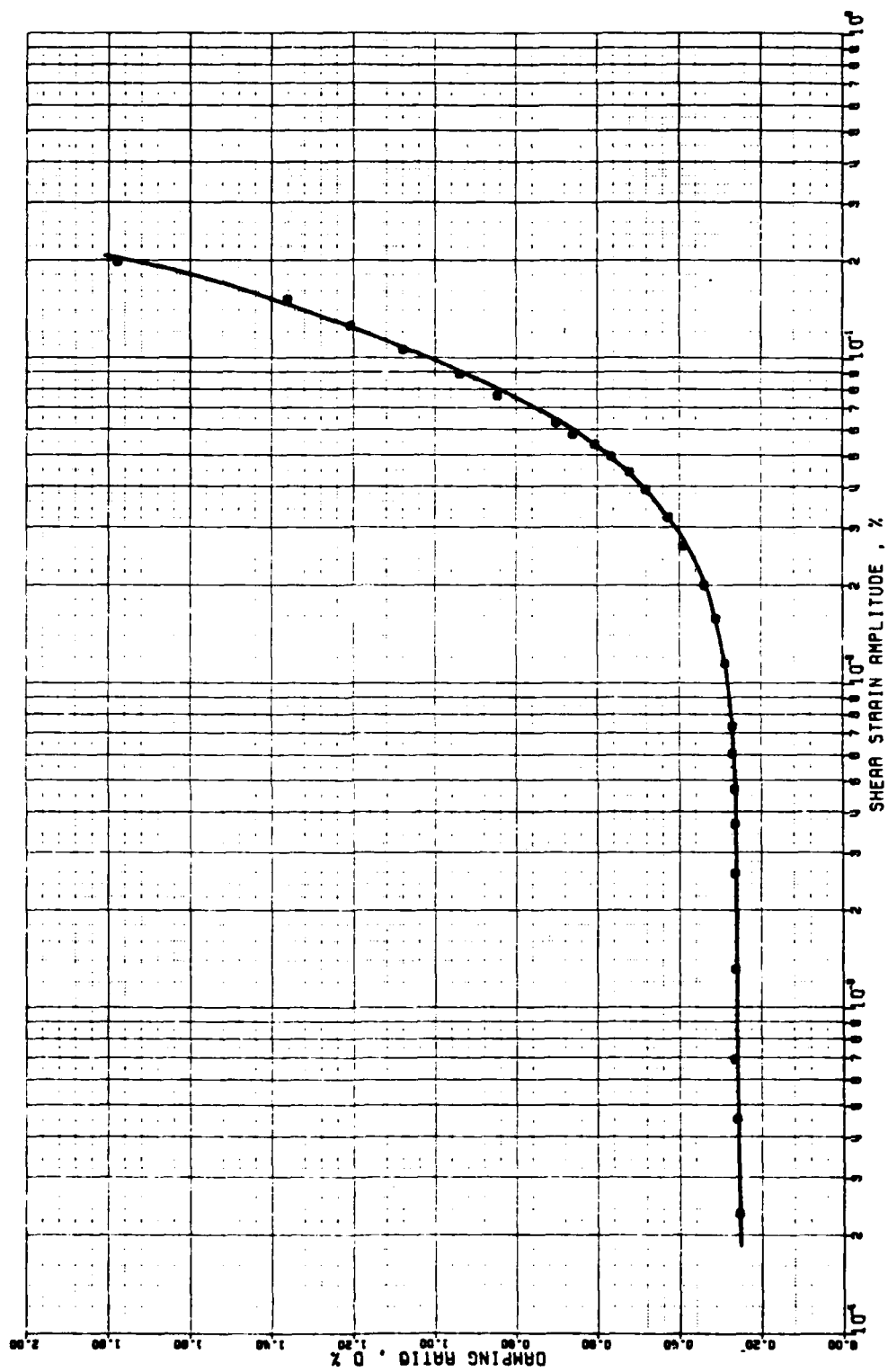
SAMPLE DEPTH = 71.32 M.



THE VARIATION OF DAMPING RATIO WITH STRAIN AMPLITUDE

DEEP CORE SAMPLES OF GULF OF MEXICO

SAMPLE DEPTH - 107.86 M.

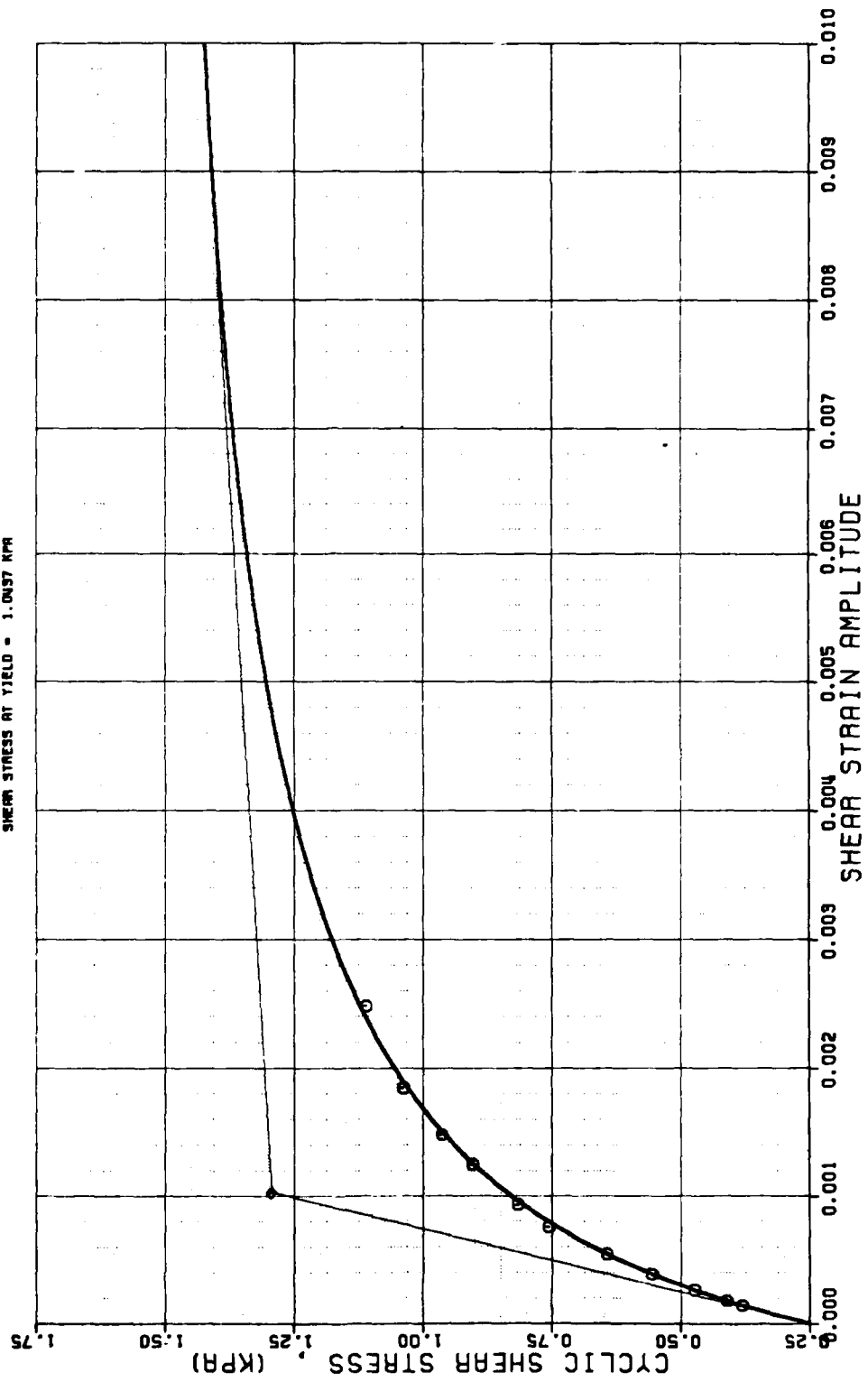


APPENDIX A-53/A-74
CYCLIC SHEAR STRESS-STRAIN CURVES

THE VARIATION OF SHEAR STRESS WITH STRAIN AMPLITUDE DEEP CORE SAMPLES OF GULF OF MEXICO

SAMPLE DEPTH = 0.24 M.

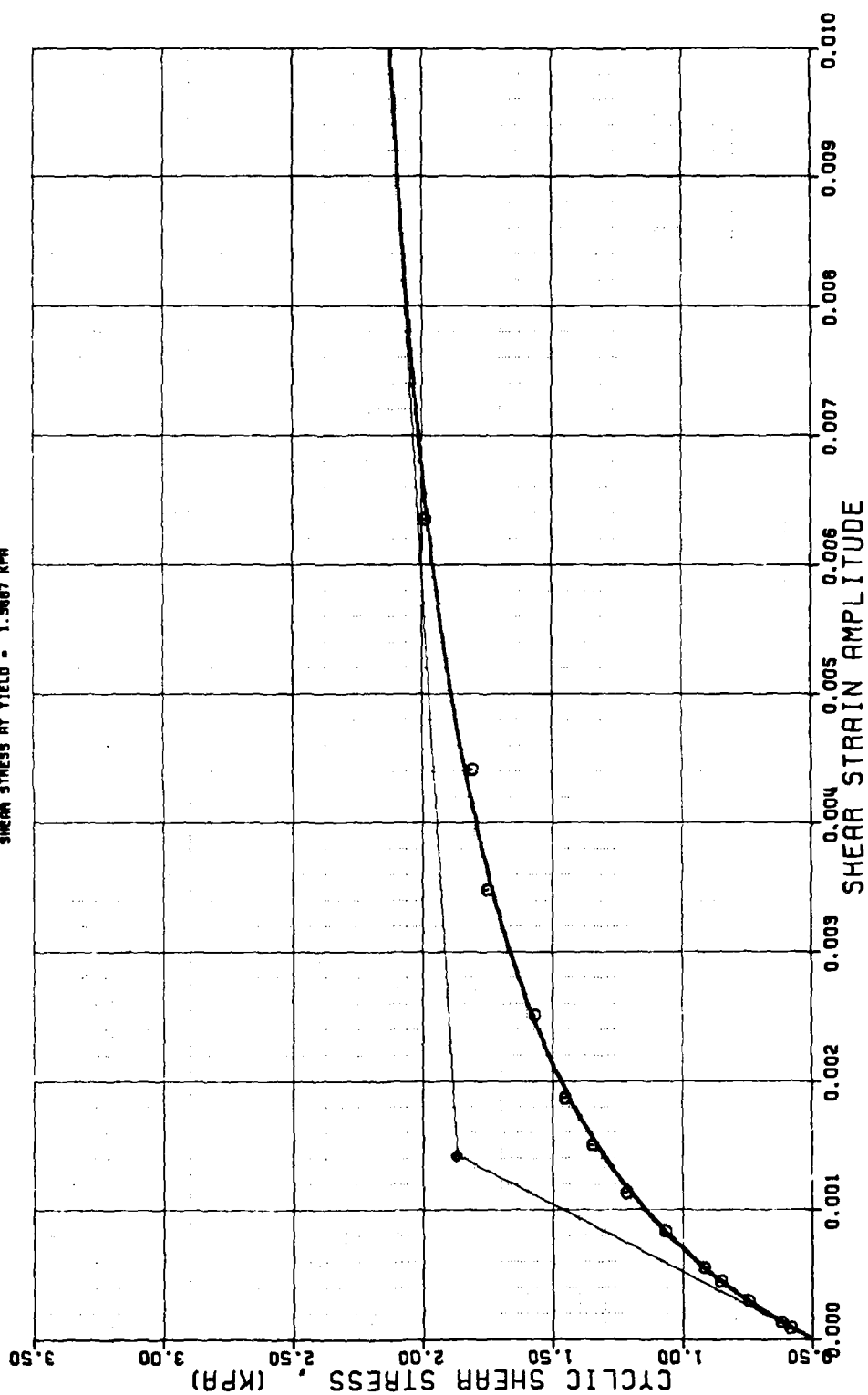
SHEAR STRESS AT YIELD = 1.0457 KPA



THE VARIATION OF SHEAR STRESS WITH STRAIN AMPLITUDE DEEP CORE SAMPLES OF GULF OF MEXICO

SAMPLE DEPTH = 2.10 M.

SHEAR STRESS AT YIELD = 1.9867 KPA

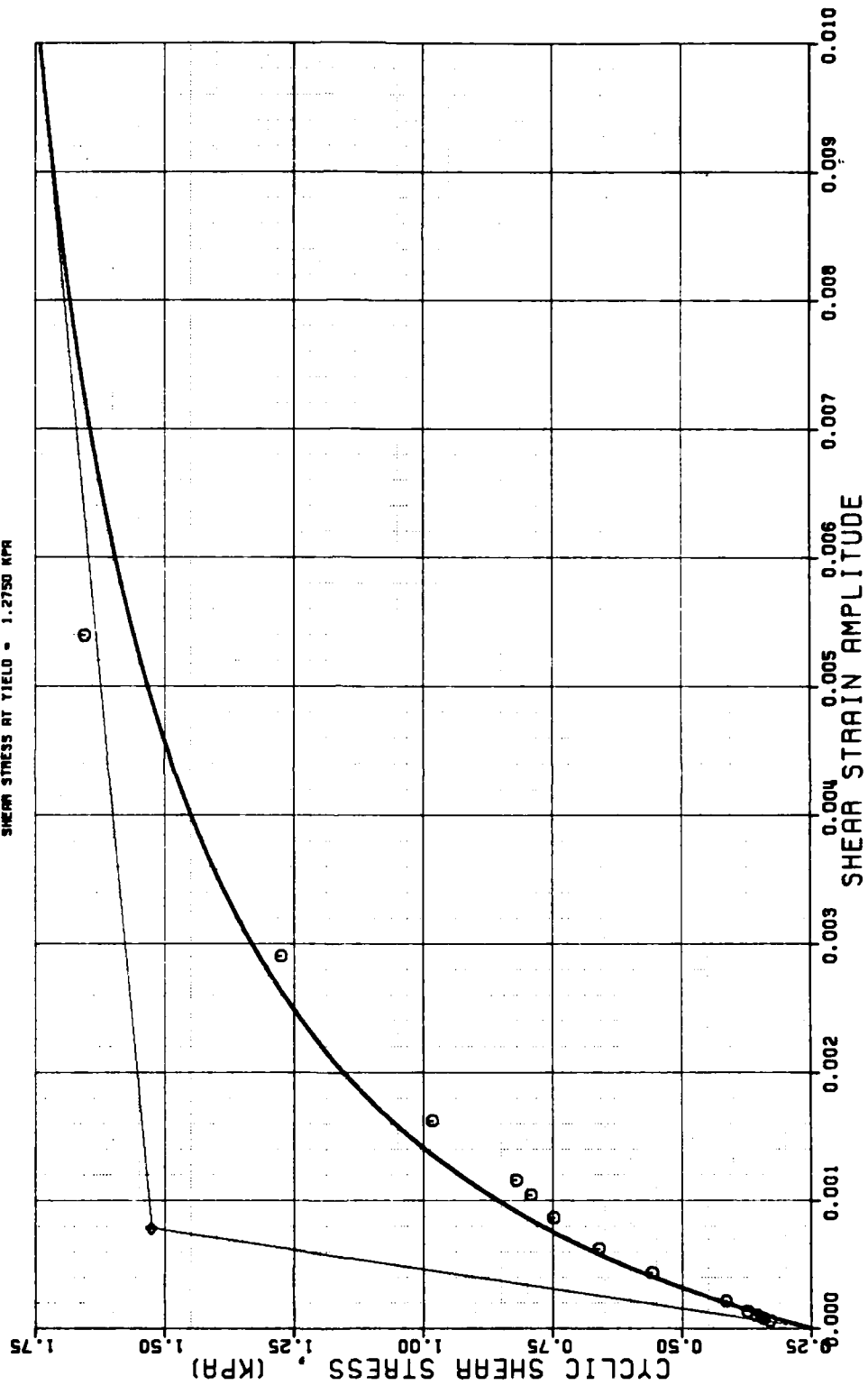


THE VARIATION OF SHEAR STRESS WITH STRAIN AMPLITUDE

DEEP CORE SAMPLES OF GULF OF MEXICO

SAMPLE DEPTH = 2.00 M.

SHEAR STRESS AT YIELD = 1.2750 KPA

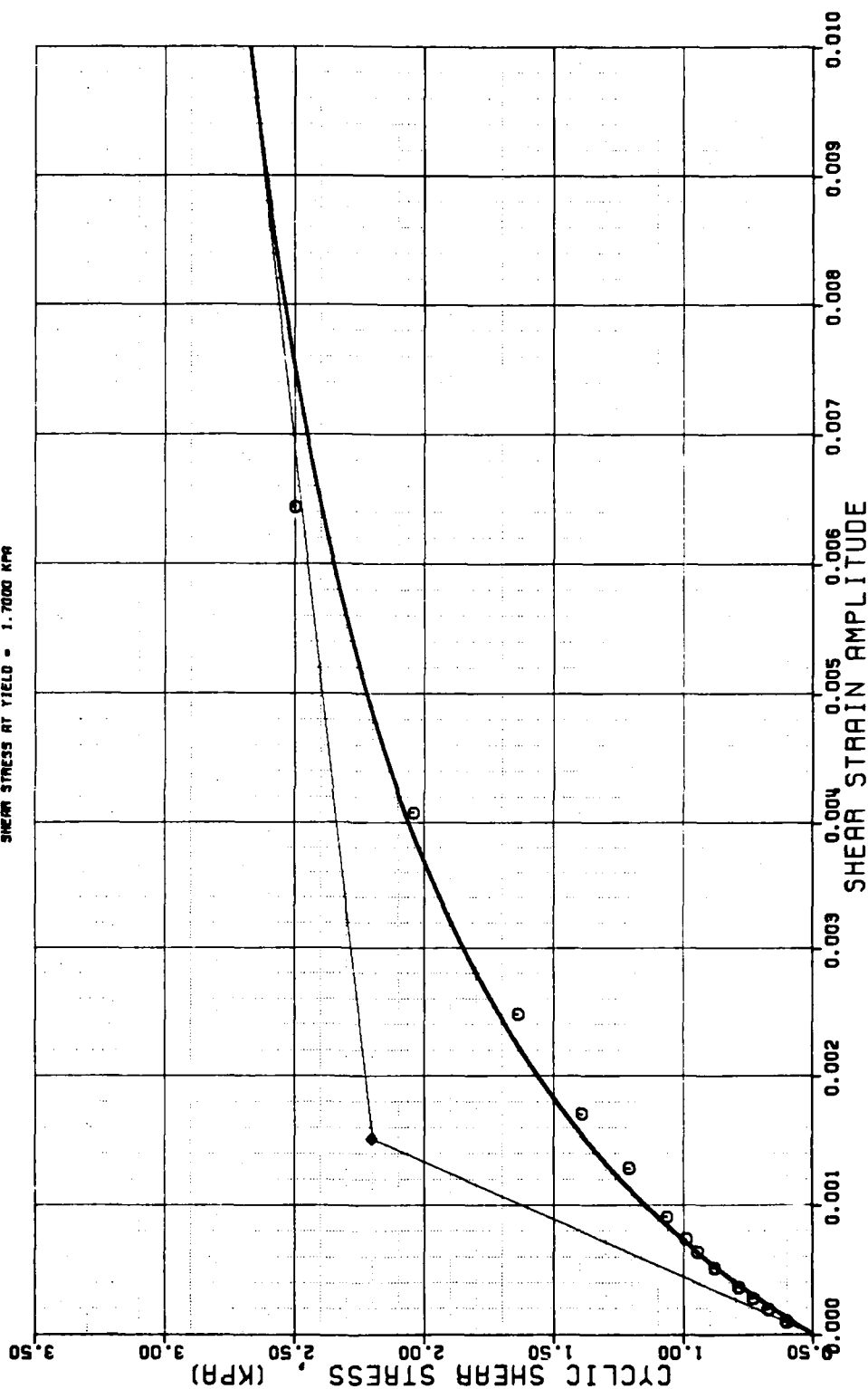


THE VARIATION OF SHEAR STRESS WITH STRAIN AMPLITUDE

DEEP CORE SAMPLES OF GULF OF MEXICO

SAMPLE DEPTH = 5.00 M.

SHEAR STRESS AT YIELD = 1.7000 KPA

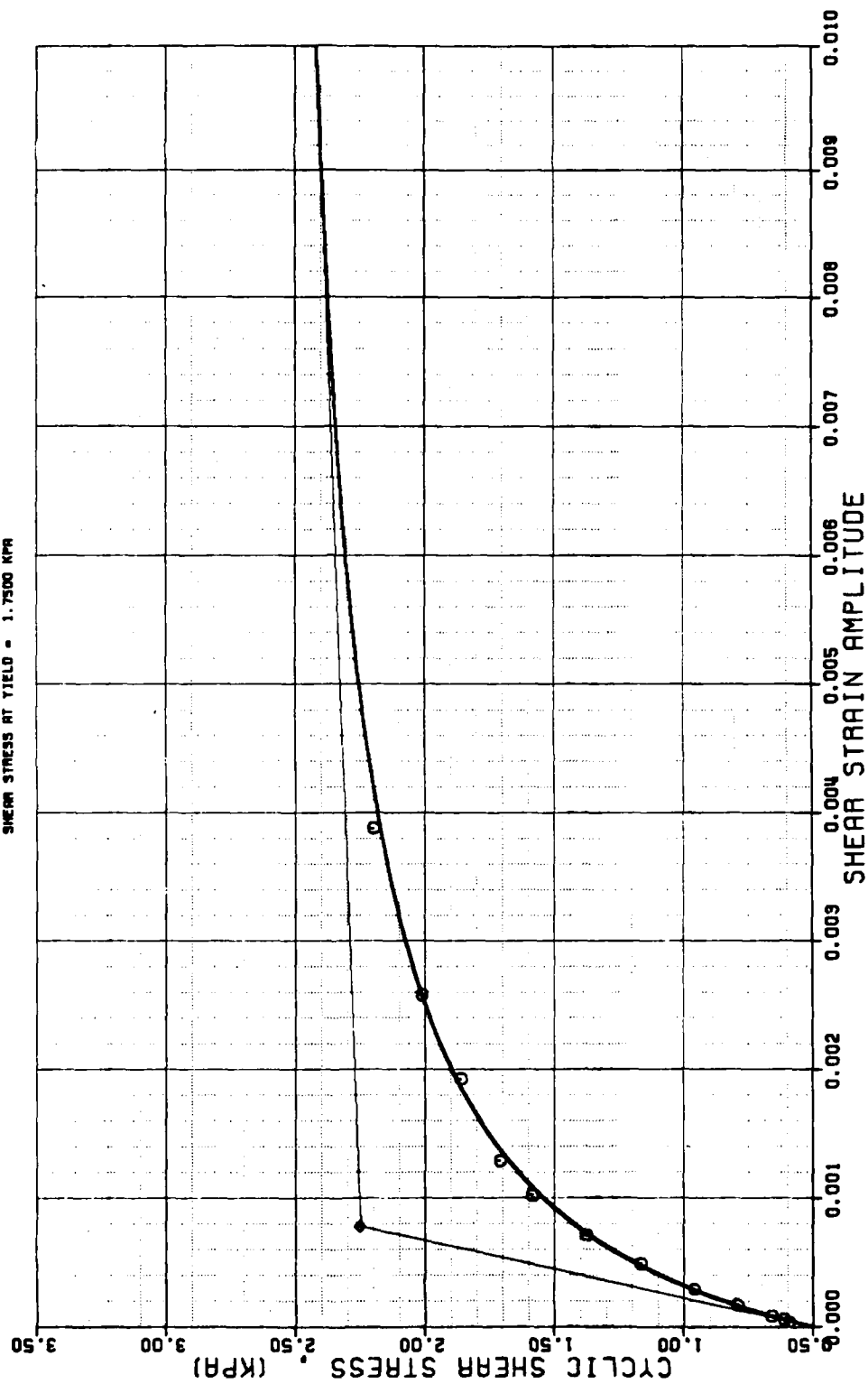


THE VARIATION OF SHEAR STRESS WITH STRAIN AMPLITUDE

DEEP CORE SAMPLES OF GULF OF MEXICO

SAMPLE DEPTH = 7.56 M.

SHEAR STRESS AT YIELD = 1.7500 KPA

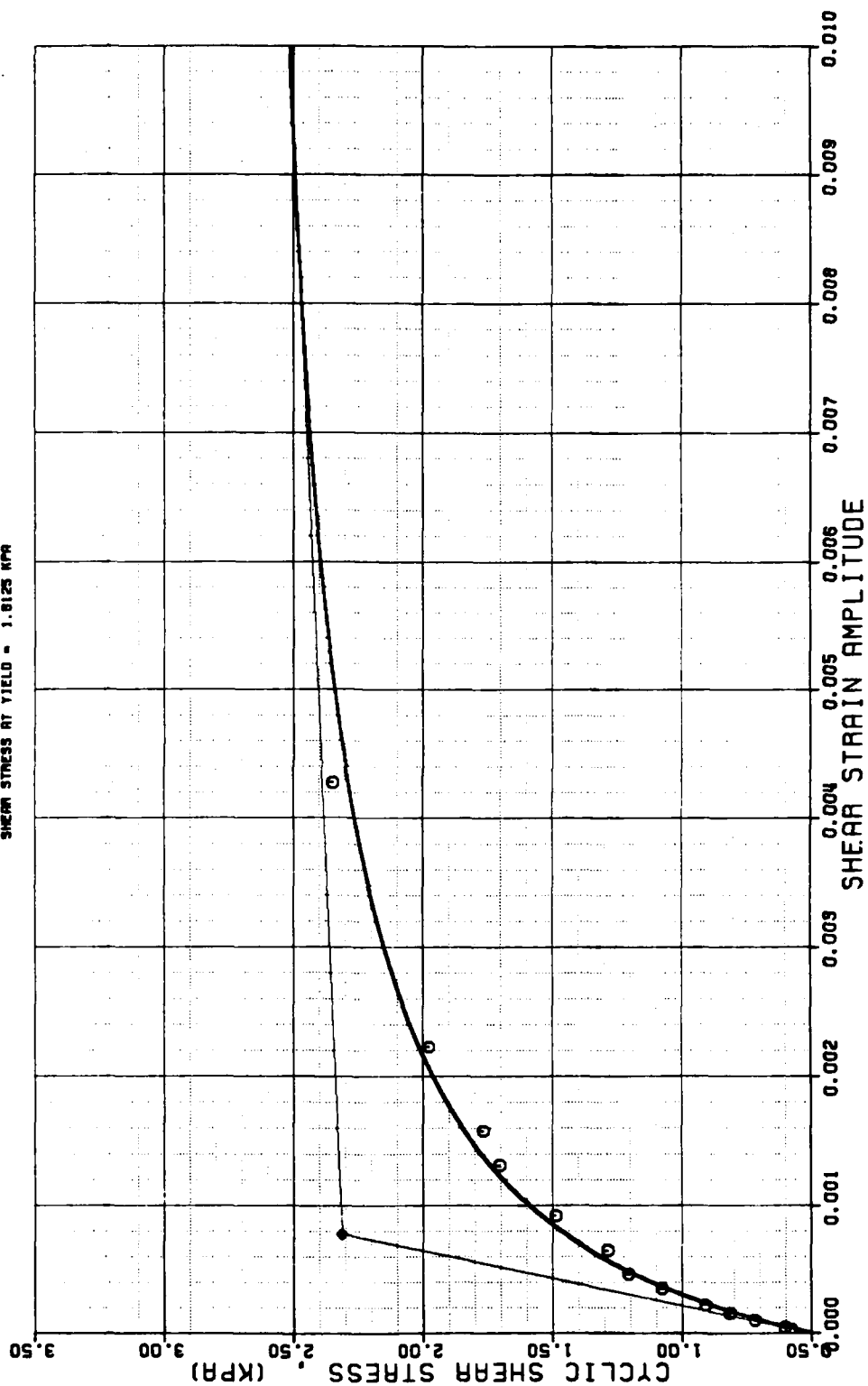


THE VARIATION OF SHEAR STRESS WITH STRAIN AMPLITUDE

DEEP CORE SAMPLES OF GULF OF MEXICO

SAMPLE DEPTH = 0.97 M.

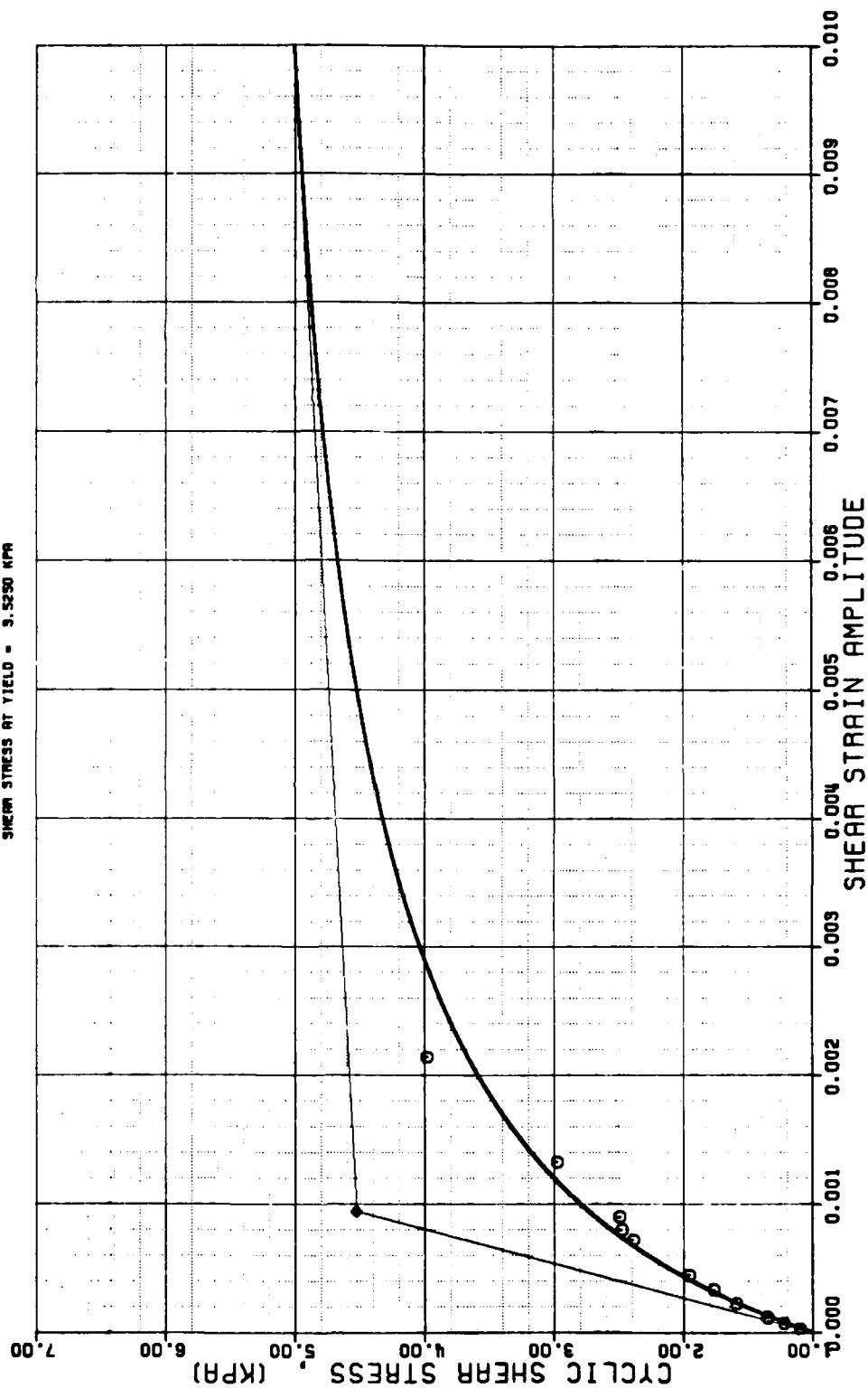
SHEAR STRESS AT YIELD = 1.8125 KPA



THE VARIATION OF SHEAR STRESS WITH STRAIN AMPLITUDE
DEEP CONE SAMPLES OF GULF OF MEXICO

SAMPLE DEPTH = 0.30 M.

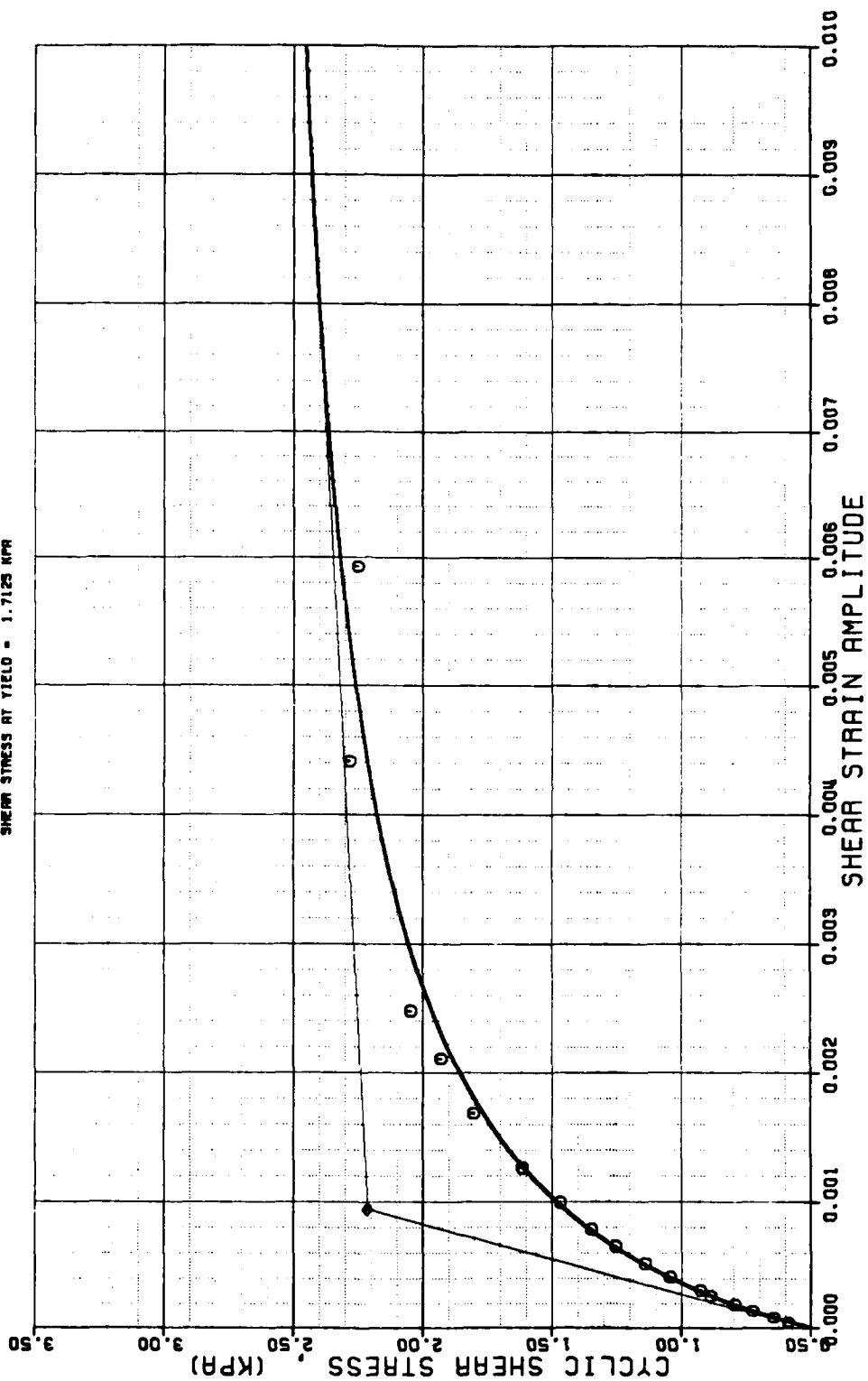
SHEAR STRESS AT YIELD = 3.5250 KPA



THE VARIATION OF SHEAR STRESS WITH STRAIN AMPLITUDE DEEP CORE SAMPLES OF GULF OF MEXICO

SAMPLE DEPTH - 12.06 M.

SHEAR STRESS AT YIELD - 1.7125 KPA

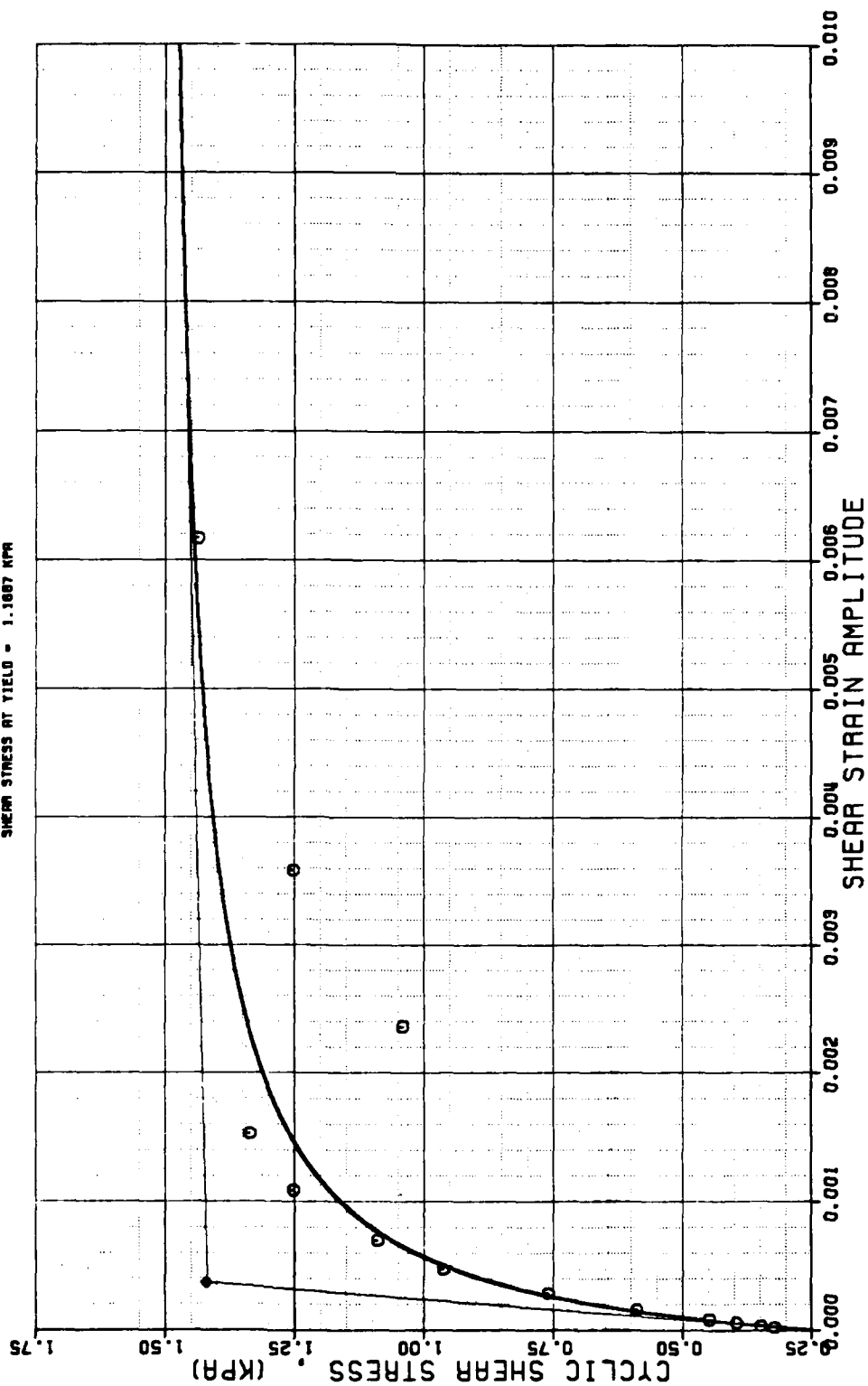


THE VARIATION OF SHEAR STRESS WITH STRAIN AMPLITUDE

DEEP CONE SAMPLES OF GULF OF MEXICO

SAMPLE DEPTH = 13.35 M.

SHEAR STRESS AT YIELD = 1.1067 KPA

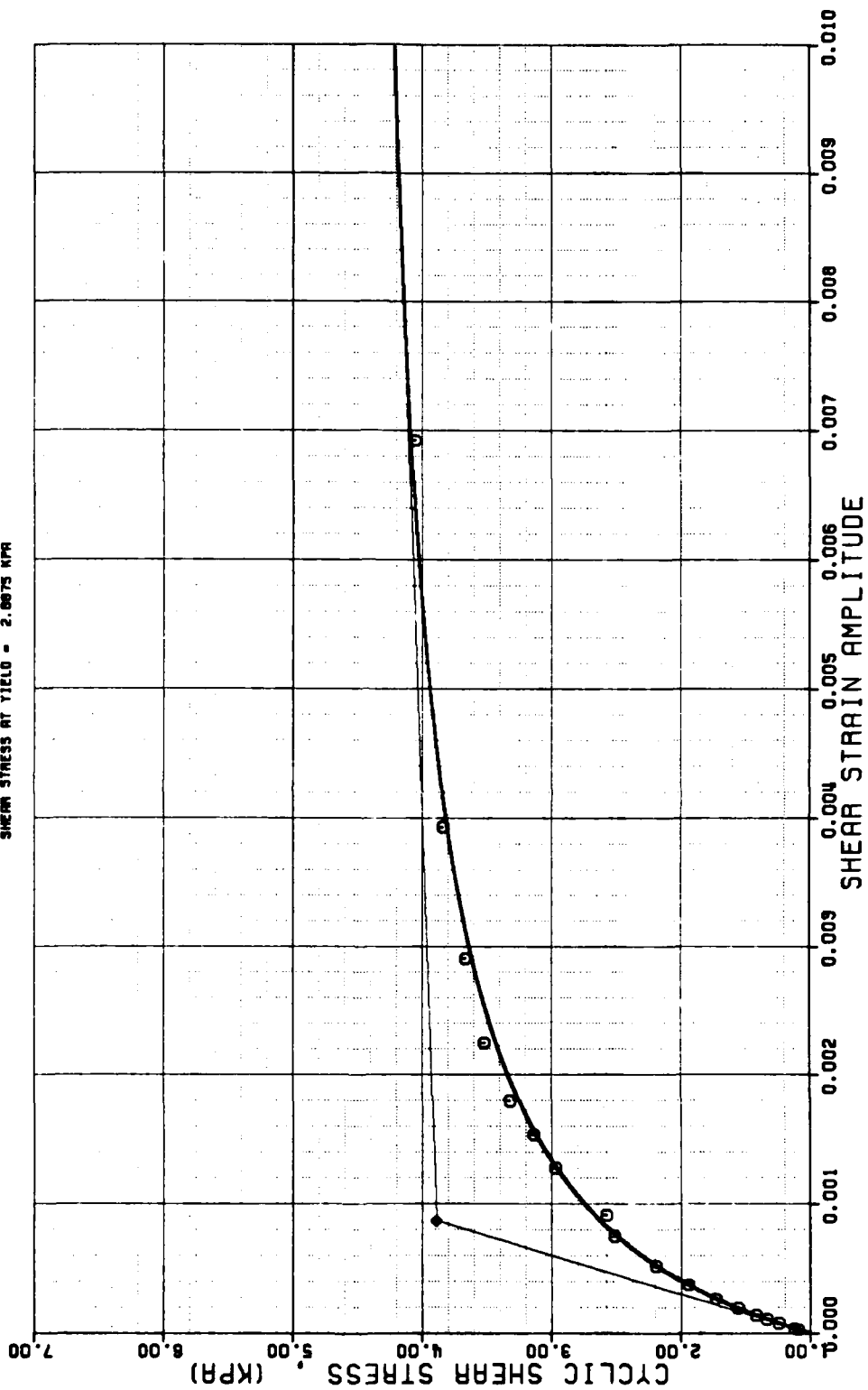


THE VARIATION OF SHEAR STRESS WITH STRAIN AMPLITUDE

DEEP CORE SAMPLES OF GULF OF MEXICO

SAMPLE DEPTH - 16.40 M.

SHEAR STRESS AT YIELD - 2.6075 KPA

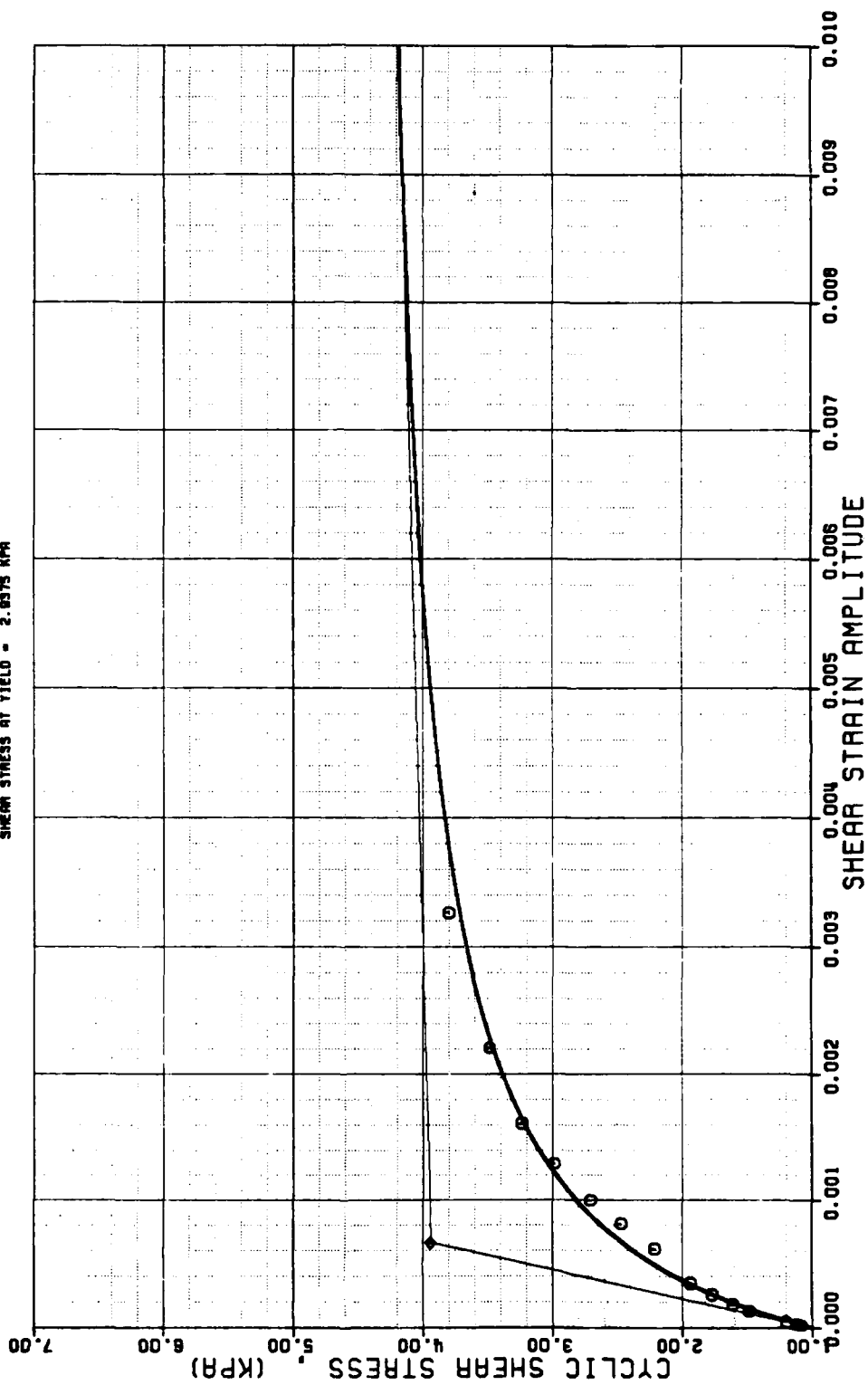


THE VARIATION OF SHEAR STRESS WITH STRAIN AMPLITUDE

DEEP CORE SAMPLES OF GULF OF MEXICO

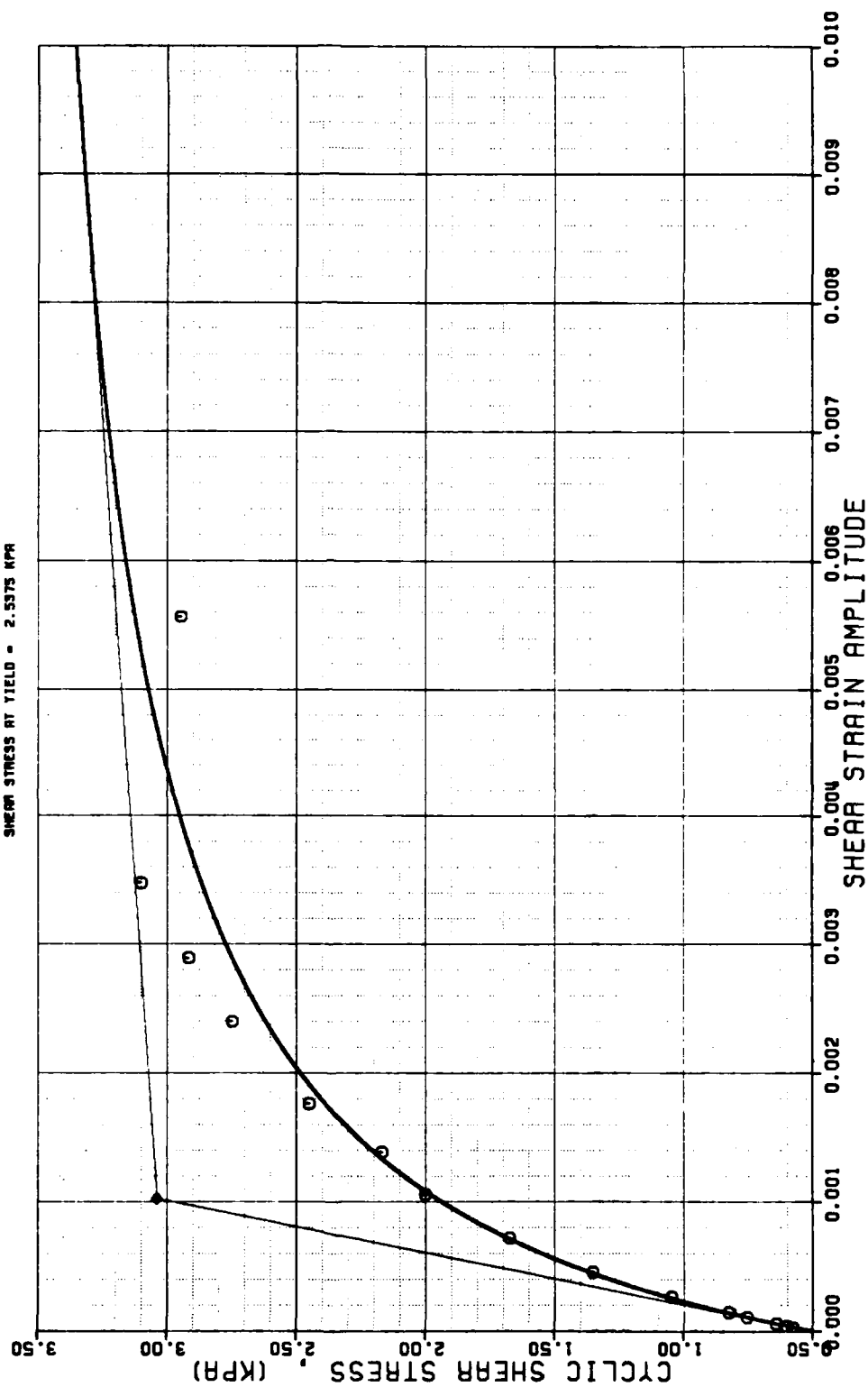
SAMPLE DEPTH = 19.45 M.

SHEAR STRESS AT YIELD = 2.9375 KPA



THE VARIATION OF SHEAR STRESS WITH STRAIN AMPLITUDE DEEP CORE SAMPLES OF GULF OF MEXICO

SAMPLE DEPTH = 22.48 M.
SHEAR STRESS AT YIELD = 2.5375 KPA

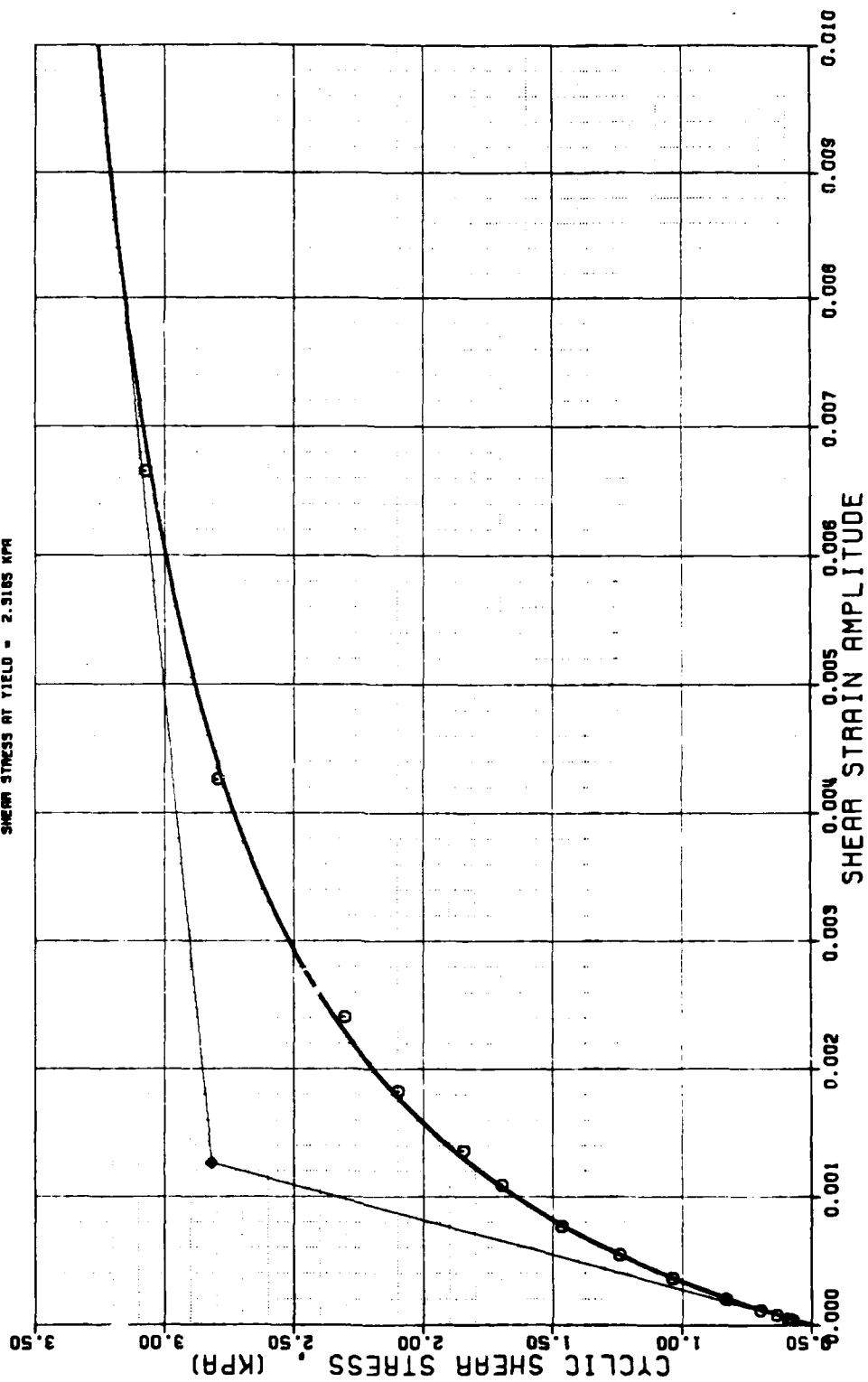


THE VARIATION OF SHEAR STRESS WITH STRAIN AMPLITUDE

DEEP CORE SAMPLES OF GULF OF MEXICO

SAMPLE DEPTH = 28.59 M.

SHEAR STRESS AT YIELD = 2.9165 KPA

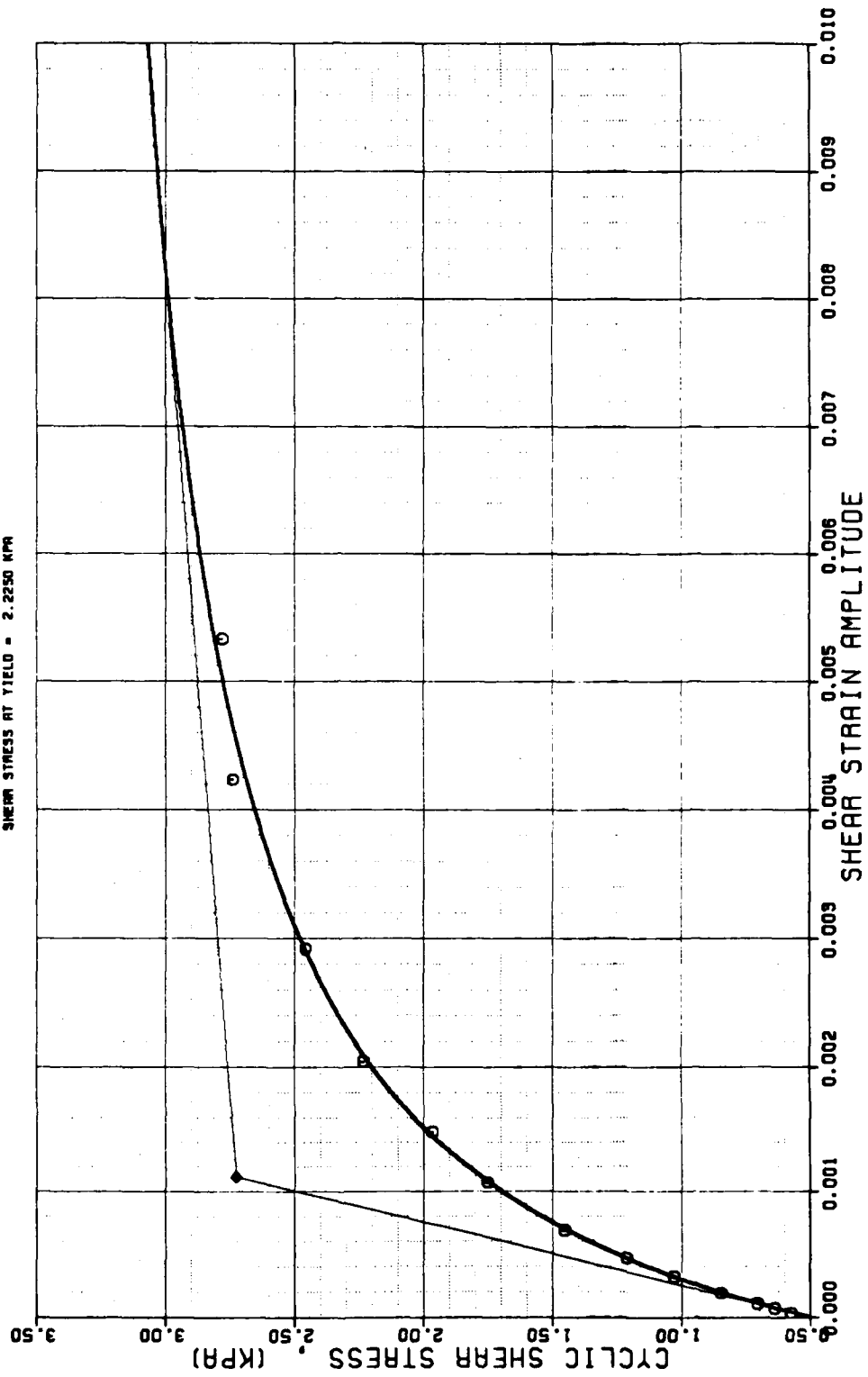


THE VARIATION OF SHEAR STRESS WITH STRAIN AMPLITUDE

DEEP CORE SAMPLES OF GULF OF MEXICO

SAMPLE DEPTH = 31.64 M.

SHEAR STRESS AT YIELD = 2.2250 KPA

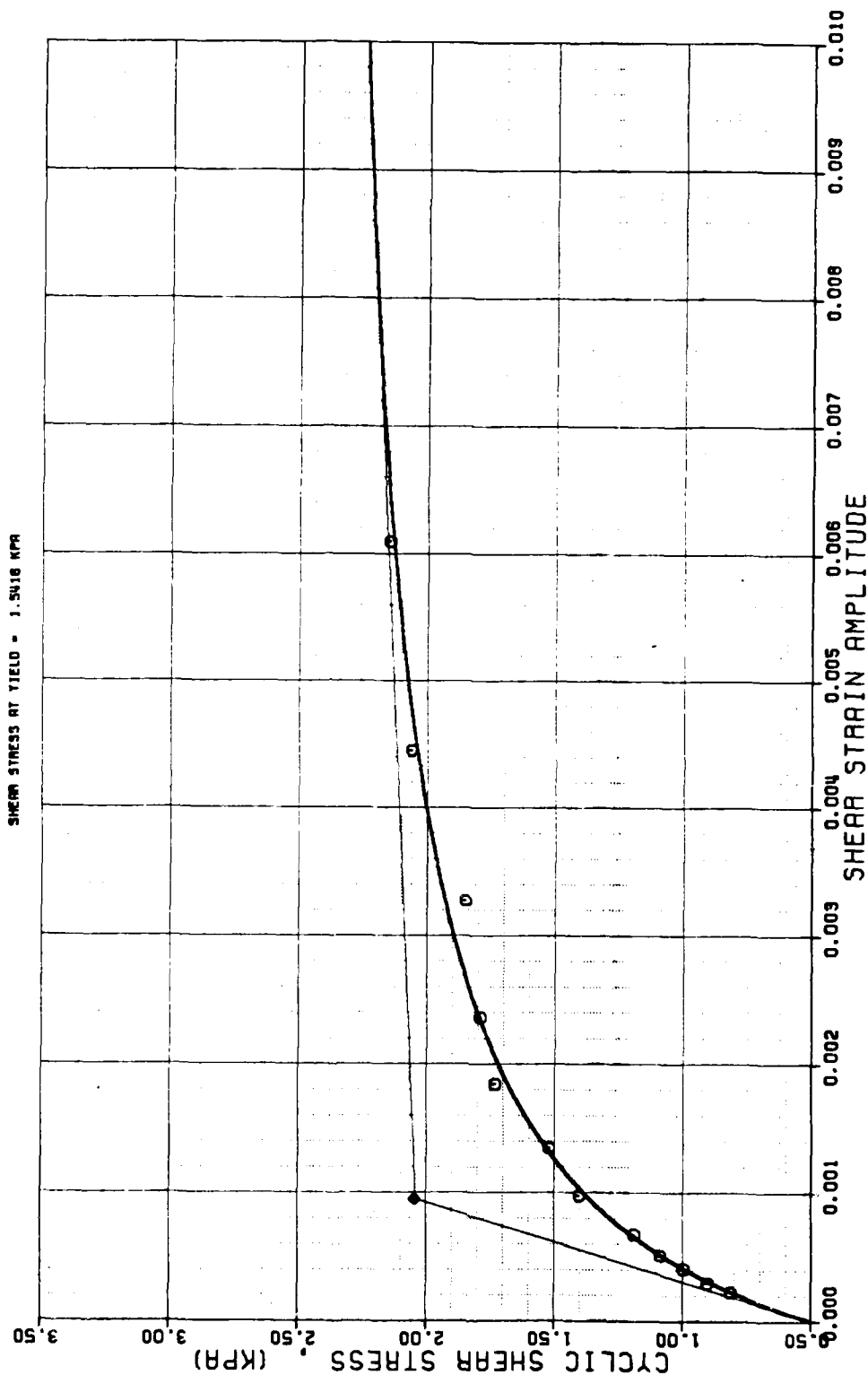


THE VARIATION OF SHEAR STRESS WITH STRAIN AMPLITUDE

DEEP CORE SAMPLES OF GULF OF MEXICO

SAMPLE DEPTH = 34.88 M.

SHEAR STRESS AT YIELD = 1.5416 KPA

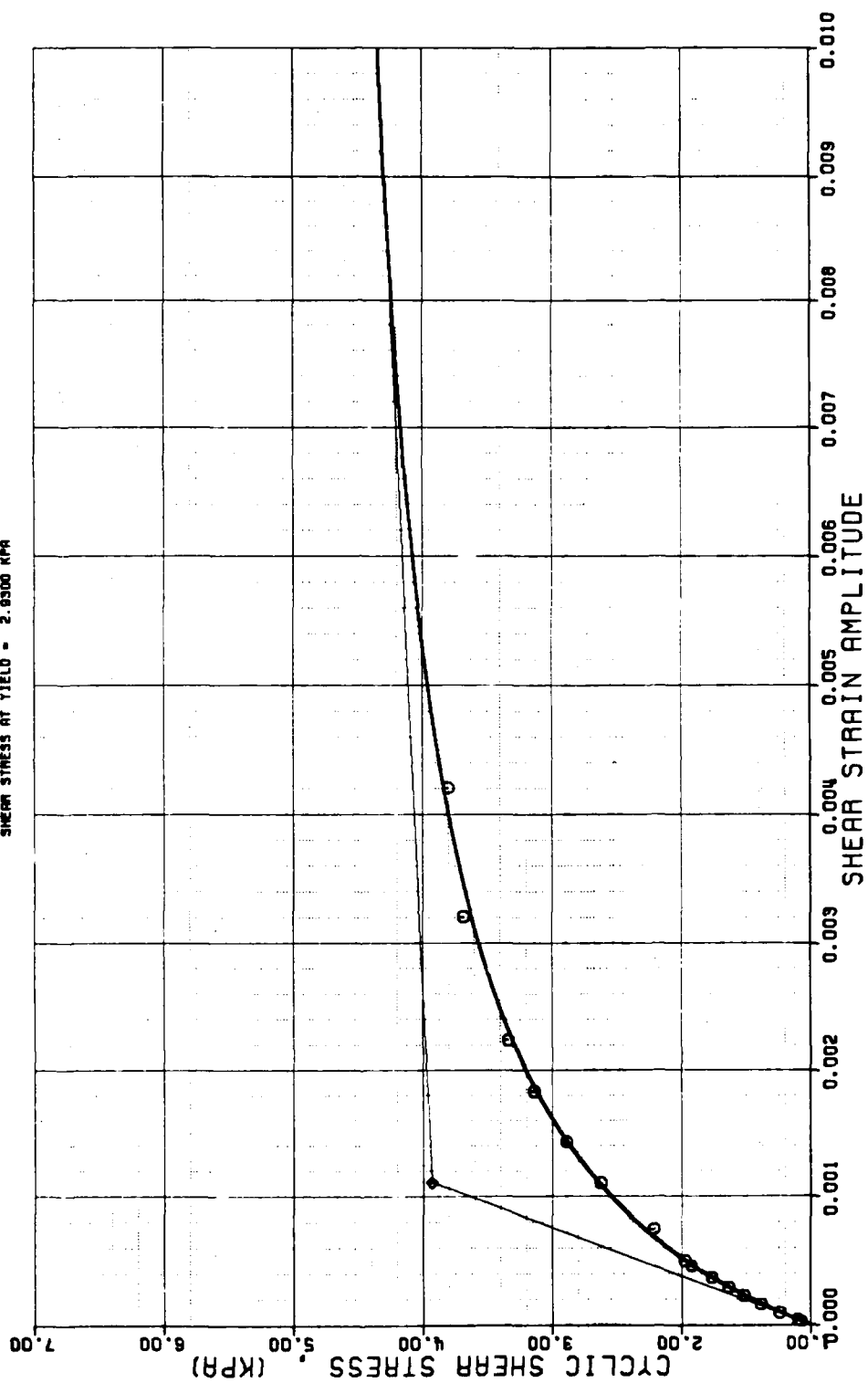


THE VARIATION OF SHEAR STRESS WITH STRAIN AMPLITUDE

DEEP CORE SAMPLES OF GULF OF MEXICO

SAMPLE DEPTH = 57.73 M.

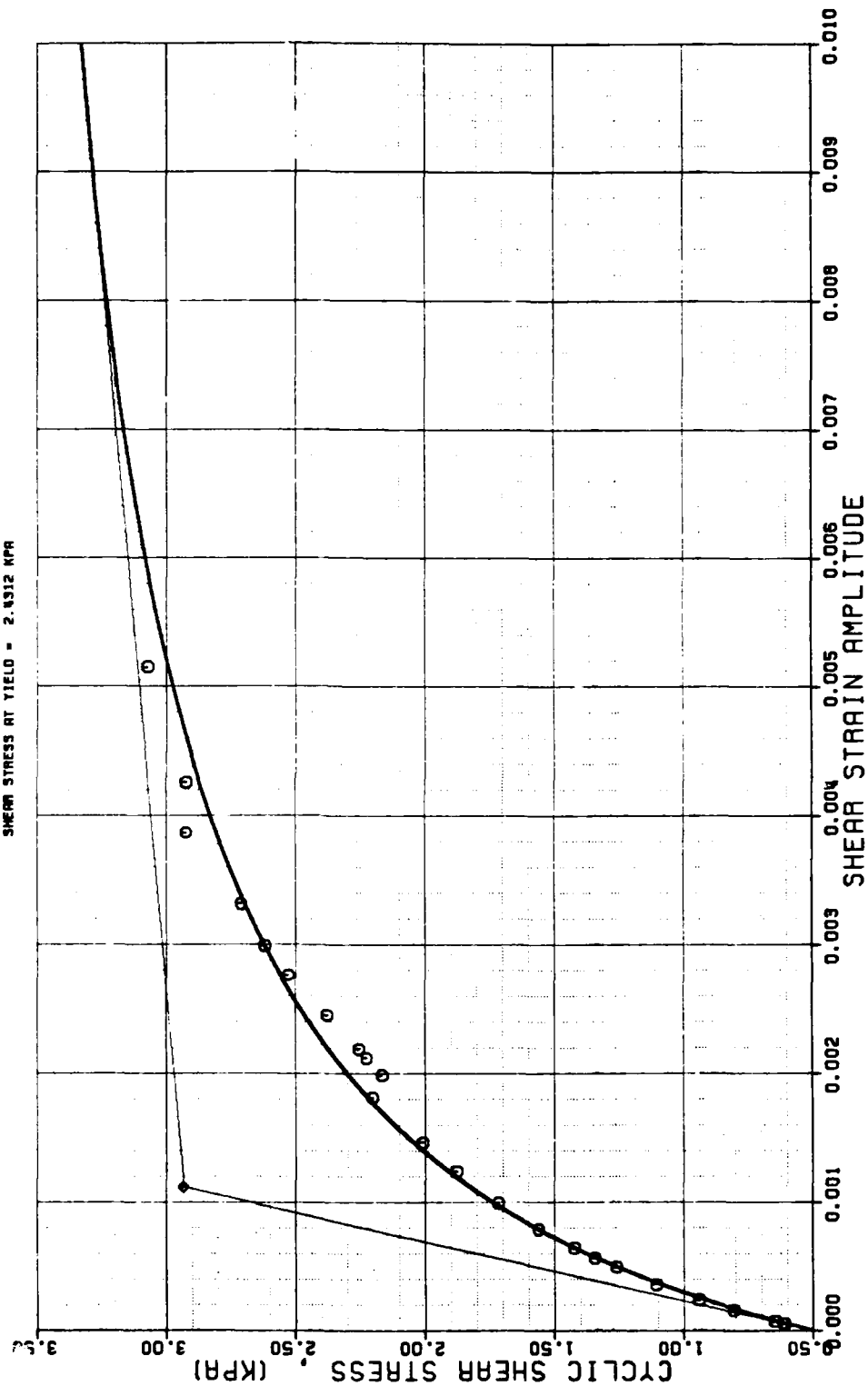
SHEAR STRESS AT YIELD = 2.9300 KPA



THE VARIATION OF SHEAR STRESS WITH STRAIN AMPLITUDE DEEP CORE SAMPLES OF GULF OF MEXICO

SAMPLE DEPTH = 40.76 M.

SHEAR STRESS AT YIELD = 2.9312 KPA

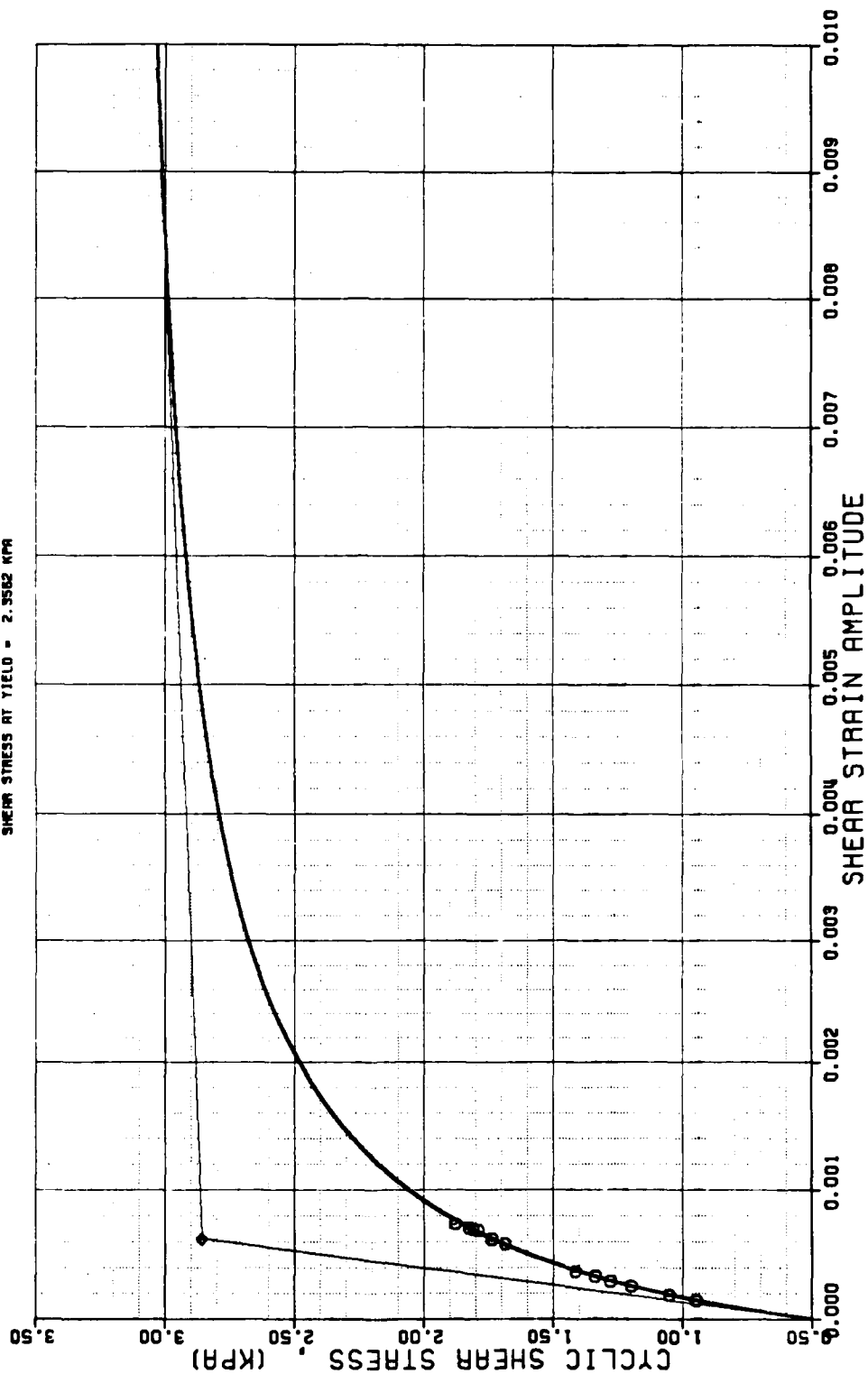


THE VARIATION OF SHEAR STRESS WITH STRAIN AMPLITUDE

DEEP CORE SAMPLES OF GULF OF MEXICO

SAMPLE DEPTH = 48.88 M.

SHEAR STRESS AT YIELD = 2.5582 KPA

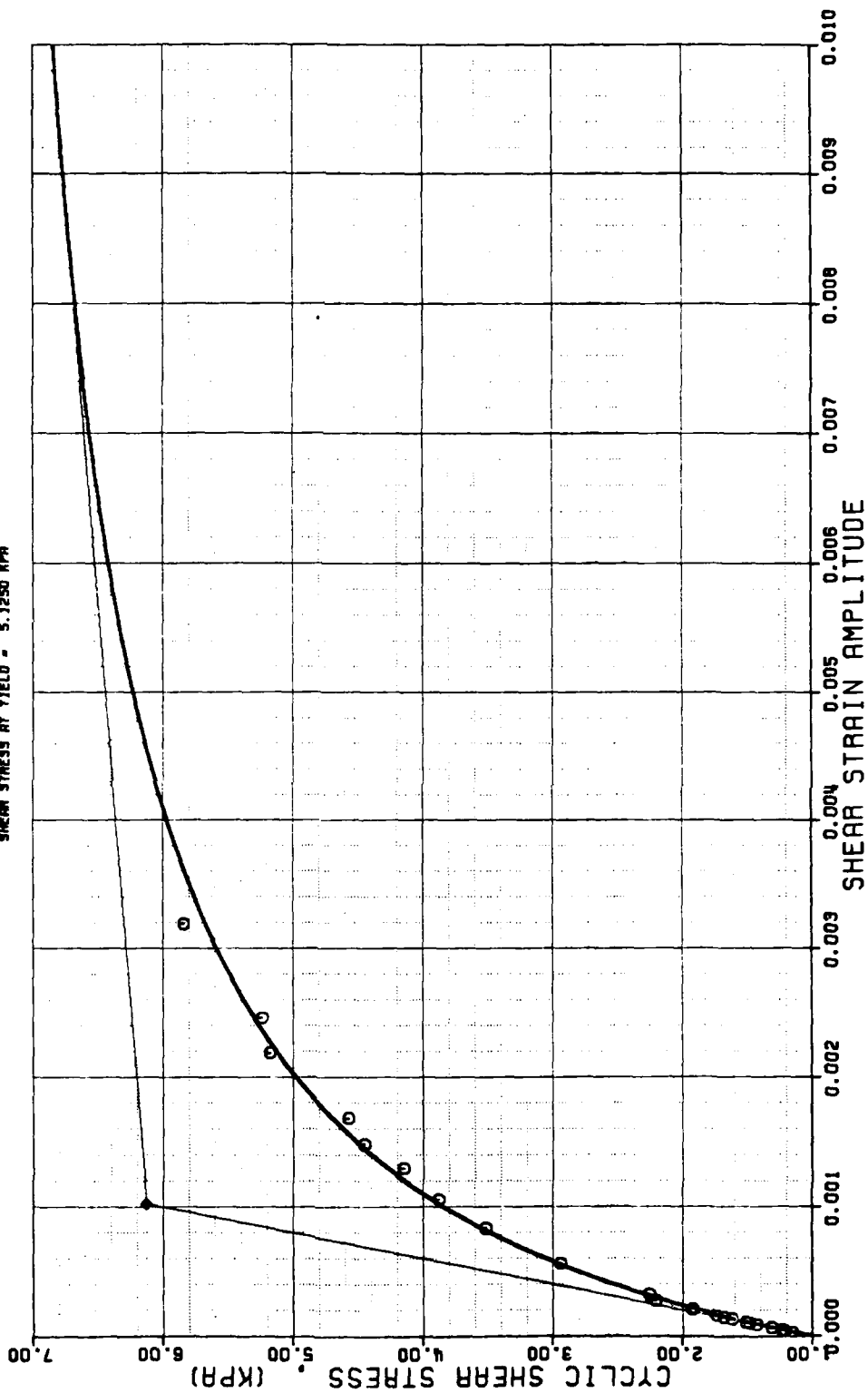


A_70

THE VARIATION OF SHEAR STRESS WITH STRAIN AMPLITUDE DEEP CORE SAMPLES OF GULF OF MEXICO

SAMPLE DEPTH = 58.07 M.

SHEAR STRESS AT YIELD = 5.1250 KPA

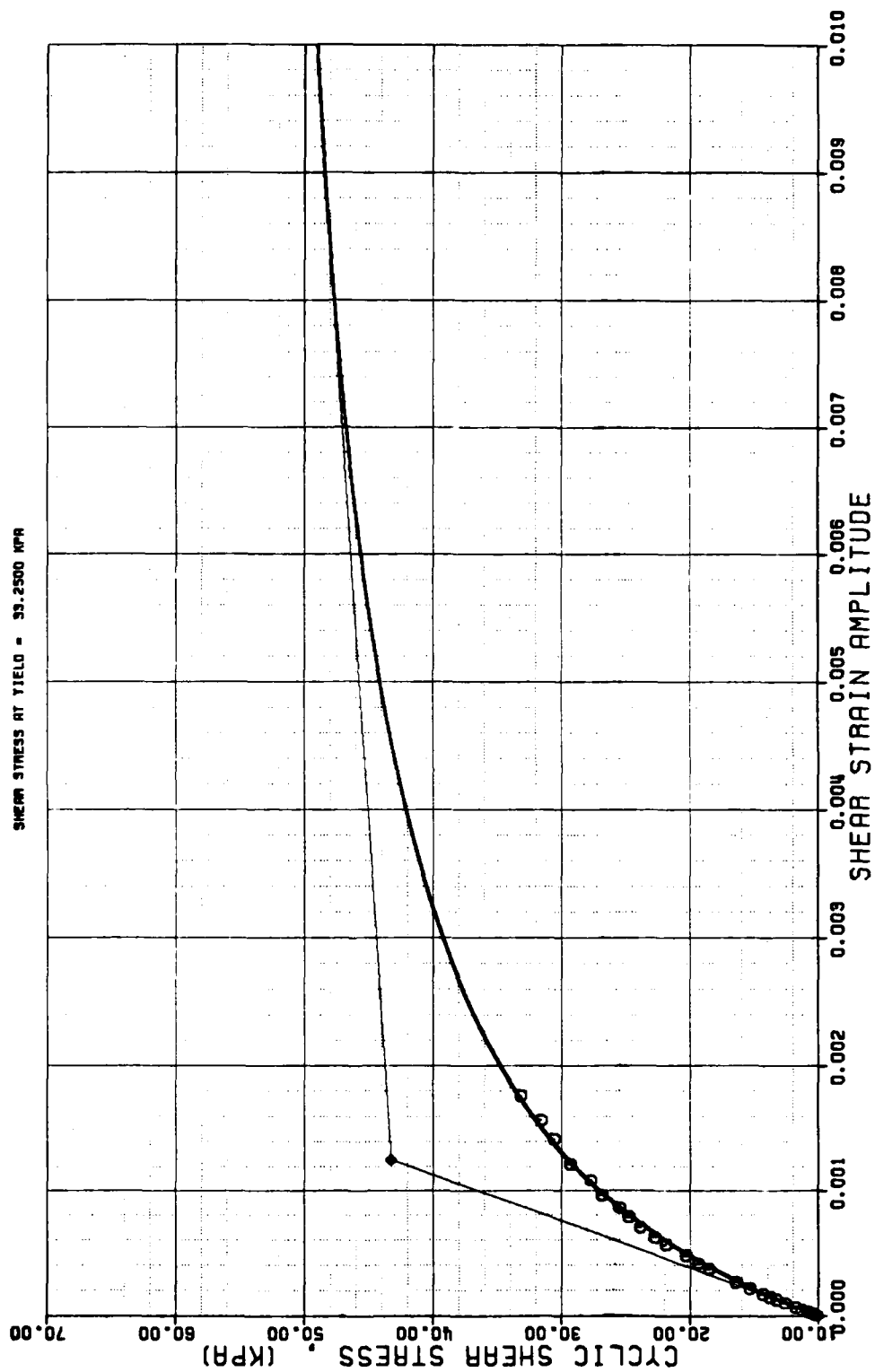


THE VARIATION OF SHEAR STRESS WITH STRAIN AMPLITUDE

DEEP CORE SAMPLES OF GULF OF MEXICO

SAMPLE DEPTH = 71.32 M.

SHEAR STRESS AT YIELD = 53.2500 KPA

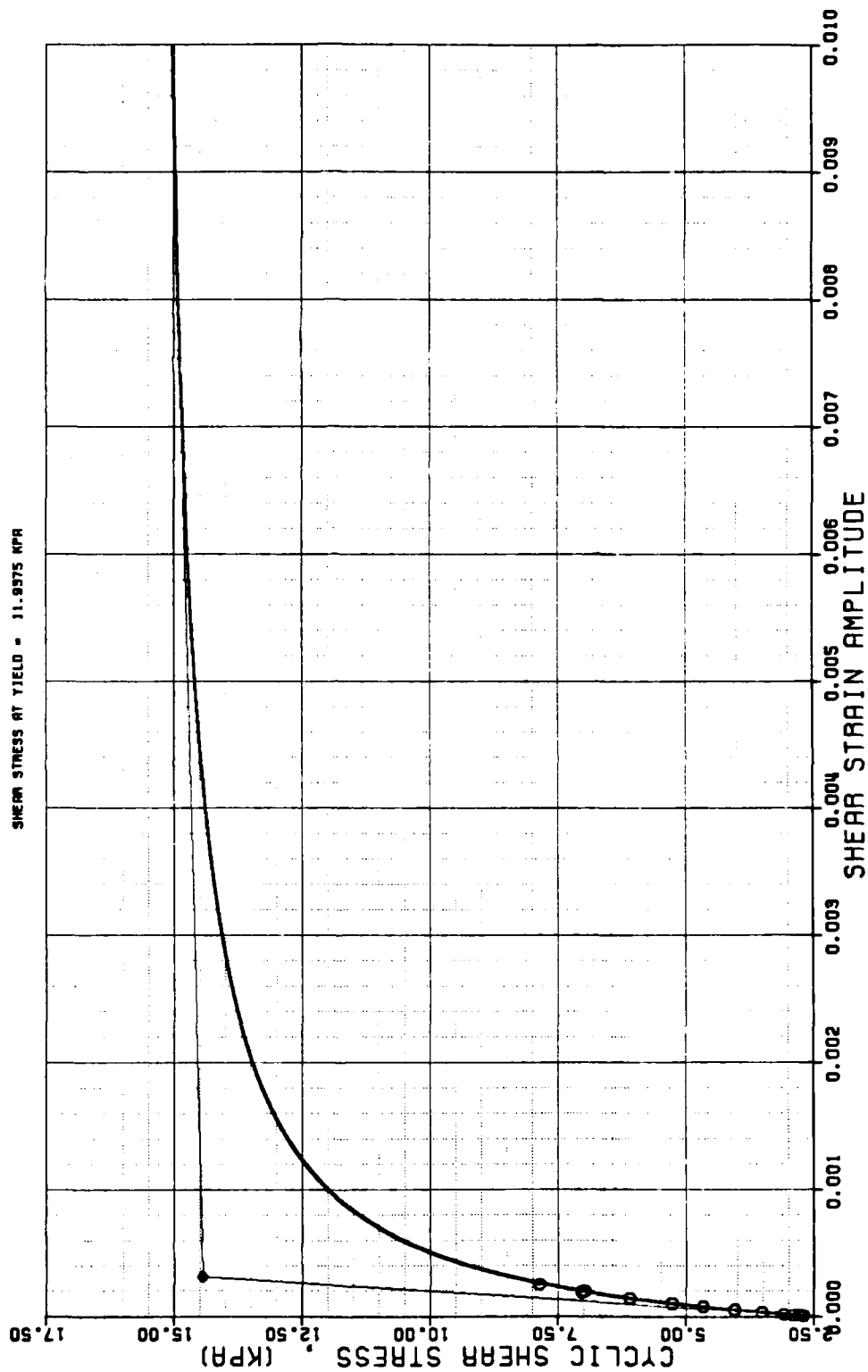


THE VARIATION OF SHEAR STRESS WITH STRAIN AMPLITUDE

DEEP CORE SAMPLES OF GULF OF MEXICO

SAMPLE DEPTH = 101.00 M.

SHEAR STRESS AT YIELD = 11.9375 KPA

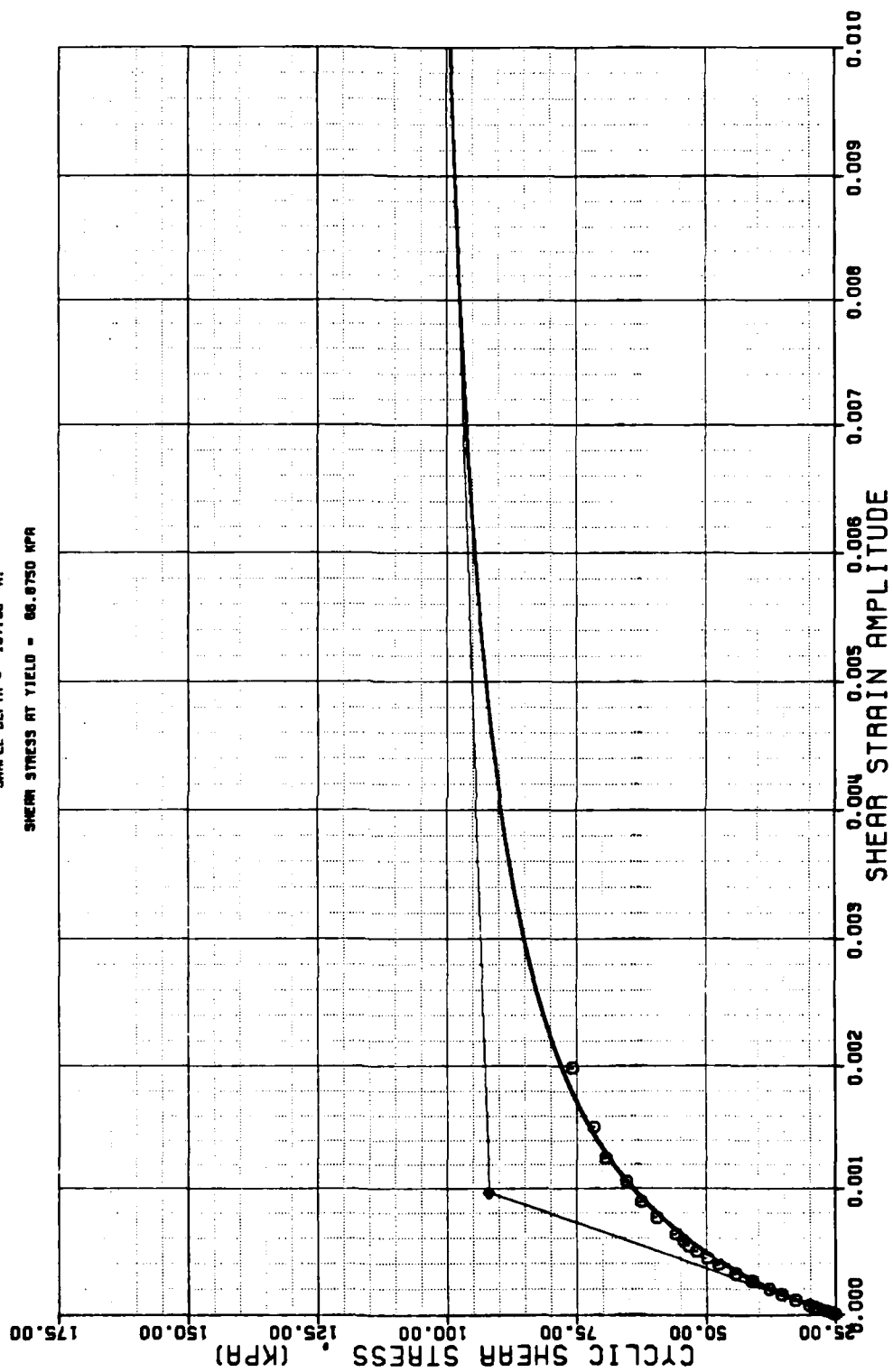


THE VARIATION OF SHEAR STRESS WITH STRAIN AMPLITUDE

DEEP CONE SAMPLES OF GULF OF MEXICO

SAMPLE DEPTH = 107.66 M.

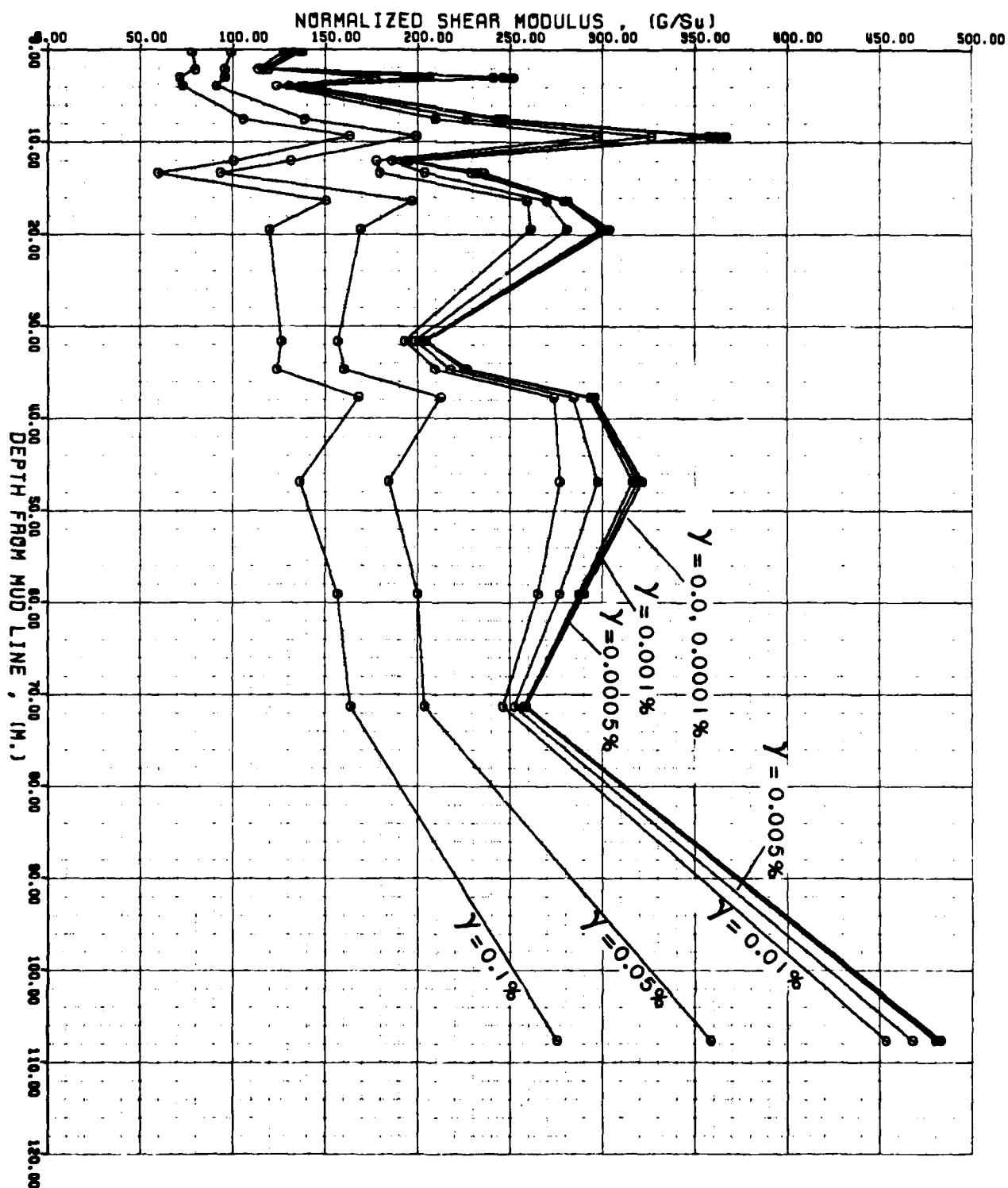
SHEAR STRESS AT YIELD = 86.8750 KPA



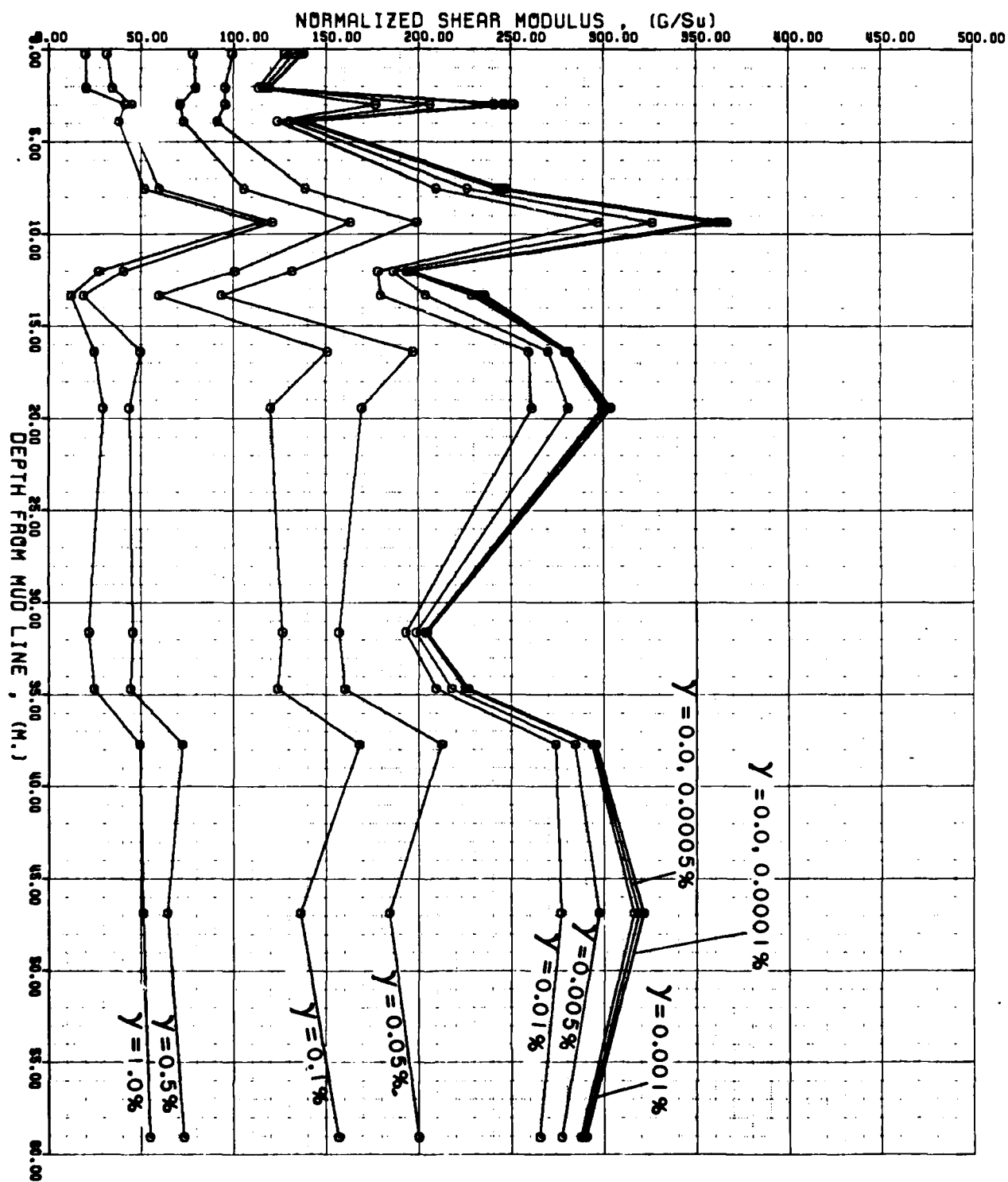
APPENDIX A-75/A-76

VARIATION OF S_v -NORMALIZED SHEAR MODULUS WITH
DEPTH FOR DIFFERENT SHEAR STRAIN VALUES

THE VARIATION OF NORMALIZED SHEAR MODULUS WITH DEPTH DEEP CORE SAMPLES OF GULF OF MEXICO



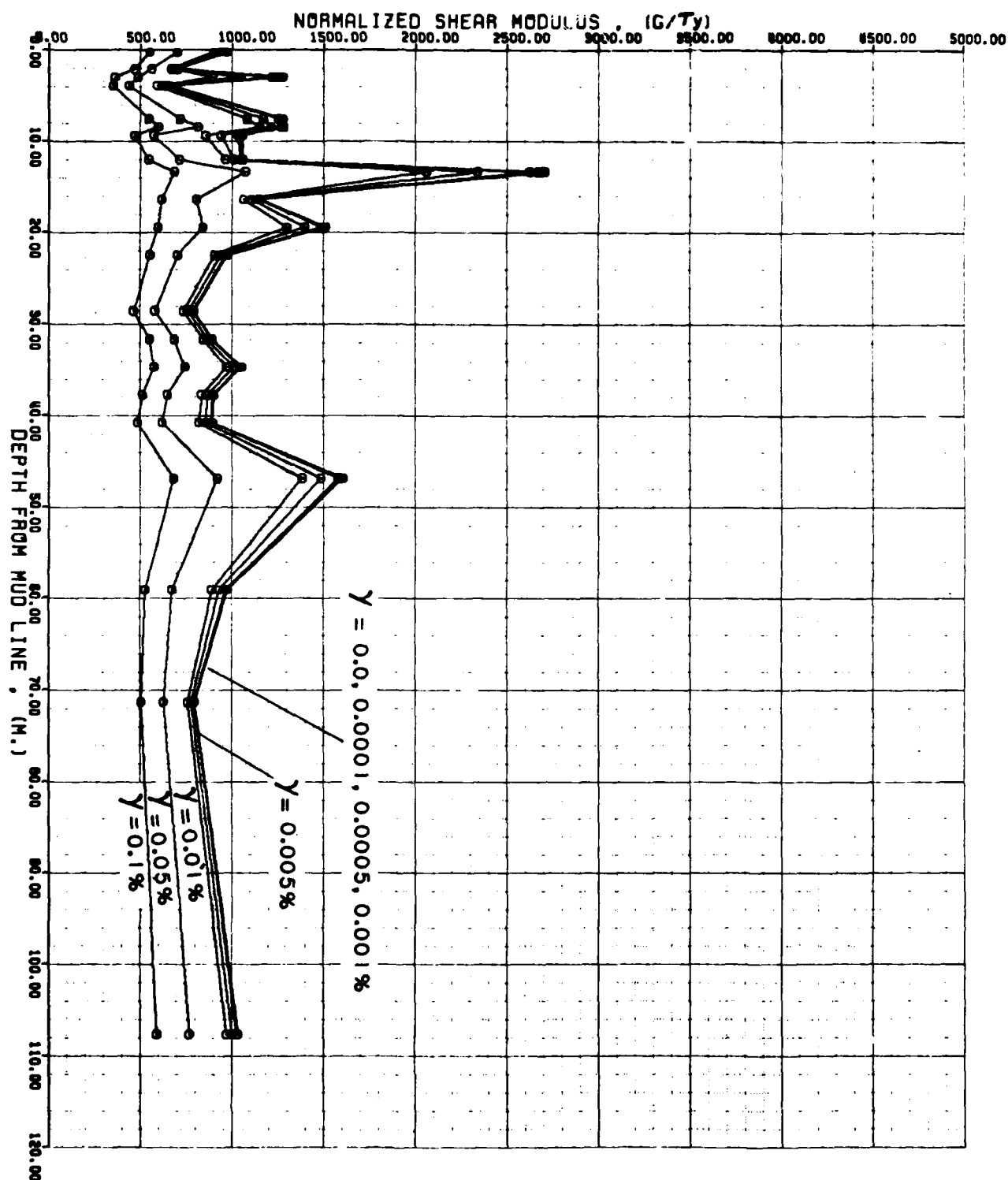
THE VARIATION OF NORMALIZED SHEAR MODULUS WITH DEPTH DEEP CORE SAMPLES OF GULF OF MEXICO



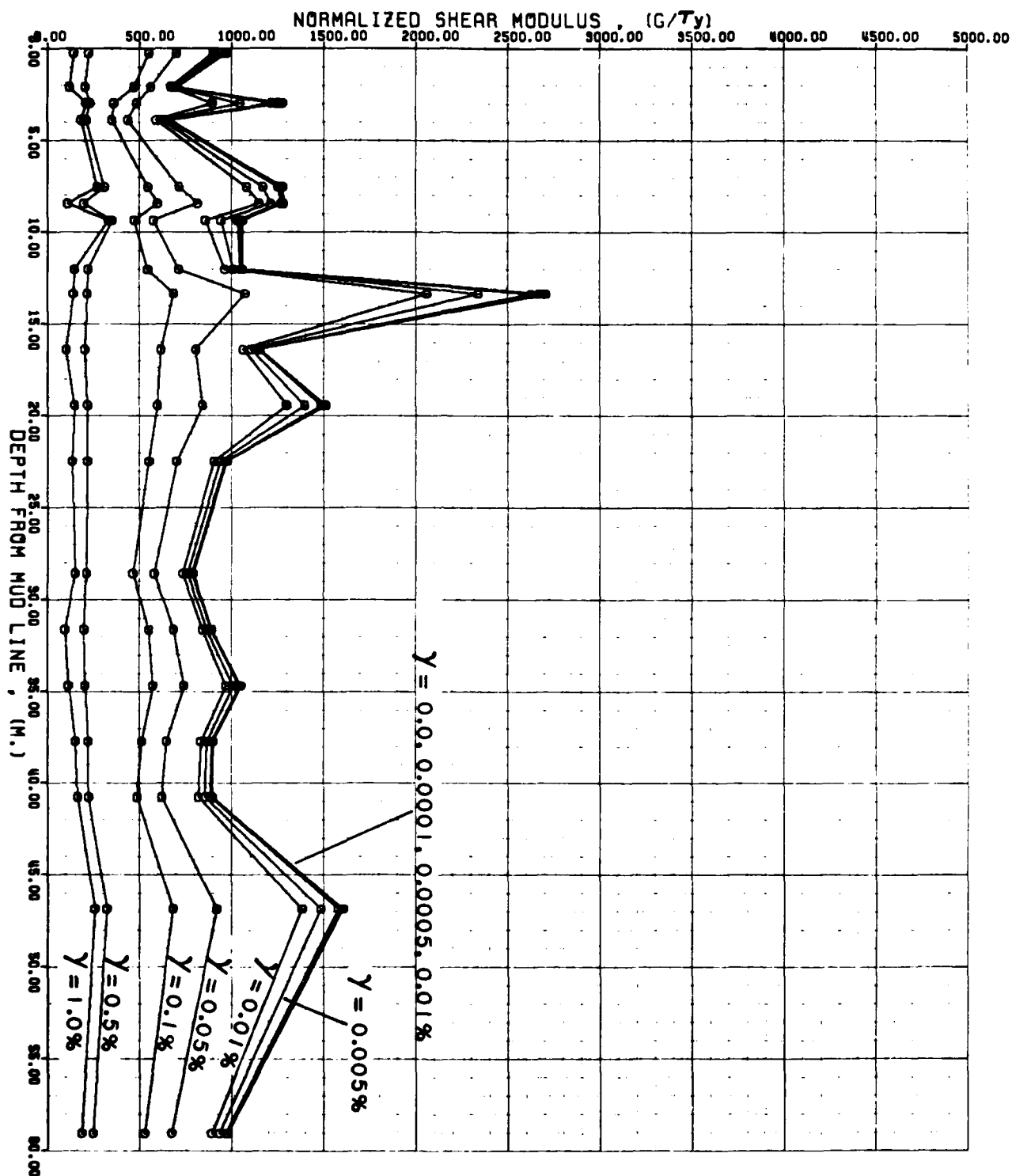
APPENDIX A-77/A-78

VARIATION OF τ_y -NORMALIZED SHEAR MODULUS WITH
DEPTH FOR DIFFERENT SHEAR STRAIN VALUES

THE VARIATION OF NORMALIZED SHEAR MODULUS WITH DEPTH DEEP CORE SAMPLES OF GULF OF MEXICO



THE VARIATION OF NORMALIZED SHEAR MODULUS WITH DEPTH DEEP CORE SAMPLES OF GULF OF MEXICO



AD-A118 157

LOUISIANA STATE UNIV BATON ROUGE DEPT OF CIVIL ENGIN--ETC F/G 8/10
CLASSIFICATION OF COASTAL SEDIMENTS.(U)
MAR 82 J N SUHAYDA; M TUMAY

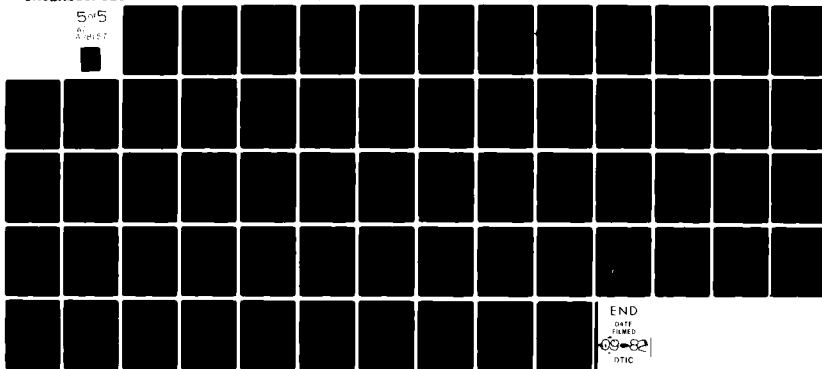
N00014-80-C-0846

UNCLASSIFIED

ML

5-5

2-15-82

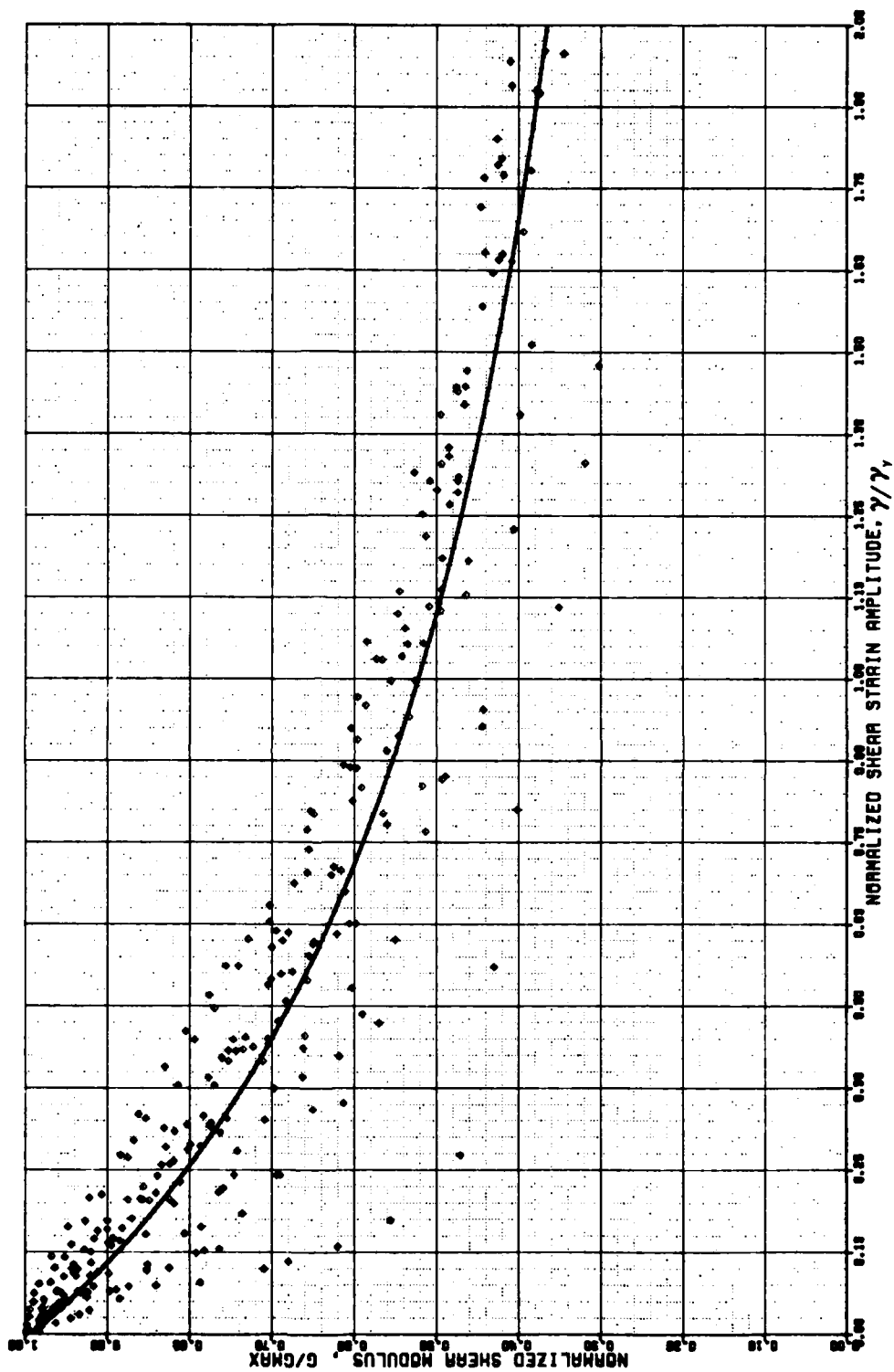


END
DATE
FILMED
09-82
DTIC

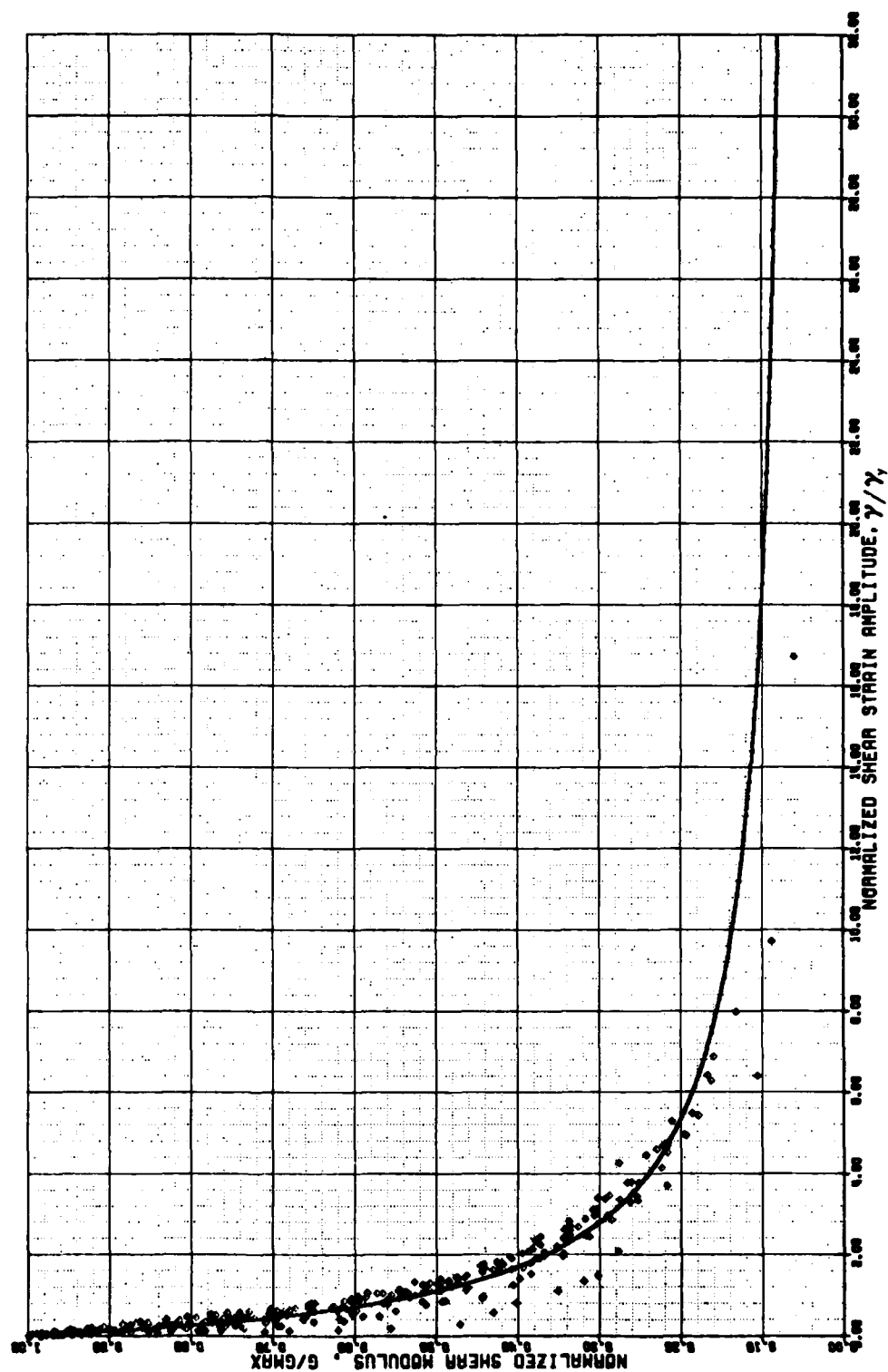
APPENDIX A-79/A-80

VARIATION OF NORMALIZED SHEAR MODULUS WITH
 γ_y - NORMALIZED SHEAR STRAIN

THE VARIATION OF SHEAR MODULUS WITH STRAIN AMPLITUDE
DEEP CORE SAMPLES OF GULF OF MEXICO



THE VARIATION OF SHEAR MODULUS WITH STRAIN AMPLITUDE
DEEP CORE SAMPLES OF GULF OF MEXICO

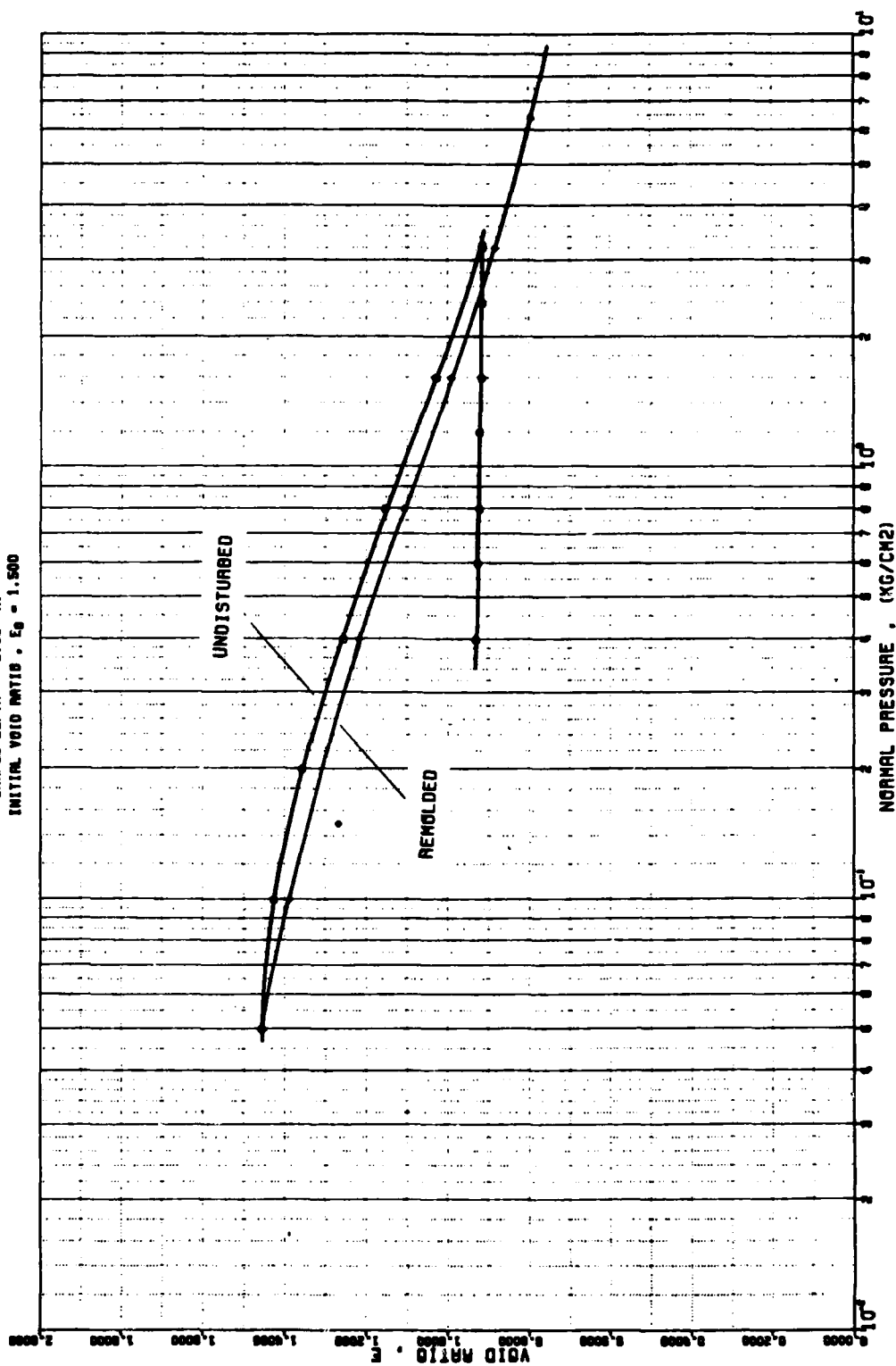


APPENDIX A-81/A-84

COMPRESSION CURVES FOR UNDISTURBED AND REMOLDED SAMPLES

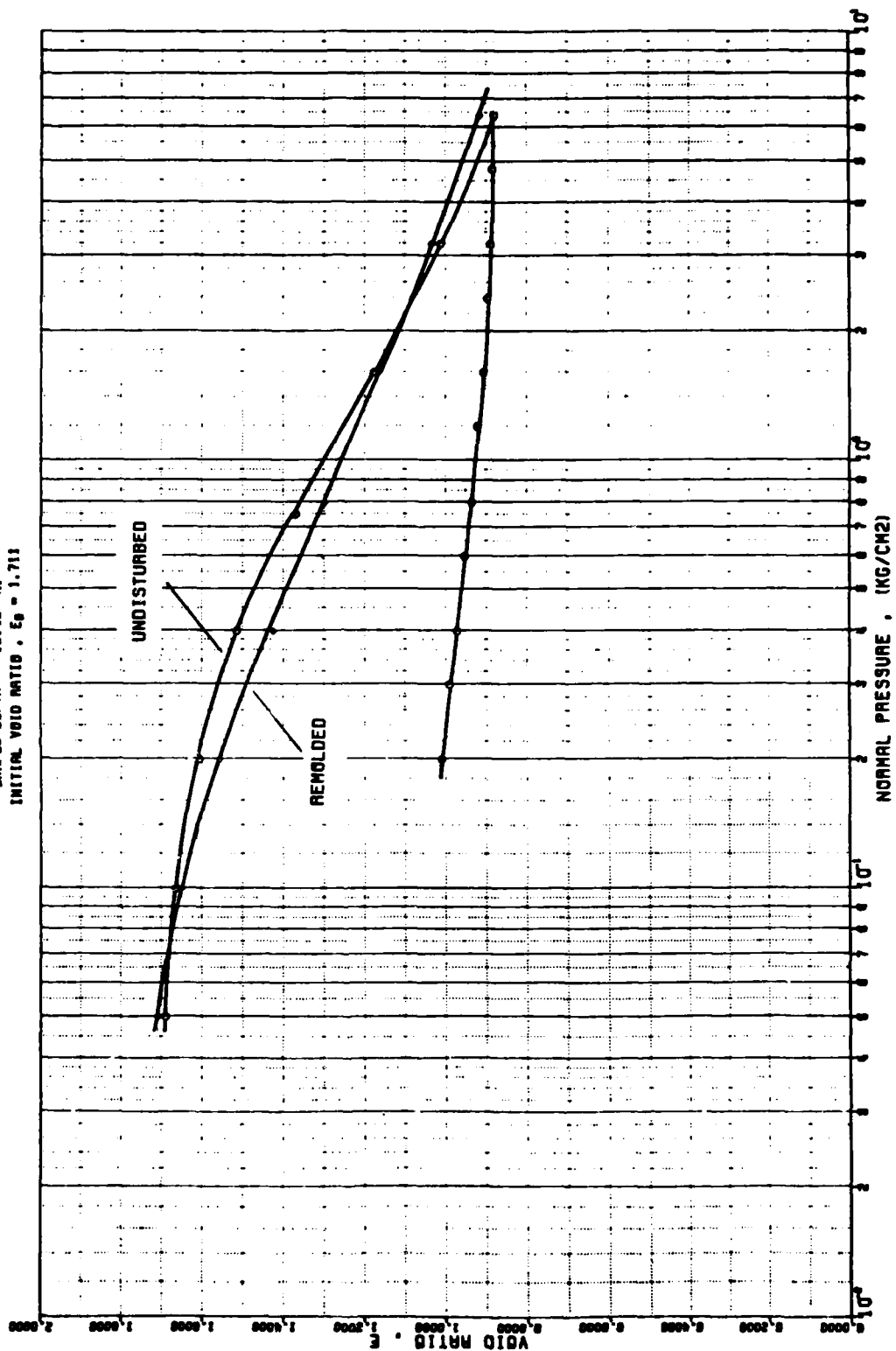
CONSOLIDATION TEST DATA DEEP CORE SAMPLES OF GULF OF MEXICO

SAMPLE DEPTH = 2.98 M.
INITIAL VOID RATIO, $e_0 = 1.500$



CONSOLIDATION TEST DATA DEEP CORE SAMPLES OF GULF OF MEXICO

SAMPLE DEPTH = 16.40 M.
INITIAL VOID RATIO, $e_0 = 1.713$

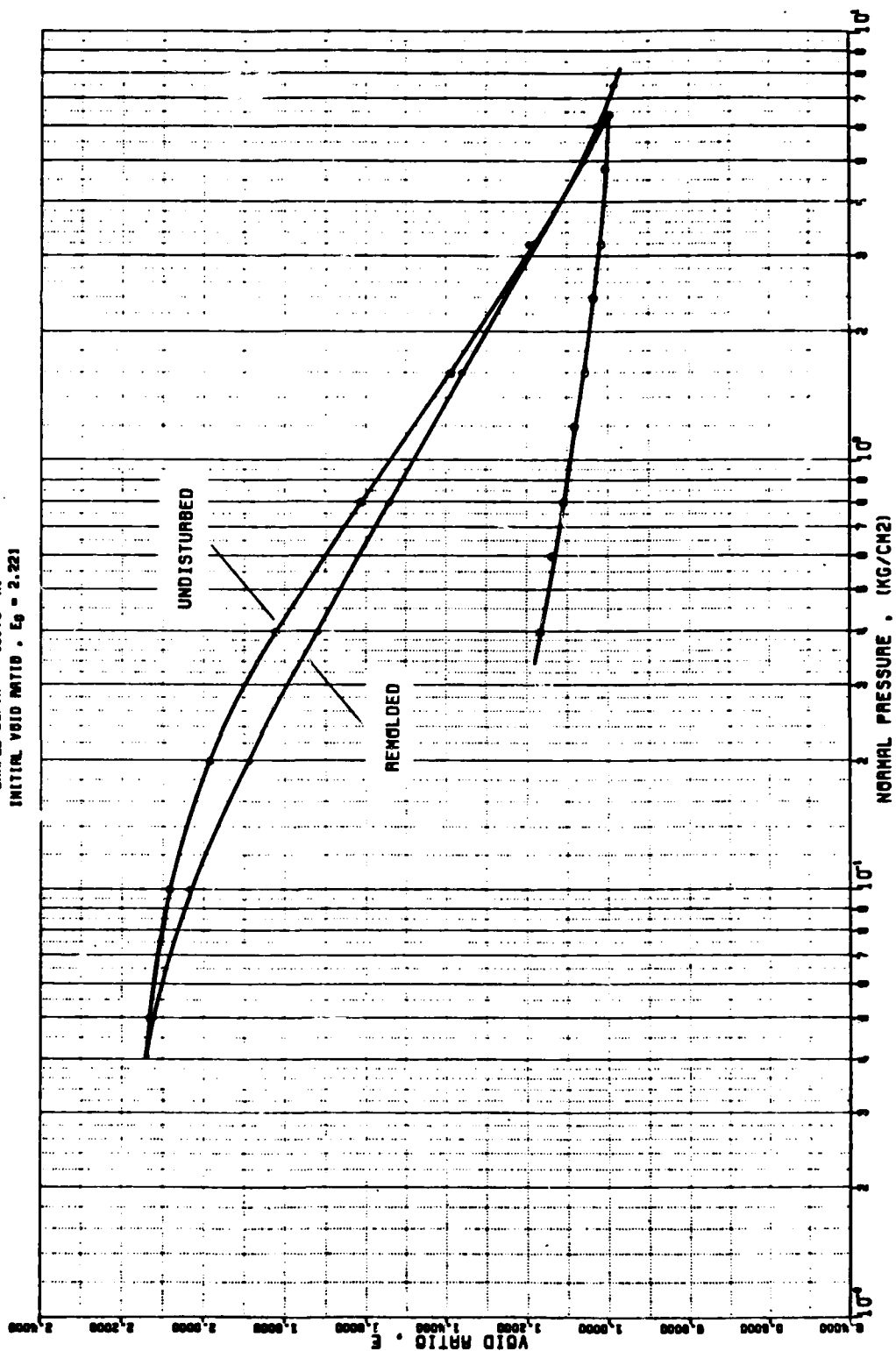


CONSOLIDATION TEST DATA

DEEP CORE SAMPLES OF GULF OF MEXICO

SAMPLE DEPTH - 40.78 M.

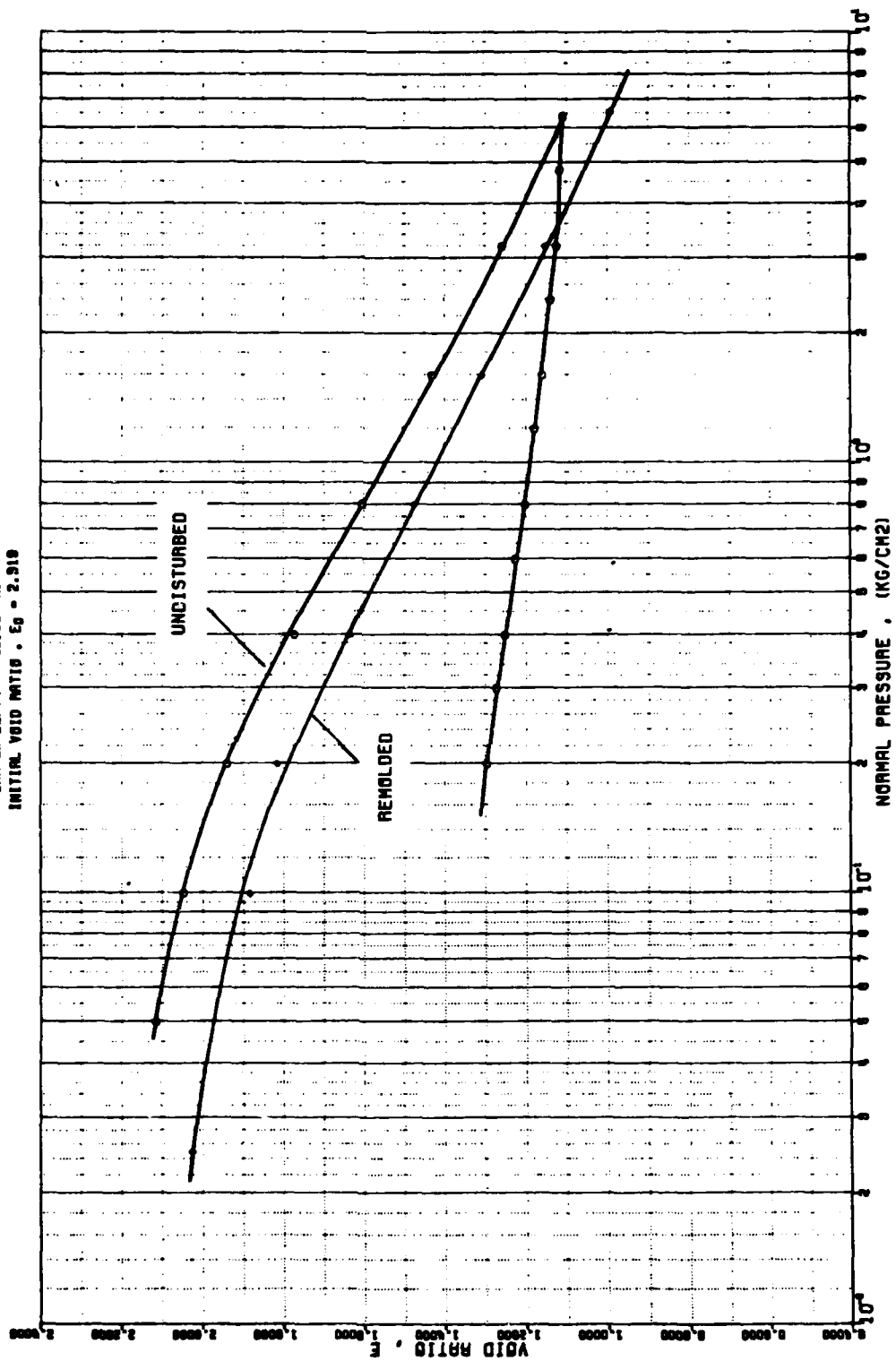
INITIAL VOID RATIO, $e_0 = 2.221$



CONSOLIDATION TEST DATA

DEEP CORE SAMPLES OF GULF OF MEXICO

SAMPLE DEPTH - 48.00 M.
INITIAL VOID RATIO $e_0 = 2.919$

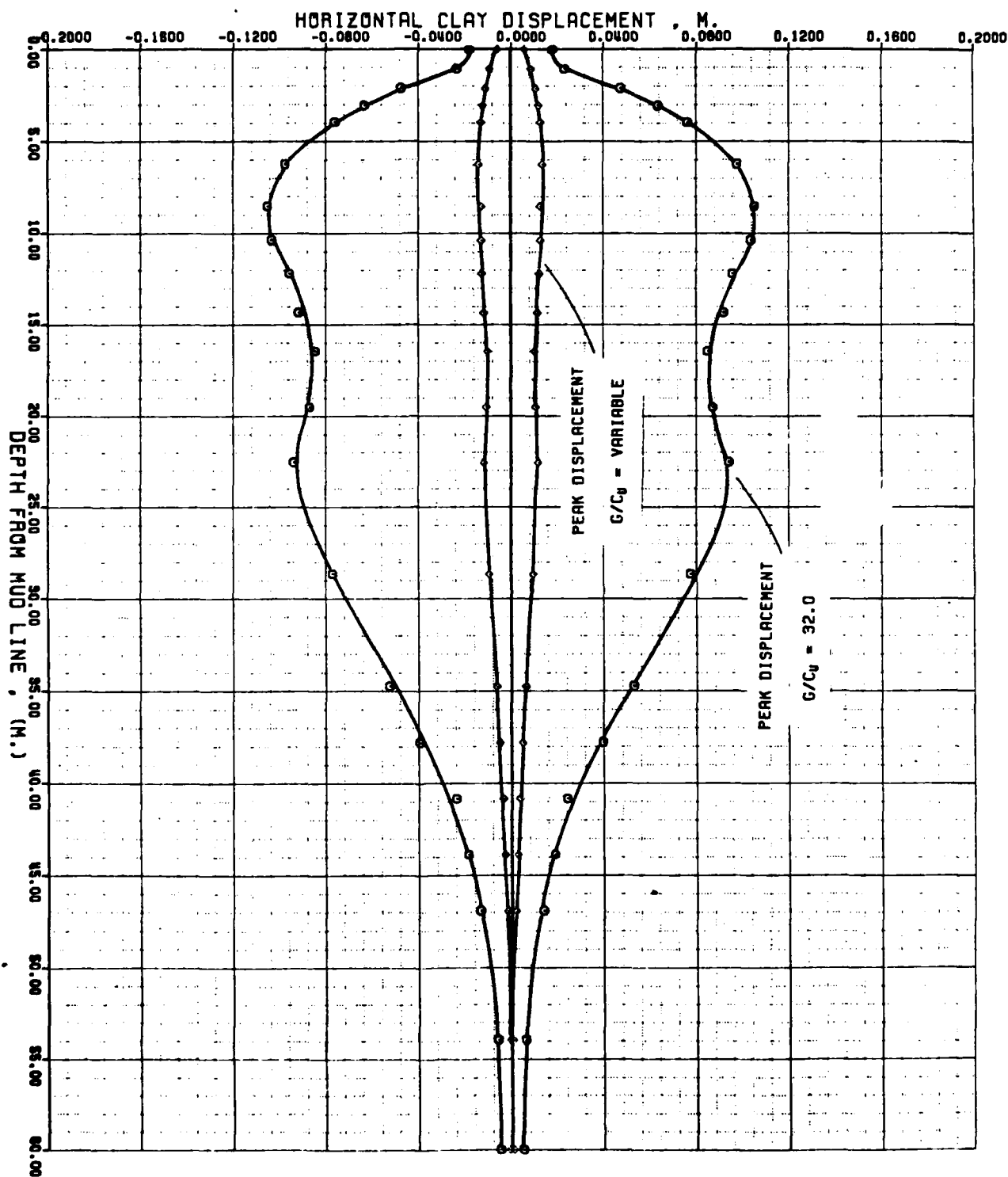


APPENDIX B
NUMERICAL ANALYSIS RESULTS

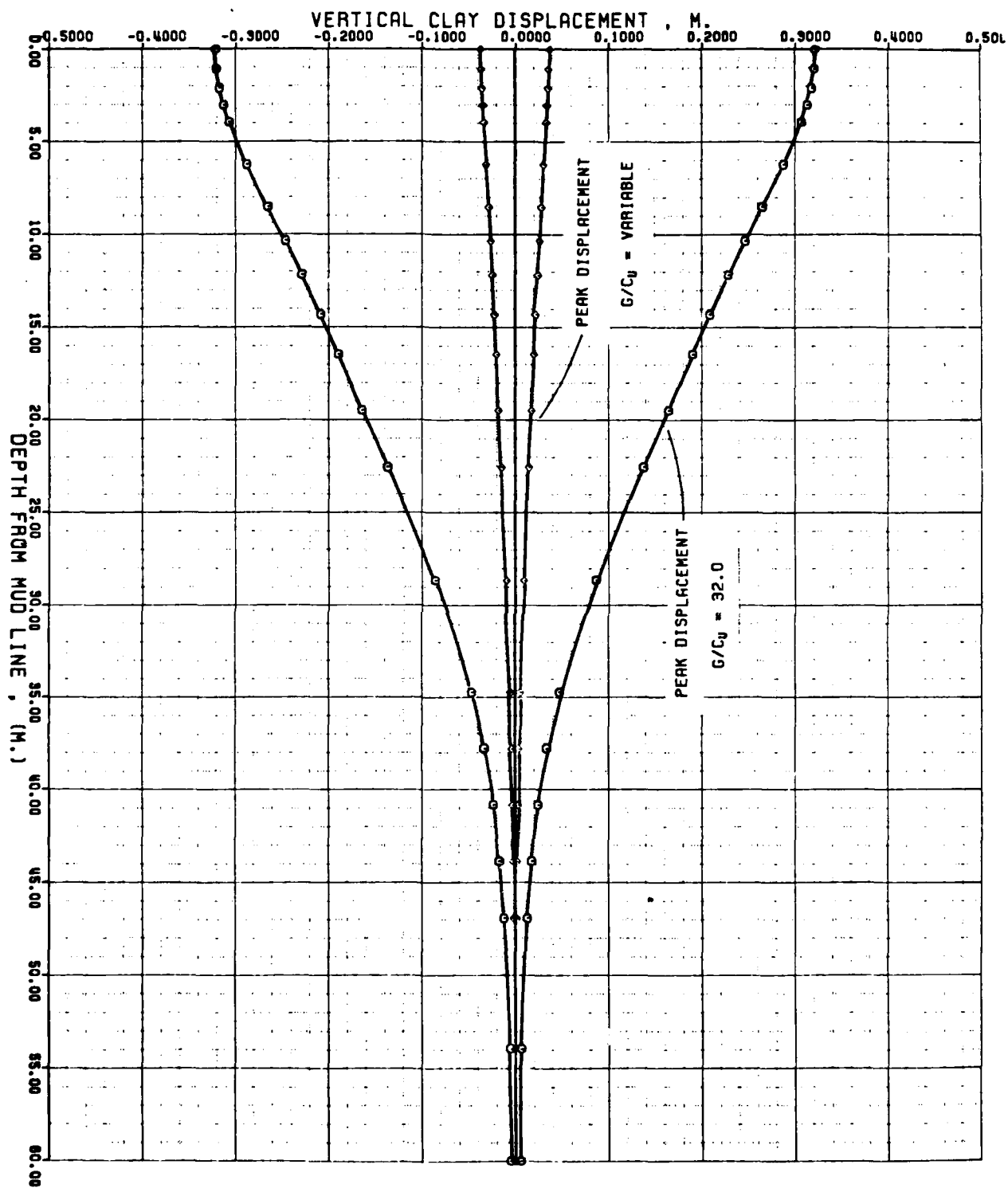
APPENDIX B-1/B-4

STATIC AND KINEMATIC PROFILES OBTAINED FROM VISCOELASTIC
SUB-BOTTOM WAVE PROPAGATION INTERACTION ANALYSIS

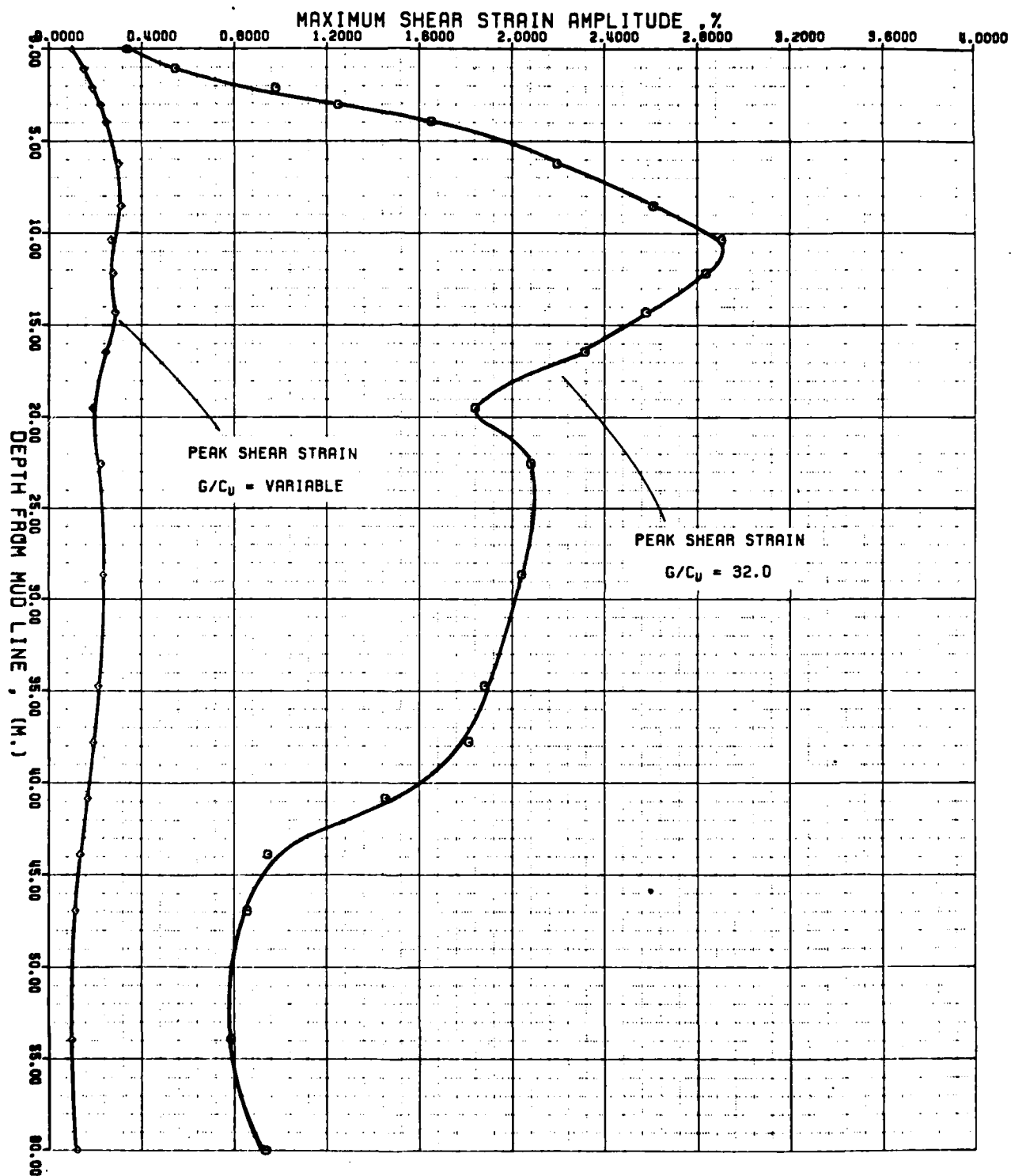
THE VARIATION OF CLAY DISPLACEMENT WITH DEPTH DEEP CORE SAMPLES OF GULF OF MEXICO



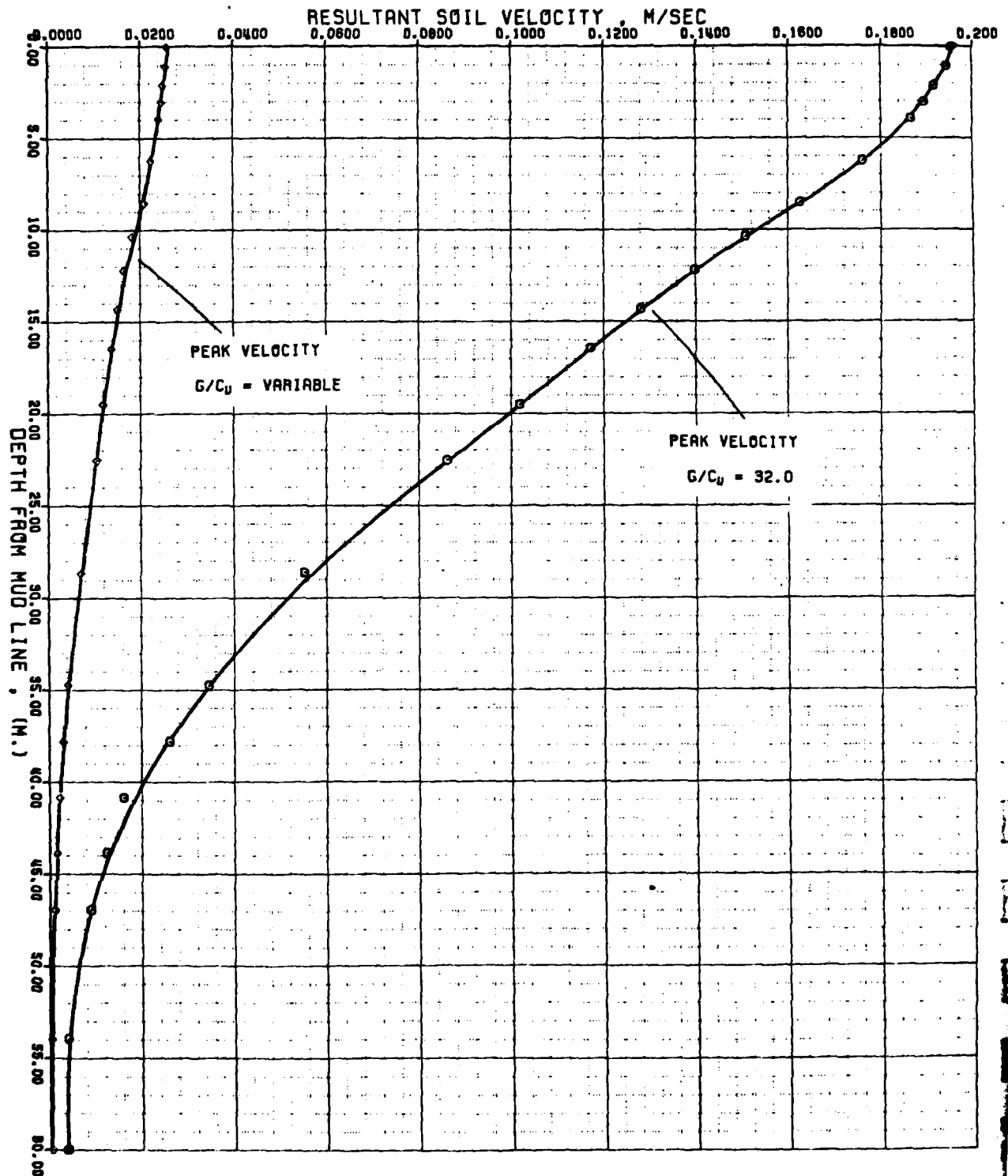
THE VARIATION OF CLAY DISPLACEMENT WITH DEPTH DEEP CORE SAMPLES OF GULF OF MEXICO



THE VARIATION OF STRAIN AMPLITUDE WITH DEPTH DEEP CORE SAMPLES OF GULF OF MEXICO



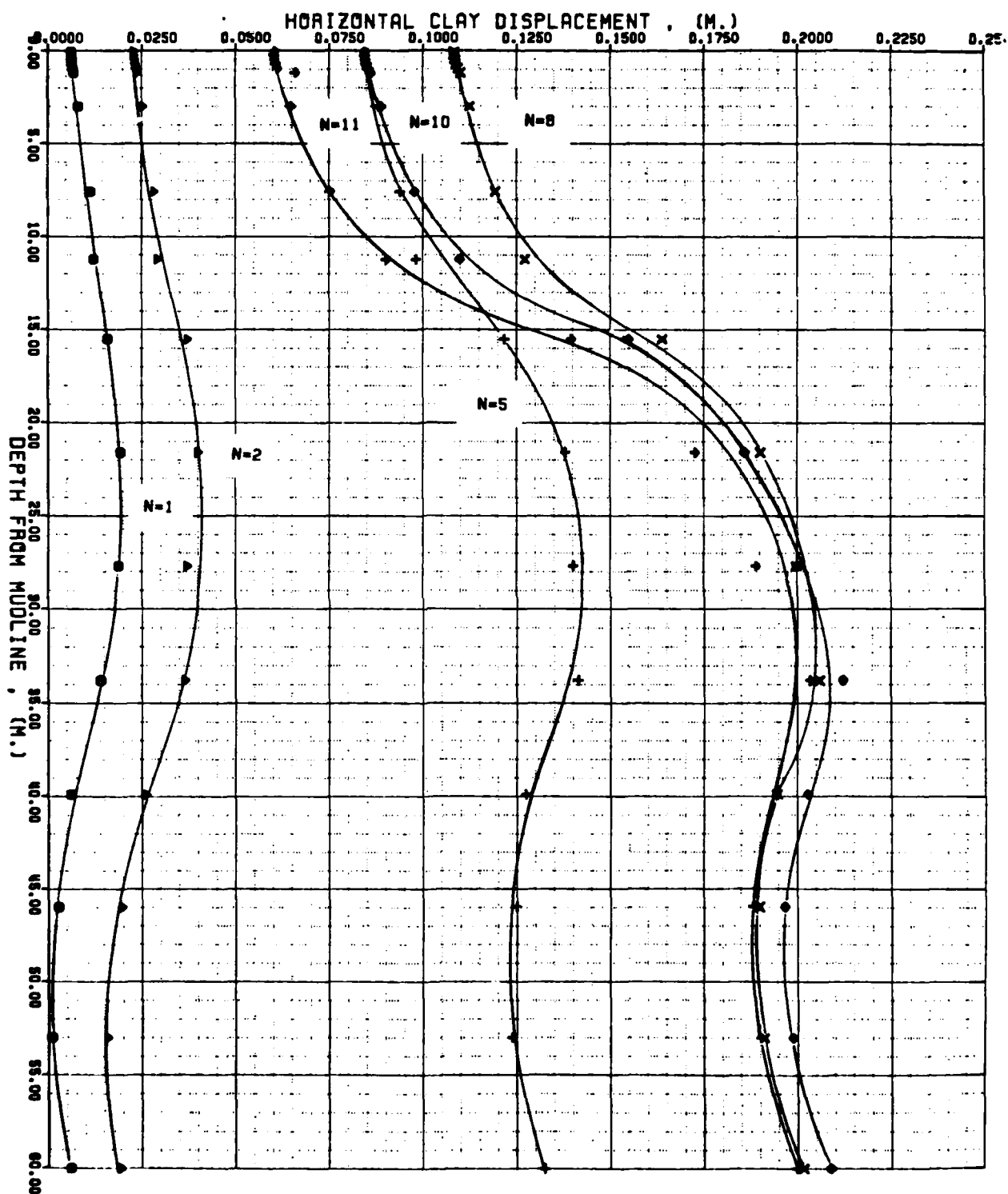
THE VARIATION OF SOIL VELOCITY WITH DEPTH DEEP CORE SAMPLES OF GULF OF MEXICO



APPENDIX B-5/B-10

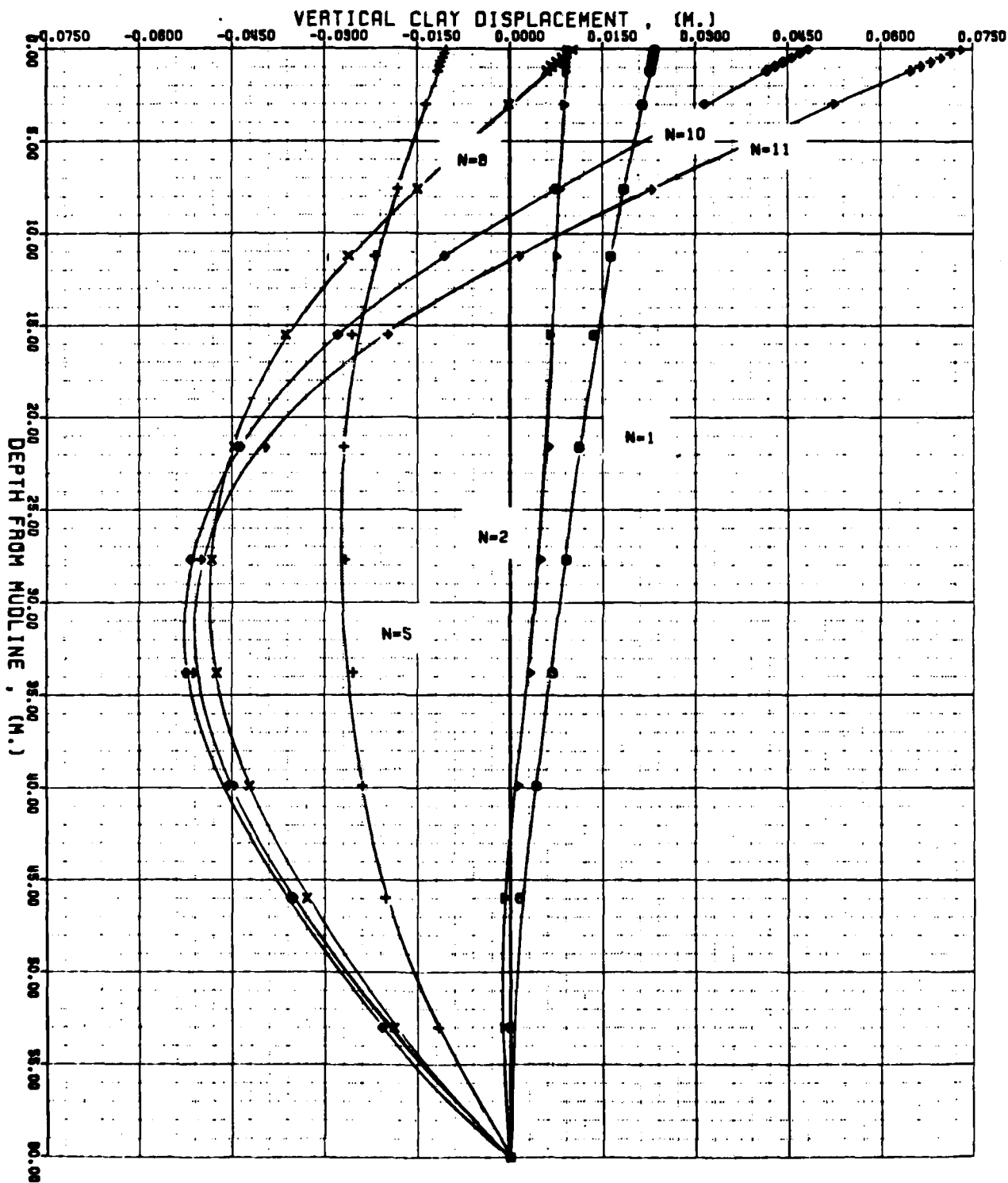
STATIC AND KINEMATIC PROFILES OBTAINED FROM NONSAP
ANALYSIS FOR THE Laterally-FREE-BOUNDARY CASE

THE VARIATION OF CLAY DISPLACEMENT WITH DEPTH DEEP CORE SAMPLES OF GULF OF MEXICO



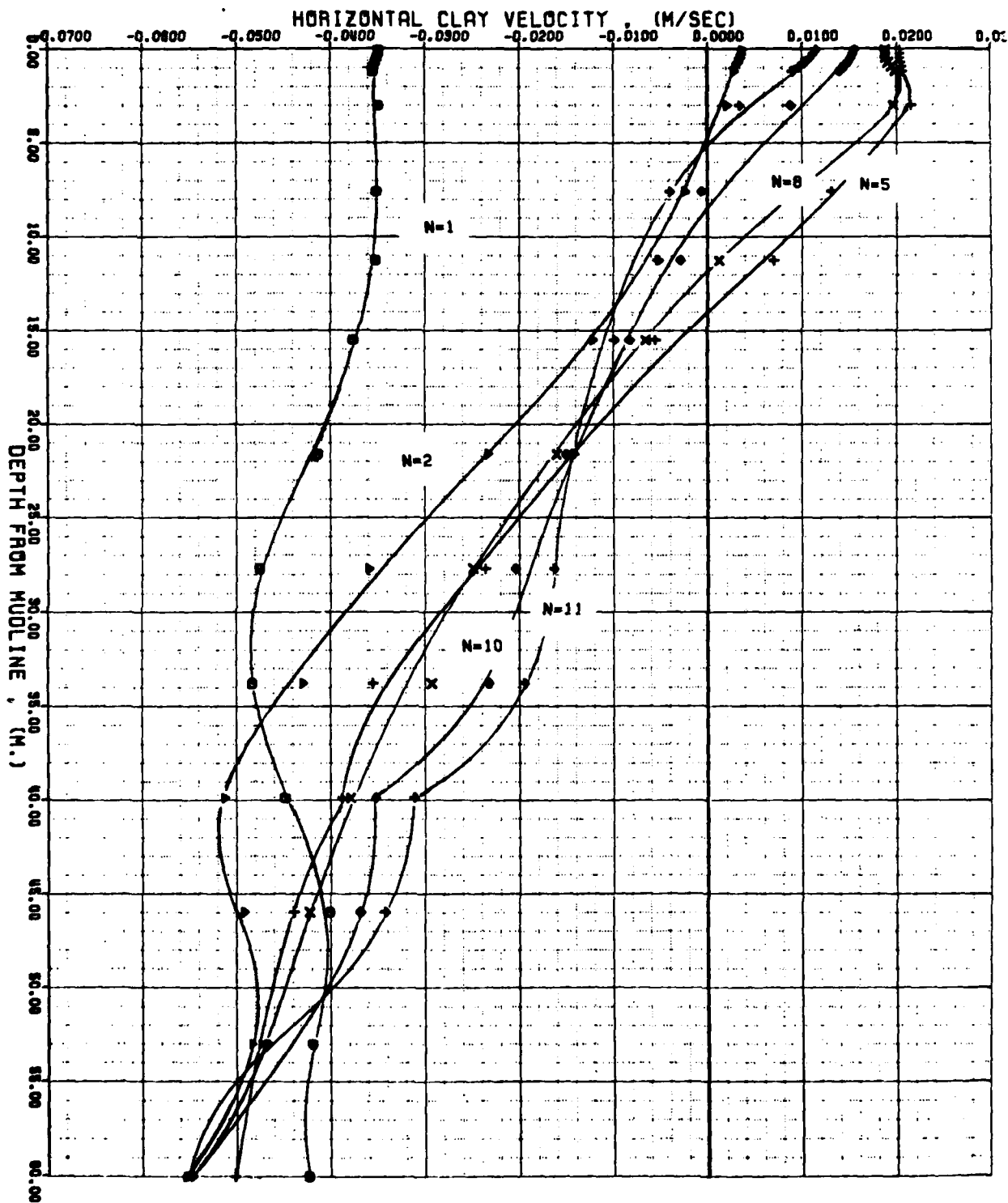
THE VARIATION OF CLAY DISPLACEMENT WITH DEPTH

DEEP CORE SAMPLES OF GULF OF MEXICO

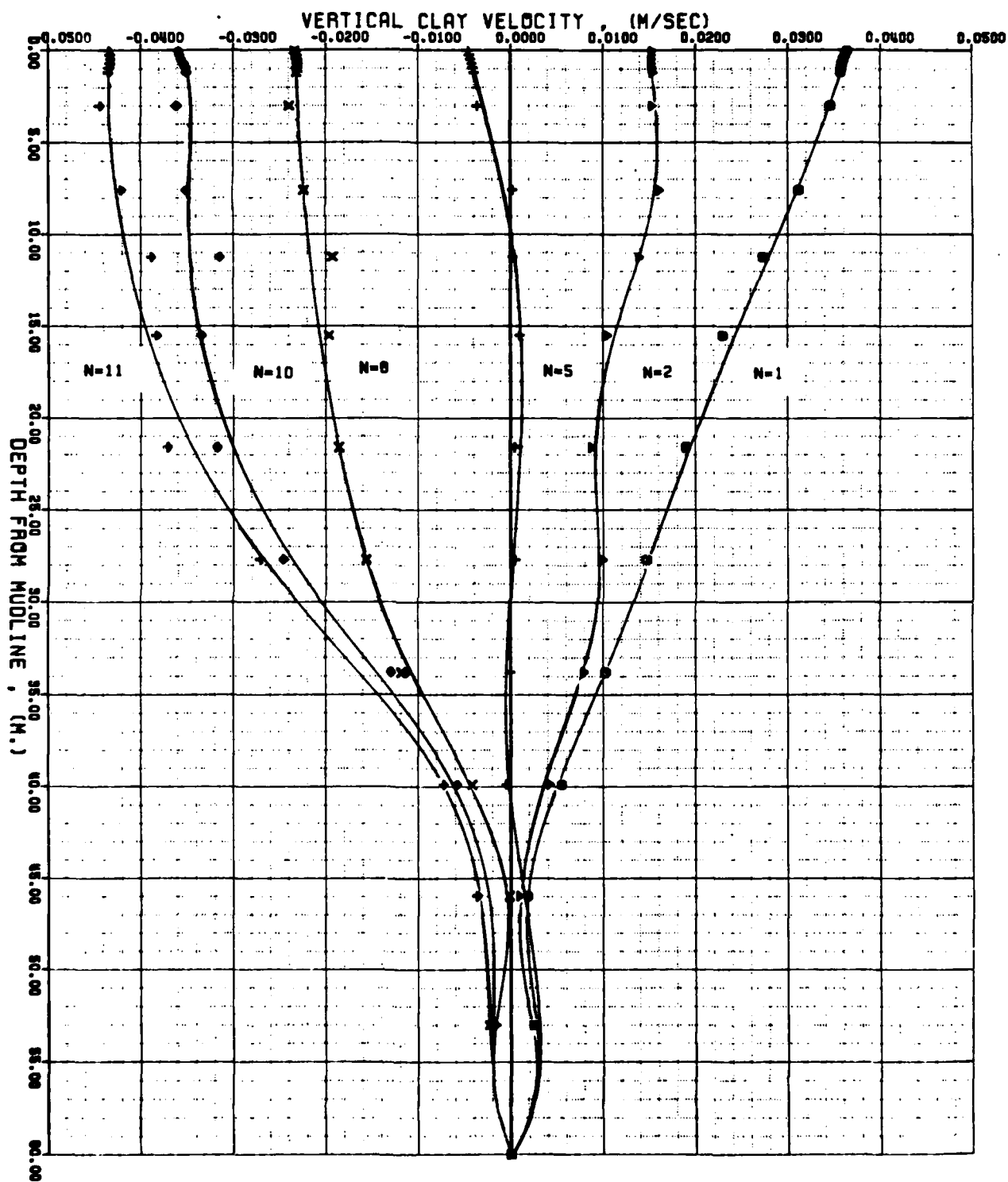


THE VARIATION OF CLAY VELOCITY WITH DEPTH

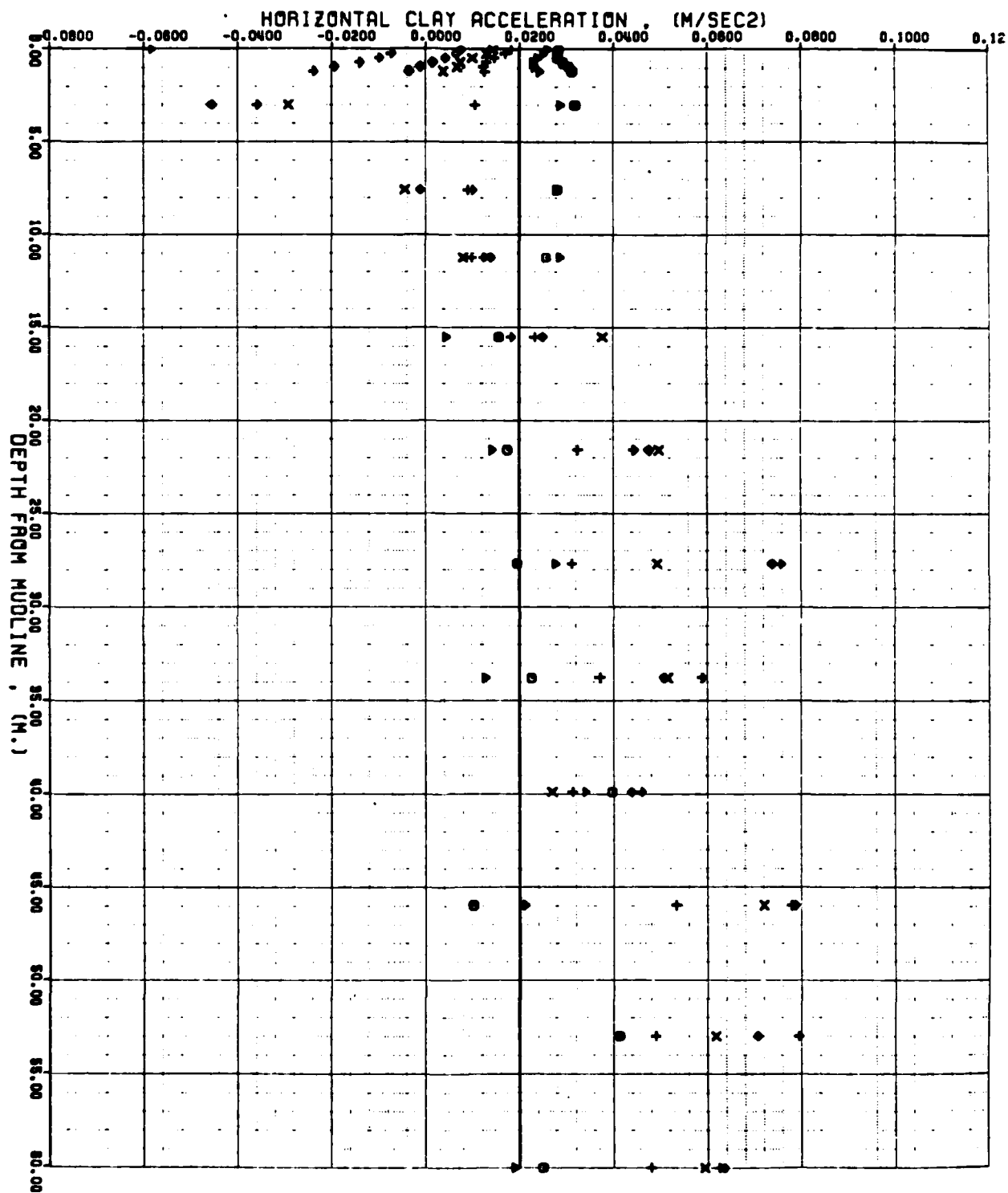
DEEP CORE SAMPLES OF GULF OF MEXICO



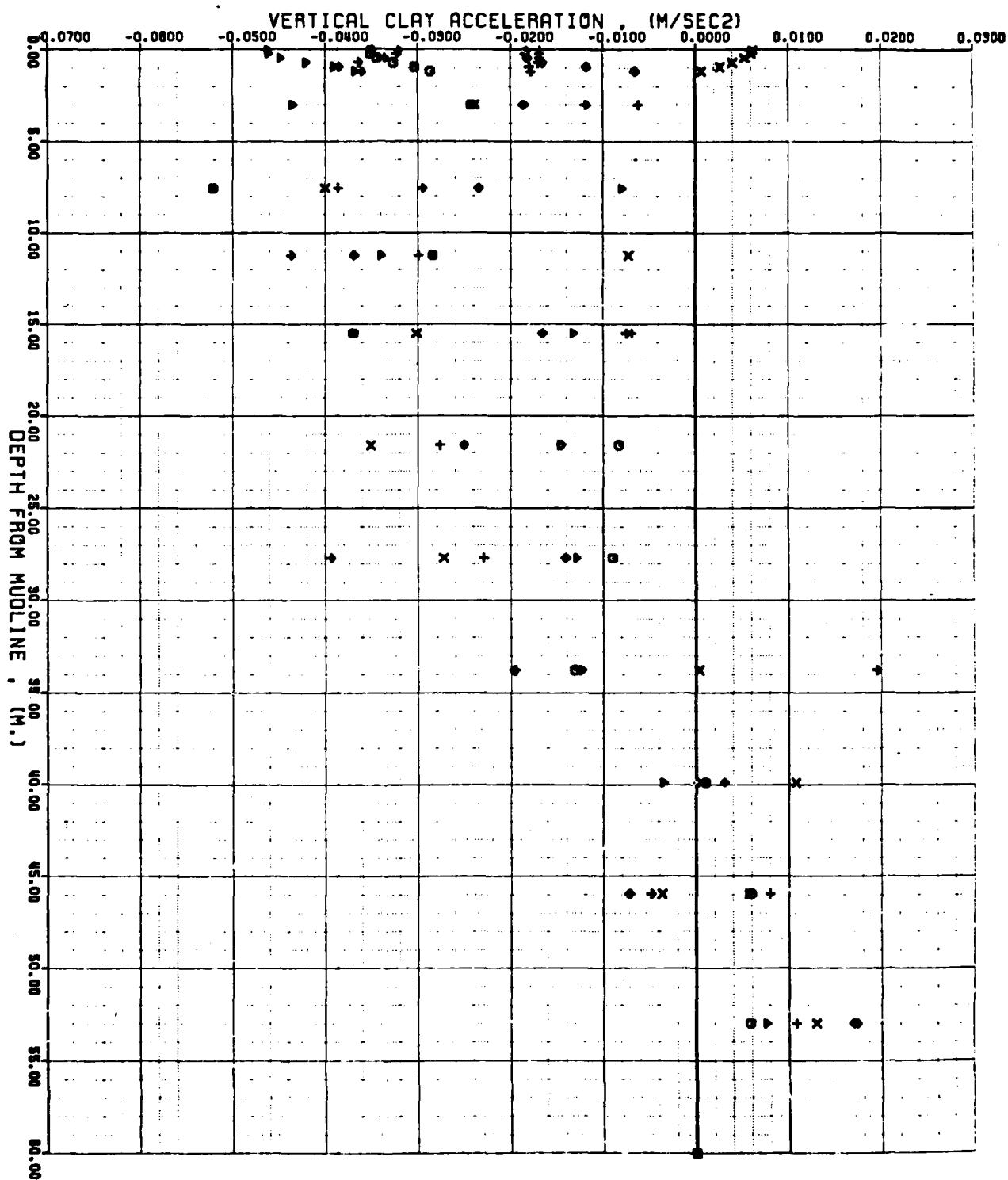
THE VARIATION OF CLAY VELOCITY WITH DEPTH DEEP CORE SAMPLES OF GULF OF MEXICO



THE VARIATION OF CLAY ACCELERATION WITH DEPTH DEEP CORE SAMPLES OF GULF OF MEXICO



THE VARIATION OF CLAY ACCELERATION WITH DEPTH DEEP CORE SAMPLES OF GULF OF MEXICO

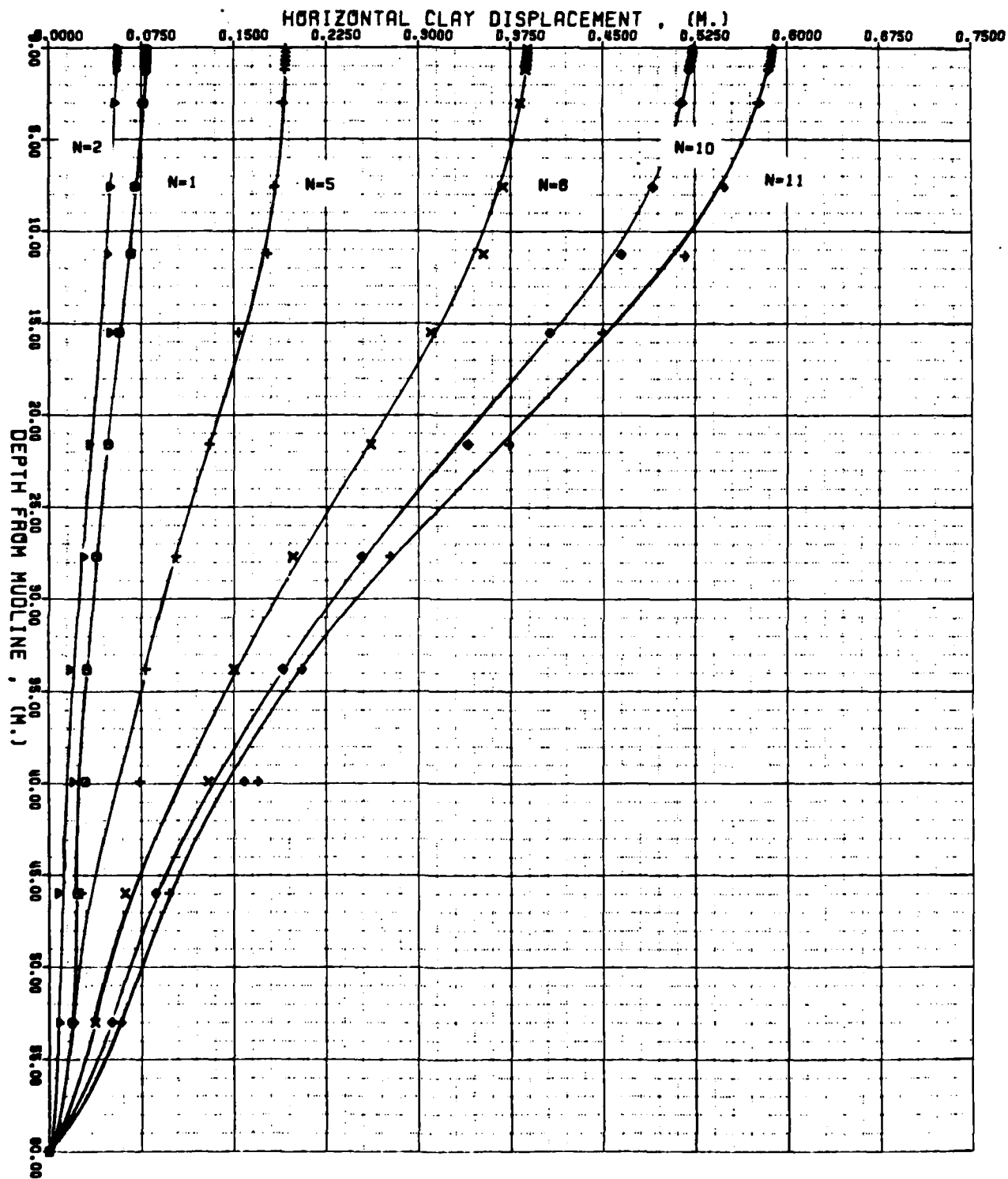


APPENDIX B-11/B-16

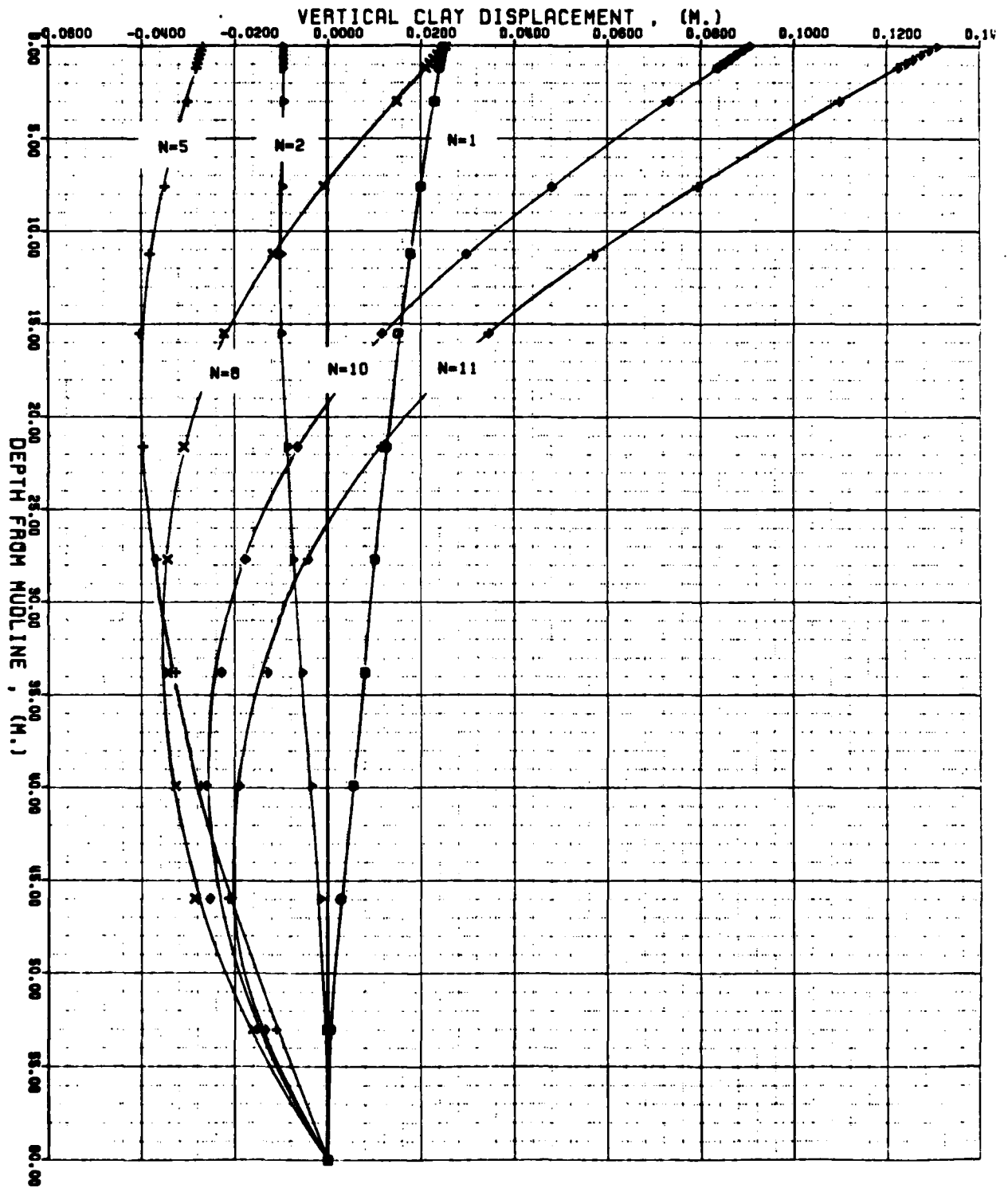
STATIC AND KINEMATIC PROFILES OBTAINED FROM NONSAP
ANALYSIS FOR THE FIXED-BOUNDARY CASE

THE VARIATION OF CLAY DISPLACEMENT WITH DEPTH

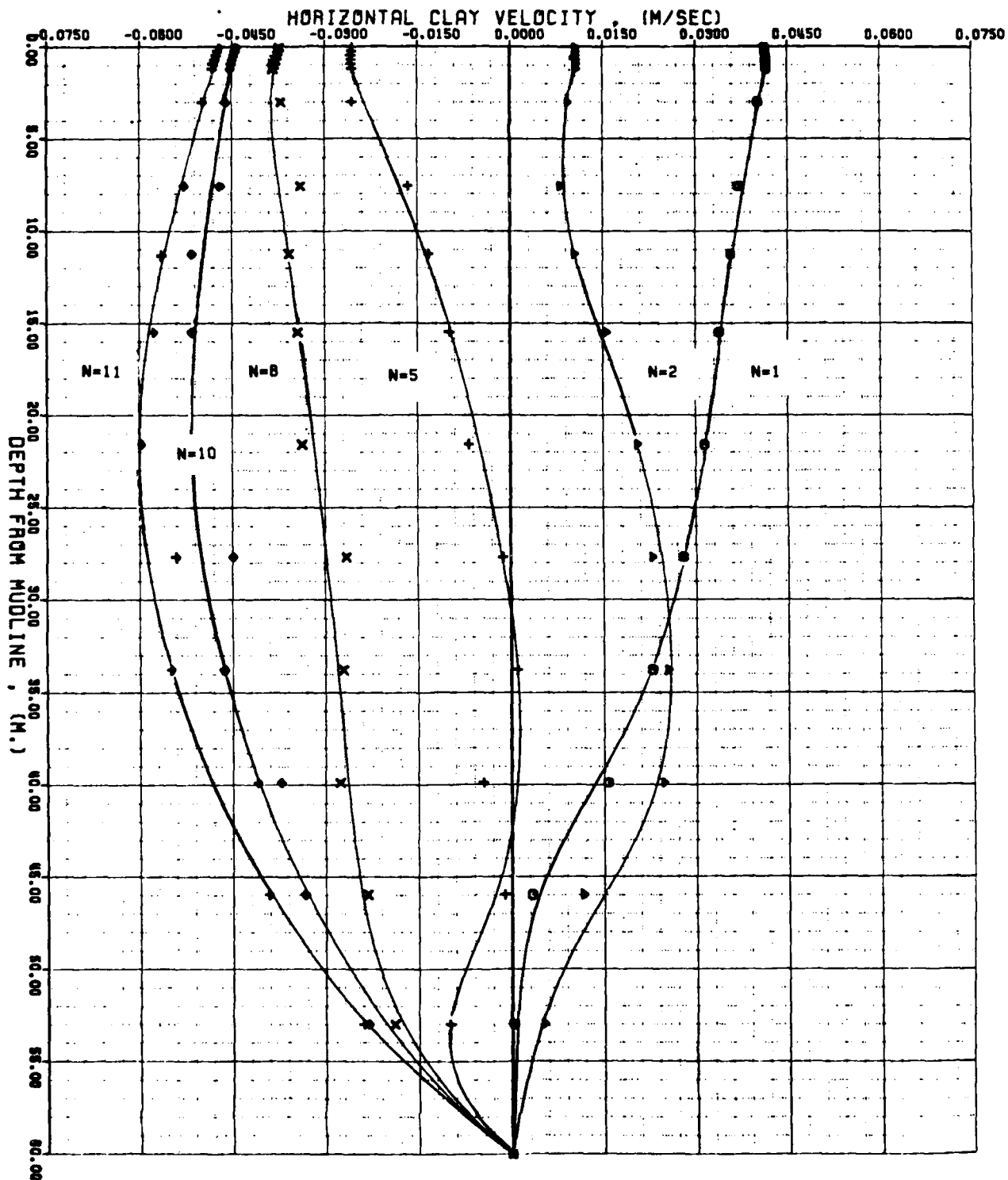
DEEP CORE SAMPLES OF GULF OF MEXICO



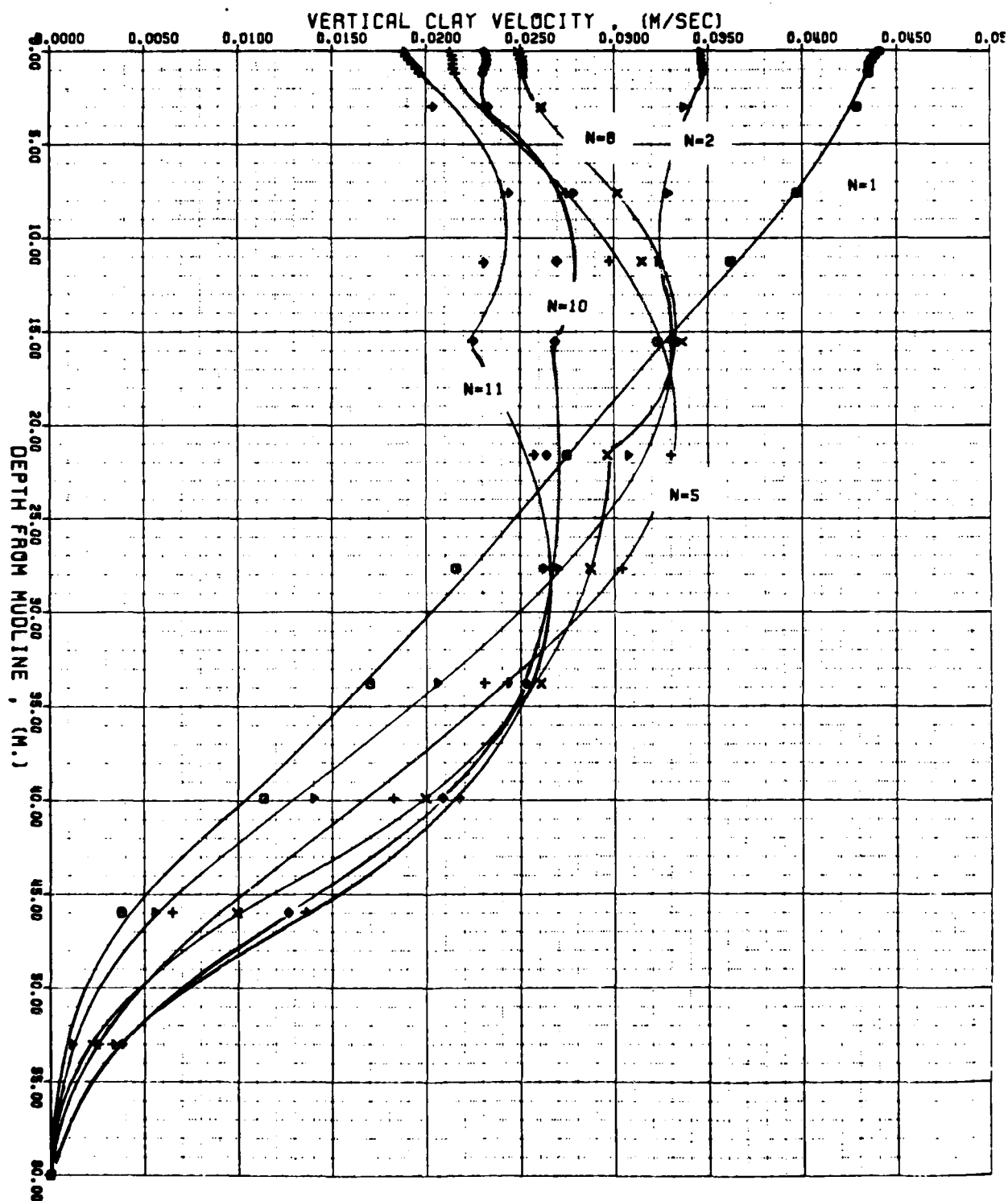
THE VARIATION OF CLAY DISPLACEMENT WITH DEPTH DEEP CORE SAMPLES OF GULF OF MEXICO



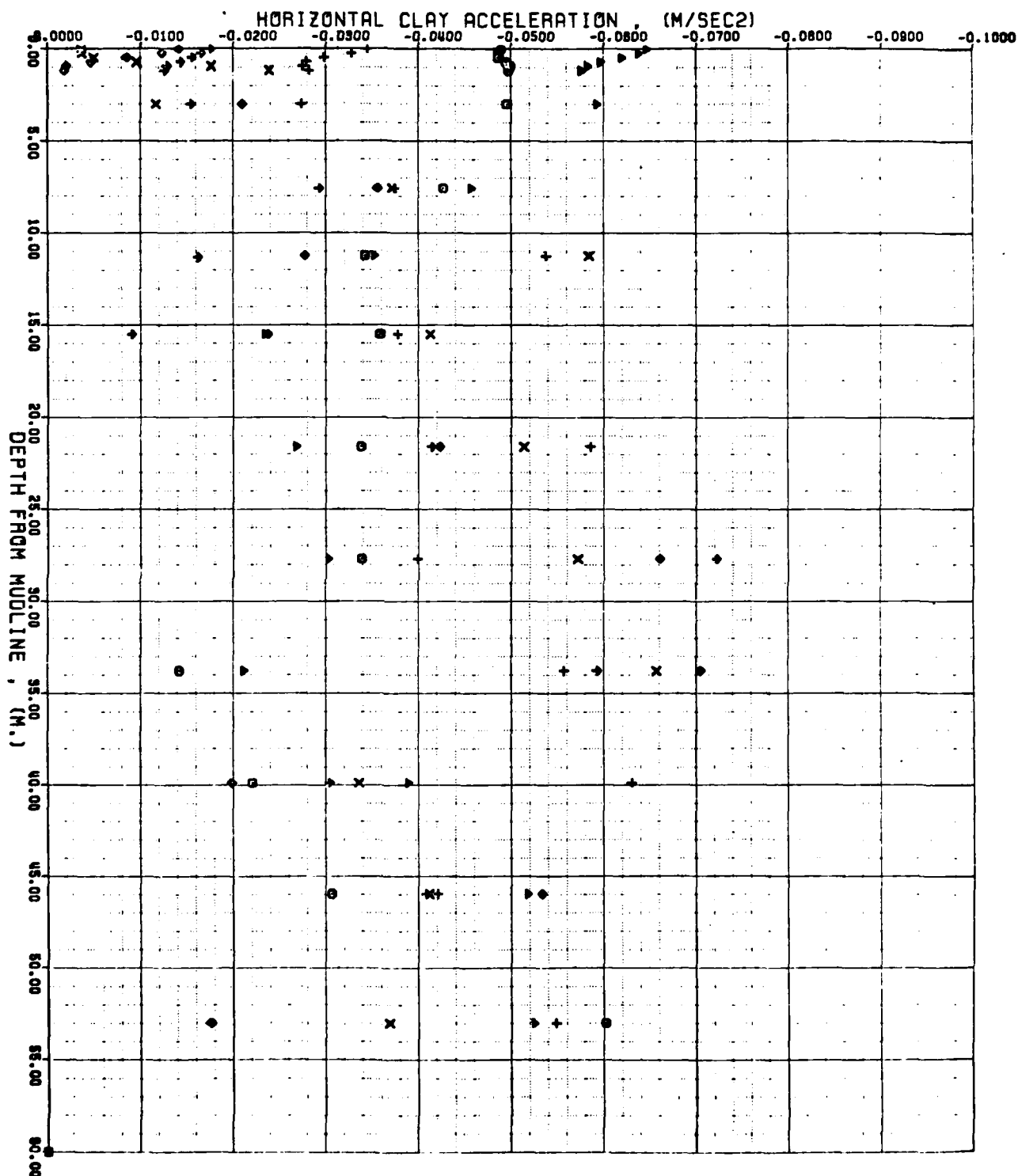
THE VARIATION OF CLAY VELOCITY WITH DEPTH DEEP CORE SAMPLES OF GULF OF MEXICO



THE VARIATION OF CLAY VELOCITY WITH DEPTH DEEP CORE SAMPLES OF GULF OF MEXICO

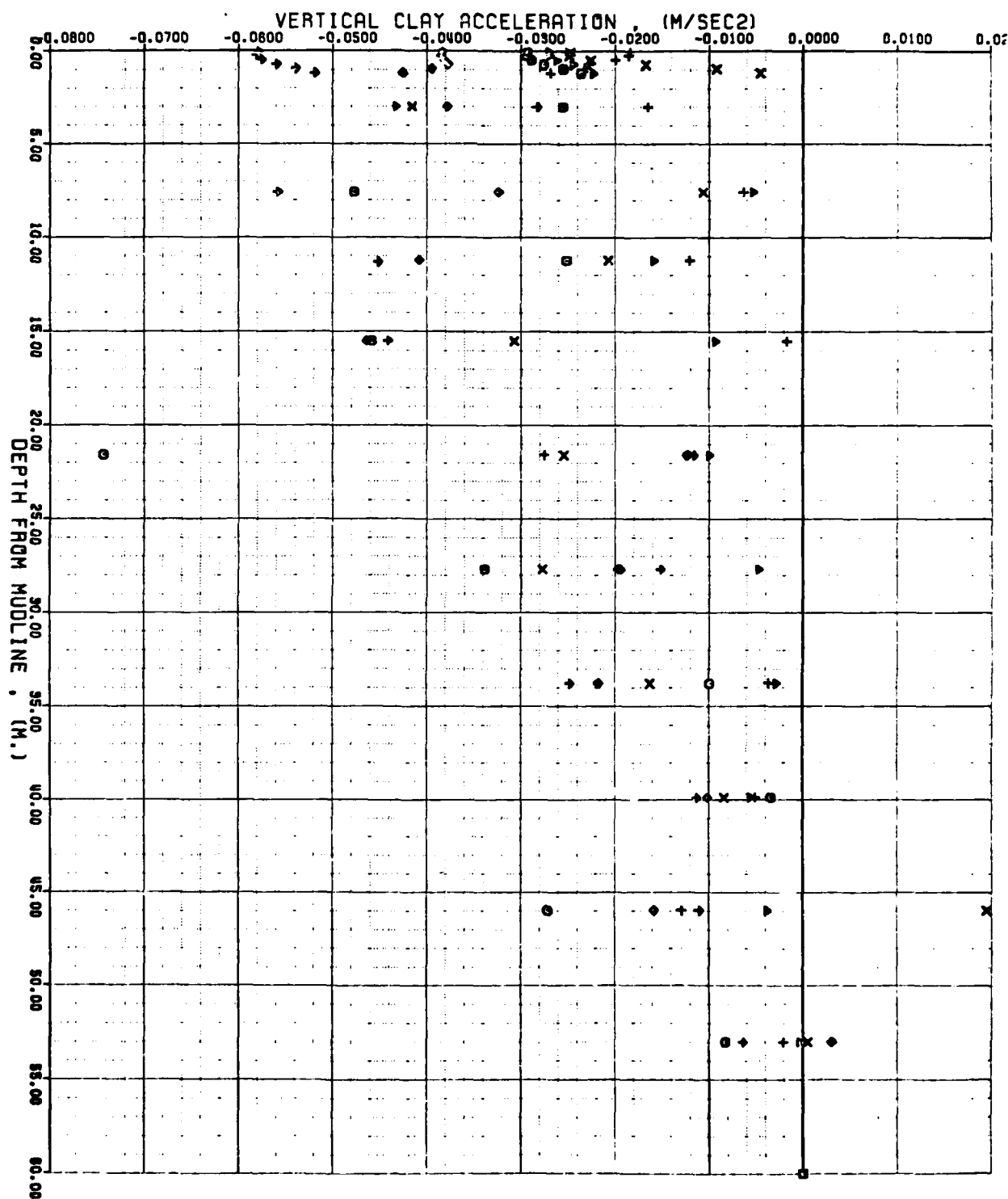


THE VARIATION OF CLAY ACCELERATION WITH DEPTH DEEP CORE SAMPLES OF GULF OF MEXICO



THE VARIATION OF CLAY ACCELERATION WITH DEPTH

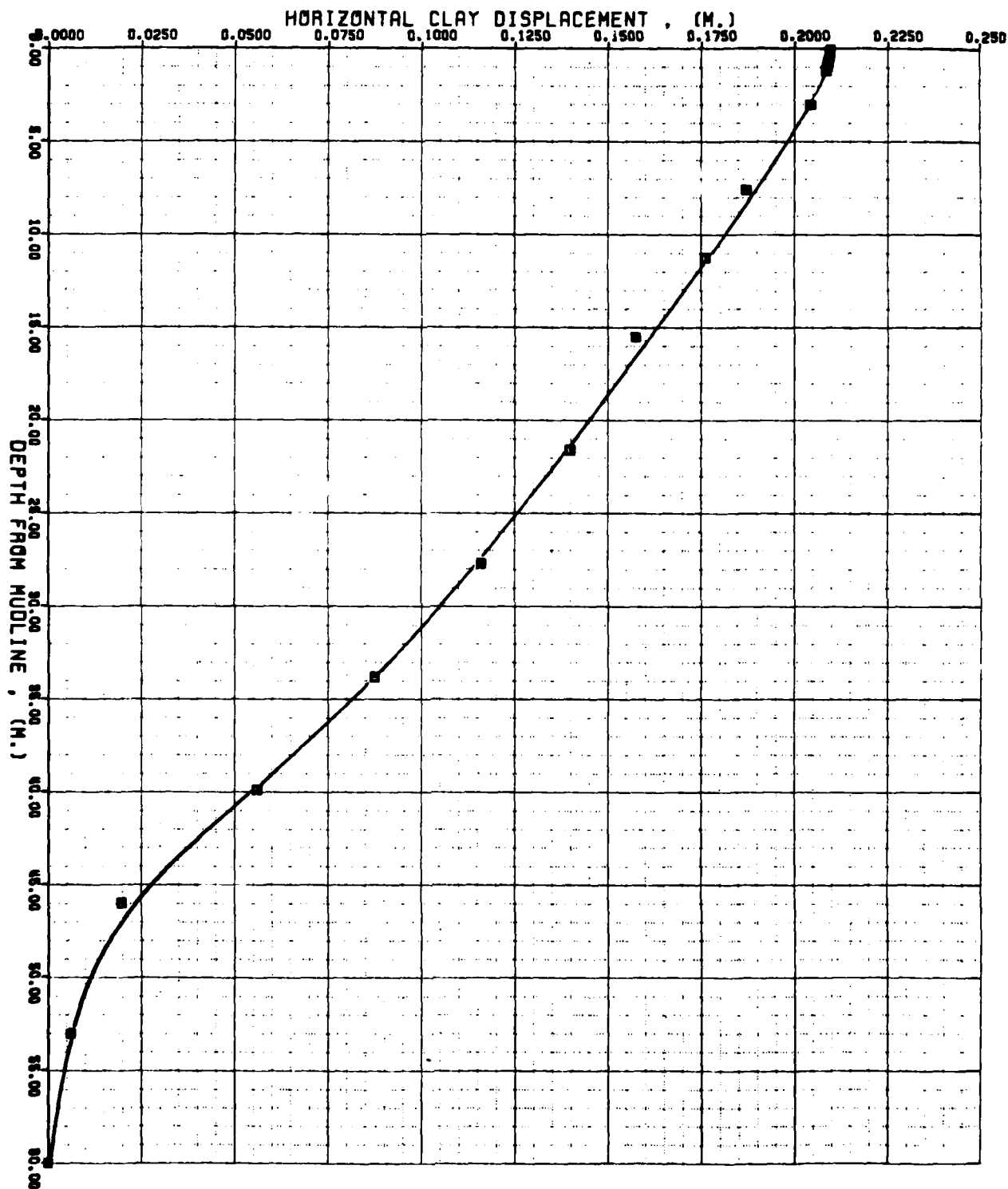
DEEP CORE SAMPLES OF GULF OF MEXICO



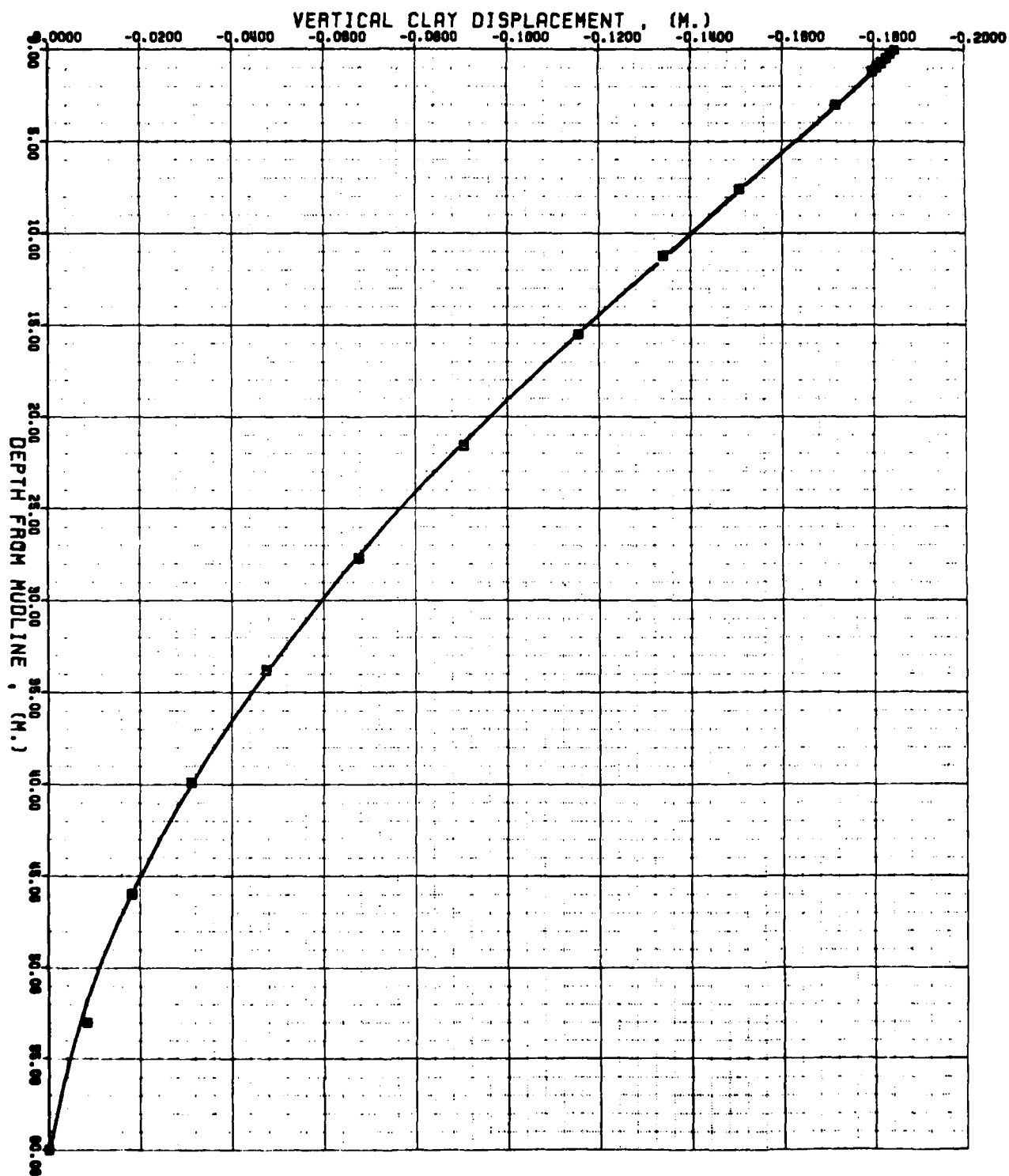
APPENDIX B-17/B-20

MAXIMUM STATIC AND KINEMATIC PROFILES OBTAINED FROM NONSAP
ANALYSIS FOR THE FIRST CYCLE OF WAVE LOADING

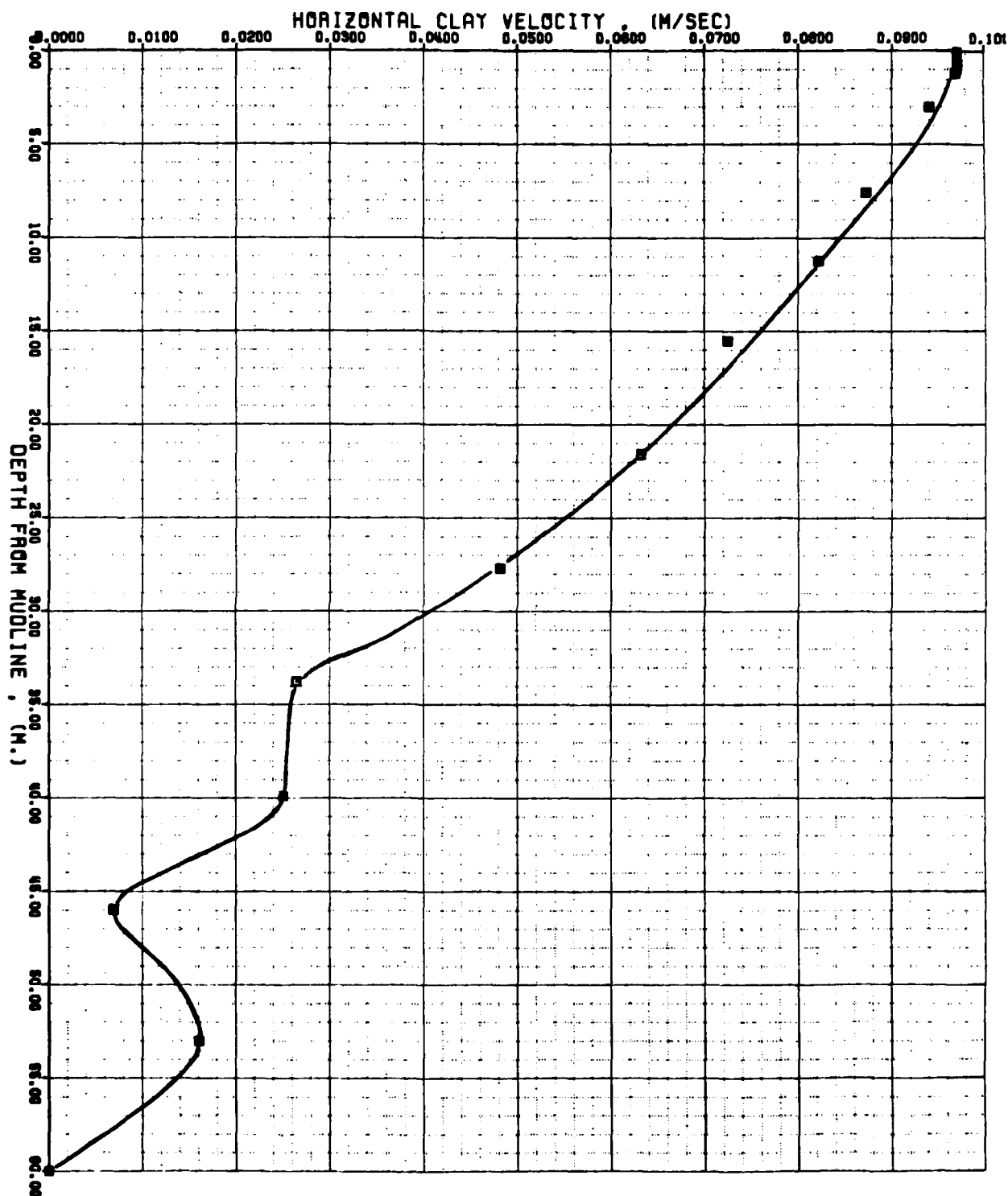
THE VARIATION OF CLAY DISPLACEMENT WITH DEPTH DEEP CORE SAMPLES OF GULF OF MEXICO



THE VARIATION OF CLAY DISPLACEMENT WITH DEPTH DEEP CORE SAMPLES OF GULF OF MEXICO

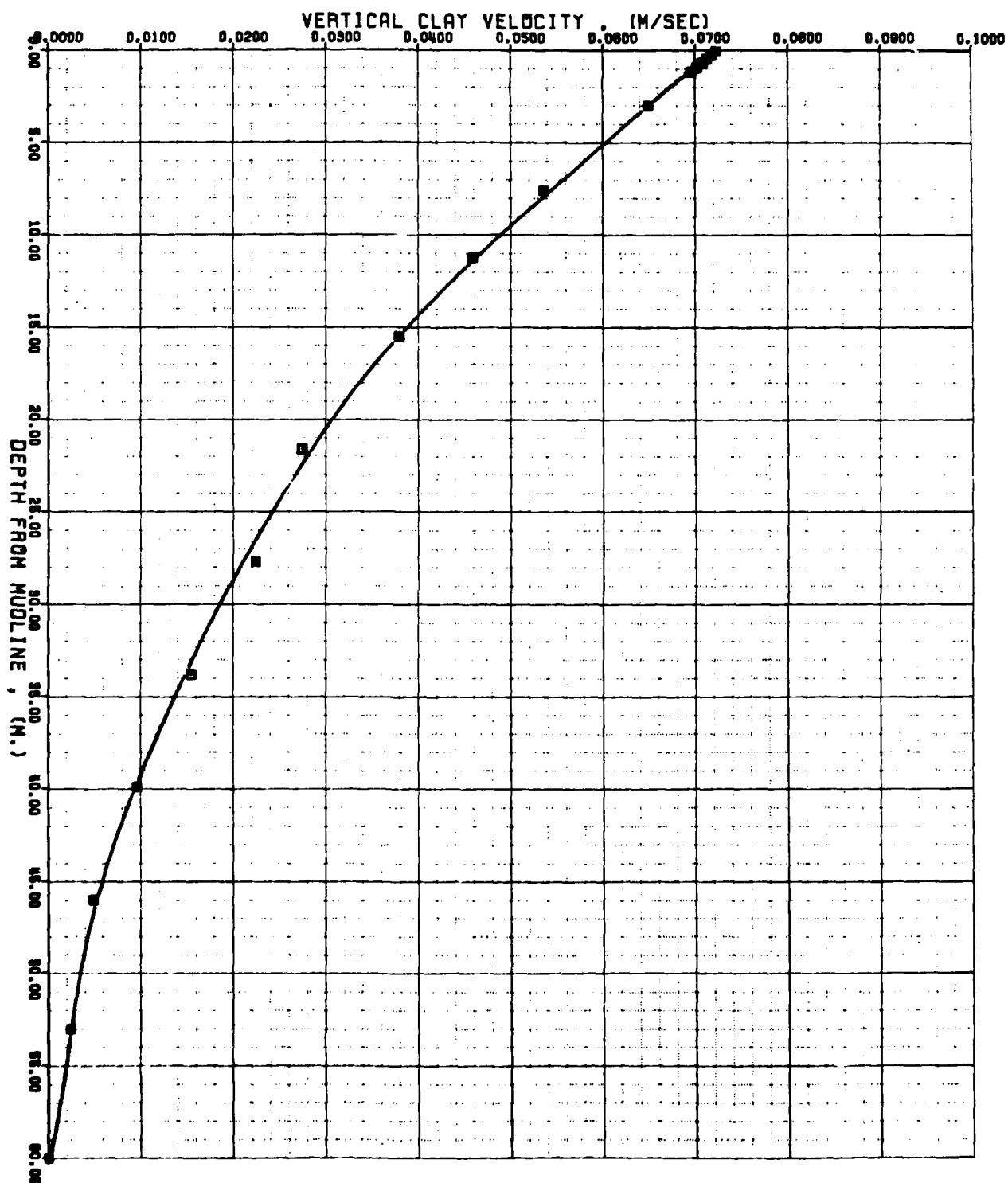


THE VARIATION OF CLAY VELOCITY WITH DEPTH DEEP CORE SAMPLES OF GULF OF MEXICO



THE VARIATION OF CLAY VELOCITY WITH DEPTH

DEEP CORE SAMPLES OF GULF OF MEXICO



APPENDIX C

COMPUTER PROGRAMS,
TYPICAL STRESS-STRAIN CURVES FROM
UNDRAINED TRIAXIAL TESTS

APPENDIX C-1

LISTING OF THE BASIC PROGRAM DEvised FOR RESONANT
COLUMN TEST DATA REDUCTION

```

1000 REM * THE NAME OF THIS PROGRAM IS 'PESONCOL'
1010 REM * WRITTEN BY J. K. POPLIN
1020 REM * LATEST REVISION - JUNE 5, 1980 - BY SIBEL PAMUKCU
1030 REM * THIS PROGRAM IS DESIGNED TO REDUCE DATA FROM
      RESONANT COLUMN TESTS
1040 DIM I$64, D1$64, D(10), L(5), D5(20), A(30)
1050 Y$="YES"
1060 G=980.66      REM ACC OF GRAVITY IN CM/SEC^2
1070 SELECT PRINT 005
1080 Z$="*"
1090 GOSUB 110
1100 GOTO 1140
1110 DEFN 110      REM * SUBROUTINE TO PRINT A LINE OF CHARACTERS
1120 FOR I=1 TO 64 PRINT Z$:NEXT I
1130 RETURN
1140 PRINT HEX(0A); "*****      DATA REDUCTION FOR RESONANT COLUM
N TESTS      *****"; HEX(0A)
1150 INPUT "IS 2.57-CM (1.4 IN.) DIAM SPECIMEN USED". P1$
1160 IF P1$<>Y$ THEN 1190
1170 J0=28.44      REM * J0 IN GM-CM-SEC^2
1180 GOTO 1230
1190 INPUT "IS 7.11-CM (2.8 IN.) DIAM SPECIMEN USED". P2$
1200 IF P2$<>Y$ THEN 2660
1210 J0=29.97      REM * J0 IN GM-CM-SEC^2
1220 GOTO 1230
1230 INPUT "DATE"          ".D$"
1240 INPUT "TEST NO"       ".T$"
1250 INPUT "IDENTIFICATION" ".I$"
1260 INPUT "DESCRIPTION OF SOIL" ".D1$"
1270 PRINT TAB(10); "*****      ENTER SOIL SPECIMEN DATA      *****
+"
1280 INPUT "WAS DIAMETER MEASURED OVER MEMBRANE ". P3$
1290 INPUT "HOW MANY DIAMETER MEASUREMENTS TO BE AVERAGED". N1
1300 D1=0
1310 PPINTUSING 1220
1320 %MEASUREMENT NO.      DIAM (CM)
      -----
1330 FOR I=1 TO N1
1340 PRINT "      ".I;"      " : INPUT D(I)
1350 D1=D1+D(I)
1360 NEXT I
1370 D=D1/N1
1380 IF P3$<>Y$ THEN 1410
1390 INPUT "DOUBLE THICKNESS OF MEMBRANE (CM) ". T1

```

```

1400 D=D-T1
1410 INPUT "HOW MANY LENGTH MEASUREMENTS TO BE AVERAGED", N2
1420 INPUT "WAS LENGTH MEASURED DIRECTLY", P4$
1430 IF P4$<>Y$ THEN 1450
1440 GOTO 1470
1450 INPUT "WAS LENGTH MEASURED BETWEEN TOP OF MOLD AND TOP OF U
PPER CAP", P5$
1460 IF P5$<>Y$ THEN 2660
1470 PRINT USING 1400
1480  XMEASUREMENT NO      LENGTH (CM)
-----
1490 L1=0
1500 FOR I= 1 TO N2
1510 PRINT "      "/I:"      " : INPUT L(I)
1520 L1=L1+L(I)
1530 NEXT I
1540 L=L1/N2
1550 IF P4$=Y$ THEN 1600
1560 IF P5$=Y$ THEN 1590
1570 L=L+10000
1580 GOTO 1600
1590 L=L+1.161
1600 INPUT "----- WET WEIGHT OF SPECIMEN (GM) - ", W1
1610 INPUT "IS DRY WEIGHT KNOWN ", R$
1620 IF R$<>Y$ THEN 1660
1630 INPUT "----- DRY WEIGHT OF SPECIMEN (GM) - ", W0
1640 W=(W1-W0)/W0
1650 GOTO 1710
1660 INPUT "IS WATER CONTENT KNOWN", R$
1670 IF R$<>Y$ THEN 2660
1680 INPUT "----- WATER CONTENT (%)      ", W
1690 W=W/100
1700 W0=W1/(1+W)
1710 V=#PI*D^2*L/4
1720 G1=W1/V: G0=W0/V
1730 J1=(W1*D^2)/(8*G)
1740 J=J1/J0
1750 B=SQR(J)
1760 FOR Y=1 TO 20
1770 A=J-B*TAN(B)
1780 IF ABS(A)<1E-06 THEN 1820
1790 B=B+A
1800 NEXT K
1810 GOTO 2660
1820 C2=(W1/V)*(2*#PI*L/B)^2

```



```

2540 PRINT USING 2550, F, T
2550 %RESONANT FREQ = ###.### HZ      RESONANT PERIOD = ###.### M
SEC
2560 PRINT USING 2570, G8, G8*20, B66, V9/100, V9/30, 48
2570 %SHEAR MODULUS = ###.###.### KN/SO M -- ###.###.### PSF
      S-WAVE VEL = ##.###.## M/SEC -- ###.###.### FT/SE
C
2580 PRINT USING 2590, S9, S9*100, D9*100
2590 %STRAIN AMP = #.##### RAD -- #.##### %
      DAMPING RATIO = ##.## %
2600 PRINT HEX(0A)
2610 SELECT PRINT 005
2620 NEXT Z
2630 SELECT PRINT 215
2640 PRINT HEX(0A); Z$="": GOSUB 10: PRINT HEX(0A)
2650 GOTO 2670
2660 PRINT "!!!!!!!!!!!!!!!!!!!! E*R*R*O*R !!!!!!!!!!!!!!"
      DOES NOT CONFORM TO PROGRAM FORMAT -----
": STOP
2670 INPUT "ARE AMPLITUDE DECAY (RUN DOWN) TEST DATA AVAILABLE";
R$
2680 SELECT PRINT 005
2690 IF R$ <> Y$ THEN 3090
2700 INPUT "SCOPE SCALE FOR COIL VOLTAGE (MV/DIV) "; S1
2710 INPUT "SCOPE SCALE FOR ACC VOLTAGE (MV/DIV) "; S2
2720 INPUT "----- FREQUENCY (HZ) ....."; F1
2730 INPUT "----- DRIVING COILS VOLTAGE (MV-RMS) ....."; C9
2740 INPUT "----- ACCEL OUTPUT VOLTAGE (MV-RMS) ....."; A9
2750 INPUT "AMPLITUDE OF ACCEL OUTPUT TRACE BEFORE POWER SHUT (D
IV) "; A(1)
2760 INPUT "NUMBER OF CONSECUTIVE AMPLITUDES READ AFTER POWER SH
UTOFF"; M
2770 PRINT "CYCLE      AMPLITUDE (DIV)
      -----"
2780 FOR K=1 TO M
2790 PRINT " "; K; "      ": INPUT A(K+1)
2800 NEXT K
2810 SELECT PRINT 215
2820 PRINT HEX(0A0A); TAB(20); "//////// DAMPING RATIO BY AMPLITU
DE DECAY METHOD //////////": PRINT HEX(0A)
2830 PRINT USING 2840, F1, C9, A9
2840 %FREQUENCY = ###.## HZ      COIL VOLTAGE = ##.###.## MV (RMS)
      ACC VOLTAGE = ##.###.## MV (RMS)
2850 PRINT USING 2860, S1, S2

```

```

2860 %SCOPE SCALES----- COILS    ###.### ## MV/DIV
                        ACCEL    ###.### ## MV/DIV
2870 PRINTUSING 2880
2880 %CYCLE      AMPLITUDE RATIO (%)
      0       10      20      30      40      50      60      70      80      90     100
      --      +-----+-----+-----+-----+-----+-----+-----+-----+-----+
2890 PRINT "0"; TAB(5); "+"; TAB(55); "*"
2900 FOR K=1 TO M
2910 V=INT(50*(A(K+1)/A(1))+5)
2920 PRINT K; TAB(5); "+"; TAB(V); "*"
2930 NEXT K
2940 PRINT HEX(0A)
2950 PRINTUSING 2960
2960 %CYCLE      DAMPING RATIO (%)
      -----
2970 D5=0
2980 FOR K=1 TO M
2990 D5(K)=(LOG(A(K)/A(K+1)))/(2*PI)
3000 PRINTUSING 3010, K, D5(K)*100
3010 ##          ###.##
3020 D5=D5+D5(K)
3030 NEXT K
3040 D6=(D5/M)
3050 N=INT(M/2)
3060 D7=(LOG(A(1)/A(N)))/(2*PI*N)
3070 PRINTUSING 3080, D6*100, D7*100
3080 %=====
      AVERAGE = ###.## %      PER MID POINT = ###.## %
3090 STOP

```

APPENDIX C-2

PART OF AN EXAMPLE REDUCED RESONANT COLUMN TEST DATA

APPENDIX C-3

LISTING OF THE BASIC PROGRAM DEVISED FOR UNDRAINED
TRIAxIAL TEST DATA REDUCTION

```

00 REM THE NAME OF THIS PROGRAM IS "NUCTSI"
110 REM THIS NEW UCTSI CAN BE USED TO REDUCE UNDRAINED TRIAXIAL
TEST DATA
120 REM WRITTEN BY J. K. POPLIN
130 REM LATEST REVISION -- MARCH 23, 1981 -- BY SIBEL PAMUKCU
140 DIM D(150), L(150), S1(150), S2(150), I1#64, I2#64, I3#64, U#64
150 SELECT PRINT 005
160 US="#(<) UNCONFINED COMPRESSION TEST (<)"
170 PRINT US
180 PRINT HEX(0A)
190 INPUT "IDENTIFICATION", I1#
200 INPUT "LOCATION", I2#
210 INPUT "BORING NO.", I3#
220 INPUT "SAMPLE NO.", I4#
230 INPUT "DEPTH", I5#
240 INPUT "DESCRIPTION OF SOIL", I6#
250 INPUT "TESTED BY", I7#
260 INPUT "DATE", I8#
270 PRINT HEX(0A): " + + + + SAMPLE DATA + + + + "
280 INPUT "INIT DIAM (M)", D1
290 A0=#PI*D1^2/4
300 INPUT "INIT LENGTH (M)", L1
310 V0=A0*L1
320 INPUT "WET WT (KN)", W0
330 INPUT "INIT WATER CONTENT (%)", W
340 G0=W0/V0
350 G1=G0/(1+W/100)
360 INPUT "LOAD CELL NO.", I9#
370 INPUT "LOAD CELL CONSTANT (MV/LB)", C1
380 C2=0.0044484/C1
390 INPUT "LVDT NO.", A1#
400 INPUT "LVDT CONSTANT (VOLT/CM)", C3
410 C4=0.01/C3
420 PRINT "----- ENTER LVDT READINGS IN VOLTS -----"
      "----- LOAD CELL READINGS IN MVOLTS -----"
430 INPUT "INITIAL LVDT READING", D0
440 INPUT "INITIAL LOAD CELL READING", L0
450 SELECT PRINT 215
460 Z$="*"
470 GOSUB 1060
480 PRINT HEX(0E): US
490 GOSUB 1060
500 PRINT HEX(0A)
510 PRINT "PROJECT IDENTIFICATION: ", I1#
520 PRINT "LOCATION: ", I2#

```

```

530 PRINT "BORING NO: ";I3$;"      SAMPLE NO: ";I9$;"      DEPTH
: ";I4$
540 PRINT "DESCRIPTION OF SOIL: ";I5$
550 PRINT "TESTED BY: ";I6$;"      DATE: ";I7$
560 PRINT "LOAD CELL NO: ";I8$;"      LVDT NO: ";A1$
570 PRINT HEX(0A);" + + + + + SAMPLE DATA + + + + + "
580 PRINT HEX(0A)
590 PRINT "DIAM: ";D1;" M.      LENGTH: ";L1;" M. "
600 PRINT "WATER CONTENT: ";W;" %      DRY UNIT WT: ";G1;"KN/M3"
610 PRINT HEX(0A)
620 SELECT PRINT 005
630 PRINT HEX(0A)
640 INPUT "TOTAL NUMBER OF READING SETS",R9
650 FOR I=1 TO R9
660 PRINT I
670 INPUT "LVDT READING: ";D
680 INPUT "LOAD CELL READING: ";L
690 PRINT HEX(0A)
700 D(I)=D
710 L(I)=L
720 NEXT I
730 M=I
740 SELECT PRINT 215
750 Z$=""
760 GOSUB 1060
770 PRINT HEX(0A)
780 PRINTUSING 790
790 %LVDT  LOAD  SAMPLE  UNIT STRAIN  CORR  LOAD  STRESS
    READ  READ  DEFORM  AREA
800 PRINTUSING 810
810 %
---- VOLT  MVOLT  M.  DEC  PCT  M2  KN  KPA  T
SF
820 PRINTUSING 830
830 %-----
-----
840 PRINT HEX(0A)
841 J=0
842 Q=0
850 FOR I=1 TO M
860 D2=C4*(D0-D(I))
870 E=D2/L1
880 A=A0/(1-E)
890 P=C2*(L(I)-L0)
900 S1(I)=P/A

```

```

910 S2(I)=S1(I)*0.01044219
920 PRINTUSING 930,D(I),L(I),D2,E,E*100,A,P,S1(I),S2(I)
930 %0.### ##.## 0.#### 0.##### 0.## 0.##### 0.### ###.### *
    ###
940 IF I=1 THEN 990
950 IF S1(I)<=J THEN 990
960 IF S2(I)<=Q THEN 990
970 J=S1(I)
980 Q=S2(I)
990 NEXT I
1000 PRINT HEX(0A)
1010 PRINTUSING 1020,J,Q,J/2,Q/2
1020 %UNCONFINED COMPRESSIVE STRENGTH = ###.### KPA , 0.#### TSF
    UNIT COHESION = ###.### KPA , 0.#### TSF
1030 Z$="*"
1040 GOSUB 1060
1050 GOTO 1100
1060 FOR K=1 TO 64
1070 PRINT Z$;
1080 NEXT K
1090 RETURN
1100 STOP

```


APPENDIX C-4

AN EXAMPLE REDUCED UNDRAINED TRIAXIAL TEST DATA

 <> UNCONFINED COMPRESSION TEST <>

PROJECT IDENTIFICATION: MUD FLOW ANALYSIS

LOCATION: MAIN PASS

BORING NO: B-6 SAMPLE NO: DEPTH: 16.40 M

DESCRIPTION OF SOIL: SOFT DARK ORGANIC

TESTED BY: S. P. DATE: AUGUST/1981

LOAD CELL NO: 1 LVDT NO: 1

+ + + + + SAMPLE DATA + + + + +

DIAM: 3.66670000E-02 M

LENGTH: 6.40500000E-02

M

WATER CONTENT: 63.0923 % DRY UNIT WT: 9.860885104747 KN/M³

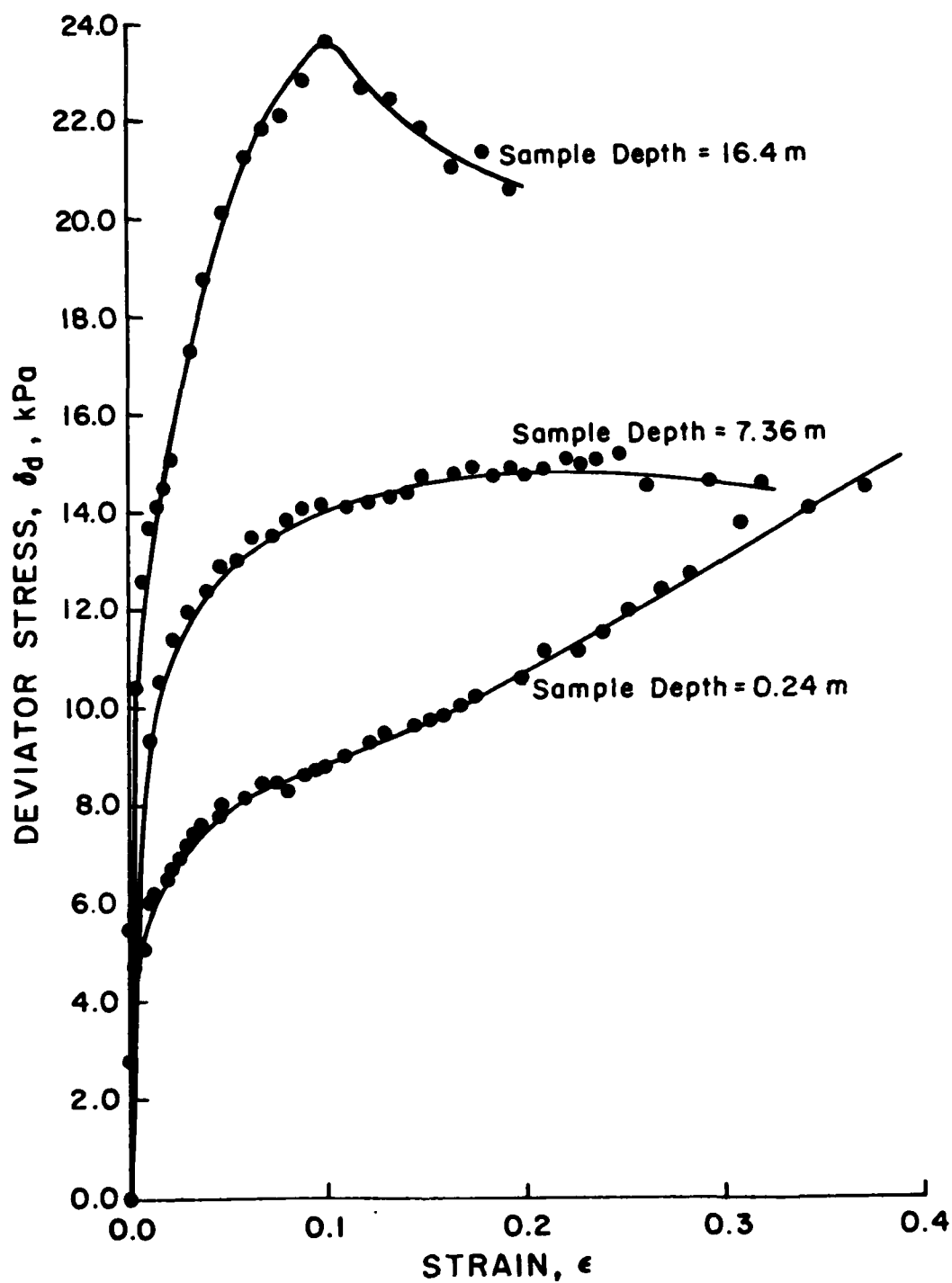
LVDT READ	LOAD READ	SAMPLE DEFORM	UNIT STRAIN		COPP AREA	LOAD	STRESS	
VOLT	MVOLT	M	DEC	PCT	M2	KN	KPA	TSF
1.648	4.11	0.0000	0.00031	0.03	0.00105	0.005	5.452	0.056
1.628	5.29	0.0002	0.00343	0.34	0.00105	0.011	10.290	0.109
1.604	5.82	0.0004	0.00718	0.71	0.00106	0.013	12.568	0.131
1.578	6.08	0.0007	0.01124	1.12	0.00106	0.014	12.599	0.142
1.552	6.21	0.0009	0.01514	1.51	0.00107	0.015	14.085	0.147
1.526	6.31	0.0012	0.01925	1.92	0.00107	0.015	14.438	0.150
1.500	6.48	0.0015	0.02341	2.34	0.00108	0.016	15.078	0.157
1.453	7.04	0.0019	0.03075	3.07	0.00108	0.018	17.251	0.180
1.395	7.46	0.0025	0.03981	3.98	0.00109	0.020	18.789	0.196
1.335	7.85	0.0031	0.04918	4.91	0.00111	0.022	20.167	0.210
1.276	8.16	0.0037	0.05829	5.83	0.00112	0.023	21.202	0.221
1.215	8.37	0.0043	0.06791	6.79	0.00113	0.024	21.812	0.227
1.155	8.51	0.0049	0.07728	7.72	0.00114	0.025	22.137	0.231
1.074	8.77	0.0057	0.08992	8.99	0.00116	0.026	22.830	0.239
0.981	9.07	0.0066	0.10444	10.44	0.00117	0.027	23.598	0.246
0.887	8.91	0.0076	0.11912	11.91	0.00119	0.027	22.617	0.236
0.791	8.96	0.0085	0.13411	13.41	0.00121	0.027	22.415	0.234
0.696	8.90	0.0095	0.14894	14.89	0.00124	0.027	21.816	0.227
0.599	8.78	0.0105	0.16409	16.40	0.00126	0.026	21.005	0.219
0.502	9.00	0.0114	0.17923	17.92	0.00128	0.027	21.385	0.223
0.405	8.87	0.0124	0.19437	19.43	0.00131	0.026	20.549	0.214

UNCONFINED COMPRESSIVE STRENGTH = 23.598 KPA : 0.2464 TSF

UNIT COHESION = 11.799 KPA : 0.1232 TSF

APPENDIX C-5

TYPICAL STRESS-STRAIN CURVES OBTAINED
FROM UNDRAINED TRIAXIAL TESTS



C_5

APPENDIX C-6

PARTS OF AN OUTPUT OF VISCOELASTIC SEA-BOTTOM WAVE
PROPAGATION INTERACTION FORTRAN COMPUTER PROGRAM

THIS CASE IS A NONLINEAR SOLUTION WITH COMPLEX
 WAVE LENGTH AND SLOPE = 1.000PERCENT
 INITIAL GUESS FOR TCU = 0.400

SWAMP FLOW INCLUDES WAVE ACTION & DOWNSLOPE EFFECTS

INPUT OPTIONS

NO OF RAJIP LAYERS=	10	
NO OF STR LAYERS=	2	
NO OF LAYERS DIVISIONS=	10	
WAVE LENGTH OPTION=	1	(0=REAL, 1=COMPLEX)
STARCH OPTION=	1	(0=LINEAR, 1=NON-LINEAR)
SMITH OPTION=	2	(1=OLD, 2=MODIFIED)
STABILITY INDEX OPTION=	1	(0= EXP READ, 1=LIQ IND READ)
NO OF SLOPES=	1	
NO OF PILES=	0	
SWAMP RAMP=	2.00	
ERROR TOLERANCE ON		
NON LINEAR SEARCH	0.010	

LAYER	THICKNESS	STRENGTH	LI	NO	STR PAC (SF)	G10	SP.WT
1	7.0000	161.1600	1.9990	0.2059	128.0600	20638.1496	96.7060
2	6.0000	151.5300	1.2430	0.1174	189.3300	28689.1749	96.7060
3	15.0000	179.1000	1.8310	0.1394	220.6200	39513.0420	96.7060
4	12.0000	200.3500	1.5690	0.1556	315.1200	63134.2920	96.7060
5	14.0000	240.0200	1.1780	0.1098	240.7800	57792.0156	96.7060
6	20.0000	275.6800	1.4550	0.1422	294.0900	81074.7312	96.7060
7	40.0000	175.9400	1.3600	0.1311	234.8500	41319.5090	96.7060
8	20.0000	186.1100	1.1160	0.1026	269.9500	58221.7835	96.7060
9	20.0000	302.6800	1.2780	0.1215	205.4700	62191.6596	96.7060
10	46.0000	359.6400	1.2230	0.1151	254.8900	91673.7374	96.7060
11	0.0	563.5700	0.3525	0.0132	362.6700	204389.9319	96.7060

• • RESULTS OF NONLINEAR SEARCH • •

G1= 17525.0531
 G10= 20638.1496
 TADRAL/STRENGTH= 0.1703
 TCU= 0.1702
 NO= 0.2059
 PERCENT ERROR= 0.0794
 ITERATION NUMBER = 4

• • RESULTS OF NONLINEAR SEARCH • •

G1= 20085.1295
 G10= 28689.1749
 TADRAL/STRENGTH= 0.3184
 TCU= 0.3182
 NO= 0.1020
 PERCENT ERROR= 0.0650

TAUHAI/STRENGTH= 0.1687
 TCU= 0.1685
 N= 0.2118
 PERCENT ERROR= 0.0364
 ITERATION NUMBER = 4

** RESULTS OF NONLINEAR SEARCH **
 G1= 89176.3822
 G10= 62191.6596
 TAUHAI/STRENGTH= 0.2328
 TCU= 0.2328
 N= 0.1323
 PERCENT ERROR= 0.0368
 ITERATION NUMBER = 4

** RESULTS OF NONLINEAR SEARCH **
 G1= 75152.1116
 G10= 91673.7378
 TAUHAI/STRENGTH= 0.2033
 TCU= 0.2033
 N= 0.1153
 PERCENT ERROR= 0.0186
 ITERATION NUMBER = 4

** RESULTS OF NONLINEAR SEARCH **
 G1= 33066.7999
 G10= 63178.2920
 TAUHAI/STRENGTH= 0.8269
 TCU= 0.8269
 N= 0.2876
 PERCENT ERROR= 0.8552
 ITERATION NUMBER = 4

** RESULTS OF NONLINEAR SEARCH **
 G1= 33150.5428
 G10= 57797.0156
 TAUHAI/STRENGTH= 0.8377
 TCU= 0.8368
 N= 0.2531
 PERCENT ERROR= 0.1957
 ITERATION NUMBER = 4

** RESULTS OF NONLINEAR SEARCH **
 G1= 50668.6190
 G10= 81074.7312
 TAUHAI/STRENGTH= 0.3949
 TCU= 0.3946
 N= 0.2274
 PERCENT ERROR= 0.0839
 ITERATION NUMBER = 4

** RESULTS OF NONLINEAR SEARCH **
 G1= 26057.7986
 G10= 41319.5988
 TAUHAI/STRENGTH= 0.3079
 TCU= 0.3068
 N= 0.2228
 PERCENT ERROR= 0.0571
 ITERATION NUMBER = 4

** RESULTS OF NONLINEAR SEARCH **
 G1= 32386.9022
 G10= 50721.7815

LAYER	DEPTH	P	G1	GP	GPP	ABS G ⁰
1	0.0	0.2059	17525.0531	17681.1849	5926.1558	18697.8851
2	7.0000	0.1820	20085.1295	20267.6586	5957.7275	21125.1628
3	13.0000	0.2849	23315.8685	23503.1913	9602.9017	25389.2836
4	28.0000	0.2876	33066.7999	33285.8387	16188.0550	36995.6769
5	40.0000	0.2531	33150.5428	33411.8002	14028.8010	36237.1287
6	54.0000	0.2274	50668.6100	51101.3619	19072.8925	54944.5612
7	74.0000	0.2228	26057.7986	26282.8364	9591.4821	27978.2502
8	114.0000	0.2118	32386.9022	32632.8168	11275.8255	34325.6262
9	134.0000	0.1323	89176.3822	89598.6462	10459.8805	50489.5116
10	154.0000	0.1153	75152.1116	75761.9618	13076.8078	77022.2666
11	200.0000	0.0132	204389.9319	204680.1036	8258.2283	208724.3938

VALUES OF CONSTANTS
 WATER DEPTH = 20.000
 TOTAL DEPTH = 220.000
 WATER SURFACE EIGHT = 48.000
 SLOPE (PERCENT) = 1.000
 WATER SURFACE EIGHT = 0.000

* * * RESPONSE VARIABLES FOR DEPTH OF 220.0 FT (DEPTH FROM HUD LINE -200.0)
 1113DA TAYLOR CYC SOIL DISPL CYC SOIL VELOCITY CYC SOIL ACCELERATION PRES DEC MAX STRAIN
 HORIZ VERT HORIZ VERT HORIZ VERT HORIZ VERT HORIZ VERT HORIZ VERT HORIZ VERT HORIZ VERT
 0.0 66.8827 -0.0001 -0.0012 0.0007 -0.0001 0.0001 0.0005 0.0005 0.0018 0.0068
 1.428 59.6314 0.0005 -0.0011 0.0006 0.0004 -0.0002 0.0004 0.0005 0.0233 0.0774
 1.757 54.5851 0.0010 -0.0005 0.0003 0.0007 -0.0004 0.0002 0.0004 0.0001 0.0709
 1.845 51.7796 0.0011 0.0003 -0.0001 0.0008 -0.0004 -0.0001 0.0004 -1.4053 0.0698
 2.513 57.5139 0.0008 0.0009 -0.0005 0.0005 -0.0003 -0.0004 0.0005 -6.3639 0.0747
 3.142 64.2467 0.0001 0.0012 -0.0007 0.0001 -0.0001 -0.0005 0.0005 -8.8918 0.0836
 3.770 71.3799 -0.0005 0.0011 -0.0006 -0.0004 0.0002 -0.0004 0.0005 -8.0233 0.0927
 4.398 76.2605 -0.0010 0.0005 -0.0003 -0.0007 0.0004 -0.0002 0.0004 -4.0001 0.0990
 5.127 77.9843 -0.0011 -0.0003 0.0001 -0.0008 0.0004 0.0001 0.0004 1.4053 0.1001
 5.455 71.5277 -0.0008 -0.0009 0.0005 -0.0005 0.0003 0.0004 0.0005 6.3639 0.0955
 6.293 66.8827 -0.0001 -0.0012 0.0007 -0.0001 0.0001 0.0005 0.0005 8.8918 0.0868

* * * RESPONSE VARIABLES FOR DEPTH OF 20.0 FT (DEPTH FROM HUD LINE - 0.0)
 LAMBDA D/SLOPE SOIL VELOCITY
 VEL HORIZ RES

0.0 -0.34286D-01-0.23112D-01 0.37952D-01
 0.62832D+00-0.34286D-01-0.22774D-01 0.29076D-01
 0.12566D+01-0.34286D-01-0.26833D-01 0.65136D-01
 0.18850D+01-0.34286D-01-0.33739D-01 0.84945D-01
 0.25133D+01-0.34286D-01-0.40854D-01 0.78290D-01
 0.31416D+01-0.34286D-01-0.45460D-01 0.54524D-01
 0.37699D+01-0.34286D-01-0.45798D-01 0.69236D-01
 0.43982D+01-0.34286D-01-0.41739D-01 0.72559D-01
 0.50285D+01-0.34286D-01-0.34833D-01 0.85385D-01
 0.56549D+01-0.34286D-01-0.27718D-01 0.72309D-01
 0.62812D+01-0.34286D-01-0.23112D-01 0.37952D-01

APPENDIX C-7

PARTS OF AN OUTPUT OF NONSAP FORTRAN COMPUTER PROGRAM

WIND FLOW ANALYSIS

CONTROL INFORMATION

```

NUMBER OF MODAL POINTS . . . . . (NUNMP) = 34
MASTER X-TRANSLATION CODE . . . . . (IDOF(1)) = 1
MASTER Y-TRANSLATION CODE . . . . . (IDOF(2)) = 0
MASTER Z-TRANSLATION CODE . . . . . (IDOF(3)) = 0
MASTER X-ROTATION CODE . . . . . (IDOF(4)) = 1
MASTER Y-ROTATION CODE . . . . . (IDOF(5)) = 1
MASTER Z-ROTATION CODE . . . . . (IDOF(6)) = 1
NUMBER OF LINEAR ELEMENT GROUPS . . . . . (NEGL) = 0
NUMBER OF NONLINEAR ELEMENT GROUPS . . . . . (NEGUL) = 1
SOLUTION MODE . . . . . (MODEX) = 2
    EQ.0, DATA CHECK
    EQ.1, EXECUTION
    EQ.2, RESTART

NUMBER OF TIME STEPS . . . . . (NSTE) = 250
TIME STEP INCREMENT . . . . . (DT) = 0.1000D-01
TIME AT SOLUTION START . . . . . (TSTART) = 0.5000D+01
PRINTING INTERVAL . . . . . (IPRI) = 50
MASS MATRIX CODE . . . . . (IMASS) = 1
    EQ.0, NO MASS EFFECTS
    EQ.1, LUMPED MASS
    EQ.2, CONSISTENT MASS
DAMPING MATRIX CODE . . . . . (IDAMP) = 1
    EQ.0, NO RAYLEIGH DAMPING
    EQ.1, RAYLEIGH DAMPING
NUMBER OF MODAL MASSES . . . . . (IMASSM) = 34
NUMBER OF MODAL DAMPERS . . . . . (IDAMPD) = 0
FREQUENCIES SOLUTION CODE . . . . . (IFREQ) = 0
    EQ.0, NO FREQUENCIES SOLUTION
    EQ.1, FREQUENCIES AND MODE SHAPES
        ARE DETERMINED
NUMBER OF TIME STEPS BETWEEN REFORMING
EFFECTIVE STIFFNESS MATRIX . . . . . (ISREF) = 50
NUMBER OF ALLOWABLE STIFFNESS REFORMATIONS
IN EACH TIME STEP . . . . . (NUNREF) = 0
NUMBER OF TIME STEPS BETWEEN

```

```

* MATERIAL CONSTANTS SET NUMBER ..... 1
DEN ..... ( DENSITY ) .. = 0.0
P ..... ( PROP(1) ) .. = 0.271372E+00
VNU ..... ( PROP(2) ) .. = 0.373023E+00
YIELD ..... ( PROP(3) ) .. = 0.208928E+01
P (HARDEN) ... ( PROP(4) ) .. = 0.605165E+02

* MATERIAL CONSTANTS SET NUMBER ..... 2
DEN ..... ( DENSITY ) .. = 0.0
P ..... ( PROP(1) ) .. = 0.376397E+00
VNU ..... ( PROP(2) ) .. = 0.362647E+00
YIELD ..... ( PROP(3) ) .. = 0.257640E+01
P (HARDEN) ... ( PROP(4) ) .. = 0.107702E+03

* MATERIAL CONSTANTS SET NUMBER ..... 3
DEN ..... ( DENSITY ) .. = 0.0
P ..... ( PROP(1) ) .. = 0.518991E+00
VNU ..... ( PROP(2) ) .. = 0.371528E+00
YIELD ..... ( PROP(3) ) .. = 0.303848E+01
P (HARDEN) ... ( PROP(4) ) .. = 0.873555E+02

* MATERIAL CONSTANTS SET NUMBER ..... 4
DEN ..... ( DENSITY ) .. = 0.0
P ..... ( PROP(1) ) .. = 0.932268E+00
VNU ..... ( PROP(2) ) .. = 0.378168E+00
YIELD ..... ( PROP(3) ) .. = 0.462258E+01
P (HARDEN) ... ( PROP(4) ) .. = 0.103676E+03

* MATERIAL CONSTANTS SET NUMBER ..... 5
DEN ..... ( DENSITY ) .. = 0.0
P ..... ( PROP(1) ) .. = 0.753907E+00
VNU ..... ( PROP(2) ) .. = 0.366325E+00
YIELD ..... ( PROP(3) ) .. = 0.333940E+01
P (HARDEN) ... ( PROP(4) ) .. = 0.618322E+02

* MATERIAL CONSTANTS SET NUMBER ..... 6
DEN ..... ( DENSITY ) .. = 0.0
P ..... ( PROP(1) ) .. = 0.956398E+00
VNU ..... ( PROP(2) ) .. = 0.363518E+00

```

* ELEMENT GROUP DATA
* ELEMENT GROUP 1 (NONLINEAR)
* ELEMENT DEFINITION
ELEMENT TYPE (SPAN(1)) .. = 2
EQ.1, TRUSS ELEMENTS
EQ.2, 2-DIM ELEMENTS
EQ.3, 3-DIM ELEMENTS
NUMBER OF ELEMENTS (SPAN(2)) .. = 16
TYPE OF NONLINEAR ANALYSIS (SPAN(3)) .. = 2
EQ.1, MATERIAL NONLINEARITY ONLY
EQ.2, TOTAL LAGRANGIAN FORMULATION
EQ.3, UPDATED LAGRANGIAN FORMULATION
* ELEMENT SUBTYPE (SPAN(5)) .. = 1
EQ.0, ALLESTHETIC ELEMENTS
EQ.1, PLANE STRAIN ELEMENTS
EQ.2, PLANE STRESS ELEMENTS
MAX NUMBER OF HOOPS DESCRIBING
ANY ONE ELEMENT (SPAN(7)) .. = 8
NUMBER OF INTEGRATION POINTS FOR
ELEMENT STIFFNESS GENERATION. (SPAN(10)) .. = 2
NUMBER OF STRESS OUTPUT TABLES (SPAN(13)) .. = 0
EQ.0, PRINT AT INTEGRATION POINTS
* MATERIAL DEFINITION
MATERIAL MODEL (SPAN(15)) .. = 6
EQ.1, ISOTROPIC
EQ.2, ORTHOTROPIC
EQ.3, VARIABLE YAMBERT MODEL
EQ.4, CURVE DESCRIPTION MODEL
EQ.5, CURVE DESCRIPTION MODEL
EQ.6, ELASTOPLASTIC (VON MISES)
EQ.7, ELASTOPLASTIC (DRUCKER-PRAGER)
EQ.8, INCOMPRESSIBLE ELASTIC (MOONEY-RIVLIN)
NUMBER OF DIFFERENT SETS OF MATERIAL
CONSTANTS (SPAN(16)) .. = 10
NUMBER OF MATERIAL CONSTANTS PER SET. .. (SPAN(17)) .. = 8
DIVISION OF STRESS ARRAY (NR)
PER INTEGRATION POINT (SPAN(18)) .. = 10

LOADS

NUMBER OF LOADS = 2
 NUMBER OF LOAD CURVES = 1
 MAX NUMBER OF POINTS IN LOAD CURVES = 251

LOAD FUNCTION NUMBER = 1
 NUMBER OF TIME POINTS = 251

TIME VALUE	FUNCTION
5.00000	0.0
5.01000	0.69969-02
5.02000	0.12300-01
5.03000	0.18669-01
5.04000	0.24949-01
5.05000	0.31220-01
5.06000	0.37500-01
5.07000	0.43780-01
5.08000	0.50059-01
5.09000	0.56330-01
5.10000	0.62600-01
5.11000	0.68870-01
5.12000	0.75140-01
5.13000	0.81400-01
5.14000	0.87660-01
5.15000	0.93910-01
5.16000	0.10020+00
5.17000	0.19640+00
5.18000	0.11270+00
5.19000	0.11890+00
5.20000	0.12510+00
5.21000	0.13130+00
5.22000	0.13750+00
5.23000	0.14370+00
5.24000	0.15000+00
5.25000	0.15620+00
5.26000	0.16240+00
5.27000	0.16860+00
5.28000	0.17480+00
5.29000	0.18100+00
5.30000	0.18720+00
5.31000	0.19340+00
5.32000	0.19960+00
5.33000	0.20580+00
5.34000	0.21200+00
5.35000	0.21790+00
5.36000	0.22380+00
5.37000	0.23020+00
5.38000	0.23630+00
5.39000	0.24240+00
5.40000	0.24850+00
5.41000	0.25460+00
5.42000	0.26070+00
5.43000	0.26670+00
5.44000	0.27280+00
5.45000	0.27880+00
5.46000	0.28480+00

MATERIAL CONSTANTS SET NUMBER 7

DEW(DENSITY).. = 0.0

Y(PROP(1)).. = 0.5529210+00

VW(PROP(2)).. = 0.373230+00

YIELD(PROP(3)).. = 0.373200+01

P (HARDEN)(PROP(4)).. = 0.1025520+03

MATERIAL CONSTANTS SET NUMBER 8

DEW(DENSITY).. = 0.0

Y(PROP(1)).. = 0.6750170+00

VW(PROP(2)).. = 0.4034200+00

YIELD(PROP(3)).. = 0.441000+01

P (HARDEN)(PROP(4)).. = 0.1277040+03

MATERIAL CONSTANTS SET NUMBER 9

DEW(DENSITY).. = 0.0

Y(PROP(1)).. = 0.8129100+00

VW(PROP(2)).. = 0.3984600+00

YIELD(PROP(3)).. = 0.4146100+01

P (HARDEN)(PROP(4)).. = 0.0475560+02

MATERIAL CONSTANTS SET NUMBER 10

DEW(DENSITY).. = 0.0

Y(PROP(1)).. = 0.1220130+05

VW(PROP(2)).. = 0.3504330+00

YIELD(PROP(3)).. = 0.6479000+01

P (HARDEN)(PROP(4)).. = 0.1300270+03

PRINT OUT FOR TIME STEP 50 (AT TIME 0.55000+01)
 1 EQUILIBRIUM ITERATIONS PERFORMED ON THIS TIME STEP TO REESTABLISH EQUILIBRIUM
 STIFFNESS REPORTED FOR THIS TIME STEP

D I S P L A C E M E N T S

NODE	X-DISPLACEMENT	Y-DISPLACEMENT	Z-DISPLACEMENT	X-ROTATION	Y-ROTATION	Z-ROTATION
1	0.0	0.2435720+00	0.0	0.0	0.0	0.0
2	0.0	0.0	0.0	0.0	0.0	0.0
3	0.0	0.2498768+00	-0.240859-01	0.0	0.0	0.0
4	0.0	-0.2709010-01	-0.2726548-01	0.0	0.0	0.0
5	0.0	0.2626380+00	-0.5325160-01	0.0	0.0	0.0
6	0.0	-0.5416800-01	-0.5723780-01	0.0	0.0	0.0
7	0.0	0.2754480+00	-0.8667530-01	0.0	0.0	0.0
8	0.0	-0.4965180-01	-0.8770500-01	0.0	0.0	0.0
9	0.0	0.2831180+00	-0.1080030+00	0.0	0.0	0.0
10	0.0	-0.5855390-01	-0.1190120+00	0.0	0.0	0.0
11	0.0	0.2648200+00	-0.1354780+00	0.0	0.0	0.0
12	0.0	-0.3543830-01	-0.1487380+00	0.0	0.0	0.0
13	0.0	0.2813030+00	-0.1595160+00	0.0	0.0	0.0
14	0.0	0.1006090-02	-0.1726690+00	0.0	0.0	0.0
15	0.0	0.2134000+00	-0.1759750+00	0.0	0.0	0.0
16	0.0	0.2687550-01	-0.1894870+00	0.0	0.0	0.0
17	0.0	0.1821870+00	-0.1981340+00	0.0	0.0	0.0
18	0.0	0.4846880-01	-0.1981500+00	0.0	0.0	0.0
19	0.0	0.1732320+00	-0.1899630+00	0.0	0.0	0.0
20	0.0	0.5685300-01	-0.2030200+00	0.0	0.0	0.0
21	0.0	0.1445170+00	-0.1939620+00	0.0	0.0	0.0
22	0.0	0.4311700-01	-0.2072620+00	0.0	0.0	0.0
23	0.0	0.1626080+00	-0.1987110+00	0.0	0.0	0.0
24	0.0	0.6417230-01	-0.2080300+00	0.0	0.0	0.0
25	0.0	0.1821600+00	-0.1948330+00	0.0	0.0	0.0
26	0.0	0.6434530-01	-0.2081890+00	0.0	0.0	0.0
27	0.0	0.1618120+00	-0.1949190+00	0.0	0.0	0.0
28	0.0	0.6448250-01	-0.2081790+00	0.0	0.0	0.0
29	0.0	0.1615550+00	-0.1949920+00	0.0	0.0	0.0
30	0.0	0.6453420-01	-0.2082430+00	0.0	0.0	0.0
31	0.0	0.1613910+00	-0.1950560+00	0.0	0.0	0.0
32	0.0	0.6454610-01	-0.2083030+00	0.0	0.0	0.0
33	0.0	0.1613190+00	-0.1951150+00	0.0	0.0	0.0
34	0.0	0.6456020-01	-0.2083620+00	0.0	0.0	0.0

V E L O C I T I E S

NODE	X-VELOCITY	Y-VELOCITY	Z-VELOCITY	X-ROTATION	Y-ROTATION	Z-ROTATION
1	0.0	0.4830640-01	0.0	0.0	0.0	0.0
2	0.0	0.0	0.0	0.0	0.0	0.0
3	0.0	0.4217650-01	-0.5164930-02	0.0	0.0	0.0
4	0.0	0.1082590-01	-0.8925870-02	0.0	0.0	0.0
5	0.0	0.4068720-01	-0.6080060-02	0.0	0.0	0.0

V E L O C I T I E S						
NODE	X-VELOCITY	Y-VELOCITY	Z-VELOCITY	X-ROTATION	Y-ROTATION	Z-ROTATION
6	0.0	0.21849D-01	-0.128975D-01	0.0	0.0	0.0
7	0.0	0.378310D-01	-0.183531D-02	0.0	0.0	0.0
8	0.0	0.267934D-01	-0.172385D-01	0.0	0.0	0.0
9	0.0	0.373650D-01	-0.165210D-02	0.0	0.0	0.0
10	0.0	0.258991D-01	-0.194087D-01	0.0	0.0	0.0
11	0.0	0.337704D-01	-0.432191D-02	0.0	0.0	0.0
12	0.0	0.281688D-01	-0.238189D-01	0.0	0.0	0.0
13	0.0	0.238708D-01	-0.528657D-02	0.0	0.0	0.0
14	0.0	0.258750D-01	-0.258653D-01	0.0	0.0	0.0
15	0.0	0.129870D-01	-0.608288D-02	0.0	0.0	0.0
16	0.0	0.248040D-01	-0.960051D-02	0.0	0.0	0.0
17	0.0	0.467534D-02	-0.271726D-01	0.0	0.0	0.0
18	0.0	0.247219D-01	-0.121962D-01	0.0	0.0	0.0
19	0.0	0.113095D-02	-0.278818D-01	0.0	0.0	0.0
20	0.0	0.233372D-01	-0.127179D-01	0.0	0.0	0.0
21	0.0	0.141270D-02	-0.270512D-01	0.0	0.0	0.0
22	0.0	0.175369D-01	-0.133888D-01	0.0	0.0	0.0
23	0.0	0.266924D-02	-0.267323D-01	0.0	0.0	0.0
24	0.0	0.182341D-01	-0.136179D-01	0.0	0.0	0.0
25	0.0	0.303589D-02	-0.267579D-01	0.0	0.0	0.0
26	0.0	0.136343D-01	-0.139603D-01	0.0	0.0	0.0
27	0.0	0.133321D-01	-0.267362D-01	0.0	0.0	0.0
28	0.0	0.352555D-02	-0.183087D-01	0.0	0.0	0.0
29	0.0	0.131133D-01	-0.265978D-01	0.0	0.0	0.0
30	0.0	0.363630D-02	-0.186819D-01	0.0	0.0	0.0
31	0.0	0.131018D-01	-0.263846D-01	0.0	0.0	0.0
32	0.0	0.361212D-02	-0.189618D-01	0.0	0.0	0.0
33	0.0	0.129237D-01	-0.260233D-01	0.0	0.0	0.0
34	0.0					

A C C E L E R A T I O N S						
NODE	X-ACCELERATION	Y-ACCELERATION	Z-ACCELERATION	X-ROTATION	Y-ROTATION	Z-ROTATION
1	0.0	-0.383528D-01	0.0	0.0	0.0	0.0
2	0.0	0.0	0.0	0.0	0.0	0.0
3	0.0	-0.108858D-01	-0.183558D-01	0.0	0.0	0.0
4	0.0	-0.228730D-01	-0.418558D-02	0.0	0.0	0.0
5	0.0	-0.619588D-01	-0.729301D-02	0.0	0.0	0.0
6	0.0	-0.238272D-02	-0.676848D-02	0.0	0.0	0.0
7	0.0	-0.340807D-01	-0.688732D-02	0.0	0.0	0.0
8	0.0	-0.183262D-01	-0.773769D-02	0.0	0.0	0.0
9	0.0	-0.505234D-01	-0.189823D-02	0.0	0.0	0.0
10	0.0	-0.599670D-01	-0.143748D-01	0.0	0.0	0.0
11	0.0	-0.377317D-01	-0.125925D-01	0.0	0.0	0.0
12	0.0	-0.320238D-01	-0.268172D-01	0.0	0.0	0.0
13	0.0	-0.563951D-01	-0.236613D-01	0.0	0.0	0.0
14	0.0	-0.586488D-01	-0.488738D-01	0.0	0.0	0.0
15	0.0	-0.453529D-01	-0.287158D-01	0.0	0.0	0.0
16	0.0	-0.482648D-01	-0.221827D-01	0.0	0.0	0.0

STRESS CALCULATIONS FOR ELEMENT GROUP 1 (2/3 CONTINUUM PLANE STRESS)

PLASTIC STRESS 90/100 STATE	STRESS-11	STRESS-22	STRESS-12	MAX STRESS	ANGLE	YIELD FUNCTION
1 PLASTIC	0.192882E+00	-0.108632E+02	0.790230E+00	0.236153E+00	3.16	0.0
2 PLASTIC	0.55318E+01	-0.87717E+01	0.104675E+01	0.560439E+01	0.16	0.355271E-10
3 PLASTIC	0.156027E+01	-0.039332E+01	-0.914580E+00	0.365155E+01	-5.20	0.0
4 PLASTIC	0.910883E+01	-0.118217E+01	-0.865930E+00	0.918167E+01	-0.81	-0.355271E-10
5 PLASTIC	-0.290427E+00	-0.127270E+02	-0.949262E+00	-0.218393E+00	-4.34	-0.355271E-10
6 PLASTIC	0.431805E+01	-0.645707E+01	-0.860225E+00	0.637571E+01	-3.04	0.0
7 PLASTIC	0.488136E+00	-0.104619E+02	0.217867E+00	0.488054E+00	1.18	0.0
8 PLASTIC	0.700932E+01	-0.409803E+01	0.264770E+00	0.701563E+01	1.36	0.0
9 PLASTIC	-0.236886E+01	-0.115583E+02	-0.158738E+01	-0.209911E+01	-9.59	0.0
10 PLASTIC	-0.126207E+01	-0.107310E+02	-0.143168E+01	-0.104852E+01	-0.52	0.355271E-10
11 PLASTIC	0.178190E+01	-0.614677E+01	-0.590323E+01	0.178190E+01	-0.43	-0.067862E-01
12 PLASTIC	0.276746E+01	-0.520707E+01	0.506006E-01	0.276889E+01	0.65	-0.238768E+00
13 PLASTIC	-0.776600E+00	-0.104420E+02	-0.125548E+01	-0.619304E+00	-7.18	0.0
14 PLASTIC	0.885273E+00	-0.922200E+01	-0.115001E+01	0.101478E+01	-6.84	0.0
15 PLASTIC	0.378705E+01	-0.581282E+01	-0.641099E+00	0.378858E+01	-3.02	-0.502852E+00
16 PLASTIC	0.536719E+01	-0.436811E+01	-0.496178E+00	0.539241E+01	-2.91	-0.351789E+00
17 PLASTIC	0.232227E+01	-0.627920E+01	-0.275473E+00	0.233108E+01	-1.03	0.0
18 PLASTIC	-0.654893E+00	-0.924495E+01	-0.205100E+01	-0.649481E+00	-1.37	0.0
19 PLASTIC	0.441138E+01	-0.381769E+01	-0.139423E+01	0.442128E+01	-9.26	0.0
20 PLASTIC	0.181700E+01	-0.680918E+01	-0.131626E+01	0.182288E+01	-0.07	0.0
21 PLASTIC	0.468868E+01	-0.381950E+01	0.517680E+00	0.472158E+01	3.64	0.0
22 PLASTIC	0.256064E+00	-0.770379E+01	0.546828E+00	0.331881E+00	3.82	0.355271E-10
23 PLASTIC	0.556288E+01	-0.246888E+01	-0.184923E+01	0.556823E+01	-12.36	0.0
24 PLASTIC	0.175687E+01	-0.677397E+01	-0.183530E+01	0.156099E+01	-12.42	0.0
25 PLASTIC	0.933195E+01	-0.572062E+00	0.947665E+00	0.943334E+01	6.11	-0.798374E+00
26 PLASTIC	0.337698E+01	-0.523187E+01	-0.576158E+00	0.340627E+01	6.39	-0.128383E+01
27 PLASTIC	0.857993E+01	-0.395919E+00	-0.226103E+01	0.916305E+01	-10.46	0.0
28 PLASTIC	0.246569E+01	-0.544787E+01	-0.229370E+01	0.328737E+01	-10.71	0.0
29 PLASTIC	0.733851E+01	-0.921652E+00	0.182388E+01	0.749399E+01	0.85	0.199800E-10
30 PLASTIC	0.382838E+01	-0.308238E+01	0.187822E+01	0.355808E+01	9.28	0.646138E-15
31 PLASTIC	0.598508E+01	-0.660888E+00	-0.236278E+01	0.688138E+01	-20.88	0.218858E-10
32 PLASTIC	0.159481E+01	-0.327670E+01	-0.239643E+01	0.252067E+01	-21.18	0.310862E-10
33 PLASTIC	0.100327E+02	-0.140848E+01	0.823459E+00	0.101209E+02	5.82	-0.301809E+01
34 PLASTIC	0.847249E+01	-0.178194E+00	0.840733E+00	0.849808E+01	5.54	-0.340201E+01
35 PLASTIC	0.908488E+01	-0.178888E+01	-0.179802E+01	0.102295E+02	-12.03	-0.325769E+01
36 PLASTIC	0.822592E+01	-0.204948E+00	-0.180151E+01	0.861197E+01	-12.09	-0.364034E+01

Commander
Naval Coastal Systems Center
ATTN: Library, Code 116.1
Panama City, Florida 32401

1 copy

Librarian
Naval Intelligence
Support Center
4301 Suitland Road
Washington, D.C. 20390

1 copy

Officer in Charge
Environmental Prediction
Research Facility
Naval Post Graduate School
Monterey, CA 93940

1 copy

Director
Amphibious Warfare Board
U.S. Atlantic Fleet
Naval Amphibious Base
Norfolk, Little Creek, VA 23520

1 copy

Commander
Amphibious Force
U.S. Pacific Fleet
Force Meteorologist
Comphibpac Code 255
San Diego, CA 92155

1 copy

Commanding General
Marine Corps Development and
Educational Command
Quantico, VA 22134

1 copy

Chief of Naval Operations
OP 987J
Department of the Navy
Washington, D.C. 20350

1 copy

Commandant
U.S. Coast Guard
ATTN: GECV/61
Washington, D.C. 20591

1 copy

National Oceanographic Data Center (D764)
Environmental Data Services
NOAA
Washington, D.C. 20235

1 copy

Defense Intelligence Agency
Central Reference Division
Code RDS-3
Washington, D.C. 20301

1 copy

DISTRIBUTION LIST

Office of Naval Research
Coastal Sciences Program
Code 422CS
Arlington, VA 22217
3 copies

Defense Documentation Center
Cameron Station
Alexandria, VA 22314
12 copies

Director
Naval Research Laboratory
ATTN: Technical Information Officer
Washington, D.C. 20375
3 copies

ONR Resident Representative
582 Federal Building
Austin, TX 78701
1 copy

Commanding Officer
Office of Naval Research Eastern/
Central Regional Office
Building 114, Section D
666 Summer Street
Boston, MA 02210
1 copy

Office of Naval Research
Code 422PO
National Space Technology
Laboratories
Bay St. Louis, MS 39529
1 copy

Office of Naval Research
Code 422PO
Washington, D.C. 22217
1 copy

Office of Naval Research
Code 100M
Washington, D.C. 22217
1 copy

Office of Naval Research
Operational Applications Division
Code 200
Arlington, VA 22217
1 copy

Commander
Naval Oceanographic Office
ATTN: Library, Code 1600
NSTL Station, MS 39529
1 copy

FILMED
9-8